

Advances in Multiphase Flow and Transport in the Subsurface Environment

Lead Guest Editor: Xiaoqing Shi

Guest Editors: Stefan Finsterle, Keni Zhang, and Dan Lu





Advances in Multiphase Flow and Transport in the Subsurface Environment

Geofluids

Advances in Multiphase Flow and Transport in the Subsurface Environment

Lead Guest Editor: Xiaoqing Shi

Guest Editors: Stefan Finsterle, Keni Zhang, and Dan Lu



Copyright © 2018 Hindawi. All rights reserved.

This is a special issue published in "Geofluids." All articles are open access articles distributed under the Creative Commons Attribution License, which permits unrestricted use, distribution, and reproduction in any medium, provided the original work is properly cited.

Editorial Board

Maurizio Barbieri, Italy
Mauro Cacace, Germany
Timothy S. Collett, USA
Cinzia Federico, Italy
Tobias P. Fischer, USA
Paolo Fulignati, Italy
Salvatore Inguaggiato, Italy

Francesco Italiano, Italy
Karsten Kroeger, New Zealand
Cornelius Langenbruch, USA
Stefano Lo Russo, Italy
John A. Mavrogenes, Australia
Ferenc Molnar, Finland
Julie K. Pearce, Australia

Daniele Pedretti, Finland
Marco Petitta, Italy
Christophe Renac, France
Andri Stefansson, Iceland
Richard E. Swarbrick, UK
Mark Tingay, Australia
Micol Todesco, Italy

Contents

Advances in Multiphase Flow and Transport in the Subsurface Environment

Xiaoqing Shi , Stefan Finsterle, Keni Zhang, and Dan Lu

Volume 2018, Article ID 2906326, 2 pages

Dynamic Behavior of CO₂ in a Wellbore and Storage Formation: Wellbore-Coupled and Salt-Precipitation Processes during Geologic CO₂ Sequestration

Jize Piao , Weon Shik Han , Sungwook Choung, and Kue-Young Kim 

Volume 2018, Article ID 1789278, 20 pages

The Form of Waiting Time Distributions of Continuous Time Random Walk in Dead-End Pores

Yusong Hou, Jianguo Jiang , and J. Wu

Volume 2018, Article ID 8329406, 6 pages

Analysis of the Influencing Factors on the Well Performance in Shale Gas Reservoir

Cheng Dai, Liang Xue, Weihong Wang, and Xiang Li

Volume 2017, Article ID 7818346, 12 pages

Study on the Oxidative Leaching of Uranium from the Lignite in the CO₃²⁻/HCO₃⁻ System

Y. Ning, Y. Li, Y. Zhang, and P. Tang

Volume 2017, Article ID 7130971, 8 pages

Simulation and Analysis of Long-Term CO₂ Trapping for the Shenhua CCS Demonstration Project in the Ordos Basin

Ying Yu, Yilian Li, Guodong Yang, Fengcheng Jiang, Sen Yang, and Yongsheng Wang

Volume 2017, Article ID 2595701, 18 pages

Numerical Modeling of CO₂ and Brine Leakage through Open Fracture in a Fault Zone: Open Channel Flow or Darcy Flow

Ning Liu, Lehua Pan, and Jianmei Cheng

Volume 2017, Article ID 9035032, 21 pages

Multiphase Flow Behavior of Layered Methane Hydrate Reservoir Induced by Gas Production

Yilong Yuan, Tianfu Xu, Xin Xin, and Yingli Xia

Volume 2017, Article ID 7851031, 15 pages

Computational Efficiency of Decoupling Approach in Solving Reactive Transport Model: A Case Study of Pyrite Oxidative Dissolution

Jixiang Huo, Fuheng Ma, and Hanzhou Song

Volume 2017, Article ID 4670103, 7 pages

Numerical Modeling of Soil Evaporation Process and Its Stages Dividing during a Drying Cycle

Jiangbo Han, Jin Lin, and Yunfeng Dai

Volume 2017, Article ID 5892867, 11 pages

Cl⁻ as a Chemical Fingerprint of Solute Transport in the Aquitard-Aquifer System of the North Jiangsu Coastal Plain, China

Qin Ge, Xing Liang, Menggui Jin, Jing Li, and Yan Liu

Volume 2017, Article ID 6131547, 16 pages

Modeling of Two-Phase Flow in Rough-Walled Fracture Using Level Set Method

Yunfeng Dai, Zhifang Zhou, Jin Lin, and Jiangbo Han

Volume 2017, Article ID 2429796, 11 pages

Numerical Investigation of the Influences of Wellbore Flow on Compressed Air Energy Storage in Aquifers

Yi Li, Keni Zhang, Litang Hu, and Jinsheng Wang

Volume 2017, Article ID 9316506, 14 pages

Quantitative Evaluation and Case Study of Risk Degree for Underground Goafs with Multiple Indexes considering Uncertain Factors in Mines

Longjun Dong, Weiwei Shu, Xibing Li, Zilong Zhou, Fengqiang Gong, and XiLing Liu

Volume 2017, Article ID 3271246, 15 pages

Editorial

Advances in Multiphase Flow and Transport in the Subsurface Environment

Xiaoqing Shi ,¹ Stefan Finsterle,² Keni Zhang,³ and Dan Lu⁴

¹School of Earth Sciences and Engineering, Nanjing University, Nanjing, China

²Finsterle GeoConsulting, Kensington, CA, USA

³Lawrence Berkeley National Laboratory, Berkeley, CA, USA

⁴Oak Ridge National Laboratory, Oak Ridge, TN, USA

Correspondence should be addressed to Xiaoqing Shi; shixq@nju.edu.cn

Received 4 February 2018; Accepted 5 February 2018; Published 4 March 2018

Copyright © 2018 Xiaoqing Shi et al. This is an open access article distributed under the Creative Commons Attribution License, which permits unrestricted use, distribution, and reproduction in any medium, provided the original work is properly cited.

Multiphase flow and transport processes in the subsurface environment are extremely important in a number of industrial and environmental applications at various spatial and temporal scales. Thus, it is necessary to identify, understand, and predict these processes to improve the production of conventional and unconventional oil and gas, to increase the safety of geological sequestration of carbon dioxide and nuclear waste disposal, and to make remediation of contaminated aquifers more effective.

The past decades have seen remarkable growth in research related to multiphase flow and transport in porous and fracture media [1–4]. Numerical models have been widely used to understand, predict, and optimize complex physical fluid flow processes combined with chemical, thermal, mechanical, and biological interactions occurring between fluids and the reservoir rocks [5–7]. Nevertheless, theoretical and practical challenges remain considerable. First, advanced mathematical models are needed to robustly and efficiently analyze the vast variety and complexity of multiphase processes. Second, application of these models to actual field site remains challenging, specifically in areas that involved strongly coupled processes, such as compressed gas energy storage, energy recovery from geothermal reservoirs as well as from coalbed methane, and gas hydrate deposits.

This special issue discusses some of the latest research outcomes in two parts: (1) theoretical fundamentals of multiphase flow and transport related numerical methods and laboratory experiments and (2) field applications to complex subsurface environments. We received 24 submissions, 13 of

which passed the initial assessment and review process. A brief summary of this issue is given in the following.

For the theoretical fundamentals, we have the following:

- (1) The paper by Y. Hou et al. investigated the anomalous dispersion of nonreactive solute particles in immobile zones and estimated the waiting time distribution. The study demonstrates that the distribution of waiting time in different dead-end pores having the similar power-law decline at early time and transiting to an exponential decline in the end. The anomalous dispersion is highly dependent on the sizes of immobile zones.
- (2) The paper by Y. Ning et al. discussed the effects on the uranium leaching efficiency of the lignite from the solid/liquid ratio, $\text{CO}_3^{2-}/\text{HCO}_3^-$ ratio, the leaching reagent concentration, and oxidants. They found the optimal solid/liquid ratio and $\text{CO}_3^{2-}/\text{HCO}_3^-$ ratio that lead to the maximum uranium leaching rate.
- (3) The paper by N. Liu et al. presented numerical simulation by an integrated wellbore-reservoir simulator (T2Well) to investigate the leakage problem along open fractures. Darcy's law in open fractures is validated by comparing the momentum model and corresponding EPM model of various apertures.
- (4) The paper by J. Huo et al. presented a decoupling approach by linear algebraic manipulations of the stoichiometric coefficients of the chemical reactions

to reduce the number of equation variables and simplifying the reactive source in the reactive transport model of pyrite oxidative dissolution.

- (5) The paper by J. Han et al. conducted numerical simulations to reproduce the bare silt soil drying process to quantitatively understand the evolutions of variables involved in the evaporation process during different stages of evaporation.
- (6) The paper by Y. Dai et al. developed an incompressible two-phase (crude oil and water) flow model incorporating interfacial forces and nonzero contact angles to accurately describe the flow characteristic of fracture scale displacements of immiscible fluids.
- (7) The paper by Y. Li et al. investigated the influences of the well screen length on compressed air energy storage in aquifers (CAESA) system performance using an integrated wellbore-reservoir simulator T2WELL.
- (8) The paper by J. Piao et al. compared coupled wellbore-reservoir and conventional equivalent porous media models to investigate dynamic behavior of CO₂ in a wellbore and storage formation during geologic CO₂ sequestration. The study demonstrates the importance of accounting for the complex thermodynamic behavior of CO₂ as it travels along the injection well and interacts with the surrounding formation. Coupled wellbore-reservoir effects may strongly affect the conditions near the injection interval and thus the injectivity, salt-precipitation potential, and other factors determining the performance and sustainability of CO₂ injection.

For the field applications, we have the following:

- (9) The paper by Y. Yu et al. performed reactive transport simulations to analyze the geochemical interactions between CO₂, formation fluid, and host rock of the major formations in the Ordos Basin and assess the CO₂ trapping capabilities for the Shenhua CO₂ capture and sequestration (CCS) project in China.
- (10) The paper by C. Dai et al. performed numerical simulations of production from a shale gas reservoir in the Sichuan Basin in China to analyze the production characteristics. They quantified the relative contributions of free and adsorbed gas to the total production rate. Moreover, they discussed the roles that the matrix, natural fractures, and the stimulated reservoir volume play in the recovery of natural gas, which determines the accuracy with which each of these components needs to be characterized or controlled.
- (11) The paper by Y. Yuan et al. conducted multiphase fluid-flow model to investigate the gas production performance from the layered hydrate reservoirs by depressurization at the offshore production test site of the Eastern Nankai Trough. They found that the dissociation zone is strongly affected by the vertical reservoir's heterogeneous structure and shows

a unique dissociation front. The beneficial production interval scheme should consider the reservoir conditions with high permeability and high hydrate saturation.

- (12) The paper by Q. Ge et al. conducted numerical simulation Cl⁻ in pore waters through the aquitard-aquifer system to understand the transport mechanism of natural tracer migration in North Jiangsu coastal plain, China.
- (13) The paper by L. Dong et al. established an evaluation index system to quantitatively assess the risk degree for underground goafs considering uncertain factors in mines. This developed system is further applied in 37 underground goafs in Dabaoshan mine, which provides an efficient guidance to both reduce the accident risk and improve the mining environment.

Acknowledgments

We are glad to share these papers with relevant communities of interest. We sincerely hope that the information, the methods, and the achievements presented in the above papers will improve the understanding of the complex multiphase flow and transport processes and solve some practical engineering problems. With the growing demands on environmentally sustainable energy production, we believe it is essential to continue improving our fundamental understanding of multiphase flow and transport processes and to advance our predictive simulation capabilities for solving challenging real-world problems. We would like to express our sincere gratitude to colleagues who performed candid and valuable reviews of the original manuscripts.

Xiaoqing Shi
Stefan Finsterle
Keni Zhang
Dan Lu

References

- [1] J. C. Parker, "Multiphase flow and transport in porous media," *Reviews of Geophysics*, vol. 27, no. 3, pp. 311–328, 1989.
- [2] C. T. Miller, G. Christakos, P. T. Imhoff, J. F. McBride, J. A. Pedit, and J. A. Trangenstein, "Multiphase flow and transport modeling in heterogeneous porous media: Challenges and approaches," *Advances in Water Resources*, vol. 21, no. 2, pp. 77–120, 1998.
- [3] C. T. Crowe, *Multiphase Flow Handbook*, C. T. Crowe, Ed., vol. 59, CRC press, 2005.
- [4] Y. S. Wu, *Multiphase Fluid Flow in Porous and Fractured Reservoirs*, Gulf Professional Publishing, 2015.
- [5] R. Helmig, *Multiphase Flow and Transport Processes in the Subsurface: A Contribution to the Modeling of Hydrosystems*, Springer-Verlag, 1997.
- [6] Z. Chen, G. Huan, and Y. Ma, *Computational Methods for Multiphase Flows in Porous Media*, Society for Industrial and Applied Mathematics, 2006.
- [7] A. Prosperetti and G. Tryggvason, *Computational Methods for Multiphase Flow*, A. Prosperetti and G. Tryggvason, Eds., Cambridge University Press, 2009.

Research Article

Dynamic Behavior of CO₂ in a Wellbore and Storage Formation: Wellbore-Coupled and Salt-Precipitation Processes during Geologic CO₂ Sequestration

Jize Piao ¹, Weon Shik Han ¹, Sungwook Choung,² and Kue-Young Kim ³

¹Department of Earth System Sciences, Yonsei University, Seoul, Republic of Korea

²Division of Earth and Environmental Sciences, Korea Basic Science Institute (KBSI), Cheongju, Republic of Korea

³Korea Institute of Geoscience and Mineral Resources, Daejeon, Republic of Korea

Correspondence should be addressed to Weon Shik Han; hanw@yonsei.ac.kr

Received 29 July 2017; Revised 15 November 2017; Accepted 19 December 2017; Published 29 January 2018

Academic Editor: Stefan Finsterle

Copyright © 2018 Jize Piao et al. This is an open access article distributed under the Creative Commons Attribution License, which permits unrestricted use, distribution, and reproduction in any medium, provided the original work is properly cited.

For investigating the wellbore flow process in CO₂ injection scenarios, coupled wellbore-reservoir (WR) and conventional equivalent porous media (EPM) models were compared with each other. In WR model, during the injection, conditions for the wellbore including pressure and temperature were dynamically changed from the initial pressure (7.45–8.33 MPa) and temperature (52.0–55.9°C) of the storage formation. After 3.35 days, the wellbore flow reached the steady state with adiabatic condition; temperature linearly increased from the well-head (35°C) to the well-bottom (52°C). In contrast, the EPM model neglecting the wellbore process revealed that CO₂ temperature was consistently 35°C at the screen interval. Differences in temperature from WR and EPM models resulted in density contrast of CO₂ that entered the storage formation (~200 and ~600 kg/m³, resp.). Subsequently, the WR model causing greater density difference between CO₂ and brine revealed more vertical CO₂ migration and counterflow of brine and also developed the localized salt-precipitation. Finally, a series of sensitivity analyses for the WR model was conducted to assess how the injection conditions influenced interplay between flow system and the localized salt-precipitation in the storage formation.

1. Introduction

As an approach for decreasing CO₂ emissions into the atmosphere, geologic carbon storage (GCS) is one of considerable solutions for relieving global climate change [1]. While operating GCS projects, CO₂, directly captured during industrial processes at fossil-fuel power plants, was injected through the wellbore and stored within the specific geologic formation covered by low-permeability caprock [2–4]. Until now, numerous GCS projects have been or are being conducted at various scales around the world to validate the safety of GCS technology [5]. For example, several pilot-scale projects were successfully completed CO₂ injection at a rate of 10,000 metric tons per year; these projects included Frio, Texas [6], Nagaoka, Japan [7], Ketzin, and Germany [8] as well as Regional Carbon Sequestration Partnership's (RCSP) Phase II program implemented by the US Department of Energy [9, 10]. In addition to pilot-scale projects, commercial-scale

projects where CO₂ was injected at an approximate rate of 1 million metric tons per year were completed or also in operation: Sleipner project in North Sea [11], Weyburn CO₂-EOR Project in Canada [12], In Salah Project in Algeria [13], and Illinois Basin-Decatur Project which is one of the Phase III projects of US Department of Energy's RCSP [14].

During the demonstration of such pilot- or commercial-scale GCS projects, transported CO₂ from the sources (e.g., coal-based power plants) must be injected through the wellbore, which is the pathway connecting the ground surface to the targeted subsurface formation [15]. Here, the wellbore is the connected open pipe while the subsurface formation is regarded as porous media. Due to the difference in their inherent configurations, within the wellbore, the inertial force is much greater than the viscous force, implying that Reynold's number can be significantly large [16]. Solution approaches to solving CO₂ transport are also different in each other. Within the wellbore, CO₂ transport belongs to the pipe

flow, which requires a solution of the Navier-Stokes equation [17]. On the other hand, once CO₂ enters porous storage formations, CO₂ transport must be explained by Darcy's law [18]. Furthermore, CO₂ injection wells were typically drilled over 1 km while penetrating multiple geologic formations. Therefore, while CO₂ migrated through the wellbore, large variations in pressure and temperature could cause to change in CO₂ phase and its thermophysical properties [19, 20].

As described, due to complexities involved during the wellbore processes, a number of studies previously drew attention and suggested that, during the CO₂ injection activity, profiles of both pressure and temperature in the wellbore could change dynamically [21–27]. For example, Lu and Connell [21] suggested that the wellbore fluids could exhibit multiphase (supercritical, liquid, gaseous CO₂, and brine) concurrently experiencing their phase changes. Furthermore, both CO₂ and brine could experience thermal alteration caused by frictional loss, thermal conduction, convection, and Joule-Thomson heating/cooling [22, 27–29]. Due to such complex alteration processes, both bottom-hole pressure and temperature would be significantly different from ones at the well-head. Subsequently, altered pressure and temperature profiles would significantly affect thermophysical properties of CO₂ such as density, viscosity, enthalpy, internal energy, and solubility [19, 26, 30–32].

When thermophysically altered CO₂ entered the storage formation, the brine within porous media would be displaced. Subsequently, the dry-out zone would be developed in the vicinity of the injection well where residual brine evaporated to dry-CO₂ while precipitating the solid salt [33, 34]. Previously, numerous studies including both experimental [35–37] and numerical studies [34, 38–41] evaluated development of dry-out zone and associated salt-precipitation. Among them, Oh et al. [36] conducted core-flooding experiments and captured the salt-precipitation at the core-inlet by using SEM images. In addition, Kim et al. [39] and Guyant et al. [40] used numerical approach to elaborate the salt-precipitation processes according to conditions for both the injection well and storage formation. In particular, within low injection rate and high permeability of the storage formation, buoyancy effect on CO₂ became dominant, and consequently, the localized salt-precipitation was developed [41] concurrently elevating pressure around the injection well [42]. Most importantly, development of the localized salt was dependent on the degree of buoyancy force on CO₂ plume, which was governed by the injection rate and thermophysical properties of CO₂. Even though thermophysical CO₂ properties could be changed significantly after CO₂ experiencing the wellbore processes, only a few studies were considered the wellbore processes impacting on CO₂ behavior in the storage formation [22, 24, 43–45].

For example, a number of previous studies neglected the wellbore flow process or interpreted the wellbore flow by adopting Darcy's law after assigning adequate rock properties [46–48]. This approach is called equivalent porous media (EPM) model. The primary reason for such simplification arises from technical difficulties solving both the wellbore and porous media flow at the same time. Nevertheless, it

is recognized that fully coupled wellbore-reservoir models, capable of accounting for nonisothermal two-phase (CO₂ and brine or water) flow, are necessary to evaluate the influence of wellbore flow on injected CO₂ within the storage formation [44, 49]. Due to this reason, the purpose of this study was to advance current understanding related to the wellbore flow process by investigating the change of both pressure and temperature profiles within the wellbore, and subsequently, CO₂ migration, and resulting accumulation of solid salt in the storage formation.

2. Method

2.1. Conceptual Model. In order to evaluate differences between equivalent porous media (EPM) and coupled wellbore-reservoir (WR) models, two base-cases which were two-dimensional radially symmetric and nonisothermal models (Case 1 and Case 2) were employed (Figures 1(a) and 1(b)). Case 1 adopted the conventional EPM approach for simulating both an injection well and a storage formation while Case 2 utilized the WR model for simulating the injection well which coupled to the storage formation. In both cases, CO₂ was injected into the storage formation which was the 40 m thick high-permeability (k) formation ($k = 3 \times 10^{-13} \text{ m}^2$ and $\phi = 0.25$) overlaid by the 50 m thick low- k sealing caprock ($k = 1 \times 10^{-17} \text{ m}^2$ and $\phi = 0.2$). These formations were positioned at a depth of 690 m below the ground surface, and their radial extent was 10,000 m. The storage formation was divided vertically into 10 layers (each layer with 4 m thickness) while the overlying sealing formation was divided into 5 layers having individually 10 m thickness. Then, they were horizontally discretized to 200 columns with the logarithmic increment from the injection well; the specific number and size of grid-blocks to the radial direction are shown in Figure 1.

For the initial condition, the hydrostatic pressure was assigned with the gradient of 10.58 kPa/m (top: 7.45 MPa to bottom: 8.33 MPa), and the geothermal gradient of 0.046°C/m was assigned with assuming the surface temperature of 20°C (model top: 52.0°C to bottom: 55.9°C). In addition, the dissolved NaCl mass fraction in the ambient brine was uniformly 15% with zero CO₂ saturation. For the boundary conditions, both top and bottom boundaries were assigned to be no-flow condition without assigning the conductive heat flow at the bottom boundary; temperature field in the model was dominantly governed by the geothermal gradient assigned to lateral boundaries. The conductive heat flows were neglected because buoyant CO₂ plume holding different temperature typically governed the temperature field adjacent to CO₂ plume and the injection well. Furthermore, the right-most side of the targeted formation at 10,000 m was set to be the Dirichlet boundary. By assuming the Dirichlet boundary, it was expected that the pressure pulse after reaching this boundary would be affected.

The primary difference between Case 1 and Case 2 was the condition for the left boundary assigned to the storage formation where CO₂ was injected. In Case 1 (EPM model), without the wellbore, CO₂ was injected into 10

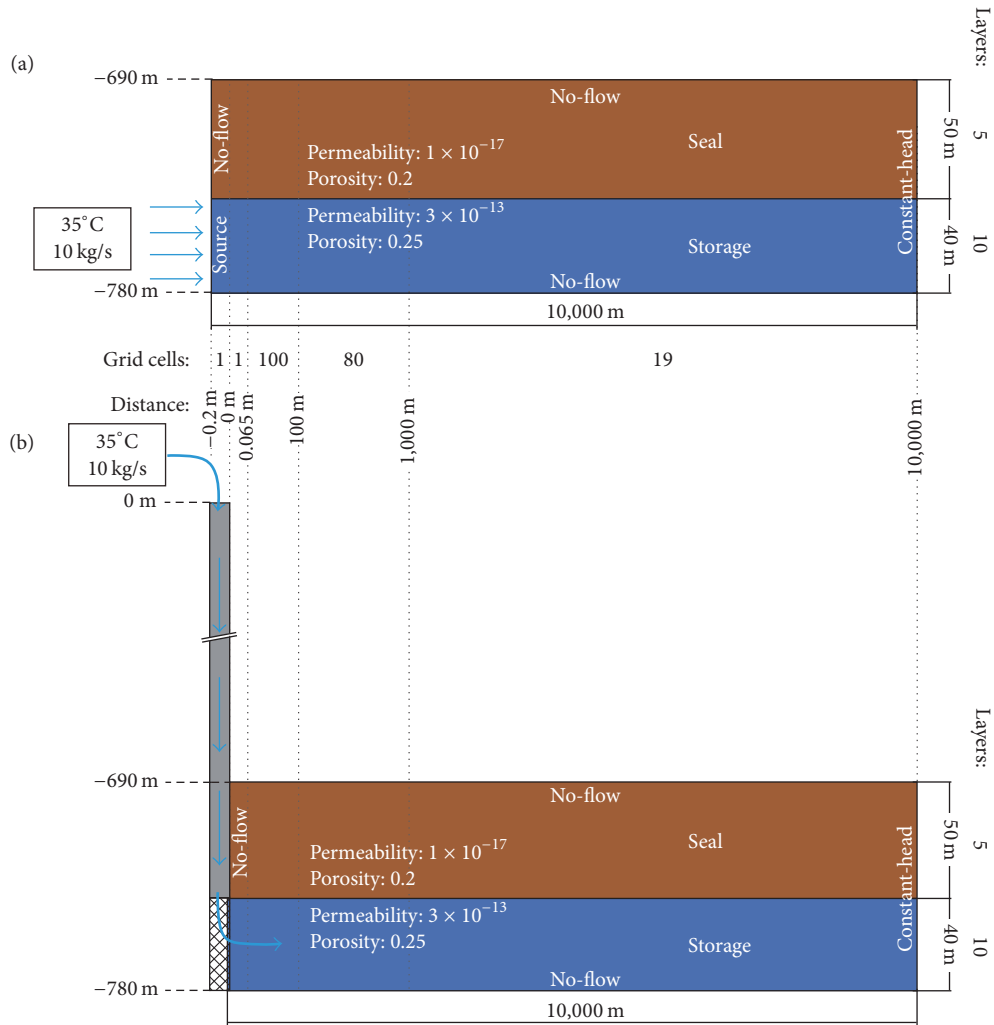


FIGURE 1: Schematic diagrams delineating the 2-dimensional radial models. (a) Case 1 targeted to evaluate the EPM model and (b) Case 2 for the WR model.

grid-blocks located at the left-most boundary with 1 kg/s injection rate (a total injection rate was 10 kg/s) during 1,095 days (3 years) (Figure 1(a)). The temperature of the injected CO₂ was maintained at 35.0°C, assuming that CO₂ velocity within the wellbore was fast enough to ignore conductive heat transfer from surroundings. Additionally, since there was no wellbore, it was assumed that the Joule Thompson effect was negligible. The ambient temperature based on assigned geothermal gradient was 54.2°C to 55.9°C in the storage formation. In Case 2 (WR model), for simulating CO₂ transport through the wellbore, the wellbore consisting of 84 grid-blocks was added to the left-most boundary from the ground surface to the bottom of target formation (Figure 1(b)). The diameter of the wellbore was set to 0.2 m. From the ground surface to the depth of 690 m (the top of the sealing formation), the 69 grid-blocks with the individual vertical size of 10 m were assigned without coupling to the surrounding formation. However, conductive heat exchange between the wellbore and the surrounding formation was considered by calculating semianalytically [24, 49]. From

the depth of 690 m to 780 m, the wellbore consisting of 15 grid-blocks was connected to the storage formation with the same dimension (sealing formation: 5 layers and storage formation: 10 layers). Among 15 grid-blocks, only 10 grid-blocks connected to the storage formation were considered to be the screen interval where CO₂ mass was injected into the storage formation. Dry CO₂ was injected from the well-head where the temperature of injected CO₂ and the injection rate was maintained at 35.0°C and 10 kg/s, respectively. In both models, the relative permeability and capillary pressure were modeled with Corey's curves [50] and van Genuchten function [51], respectively. The mathematical expressions and input parameters for Corey and van Genuchten functions were presented in Table 1.

Finally, in addition to Cases 1 and 2, 6 subcases of Case 2 were developed to evaluate different injection conditions for the WR model (Table 2). Three parameters including the injected CO₂ temperature, the injection rate, and the wellbore diameter were determined to analyze the role of the wellbore process on injected CO₂. Particularly, the injected

TABLE 1: Parameters and properties used in the basecase model. The definitions of symbols are explained in nomenclature.

Parameters for formation	Values
Permeability	
Storage formation	$3 \times 10^{-13} \text{ m}^2$
Sealing formation	$1 \times 10^{-17} \text{ m}^2$
Porosity	
Storage formation	0.25
Sealing formation	0.2
Salinity	
Surface pressure	$1.01 \times 10^5 \text{ Pa}$
Pressure gradient	$10,577.8 \text{ Pa/m}$
Surface temperature	20°C
Temperature gradient	0.0461°C/m
Thermal conductivity	$2.51 \text{ W/m}^\circ \text{C}$
Parameters for injection	Values
Injection rate	10 kg/s
Injection temperature	35°C
Wellbore diameter	0.2 m
Parameters for transport	Values
Relative permeability	Corey's model $k_{rG} = (1 - \bar{S})^2(1 - \bar{S}^2)$; $k_{rL} = \bar{S}^4$ $\bar{S} = (S_L - S_{lr}) / (1 - S_{lr} - S_{gr})$ $S_{lr} = 0.3, S_{gr} = 0.05$
Capillary pressure	van Genuchten model $P_c = -P_0 \left((S^*)^{-1/\lambda'} - 1 \right)^{(1-\lambda')}$ $S^* = (S_L - S_{lr}) / (S_{is} - S_{lr})$
Storage formation	$\lambda' = 0.46, S_{lr} = 0.2, 1/P_0 = 1 \times 10^{-4} \text{ Pa}^{-1}$
Sealing formation	$\lambda' = 0.25, S_{lr} = 0.2, 1/P_0 = 1 \times 10^{-5} \text{ Pa}^{-1}$

TABLE 2: Description of sensitivity scenarios.

Case	Injection temperature ($^\circ \text{C}$)	Injection rate (kg/s)	Wellbore diameter (m)
Case 2	35	10	0.2
Case 2-1	45	10	0.2
Case 2-2	60	10	0.2
Case 2-3	35	5	0.2
Case 2-4	35	50	0.2
Case 2-5	35	10	0.13
Case 2-6	35	10	0.05

CO_2 temperatures were selected from relatively high values (35°C – 60°C) even though the high injected CO_2 temperature will cause a high energetic cost because of heating up CO_2 [52].

2.2. Numerical Simulator. In this study, two simulators were compared; one for the EPM model applying to Case 1 was TOUGH2/ECO2N [53, 54] and the other for the WR model in Case 2 was T2Well/ECO2N [24, 55]. TOUGH2 is the

numerical simulator capable of simulating nonisothermal multiphase and multicomponent fluids in multidimensional porous and fractured media [53]. The ECO2N is a fluid property module that describes the thermophysical properties of H_2O - NaCl - CO_2 system [54, 56]. T2Well/ECO2N, which is the suite of the TOUGH2/ECO2N, is the integrated simulator capable of accounting for both wellbore and storage subdomain where they are controlled by different governing equations [24]. Specifically, the viscous flow within the wellbore was predicted from one-dimensional momentum equation while porous media representing the storage formation were simulated with two-dimensional multiphase version of Darcy's law.

For the specific details regarded to TOUGH2, Pruess et al. [53] can be referred. Here, the governing equations related to T2Well/ECO2N are only explained; the primary governing equations representing mass, energy, and momentum within the wellbore and the storage formation are listed in Table 3. As shown in Table 3, the primary difference between porous medium and the wellbore is consideration of both kinetic ($\mathbf{u}_\beta^2/2$) and potential ($g z \cos \theta$) energy terms in the energy flux and accumulation equations of the wellbore model. Therefore, while CO_2 migrates through the wellbore, variations in both potential and kinetic energies interactively change the energy state of CO_2 within the wellbore. Additionally, fluid velocities within the wellbore are determined by the mixture velocity (u_m) and the drift velocity (u_d), which is calculated from the Drift-Flux-Model (DFM) [57]. Specifically, u_m is calculated by solving following momentum equation [55]:

$$\begin{aligned} \frac{\partial}{\partial t} (\rho_m u_m) + \frac{1}{A} \frac{\partial}{\partial z} [A (\rho_m u_m^2 + \gamma)] \\ = - \frac{\partial P}{\partial z} - \frac{\Gamma_w f \rho_m |\mathbf{u}_m| \mathbf{u}_m}{2A} - \rho_m g \cos \theta, \end{aligned} \quad (1)$$

where γ is expressed with the following equation: $\gamma = (S_G/(1 - S_G))(\rho_G \rho_L \rho_m / \rho_m^{*2})[(C_0 - 1)u_m + u_d]^2$, which explains the slip between gas and liquid phases. Subsequently, u_d is calculated with a function of gas saturation (S_G) and other fluid properties:

$$u_d = \frac{(1 - C_0 S_G) u_c K(S_G, K_w, C_0) m(\theta)}{C_0 S_G \sqrt{\rho_G / \rho_L} + 1 - C_0 S_G}. \quad (2)$$

In (2), the characteristic velocity (u_c) indicates the rising velocity of gaseous bubble in a liquid column and $m(\theta)$ denotes the inclination effect of the wellbore. The function for $K(\cdot)$ is used for smooth transition of drift velocity between the bubble rising stage and the film flooding stage. Other terms in (2) can be found in the nomenclature. Further details about the T2Well/ECO2N simulator can be found in Pan et al. [55].

In regard to the salt-precipitation process occurring adjacent to the injection well, a number of previous studies have been conducted with TOUGH2/ECO2N [34, 38–42]. However, only a few studies considered the influence of salinity on both wellbore and reservoir flow [25, 58]. In TOUGH2/ECO2N, the salt-precipitation occurred when water vaporized into dry supercritical CO_2 , which was

TABLE 3: Governing equations utilized in T2Well/ECO2N, which represents fluids through the wellbore and storage formation. The definitions of symbols are explained in nomenclature.

Description	Equation
Conservation of mass and energy	$\frac{d}{dt} \int_{V_n} M^\kappa dV_n = \int_{\Gamma_n} \mathbf{F}^\kappa \cdot \mathbf{n} d\Gamma_n + \int_{V_n} q^\kappa dV_n$
Mass accumulation	$M^\kappa = \phi \sum_{\beta} S_{\beta} \rho_{\beta} X_{\beta}^{\kappa}$, for each mass component κ
Mass flux	$\mathbf{F}^\kappa = \sum_{\beta} \mathbf{u}_{\beta} \rho_{\beta} X_{\beta}^{\kappa}$, for each mass component κ
Porous medium	
Energy flux	$\mathbf{F}^{NK1} = -\lambda \nabla T + \sum_{\beta} h_{\beta} \rho_{\beta} \mathbf{u}_{\beta}$
Energy accumulation	$M^{NK1} = (1 - \phi) \rho_R C_R T + \phi \sum_{\beta} \rho_{\beta} S_{\beta} \mathbf{u}_{\beta}$
Darcy velocity	$\mathbf{u}_{\beta} = -k \frac{k_{r\beta}}{\mu_{\beta}} (\nabla P_{\beta} - \rho_{\beta} \mathbf{g})$ Darcy's Law for each phase β , with $P_{\beta} = PG + Pc$
Wellbore	
Energy flux	$\mathbf{F}^{NK1} = -\lambda \nabla T + \sum_{\beta} \rho_{\beta} S_{\beta} \mathbf{u}_{\beta} \left(h_{\beta} + \frac{\mathbf{u}_{\beta}^2}{2} + \mathbf{g}z \cos \theta \right)$
Energy accumulation	$M^{NK1} = \sum_{\beta} \rho_{\beta} S_{\beta} \left(U_{\beta} + \frac{\mathbf{u}_{\beta}^2}{2} + \mathbf{g}z \cos \theta \right)$
Phase velocity	$u_G = C_0 \frac{\rho_m}{\rho_m^*} u_m + \frac{\rho_L}{\rho_m^*} u_d$ Drift-flux model $u_L = \frac{(1 - S_G C_0) \rho_m}{(1 - S_G) \rho_m^*} u_m - \frac{S_G \rho_G}{(1 - S_G) \rho_m^*} u_d$ Drift-flux model

Source: modified after Pan et al. [49].

accounted for the equations of states developed by Spycher and Pruess [32]. The precipitation of salt is able to cause to reduction in both porosity and permeability adjacent to the injection well. In this work, reduction of porosity and permeability due to the salt-precipitation was calculated using a “tubes-in-series” model [53, 59].

$$\frac{k}{k_0} = \theta_s^2 \frac{1 - \Gamma + \Gamma/\omega^2}{1 - \Gamma + \Gamma [\theta_s / (\theta_s + \omega - 1)]^2} \quad (3)$$

$$\theta_s^2 = \frac{1 - S_s - \phi_r}{1 - \phi_r} \quad (4)$$

$$\omega = 1 - \frac{1/\Gamma}{1/\phi_r - 1}, \quad (5)$$

where k/k_0 denotes the permeability reduction factor. ω is calculated by two independent geometric parameters such as fraction of original porosity ($\phi_r = \phi/\phi_0$) and fractional length of pore body (Γ). According to few previous studies, both ϕ_r and Γ were set to be 0.8 [38, 39].

2.3. Gravity Number. The buoyancy effect is one of the significant factors for determining distribution of both CO₂ plume and associated salt-precipitation [41, 42]. In order to quantitatively assess distribution of salt-precipitation in two cases, the gravity number (N_{gv}) was chosen for evaluating the buoyancy effect on the CO₂ plume in the storage formation.

N_{gv} defined below measures the degree of strength of gravity to viscous forces [60]:

$$N_{gv} = \frac{k_v L_s \Delta \rho \mathbf{g}}{H u_i \mu}. \quad (6)$$

where k_v is the vertical permeability, H is the thickness of the storage formation, and L_s , as a characteristic length, is chosen to be equal to the horizontal length of the storage formation. $\Delta \rho$ is the density difference between CO₂ and brine, u_i is the total averaged velocity to the horizontal direction predicted from grid-blocks between wellbore and storage formations, and μ is CO₂ viscosity. In (6), greater N_{gv} indicates dominance of the gravity force on CO₂ plume [61].

3. Comparison of EPM and WR Models (Case 1 versus Case 2)

3.1. Analyses of Wellbore Flow Conditions

3.1.1. Characterization of Multiple Stages in the Wellbore. In Case 1 (EPM model), CO₂ holding constant temperature of 35.0°C was injected into the storage formation (formation pressure from 7.95 MPa to 8.33 MPa) at a constant rate of 10 kg/s throughout the simulation time (Figure 1(a)). Following the injection conditions, CO₂ injected into the storage formation was in supercritical phase consistently preserving its density and viscosity approximately larger than 600 kg/m³ and 5.0 × 10⁻⁵ Pa-s, respectively.

In Case 2 (WR model), CO₂ holding 35.0°C was injected from the well-head at a rate of 10 kg/s (Figure 1(b)). Once CO₂ was entered from the well-head, it transported through the 780 m depth wellbore (Figure 2(a)) while experiencing thermal disequilibrium processes such as heat convection, conduction, frictional effect, and Joule-Thomson effect [21, 27]. Consequently, the temperature of CO₂ reaching the well-bottom was changed from 35.0°C (at the well-head) to approximately 52.0°C. Due to such dynamic disturbance in both temperature and pressure within the wellbore, the thermodynamic properties of CO₂ entering from the well-head were also different with ones reaching the well-bottom.

Figures 2(b)–2(d) showed changes in CO₂ saturation, pressure, and temperature throughout the wellbore during 100 days after CO₂ injection began. According to CO₂ saturation profile in Figure 2(b), three stages were characterized. Stage I (0 to 1.2×10^{-5} day (=1 sec)) defined the status of the wellbore where brine was fully saturated in the well; both pressure and temperature remained hydrostatic and geothermal gradient conditions, initially assigned to the model (Stage I in Figures 2(c) and 2(d)). During Stage II (1.2×10^{-5} day (=1 sec) to 1.2×10^{-2} day (=17.3 min)), the wellbore transitioned from single (or brine) to multiphase conditions where both brine and CO₂ coexisted; the dynamic interface (dashed purple-line in Figures 2(c) and 2(d)) between injected CO₂ and brine was developed. In addition, the phase transition of CO₂ from gaseous to supercritical phase was observed at a depth of 468 m for the first time (3.2×10^{-3} day), which dynamically evolved with time (Figure 2(b)). Approximately after 3.35 day, gaseous CO₂ in the wellbore completely transitioned to supercritical phase.

Immediately after CO₂ injection began at Stage II, CO₂ suddenly pushed brine from the well-head, and therefore, increase in CO₂ saturation was observed at the well-head (Figure 2(b)). Due to the encroachment of CO₂ from the well-head, brine positioned at the well-bottom needed to enter the storage formation in which permeability (3×10^{-13} m²) and capillary pressure were significantly smaller and larger than the wellbore ones, respectively. Because of contrasts in both permeability and capillary pressure between the wellbore and storage formation, the pressure at the wellbore was built up and reached its peak at 2.3×10^{-4} day (Figure 2(c)). Then, subsequent pressure reduction implies that brine at the well-bottom was getting entered the storage formation with continuous CO₂ injection from the well-head. Gradual decrease in the wellbore pressure was observed until the wellbore was completely replaced by CO₂ at 1.2×10^{-2} day (Figure 2(c)).

The temperature profile was somewhat similar to pressure one. At Stage I, temperature ranged from the well-head to well-bottom was 20.0°C to 56.0°C (Figure 2(d)). Then, CO₂ with temperature of 35.0°C was injected from the well-head. While 35.0°C CO₂ displaced the brine from the well-head, relatively warm brine (approximately 50.0–56.0°C) positioned at the bottom of the wellbore entered the storage formation (Stage II). Concurrently, low-temperature brine (20.0°C) was pushed from the well-head to the deeper part of the wellbore by injected CO₂. While the injected CO₂ pushed

low-temperature brine downward, diverse thermal processes including thermal convection, conduction, frictional effect, and Joule-Thomson effect occurred concurrently. However, because thermal convection representing the movement of shallow cold-brine toward the well-bottom was more dominant than other thermal effects, overall decrease in temperature was observed in the wellbore.

Immediately after Stage III at 1.2×10^{-2} day, the wellbore was completely replaced by the injected CO₂. Soon, both pressure and temperature increased together (6.9×10^{-2} day). This positive relationship can be attributed to Joule-Thomson effect ($(\partial T/\partial P)_H$), which defines change in temperature during (de)compression of CO₂ based on its counterpart of pressure change under the isenthalpic condition [62]. After 3.35 day, profiles for both pressure and temperature reached the steady-state condition while CO₂ in the wellbore completely became supercritical phase (Figure 2(b)). In summary, due to thermal processes such as frictional effect, heat conduction, and Joule-Thomson effect, temperature of CO₂ which entered the storage formation reached approximately 51–52°C, which was greater than injected CO₂ (35°C) but lower than temperature (54–55°C) of the storage formation.

3.1.2. Variations in Thermophysical Properties of Injected CO₂.

Figure 3 showed contours for density, viscosity, specific enthalpy, and Joule-Thomson coefficient of CO₂ dependent on temperature and pressure, which were predicted from Span and Wagner [63]. Figures 3(a) and 3(b) delineated relatively wide ranges covering pressure from 0 to 30 MPa and temperature from 0 to 200°C. Therefore, appropriate ranges for pressure (6 to 10 MPa) and temperature (20 to 80°C) were selected, and CO₂ injection condition was examined for both cases (Figures 3(c) and 3(d)).

The CO₂ injection condition for Case 1 (EPM model; purple symbols) was plotted at 1,095 days (Figure 3(c)). After 1,095 days, pressure from the top to the bottom of the storage formation was changed from 9.16 to 9.26 MPa while maintaining 35°C. At this condition, the injected CO₂ was completely supercritical phase with relatively large density (approximate 650 kg/m³) and viscosity (approximate 5.2×10^{-5} Pa·s) (Figure 3(c)).

For Case 2 (WR model), 4 profiles were selected; one was at the end of Stage II (1.2×10^{-2} day in Figure 2(b)) immediately after the wellbore was completely filled with CO₂; at this time, the injected CO₂ experienced phase transition from gaseous to supercritical phase at 155 m depth (Point A in Figures 2(b) and 3(c)). Presence of both gaseous and supercritical CO₂ within the wellbore resulted in dynamic (or nonlinear) profile of CO₂. At the well-head, temperature and pressure were 35°C and 6.96 MPa, which was plotted below the critical point (31.1°C and 7.38 MPa) of CO₂. Then, at 155 m (Point A) temperature dropped to 32.6°C ($\Delta T = -2.4^\circ\text{C}$) while pressure increased to 7.37 MPa ($\Delta P = +0.4$ MPa). Similar to Han et al. [27] and Lu and Connell [21], decrease in CO₂ temperature occurred in the wellbore due to heat conduction with the surrounding formation; the temperature of the surrounding formation was 27.1°C in this depth. From the ground surface to 155 m, gaseous CO₂ in the wellbore holds

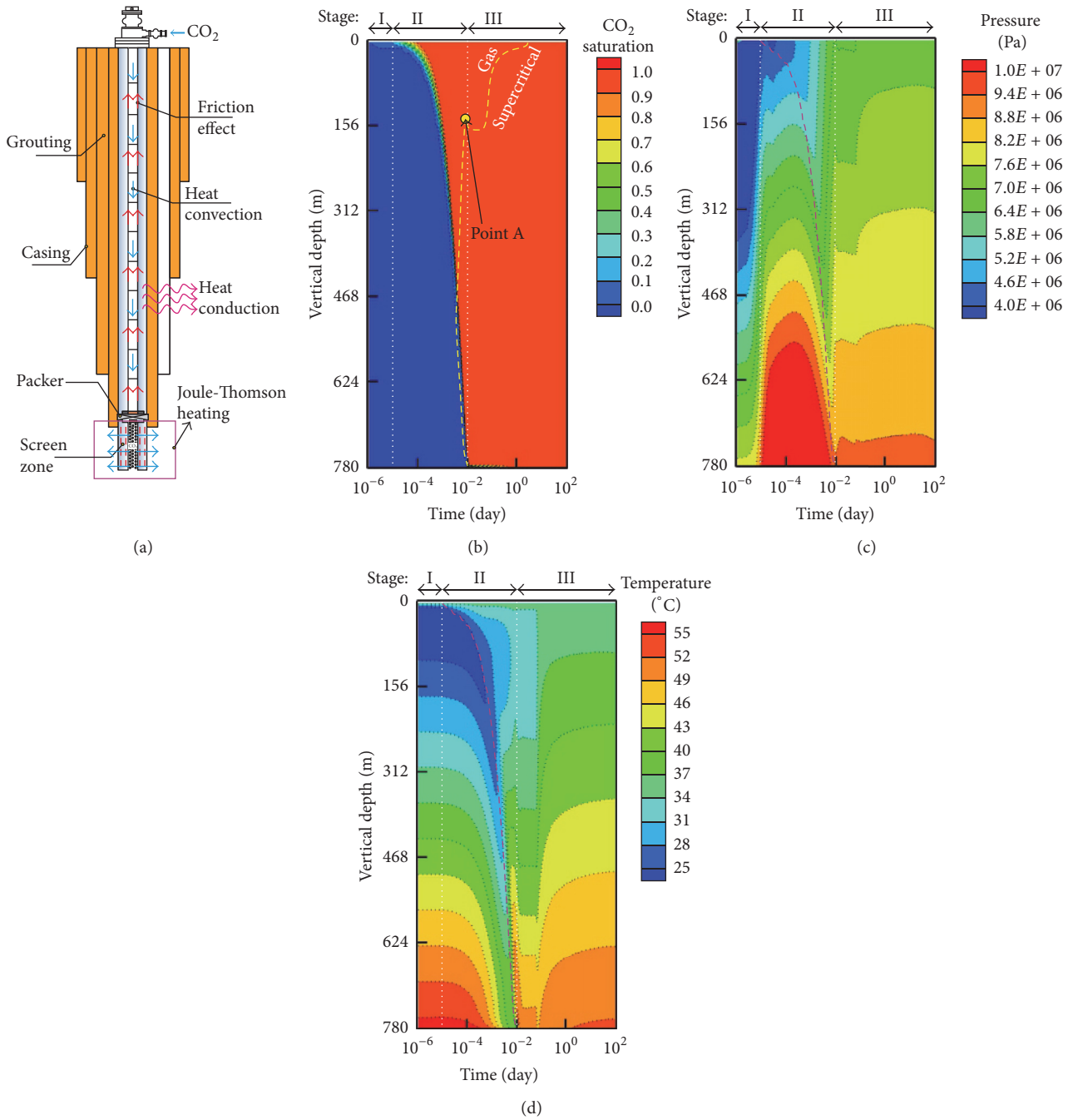


FIGURE 2: Changes in thermophysical properties of CO₂ within the wellbore during 100 days; (a) a schematic diagram delineating CO₂ transport within the wellbore and associated thermal effects; profiles for (b) CO₂ saturation [-], (c) pressure [Pa], and (d) temperature [°C]. The two white dotted lines define the initiation of each different stage while injected CO₂ is displacing the brine in the wellbore (1.2×10^{-5} (=1 sec) and 1.2×10^{-2} (=17.3 min)). The yellow dashed line in (b) represents the interface between gaseous and supercritical CO₂ phase. The purple dashed lines shown in (c) and (d) indicate the dynamic interface between CO₂ and brine.

its density from 219 to 326 kg/m³, viscosity from 2.0×10^{-5} to 2.3×10^{-5} Pa-s, and Joule-Thomson coefficient decreasing from 9.1 to 8.2°C/MPa. Deeper than 155 m, gaseous CO₂ transitioned to supercritical phase. Both temperature and pressure increased nonlinearly while deviating from isenthalpic lines (300–350 kJ/kg in Figure 3(d)), implying that supercritical CO₂ in the wellbore did not reach the adiabatic condition yet;

thus, various thermal processes including thermal conduction and friction actively affected CO₂ temperature. When CO₂ arrived at the well-bottom, its temperature reached 52.2°C with elevated pressure of 9.5 MPa. Compared to Case 1 (35°C), CO₂ temperature at the well-bottom increased (ΔT) +17.2°C. Due to significant discrepancy in CO₂ temperature from these two cases, thermodynamic properties of CO₂ were

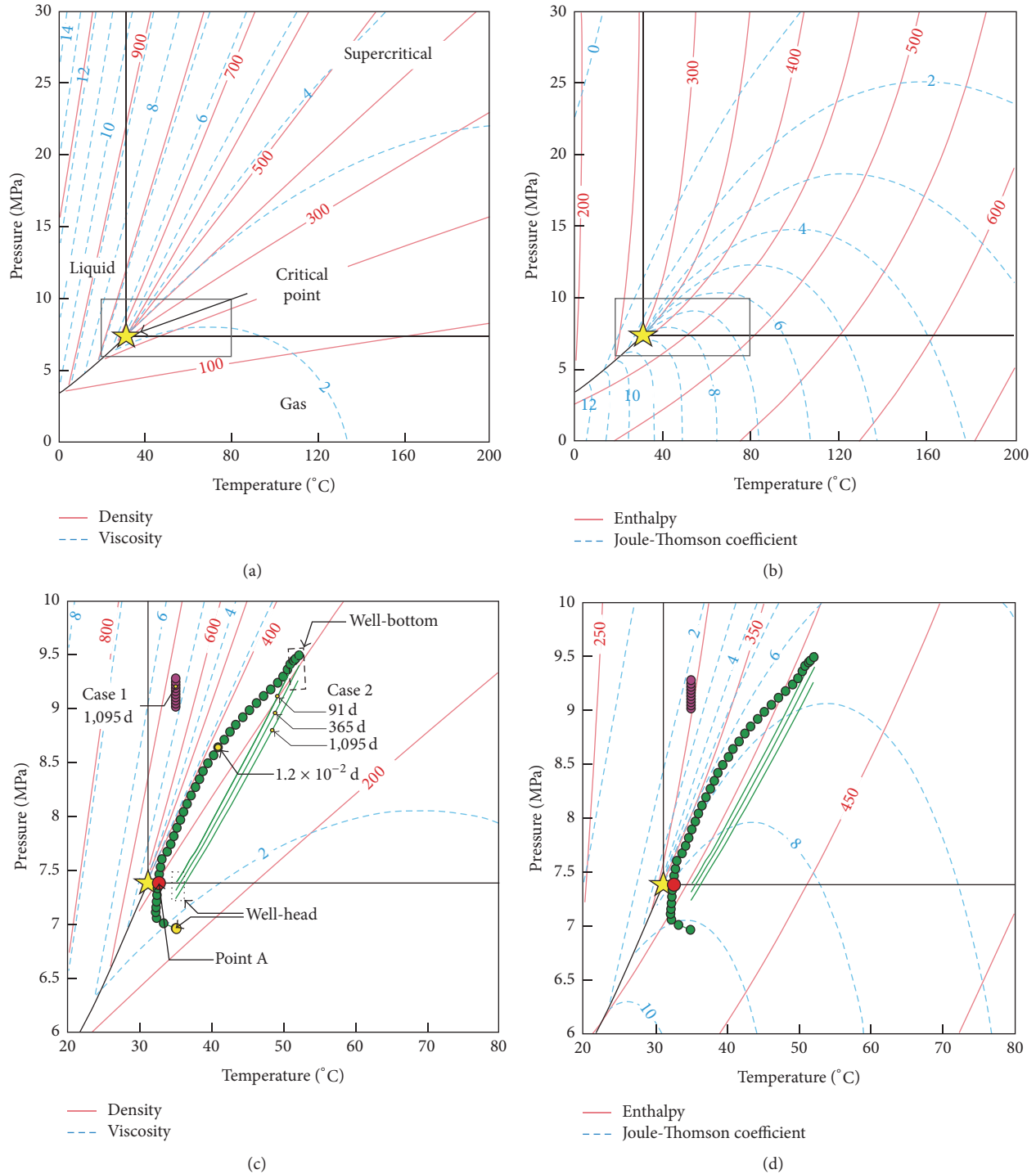


FIGURE 3: Contours of (a) density [kg/m^3] and viscosity [10^{-5} Pa·s] and (b) enthalpy [kJ/kg] and Joule-Thomson coefficient [$^{\circ}\text{C}/\text{MPa}$] in P - T space. Gray box represents a suitable condition for the wellbore during geologic CO_2 sequestration (P : 6 to 10 MPa and T : 20 to 80 $^{\circ}\text{C}$). (c) and (d) represent contours for density, viscosity, enthalpy, and Joule-Thomson coefficient in P - T regime suitable for the wellbore. Purple symbols represent the conditions for CO_2 injection in Case 1. Green symbols and lines represent the conditions for the wellbore in Case 2.

also different which affected the behavior of CO_2 transport in the storage formation.

The other three profiles (91, 365, and 1,095 days) were selected during Stage III. These profiles were paralleled to

isenthalpic lines, implying that CO_2 within the wellbore reached the adiabatic condition (Figures 3(c) and 3(d)). In this condition, Joule-Thomson effect on CO_2 temperature would be more significant than any other thermal processes

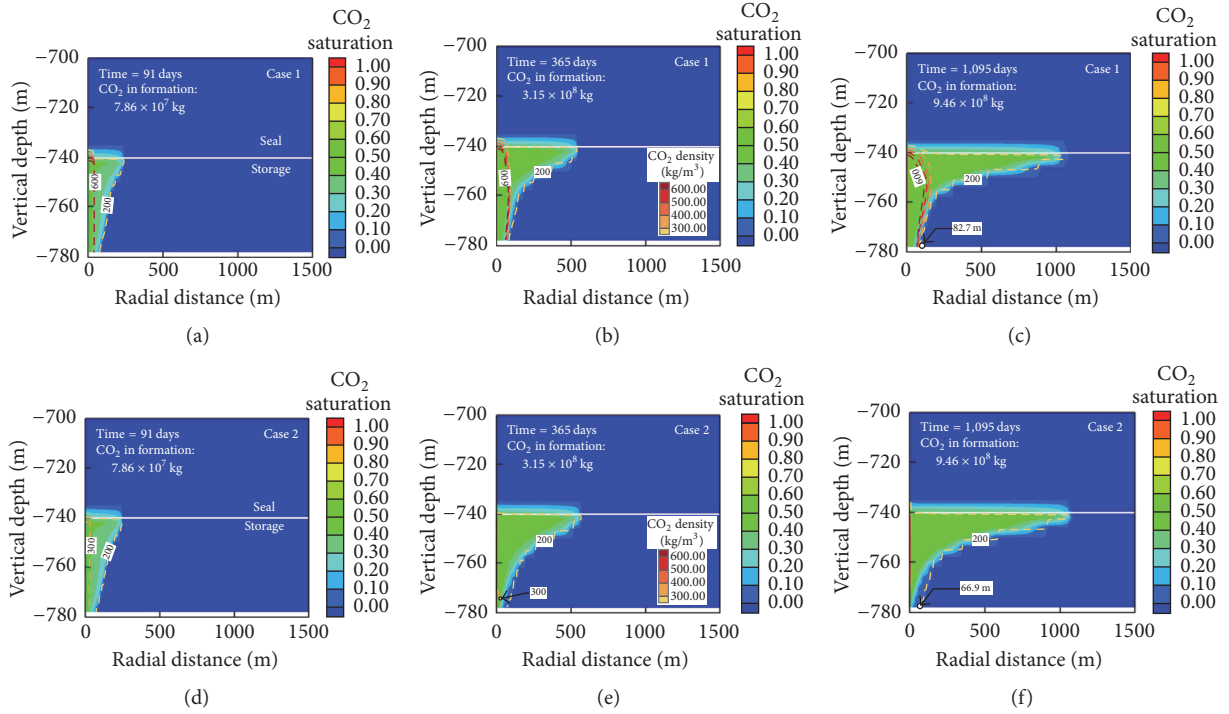


FIGURE 4: Distribution of CO₂ saturation [-] shown as color contours and CO₂ density [kg/m³] as dashed lines at a series of times (91, 365, 1,095 days). (a), (b), and (c) were simulated from the EPM model (Case 1) while (d), (e), and (f) were from the WR model (Case 2). The isodense lines represent the magnitude of density which follows the legend shown in (b) and (e).

[21]. As seen in Figure 3(d), Joule-Thomson coefficient having positive values decreased from 8.8 to 6.4°C/MPa as approaching to the well-bottom; positive values of Joule-Thomson coefficient imply the adiabatic heating with CO₂ compression, and its effect was relatively large at the shallow depth. All these three profiles revealed that gaseous CO₂ filled the small portion of the well-head even after the arrival of the adiabatic condition. In addition, it is observed that the wellbore pressure slightly decreased with time; the small drop of the well-bottom pressure between 91 and 1,095 days was (ΔP) -0.2 MPa (9.5 to 9.3 MPa). Correspondingly, CO₂ density and viscosity at the well-bottom were decreased, ($\Delta \rho$) -19.9 kg/m³ (311.7 to 291.8 kg/m³) and ($\Delta \mu$) -0.1 × 10⁻⁵ Pa·s (2.5 to 2.4 × 10⁻⁵ Pa·s), respectively (Figure 3(c)).

Overall, when comparing to CO₂ density and viscosity from Case 2 (WR model), Case 1 (EPM model) was 680.0 kg/m³ and 5.4 × 10⁻⁵ Pa·s, respectively, at 1,095 days. As seen, discrepancies in thermophysical properties of CO₂ were significant when two different injection schemes were used even with the same injection rate. This discrepancy became primary reasons for different distribution of CO₂ plume within the storage formation and subsequently the patterns for the salt-precipitation, which will be discussed in following section.

3.2. Analyses of Storage Formation Conditions

3.2.1. Patterns for CO₂ Migration in the Storage Formations.

Figure 4 showed the distribution of CO₂ saturation after

91, 365, and 1,095 days of CO₂ injection; Figures 4(a)–4(c) and Figures 4(d)–4(f) were simulated with the EPM model (Case 1) and WR model (Case 2), respectively. Comparing two cases, the same mass of CO₂ was injected into the storage formation (9.46 × 10⁸ kg during 1,095 days), and consequently, CO₂ plume migrated the equal distance of 1,048 m at the interface between the caprock and storage formation (Figures 4(c) and 4(f)). Nevertheless, at the bottom of the storage formation, the frontal location of CO₂ plume was different (82.7 m and 66.9 m for Case 1 and Case 2, resp.), implying that more CO₂ migrated vertically in Case 2, and therefore, more counterflowing brine was developed. According to (6), N_{gv} for each case was calculated and listed in Table 4. As expected, N_{gv} in Case 2 (2.76) was greater than Case 1 (2.20), implying that the buoyancy force acting on the CO₂ plume was greater in Case 2.

In Case 1, density and viscosity of CO₂ in the storage formation were greater than ~600 kg/m³ (Figures 4(a)–4(c)) and ~5.0 × 10⁻⁵ Pa·s, respectively (contour lines of CO₂ viscosity were not plotted because they were similar to the isodense lines). However, density and viscosity decreased to ~200 kg/m³ and ~2.0 × 10⁻⁵ Pa·s, respectively, while approaching to the margin of the CO₂ plume. In Case 2, CO₂ density was relatively small, showing the range of 200 to 300 kg/m³ (Figures 4(d)–4(f)); CO₂ density greater than 300 kg/m³ appeared only next to the injection well until 91 days (Figure 4(d)). In addition, CO₂ viscosity ranged from 2.4 × 10⁻⁵ Pa·s adjacent to the wellbore to 2.0 × 10⁻⁵ Pa·s at the margin of the CO₂ plume. Differences in CO₂ properties

TABLE 4: Predicted gravity number for multiple cases as well as associated parameters used in (6).

Case	Time (d)	u_i (m/s)	ρ_{brine} (kg/m ³)	ρ_{CO_2} (kg/m ³)	μ (Pa·s)	N_{gv}
Case 1	91	3.80×10^{-3}	1097.7	557.4	4.5×10^{-5}	2.33
	365	3.84×10^{-3}	1098.1	575.8	4.6×10^{-5}	2.17
	1,095	3.89×10^{-3}	1098.5	571.0	4.5×10^{-5}	2.20
Case 2	91	8.73×10^{-3}	1088.3	294.7	2.4×10^{-5}	2.78
	365	9.03×10^{-3}	1084.7	287.2	2.4×10^{-5}	2.74
	1,095	9.41×10^{-3}	1097.1	277.0	2.3×10^{-5}	2.76
Sensitivity Scenarios						
Case 2-1	1,095	1.09×10^{-2}	1096.5	248.0	2.2×10^{-5}	2.56
Case 2-2	1,095	1.26×10^{-2}	1095.0	223.6	2.2×10^{-5}	2.32
Case 2-3	1,095	5.23×10^{-3}	1097.5	251.4	2.2×10^{-5}	5.36
Case 2-4	1,095	2.49×10^{-2}	1098.1	486.5	3.6×10^{-5}	0.51
Case 2-5	1,095	9.27×10^{-3}	1097.2	280.4	2.3×10^{-5}	2.77
Case 2-6	1,095	4.07×10^{-3}	1098.5	570.7	4.5×10^{-5}	2.12

ρ_{brine} , ρ_{CO_2} , and μ are the average value of brine density, CO₂ density, and CO₂ viscosity in the storage formation, respectively.

such as density and viscosity in these two cases were amplified even after more CO₂ was injected into the storage formation.

3.2.2. Patterns for Salt-Precipitation and CO₂/Brine Flow. At the dry-out zone, different patterns for the salt-precipitation also appeared in these two cases (Figure 5). Here, the “dry-out zone” was defined as a zone where brine had been replaced by injected CO₂, and consequently, its CO₂ saturation approximately reached unity [34]. At the front of the dry-out zone (the interface of dry-CO₂ and brine), pure H₂O is continuously vaporized while remaining the solid salt in the pore. Degree and configuration of precipitated salt were governed by two factors; one was the migration speed of the dry-out front, which was governed by viscous force (e.g., injection rate and horizontal permeability of the storage formation). The others were factors governing buoyancy force (e.g., CO₂ density, the rate for counterflowing brine, and vertical permeability of the storage formation). Additionally, the amount of salt (or salinity) supplied by the counterflowing brine also governed the amount of precipitated salt [37].

In Case 1 (EPM model) following the conventional modeling approach (1 kg/s of CO₂), distribution of horizontal CO₂ flux along the radial distance was almost uniform (e.g., 4.4×10^{-3} kg/(s·m²) at 9.04 m at 1,095 days) (Figures 5(a) and 5(b)). In contrast, the counterflowing brine with its magnitude of 1.5×10^{-7} kg/(s·m²) flew opposite to CO₂ flux at 9.04 m (Figure 5(c)). The detailed snap-shots of the growing salt-precipitation were plotted at 91, 365, and 1,095 days in Figures 6(a)–6(c). As seen, the salt was uniformly accumulated throughout the entire thickness of the storage formation with its saturation of approximately 0.04. Correspondingly, the average permeability reduction (k/k_0) calculated from (3) was 65.1% in 1,095 days. Slightly elevated salt saturation appeared at both nearby the wellbore and the interface between sealing and storage formations. Adjacent to the wellbore, the salt saturation increased to be 0.06 due to the

complete vaporization of residual brine. At the interface of the sealing formation, the salt saturation was increased due to H₂O vaporization from the inflowing brine. According to Kim et al. [39], residual brine flew from the sealing formation to the dry-out zone where brine was completely displaced by injected dry-CO₂ (Figure 5(c)). Consequently, the maximum salt saturation and the k/k_0 reached 0.078 and 39.2%, respectively.

The WR model (Case 2) was able to predict the profiles for both horizontal and vertical CO₂ mass flow rates within the wellbore (Figure 5(d)). Above the interface (740 m) between the storage and sealing formations, the vertical CO₂ mass flow rate was consistently 10 kg/s because the wellbore was fully cased (red circle in Figure 5(d)). However, once CO₂ entered the screened interval (740 to 780 m), the vertical CO₂ mass flow rate decreased with the depth almost linearly and finally reached zero at the well-bottom. In this interval, the horizontal CO₂ mass flow rate reflected the actual CO₂ injection rate (blue circles in Figure 5(d)). As seen in Figures 5(a) and 5(d), the actual CO₂ injection rates from both cases were different; in Case 2, the actual CO₂ injection rates were larger at the upper storage formation except the interface similar to Vilarrasa et al. [64] and decreased toward the well-bottom. However, throughout the entire thickness, the average actual CO₂ injection rate was the same as the injection rate assigned to Case 1 (i.e., 10 kg/s).

Due to magnitude difference of actual CO₂ injection rates throughout the screen interval, both viscous and buoyancy forces differently acted on CO₂ plume between Case 1 and Case 2 [44]. Furthermore, relatively warm CO₂ (e.g., 52°C) entered from the wellbore to the storage formation also amplified the buoyancy effect on CO₂ plume (Figure 3(c)). Due to these reasons, in Case 2, the injected CO₂ plume rose rapidly, inducing more counterflowing brine flux (5.0×10^{-6} kg/(s·m²) at 8 m at 1,095 days) along the bottom of the storage formation (Figure 5(f)). Because of

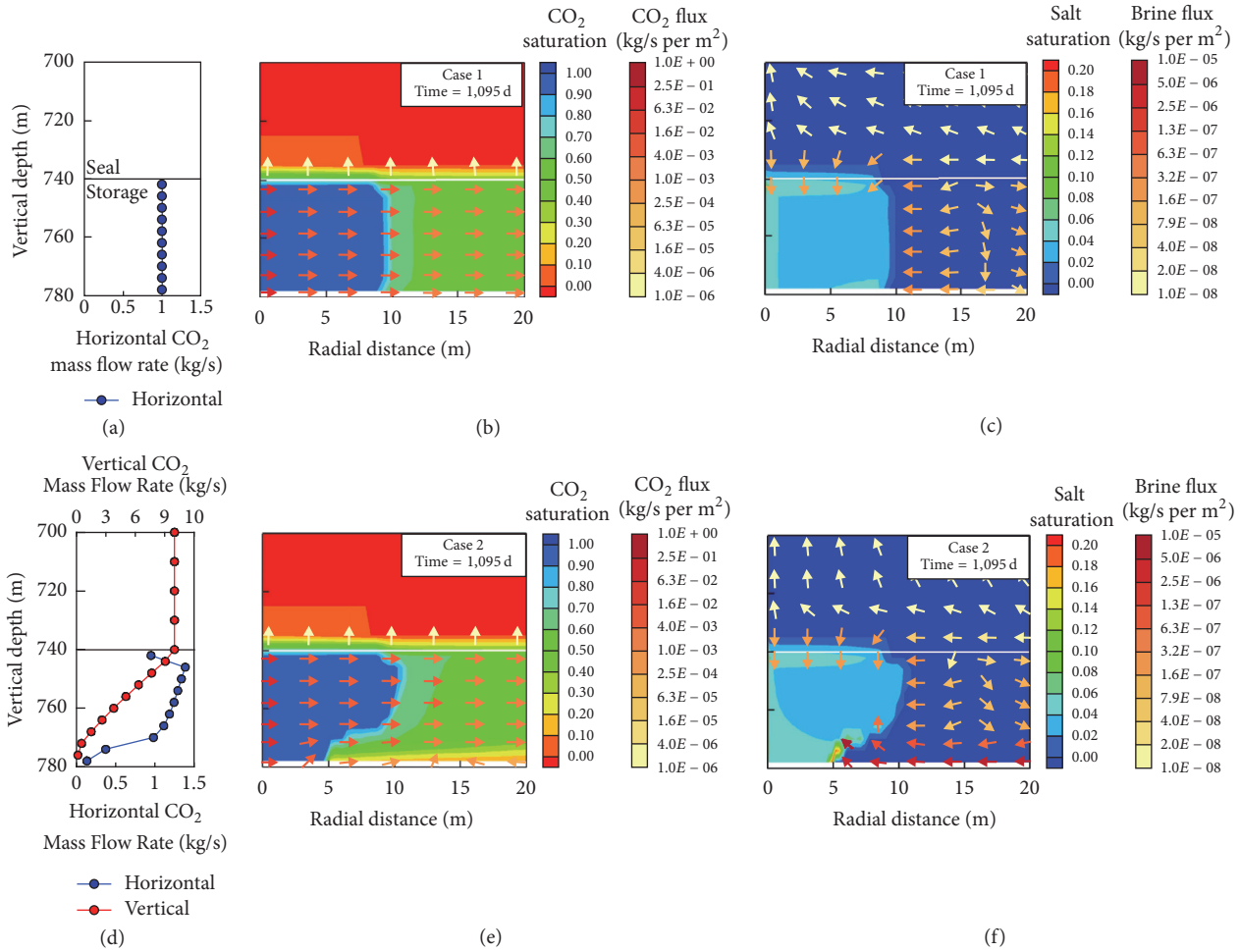


FIGURE 5: Flux patterns for CO₂ and brine near the injection well after the injection of 1,095 days. (a) and (d) predicted CO₂ mass flow rate [kg/s] within grid-blocks representing the wellbore; blue circles are horizontal CO₂ mass flow rate from the wellbore to the storage formation and red symbols are vertical CO₂ mass flow rate within the wellbore. (b) and (e) indicate CO₂ flux [kg/(s·m²)] with CO₂ saturation. (c) and (f) indicate brine flux [kg/(s·m²)] with salt saturation. The arrows indicate directions for both CO₂ and brine flux, and the colors represent their magnitude.

strong buoyancy effect on the CO₂ plume, the configuration of the dry-out zone where the salt was precipitated was nonuniform. In particular, the localized salt-peak was developed due to additional supply of salinity by counterflowing brine.

At the zone where the localized salt was precipitated, the maximum salt saturation reached almost equal to porosity (0.25) implying significant deterioration of permeability; the cumulated salt-barrier restricted horizontal propagations of both CO₂ and pressure, consequently reducing effectiveness of the injection well. Figures 6(d)–6(f) showed the development of salt-precipitation at 91, 365, and 1,095 days. According to Figure 6(f), it is distinct that the lower part of the dry-out front stopped expanding after 365 days when the localized salt-peak was developed.

4. Sensitivity Analyses for WR Model

In order to further evaluate the influence of wellbore processes on complete CO₂ injection scenarios and associated

salt-precipitation, sensitivity analyses were conducted by varying the injection conditions such as injected CO₂ temperature, injection rate, and wellbore diameter. Then, outputs from developed sensitivity scenarios were compared relative to the base-case representing Case 2 (Table 2).

4.1. Effect of Injected CO₂ Temperature at the Well-Head. Case 2 (35°C), Case 2-1 (45°C), and Case 2-2 (60°C) were designed to evaluate the influence of injected CO₂ temperature while fixing the injection rate of 10 kg/s and the wellbore diameter of 0.2 m. After 1,095 days, CO₂ profiles predicted from three cases became parallel to isenthalpic lines, implying that CO₂, after completely displacing brine within the wellbore, reached the adiabatic condition (Figure 7(a)). While constraining the injection rate, different injected CO₂ temperature resulted in prediction of different well-head pressures ($P_{\text{Case 2}} = 7.24$ MPa, $P_{\text{Case 2-1}} = 7.54$ MPa and $P_{\text{Case 2-2}} = 7.79$ MPa). Nevertheless, the well-bottom pressures were relatively consistent ($P_{\text{Case 2}} = 9.26$ MPa, $P_{\text{Case 2-1}} = 9.29$ MPa, $P_{\text{Case 2-2}} = 9.30$ MPa). Within the wellbore, the hydrostatic pressure

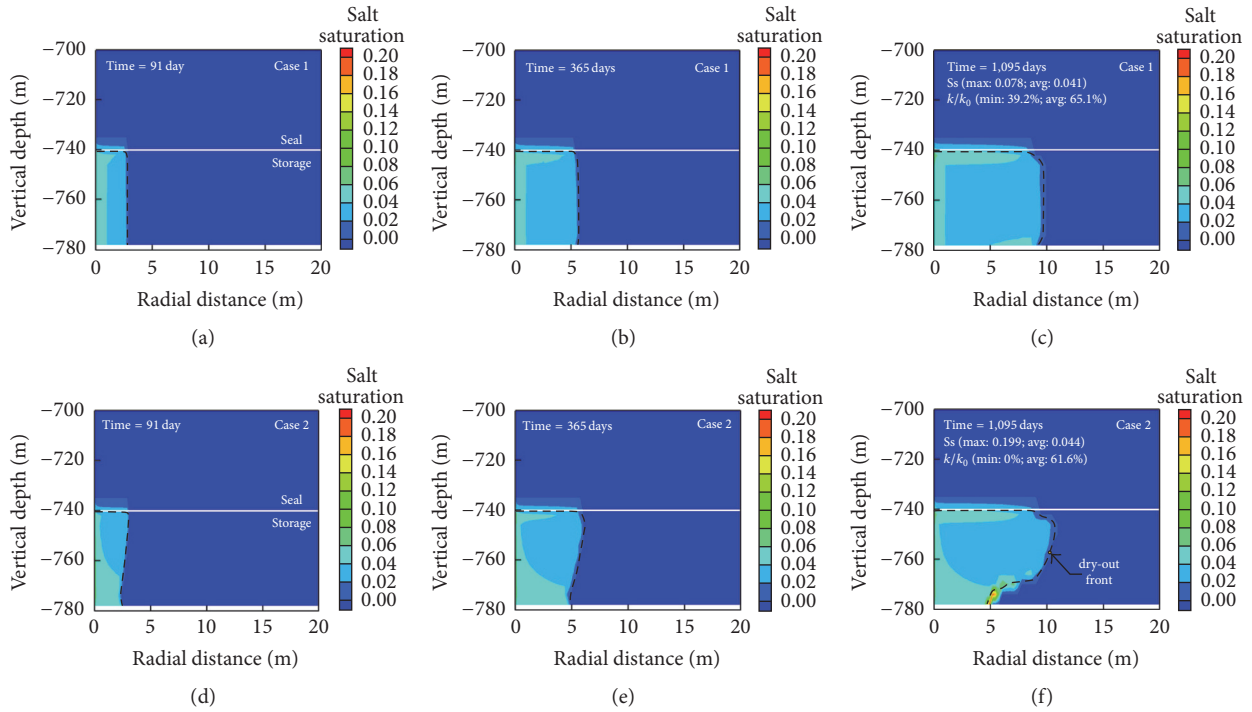


FIGURE 6: Distribution of salt saturation [-] shown as color contours and the dry-out front as dashed lines at a series of times (91, 365, and 1,095 days). (a), (b), and (c) were simulated from the EPM model (Case 1), but (d), (e), and (f) were from the WR model (Case 2).

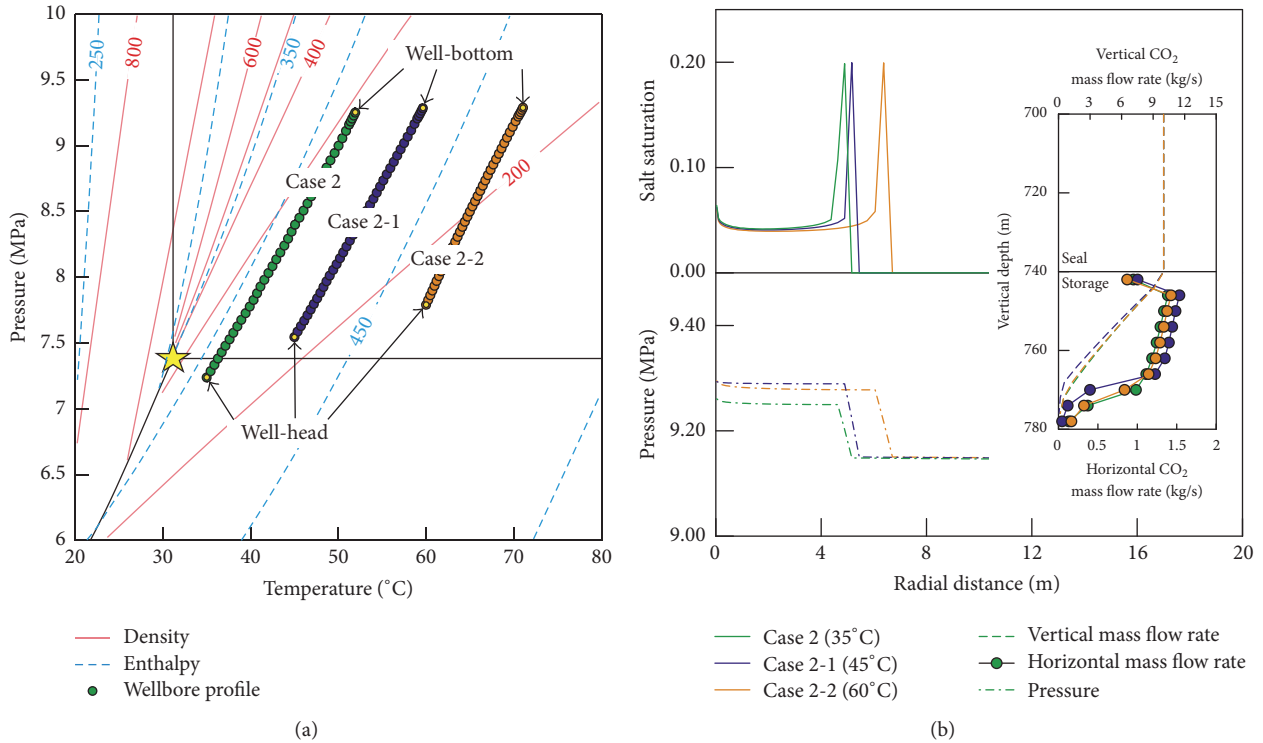


FIGURE 7: (a) Changes of CO₂ properties (density [kg/m³] and enthalpy [kJ/kg]) within the wellbore and (b) development of salt saturation [-] and built-up pressure [MPa] at the bottom layer. The small figure represents both horizontal and vertical CO₂ mass flow rate [kg/s] within the wellbore at three different injection temperatures (35, 45, and 60°C) after 1,095 days.

(P_{bottom}) at the well-bottom can be expressed to be $P_{\text{bottom}} = P_{\text{head}} + \rho_{\text{CO}_2} \mathbf{g}H$. The same injection rate (10 kg/s) indicates that P_{bottom} should be consistent at all cases. However, the magnitude of the second term ($\rho_{\text{CO}_2} \mathbf{g}H$) at the right-side varied because ρ_{CO_2} decreased with the increase in injected CO_2 temperature; for example, ρ_{CO_2} at the well-bottom was 291.8 kg/m³, 251.6 kg/m³, and 216.8 kg/m³ in Cases 2, 2-1, and 2-2, respectively. While maintaining the same P_{bottom} , decrease in $\rho_{\text{CO}_2} \mathbf{g}H$ resulted in elevated P_{head} as appeared in Figure 7(a). Due to this reason, CO_2 existed as gaseous phase adjacent to the well-head in Case 2, but no more gaseous CO_2 was present as the injected CO_2 temperature was increased.

Within the storage formation, all cases showed the accumulation of localized salt, but the peak was closer to the well as the injected CO_2 temperature decreased (Figure 7(b)); the localized salt-peak was positioned at 4.89 m, 5.16 m, and 6.37 m in Case 2 (35°C), Case 2-1 (45°C), and Case 2-2 (60°C), respectively. Previously, Kim et al. [41] noted that the localized salt-peak was developed closer to the injection well as the buoyancy effect was stronger (or greater N_{gv} , greater temperature). As seen, in our study, calculated N_{gv} of Case 2, Case 2-1, and Case 2-2 was 2.76, 2.56 and 2.32, respectively (Table 4). The relationship between injected CO_2 temperature and N_{gv} was inconsistent with the previous premise defining that less dense (or warm) CO_2 promoted vertical migration more. According to the Mass Flux equation ($F^K = \sum_{\beta} \mathbf{u}_{\beta} \rho_{\beta} X_{\beta}^K$) shown in Table 3, if CO_2 completely displaced brine adjacent to the wellbore (assuming a single-phase and single-component), the Mass Flux equation can be simplified to be the $\mathbf{F}_{\text{CO}_2} = \mathbf{u}_{\text{CO}_2} \rho_{\text{CO}_2}$. Here, average horizontal CO_2 mass flow rate (\mathbf{I}_r) is expressed to be $\mathbf{I}_r = \mathbf{F}_{\text{CO}_2} \cdot \mathbf{A}_i$. In this study, \mathbf{I}_r was 1 kg/s at 10 grid-blocks of the screen interval and the interface area (\mathbf{A}_i) of the grid-blocks was fixed to be 2.51 m². Correspondingly, \mathbf{F}_{CO_2} was constant, resulting in the fact that any change in ρ_{CO_2} should accompany variation in \mathbf{u}_{CO_2} . For example, in Case 2, Case 2-1, and Case 2-2 increase in the injected CO_2 temperature accompanied the decrease in ρ_{CO_2} , which resulted in elevated \mathbf{u}_{CO_2} within the storage formation.

Subsequently, in (6), increase in \mathbf{u}_{CO_2} , which was included in the denominator, decreased N_{gv} even if $\Delta\rho$ increased due to increasing the injected CO_2 temperature. Due to this complicated relation, increase in injected CO_2 temperature ultimately decreased the buoyancy effect on CO_2 plume while enhancing viscous force (or enhancing \mathbf{u}_{CO_2}). Additionally, the magnitude of the salt-peak (solid-line) was similar in all cases (approximately 0.19), implying that different CO_2 temperature did not cause to variation in the size of the salt-peak. Nevertheless, the location of the salt-peak was different and also coincident to the realm where the pressure (dot-dashed) was built up, implying that the salt-peak served as a local barrier which prevented the propagation of pressure pulse to the far-region.

4.2. Effect of Injection Rate. The effect of injection rate on the wellbore process and associated salt-precipitation was investigated throughout Case 2-3 (5 kg/s), Case 2 (10 kg/s), and Case 2-4 (50 kg/s) (Table 2). After 1,095 days, CO_2 profiles

in all cases reached the adiabatic condition (Figure 8(a)). At the well-head, greater injection rate pushing more CO_2 to the well-bottom induced larger well-head pressure ($P_{\text{Case 2-3}} = 7.10$ MPa, $P_{\text{Case 2}} = 7.24$ MPa, and $P_{\text{Case 2-4}} = 8.06$ MPa). Likewise, the well-bottom pressure was elevated ($P_{\text{Case 2-3}} = 9.03$ MPa, $P_{\text{Case 2}} = 9.26$ MPa, and $P_{\text{Case 2-4}} = 11.63$ MPa).

Under the adiabatic condition, change in pressure accompanied variation of temperature. For example, CO_2 profile in Case 2-4 (50 kg/s) approximately lied along $\sim 5^\circ\text{C}/\text{MPa}$ contour line for Joule-Thomson coefficient shown in Figure 3(d). Considering that such a high injection rate minimized thermal exchange between CO_2 within the wellbore and the surrounding formation, pressure difference ($\Delta P_{\text{Case 2-4}} = 11.63 - 8.06 = 3.57$ MPa) between the well-bottom and well-head resulted in change of temperature $\Delta T_{\text{Case 2-4}} = \sim 5^\circ\text{C}/\text{MPa} \times 3.57 \text{ MPa} = \sim 17.85^\circ\text{C}$, which was similar to the model-predicted temperature difference ($\Delta T_{\text{Case 2-4}} = 17^\circ\text{C}$) between the well-bottom (52°C) and well-head (35°C) (Figure 8(a)). For Cases 2-3 (5 kg/s) and 2 (10 kg/s), CO_2 profiles for relatively small injection rates fell on large Joule-Thomson coefficient ($8.7\sim 7.3^\circ\text{C}/\text{MPa}$) shown in Figure 3(d). By applying the same principle, it can be concluded that the wellbore dynamic model reasonably proved temperature disturbance on CO_2 under the adiabatic condition.

Within the storage formation, the salt-peak only occurred when the injection rate was small (Cases 2-3 and 2 in Figure 8(b)). In particular, the smaller injection rate caused to the development of the salt-peak closer from the wellbore. For example, in Case 2-3, the localized salt-precipitation was developed at 0.65 m from the injection well by surrounding the half of the screen interval (from the well-bottom to 760 m). Similarly, in the magnified figure of Figure 8(a), CO_2 profile in Case 2-3 was not linear at the well-bottom; the slope of CO_2 profile was different from 760 to 780 m due to the development of salt-barrier. Because the salt-barrier was developed immediately next to the wellbore, the horizontal CO_2 mass flow rate became almost zero (blue circles in the small figure of Figure 8(b)). Without CO_2 entering the storage formation, the built-up pressure was small ($\Delta P = 0.5$ MPa; from 8.3 MPa to 8.8 MPa) (blue dot-dashed line in Figure 8(b)). This negligible change in pressure within the storage formation implies that the developed salt-barrier effectively segregated the pressure propagation from the wellbore to the storage formation.

In high injection rate (Case 2-4, 50 kg), the elevated viscous force minimized the development of the salt-peak. Therefore, the salt-accumulation horizontally extended to 27.1 m while developing the uniform salt saturation of 0.03 (Figure 8(b)). The pressure in the storage formation increased due to high injection rate but decreased logarithmically from the wellbore. In the wellbore, vertical CO_2 mass flow rate decreased linearly from 740 m to the well-bottom (orange dashed line in the small figure of Figure 8(b)). Meanwhile, the horizontal CO_2 mass flow rate was 5 kg/s in each grid-block except at the interface of the seal and the well-bottom. Finally, the calculated N_{gv} of Case 2-3 where the dry-out front was only extended to 0.65 m was the largest (5.36), but the N_{gv} of Case 2-4 was only 0.51 with the extended dry-out front to be 27.10 m (Table 4).

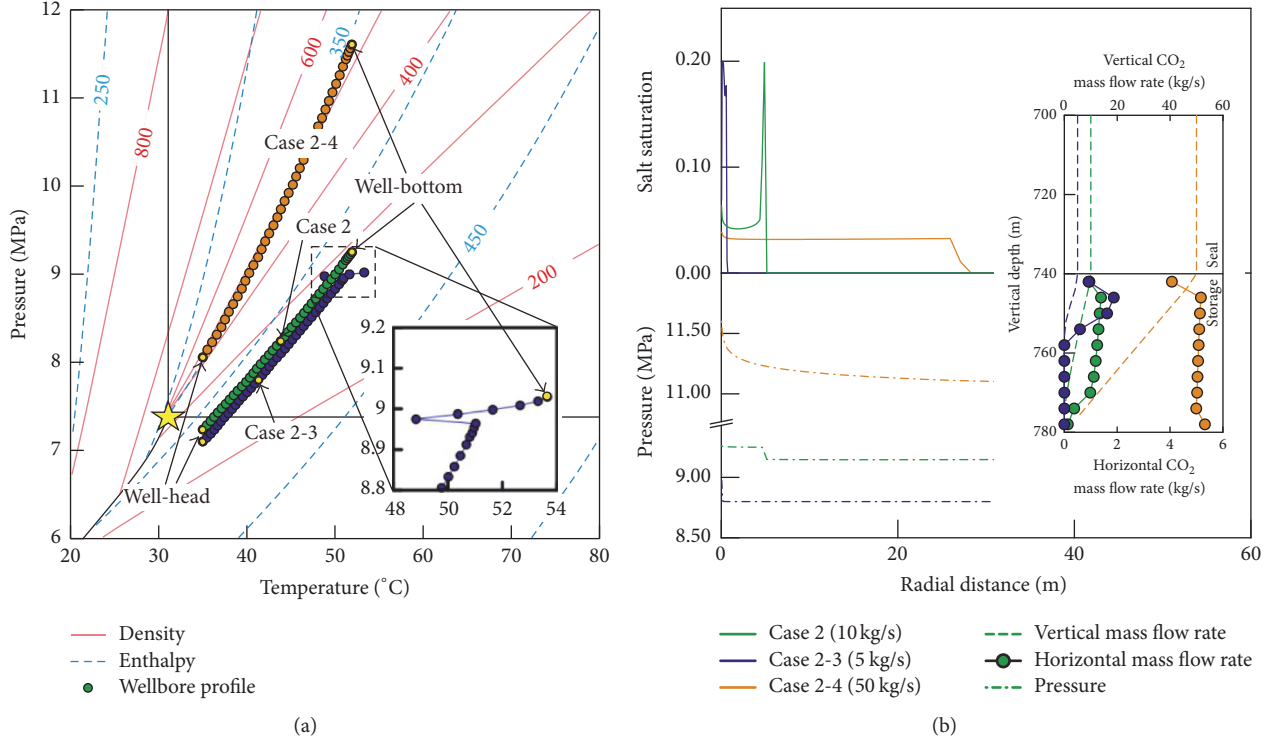


FIGURE 8: (a) Changes of CO₂ properties (density [kg/m³] and enthalpy [kJ/kg]) within the wellbore and (b) development of salt saturation [-] and built-up pressure [MPa] at the bottom layer. The small panel represents both horizontal and vertical CO₂ mass flow rate [kg/s] within the wellbore at three different injection rates (5, 10, and 50 kg/s) after 1,095 days.

4.3. Effect of Wellbore Diameter. In this study, after fixing the injected CO₂ temperature (35°C) and rate (10 kg/s), the wellbore diameter was varied at Case 2-6 (0.05 m), Case 2-5 (0.13 m), and Case 2 (0.2 m) (Table 2). As shown in Figure 9(a), CO₂ profiles of both Case 2 and Case 2-5 were almost parallel to isenthalpic lines, indicating the arrival of the adiabatic condition. CO₂ profile of Case 2-5 was slightly shifted from Case 2; discrepancies were $\Delta P_{\text{well-head}} = 0.06$ MPa, $\Delta P_{\text{well-bottom}} = 0.01$ MPa, and $\Delta T_{\text{well-bottom}} = 0.52$ °C, respectively. Similarly, magnitudes of vertical and horizontal CO₂ mass flow rates were nearly the same, and thus, both configuration of the precipitated salt-barrier and built-up pressure were almost equivalent (Figure 9(b)). N_{gv} for Case 2 and Case 2-5 also showed similar values, 2.76 and 2.77, respectively (Table 4).

When the wellbore diameter decreased furthermore to 0.05 m (Case 2-6), CO₂ profile was changed significantly (Figure 9(a)). First of all, the pressure profile was overturned. Previously, both Case 2 and Case 2-5 revealed that the wellbore pressure was elevated with increase in depth, and thus, the well-bottom pressure was the highest. However, in Case 2-6, the well-head pressure was the highest one (9.9 MPa after 1,095 days), and the pressure decreased along the depth, reaching to 9.1 MPa adjacent to the interface (746 m depth) (the magnified figure in Figure 9(a)). Below 746 m, the pressure overturned with increasing both ($\Delta P =$) 0.2 MPa and ($\Delta T =$) 0.4°C to the well-bottom. In order to understand pressure overturn within the wellbore, it is

important to understand the relationship between gravitation and frictional forces.

While CO₂ migrates through the wellbore, both gravity and frictional forces must leverage each other. Here, the gravitational force can be calculated from $\mathbf{F}_g = \rho_{\text{CO}_2} V_{\text{CO}_2} \mathbf{g}$; V_{CO_2} is CO₂ volume. The frictional force ($\mathbf{F}_f = \boldsymbol{\tau}_w \Gamma_w l_w$) can be obtained by multiplying the shear stress ($\boldsymbol{\tau}_w$) to the perimeter of wellbore ($\Gamma_w = \pi d$, d is the wellbore diameter) and the wellbore length (l_w). Considering that the wellbore is completely filled with CO₂ after 1,095 days, the shear stress ($\boldsymbol{\tau}_w$) can be calculated with the following equation [55]:

$$\boldsymbol{\tau}_w = \frac{1}{2} f \rho_{\text{CO}_2} |\mathbf{u}_{\text{CO}_2}| \mathbf{u}_{\text{CO}_2}. \quad (7)$$

Here, the friction coefficient (f) is dependent on the Reynolds number ($\text{Re} = \rho_{\text{CO}_2} u_{\text{CO}_2} d / \mu_{\text{CO}_2}$) within the wellbore. Then, \mathbf{F}_f can be expressed as

$$\mathbf{F}_f = \boldsymbol{\tau}_w \Gamma_w l_w = \frac{1}{2} f \rho_{\text{CO}_2} |\mathbf{u}_{\text{CO}_2}| \mathbf{u}_{\text{CO}_2} \Gamma_w l_w. \quad (8)$$

As described before, the vertical mass flow rate is $\mathbf{I}_r = \mathbf{F}_{\text{CO}_2}$. $A = \rho_{\text{CO}_2} \mathbf{u}_{\text{CO}_2} \pi (d/2)^2$. Subsequently, \mathbf{I}_r can be rearranged by replacing \mathbf{u}_{CO_2} in \mathbf{F}_f shown in

$$\mathbf{F}_f = 8f \frac{\mathbf{I}_r^2}{\rho_{\text{CO}_2} \pi d^3} l_w. \quad (9)$$

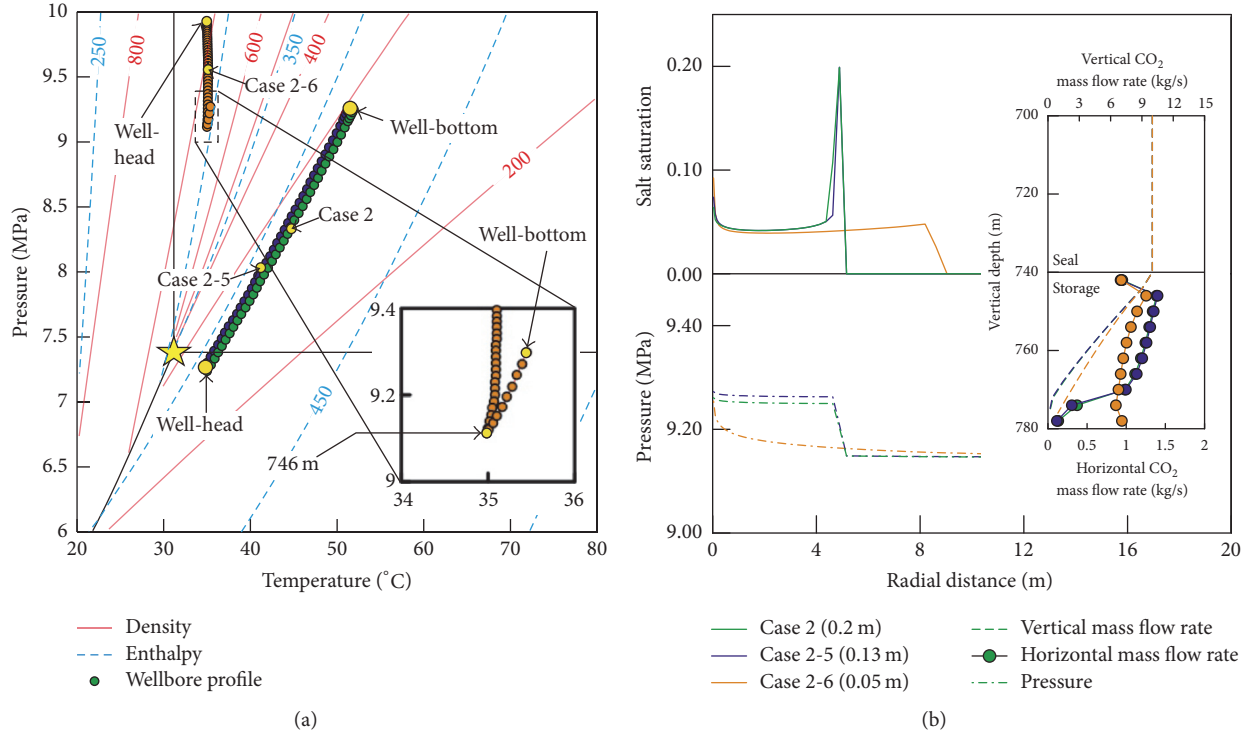


FIGURE 9: (a) Changes of CO₂ properties (density [kg/m³] and enthalpy [kJ/kg]) within the wellbore and (b) development of salt saturation [-] and built-up pressure [MPa] at the bottom layer. The small figure represents both horizontal and vertical CO₂ mass flow rate [kg/s] within the wellbore with three different wellbore diameters (0.05, 0.13, and 0.2 m) after 1,095 days.

When the CO₂ injection rate was constant at the well-head, the vertical CO₂ mass flow rate (I_r) was also invariable from the well-head to the interface (the orange dashed line in the small figure of Figure 9(b)). At constant I_r , (9) represents the fact that F_f is dependent on friction coefficient (f), CO₂ density (ρ_{CO_2}), and wellbore diameter (d) and length (l_w). In particular, the third power of wellbore diameter (d^3) in (9) indicates that the wellbore diameter can influence F_f more than any other parameters. For example, when the wellbore diameter was decreased 4 times from 0.2 m (Case 2) to 0.05 m (Case 2-6), the average F_f per unit depth between the well-head and 746 m increased from 0.5 N/m to 16.0 N/m (32 times). However, the average F_g per unit depth decreased from 82.2 N/m to 13.8 N/m (approximately 6 times). As seen, when the wellbore diameter was sufficiently small (e.g., 0.05 m), F_f was large enough to exceed F_g , which induced the overturn of the pressure profile.

Within the wellbore, the pressure relationship between two grid-blocks next to each other can be written as $P_2A = P_1A + F_g - F_f$. Here, P_1 is the pressure of the grid-block 1 positioning above the grid-block 2, and A is the cross-section area between two grid-blocks. When F_f was greater than F_g ($F_f > F_g$), P_1 should be greater than P_2 ($P_1 > P_2$), indicating that the well-head pressure was the largest along the wellbore and decreased with the depth, as seen in Case 2-6. The similar pressure profile along the wellbore was also observed by Pan et al. [24] who simulated the wellbore processes at a 100 kg/s injection rate.

Interestingly, at Case 2-6 (0.05 m), pressure was increased again with the depth below 746 m (the magnified figure in Figure 9(a)). It can be attributed to decrease in vertical CO₂ mass flow rate (I_r) at the screen interval where horizontal CO₂ mass flow rate increased (the orange circle in the small figure of Figure 9(b)). Decrease in I_r induced a decrease in F_f as seen in (9). Therefore, at the screen interval, F_g overcame F_f in turn; for example, from 746 m to the well-bottom average F_g and F_f per unit depth were 13.3 N/m and 3.9 N/m, respectively.

In addition to the pressure profile, the temperature profile along the wellbore was also perturbed due to the variation in the wellbore diameter. Different from Cases 2 and 2-5, CO₂ profile in Case 2-6 was not situated at the isenthalpic condition; from the well-head to 746 m, temperature change was negligible ($\Delta T = 0^\circ\text{C}$), and from 746 m to the well-bottom CO₂ temperature was slightly increased ($\Delta T = 0.4^\circ\text{C}$) (the magnified figure in Figure 9(a)). From the well-head to 746 m, no change in CO₂ temperature indicates that CO₂ in the wellbore did not experience major thermal disturbances due large vertical CO₂ velocity. However, below 746 m, decrease in I_r accompanied the reduction of u_{CO_2} , resulting to slight enhancement of thermal conduction between storage formation and the wellbore. Nevertheless, due to lack of thermal perturbation in Case 2-6, temperature of CO₂ entering the storage formation was almost the same to one for Case 1 (EPM model) (Figures 3(c) and 9(a)). Thermophysical properties of CO₂ entering the storage formation were similar

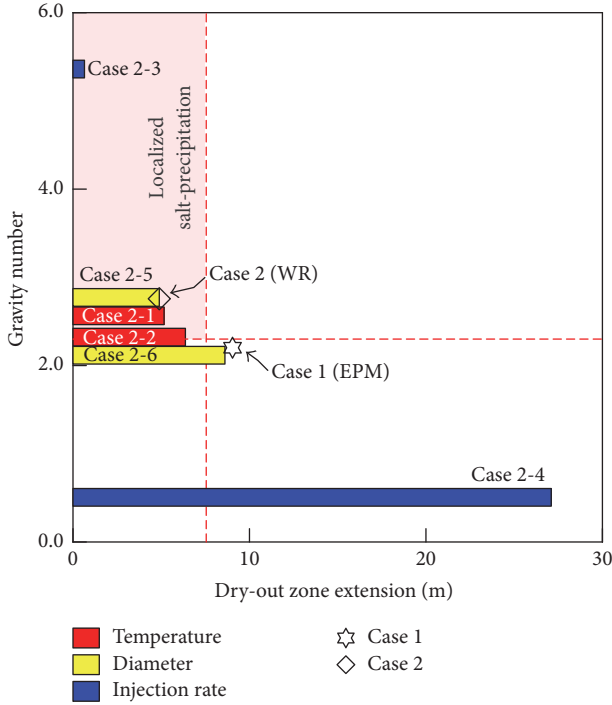


FIGURE 10: Relationship delineating between gravity number and the location of dry-out front after 1,095 days. The red box indicates the area developing the localized salt-precipitation.

to each other. As shown in Figure 9(b), the dry-out front expanded to similar distance (8.61 m) to Case 1 where the dry-out front expanded to 9.04 m without developing the localized salt-precipitation (Figure 5(c)). The calculate N_{gv} was also similar to each other (Case 2-6: 2.12 and Case 1: 2.20), which implies that the injection condition from the small diameter wellbore could mimic one for Case 1 (EPM model) under the specific conditions.

4.4. Gravity Number versus Dry-Out Front. Development of salt-barrier and its extent from the wellbore were governed by dominance between buoyancy and viscous forces, which was estimated from gravity number (N_{gv}) (Table 4). Interestingly, N_{gv} revealed the negative relationship with the extension of the dry-out front (Figure 10); the threshold of the N_{gv} developing the localized salt-barrier was approximately 2.3. At that time, the extent of localized salt-barrier was less than 8 m from the injection well. In Case 1 (the EPM model), the 10 grid-blocks imitated the wellbore where CO_2 flow was solved with Darcy's law (Figure 1(a)). Here, the salt saturation uniformly extended to 9.04 m from the wellbore without developing the localized salt-precipitation (the star symbol in Figure 10). Whereas in Case 2 (diamond symbol) adopting the WR model, N_{gv} increased while developing the localized salt-barrier, and the dry-out front became smaller than 4.89 m.

For the sensitivity study of the wellbore diameter, both predicted N_{gv} and dry-out extent were almost the same in both Case 2 (0.2 m) and Case 2-5 (0.13 m). However, when the wellbore diameter decreased further to 0.05 m (Case

2-6), the viscous force became dominant in the storage formation. Consequently, the salt was precipitated uniformly to 8.61 m. Indeed, the 0.05 m diameter wellbore behaved similarly to Case 1 (EPM model). Effect of the injected CO_2 temperature was minimal (Case 2, Case 2-1, and Case 2-2) (Figure 10). While the temperature of injected CO_2 increased, CO_2 density was decreased, which resulted in elevated CO_2 velocity (\mathbf{u}_{CO_2}) within the storage formation (see discussion in Section 4.1). Due to the elevated \mathbf{u}_{CO_2} , viscous force became dominant, and thus, the dry-out front was extended further (Case 2-1: 5.16 m and Case 2-2: 6.37 m).

Finally, sensitivity analysis with the injection rate (Case 2-3, Case 2, and Case 2-4) revealed that the injection rate plays a significant role in the dry-out zone extent and development of the localized salt-precipitation (Figure 10). When the injection rate decreased to the 5 kg/s, the localized salt-barrier was developed immediately adjacent to wellbore (0.65 m). Consequently, the salt-barrier prevented the CO_2 entering the storage formation. On the contrary, the large injection rate (50 kg/s) significantly enhanced viscous force of CO_2 plume in the storage and extended the dry-out front to the furthest distance (27.10 m) in all cases without the development of localized salt-precipitation.

5. Discussion

The numerical studies varying multiple CO_2 injection scenarios were conducted to elaborate the relationship between the wellbore process and associated changes occurred within the storage formation. Due to the complex involving wellbore flow and the salt-precipitation, the dynamic changes of CO_2 properties and wellbore conditions were necessary to be evaluated. Here, the transient, coupled wellbore-reservoir model aided to simulate the CO_2 flow more precisely than conventional EPM model for various injection scenarios in geologic CO_2 sequestration. For example, migration patterns of CO_2 plume, which was governed by thermodynamic properties of CO_2 , could affect the storage capacity and possibly leakage potentials [65]. The resulting development of the localized salt-barrier was able to significantly influence the injectivity [40, 41].

In the simulation studies, a few limitations were included. The injected CO_2 temperature at the well-head was chosen to be higher than the critical temperature. Therefore, the injected CO_2 from the well-head was always to be supercritical state. However, in the field implementation, the high CO_2 temperature implies high energetic cost requiring for heating up CO_2 [52]. Therefore, for the consideration of economically optimum CCS operations, the injection of gaseous CO_2 should be evaluated using the wellbore dynamic model too. In addition, dependent on conditions of the storage formation, the rate of conductive heat transfer between CO_2 plume and formation fluid would be different as well as the magnitude of salt-precipitation [66]. In this work, assigned temperature and pressure gradients in the model were greater than ones for typical sedimentary basins. In particular, conditions for the storage formation such as temperature, pressure gradients, and the injection depth were referred from the first pilot-scale CO_2 injection

project at Yeong-il embayment in Korea, which is located close to the tectonically active region in Japan [67]. Due to consideration of relatively warm and pressurized storage formation, CO₂ plume behavior within both the wellbore and the storage formation could be different from CO₂ injected in conventional sedimentary basins. Finally, even if this study did not consider, properties of the storage formation involving permeability, porosity, heterogeneity, burial depth, and lithology of the storage formation could influence CO₂ flux entering from the wellbore to the storage formation and resulting salt-precipitation. Nevertheless, such effects were not considered here, but they are equally important to be evaluated.

6. Conclusions

The WR model (Case 2) was selected to simulate fluid flows in both the wellbore and the storage formation. Additionally, the EPM model (Case 1) was compared to the WR model (Case 2) for evaluating any discrepancies (Figure 1). After considering the wellbore flow process, entering CO₂ mass flow rate, CO₂ phase, and thermodynamic properties at the screen interval can be predicted more accurately. Consequently, the patterns of CO₂ plume and salt-precipitation at the storage formation showed different distribution between two cases. The precipitated salt in Case 2 served as a barrier to prevent horizontal propagation of CO₂ plume from the injection well and also deteriorate the injectivity. Then, the transient, coupled wellbore-reservoir model can simulate the CO₂ flow more precisely than conventional EPM model for various injection scenarios in GCS. Additionally, under the different injection conditions (injected CO₂ temperature, injection rate, and wellbore diameter) the simulation results, such as pressure build-up, CO₂ migration, and patterns of salt-precipitation, showed various values. Therefore, through a series of multiple simulations, it can be concluded that the wellbore flow processes can play an important role in the CO₂ injection scenarios and significantly influence the changes which occurred by CO₂ injection in the storage formation. The dynamic changes of CO₂ properties and wellbore conditions are necessary for modeling the CO₂ migration and development of salt-precipitation at the storage formation. For example, patterns of CO₂ plume, which was determined by thermodynamic properties of CO₂, can particularly affect the storage capacity and possibly leakage potentials. In addition, development of the localized salt-barrier can significantly influence the injectivity. Therefore, this study not only deepens understanding of wellbore flow process but also can provide theoretical support for the commercial-scale of CO₂ injection projects.

Nomenclature

A : Cross-sectional area, m²
 C_0 : Shape factor
 C_R : Heat capacity of the rock, J/kg-K
 g : Acceleration of gravity vector, m/s²

f : The fanning friction coefficient, dimensionless
 F : Mass or energy flux vector, kg/m²·s or W/m²
 h : Specific enthalpy, J/kg
 k : Permeability, m²
 k_0 : Initial permeability, m²
 k_r : Relative permeability, m²
 K_u : Kutateladze number
 M : Mass accumulation term, kg/m³
 n : Outward unit normal vector
 P : Pressure, Pa
 P_0 : The strength coefficient
 P_c : Capillary pressure, Pa
 q : Mass or heat source term, kg/m³·s or W/m³
 S : Saturation
 S_{gr} : Supercritical-phase CO₂ residual saturation
 S_{lr} : Brine residual saturation
 S_{ls} : Saturated brine saturation
 t : Time, s
 T : Temperature, °C
 u : Velocity, m/s
 U : Internal energy, J/kg
 V_n : Volume, m³
 X : Mass fraction
 z : Z-coordinate (positive upward), m.

Greek Letters

Γ : The fractional length of the pore bodies, m
 Γ_n : Area of closed surface, m²
 Γ_w : The perimeter of the well cross-section, m
 θ : Angle between wellbore and vertical direction, °
 λ : Thermal conductivity, W/°C·m
 λ' : The parameter depending on pore geometry
 μ : Dynamic viscosity, kg/m·s
 ρ : Density, kg/m³
 ρ_m^* : Profile-adjusted average density, kg/m³
 ρ_m : The density of the gas-liquid mixture, kg/m³
 ϕ : Porosity
 ϕ_r : The fraction of original porosity at which permeability is reduced to zero
 ϕ_0 : Initial Porosity.

Subscripts and Superscripts

β : Phase index
 d : Drift
 G : Gas
 κ : Component index
 L : Liquid
 m : Mixture
 $NK1$: Energy component

R: Rock
 $r\beta$: Relative for phase β
 S: Solid.

Conflicts of Interest

The authors declare that there are no conflicts of interest regarding the publication of this paper.

Acknowledgments

This research was partially supported by Demonstration-Scale Offshore CO₂ Storage Project in Pohang, Basin, Republic of Korea, funded from Energy Efficiency & Resources of the Korea Institute of Energy Technology Evaluation and Planning (KETEP) which was granted financial resource from the Ministry of Trade, Industry & Energy, Republic of Korea (no. 20162010201980) and also supported by Basic Science Research Program through the National Research Foundation of Korea (NRF) funded by the Ministry of Education (no. 2016R1D1A1B01008715). The authors also acknowledge financial support by the Basic Research Project of the Korea Institute of Geoscience and Mineral Resources (KIGAM) funded by the Ministry of Science and ICT.

References

- [1] IPCC, *Special Report on Carbon Dioxide Capture and Storage*, Cambridge University Press, Cambridge, U.K, 2005.
- [2] H. Audus, "Greenhouse gas mitigation technology: An overview of the CO₂ capture and sequestration studies and further activities of the IEA greenhouse gas R&D programme," *Energy*, vol. 22, no. 2-3, pp. 217–221, 1997.
- [3] S. Bachu, "CO₂ storage in geological media: role, means, status and barriers to deployment," *Progress in Energy and Combustion Science*, vol. 34, no. 2, pp. 254–273, 2008.
- [4] J. T. Birkholzer, C. M. Oldenburg, and Q. Zhou, "CO₂ migration and pressure evolution in deep saline aquifers," *International Journal of Greenhouse Gas Control*, pp. 203–220, 2015.
- [5] K. Michael, A. Golab, V. Shulakova et al., "Geological storage of CO₂ in saline aquifers—a review of the experience from existing storage operations," *International Journal of Greenhouse Gas Control*, vol. 4, no. 4, pp. 659–667, 2010.
- [6] S. D. Hovorka, S. M. Benson, C. Doughty et al., "Measuring permanence of CO₂ storage in saline formations: the Frio experiment," *Environmental Geosciences*, vol. 13, no. 2, pp. 105–121, 2006.
- [7] K. Sato, S. Mito, T. Horie et al., "Monitoring and simulation studies for assessing macro- and meso-scale migration of CO₂ sequestered in an onshore aquifer: Experiences from the Nagaoka pilot site, Japan," *International Journal of Greenhouse Gas Control*, vol. 5, no. 1, pp. 125–137, 2011.
- [8] H. Würdemann, F. Möller, M. Kühn et al., "CO₂ SINK-From site characterisation and risk assessment to monitoring and verification: One year of operational experience with the field laboratory for CO₂ storage at Ketzin, Germany," *International Journal of Greenhouse Gas Control*, vol. 4, no. 6, pp. 938–951, 2010.
- [9] J. Litynski, S. Plasynski, L. Spangler et al., "U.S. Department of Energy's Regional Carbon Sequestration Partnership Program: Overview," *Energy Procedia*, vol. 1, no. 1, pp. 3959–3967, 2009.
- [10] J. Litynski, T. Rodosta, D. Vikara, and R. Srivastava, "U.S. DOE's R&D Program to develop infrastructure for carbon storage: Overview of the regional carbon sequestration partnerships and other R&D field projects," *Energy Procedia*, vol. 37, pp. 6527–6543, 2013.
- [11] T. A. Torp and J. Gale, "Demonstrating storage of CO₂ in geological reservoirs: The Sleipner and SACS projects," *Energy*, vol. 29, no. 9-10, pp. 1361–1369, 2004.
- [12] C. Preston, M. Monea, W. Jazrawi et al., "IEA GHG Weyburn CO₂ monitoring and storage project," *Fuel Processing Technology*, vol. 86, no. 14-15, pp. 1547–1568, 2005.
- [13] A. Mathieson, J. Midgely, I. Wright, N. Saoula, and P. Ringrose, "In Salah CO₂ storage JIP: CO₂ sequestration monitoring and verification technologies applied at Krechba, Algeria," *Energy Procedia*, vol. 4, pp. 3596–3603, 2011.
- [14] R. J. Finley, S. M. Frailey, H. E. Leetaru, O. Senel, M. L. Couëslan, and S. Marsteller, "Early operational experience at a one-million tonne CCS demonstration project, Decatur, Illinois, USA," *Energy Procedia*, vol. 37, pp. 6149–6155, 2013.
- [15] J. M. Nordbotten, M. A. Celia, S. Bachu, and H. K. Dahle, "Semi-analytical solution for CO₂ leakage through an abandoned well," *Environmental Science & Technology*, vol. 39, no. 2, pp. 602–611, 2005.
- [16] B. Hof, C. W. H. Van Doorne, J. Westerweel et al., "Experimental observation of nonlinear traveling waves in turbulent pipe flow," *Science*, vol. 305, no. 5690, pp. 1594–1598, 2004.
- [17] C. E. Brennen, *Fundamentals of Multiphase Flows*, Cambridge University Press, 2005.
- [18] S. E. Ingebritsen, W. E. Sanford, and C. E. Neuzil, "Groundwater in Geologic Processes," Cambridge University Press, New York, NY, USA, Second edition, 2006.
- [19] E. Lindeberg, "Modelling pressure and temperature profile in a CO₂ injection well," *Energy Procedia*, vol. 4, pp. 3935–3941, 2011.
- [20] C. M. Oldenburg, C. Doughty, C. A. Peters, and P. F. Dobson, "Simulations of long-column flow experiments related to geologic carbon sequestration: Effects of outer wall boundary condition on upward flow and formation of liquid CO₂," *Greenhouse Gases: Science and Technology*, vol. 2, no. 4, pp. 279–303, 2012.
- [21] M. Lu and L. D. Connell, "Non-isothermal flow of carbon dioxide in injection wells during geological storage," *International Journal of Greenhouse Gas Control*, vol. 2, no. 2, pp. 248–258, 2008.
- [22] M. Lu and L. D. Connell, "Transient, thermal wellbore flow of multispecies carbon dioxide mixtures with phase transition during geological storage," *International Journal of Multiphase Flow*, vol. 63, pp. 82–92, 2014.
- [23] X. Li, R. Xu, L. Wei, and P. Jiang, "Modeling of wellbore dynamics of a CO₂ injector during transient well shut-in and start-up operations," *International Journal of Greenhouse Gas Control*, vol. 42, pp. 602–614, 2015.
- [24] L. Pan, C. M. Oldenburg, K. Pruess, and Y.-S. Wu, "Transient CO₂ leakage and injection in wellbore-reservoir systems for geologic carbon sequestration," *Greenhouse Gases: Science and Technology*, vol. 1, no. 4, pp. 335–350, 2011.
- [25] D. Liu, Y. Li, L. Xu, and Y. Yu, "Numerical investigation of the influence of interaction between wellbore flow and lateral reservoir flow on CO₂ geological sequestration," *Environmental Earth Sciences*, vol. 74, no. 1, pp. 715–726, 2015.

- [26] M. Lu and L. D. Connell, "The transient behaviour of CO₂ flow with phase transition in injection wells during geological storage - Application to a case study," *Journal of Petroleum Science and Engineering*, vol. 124, pp. 7–18, 2014.
- [27] W. S. Han, G. A. Stillman, M. Lu, C. Lu, B. J. McPherson, and E. Park, "Evaluation of potential nonisothermal processes and heat transport during CO₂ sequestration," *Journal of Geophysical Research: Solid Earth*, vol. 115, no. 7, Article ID B07209, 2010.
- [28] C. M. Oldenburg, "Joule-Thomson cooling due to CO₂ injection into natural gas reservoirs," *Energy Conversion and Management*, vol. 48, no. 6, pp. 1808–1815, 2007.
- [29] V. Vilarrasa and J. Rutqvist, "Thermal effects on geologic carbon storage," *Earth-Science Reviews*, vol. 165, pp. 245–256, 2017.
- [30] J. Henniges, A. Liebscher, A. Bannach et al., "P-T- ρ and two-phase fluid conditions with inverted density profile in observation wells at the CO₂ storage site at Ketzin (Germany)," *Energy Procedia*, vol. 4, pp. 6085–6090, 2011.
- [31] V. Vilarrasa, O. Silva, J. Carrera, and S. Olivella, "Liquid CO₂ injection for geological storage in deep saline aquifers," *International Journal of Greenhouse Gas Control*, vol. 14, pp. 84–96, 2013.
- [32] N. Spycher and K. Pruess, "CO₂-H₂O mixtures in the geological sequestration of CO₂. II. Partitioning in chloride brines at 12–100°C and up to 600 bar," *Geochimica et Cosmochimica Acta*, vol. 69, pp. 3309–3320, 2005.
- [33] K. Pruess and J. García, "Multiphase flow dynamics during CO₂ disposal into saline aquifers," *Environmental Geology*, vol. 42, no. 2-3, pp. 282–295, 2002.
- [34] L. André, Y. Peysson, and M. Azaroual, "Well injectivity during CO₂ storage operations in deep saline aquifers - Part 2: Numerical simulations of drying, salt deposit mechanisms and role of capillary forces," *International Journal of Greenhouse Gas Control*, vol. 22, pp. 301–312, 2014.
- [35] G. Bacci, A. Korre, and S. Durucan, "An experimental and numerical investigation into the impact of dissolution/precipitation mechanisms on CO₂ injectivity in the wellbore and far field regions," *International Journal of Greenhouse Gas Control*, vol. 5, no. 3, pp. 579–588, 2011.
- [36] J. Oh, K.-Y. Kim, W. S. Han, T. Kim, J.-C. Kim, and E. Park, "Experimental and numerical study on supercritical CO₂/brine transport in a fractured rock: Implications of mass transfer, capillary pressure and storage capacity," *Advances in Water Resources*, vol. 62, pp. 442–453, 2013.
- [37] Y. Peysson, L. André, and M. Azaroual, "Well injectivity during CO₂ storage operations in deep saline aquifers-Part I: Experimental investigation of drying effects, salt precipitation and capillary forces," *International Journal of Greenhouse Gas Control*, vol. 22, pp. 291–300, 2014.
- [38] H. Alkan, Y. Cinar, and E. B. Ülker, "Impact of Capillary Pressure, Salinity and In situ Conditions on CO₂ Injection into Saline Aquifers," *Transport in Porous Media*, vol. 84, no. 3, pp. 799–819, 2010.
- [39] K.-Y. Kim, W. S. Han, J. Oh, E. Park, and P.-K. Lee, "Flow Dynamics of CO₂/brine at the Interface Between the Storage Formation and Sealing Units in a Multi-layered Model," *Transport in Porous Media*, vol. 105, no. 3, pp. 611–633, 2014.
- [40] E. Guyant, W. S. Han, K.-Y. Kim, M.-H. Park, and B.-Y. Kim, "Salt precipitation and CO₂/brine flow distribution under different injection well completions," *International Journal of Greenhouse Gas Control*, vol. 37, pp. 299–310, 2015.
- [41] K.-Y. Kim, W. S. Han, J. Oh, T. Kim, and J.-C. Kim, "Characteristics of salt-precipitation and the associated pressure build-up during CO₂ storage in saline aquifers," *Transport in Porous Media*, vol. 92, no. 2, pp. 397–418, 2012.
- [42] K. Pruess and N. Müller, "Formation dry-out from CO₂ injection into saline aquifers: 1. effects of solids precipitation and their mitigation," *Water Resources Research*, vol. 45, no. 3, Article ID W03402, 2009.
- [43] M. Bahonar, J. Azaiez, and Z. Chen, "Transient nonisothermal fully coupled wellbore/reservoir model for gas-well testing, part 1: Modelling," *Journal of Canadian Petroleum Technology*, vol. 50, no. 9-10, pp. 37–50, 2011.
- [44] D. Liu, Y. Li, S. Song, and R. Agarwal, "Simulation and analysis of lithology heterogeneity on CO₂ geological sequestration in deep saline aquifer: a case study of the Ordos Basin," *Environmental Earth Sciences*, vol. 75, pp. 1–13, 2016.
- [45] K. Rasmusson, C.-F. Tsang, Y. Tsang et al., "Distribution of injected CO₂ in a stratified saline reservoir accounting for coupled wellbore-reservoir flow," *Greenhouse Gases: Science and Technology*, vol. 5, no. 4, pp. 419–436, 2015.
- [46] L. André, M. Azaroual, and A. Menjot, "Numerical simulations of the thermal impact of supercritical CO₂ injection on chemical reactivity in a carbonate saline reservoir," *Transport in Porous Media*, vol. 82, pp. 247–274, 2010.
- [47] T. Giorgis, M. Carpita, and A. Battistelli, "2D modeling of salt precipitation during the injection of dry CO₂ in a depleted gas reservoir," *Energy Conversion and Management*, vol. 48, no. 6, pp. 1816–1826, 2007.
- [48] T. J. Tambach, D. Loeve, C. Hofstee, W.-J. Plug, and J. G. Maas, "Effect of CO₂ Injection on Brine Flow and Salt Precipitation After Gas Field Production," *Transport in Porous Media*, vol. 108, no. 1, pp. 171–183, 2015.
- [49] L. Pan, B. Freifeld, C. Doughty, and S. Zakem, "Fully coupled wellbore-reservoir modeling of geothermal heat extraction using CO₂ as the working fluid," *Geothermics*, vol. 53, pp. 100–113, 2015.
- [50] A. T. Corey, "The Interrelation between gas and oil relative permeabilities," *Producers Monthly*, vol. 19, p. 38, 1954.
- [51] M. T. van Genuchten, "A closed-form equation for predicting the hydraulic conductivity of unsaturated soils," *Soil Science Society of America Journal*, vol. 44, no. 5, pp. 892–898, 1980.
- [52] S. Goodarzi, A. Settari, M. D. Zoback, and D. W. Keith, "Optimization of a CO₂ storage project based on thermal, geochemical and induced fracturing effects," *Journal of Petroleum Science and Engineering*, vol. 134, pp. 49–59, 2015.
- [53] K. Pruess, C. Oldenburg, and G. Moridis, *TOUGH2 User's Guide, Version 2*, Lawrence Berkeley National Laboratory, Berkeley, Calif, USA, 1999.
- [54] L. Pan, N. Spycher, C. Doughty, and K. Pruess, "ECO2N V. 2.0: A New TOUGH2 Fluid Property Module for Mixtures of Water, NaCl, and CO₂," Tech. Rep. LBNL–6930E, 2014.
- [55] L. Pan, C. Oldenburg, Y. Wu, and K. Pruess, "T2Well/ECO2N version 1.0: multiphase and non-isothermal model for coupled wellbore-reservoir flow of carbon dioxide and variable salinity water," Tech. Rep. LBNL-4291E, Lawrence Berkeley National Laboratory, Berkeley, Calif, USA, 2011.
- [56] K. Pruess, *ECO2N: A TOUGH2 Fluid Property Module for Mixtures of Water, NaCl, and CO₂*, Lawrence Berkeley National Laboratory, Berkeley, Calif, USA, 2005.
- [57] H. Shi, J. A. Holmes, L. J. Durlofsky et al., "Drift-flux modeling of two-phase flow in wellbores," *SPE Journal*, vol. 10, no. 1, pp. 24–33, 2005.

- [58] P. Jiang, X. Li, R. Xu et al., "Thermal modeling of CO₂ in the injection well and reservoir at the Ordos CCS demonstration project, China," *International Journal of Greenhouse Gas Control*, vol. 23, pp. 135–146, 2014.
- [59] A. Verma and K. Pruess, "Thermohydrological conditions and silica redistribution near high-level nuclear wastes emplaced in saturated geological formations," *Journal of Geophysical Research: Atmospheres*, vol. 93, no. 2, pp. 1159–1173, 1988.
- [60] D. Zhou, F. J. Fayers, and F. M. Orr, "Scaling of multiphase flow in simple heterogeneous porous media," *Society of Petroleum Engineers*, vol. 12, no. 3, 1997.
- [61] S. Taku Ide, K. Jessen, and F. M. Orr Jr., "Storage of CO₂ in saline aquifers: Effects of gravity, viscous, and capillary forces on amount and timing of trapping," *International Journal of Greenhouse Gas Control*, vol. 1, no. 4, pp. 481–491, 2007.
- [62] A. Cooksy, *Physical Chemistry Thermodynamics, Statistical Mechanics, Kinetics*, Pearson Education, New Jersey, NJ, USA, 2013.
- [63] R. Span and W. Wagner, "A new equation of state for carbon dioxide covering the fluid region from the triple-point temperature to 1100 K at pressures up to 800 MPa," *Journal of Physical and Chemical Reference Data*, vol. 25, no. 6, pp. 1509–1596, 1996.
- [64] V. Vilarrasa, J. Carrera, D. Bolster, and M. Dentz, "Semianalytical Solution for CO₂ Plume Shape and Pressure Evolution During CO₂ Injection in Deep Saline Formations," *Transport in Porous Media*, vol. 97, no. 1, pp. 43–65, 2013.
- [65] K. Pruess, "Numerical studies of fluid leakage from a geologic disposal reservoir for CO₂ show self-limiting feedback between fluid flow and heat transfer," *Geophysical Research Letters*, vol. 32, no. 14, pp. 1–4, 2005.
- [66] W. S. Han, K.-Y. Kim, E. Park, B. J. McPherson, S.-Y. Lee, and M.-H. Park, "Modeling of spatiotemporal thermal response to CO₂ injection in saline formations: interpretation for monitoring," *Transport in Porous Media*, vol. 93, no. 3, pp. 381–399, 2012.
- [67] J. Hwang, S. Baek, H. Lee, W. Jung, and W. Sung, "Evaluation of CO₂ storage capacity and injectivity using a relief well in a saline aquifer in Pohang basin, offshore South Korea," *Geosciences Journal*, vol. 20, no. 2, pp. 239–245, 2016.

Research Article

The Form of Waiting Time Distributions of Continuous Time Random Walk in Dead-End Pores

Yusong Hou, Jianguo Jiang , and J. Wu

School of Earth Sciences and Engineering, Nanjing University, Nanjing, China

Correspondence should be addressed to Jianguo Jiang; jianguo.jiang@nju.edu.cn

Received 22 July 2017; Revised 16 November 2017; Accepted 12 December 2017; Published 8 January 2018

Academic Editor: Dan Lu

Copyright © 2018 Yusong Hou et al. This is an open access article distributed under the Creative Commons Attribution License, which permits unrestricted use, distribution, and reproduction in any medium, provided the original work is properly cited.

Anomalous dispersion of solute in porous media can be explained by the power-law distribution of waiting time of solute particles. In this paper, we simulate the diffusion of nonreactive tracer in dead-end pores to explore the waiting time distributions. The distributions of waiting time in different dead-end pores show similar power-law decline at early time and transit to an exponential decline in the end. The transition time between these two decline modes increases with the lengths of dead-end pores. It is well known that power-law distributions of waiting time may lead to anomalous (non-Fickian) dispersion. Therefore, anomalous dispersion is highly dependent on the sizes of immobile zones. According to the power-law decline, we can directly get the power index from the structure of dead-end pores, which can be used to judge the anomalous degree of solute transport in advance.

1. Introduction

Anomalous dispersion widely exists in solute transport in ground water or in other porous media [1–7], which makes it difficult to simulate solute transport by traditional advection-dispersion equation. In recent years, scholars have developed a few models to describe the anomalous transport such as continuous time random walk (CTRW) [8–12] and fractional advection-dispersion equation [13–16]. The simulations by CTRW can agree well with the experimental data by fitting the transfer probability density function $\varphi(x, t)$ [2, 17]. Assume $\varphi(x, t)$ has the form $\varphi(x, t) = \phi(x)\psi(t)$, where $\psi(t)$ denotes the waiting time distribution between two successive jumps. Corresponding to anomalous transport, $\psi(t)$ should follow a power-law decline, that is, $\psi(t) \sim t^{-1-\alpha}$ with $0 < \alpha < 2$ [17]. Many researchers have investigated the form of $\psi(t)$ by simulating the transport of solute in porous media [18–21], which may show power-law decline. However, fitting parameters from transport data in complex fluid fields are not suitable to uncover the physical mechanism of the power-law decline. An alternative way for the investigation of the form of $\psi(t)$ is to directly simulate the motion of solute particles in immobile zones. In this paper, we construct the dead-end pores as immobile zones and simulate the waiting time distributions to explore the modes of solute transport.

$\psi(t)$ is more likely to show an exponential decline than a power-law decline because particles in stagnant zones are determined by diffusion equation. As many experiments show, an anomalous transport eventually converts to a Fickian process [2, 19]. Consequently, in the mathematical models, the power-law decline is often truncated arbitrarily by an exponential decline in the assumption of $\psi(t)$ [4, 9]. However, why does there exist a power-law decline of waiting time distribution? When does a power-law decline begin to convert to an exponential decline? In addition, it is not clear which factors determine the value of the power index α . To explore the general form of waiting time distribution function, we directly simulate $\psi(t)$ in dead-end pores. In this paper, we select three types of dead-end pores. By these dead-end pores with different sizes and shapes, we aim to get a universal form of $\psi(t)$, which may show both the power-law part (corresponding to anomalous transport) and the exponential decline part (Fickian transport). In addition, from our simulations, we expect to get the index α which describes the anomalous degree.

2. Method of Simulation

In the framework of CTRW model for solute transport, the distribution of waiting time between two successive jumps

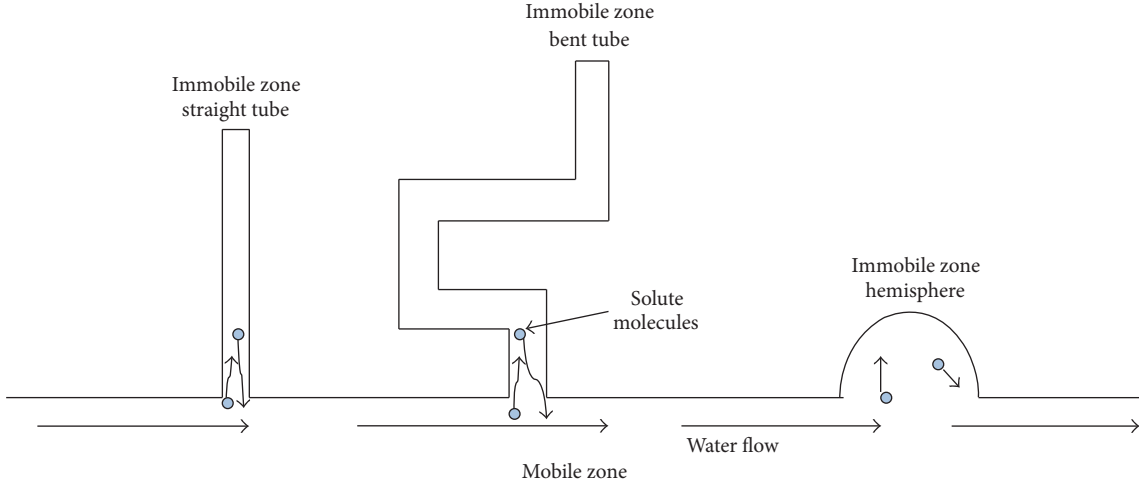


FIGURE 1: The schematic diagram of mobile zone and immobile zone. Three types of dead-end pores, that is, straight tube, bent tube, and hemisphere, represent the immobile zones.

determines whether the dispersion is anomalous or not. For simplicity, skipping over the displacement distribution $\phi(x)$ of jumps, we only investigate the waiting time distribution $\psi(t)$. In our physical picture, waiting events happen when nonreactive particles are trapped in immobile zones. Dead-end pores are typical immobile zones. The flow velocity in a dead-end pore is zero and solute particles escape only by diffusion. The waiting time is the period from entering a dead-end pore to moving out of it. We consider three types of dead-end pores: straight tube, bent tube, and hemisphere as illustrated in Figure 1. These three dead-end pores lie above the flow tube which represents the mobile zone. Tracer particles on the interface between the flow tube and dead-end pores may enter the dead-end pore by diffusion. We begin to count waiting time when the particles pass through interfaces to dead-end pores and end counting when particles pass through interfaces to the flow tube.

For simplicity, we use the surviving probability $P(t)$ in the immobile zone to describe the waiting time distribution $\psi(t)$; the relation between them can be written as

$$P(t) = 1 - \int_0^t \psi(\tau) d\tau = \int_t^\infty \psi(\tau) d\tau, \quad (1)$$

or $\Psi(t) = -dP(t)/dt$. Compared to $P(t)$, $\Psi(t)$ fluctuates more violently as the derivative enlarges the fluctuations of simulated values of $P(t)$.

$P(t)$ can be directly calculated by counting the number of particles in the dead-end pores and the particles will not be tracked when they move out of immobile zones. Then, $\psi(t)$ is obtained from the derivative of $P(t)$. However, the probability $P(t)$ is very small when the time is large, especially if $P(t)$ decreases in an exponential form. By conventional particle tracing method with each particle of the same weight, $P(t)$ is proportional to the number of particles staying in the immobile zone. The number corresponding to small $P(t)$ is zero or fluctuates violently. To simulate $P(t)$ in a wide range, variable weight for tracing particles is adopted in this paper. In recent years the pruned-enriched method has been

developed to simulate the random walk with variable weight [22–24]. We use the pruned-enriched method to adjust the weight according to $P(t)$. At the beginning of simulation, each particle is released at the interface between the flow tube and dead-end pores with the same weight $W(0) = 1$. Consider the case that the simulated particle is still in the dead-end pore at the time $t = n\Delta t$. Define $r = W(t)/P(t)$. If $r > 1$, this particle is split in $\text{Int}(r)$ (the integer part of r) copies and each copy continues to diffuse with a new weight $W_{\text{new}} = W(t)/\text{Int}(r)$. If $r \leq 1$, we continue to simulate the diffusion of the particle with probability $r' = 1/\text{Int}(1/r)$ and the new weight W_{new} is adjusted to $W(t)/r'$. In other words, the simulation of the particle is ceased with the probability $1 - r'$. $P(t)$ is updated in every step. By the scheme of variable weight, the smallest probability we could simulate can be reduced by many orders of magnitude. In the whole range of simulated time, the number of samples for each t has a nearly uniform distribution. Without the scheme of variable weights, the number of visited samples is proportional to $P(t)$ and decreases sharply with t , which leads to violent oscillation of simulated $P(t)$.

3. Results and Discussion

For most heavy metal ions, the order of magnitude of diffusion coefficient is about $10^{-10} \text{ m}^2/\text{s}$. In this paper, the diffusion coefficient of solute is set to be $4 \times 10^{-10} \text{ m}^2/\text{s}$. When tracer particles enter the dead-end pores through the interface, we start the time. When particles escape from the dead-end pores, the tracing process of this particle will be terminated. For simplicity, particles after escaping from a dead-end pore cannot be allowed to enter the same dead-end pore again because they drift in the flow tube (mobile zone). Firstly, we consider the surviving probability $P(t)$ in large dead-end pores. The lengths of straight tube and bent tube are both taken 10 mm and the radius of hemisphere is taken 15 mm. Figure 2 shows the power-law decrease of simulated $P(t)$ and $\psi(t)$. The $P(t)$ and $\psi(t)$ in bent tube and in

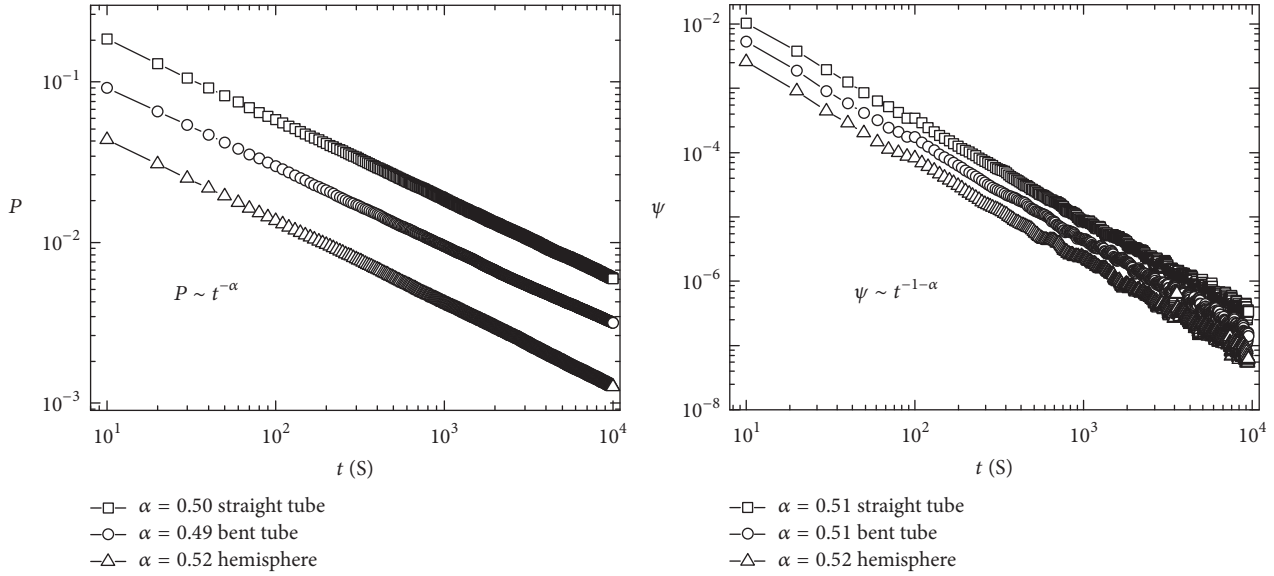


FIGURE 2: The power-law form of the surviving probability $P(t)$ and the waiting time distribution $\Psi(t)$ in dead-end pores at early time. The power α approximates to 0.5 for each type of dead-end pore.

hemisphere are reduced by the factor 1/2 and 1/4, respectively, which makes the comparison in Figure 2 clear without altering the power law. We take the values of power from the data of $P(t)$ because $\psi(t)$ has more violent fluctuations. During the time interval $10\text{ s} - 10^4\text{ s}$, $P(t)$ decays in a power law, that is, $P(t) \sim t^{-\alpha}$. Corresponding to straight tube, bent tube, and hemisphere, the value of α is 0.50, 0.49, and 0.52, respectively. They are close to 0.5. Thus, it is reasonable to suppose that the power α is approximately equal to 0.5 in these three types of dead-end pores.

Let us discuss the physical meaning of the simulated results. This power-law form of $P(t)$ with $\alpha = 0.5$ results in anomalous dispersion, which can also be described by time-fractional advection-dispersion equation (tFADE). If the waiting time distribution has the form $\psi(t) \sim t^{-1-\alpha}$, the concentration $C(x, t)$ can be written as [25]

$$\frac{\partial C(x, t)}{\partial t} = {}_0D_t^{1-\alpha} L[C(x, t)], \quad (2)$$

where ${}_0D_t^{1-\alpha}$ is the fractional Riemann-Liouville operator; that is,

$${}_0D_t^{1-\alpha} f(t) = \frac{1}{\Gamma(\alpha)} \frac{\partial}{\partial t} \int_0^t d\tau \frac{f(\tau)}{(t-\tau)^{1-\alpha}}. \quad (3)$$

Here, $L[C(x, t)]$ is the operator representing dispersion. Therefore, the fractional order of time derivation is about 0.5 if anomalous dispersion is caused by solute trapping in long dead-end pores.

The sizes of above dead-end pores are set large in the simulations. Let us consider the dead-end pores with short length. Tracer particles can jump out of them easily. Which form does surviving probability density $P(t)$ show? To investigate it, we set the length of straight tubes to be 1 mm, 2 mm, 3 mm, and 4 mm, respectively. The diffusion coefficient is the

same as above. The simulated $P(t)$ and $\psi(t)$ are illustrated in Figure 3. At the early time, $P(t)$ and $\psi(t)$ in each straight tube decrease with the power law. As time increases, $P(t)$ and $\psi(t)$ deviate from the power-law decline. The shorter the length is, the earlier the deviation happens. Therefore, anomalous dispersion strongly depends on the sizes of dead-end pores. The duration of anomalous dispersion becomes longer as the length of dead-end pore increases.

Now let us consider the form of $P(t)$ at large time in small dead-end pores. We also investigate three types of dead-end pores, that is, straight tube, bent tube, and hemisphere, but their sizes are shortened. The length of straight tube and bent tube is set to be 2 mm and 3 mm, respectively. The radius of hemisphere is set to be 3 mm. Using the particle tracing method with viable weight, we can simulate the surviving probability $P(t)$ with a high resolution. Figure 4 shows that $\log(P(t))$ and $\log(\psi(t))$ are linear with time t in every type of dead-end pore, which indicates the exponential decline when t is large. The exponential decline can be easily explained by immobile-mobile model [26] by neglecting the variability of concentration in immobile zones, which reads

$$\frac{\partial C_{\text{im}}(x, t)}{\partial t} = -\beta(C_{\text{im}} - C_{\text{m}}), \quad (4)$$

where C_{im} and C_{m} represent the concentration in dead-end pores (immobile zones) and in flow tube (mobile zones), respectively. $C_{\text{im}}(x, t)$ is proportional to $P(t)$. If $C_{\text{m}} = 0$ at large t because of drift with water flow, C_{im} decreases as $C_{\text{im}} \sim e^{-\beta t}$, that is, an exponential decline.

From simulations above, we can see that surviving probability $P(t)$ decreases with time in a power law at early time and in an exponential form at large time. The power law with $\alpha \approx 0.5$ corresponds to an anomalous dispersion, while the exponential decline corresponds to a Fickian dispersion. Therefore, it is important to determine the transition time

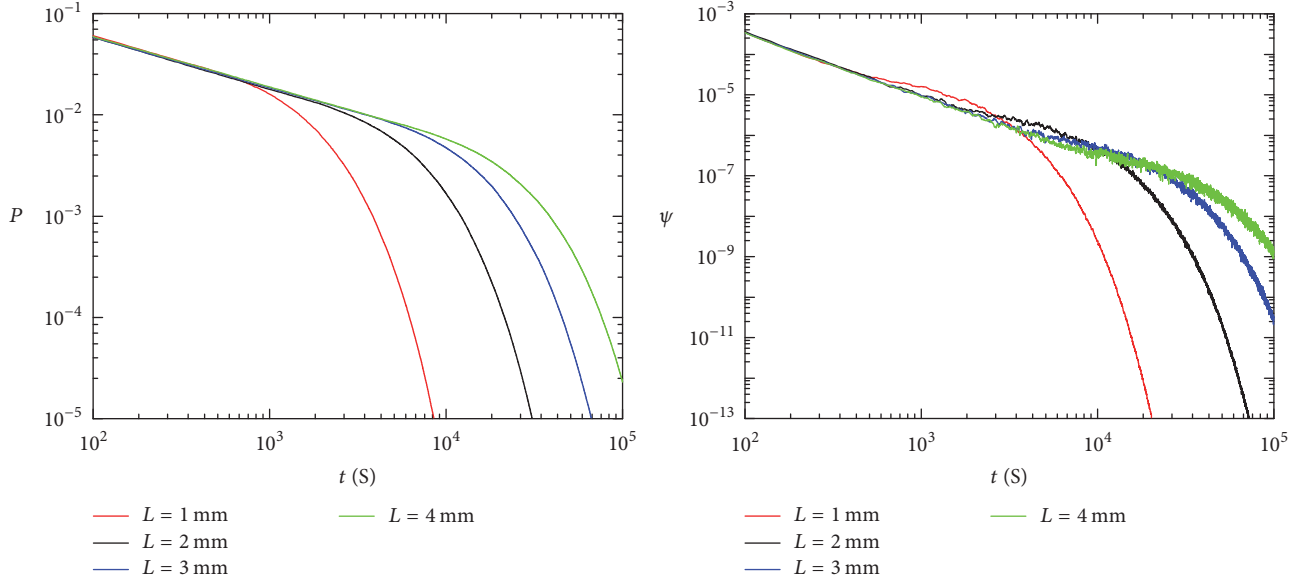


FIGURE 3: The deviation from the power-law decline of $P(t)$ and $\Psi(t)$ in straight tubes of different length L as t increases. The shorter the length is, the faster the deviation happens.

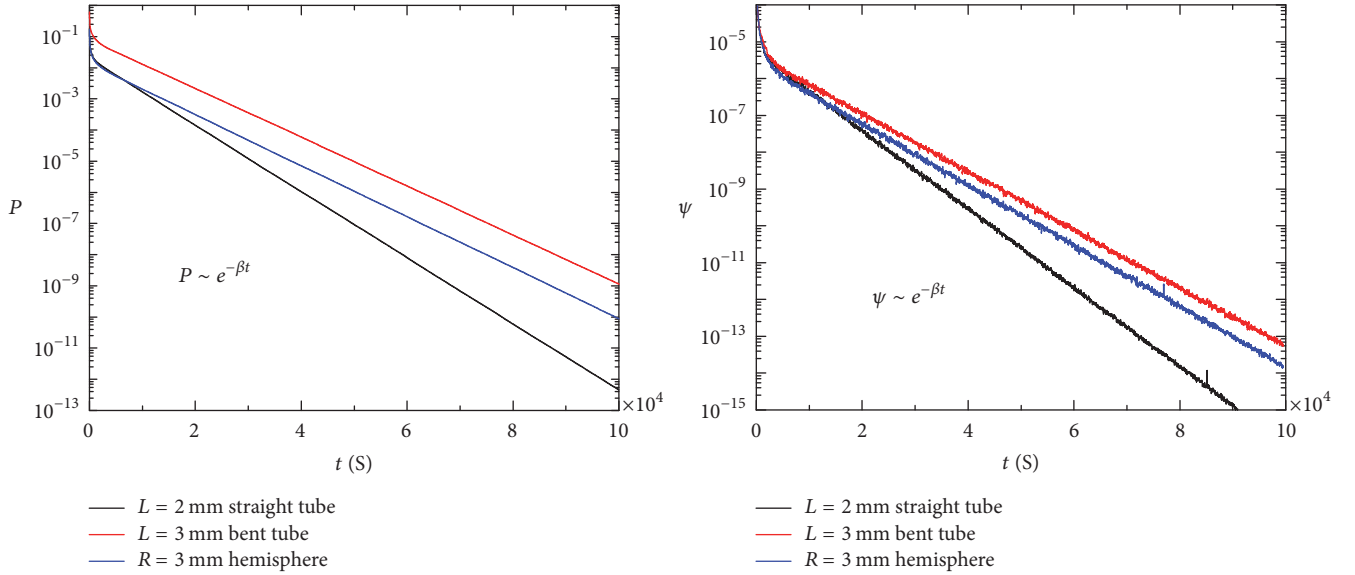


FIGURE 4: The exponential decrease of $P(t)$ and $\Psi(t)$ at large time for each type of dead-end pore.

T_t at which the decline transits from a power law to an exponential form. To get the transition time T_t , we first calculate the exponent β in (4). T_t has a close relation with the reciprocal of β . For simplicity, we use a straight tube as the dead-end pore. The diffusion equation about the concentration $C(x, t)$ in the tube can be written as

$$\frac{\partial C(x, t)}{\partial t} = D_m \frac{\partial^2 C(x, t)}{\partial x^2} \quad (0 \leq x \leq L), \quad (5)$$

where L is the length of the straight tube and $P(t) = \int_0^L C(x, t) dx$. The interface between the straight tube and the mobile zone is located at $x = 0$. As tracer particles move out of

the straight tube, they are not allowed to enter again because of drift with flow. Consequently, the boundary condition at $x = 0$ can be set as $C(0, t) = 0$. The condition of reflecting boundary at $x = L$ is written as $\partial C(x, t)/\partial x|_{x=L} = 0$. By the method of variable separation, $C(x, t)$ has the form $C(x, t) = X(x)e^{-\beta t}$ and we can get the minimum of β ; that is,

$$\beta_{\min} = \frac{\pi^2 D_m}{4L^2}. \quad (6)$$

Other eigenvalues of β are much larger than β_{\min} and the modes with large β decrease more rapidly than the mode with β_{\min} . Neglecting the modes with large β , β in $C(x, t) =$

TABLE 1: The comparison between the β fitted by $P(t) \sim e^{-\beta t}$ and the β_{\min} of (6).

L (mm)	β (s^{-1})	β_{\min} (s^{-1})	β/β_{\min}
1	9.72×10^{-4}	9.87×10^{-4}	0.98
2	2.44×10^{-4}	2.47×10^{-4}	0.99
3	1.08×10^{-4}	1.10×10^{-4}	0.98
4	6.10×10^{-4}	6.20×10^{-4}	0.99

$X(x)e^{-\beta t}$ approximates to β_{\min} . We fit the β of straight tubes of different length according to $P(t) \sim e^{-\beta t}$ and compare them with the values of β_{\min} calculated from (6). Table 1 shows the values of β and β_{\min} . The two sets of values are very close. In hemisphere dead-end pores, β can also be approximated by β_{\min} as the tube despite replacing L with R and adding a coefficient.

Now let us discuss the transition time T_t at which the decline of $P(t)$ transits from a power-law form to an exponential decline form. In Figure 3, T_t is the time when the curve deviates from the straight line. Comparing the transition time T_t to $1/\beta$ in Table 1, we can find that T_t is located in the range of time $[1/2\beta, 1/\beta]$. Since β is very close to β_{\min} (illustrated in Table 1), T_t is approximately proportional to the square of length L and inversely proportional to D_m as shown in (6). As T_t represents the transition time from power-law decline to exponential decline, the enduring time of anomalous dispersion has the same relation with the length L and D_m as that in (6).

4. Conclusions

In this paper, we investigate the waiting time distribution $\psi(t)$ of nonreactive solute particles in immobile zones, which are represented by dead-end pores. Three types of dead-end pores, straight tube, bent tube, and hemisphere, are simulated. When a dead-end pore is large enough, $\psi(t)$ follows a power-law distribution, that is, $\psi(t) \sim t^{-1-\alpha}$. All the simulated dead-end pores in this paper show that the values of α are very close to 0.5. According to CTRW theory, this power-law distribution results in anomalous dispersion [17, 25]. If dead-end pore is finite, $\psi(t)$ follows an exponential decrease finally. Therefore, the transport is anomalous at early time and is Fickian at later time. The transition time T_t is proportional to the square of the length of dead-end pores and inversely proportional to the diffusion coefficient of solute. From CTRW theory, we could use T_t to sign the transition time from anomalous transport to Fickian transport. Thus, we can draw the conclusion that anomalous transport phenomena will be more easily observed in the porous media with large immobile zones.

In practice, dead-end pores may be very long, such as the fractures in fracture porous media. In this case, the waiting time distribution can seem as a power-law distribution during the whole observation period. Therefore, anomalous dispersion lasts for the whole observation period. The power-law distribution of $\psi(t)$ has a close relation with fractional dispersion equation [25]. According to our simulations, the fractional order of time derivative approximates to 0.5 when

using tFADE (i.e., (2)) to describe this class of anomalous dispersion.

Conflicts of Interest

The authors declare that they have no conflicts of interest.

Acknowledgments

This study was supported by the National Key Research and Development Program of China (Grant no. 2016YFC040280801), the National Natural Science Foundation of China- (NSFC-) Xinjiang project (Grant no. U1503282), and NSFC projects (Grant no. 41672233).

References

- [1] E. E. Adams and L. W. Gelhar, "Field study of dispersion in a heterogeneous aquifer: 2. spatial moments analysis," *Water Resources Research*, vol. 28, no. 12, pp. 3293–3307, 1992.
- [2] M. Levy and B. Berkowitz, "Measurement and analysis of non-fickian dispersion in heterogeneous porous media," *Journal of Contaminant Hydrology*, vol. 64, no. 3-4, pp. 203–226, 2003.
- [3] U. M. Scheven, D. Verganelakis, R. Harris, M. L. Johns, and L. F. Gladden, "Quantitative nuclear magnetic resonance measurements of preasymptotic dispersion in flow through porous media," *Physics of Fluids*, vol. 17, no. 11, Article ID 117107, pp. 1–7, 2005.
- [4] Y. Zhang, H. Xu, X. Lv, and J. Wu, "Diffusion in relatively homogeneous sand columns: a scale-dependent or scale-independent process?" *Entropy*, vol. 15, pp. 4376–4391, 2013.
- [5] E. Crevacore, T. Tosco, R. Sethi, G. Boccardo, and D. L. Marchisio, "Recirculation zones induce non-fickian transport in three-dimensional periodic porous media," *Physical Review E: Statistical, Nonlinear, and Soft Matter Physics*, vol. 94, no. 5, Article ID 053118, 2016.
- [6] A. Tyukhova, M. Dentz, W. Kinzelbach, and M. Willmann, "Mechanisms of anomalous dispersion in flow through heterogeneous porous media," *Physical Review Fluids*, vol. 1, Article ID 074002, 2016.
- [7] A. Nissan, I. Dror, and B. Berkowitz, "Time-dependent velocity-field controls on anomalous chemical transport in porous media," *Water Resources Research*, vol. 53, pp. 3760–3769, 2017.
- [8] B. Berkowitz, G. Kosakowski, G. Margolin, and H. Scher, "Application of continuous time random walk theory to tracer test measurements in fractured and heterogeneous porous media," *Groundwater*, vol. 39, no. 4, pp. 593–604, 2001.
- [9] M. Dentz, A. Cortis, H. Scher, and B. Berkowitz, "Time behavior of solute transport in heterogeneous media: transition from anomalous to normal transport," *Advances in Water Resources*, vol. 27, no. 2, pp. 155–173, 2004.

- [10] R. Połoczański, A. Wyłomańska, M. Maciejewska, A. Szczurek, and J. Gajda, “Modified cumulative distribution function in application to waiting time analysis in the continuous time random walk scenario,” *Journal of Physics A: Mathematical and Theoretical*, vol. 50, no. 3, Article ID 034002, 2017.
- [11] A. Puyguiraud, M. Dentz, and P. Gouze, “Transport upscaling from pore-to Darcy-scale: incorporating pore-scale berea sandstone lagrangian velocity statistics into a Darcy-scale transport CTRW model,” in *EGU General Assembly Conference Abstracts*, vol. 19, p. 10943, 2017.
- [12] M. F. Shlesinger, “Origins and applications of the montroll-weiss continuous time random walk,” *The European Physical Journal B*, vol. 90, no. 5, 93 pages, 2017.
- [13] R. Metzler and J. Klafter, “The random walk’s guide to anomalous diffusion: a fractional dynamics approach,” *Physics Reports*, vol. 339, no. 1, pp. 1–77, 2000.
- [14] Y. Zhang, D. A. Benson, and D. M. Reeves, “Time and space nonlocalities underlying fractional-derivative models: distinction and literature review of field applications,” *Advances in Water Resources*, vol. 32, no. 4, pp. 561–581, 2009.
- [15] J. F. Kelly and M. M. Meerschaert, “Space-time duality for the fractional advection-dispersion equation,” *Water Resources Research*, vol. 53, pp. 3464–3475, 2017.
- [16] R. Schumer, D. A. Benson, M. M. Meerschaert, and S. W. Wheatcraft, “Eulerian derivation of the fractional advection-dispersion equation,” *Journal of Contaminant Hydrology*, vol. 48, no. 1–2, pp. 69–88, 2001.
- [17] B. Berkowitz, A. Cortis, M. Dentz, and H. Scher, “Modeling Non-fickian transport in geological formations as a continuous time random walk,” *Reviews of Geophysics*, vol. 44, no. 2, Article ID RG2003, 2006.
- [18] B. Bijeljic and M. J. Blunt, “Pore-scale modeling and continuous time random walk analysis of dispersion in porous media,” *Water Resources Research*, vol. 42, no. 1, Article ID W01202, 2006.
- [19] B. Berkowitz and H. Scher, “Exploring the nature of non-fickian transport in laboratory experiments,” *Advances in Water Resources*, vol. 32, no. 5, pp. 750–755, 2009.
- [20] B. Bijeljic, A. Raeini, P. Mostaghimi, and M. J. Blunt, “Predictions of non-fickian solute transport in different classes of porous media using direct simulation on pore-scale images,” *Physical Review E: Statistical, Nonlinear, and Soft Matter Physics*, vol. 87, no. 1, Article ID 013011, 2013.
- [21] J. Jiang and J. Wu, “Continuous time random walk in homogeneous porous media,” *Journal of Contaminant Hydrology*, vol. 155, pp. 82–86, 2013.
- [22] T. Prellberg and J. Krawczyk, “Flat histogram version of the pruned and enriched rosenbluth method,” *Physical Review Letters*, vol. 92, no. 12, pp. 120602–1, 2004.
- [23] J. Jiang, Y. Huang, and J. Wu, “Can the pruned-enriched method be used for the simulation of fluids?” *Journal of Statistical Physics*, vol. 136, no. 5, pp. 984–988, 2009.
- [24] J. Jiang and J. Wu, “Simulation of continuous-time random walks by the pruned-enriched method,” *Physical Review E*, vol. 84, Article ID 036710, 2011.
- [25] E. Barkai, R. Metzler, and J. Klafter, “From continuous time random walks to the fractional Fokker-Planck equation,” *Physical Review E: Statistical Physics, Plasmas, Fluids, and Related Interdisciplinary Topics*, vol. 61, no. 1, pp. 132–138, 2000.
- [26] P. P. Wang, C. Zheng, and S. M. Gorelick, “A general approach to advective-dispersive transport with multirate mass transfer,” *Advances in Water Resources*, vol. 28, no. 1, pp. 33–42, 2005.

Research Article

Analysis of the Influencing Factors on the Well Performance in Shale Gas Reservoir

Cheng Dai,¹ Liang Xue,^{2,3} Weihong Wang,¹ and Xiang Li⁴

¹State Key Laboratory of Shale Oil and Gas Enrichment Mechanisms and Effective Development, Sinopec Group, Beijing 100083, China

²Department of Oil-Gas Field Development, College of Petroleum Engineering, China University of Petroleum, Beijing 102249, China

³State Key Laboratory of Petroleum Resources and Prospecting, China University of Petroleum, Beijing 102249, China

⁴College of Engineering, Peking University, Beijing 100871, China

Correspondence should be addressed to Liang Xue; xueliang@pku.edu.cn

Received 13 July 2017; Revised 12 October 2017; Accepted 29 October 2017; Published 26 December 2017

Academic Editor: Stefan Finsterle

Copyright © 2017 Cheng Dai et al. This is an open access article distributed under the Creative Commons Attribution License, which permits unrestricted use, distribution, and reproduction in any medium, provided the original work is properly cited.

Due to the ultralow permeability of shale gas reservoirs, stimulating the reservoir formation by using hydraulic fracturing technique and horizontal well is required to create the pathway of gas flow so that the shale gas can be recovered in an economically viable manner. The hydraulic fractured formations can be divided into two regions, stimulated reservoir volume (SRV) region and non-SRV region, and the produced shale gas may exist as free gas or adsorbed gas under the initial formation condition. Investigating the recovery factor of different types of shale gas in different region may assist us to make more reasonable development strategies. In this paper, we build a numerical simulation model, which has the ability to take the unique shale gas flow mechanisms into account, to quantitatively describe the gas production characteristics in each region based on the field data collected from a shale gas reservoir in Sichuan Basin in China. The contribution of the free gas and adsorbed gas to the total production is analyzed dynamically through the entire life of the shale gas production by adopting a component subdivision method. The effects of the key reservoir properties, such as shale matrix, secondary natural fracture network, and primary hydraulic fractures, on the recovery factor are also investigated.

1. Introduction

With the growing demand on cleaner energy to sustain the global economy, the exploration and development of natural gas have attracted wide attention in the recent years. Shale gas, as a newly developed unconventional energy source, is expected to play a more important role. Shale formations are widely distributed in the earth's crust. The Global Shale Gas Initiative estimates that there are 688 shale formations in 142 basins worldwide. This provides vast potential space for shale gas to be accumulated in biogenic manner, thermogenic manner, or the combined biogenic-thermogenic manner [1]. The Energy Information Administration (EIA) in 2013 estimated approximately 7,300 tcf shale gas resources in 137 shale formations in 41 countries that are technically recoverable, and 32% of the total estimated natural gas resources are in shale formation [2]. The most distinctive characteristics of shale gas reservoir are its extremely low permeability and

porosity, which had made the shale formation be treated as source rock and seal previously. However, with the application of advanced technologies, such as multistage hydraulic fracturing and horizontal wells, it is possible to develop the organic-rich shale reservoir in an economic viable manner.

The flow mechanisms during the shale gas production are much more complicated than those in conventional gas reservoir due to the complex multiscale gas transport mechanisms in the stimulated shale gas reservoir. The shale gas can be adsorbed on the organic matter, and thus the desorption may be crucial for the ultimate gas recovery in shale formation if the organic content in the shale matrix is high [3]. The desorbed gas combined with free gas in intergranular pores needs to transport through the dominant nanopores in the shale matrix. Since the mean free path of the gas molecule can be smaller than the pore radius in the nanopores, the diffusion can greatly improve the gas transport speed in this process which is now characterized by

Knudsen diffusion. Many corrections to obtain the apparent permeability of shale matrix have been proposed to take the non-Darcy flow behavior and gas slippage effect into account [4–6]. The gas can then be travelled through a complex fracture network induced by hydraulic fracturing stimulation process, which creates a high permeable region called stimulated reservoir volume (SRV) [7, 8]. Mainly, two types of fractures are involved in this SRV region: the widely distributed reactivated preexisting natural fractures with complex geometry and the newly created sparsely distributed hydraulic fractures with relatively less complex geometry. When these two types of fracture system are well connected, the SRV region with enhanced permeability can greatly improve the well performance in low-permeable reservoirs [9, 10].

Numerical simulation of shale gas production is challenging. Generally, there exist two common conceptual approaches in the literatures: the dual/multiple porosity/permeability model and discrete fracture model. The dual-porosity model proposed by Warren and Root [11] has been widely used in well-connected small-scale fracture systems, such as natural fracture system [12–16]. In this approach, the reservoir is characterized by two overlapping continua to represent fractures and matrix. The flow interaction between these continua is described by using a transfer function called the shape factor. Due to the simplification on the complex geometry of the fractures, this approach cannot account explicitly for the effect of the individual fractures on the flow characteristics. Discrete fracture model method (DFM) can overcome the limitation of dual porosity method and take the realistic fracture geometry into account [17]. It is common to use unstructured grid during the simulation of the fluid flow process to make the grid system consistent with the geometry of each fracture. Due to the computational cost of this approach, DFM is usually applied when a small number of large-scale fractures play dominant roles in fluid flow. Recently, the embedded discrete fracture method (EDFM) has gained more interests when numerically characterizing the fractured reservoir [18, 19]. The conception of EDFM was proposed by Lee et al. [20, 21] by taking advantage of both dual-porosity model and discrete fracture model. EDFM characterizes the medium matrix by using structured grid and embeds the discrete fractures into the matrix grid by handling the intersection between fractures and matrix; thus all the issues associated with the mathematical difficulties of unstructured grid vanish.

The United States leads the shale gas production worldwide. EIA estimates that 15 trillion cubic feet of natural gas were produced in 2016 from shale gas wells, which takes up 47% of total natural gas production. China is the third country that commercializes the shale gas production after US and Canada, and Fuling shale gas play has been the dominant shale gas reservoir in China by far since its beginning of shale gas production in 2012. The shale gas production in China is still at its early stage, and the influence of many key reservoir properties and hydraulic fracturing design parameters on the well performance remains unclear. In this paper, we built a dual-porosity-based numerical model that is capable of considering the above special flow mechanisms

to investigate contributions of free and adsorbed gas to the total production and the effect of the matrix permeability, the number of hydraulic fracturing stages, the conductivity of primary hydraulic fractures, half-length of primary hydraulic fractures, and the conductivity and development level of secondary fracture network on the recovery factors in SRV and non-SRV regions according to the field data collected from a shale gas field in Sichuan Basin. All these investigations are crucial to the reasonable design of development plan for shale gas production. A component subdivision method implemented in the UNCONG simulator is used to explicitly characterize the free gas and adsorbed gas produced from SRV and non-SRV regions, which makes the sensitivity analysis presented here unique and more complete compared with the previous works based on commercial simulators.

The rest of the paper is arranged as follows: the mathematical and numerical model to describe the gas flow process in the specified shale gas reservoir and the component subdivision method to differentiate the effect of free gas and adsorbed gas are presented in Section 2; the contributions of free gas and adsorbed gas to the total gas production are analyzed by using “component subdivision method” and the influences of reservoir properties and hydraulic fracturing parameters on the well performance are studied in Section 3; and finally conclusions are drawn based on all the analysis results in Section 4.

2. Methodology

2.1. Mathematical Model of the Fluid Flow. The entire shale gas reservoir system is divided into two types of media based on the concept of dual-porosity model: matrix and fracture system. The gas flow model in each type of medium is built based on its distinctive flow characteristics. The existence of massive nanopores in shale reservoirs leads to a large amount of gas adsorbed on the pore walls in the shale matrix. The amount of adsorbed gas can vary from 35 to 58% in Barnett shale to 60–85% in Lewis shale [22]. In reality, when the desorbed gas combined with free gas flows in the shale reservoir, it is difficult to differentiate them and quantify their contributions to the total gas production in the wellhead separately. However, it is crucial to understand the dynamic production characteristics of adsorbed gas and free gas in order to design the reasonable strategy to develop shale gas. To explicitly characterize the contribution of these two types of shale gas, we adopted the “component subdivision” method proposed by Yang et al. [23], where the free gas and adsorbed gas are numerically treated as two different components and they can be marked separately but modeled simultaneously as a unified flow system. This method is based on the compositional reservoir simulation model. The basic principle to build the flow model is the mass conservation for each component in different medium.

In the shale matrix, for a specific component c , the mass conservation law can be written as

$$\int \frac{\partial}{\partial t} [\phi (S_g y_c \rho_g)] dV + \int (y_c q_g) dA + (q_c^s) = 0, \quad (1)$$

where V and A are the control volume and area, ϕ is the porosity, S_g is the saturations of gas, ρ_g are the mole densities of oil and gas, y_c is the mole fraction of gas, q_g is the mole flux of gas, and q_c^s is mole flux of the adsorbed component c entering the matrix pore, and it can be computed as

$$q_c^s = \rho_m (C_{c0} - C_c^\infty) \frac{1}{\Delta t}, \quad (2)$$

where ρ_m is the matrix density, Δt is the time interval, C_{c0} is the initial adsorption concentration during this time interval, and C_c^∞ is the equilibrium adsorption concentration. C_c^∞ can be determined based on the Langmuir isothermal adsorption curve:

$$\overline{C}_c = V_{Lc} \frac{y_c P_g}{P_{Lc} + \sum_c y_c P_g}, \quad (3)$$

where V_{Lc} is the Langmuir volume representing the maximum adsorption volume of the shale matrix and P_{Lc} is the Langmuir pressure representing the pressure at which 50% of the Langmuir volume can be adsorbed.

In the fracture system, for a specific component c , the mass conservation equation can be written as

$$\int \frac{\partial}{\partial t} [\phi (S_g y_c \rho_g)] dV + \int (y_c q_g) dA + (q_c^W) = 0. \quad (4)$$

One main difference of flow mechanisms between matrix and fracture system is that there is no need to take the adsorption effect in the fracture system because the fractures essentially act as the main flow path, not a storage space as the matrix does. In addition, it is required to take the intersections between the fractures and wellbore into consideration to accurately characterize the fracture flow, and q_c^W is the mole flux to describe this effect. The flow between matrix and fractures can be considered as the fluid exchange between two different control volumes and can be computed as the flow term ($y_c q_g$). The flux between two adjacent cells can be estimated via Darcy's law:

$$(q_g)_{ij} = \frac{\rho_g k_{rg}}{\mu_g} T_{ij} [\Phi_i - \Phi_j], \quad (5)$$

where k_{rg} is relative permeability, μ_g is viscosity, and $\Phi_i - \Phi_j$ is the potential difference between cells i and j . The transmissibility T_{ij} is calculated by volume-weighted average.

$$T_{ij} = \left(\frac{V_i}{k_i} + \frac{V_j}{k_j} \right)^{-1}, \quad (6)$$

where V_i and V_j are the volumes of cells i and j , while k_i and k_j are the apparent permeabilities of cells i and j , respectively.

In dual-porosity-dual-permeability (DPDP) model, the transmissibility between a matrix cell and its corresponding fracture cell is defined as

$$T_{mf} = V \left(\frac{f_x k_x}{L_x^2} + \frac{f_y k_y}{L_y^2} + \frac{f_z k_z}{L_z^2} \right), \quad (7)$$

where V is the grid volume. The fracture spacing along the x , y , and z directions is represented by L_x , L_y , and L_z and k_x , k_y , and k_z are the matrix permeability of the three directions, respectively. f_x , f_y , and f_z are dimensionless parameters related to the geometric information of fracture, which are equal to π^2 for sugar cube model.

The flow between hydraulic fracture and well is calculated by the following equation:

$$(q_g)_{i,\text{well}} = \frac{\rho_g k_{rg}}{\mu_g} \cdot \text{wi} \cdot k_i [\Phi_{\text{well}} - \Phi_i], \quad (8)$$

where wi is well index which represents the conductivity between well and the hydraulic fracture and $\Phi_{\text{well}} - \Phi_i$ is the potential difference between well and cell i . In an orthogonal grid, one option is to use Peaceman's formula to compute well index.

If the well is parallel to z direction,

$$\text{wi}_z = \frac{2\pi D_z \cdot \sqrt{k_x k_y}}{k_z [\ln(r_{0,z}/r_w) + s]}, \quad (9)$$

$$r_{0,z} = 0.28 \frac{\left[(k_y/k_x)^{1/2} \Delta X^2 + (k_x/k_y)^{1/2} \Delta Y^2 \right]^{1/2}}{(k_y/k_x)^{1/4} + (k_x/k_y)^{1/4}}.$$

If the well is parallel to y direction,

$$\text{wi}_y = \frac{2\pi D_y \sqrt{k_x k_z}}{k_y [\ln(r_{0,y}/r_w) + s]}, \quad (10)$$

$$r_{0,y} = 0.28 \frac{\left[(k_z/k_x)^{1/2} \Delta X^2 + (k_x/k_z)^{1/2} \Delta Z^2 \right]^{1/2}}{(k_z/k_x)^{1/4} + (k_x/k_z)^{1/4}}.$$

If the well is parallel to x direction,

$$\text{wi}_x = \frac{2\pi D_x \sqrt{k_y k_z}}{k_x [\ln(r_{0,x}/r_w) + s]}, \quad (11)$$

$$r_{0,x} = 0.28 \frac{\left[(k_z/k_y)^{1/2} \Delta Y^2 + (k_y/k_z)^{1/2} \Delta Z^2 \right]^{1/2}}{(k_z/k_y)^{1/4} + (k_y/k_z)^{1/4}},$$

where r_w is well radius. D_x , D_y , and D_z are the projection lengths of the perforation interval onto the x -axis, y -axis, and z -axis; s is the skin factor; ΔX , ΔY , and ΔZ are the size of the fracture grid block.

As mentioned before, the Knudsen diffusion needs to be considered into the gas transport in shale matrix. This effect can be described by adding a correction term to the apparent permeability under the same pressure gradient:

$$\frac{k_a}{k_\infty} = 1 + \frac{b}{P}, \quad (12)$$

where k_a and k_∞ are the apparent permeability and the intrinsic permeability, respectively, P is the reservoir pressure, and b is the correction coefficient of Knudsen diffusion.

The correction coefficient can be determined through fitting the experiment data.

Non-Darcy flow may occur in high permeable area, such as hydraulic fractures. In reservoir simulation, the phenomenon of non-Darcy flow is characterized by Forchheimer equation:

$$T_{ij} \cdot [\Phi_{g,j} - \Phi_{g,i}] = \frac{k_{rg}}{\mu} x_{c,g} q_{c,g;ij} + C\beta\bar{\rho}_g \left(\frac{\bar{k}}{A_{ij}} \right) \frac{(q_{c,g;ij})^2}{[x_{c,g}\rho_g]^2}, \quad (13)$$

where C is the unit converge unit converter and β is Forchheimer coefficient. Forchheimer coefficient also can be measured through experiment data fitting.

2.2. Component Subdivision Method. In order to quantify the distributions of free and adsorbed gas in different regions, ‘‘component subdivision’’ method is used. The free and adsorbed gas from SRV and non-SRV region are treated as different components with the same PVT features in (1), namely, SRV free gas, SRV adsorbed gas, non-SRV free gas, and non-SRV adsorbed gas, respectively. The PVT features are calculated by flash calculation according to PR Equation of State in this study. According to Langmuir equation (3), one component’s adsorbed content is in equilibrium with its partial pressure in the vapor phase. In the component subdivision method used here, a specific type of shale gas (free or adsorbed gas) produced from a specific region (SRV or non-SRV) is treated as an independent ‘‘component’’; it should be in equilibrium with the total methane’s partial pressure rather than its own partial pressure. The mole fraction of methane gas y_c can be defined as

$$y_c = y_1 + y_2 + y_3 + y_4, \quad (14)$$

where y_1 , y_2 , y_3 , and y_4 represent the mole fractions of free gas from SRV region, adsorbed gas from SRV region, free gas from non-SRV region, and adsorbed gas from non-SRV region. Langmuir equation (3) in component subdivided method is modified as

$$\bar{C}_c = V_{Lc} \frac{(y_1 + y_2 + y_3 + y_4) P_g}{1.0 + \sum_c y_c P_g}. \quad (15)$$

In the beginning of the shale gas production, only free gas flows into the wellbore and no adsorbed gas has been produced yet; thus the mole fractions of adsorbed components, y_2 and y_4 , need to be set as zero.

2.3. Numerical Model of the Shale Gas Reservoir. To implement the mathematical model developed above, we built a numerical model based on dual-porosity-dual-permeability (DPDP) concepts to investigate the effects of all parameters on the well performance. The reservoir properties data used in this numerical model were obtained from the field measurement data in a shale gas reservoir located in Sichuan basin. These productive marine shale formations are mainly

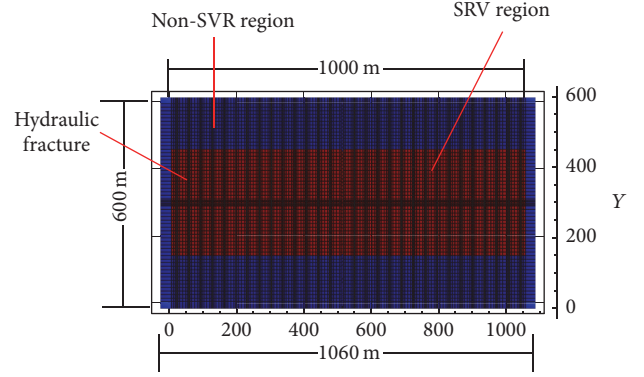


FIGURE 1: Numerical model of the shale gas reservoir.

TABLE 1: Key properties of shale reservoir model.

Property	Value
Reservoir dimension	1060 m × 600 m × 50 m
Grid system	332 × 61 × 6
Matrix porosity	4.05%
Matrix permeability	1 × 10 ⁻⁴ mD
Secondary fracture network porosity	0.45%
Secondary fracture network permeability	5 × 10 ⁻⁴ mD
Secondary fracture spacing	30 m
Primary hydraulic fracture conductivity	0.1 mD·m
Primary hydraulic half-length	150 m
Pressure gradient	1.55
Langmuir pressure	6 MP
Langmuir volume	2.5 m ³ /t

lower Silurian Longmaxi and Ordovician Wufeng with the burial depth of 2,500 meters and formation temperature of 85°C. Almost all the wells are hydraulically fractured horizontal wells with multiple transverse fractures. Here, we built a single-well model by using the simulation code UNCONG developed by Li et al. [24] as shown in Figure 1, and the key shale reservoir properties are listed in Table 1 for the base model used in the following analyses. All the main formation properties used in this study are collected from well logging and lab experiments in the Fuling shale gas play. It is assumed that the length of the horizontal well is 1000 m with 30 hydraulic fracturing stages. The half-length of the hydraulic fractures is 150 m. The hydraulic fractures are depicted as black lines in Figure 1, which are characterized by using local grid refinement method in the numerical models. Due to the natural fracture reactivation after the hydraulic fracturing, there would be a secondary fracture network around the primary hydraulic fractures. Here, we used the spacing between two fracture layers to represent the complexity or the developed level of the secondary fracture network as done in Warren and Root [11]. The less the spacing is, the more complex or developed the secondary fracture network is. In Figure 1, the secondary fracture network is depicted in red color, and it also indicates the coverage area of the SRV region. The non-SRV region as depicted in Figure 1

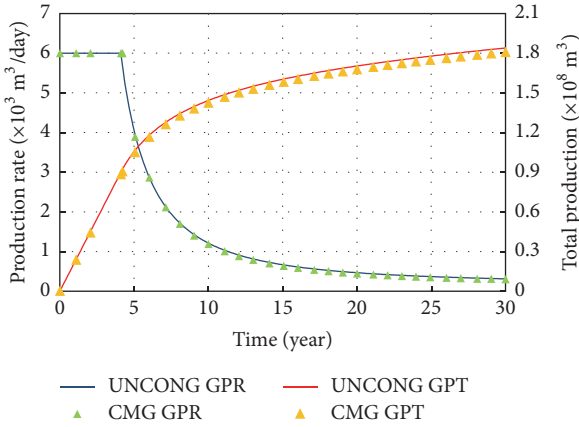


FIGURE 2: Comparison results of UNCONG and CMG.

in blue color has not experienced any stimulation and thus holds the properties of the shale matrix. According to the geological and well logging data, the original-gas-in-place (OGIP) is $4.76 \times 10^8 \text{ m}^3$ and the adsorbed gas takes up 40% of the OGIP, and the OGIP in the SRV region and non-SRV region is, respectively, $2.25 \times 10^8 \text{ m}^3$ and $2.52 \times 10^8 \text{ m}^3$.

We first validated our simulator UNCONG by comparing the simulation results with those obtained through commercial simulator CMG on the basis of the base case. Figure 2 shows the production rate and total production of gas from UNCONG and CMG. As can be observed in the Figure, the results of production rate obtained from UNCONG are very similar to those obtained from CMG. There are slight differences in the comparison results of total production, especially in the late stage of the total production curve, due to the accumulation effect of the total production with time, but the accuracy of the UNCONG simulator can be accepted. The main reason why we used UNCONG but not CMG or other commercial simulators is that they do not have the ability to quantify the contribution of different types of gas produced from different regions. This function has been developed in UNCONG and can aid us to implement the sensitivity analysis in this work.

3. Result Analysis

3.1. Contributions of the Adsorbed and Free Gas to the Production. The adsorbed gas and free gas production behaviors are investigated explicitly and separately by using the “component subdivision” method. In the base model, the horizontal well is producing shale gas at the prescribed production rate of $60,000 \text{ m}^3$, and the minimum bottomhole pressure is set as 6 MPa, which is consistent with the working condition in Fuling gas field. Figure 3 depicts the characteristics of adsorbed, free, and total shale gas production in terms of both production rate and cumulative production. It indicates that, under this working schedule, this well can produce shale gas stably in the first 4 years and then the production starts to decline. The cumulative production after 30 years can be as much as $1.81 \times 10^9 \text{ m}^3$.

To clearly show the contributions of the adsorbed and free gas on the total production, the entire production life of

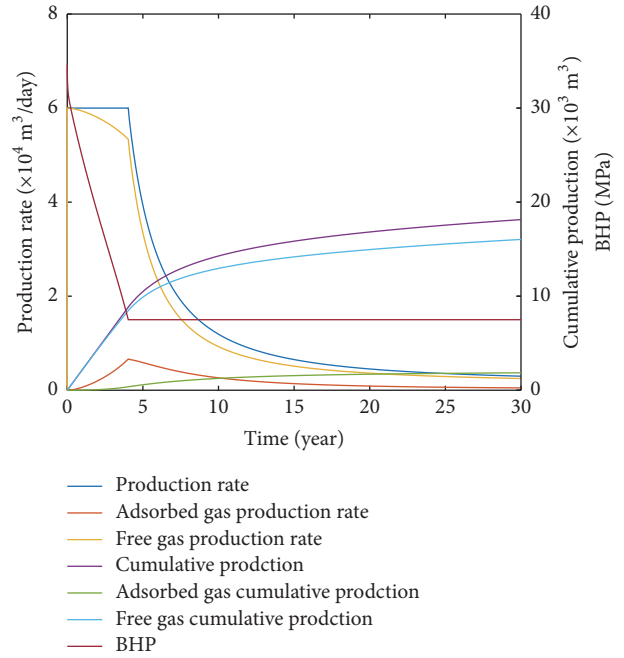


FIGURE 3: The production rate and cumulative production of base model.

this well is divided into three stages based on its production characteristics: the first stage starts from the beginning to the end of the stable production; the second stage starts from the beginning of the production decline and ends after 10 years of production; and the third stage covers the period when the shale gas production enters its late stable production.

As shown in Figure 4, in the first stage, the shale gas can be produced at relatively stable rate of roughly $6 \times 10^4 \text{ m}^3$, and the total gas production is dominated by free gas in the SRV region. With decreasing the reservoir pressure, the free gas production starts decreasing and the gas used to be adsorbed on the matrix begins to desorb and the adsorbed gas production climbs up. At the end of the first stage, the production rate of the adsorbed gas approaches to the maximum at the rate of $6.5 \times 10^3 \text{ m}^3$. Our finding is consistent with Wang [25] who states that the existence of adsorption gas has a more obvious effect on the production decline in the early stage and this is contrary to the common belief that the adsorption gas becomes important only when the average pressure in the reservoir drops to a certain level. In the second stage, the production rate starts declining. Due to the relatively easy depletion of the free gas, most of the free gas has been produced in the first stage, which leads the contribution of the adsorbed gas to become more obvious in the second stage. In the third stage, the production rate remains at a low level. The produced gas is dominated by the free gas in the non-SRV region. At the end of the 30 years, 73.76% of the total production rate is composed of the free gas in the non-SRV region.

Figure 5 indicates that, during the 30-year production period, the cumulative gas production is composed of the free gas in the SRV region with 67.57%, free gas in the non-SRV region with 20.81%, the adsorbed gas in the SRV region with

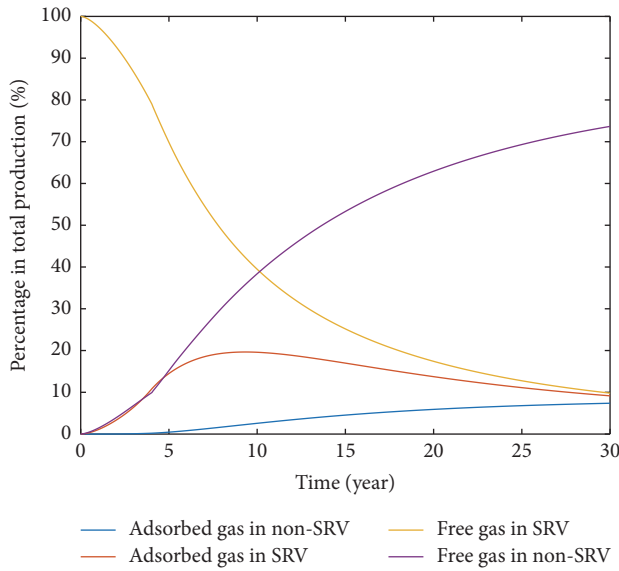


FIGURE 4: The fractions of free gas and absorbed gas in SRV and non-SRV regions in terms of production rate.

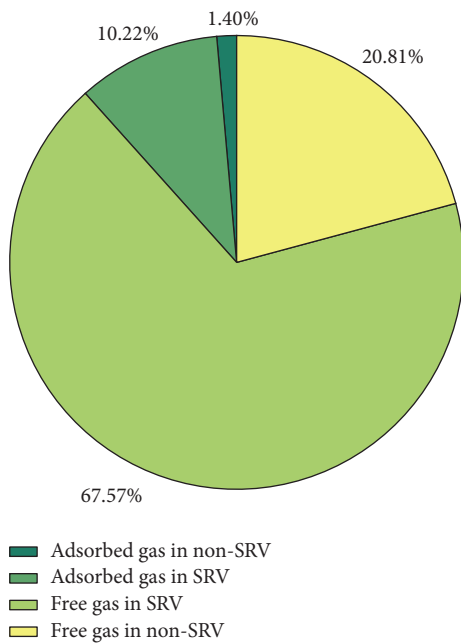


FIGURE 5: The fractions of free gas and absorbed gas in SRV and non-SRV regions in terms of cumulative production.

10.22%, and the adsorbed gas in the non-SRV region with 1.40%. The free gas still greatly dominates the overall shale gas production, even though the adsorbed gas takes up 40% of the OGIP.

3.2. The Effect of the Matrix Permeability on the Recovery Factor. After analyzing the production dynamics in the above section, we focused on the effect of the postfracturing reservoir properties on the recovery factor in different regions, that is, the ratio of recovered gas at a specific production time

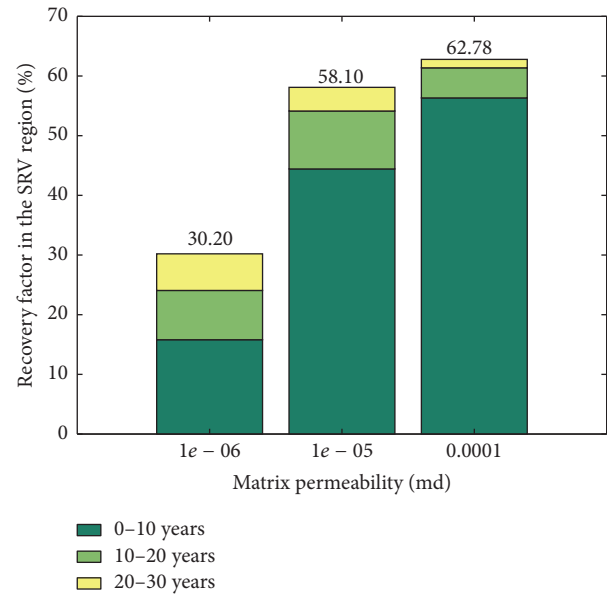


FIGURE 6: The effect of matrix permeability on the recovery factor in SRV region.

and original-gas-in-place in the SRV and non-SRV regions. For the purpose of result presentation, we divided the 30-year production period into three 10-year intervals so that the dynamic change of the recovery factor can be better studied.

To investigate the effect of matrix permeability, we selected 3 typical values in the range of the field observed matrix permeability in the shale gas reservoir: 1×10^{-4} mD, 1×10^{-5} mD, and 1×10^{-6} mD, respectively. Figure 6 shows the effect of the matrix permeability on the recovery factor in the SRV region. The result implies that the matrix permeability can severely affect the recovery factor in the SRV region, and the recovery factor in the SRV region decreases with decreasing the matrix permeability. Along the time line, the recovery factor decreases dramatically, which is understandable due to the rapid production decline in the ultra-low-permeable reservoir. In the non-SRV region, the effective recovery is largely determined by the matrix permeability, since the hydraulic fracturing stimulation has no effect on this part of the reservoir. Figure 7 shows the effect of the matrix permeability on the recovery factor in the non-SRV. In general, it shows the same tendency as that in the SRV region, that is, the lower the matrix permeability is, the smaller the recovery factor is. However, one noticeable point in this analysis is that the shale gas in the non-SRV region almost cannot be recovered at all when the matrix permeability is lower than 1×10^{-6} mD.

3.3. The Effect of the Secondary Fracture Network Properties on the Recovery Factor. In this section, the effect of the properties of the secondary fracture network on the recovery factor in different region of shale gas reservoir is investigated. Two main properties, the density and the permeability of the secondary fracture network, are selected here.

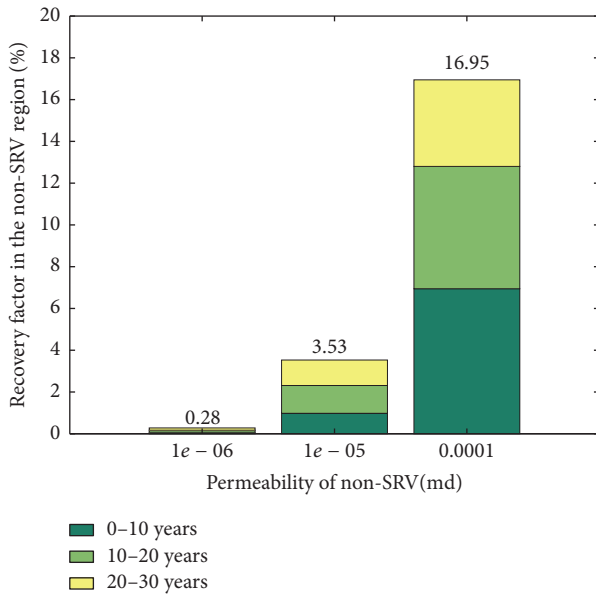


FIGURE 7: The effect of matrix permeability on the recovery factor in non-SRV region.

As mentioned before, the density of the fracture network can be described by using the spacing of the fracture layer in the dual-porosity model. Here, we used 5 different values of fracture layer spacing, 10, 15, 20, 25, and 30, respectively. Figure 8(a) shows the effect of the secondary fracture network density on the recovery factor in SRV region. It can be found that the effect of secondary fracture network density on the recovery factor in the SRV region is not obvious for the base case, where matrix permeability is 1×10^{-4} mD. For comparison purpose, a new simulation based on the matrix permeability of 1×10^{-5} mD is performed. When the matrix permeability is decreased, the effect of secondary fracture network density on the recovery factor becomes more profound. It indicates that it is not helpful to create a more complex secondary fracture network to improve the recovery factor in the SRV region if the matrix permeability in this region is already relatively high. Figure 8(b) shows the effect of the secondary fracture network density on the recovery factor in the non-SRV region. It can be found that the complex fracture network is always helpful to improve the recovery factor in the non-SRV region, since it increases the contact area with the non-SRV region.

To investigate the fracture network permeability on the recovery factor in different regions, 4 typical values are selected in this analysis. They are 0.001 mD, 0.005 mD, 0.01 mD, and 0.1 mD, respectively. Figure 9 shows the analysis results. It indicates a similar tendency to the effect of the fracture network complexity. Improving the permeability of the fracture network has a more profound effect on the non-SRV region than on the SRV region. If the hydraulic fracturing cannot create the primary fractures but only a secondary fracture network, then it is obvious that the secondary fracture network permeability can have a severe effect on the recovery factor in both SRV and non-SRV regions, as shown in Figure 10. However, it also can be observed that

the recovery factor can be very small when the secondary fracture network permeability is low, which indicates that the creation of primary hydraulic fractures can alleviate the requirement on the secondary fracture network permeability. Therefore, in practice, it would be more favorable to create primary hydraulic fractures with moderate complex and permeable secondary fracture network than to just create a more uniform fracture network.

3.4. The Effect of the Primary Hydraulic Fracture Properties on the Recovery Factor. Three main properties of the hydraulic fractures on the recovery factor are investigated in this section. They are the number of hydraulic fracturing stages, fracture conductivity, and the half-length of the hydraulic fractures, respectively. For the stages number, simulation results based on three cases are compared, 10, 20, and 30. Figure 11 shows the effect of the stage numbers on the recovery factors in SRV and non-SRV regions. It can be found that the recovery factors in both SRV and non-SRV regions are not influenced when the number of the hydraulic fracturing stages is decreased from 30 in the base case to 20. However, when further reducing the stage numbers to 10, the recovery factors are severely affected. To search for the reason behind the phenomenon, the pressure distribution with the different stage numbers is plotted in Figure 12 (the pressure distribution with stage number of 20 is very similar to that with 30 and thus it is not plotted). It can be observed that the pressure drops uniformly along the horizontal well (it forms a large blue rectangle) when the stage number is 30, but the pressure drawdown when the stage number is 10 forms several sections (small blue rectangular) and each section is separated relative to the others. Recall that our horizontal well is 1000 m, and each hydraulic fracturing stage is associated with secondary fracture network with the width of 30 m on one side. The spacing between two hydraulic fractures is about 33.3 m if the stage number is 30. Therefore, the pressure system associated with each primary hydraulic fracture is well connected. However, the spacing between two hydraulic fractures is about 100 m if the stage number is 10. It means that there would be a 40 m wide space which is not stimulated by hydraulic fracturing process, and thus the pressure system associated with each primary hydraulic fracture is independent of the others. In the design of the hydraulic fracturing, it requires increasing the stage number to create a fracture system (including primary hydraulic fractures and the reactivated natural fractures) that can form a well-connected SRV region, and it is not worthy of further increasing the stage number when this requirement can be satisfied.

Four typical values of hydraulic fracture conductivity are selected to investigate the effect on shale gas production. They are 0.1, 0.5, 1, and 10 mD·m, respectively. Figure 13 shows the effect of the hydraulic fracture conductivity on the recovery factor in different regions. It can be seen that in general higher hydraulic fracture conductivity is favorable to improve recovery factors in both SRV and non-SRV regions.

The half-length of the hydraulic fractures has an effect on the SRV area and thus on the estimation of the OGIP in SRV and non-SRV regions. Here, three cases of designed hydraulic

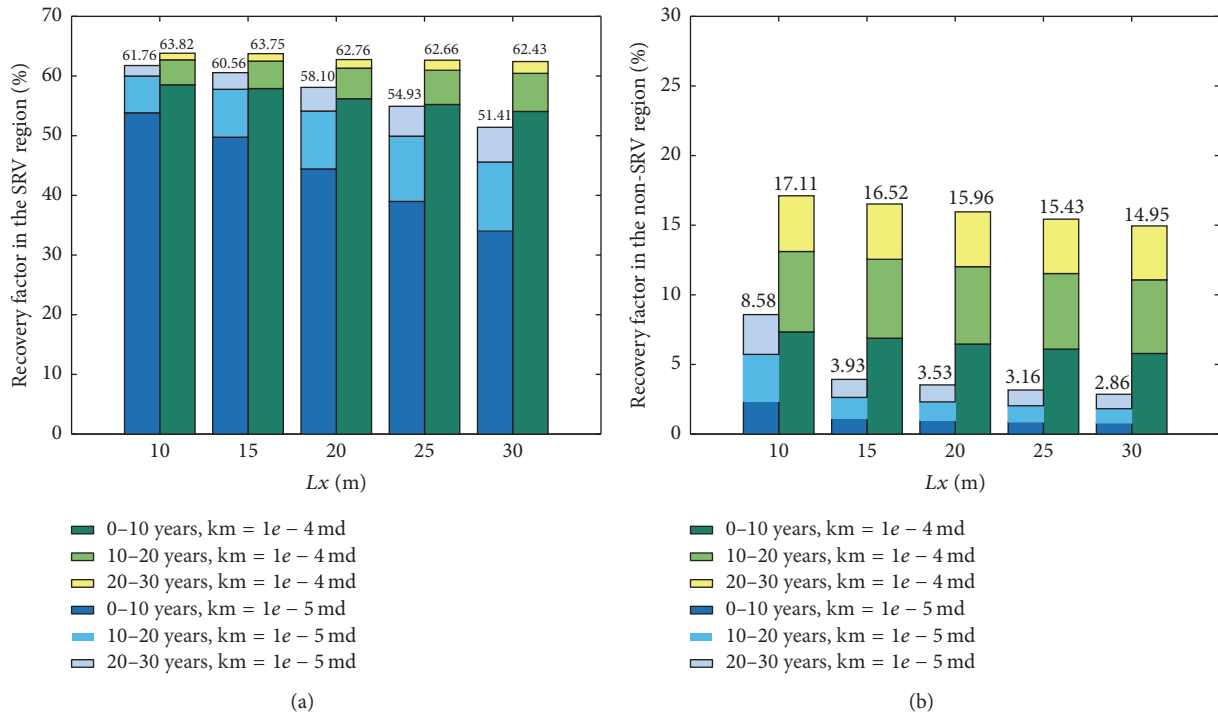


FIGURE 8: The effect of secondary fracture network density on the recovery factor: (a) SRV region and (b) non-SRV region.

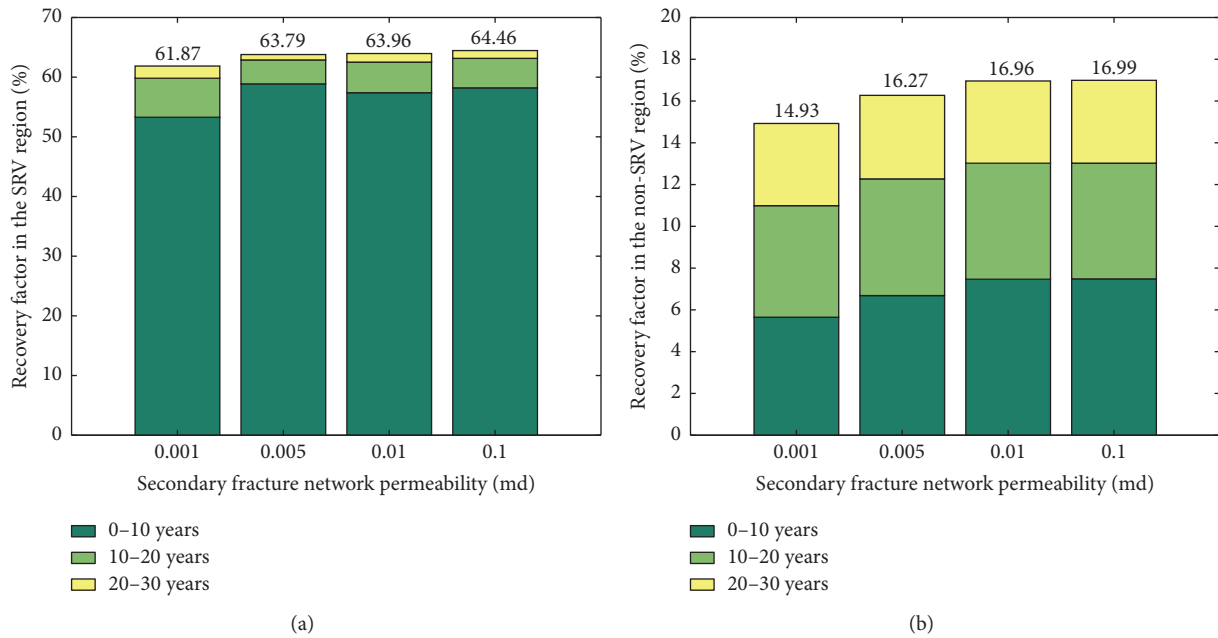


FIGURE 9: The effect of secondary fracture network permeability on the recovery factor: (a) SRV region; (b) non-SRV region.

fracture half-length are selected, that is, 150 m, 130 m, and 110 m., and the corresponding OGIPs in SRV region are $2.25 \times 10^9 \text{ m}^3$, $1.95 \times 10^9 \text{ m}^3$, and $1.65 \times 10^9 \text{ m}^3$. Figure 14 shows the effect of the half-length of the hydraulic fractures on the recovery factors in SRV and non-SRV regions. It can be observed that the half-length only has a moderate effect on the recovery factor in SRV region. But the effect of half-length on the recovery factor in non-SRV region is profound. With

the increase of the half-length, the recovery factor in the non-SRV region increases.

4. Conclusion

This work built a numerical model to analyze the gas production characteristics in shale gas reservoir and used the field data collected from a shale gas play in Sichuan Basin

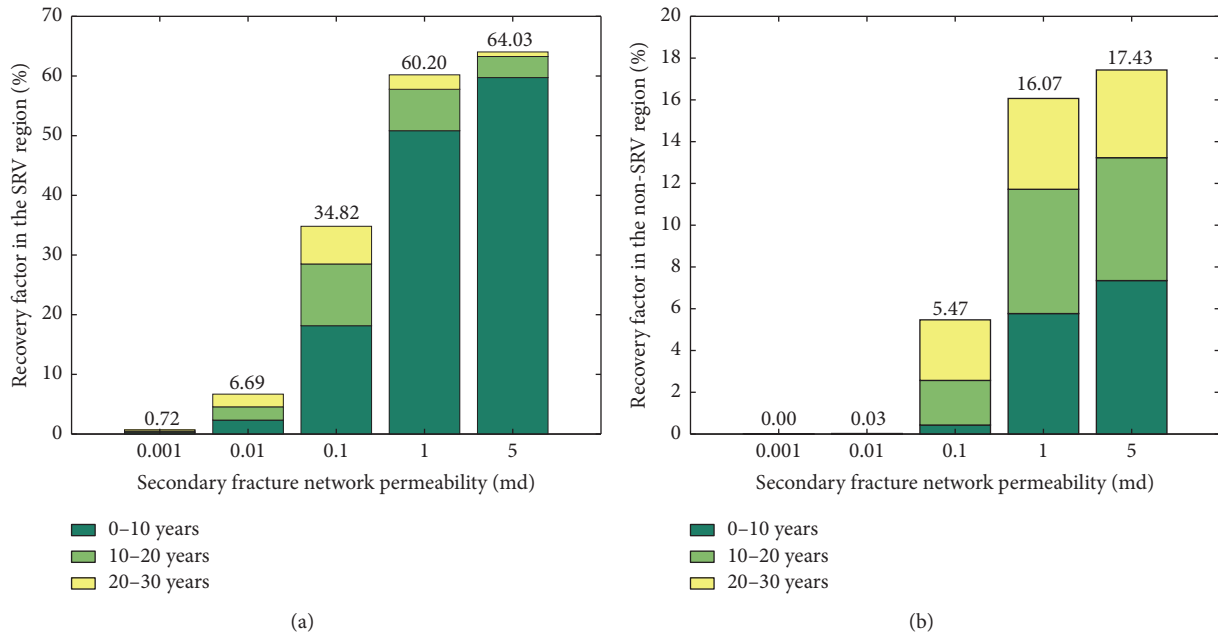


FIGURE 10: The effect of secondary fracture network permeability on the recovery factor without primary hydraulic fractures: (a) SRV region; (b) non-SRV region.

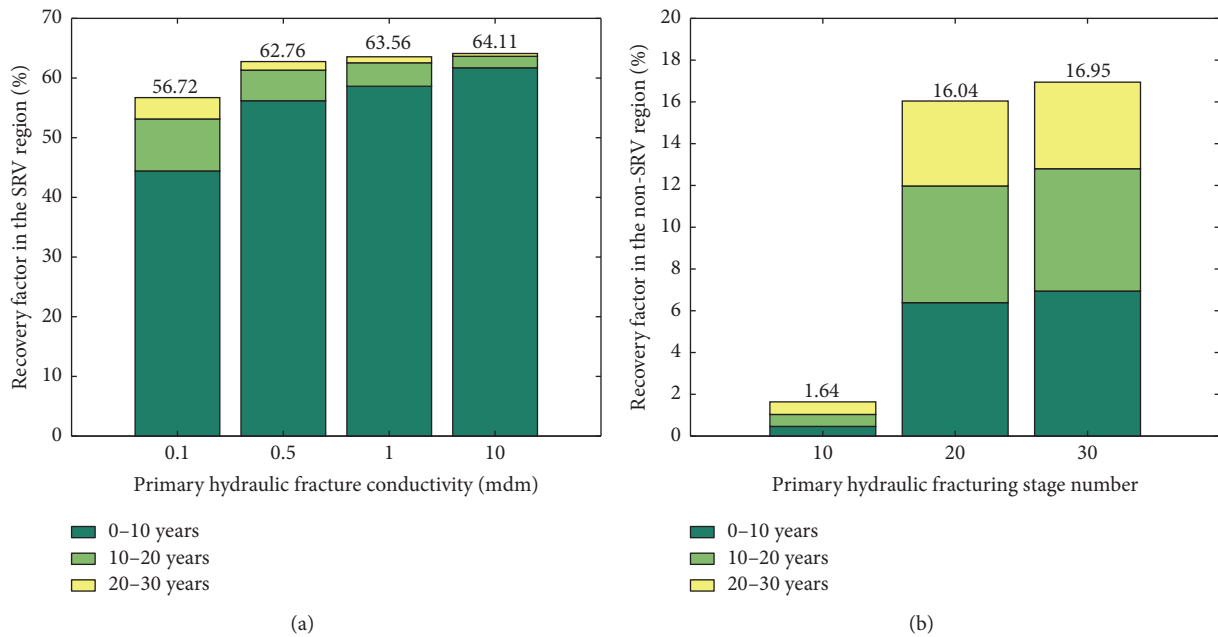


FIGURE 11: The effect of primary hydraulic fracturing stage number on the recovery factor: (a) SRV region; (b) non-SRV region.

in China to investigate the influence of various factors on the production characteristics. It leads to the following key findings:

- (1) The contribution of adsorbed gas and free gas from different regions to the total gas production was explicitly and separately studied by using a “component subdivision method.” Free gas in the SRV region dominates the initial gas production. The adsorbed

gas production increases as the pressure of the shale reservoir gradually decreases and approaches the maximum value at the end of the initial stable production stage. When gas production declines, the production of adsorbed gas can alleviate the decline level by compensating the sharp decline of free gas production in the SRV region. When the gas production comes into the late stable production stage, the free gas in the non-SRV region dominates the gas production.

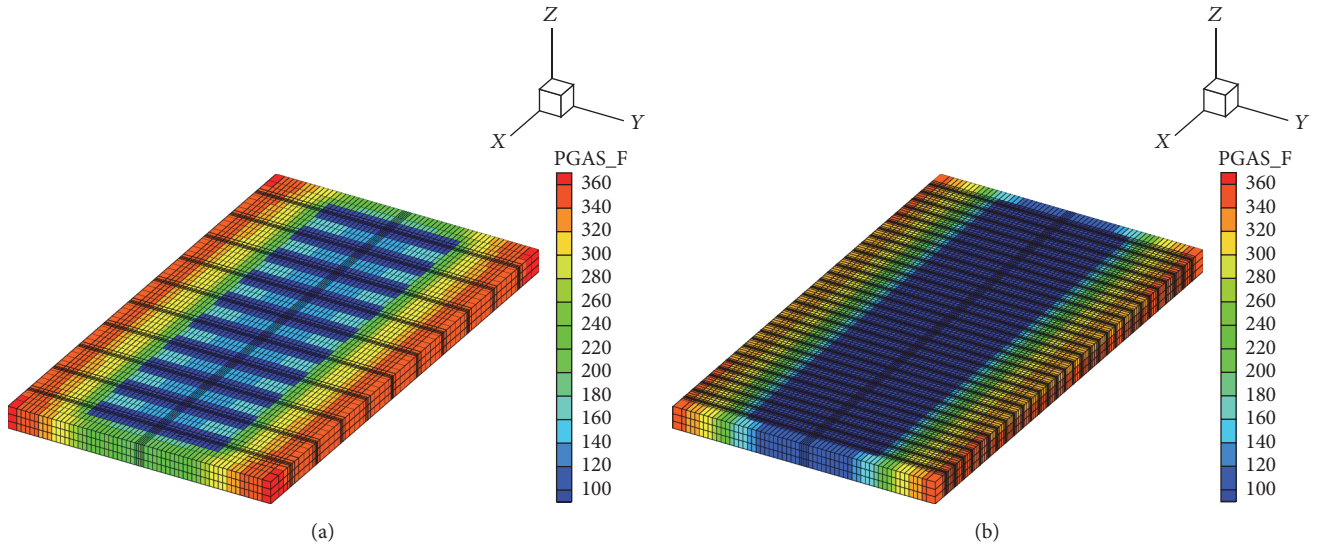


FIGURE 12: The pressure distribution with different hydraulic fracturing stage number: (a) 10 and (b) 20.

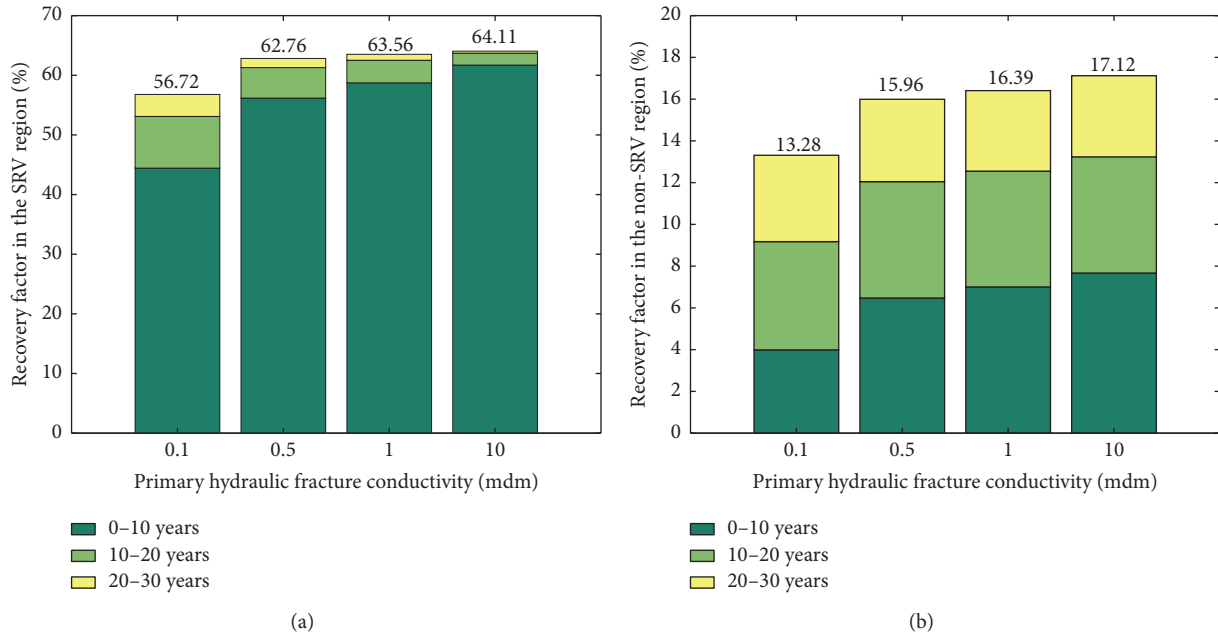


FIGURE 13: The effect of primary hydraulic fracture conductivity on the recovery factor: (a) SRV and (b) non-SRV regions.

In terms of the cumulative production, free gas is the main component in the total gas production.

- (2) The shale matrix permeability in the SRV region has a profound effect on recovery factor in the SRV region as matrix permeability in the non-SRV region does to recovery factor in the non-SRV region. Higher matrix permeability has a positive effect on the recovery factor.
- (3) The density and the permeability of the secondary natural fracture network have more obvious effect on the recovery factor in the non-SRV region than that in SRV region. The existence of the primary hydraulic

fractures is necessary even if a well-connected secondary natural fracture network can be created by hydraulic fracturing.

- (4) The stage number of the hydraulic fracturing needs to be sufficiently large to create a unified pressure system along the horizontal well. The conductivity and half-length of the primary hydraulic fractures have positive effects on the recovery factor in both SRV and non-SRV regions.

Conflicts of Interest

The authors declare that they have no conflicts of interest.

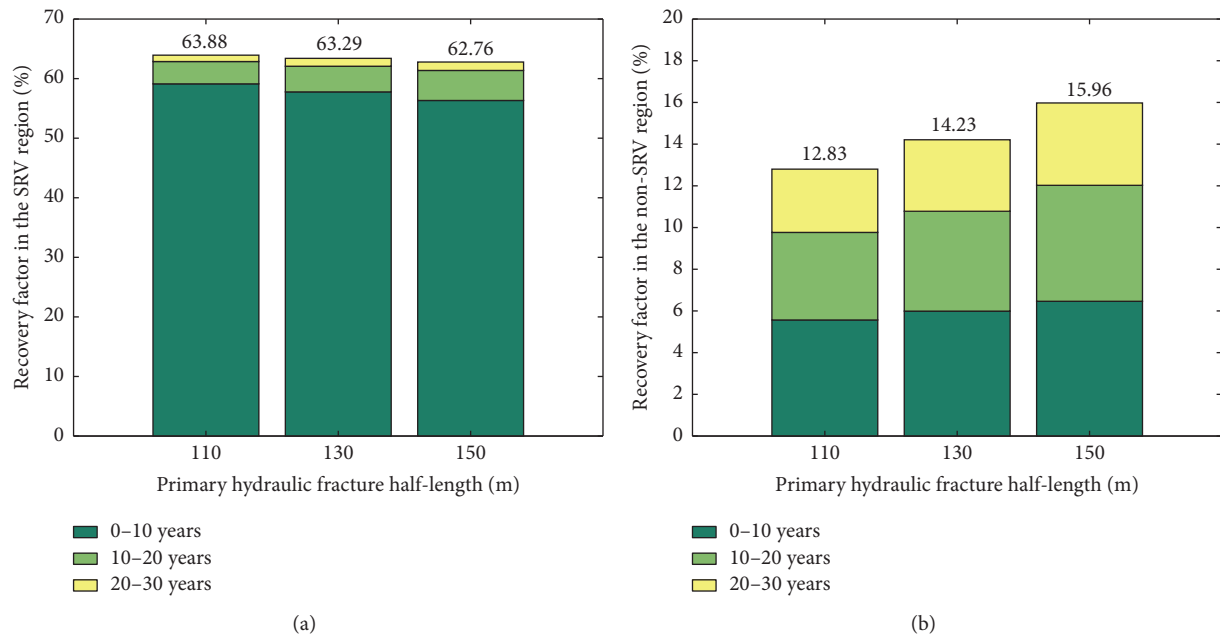


FIGURE 14: The effect of primary hydraulic fracture half-length of fracture on the recovery factor: (a) SRV and (b) non-SRV regions.

Acknowledgments

This work is funded by the National Natural Science Foundation of China (Grant no. 41402199), National Science and Technology Major Project (Grants nos. 2016ZX05037003 and 2016ZX05060002), the Science Foundation of China University of Petroleum, Beijing (Grant no. 2462014YJRC038), China Postdoctoral Science Foundation (Grant no. 2016M591353), and the Science Foundation of Sinopec Group (Grant no. P16058).

References

- [1] J. B. Curtis, "Fractured shale-gas systems," *AAPG Bulletin*, vol. 86, no. 11, pp. 1921–1938, 2002.
- [2] H. Sun, A. Chawathe, H. Hoteit, X. Shi, and L. Li, "Understanding shale gas production mechanisms through reservoir simulation," *Journal of Chemical Physics*, vol. 36, pp. 317–352, 2014.
- [3] W. Yu and K. Sepehrnoori, "Simulation of gas desorption and geomechanics effects for unconventional gas reservoirs," *Fuel*, vol. 116, pp. 455–464, 2014.
- [4] F. Civan, "Effective correlation of apparent gas permeability in tight porous media," *Transport in Porous Media*, vol. 82, no. 2, pp. 375–384, 2010.
- [5] H. Darabi, A. Ettehad, F. Javadpour, and K. Sepehrnoori, "Gas flow in ultra-tight shale strata," *Journal of Fluid Mechanics*, vol. 710, pp. 641–658, 2012.
- [6] H. Singh, F. Javadpour, A. Ettehadtavakkol, and H. Darabi, "Nonempirical apparent permeability of shale," *SPE Reservoir Evaluation and Engineering*, vol. 17, no. 3, pp. 414–424, 2014.
- [7] M. J. Mayerhofer, E. P. Lonon, C. Rightmire, D. Walser, C. L. Cipolla, and N. R. Warplnskl, "What is stimulated reservoir volume?" *SPE Production and Operations*, vol. 25, no. 1, pp. 89–98, 2010.
- [8] J. Sun, G. Niu, and D. Schechter, "Numerical simulation of stochastically-generated complex fracture networks by utilizing core and microseismic data for hydraulically fractured horizontal wells in unconventional reservoirs— a field case study," in *Proceedings of the SPE Eastern Regional Meeting*, vol. 2016, Canton, Ohio, USA, 13–15 September.
- [9] R. Hull, H. Bello, P. L. Richmond, B. Suliman, D. Portis, and R. Meek, "Variable stimulated reservoir volume (SRV) simulation: eagle ford shale case study," *Society of Petroleum Engineers*, 2013.
- [10] Y.-L. Zhao, L.-H. Zhang, J.-X. Luo, and B.-N. Zhang, "Performance of fractured horizontal well with stimulated reservoir volume in unconventional gas reservoir," *Journal of Hydrology*, vol. 512, pp. 447–456, 2014.
- [11] J. E. Warren and P. J. Root, "The behavior of naturally fractured reservoirs," *Society of Petroleum Engineers Journal*, vol. 3, pp. 245–255, 1963.
- [12] S. T. Luthy, "Dual-Porosity Reservoir Modeling of the Fractured Hanifa Reservoir, Abqaiq Field, Saudi Arabia," *AAPG Bulletin*, vol. 5, 1995.
- [13] P. Sarma and K. Aziz, "New transfer functions for simulation of naturally fractured reservoirs with dual-porosity models," *SPE Journal*, vol. 11, no. 3, pp. 328–340, 2006.
- [14] H. Lu, G. Di Donato, and M. J. Blunt, "General transfer functions for multiphase flow in fractured reservoirs," *SPE Journal*, vol. 13, no. 3, pp. 289–297, 2008.
- [15] B. Gong, M. Karimi-Fard, and L. J. Durlofsky, "Upscaling discrete fracture characterizations to dual-porosity, dual-permeability models for efficient simulations of flow with strong gravitational effects," *SPE Journal*, vol. 13, no. 1, pp. 58–67, 2008.
- [16] S. Geiger, M. Dentz, and I. Neuweiler, "A novel multirate dual-porosity model for improved simulation of fractured and multiporosity reservoirs," *SPE Journal*, vol. 18, no. 4, pp. 670–684, 2013.
- [17] M. Karimi-Fard, L. J. Durlofsky, and K. Aziz, "An efficient discrete-fracture model applicable for general-purpose reservoir simulators," *SPE Journal*, vol. 9, no. 2, pp. 227–236, 2004.

- [18] A. Moïnfar, A. Varavei, K. Sepehrnoori, and R. T. Johns, "Development of an efficient embedded discrete fracture model for 3D compositional reservoir simulation in fractured reservoirs," *SPE Journal*, vol. 19, no. 2, pp. 289–303, 2014.
- [19] X. Yan, Z. Huang, J. Yao, Y. Li, and D. Fan, "An efficient embedded discrete fracture model based on mimetic finite difference method," *Journal of Petroleum Science and Engineering*, vol. 145, pp. 11–21, 2016.
- [20] S. H. Lee, C. L. Jensen, and M. F. Lough, "Efficient finite-difference model for flow in a reservoir with multiple length-scale fractures," *SPE Journal*, vol. 5, no. 3, pp. 268–275, 2000.
- [21] S. H. Lee, M. F. Lough, and C. L. Jensen, "Hierarchical modeling of flow in naturally fractured formations with multiple length scales," *Water Resources Research*, vol. 37, no. 3, pp. 443–455, 2001.
- [22] A. Darishchev, P. Lemouzy, and P. Rouvroy, "On Simulation of Flow in Tight and Shale Gas Reservoirs," in *Proceedings of the SPE Unconventional Gas Conference and Exhibition*, Society of Petroleum Engineers, Muscat, Oman, 2013.
- [23] T. Yang, X. Li, and D. Zhang, "Quantitative dynamic analysis of gas desorption contribution to production in shale gas reservoirs," *Journal of Unconventional Oil and Gas Resources*, vol. 9, pp. 18–30, 2015.
- [24] X. Li, D. Zhang, and S. Li, "A multi-continuum multiple flow mechanism simulator for unconventional oil and gas recovery," *Journal of Natural Gas Science and Engineering*, vol. 26, pp. 652–669, 2015.
- [25] H. Wang, "What factors control shale-gas production and production-decline trend in fractured systems: a comprehensive analysis and investigation," *Society of Petroleum Engineers Journal*, vol. 22, no. 02, pp. 562–581, 2017.

Research Article

Study on the Oxidative Leaching of Uranium from the Lignite in the $\text{CO}_3^{2-}/\text{HCO}_3^-$ System

Y. Ning, Y. Li, Y. Zhang, and P. Tang

School of Environmental Studies, China University of Geosciences, Wuhan 430074, China

Correspondence should be addressed to Y. Li; yl.li@cug.edu.cn

Received 14 July 2017; Revised 19 October 2017; Accepted 12 November 2017; Published 19 December 2017

Academic Editor: Dan Lu

Copyright © 2017 Y. Ning et al. This is an open access article distributed under the Creative Commons Attribution License, which permits unrestricted use, distribution, and reproduction in any medium, provided the original work is properly cited.

$\text{Na}_2\text{CO}_3/\text{NaHCO}_3$ mixtures with different oxidants were used to leach uranium in the lignite which was obtained from Lincang, Yunnan province. The experimental results showed that the optimal solid/liquid ratio and $\text{CO}_3^{2-}/\text{HCO}_3^-$ ratio for uranium leaching were 1 : 20 (g/mL) and 2 : 1, respectively. With the increase of carbon concentration from 0.1 mol/L to 1.1 mol/L, the leaching efficiency of uranium increased from 14.64% to 42.39% after 6 h leaching. The oxidants could significantly enhance the uranium leaching efficiency, which was up to 72.23% by injecting O_2 at 1.5 L/min after 12 h leaching. The oxidative leaching process of uranium from the lignite was better fitted to the pseudo-second-order reaction model. The sequential extraction results illustrated that the oxidants could effectively enhance the leaching of organic matter bound uranium in the lignite, which was decreased from 76.86 mg/kg to 9.00 mg/kg by injecting O_2 . The infrared spectrum analysis demonstrated that the corresponding transmittance at about 3197 cm^{-1} was prominently reduced after the oxidative leaching, which intimated that the phenolic and alcoholic hydroxyl might be the main functional groups combined with uranium in the lignite.

1. Introduction

The radiation pollution caused by the consumption of the uranium-bearing coals has gradually aroused great public concern [1]. The average uranium content of coals in China was 2.31 mg/kg based on analyses of 1535 coal samples [2]. Though the content of uranium in coals is relatively low, high abundance of uranium in coals was found in some regions of China. The concentration of uranium in the Late Permian coals was 111 mg/kg from the Heshan coalfield of southern China [3], and it was 153 mg/kg in the lignite from the Yanshan coalfield of Yunnan province [4]. Moreover, the uranium content of coals could be extremely high in individual regions that could be used as uranium resources. For instance, the uranium concentration in coals from the Yili Basin of Xinjiang province was up to 7207 mg/kg [5].

In order to reduce the environment pollution, some study tried to leach the uranium from the combustion products of the uranium-bearing coals in recent years [6, 7]. However, the uranium leaching efficiency generally decreased with the increase of combustion temperature and time [8]. To prevent

the reduction of the leaching efficiency, the combustion process needs to be strictly controlled while leaching uranium from the combustion products. In addition, although the uranium tends to be concentrated in the bottom ash and fly ash during the coal combustion [9], some of the fine particles containing uranium (especially the submicron particles) were difficult to be captured by the air pollution control devices, and those fine particles usually diffused into the air and led to uranium pollution in the environment [10].

Considering the environmental pollution caused by uranium-bearing coals and the potential economic value of the uranium in the coals, leaching uranium from the uranium-bearing coals such as lignite can efficiently reduce the radiation pollution and brings economic benefits. The study of the leaching of uranium from coals has been started since the 1950s [8] and the leaching reagents were mainly sulfuric acid, nitric acid, and other inorganic acids. However, these techniques could bring new problems. As the organic matter in coals partially dissolves in the leaching reagent during the acid leaching process, it is difficult to separate the liquid phase from the solid leaching residue. Moreover,

the coals are difficult to be reused after leaching with the inorganic acids.

Otherwise, the effect of the oxidants on the uranium leaching was studied as well. It has been proved that the oxidants could enhance the leaching efficiency of uranium. U(IV) in the tailing could be oxidized to U(VI) by air, H_2O_2 , O_3 , NaClO_3 , H_2SO_5 , MnO_2 , and KMnO_4 [11–13]. The study of Shlewit and Alibrahim [14] revealed that the removing ratio of uranium in the phosphate polluted soil increased from 30% to 60% by adding H_2O_2 . Francis et al. [12] found that the uranium leaching efficiency in the soil increased by about 10% when adding 20 mg/g KMnO_4 .

The objective of the study is to enhance the uranium leaching efficiency based on the premise that the coals after leaching are suitable for reuse. Therefore, the $\text{CO}_3^{2-}/\text{HCO}_3^-$ systems with different oxidants were used to leach uranium in the lignite, which was obtained from Lincang, Yunnan province. Specifically, we sought to determine the following:

- (1) The effect of the solid/liquid ratio (S/L ratio), $\text{CO}_3^{2-}/\text{HCO}_3^-$ ratio, the leaching reagent concentration, and oxidants on the uranium leaching efficiency of the lignite
- (2) The kinetics and the mechanism of the uranium leaching process in the lignite.

2. Methods and Techniques

2.1. Materials. The lignite from Lincang City, southwest of Yunnan province, China, which contained 102.10 mg/kg uranium, was used in this study. The lignite samples were ground, using a Hubei Geological Research Laboratory GSXX-4 planetary ball mill, to a homogeneous dry powder of less than 200 mesh. The chemical compositions of the lignite were analyzed by a PANalytical Axios mAX X-ray fluorescence (XRF) spectrometry (Table 1).

30% aqueous H_2O_2 , NaClO solution with 5% available chlorine, KMnO_4 , $\text{K}_2\text{S}_2\text{O}_8$, NaHCO_3 , and Na_2CO_3 were purchased from the Sinopharm Chemical Reagent Company. All the chemicals used in the experiments were of analytical purity grade. High purity O_2 (99.5%) was purchased from the Wuhan Iron and Steel (Group) Corporation.

2.2. Analytical Method. The total uranium content in the lignite was determined by the method from Dai et al. [15] and the modified sequential extraction procedure proposed by Xiong et al. [16] was used to analyze the speciation of uranium in the lignite. The concentration of uranium was analyzed using a PerkinElmer Sciex ELAN DRC-II inductively coupled plasma-mass spectrometer (ICP-MS). Fourier transform infrared (FTIR) spectra of the samples were recorded between 400 and 4000 cm^{-1} at a constant temperature (20°C) on a Nicolet 6700 FTIR spectrometer. pH was measured using a Thermo Orion model 868 pH-meter.

2.3. Carbonate/Bicarbonate Leaching Experiment. Various S/L ratios, $\text{CO}_3^{2-}/\text{HCO}_3^-$ ratios, and the concentrations of the leaching reagent were designed to determine the optimal conditions for the alkaline leaching of uranium from the

TABLE 1: Chemical compositions of the lignite (wt.%) (ash basis).

Na_2O	0.221
MgO	1.552
Al_2O_3	19.026
SiO_2	40.335
P_2O_5	0.094
SO_3	10.543
K_2O	2.399
CaO	6.349
TiO_2	0.829
MnO	0.545
Fe_2O_3	17.023
NiO	0.135
CuO	0.064
ZnO	0.055
GeO_2	0.126
As_2O_3	0.09
Rb_2O	0.049
SrO	0.078
Y_2O_3	0.064
ZrO_2	0.022
WO_3	0.106
PbO	0.053
Cl	0.109
U	0.134

lignite. The temperature and the shaking speed in the leaching experiments were 25°C and 150 r/min, respectively. The leachates were centrifuged at 5000 r/min for 5 min and the supernatants were collected for the uranium content analysis. The uranium leaching efficiency was defined as the ratio of the uranium content in the leaching solution to the total amount of uranium in the lignite, expressed as a percentage.

2.4. Oxidative Leaching Experiment. Under the optimal S/L ratio and $\text{CO}_3^{2-}/\text{HCO}_3^-$ ratio, four oxidants, which were 30% aqueous H_2O_2 , NaClO solution with 5% available chlorine, KMnO_4 , and $\text{K}_2\text{S}_2\text{O}_8$, were selected to assess the effect of oxidation on the leaching efficiency of uranium from the lignite. In the experiment, the concentration of the leaching agent was 0.5 mol/L. Besides, the dosage of H_2O_2 and NaClO solution was defined as the volume ratio of the oxidant to the leaching agent, while the dosage of KMnO_4 and $\text{K}_2\text{S}_2\text{O}_8$ was defined as the mass ratio of the oxidant to the lignite sample.

2.5. Kinetic Experiment. Kinetic experiments were conducted using 0.5 mol/L of the leaching agent with the optimal S/L ratio, $\text{CO}_3^{2-}/\text{HCO}_3^-$ ratio, and the oxidant dosage for a period of 24 h. In addition, high purity oxygen (99.5%) was injected to the leaching agent at a constant rate of 1.5 L/min in order to compare the leaching efficiency. Samples were collected at different predetermined time intervals to evaluate the kinetic performance of the uranium leaching process.

The leaching of uranium can be interpreted as the uranium desorption from the lignite. The pseudo-first-order

equation and the pseudo-second-order equation were applied to investigate the leaching kinetic [17].

The pseudo-first-order equation can be formulated as follows:

$$\frac{dQ_t}{dt} = -k_1 (Q_t - Q_e), \quad (1)$$

where k_1 is the rate constant and Q_e and Q_t are the solid-phase concentrations of uranium in the lignite at equilibrium and any time t . With the initial condition of $Q_t = Q_0$ at $t = 0$, (1) is integrated and yields the following:

$$Q_t = Q_e + (Q_0 - Q_e) \exp(-k_1 t). \quad (2)$$

The value of Q_t is calculated according to

$$Q_t = Q_0 - \frac{(C_t - C_0) V_L}{m_s}, \quad (3)$$

where C_0 is the initial concentration of uranium in the leaching solution (mg/L), C_t is the concentration of uranium in the leaching solution at t (mg/L), V_L is the volume of the leaching solution, and m_s is the mass of the lignite.

The pseudo-second-order equation is expressed as follows:

$$\frac{dQ_t}{dt} = -k_2 (Q_t - Q_e)^2, \quad (4)$$

where k_2 is the rate constant. With the initial condition of $Q_t = Q_0$ at $t = 0$, (4) is integrated and yields

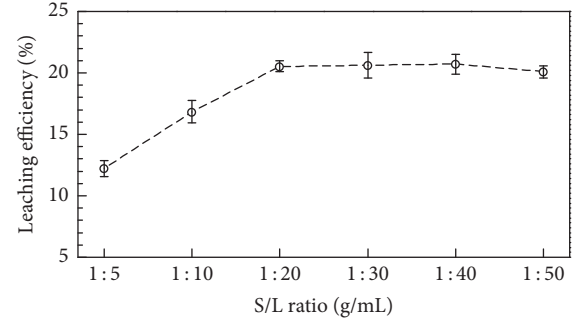
$$Q_t = Q_e + \frac{Q_e - Q_0}{k_2 t (Q_e - Q_0) - 1}. \quad (5)$$

According to the kinetic equations, the rate constants (k_1 and k_2) and the theoretical capacity of the uranium leaching efficiency were computed using the nonlinear fitting.

2.6. Leaching Mechanism Analysis. The leachates collected from the kinetic experiments were centrifuged at 5000 r/min for 5 min and the residues washed with deionized water were taken for the sequential extraction and FTIR analysis. The mechanism of uranium leaching from the lignite was analyzed based on the comparisons of the sequential extraction for the uranium speciation in the lignite before and after leaching. Furthermore, FTIR spectra were used to investigate the leaching process.

3. Experimental Results

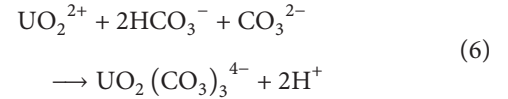
3.1. The Effect of S/L Ratios on the Uranium Leaching of the Lignite. The leaching efficiency of uranium in 0.5 mol/L Na_2CO_3 solution under various S/L ratios is shown in Figure 1. After 6 h reaction, the leaching process tends to be in equilibrium. The results indicate that, with the decrease of S/L ratio, the leaching efficiency of uranium increases gradually and is up to $20.54 \pm 0.46\%$ at the optimal S/L ratio of 1:20 g/mL. However, a further decrease of S/L ratio does not lead to an observable increase of the uranium leaching efficiency.



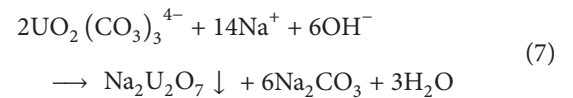
—○— Leaching efficiency

FIGURE 1: The leaching efficiency of uranium in 0.5 mol/L Na_2CO_3 solution at various S/L ratios.

3.2. The Effect of the Concentration of Leaching Agents and the $\text{CO}_3^{2-}/\text{HCO}_3^-$ Ratio on the Uranium Leaching Efficiency. Figure 2 shows the leaching efficiency of uranium by different concentration of the leaching agents and $\text{CO}_3^{2-}/\text{HCO}_3^-$ ratio at the optimal S/L ratio after 6 h leaching. It can be observed that the leaching efficiency of uranium increases with the concentration of the leaching agent. The maximum uranium leaching efficiency of the 0.1 mol/L, 0.3 mol/L, 0.5 mol/L, 0.7 mol/L, 0.9 mol/L, and 1.1 mol/L leaching agent is 15.21%, 19.28%, 23.74%, 26.30%, 40.69%, and 42.39%, respectively. The main reaction in the solution can be expressed as follows [11]:



With the increase of NaHCO_3 in the leaching agent, the ultimate pH of the leaching agent gradually declines (as shown in Figure 3). As the concentration of the leaching agent ranges from 0.5 mol/L to 1.1 mol/L, the maximum leaching efficiency of uranium is achieved when the $\text{CO}_3^{2-}/\text{HCO}_3^-$ ratio is 2:1, which can be the optimal $\text{CO}_3^{2-}/\text{HCO}_3^-$ ratio for the leaching of uranium in the study. Furthermore, the ultimate pH in the leaching experiment under the optimal $\text{CO}_3^{2-}/\text{HCO}_3^-$ ratio is around 9.70. Some studies have shown that $[\text{UO}_2(\text{CO}_3)_3]^{4-}$ could combine with OH^- to produce sodium diuranate precipitation at pH values above 11 (see (7)). Santos and Ladeira [18] found out that, in the pH range of 9~10.2, the precipitation of sodium diuranate could be reduced by using $\text{NaCO}_3/\text{NaHCO}_3$ mixture, which is similar to the result obtained in our study



3.3. The Effect of the Oxidant on the Uranium Leaching Efficiency. Figure 4(a) compares the uranium leaching efficiencies at different dosages of oxidants after 6 h leaching. In the experiment, the concentration of the leaching agent was 0.5 mol/L and the $\text{CO}_3^{2-}/\text{HCO}_3^-$ ratio was 2:1. The results

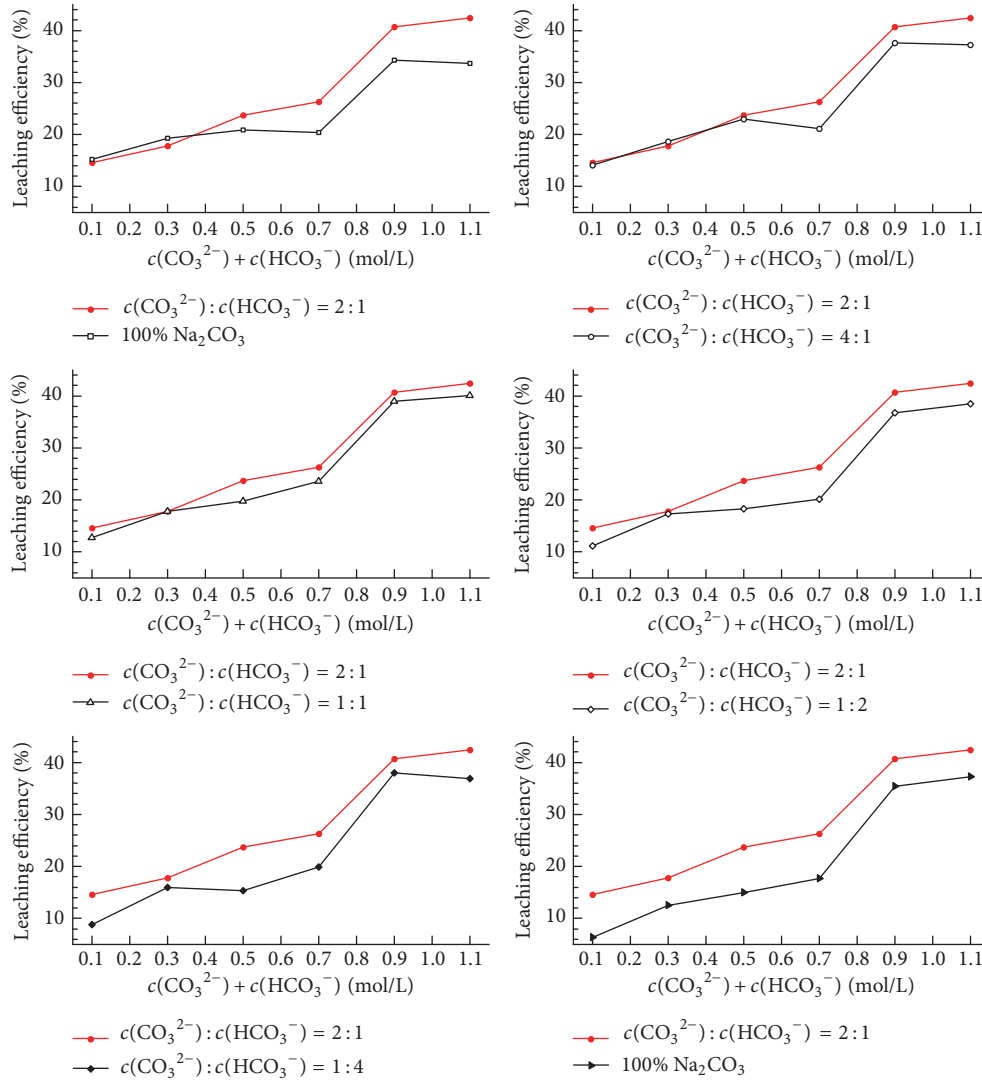


FIGURE 2: The leaching efficiency at various leaching agent concentrations and mixture ratios.

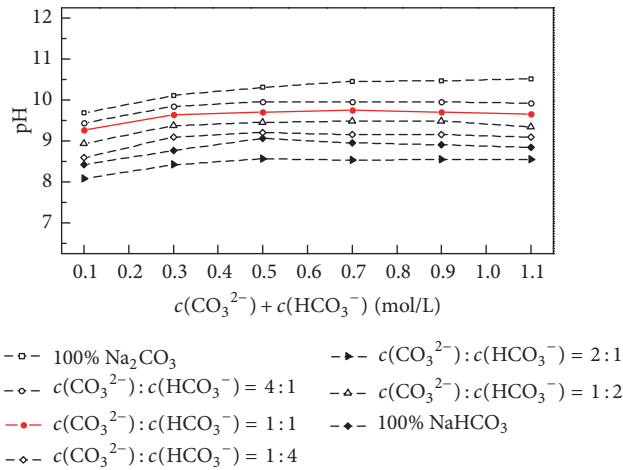


FIGURE 3: The ultimate pH at various leaching agent concentrations and mixture ratios.

indicate that the oxidants can enhance the uranium leaching efficiency. It is concluded that the optimal dosage of KMnO_4 and $\text{K}_2\text{S}_2\text{O}_8$ is 2 wt.% while the corresponding leaching efficiency of uranium is 34.71% and 50.45%, respectively. Besides, the optimal dosage of H_2O_2 (30% aqueous solution) and NaClO solution (5% available chlorine) is 1 vol.% with the corresponding leaching efficiencies 39.57% and 41.26%, respectively.

Moreover, as the dosage of NaClO solution increases from 4 vol.% to 16 vol.%, the ultimate pH in the solution continually increases from 9.97 to 11.65 (Figure 4(b)) as the hydrolysis of ClO^- , which leads to the occurrence of (7) and reduces the uranium leaching efficiency from 41.98% to 29.88%. Besides, the oxidative leaching experiment with a high dosage of H_2O_2 cannot be carried out, as the leaching agent reacts violently with H_2O_2 (which is actually a weak acid) at a dosage of 16 vol.%. Furthermore, the ultimate pH of the leaching solutions containing KMnO_4 and $\text{K}_2\text{S}_2\text{O}_8$ is reduced very slightly.

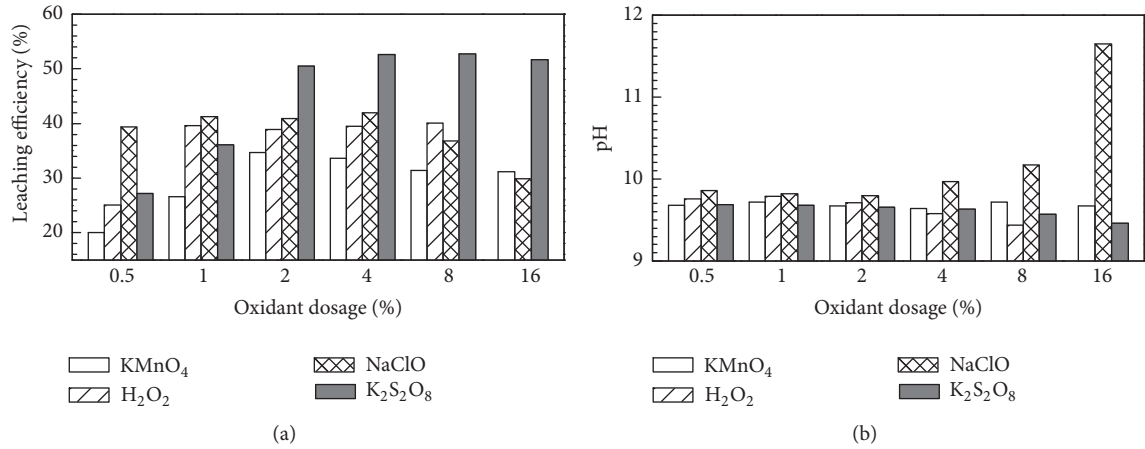


FIGURE 4: The effect of the oxidant on the uranium leaching efficiency and the ultimate pH.

3.4. Kinetics of the Leaching of Uranium from the Lignite.

Figure 5 depicts the time variation of the uranium leaching efficiency from the lignite. The results show that the significant increases in the leaching efficiency of uranium are correlated with the addition of oxidants. In the experiment without adding any oxidant, the leaching process approaches equilibrium within 4 h and the corresponding uranium leaching efficiency is only 29.10%. On the contrast, the leaching process reaches equilibrium at the shortest time of about 2 h with the addition of 1 vol.% H₂O₂ (30% aqueous solution) and the leaching efficiency is up to 43.51%. On the other hand, the equilibrium time of about 6 h is needed for the leaching process with the addition of 2 wt.% KMnO₄ and K₂S₂O₈, the corresponding leaching efficiency of which is 42.35% and 48.34%, respectively. Furthermore, under the condition of adding 1 vol.% NaClO solution (5% available chlorine) and injecting O₂ at a constant rate of 1.5 L/min, it takes about 12 h for the leaching process to attain the equilibrium state and, correspondingly, the uranium leaching efficiency of 52.06% and 72.23% is achieved, respectively.

Figure 6 displays the kinetics of the leaching of uranium from the lignite. The pseudo-first-order and pseudo-second-order equations that are applied to describe the kinetics of the leaching process and the kinetic parameters are listed in Table 2. The correlation coefficients (r^2) of the two kinetic equations reveal that the leaching process with the five oxidants is better fitted to the pseudo-second-order model, in which the maximum r^2 is 0.989 under the condition of injecting O₂. On the contrary, the leaching process without oxidant is better fitted to the pseudo-first-order model and the corresponding r^2 is 0.957. The better applicability of the pseudo-first-order model may be due to the strong affinity of the lignite to uranium, which also shows that the leaching efficiency is mainly dependent on the amount of the leachable uranium in the lignite.

Further analysis of the values of Q_e shows that when the leaching process reaches the equilibrium state, the solid-phase-concentration of uranium in the lignite samples is much lower in the oxidative leaching process with the five oxidants, which tally with the experimental results. Thus, the

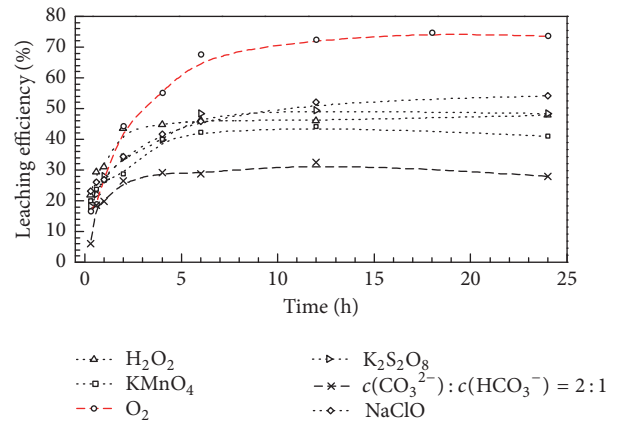


FIGURE 5: The leaching efficiency of uranium from lignite over a period of time.

use of the oxidant to enhance the leaching of uranium from the lignite is an effective option, not only because the oxidant can oxidize U(IV) to the significantly more soluble U(VI), but also because it can degrade the organic matter in the lignite to reduce the speciation which is difficult to leach, such as the organic matter bound uranium. This is what we are going to discuss in the following sections.

3.5. Sequential Extraction Experiment. Figure 7 shows the contents of the speciation of uranium in the lignite samples before and after leaching experiment by the sequential extraction procedure. The result indicates that the main speciation of uranium in the original lignite is the organic matter bound, which significantly decreased in the oxidative leaching process. At the conditions of adding H₂O₂, K₂S₂O₈, NaClO, and O₂, the organic matter bound uranium is reduced from 76.86 mg/kg to 38.89 mg/kg, 27.27 mg/kg, 25.72 mg/kg, 23.39 mg/kg, and a minimum of 9.00 mg/kg, respectively, while, in the experiment without adding any oxidant, it is decreased to 45.34 mg/kg only.

Otherwise, the reduction of the Fe-Mn oxides bound, sulfide bound, and aluminosilicate bound uranium in the

TABLE 2: Kinetic parameters for the leaching of uranium from the lignite.

Run	Experimental data		Pseudo-first-order kinetic				Pseudo-second-order kinetic			
	C_e (mg·L ⁻¹)	Q_e (mg·kg ⁻¹)	Q_0 (mg·kg ⁻¹)	k_1 (h ⁻¹)	Q_e (mg·kg ⁻¹)	r^2	Q_0 (mg·kg ⁻¹)	k_2 (kg·mg ⁻¹ ·h ⁻¹)	Q_e (mg·kg ⁻¹)	r^2
(a)	3.76	27.00	97.77	0.40	27.32	0.988	100.65	0.0065	18.13	0.989
(b)	2.76	46.88	93.41	0.60	51.13	0.874	99.84	0.028	49.14	0.935
(c)	2.47	52.75	97.19	0.74	54.03	0.940	101.94	0.028	51.05	0.973
(d)	2.44	53.28	99.97	1.49	55.29	0.965	102.48	0.054	52.78	0.982
(e)	2.09	60.30	97.10	0.96	60.04	0.892	101.63	0.053	58.79	0.937
(f)	1.43	73.50	102.75	1.23	71.92	0.957	104.37	0.12	72.67	0.861

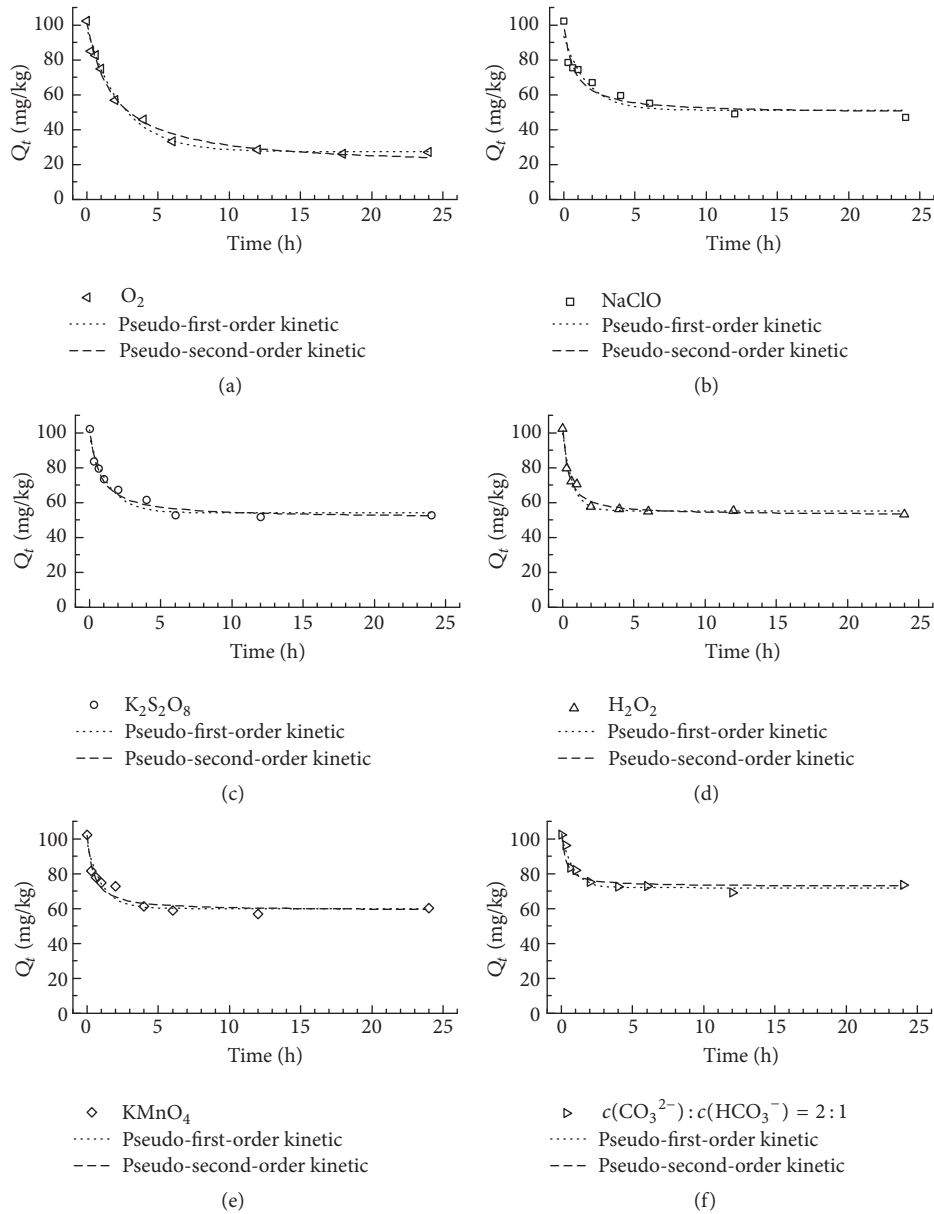


FIGURE 6: Kinetics of the leaching of uranium from the lignite.

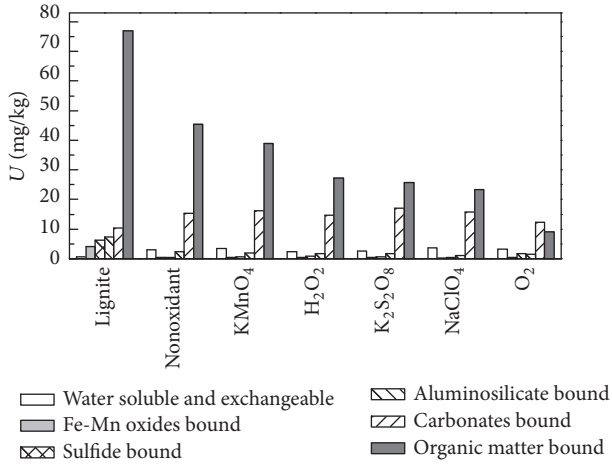


FIGURE 7: The speciation of uranium in the lignite before and after leaching.

leaching experiments is similar. In addition, a small amount of $[\text{UO}_2(\text{CO}_3)_3]^{4-}$ in the leachate can be adsorbed onto the lignite sample, which will easily be desorbed again during the sequential extraction procedure. Therefore, the contents of the water soluble and carbonates bound uranium in the lignite samples increase slightly after leaching.

The reduction of the organic matter bound uranium shows significant positive relationship with the corresponding uranium leaching efficiency, which illustrates that the leaching efficiency mainly depends on the leaching of the organic matter bound uranium in the lignite.

Among the five oxidants, the reduction of the organic matter bound uranium in the lignite by injecting O_2 is much more efficient, and the main reasons can be explained as follows: (1) dissolved oxygen (DO) consumed during the leaching process can be continuously supplied by the injection of O_2 at a constant rate of 1.5 L/min, which maintains a supersaturated state of DO in the leaching agent; (2) the lignite sample agitated by the injection of O_2 is well-mixed in the leaching agent, which increases the contact area between the powdered lignite samples, the leaching agent, and O_2 and therefore enhances the oxidative leaching.

3.6. FTIR Analysis. Figure 8 compares the FTIR spectra of the lignite samples before and after oxidative leaching. The main bands in the infrared spectrum of the original lignite and corresponding assignments are as follows: (1) the intense band at about 3197 cm^{-1} is attributed to the O-H stretching vibrations of alcohols and phenols; (2) the band at about 2919 cm^{-1} is caused by the C-H stretching vibrations of aliphatic structures; (3) the band at about 1610 cm^{-1} is assigned to the C=C stretching vibrations of aromatic rings; (4) the band at about 1437 cm^{-1} is ascribed to the C-H bending vibrations of aliphatic groups; (5) the band at about 1278 cm^{-1} can be attributed to the C-O stretching of phenolic groups; (6) the band at about 1031 cm^{-1} is generally attributed to C-O stretching of ethers and phenols [19–21]. According to the spectrum, the original lignite is rich in oxygen-containing functional groups and aromatic rings.

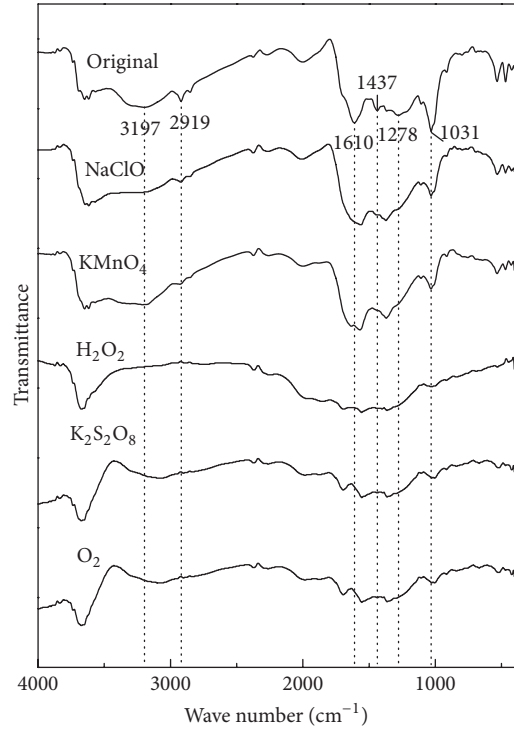


FIGURE 8: The FTIR spectra of the lignite before and after oxidative leaching.

In the infrared spectra of the lignite after oxidative leaching, the peak at about 3197 cm^{-1} significantly reduces, which indicates that the content of hydroxyl groups in alcohols and phenols decreases by oxidation. The infrared spectra adsorption peaks at 2919 cm^{-1} , 1610 cm^{-1} , 1437 cm^{-1} , 1278 cm^{-1} , and 1031 cm^{-1} also experience a decrease in the oxidative leaching process with O_2 , H_2O_2 , and $\text{K}_2\text{S}_2\text{O}_8$.

The lignite belongs to the low rank coal with a low degree of coalification, which contains a large quantity of humic acid and fulvic acid. It has been studied previously that humic acid provides a lot of functional groups which are able to combine with the metal ions, including the carboxyl [22], phenolic hydroxyl, and alcoholic hydroxyl [23]. In the study, the phenolic hydroxyl and alcoholic hydroxyl groups may be the major functional groups combined with uranium. We conclude that the main reason for the enhancement of the uranium leaching efficiency is the effective degradation of these functional groups by the oxidants.

4. Conclusions

In this study, the effects of the S/L ratio, $\text{CO}_3^{2-}/\text{HCO}_3^-$ ratio, the leaching reagent concentration, and oxidants on the uranium leaching efficiency of the lignite were discussed. Some conclusions can be drawn as follows.

- (1) The leaching of uranium from the lignite by $\text{Na}_2\text{CO}_3/\text{NaHCO}_3$ mixture is efficient under the optimal solid/liquid ratio and $\text{CO}_3^{2-}/\text{HCO}_3^-$ ratio, which are 1:20 (g/mL) and 2:1, respectively.
- (2) The five oxidants, H_2O_2 , NaClO , KMnO_4 , $\text{K}_2\text{S}_2\text{O}_8$, and O_2 , can significantly enhance the leaching of uranium

in the lignite. And the use of O₂ is the most efficient option which increases the leaching efficiency up to 72.23% after 12 h reaction.

(3) According to the kinetic results, the pseudo-second-order model is suitable to describe the kinetics of oxidative leaching process, and the maximum r^2 is 0.989 in the leaching experiment by injecting O₂.

(4) The organic matter bound uranium, which is the main speciation of uranium in the lignite, can be effectively reduced from 76.86 mg/kg to 9.00 mg/kg by injecting O₂.

(5) The FTIR analyses indicate that the phenolic and alcohol hydroxyl functional groups combined with uranium in the lignite are observably reduced by the oxidants, which may lead to the enhancement of the leaching efficiency of uranium.

Conflicts of Interest

The authors declare that there are no conflicts of interest regarding the publication of this manuscript.

Acknowledgments

This work was partially supported by the National Natural Science Foundation of China (NSFC, no. 41572233). The authors thank Weiyi Huang, Danqing Liu, and Chen Jing for invaluable contributions to this work.

References

- [1] Z. Papp, Z. Dezső, and S. Daróczy, "Significant radioactive contamination of soil around a coal-fired thermal power plant," *Journal of Environmental Radioactivity*, vol. 59, no. 2, pp. 191–205, 2002.
- [2] J. Yang, "Concentration and distribution of uranium in Chinese coals," *Energy*, vol. 32, no. 3, pp. 203–212, 2007.
- [3] S. Dai, W. Zhang, V. V. Seredin et al., "Factors controlling geochemical and mineralogical compositions of coals preserved within marine carbonate successions: A case study from the Heshan Coalfield, southern China," *International Journal of Coal Geology*, vol. 109–110, pp. 77–100, 2013.
- [4] S. Dai, D. Ren, Y. Zhou et al., "Mineralogy and geochemistry of a superhigh-organic-sulfur coal, Yanshan Coalfield, Yunnan, China: Evidence for a volcanic ash component and influence by submarine exhalation," *Chemical Geology*, vol. 255, no. 1–2, pp. 182–194, 2008.
- [5] S. Dai, J. Yang, C. R. Ward et al., "Geochemical and mineralogical evidence for a coal-hosted uranium deposit in the Yili Basin, Xinjiang, northwestern China," *Ore Geology Reviews*, vol. 70, pp. 1–30, 2015.
- [6] X. Lei, G. Qi, Y. Sun, H. Xu, and Y. Wang, "Removal of uranium and gross radioactivity from coal bottom ash by CaCl₂ roasting followed by HNO₃ leaching," *Journal of Hazardous Materials*, vol. 276, pp. 346–352, 2014.
- [7] Y. L. Sun, G. X. Qi, X. F. Lei, H. Xu, and Y. Wang, *Extraction of Uranium in Bottom Ash Derived from High-Germanium Coals*, vol. 31, pp. 589–597, 2016.
- [8] F. J. Hurst, "Recovery of uranium from lignites," *Hydrometallurgy*, vol. 7, no. 4, pp. 265–287, 1981.
- [9] Y. Zhang, M. Shi, J. Wang et al., "Occurrence of uranium in Chinese coals and its emissions from coal-fired power plants," *Fuel*, vol. 166, pp. 404–409, 2016.
- [10] J. Yang, D. Liu, Y. Wang et al., "Release and the interaction mechanism of uranium and alkaline/alkaline-earth metals during coal combustion," *Fuel*, vol. 186, pp. 405–413, 2016.
- [11] C. F. V. Mason, W. R. J. R. Turney, B. M. Thomson, N. Lu, P. A. Longmire, and C. J. Chisholm-Brause, "Carbonate leaching of uranium from contaminated soils," *Environmental Science & Technology*, vol. 31, no. 10, pp. 2707–2711, 1997.
- [12] C. W. Francis, M. E. Timpson, and J. H. Wilson, "Bench- and pilot-scale studies relating to the removal of uranium from uranium-contaminated soils using carbonate and citrate lixiviants," *Journal of Hazardous Materials*, vol. 66, no. 1–2, pp. 67–87, 1999.
- [13] J. H. Kim, H. C. Cho, and K. Han, "Leaching behavior of U and V from a Korean uranium ore using Na₂CO₃ and KOH," *Geosystem Engineering*, vol. 17, no. 2, pp. 113–119, 2014.
- [14] H. Shlewit and M. Alibrahim, "Recovery of uranium from phosphate by carbonate solutions," *Journal of Radioanalytical and Nuclear Chemistry*, vol. 275, no. 1, pp. 97–100, 2008.
- [15] S. Dai, X. Wang, Y. Zhou et al., "Chemical and mineralogical compositions of silicic, mafic, and alkali tonsteins in the late permian coals from the Songzao Coalfield, Chongqing, Southwest China," *Chemical Geology*, vol. 282, no. 1–2, pp. 29–44, 2011.
- [16] J. Y. Xiong, H. X. Li, Z. B. Dong, S. Zhang, N. B. Qian, and C. L. Wu, "Study on the Occurrence of Ferrum in Coal by Ultrasound-assisted Sequential Chemical Extraction," *Environmental Science*, vol. 34, pp. 4490–4494, 2013.
- [17] J. Y. Tseng, C. Y. Chang, C. F. Chang et al., "Kinetics and equilibrium of desorption removal of copper from magnetic polymer adsorbent," *Journal of Hazardous Materials*, vol. 171, pp. 370–377, 2009.
- [18] E. A. Santos and A. C. Q. Ladeira, "Recovery of uranium from mine waste by leaching with carbonate-based reagents," *Environmental Science & Technology*, vol. 45, no. 8, pp. 3591–3597, 2011.
- [19] X. He, B. Xi, Z. Wei et al., "Spectroscopic characterization of water extractable organic matter during composting of municipal solid waste," *Chemosphere*, vol. 82, no. 4, pp. 541–548, 2011.
- [20] L. Li, Z. Wei, L. ZY, J. Wang, Q. S. Zhou, and J. Guo, "Kinetic and thermodynamic studies on the adsorption of U (VI) onto humic acid," *Desalination & Water Treatment*, vol. 54, pp. 2541–2545, 2015.
- [21] S. Xue, K. Wang, Q. L. Zhao, and L. L. Wei, "Chlorine reactivity and transformation of effluent dissolved organic fractions during chlorination," *Desalination*, vol. 249, no. 1, pp. 63–71, 2009.
- [22] K. Schmeide, S. Sachs, M. Bubner, T. Reich, K. H. Heise, and G. Bernhard, "Interaction of uranium (VI) with various modified and unmodified natural and synthetic humic substances studied by EXAFS and FTIR spectroscopy," *Inorganica Chimica Acta*, vol. 351, no. 1, pp. 133–140, 2003.
- [23] S. M. Yakout, S. S. Metwally, and T. El-Zakla, "Uranium sorption onto activated carbon prepared from rice straw: Competition with humic acids," *Applied Surface Science*, vol. 280, pp. 745–750, 2013.

Research Article

Simulation and Analysis of Long-Term CO₂ Trapping for the Shenhua CCS Demonstration Project in the Ordos Basin

Ying Yu,¹ Yilian Li,¹ Guodong Yang,² Fengcheng Jiang,¹ Sen Yang,¹ and Yongsheng Wang³

¹*School of Environmental Studies, China University of Geosciences, Wuhan 430074, China*

²*College of Resources and Environmental Engineering, Wuhan University of Science and Technology, Wuhan 430081, China*

³*China Shenhua Coal Liquefaction Co., Ltd. Ordos, Ordos 017209, China*

Correspondence should be addressed to Yilian Li; yl.li@cug.edu.cn

Received 14 July 2017; Revised 21 October 2017; Accepted 12 November 2017; Published 10 December 2017

Academic Editor: Xiaoqing Shi

Copyright © 2017 Ying Yu et al. This is an open access article distributed under the Creative Commons Attribution License, which permits unrestricted use, distribution, and reproduction in any medium, provided the original work is properly cited.

The Shenhua CO₂ capture and sequestration (CCS) project has achieved its goal of injecting 100,000 tons/year CO₂ into the saline aquifers of the Ordos Basin. This study analyzes the geochemical interactions between CO₂, formation fluid, and host rock of the major formations in the Ordos Basin, assesses the CO₂ trapping capabilities, and predicts the final mineral forms of injected CO₂. Reactive transport simulations are performed using a 2D radial model, which represents a homogeneous formation. The results show that 80% of injected CO₂ remains as free supercritical gas in each formation after injection, while most of CO₂ is sequestered in different carbonate mineral assemblages after 10,000 years. The CO₂ mineral trapping capacities of the Shiqianfeng and Shihezi formations are smaller than the Liujiagou formation. Calcite, dawsonite, and siderite are stable CO₂ trapping minerals, while dolomite, ankerite, and magnesite are not. The increase in porosity and permeability of the three formations in the first 100 years agrees with the observation from the Shenhua CCS Project. Also the decrease in porosity and permeability after 100 years shows agreement with other modelling studies using the similar methods. These results are useful for the evaluation of the geochemical process in long-term CO₂ geological storage.

1. Introduction

The global average surface temperature growing in decades has increased the worries about global warming [1]. The excess emission of greenhouse gas (mainly CO₂) is considered as the principal culprit [2, 3]. Therefore, CO₂ capture and sequestration (CCS) has been proposed—especially CO₂ geological storage (CGS), which becomes one of the most effective methods to mitigate the greenhouse effect [4, 5].

Among CGS studies, the migration patterns of CO₂ and geochemical responses induced by CO₂ injection have been focused on. The results indicate that physical properties of fluid and host rock control the way CO₂ moves, while chemical processes dominate the fate of CO₂ [6–8]. Factors affecting CO₂ migration mainly include the following: (1) density difference of fluid; (2) penetration pathway; (3) capillary pressure; (4) injection rates; and (5) formation pressure [9–11]. However, CO₂ plume beneath caprocks barely

moves without injection pressure as driven force, although molecular diffusion/dispersion and convective mixing occur in the CO₂ bearing zone. After injection, the CO₂-water-rock interactions dominate the CO₂ trapping mechanisms, which have great effect on the long-term safety of CO₂ geological storage.

CO₂-water-rock interactions have been widely studied with laboratory experiment and numerical simulation. Several researchers have investigated the reactive transport processes based on field conditions. Cipolli et al. [12] studied the CO₂ injection into the serpentine in Italy by EQ 3/6. Gaus et al. [13] modelled the CO₂ diffusion through the caprock at the Sleipner project using PHREEQC. Audigane et al. [14] simulated the CO₂ injection into a saline aquifer at the Sleipner project using TOUGHREACT. These studies indicate that dissolution of host rock contributes to the CO₂ mineral trapping. The pattern of mineral dissolution and precipitation is different under different field conditions [7, 8, 15].

Some other studies have focused on several specific minerals involved in CO₂-water-rock interactions. Xu et al. [16–18] simulated the CO₂-water-rock interactions using TOUGHREACT; they found dissolution of calcite and aluminosilicate and precipitation of ankerite, dawsonite, siderite, magnesite, calcite, and dolomite. Wigand et al. [19] conducted experiments under in situ conditions of the Bunter Sandstone Formation in Europe and observed dolomite dissolution and smectite precipitation. Okuyama et al. [20] simulated the CO₂-water-rock interactions induced by CO₂ injection in the Tokyo Bay area by TOUGHREACT, and dissolution of plagioclase and precipitation of dawsonite were observed. Their studies indicate that dissolution of carbonate minerals is regarded as dominant reaction in a short time [21, 22]. Meanwhile, precipitation of trapping minerals depends on the primary mineral assemblages [23].

For a specific site or formation, CO₂-water-rock interactions are different due to different hydrogeochemical conditions, which are worth investigating to enhance our understanding of CO₂ evolution in each CGS project. The Shenhua CCS Project has finished its goal of injecting 100,000 tons/year CO₂ into the onshore saline aquifers of the Ordos Basin by the end of 2013, with CO₂ captured from the Shenhua Direct Coal Liquefaction Company [24]. As the first integrated CGS project in China, the Shenhua CCS Project has attracted extensive research interest. Wang [25] and Yang [26] explored the mechanism of reactions between the CO₂ fluid and the Shiqianfeng/Shihezi formation in the Ordos Basin, using a high pressure reactor simulating the underground conditions. Tao [27] investigated the mineralization of CO₂ in the Liujiagou formation using the same equipment. However, experimental studies are limited by time scales, and CO₂ mineral trapping that immobilizes CO₂ permanently is a long-term process.

The objective of this study is to investigate the long-term CO₂-water-rock interactions based on the three formations at the Shenhua CCS site. In addition, pH changes and mineral dissolution/precipitation caused by CO₂ injection are analyzed. The supercritical CO₂ flow and geochemical reactions are modelled by TOUGHREACT, which coupled simulate subsurface multiphase fluid and heat flow, solute transport, and chemical reactions. Furthermore, the simulated geochemical processes in the three formations are compared with other experimental and modelling studies. The results from this study can be useful for the evaluation of long-term CO₂ geological storage and the geochemical process for practical implementations of CCS.

2. Geological Setting

The Shenhua CCS Project is located in the east section of the northern Yishan Slope in the Ordos Basin, which is an ideal place for large-scale CO₂ storage in geological formations in China [28]. The Triassic and Permian sandstone of the Ordos Basin are recognized as deep saline aquifers that have significant potential for CO₂ geological sequestration. The sedimentary thickness is more than 1500 m from Ordovician to Lower Triassic in the study area. Five reservoir-caprock assemblages (Liujiagou, Shiqianfeng, Shihezi, Shanxi, and

Majiagou) have been identified according to the previous studies [24, 29]. In this study, the Liujiagou, Shiqianfeng, and Shihezi formations are selected as the target layers for simulations (Figure 1), because they are major formations for CO₂ geological storage at the Shenhua CCS Project [24]. The fractures in the three formations are less developed with minor sizes and have little impact on the CO₂ geological storage [30].

2.1. Formation Characterization. The Liujiagou formation is at depths of 1576–1699 m. The interbedded seal is 5–15 m thick and discontinuous, characterized as silty mudstone or muddy siltstone. The reservoir formation is 123 m thick mainly composed of arkoses and lithic feldspathic sandstone. The porosity and permeability of the reservoir are 6.3–10% and 0.02×10^{-15} – 2.81×10^{-15} m², respectively [24, 27, 30].

The Shiqianfeng formation is situated at depths of 1699–1990 m. The caprock is 26.2–103.6 m thick and characterized as silty mudstone or muddy siltstone, which is relatively continuous. The reservoir is 292 m thick and mainly composed of floodplain feldspathic quartz sandstone, with porosity and permeability 5–12.9% and 0.1×10^{-15} – 6.58×10^{-15} m², respectively [24, 25, 30].

The Shihezi formation is located at depths of 1990–2232 m. There is relatively pure mudstone in the upper Shihezi formation as a 116 m thick regional seal. The reservoir is 126 m thick and mainly composed of feldspathic quartz sandstone and feldspathic litharenite. The porosity and permeability of the reservoir are 8.8–12.6% and 1.23×10^{-15} – 5.99×10^{-15} m², respectively [24, 26, 30].

The details of mineral composition of the three formations and selected secondary minerals are given in Table 1. Considering the availability of kinetic data, we adjust the primary minerals used in the simulations referring to Xu et al. [18, 31]. According to the equilibrium batch modelling and previous studies of CO₂-water-rock interactions [7, 31], almost all the possible secondary minerals are considered in the simulations. The average temperature and pressure gradient of the study area are estimated as 30°C/km and 100 bar/km, respectively.

2.2. Formation Fluid Chemistry. In the Liujiagou formation, the groundwater is dominated by Ca-Na-Cl water type and highly mineralized with a total dissolved solid content (TDS) of 56 g/L. In the Shiqianfeng formation, the groundwater is also dominated by Ca-Na-Cl water type and highly mineralized with a TDS of 31.2 g/L. In the Shihezi formation, the groundwater is dominated by Na-Ca-Cl water type and lowly mineralized with a TDS of 9.39 g/L. The details of aqueous chemical concentrations are given in Table 2 [26, 27, 32].

Before simulating CO₂ injection, batch simulations are conducted to equilibrate the primary minerals with in situ water at the formation temperature and CO₂ partial pressure. The resulting water chemistry is used as the initial aqueous concentrations for reactive transport simulations [18, 33].

3. Simulation Methods

3.1. Governing Equations. TOUGHREACT is a comprehensive nonisothermal multicomponent reactive fluid flow and

Stratum			Group	Thickness (m)	Lithologic section	Lithologic characteristics	
Period	System	Series					
Cenozoic	Quaternary			0-30		Grayish yellow gravel layer	
Mesozoic	Cretaceous		Luohe	0-137		Sandstone intercalated with mudstone	
		Jurassic	Middle	Anding	80-150		
			Zhiluo	200-400			
	Lower		Yanan	250-300			
	Triassic	Upper		Yanchang	790-1415		
				Zhifang	300-530		
		Lower	Heshanggou		47-169		
			Litujiagou	Upper	202-422		
				Middle			
	Lower						
Upper Paleozoic	Permian	Upper	Shiqianfeng	Upper	200-345		
				Lower			
			Shihezi	Upper		200-340	
				Lower			80-200
		Carboniferous		Shanxi	37-125		
				Taiyuan	22-276		
				Benxi	15-58		
			Lower Paleozoic	Ordovician	Lower	Majiagou	100-1000

FIGURE 1: Lithologic and stratigraphic sequence of the Ordos Basin, illustrating the positions and geological characteristics of the main injection formations (modified from Li et al. [29]).

geochemical transport simulator [18] used in this study. The multiphase flow, heat flow, and chemical transport are governed by the principle of mass (energy) conservation. The general conservation equation can be written as follows:

$$\frac{\partial M_{\kappa}}{\partial t} = -\nabla F_{\kappa} + q_{\kappa}, \quad (1)$$

where the subscript κ is the mass component or heat component, M_{κ} is the mass or energy of component κ , t is the time,

F_{κ} denotes the mass or heat flux, and q_{κ} is the sources or sinks. The calculation here contains the component in all phases.

After space and time discretization, the governed equations for fluid flow are transformed to a set of coupled nonlinear algebraic equations and can be solved by Newton-Raphson iteration methods [18]. The thermodynamic variables such as fluid velocities and phase saturations are obtained and used for chemical transport simulation.

TABLE 1: Mineral composition of formations [25–27] and possible secondary minerals used in the simulations.

Minerals of formations	Mineral modelled	Chemical composition	Volume fraction (vol.%)		
			Liujiagou	Shiqianfeng	Shihezi
<i>Primary minerals</i>					
Quartz	Quartz	SiO ₂	27	65	66
Alkali-feldspar	K-feldspar	KAlSi ₃ O ₈	14	9	0
Plagioclase	Oligoclase	Ca _{0.2} Na _{0.8} Al _{1.2} Si _{2.8} O ₈	24	16	6
Illite	Illite	K _{0.6} Mg _{0.25} Al _{1.8} (Al _{0.5} Si _{3.5} O ₁₀)(OH) ₂	17	4.5	18.5
Kaolinite	Kaolinite	Al ₂ Si ₂ O ₅ (OH) ₄	6	0	0
Chlorite	Chlorite	Mg _{2.5} Fe _{2.5} Al ₂ Si ₃ O ₁₀ (OH) ₈	8.5	0	0
Smectite	Smectite-Na	Na _{0.290} Mg _{0.26} Al _{1.77} Si _{3.97} O ₁₀ (OH) ₂	1.75	1.25	1.75
	Smectite-Ca	Ca _{0.145} Mg _{0.26} Al _{1.77} Si _{3.97} O ₁₀ (OH) ₂	1.75	1.25	1.75
Calcite	Calcite	CaCO ₃	0	3	3
Dolomite	Dolomite	CaMg(CO ₃) ₂	0	0	3
<i>Secondary minerals</i>					
	Magnesite	MgCO ₃			
	Albite	NaAlSi ₃ O ₈			
	Siderite	FeCO ₃			
	Ankerite	CaMg _{0.3} Fe _{0.7} (CO ₃) ₂			
	Dawsonite	NaAlCO ₃ (OH) ₂			
	Hematite	Fe ₂ O ₃			
	Halite	NaCl			
	Anhydrite	CaSO ₄			

TABLE 2: Aqueous concentrations of in situ water [26, 27, 32] and initial aqueous concentrations for simulations.

Components	Liujiagou		Shiqianfeng		Shihezi	
	(mg/L)	(mol/kg H ₂ O)	(mg/L)	(mol/kg H ₂ O)	(mg/L)	(mol/kg H ₂ O)
Na ⁺	7816	1.09	4560	4.19 × 10 ⁻¹	2356	1.97 × 10 ⁻¹
Ca ²⁺	14511.02	1.32 × 10 ⁻²	6450	5.66 × 10 ⁻²	106733	2.70 × 10 ⁻⁵
Mg ²⁺	894.6	7.09 × 10 ⁻⁷	198.72	5.59 × 10 ⁻¹³	4.47	2.25 × 10 ⁻⁵
K ⁺	34.15	6.84 × 10 ⁻⁵	24.453	1.82 × 10 ⁻³	76.42	2.87 × 10 ⁻⁵
Fe ²⁺	2.24	1.02 × 10 ⁻⁴	19.04	1.25 × 10 ⁻⁵	27.47	9.52 × 10 ⁻¹¹
Cl ⁻	39739.84	1.12	17940	5.06 × 10 ⁻¹	5339.34	1.50 × 10 ⁻¹
SO ₄ ²⁻	2075.01	3.93 × 10 ⁻⁴	1940	1.85 × 10 ⁻²	46.28	2.26 × 10 ⁻⁷
HCO ₃ ⁻	25.22	1.77 × 10 ⁻³	56.852	6.50 × 10 ⁻⁴	520.26	4.57 × 10 ⁻²
AlO ₂ ⁻	0.1845	1.32 × 10 ⁻⁸	0.00324	2.77 × 10 ⁻⁸	0.0057	7.59 × 10 ⁻⁸
SiO ₂ (aq)	1.18	5.15 × 10 ⁻⁴	708	5.89 × 10 ⁻⁴	19.5	6.63 × 10 ⁻⁴
pH		7.03		6.68		7.92
Temperature		55°C		62°C		67°C

Note. Data under mg/L are aqueous concentrations of in situ water; data under mol/kg H₂O are the initial aqueous concentrations for simulations.

To reproduce a geochemical system, the concentrations of aqueous complexes composed of basis species are expressed as

$$c_i = K_i^{-1} \gamma_i^{-1} \prod_j^{N_c} c_j^{v_{ij}} \gamma_j^{v_{ij}}, \quad (2)$$

where c is the molal concentration of aqueous components, γ is the thermodynamic activity coefficient, K is the equilibrium constant, subscripts i and j mean the index of the aqueous complexes and basis species, respectively, the subscript i also means the i th reaction to composing the i th

aqueous complexes, v_{ij} is the stoichiometric coefficient of j th basis species in the i th reaction, and N_c is the total number of basis species.

For the dissolution and precipitation of equilibrium minerals, the mineral saturation ratio is expressed as

$$\Omega_m = K_m^{-1} \prod_{j=1}^{N_c} c_j^{v_{mj}} \gamma_j^{v_{mj}}, \quad (3)$$

where subscript m is the equilibrium mineral index and K_m is the corresponding equilibrium constant. Meanwhile the

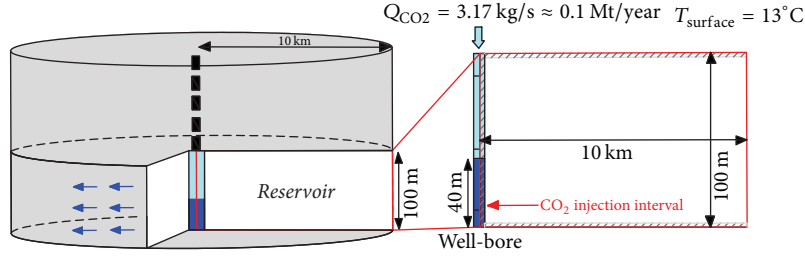


FIGURE 2: Schematic representation of the 2D radial model.

dissolution and precipitation of kinetic minerals are modelled with a rate expression given by Lasaga et al. [34]:

$$r_n = \pm k_n A_n \left| 1 - \Omega_n^{\theta} \right|^{\eta}, \quad (4)$$

where k is the rate constant, A is the specific reactive surface area, Ω is the kinetic mineral saturation ratio which is defined as (3), subscript n is the kinetic mineral index, and parameters θ and η are determined from experiment or taken as equal to one.

Reactions involving aqueous and gaseous phases are assumed to be at equilibrium and the governing equation according to the Mass-Action Law is as follows:

$$p_f \Gamma_f K_f = \prod_{j=1}^{N_c} c_j^{v_{fj}} \gamma_j^{v_{fj}}, \quad (5)$$

where p is the partial pressure of gas and Γ is the gas fugacity coefficient.

Porosity changes of the medium are directly calculated from the volume changes as a result of mineral precipitation and dissolution [18]. The calculation of permeability changes in TOUGHREACT depends on the medium type.

3.2. Model Setup and Simulation Parameters. In this study, we focus on the long-term CO_2 -water-rock interactions in reservoir; therefore we simplify the three formations as homogeneous sandstones. A two-dimensional (2D) radial model is applied with thickness of 100 m and an external radius of 10 km (Figure 2). The model contains 10 layers in the vertical direction, and it is divided into 101 radial grid elements logarithmically increasing from the injection well in the radial direction. The injection well is modelled as a circular grid element of $R = 0.2$ m, while the outermost grid is specified with a large volume of 10^{50} m^3 representing an infinite lateral boundary. The top and bottom boundaries of the model are regarded as impermeable layers. Similar models have been used in previous studies [8, 31, 33]. The injection interval is 40 m thick at the bottom of the injection well. CO_2 is injected into the formation at a constant rate of 3.17 kg/s for three years. The fluid flow and geochemical transport simulation are running for 10,000 years, which is a reasonable time scale for CO_2 long-term sequestration [15, 33, 35, 36].

The hydrogeological and petrophysical parameters are based on the actual underground conditions. The initial pressures of the Liujiagou, Shiqianfeng, and Shihezi formations

are 16 MPa, 18.9 MPa, and 21 MPa, respectively, while the temperatures are 55°C, 62°C, and 67°C, respectively. The initial mineral compositions and aqueous concentrations are presented in Section 2. The initial porosities of the Liujiagou, Shiqianfeng, and Shihezi formations used in the simulations are 10%, 12.9%, and 12.6%, while the permeabilities are $2.81 \times 10^{-15} \text{ m}^2$, $6.58 \times 10^{-15} \text{ m}^2$, and $5.99 \times 10^{-15} \text{ m}^2$, respectively. Alkali-feldspar and plagioclase are modelled as K-feldspar and oligoclase, and smectite is regarded as a combination of 50% smectite-Na and smectite-Ca referring to previous studies [16, 17]. Capillary pressure and relative permeability are calculated from the models of van Genuchten [37] and Corey [38]. The details are given in Table 3. Other parameters are taken from Xu et al. [31].

4. Results and Discussion

4.1. Time Evolution of CO_2 Trapping Mechanisms. Injected CO_2 can be directly trapped as free-gas (supercritical fluid) by low-permeability caprocks and then dissolves into groundwater and reacts with rock minerals leading to precipitation of carbonates [16]. The whole process can be classified as three trapping mechanisms: free-gas trapping, solubility trapping, and mineral trapping. Using TOUGHREACT as the simulator, the abundance of CO_2 trapped in different mechanisms can be calculated from

$$M_{\text{CO}_2}^g = \sum_{n=1} (V_n \phi_n Sg_n Dg_n) \quad (6)$$

$$M_{\text{CO}_2}^l = \sum_{n=1} (V_n \phi_n Sl_n Dl_n X_{\text{CO}_2}) \quad (7)$$

$$M_{\text{CO}_2}^s = \sum_{n=1} (V_n (1 - \phi_n) SM_{\text{CO}_2}), \quad (8)$$

where the superscripts g , l , and s indicate CO_2 trapped as free-gas, aqueous phase, and minerals, respectively, M_{CO_2} is the CO_2 trapping capacity, the subscript n is the index of grid blocks, V is the volume, ϕ is the porosity, Sg and Sl are the gas saturation and liquid saturation, Dg and Dl are the density of gas and liquid phase, X_{CO_2} is the mass fraction of CO_2 in aqueous phase, and SM_{CO_2} is CO_2 mineral trapping capacity per unit volume medium.

The evolution of CO_2 trapping mechanisms of the three formations over time is shown in Figures 3(a), 3(b), and 3(c). During the injection period (the first three years), the CO_2 trapping mechanisms in the three formations are similar.

TABLE 3: Hydrogeological parameters of the three formations used in this study.

Parameters	Liujiaogou formation	Shiqianfeng formation	Shihezi formation
Permeability (m ²)	2.81×10^{-15}	6.58×10^{-15}	5.99×10^{-15}
Porosity	0.100	0.129	0.126
Pore compressibility (Pa ⁻¹)	4.5×10^{-10}	4.5×10^{-10}	4.5×10^{-10}
Rock grain density (kg/m ³)	2600	2600	2600
Temperature (°C)	55	62	67
Pressure (MPa)	16	18.9	21
Salinity (wt.%)	6	3	0.9
Residual gas saturation, S_{gr}	0.05	0.05	0.05
Residual liquid saturation, S_{lr}	0.3	0.3	0.3
van Genuchten, P_0 (kPa)	19.61	19.61	19.61
van Genuchten, λ (1/Pa)	0.457	0.457	0.457

The CO₂ free-gas trapping and CO₂ solubility trapping keep growing, while the CO₂ mineral trapping remains inactive. At the end of injection period, 80% of injected CO₂ remains as free-gas in each formation. Then the CO₂ free-gas trapping decreases, while the CO₂ solubility trapping continues rising up. The CO₂ mineral trapping in the three formations starts at the 100 years and the final CO₂ mineral trapping capacity is almost the same (nearly all the CO₂ gases are trapped in minerals at 10,000 years).

Standard deviation is usually used to quantify the dispersion degree of a set of data [39]. In this study, there are three CO₂ amounts for the three formations under each CO₂ trapping mechanism. They are regarded as a set of data, the standard deviation of which is calculated to quantify the difference among the three CO₂ amounts. As shown in Figure 3(d), each line denotes one trapping mechanism. The standard deviations of the three trapping mechanisms increase greatly from 100 years, which corresponds to the beginning of CO₂ mineral trapping. After that then the difference of mineral trapping capacities becomes the largest. The different CO₂ mineral trapping capacities affect the CO₂ amounts of the other two trapping mechanisms. Thus the standard deviation peaks of the three trapping mechanisms occur at about 1000–2000 years. It can be concluded that the evolution of CO₂ trapping mechanisms is dominated by the CO₂-water-rock interactions in a large time scale (more than 1000 years). CO₂-water-rock interactions should be the key factor for the evaluation of long-term CO₂ geological storage.

To assess the CO₂ mineral trapping capability of the three formations, we calculate the abundance of CO₂ sequestered in minerals (Figure 4) using

$$M_{CO_2, \min_a} = \sum_{n=1}^{n_{\max}} (V_n (1 - \phi_n) V_a W_{CO_2, \min_a} \rho_{\text{rock}}), \quad (9)$$

where the superscript a means the CO₂ trapping mineral, ρ_{rock} is the density of the host rock 2600 kg/m³, and W_{CO_2, \min_a} is the molecular weight percent of CO₂ in mineral a .

CO₂ is injected into the formation at the constant rate of 3.17 kg/s (100,000 tons/year) for three years, and thus the total amount of injected CO₂ in each formation is 3×10^8 kg. At the end of simulation, the CO₂ mineral trapping capacities of

the Liujiaogou, Shiqianfeng, and Shihezi formations are 2.99×10^8 kg, 2.85×10^8 kg, and 2.79×10^8 kg, respectively. In the Liujiaogou formation, the amounts of CO₂ immobilized in calcite, dawsonite, and siderite are 2.07×10^8 kg, 4.61×10^7 kg, and 4.59×10^7 kg, respectively. In the Shiqianfeng formation, the amounts of CO₂ immobilized in calcite and dawsonite are 1.84×10^8 kg and 1.01×10^8 kg. In the Shihezi formation, the amounts of CO₂ immobilized in calcite, dawsonite, and magnesite are 1.49×10^8 kg, 1.42×10^7 kg, and 1.16×10^8 kg, respectively (Figure 4). It can be inferred that calcite is a common CO₂ trapping mineral, while dawsonite, siderite, and magnesite precipitation depend on specific formation conditions.

4.2. pH Changes. CO₂ dissolution induces a series of acidic reactions, lowering the pH of the formation water. Figure 5 shows the pH spatial distribution of the Liujiaogou formation at different times, which is similar to the cases of the Shiqianfeng and Shihezi formations (not shown). Figure 5 also infers the spatial distribution of CO₂ plume. We select points A, B, and C to represent CO₂-rich zone and near-well and far-well zone and take point C as a reference point.

As shown in Figure 6, pH at points A and B falls sharply during the injection period (the first three years) and increases distinctly after hundreds of years. The changes of pH at point A lag behind point B because point B is beneath point A, which is closer to the injection interval. It can be concluded that the decrease in pH is caused by CO₂ dissolution (Reaction 1 in Table 4), while the increase in pH is resulting from mineral dissolution (Reaction 2–5 in Table 4).

We take the pH at different times as a set of data and calculate the standard deviations to show the different buffering degrees in the three formations. For the Liujiaogou, Shiqianfeng, and Shihezi formations, the buffering degrees are quantified as 1.447, 0.977, and 0.318 at point A and 1.814, 1.376, and 1.160 at point B, respectively. Hence, the descending order of the amounts of dissolved minerals for the three formations is as follows: the Liujiaogou formation, the Shiqianfeng formation, and the Shihezi formation.

4.3. Mineral Dissolution. Point C is regarded as a reference point in far-well zone, mineral dissolution and precipitation

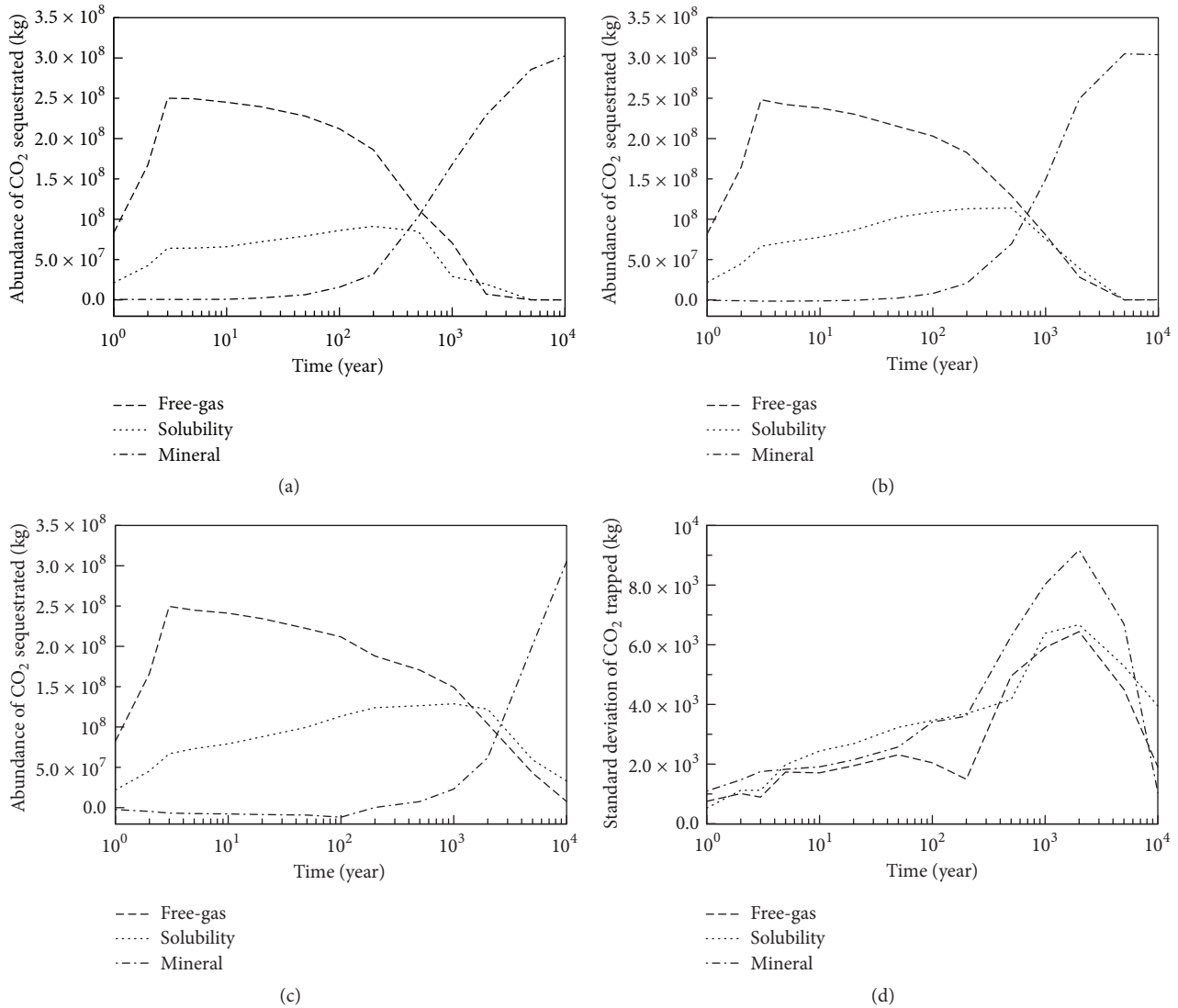


FIGURE 3: The evolution of the injected CO₂ in different trapping mechanisms for the Liujiagou formation (a), the Shiqianfeng formation (b), and the Shihezi formation (c) and the evolution of standard deviations for different trapping mechanisms (d) over time.

of which are not affected by CO₂-water-rock interactions. Then we deduce the changes in mineral and ion of point C from points A and B to analyze the geochemical reactions induced by CO₂ injection (Figures 7, 8, and 9). Figure 7 shows the mineral dissolution induced by CO₂-water-rock interactions in the three formations, which is consistent with the quantified pH buffering degrees in Section 4.2.

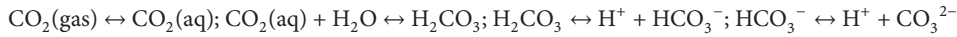
Oligoclase, smectite-Ca, and illite are common initial minerals in the three formations. As shown in Figure 7, oligoclase dissolves steadily and supplies Ca²⁺ and Mg²⁺. The amounts of dissolved oligoclase at point A are very close to that at point B. However, more dissolved oligoclase occurs in the Liujiagou and Shiqianfeng formations due to the higher initial oligoclase abundance. Smectite-Ca firstly precipitates with sufficient Ca²⁺ and Mg²⁺ in the first 5000 years. Then it dissolves to provide Ca²⁺ and Mg²⁺, which are needed for precipitation of other minerals. Illite only dissolves at

point A in the Liujiagou and Shiqianfeng formations that can release Mg²⁺ and K⁺. K-feldspar is an initial mineral in both the Liujiagou and Shiqianfeng formations, while it only dissolves at point B of these formations and supplies K⁺ (Figures 7(b) and 7(d)). Chlorite only dissolves in the Liujiagou formation as an initial mineral, releasing Mg²⁺ and Fe²⁺ (Figures 7(a) and 7(b)). In addition, as albite is a selected secondary mineral in the three formations, the decrease in volume fraction of albite (Figures 7(e) and 7(f)) is due to the greater precipitation of albite at point C than at points A and B, which suggests CO₂ is unfavorable for albite precipitation.

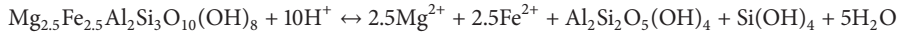
It can be inferred that oligoclase and smectite-Ca are Ca²⁺ sources in the three formations. Mg²⁺ is supplied by smectite-Ca, illite, and chlorite in the Liujiagou formation, smectite-Ca and illite in the Shiqianfeng formation, and smectite-Ca in the Shihezi formation. K⁺ in the Liujiagou and Shiqianfeng formations is provided by illite and K-feldspar

TABLE 4: The main dissolution reactions in this study.

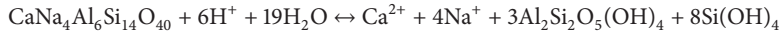
Reaction 1: dissolution of CO_2 :



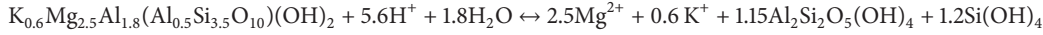
Reaction 2: dissolution of chlorite:



Reaction 3: dissolution of oligoclase:



Reaction 4: dissolution of illite:



Reaction 5: dissolution of albite

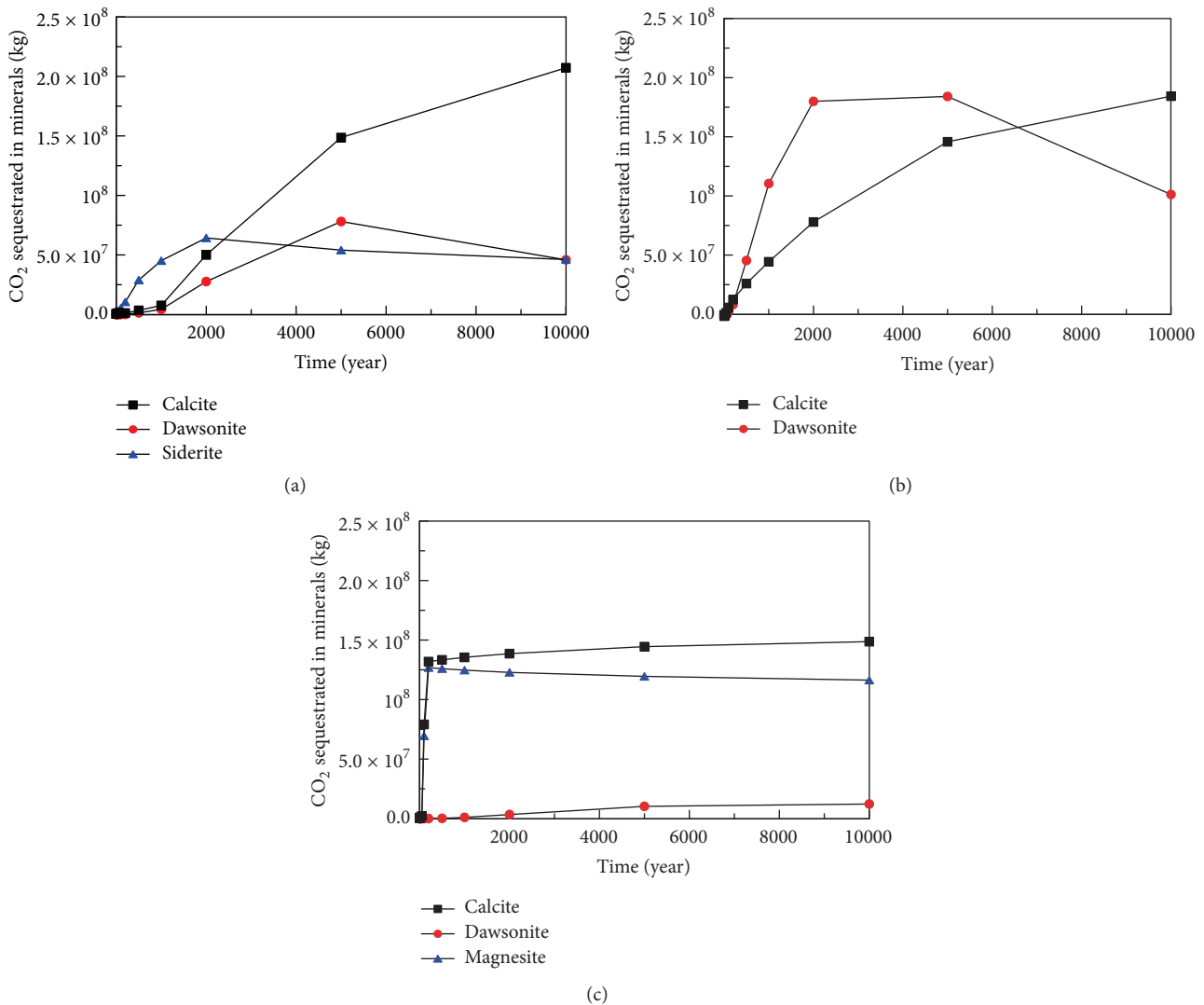
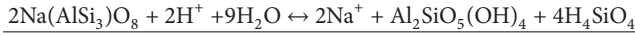


FIGURE 4: The amounts of CO_2 sequestered in minerals for the Liujiagou formation (a), Shiqianfeng formation (b), and Shihezi formation (c) at different times.

dissolution, respectively. Fe^{2+} is only provided by chlorite in the Liujiagou formation. Na^+ is sourced from oligoclase in the three formations.

Figure 8 shows the changes in aqueous concentrations induced by CO_2 -water-rock interactions. As mentioned

above, mineral dissolution might increase the concentrations of Na^+ , Fe^{2+} , Mg^{2+} , Ca^{2+} , and K^+ in the formation water. However, the concentration changes of K^+ and Fe^{2+} in the three formations remain zero (Figure 8). The changes of Mg^{2+} in the Liujiagou and Shihezi formations remain zero after 400

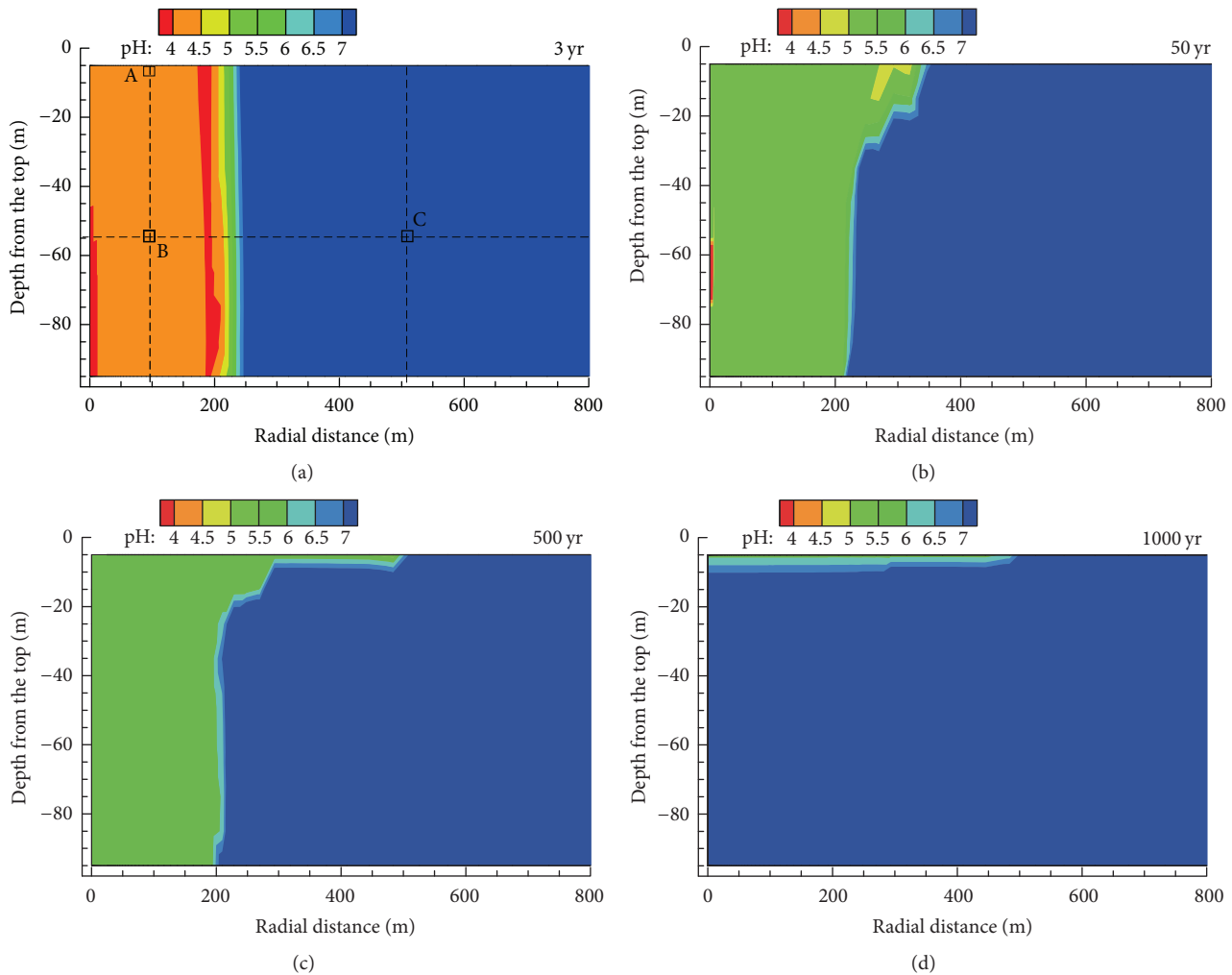


FIGURE 5: The pH spatial distribution of the Liujiagou formation at different times.

years and 200 years, respectively. The maximum reduction of Ca^{2+} occurs in the Liujiagou formation and the minimum in the Shihezi formation (Figures 8(a), 8(b), 8(e), and 8(f)). The concentration of Na^+ in the Liujiagou and Shiqianfeng formations decreases in the first 30 years and then increases with a different extent (Figures 8(a), 8(b), 8(c), and 8(d)). For Shihezi formation, Na^+ increases after 100 years (Figures 8(e) and 8(f)). It can be inferred that the aqueous concentration changes are affected not only by mineral dissolution but also by mineral precipitation. Then we investigate the mineral precipitation combined with aqueous concentrations changes in Section 4.4.

4.4. Mineral Precipitation. In the Liujiagou formation (Figures 7–9(a–b)), illite and K-feldspar are initial minerals. It can be inferred from the changes in the concentration of K^+ (Figures 8(a) and 8(b)) that K-feldspar precipitation at point A is due to illite dissolution, while precipitation of illite at point B results from K-feldspar dissolution. Similarly, ankerite and siderite precipitate with chlorite dissolution providing Fe^{2+} . More chlorite dissolves at point A compared

to point B due to lower pH, leading to more ankerite and siderite precipitation at point A. Precipitation of ankerite also needs Ca^{2+} and Mg^{2+} , which suggest that more Ca^{2+} and Mg^{2+} are provided at point A compared to point B.

For the Liujiagou formation (Figures 7–9(a–b)), Ca^{2+} is released by oligoclase dissolution constantly, which is used for precipitation of smectite-Ca, calcite, and ankerite in the first 5000 years. During this period, Ca^{2+} provided by oligoclase dissolution and consumed by smectite-Ca precipitation at point A is close to that at point B (Figure 8(a, b) and Figure 9(a, b)). Hence the minor precipitation of calcite at point A left more Ca^{2+} for precipitation of ankerite than point B. In addition, smectite-Ca and ankerite all disappear at the end of simulation so that the final calcite abundances at points A and B are consistent.

The concentration of Mg^{2+} in the Liujiagou formation firstly increases due to chlorite dissolution. Then smectite-Ca and illite dissolution also provide Mg^{2+} at point A. Meanwhile, Mg^{2+} at point B is released by minor dissolution of smectite-Ca and chlorite and consumed by illite precipitation. Hence, there is more Mg^{2+} at point A for precipitation of

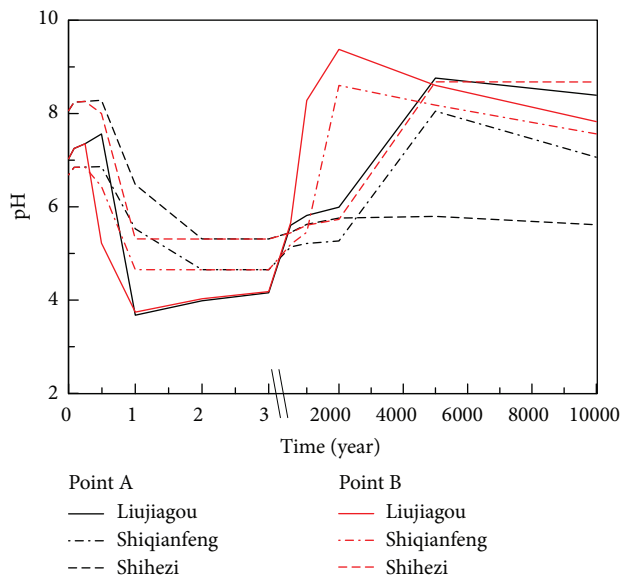


FIGURE 6: The evolution of pH at point A and point B for the Liujiagou, Shiqianfeng, and Shihezi formations over time.

ankerite. Na^+ released by oligoclase dissolution at point A is close to that at point B. Then the larger increase in Na^+ at point A can be explained by additional albite dissolution and minor smectite-Na precipitation. Dawsonite precipitates at both points A and B with sufficient Na^+ and high CO_2 saturation. However, CO_2 moves upward by buoyance in the near-well zone (point B) so that dawsonite at point B disappears at the end of simulation.

In the Shiqianfeng formation (Figures 7–9(c-d)), illite and K-feldspar are also initial minerals. The changes in concentration of K^+ also remain zero. Therefore, all dissolved illite is transformed into K-feldspar at point A as the case in the Liujiagou formation. However, K-feldspar precipitation also occurs at point B due to illite dissolution providing K^+ in the first 5000 years, and after that then K-feldspar dissolves to supply K^+ for illite precipitation. It can be inferred that illite is transformed into K-feldspar with higher CO_2 saturation and lower pH (Figure 6) in the Liujiagou and Shiqianfeng formations, while it reverses with lower CO_2 saturation and higher pH. Besides, precipitation of ankerite and siderite does not occur without chlorite providing Fe^{2+} .

For Shiqianfeng formation (Figures 7–9(c-d)), Ca^{2+} is also released by oligoclase and used for precipitation of smectite-Ca and calcite in the first 5000 years. Then smectite-Ca dissolves to provide more Ca^{2+} for calcite precipitation. At the end of simulation, the final calcite abundance at point A is consistent with that at point B. Mg^{2+} released by illite dissolution is used for precipitation of smectite-Ca and smectite-Na in the first 5000 years. Then smectite-Ca dissolves to supply Mg^{2+} , which is used for precipitation of smectite-Na at point A and precipitation of smectite-Na and illite at point B. Thus minor smectite-Na precipitation occurs at point B than point A. Na^+ released by oligoclase contributes to the precipitation of smectite-Na and dawsonite. There is

more dawsonite precipitates in the Shiqianfeng formation than the Liujiagou formation, without ankerite and siderite immobilizing the injected CO_2 . As a result, there are less Na^+ and minor smectite-Na precipitation in the Shiqianfeng formation.

In the Shihezi formation (Figures 7–9(e-f)), illite is an initial mineral, while K-feldspar is not (Table 1). Thus illite might be the only K^+ source. However, it does not dissolve to provide K^+ for K-feldspar precipitation at point A (Figure 7(e) and Figure 9(e)) with low pH and high CO_2 saturation (Figures 5 and 6), although 18.5% (volume fraction) of host rock is illite (Table 1). Also, there is no K^+ exchange between illite and K-feldspar at point B (Figures 7(f) and 9(f)). Ankerite and siderite does not precipitate because there is no chlorite (Table 1) supplying Fe^{2+} .

For Shihezi formation (Figures 7–9(e-f)), Ca^{2+} released by dolomite is consumed by precipitation of calcite in the first 50 years. Then calcite exchanges Ca^{2+} with dolomite in the next 150 years. However, calcite and dolomite are unstable due to low pH and high CO_2 saturation, and both of them disappear after 200 years. Then calcite precipitates again with pH increases due to dissolution of oligoclase and albite. Mg^{2+} , after an initial increase due to dolomite dissolution, is consumed by precipitation of smectite-Na and smectite-Ca. Na^+ released by oligoclase and albite is used for precipitation of smectite-Na and dawsonite. More dawsonite precipitates at point A compared to point B due to the higher CO_2 saturation at point A.

Mineral dissolution and precipitation induced by the injected CO_2 are analyzed by comparison of the three observation points (points A, B, and C) in the three formations. It can be inferred that quartz sandstones in the Shiqianfeng and Shihezi formations have lower pH buffering capacity. Illite and K-feldspar exchanged K^+ when they are both initial minerals. Chlorite is a key initial mineral providing Fe^{2+} for precipitation of ankerite and siderite. Calcite, dawsonite, and siderite are stable CO_2 trapping minerals, while ankerite, dolomite, and magnesite are not.

4.5. Distribution of Mineral Abundance. As described in Sections 4.2–4.4, the CO_2 -water-rock interactions are mostly affected by variations in the initial mineral compositions. The mineral abundance changes at the end of simulation induced by CO_2 -water-rock interactions are further analyzed in this part.

Figure 10 shows the mineral distribution of the three formations in the radial direction at the end of simulation at depths of -5 m and -55 m. According to pH changes and mineral alteration, the modelling system can be divided into three regions, which are CO_2 bearing zone, low gas saturation zone, and far-well zone. The initial mineral compositions of the three zones are the same. However, much more significant dissolution and precipitation of minerals occur in CO_2 bearing zone compared with far-well zone. Besides, CO_2 bearing zones at the end of simulation are also similar in shape to the CO_2 plume at the end of injection period (Figures 10 and 5), which indicates that the injected CO_2 barely moves after injection.

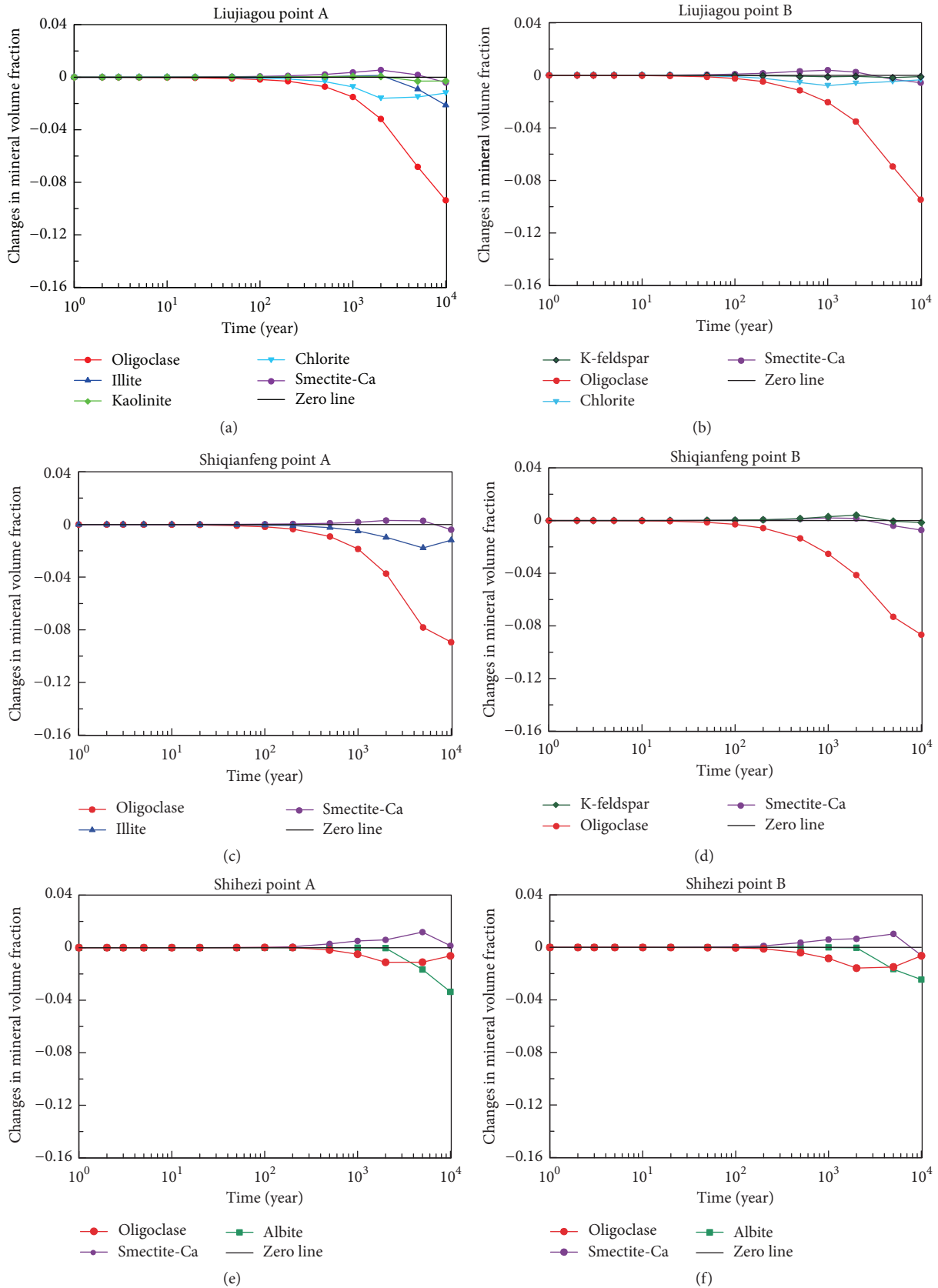


FIGURE 7: The evolution of dissolved minerals at points A and B for the Liujiagou formation (a, b), Shiqianfeng formation (c, d), and Shihezi formation (e, f) over time.

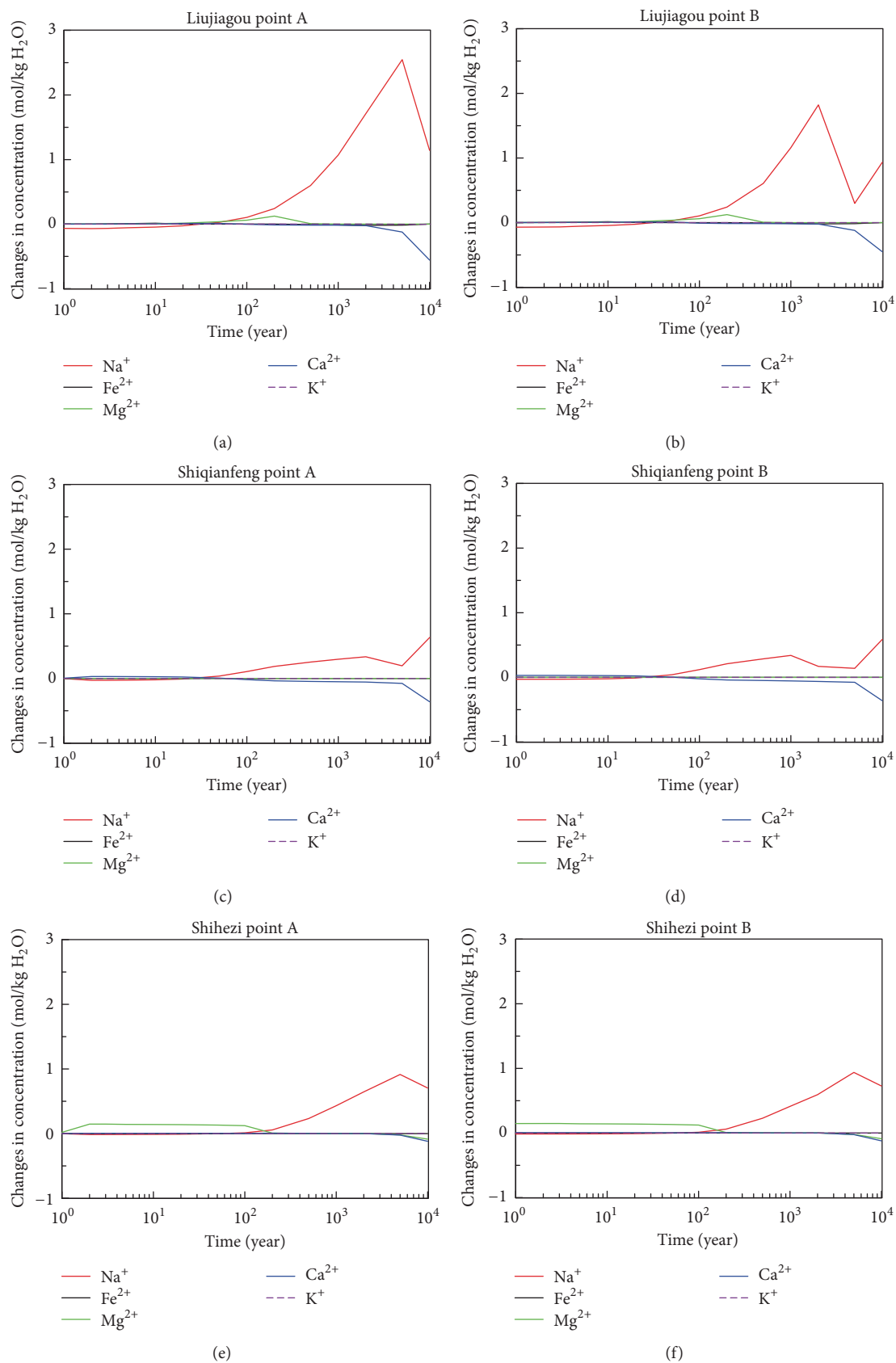


FIGURE 8: The evolution of changes in aqueous concentrations at points A and B for the Liujiagou formation (a, b), Shiqianfeng formation (c, d), and Shihezi formation (e, f) over time.

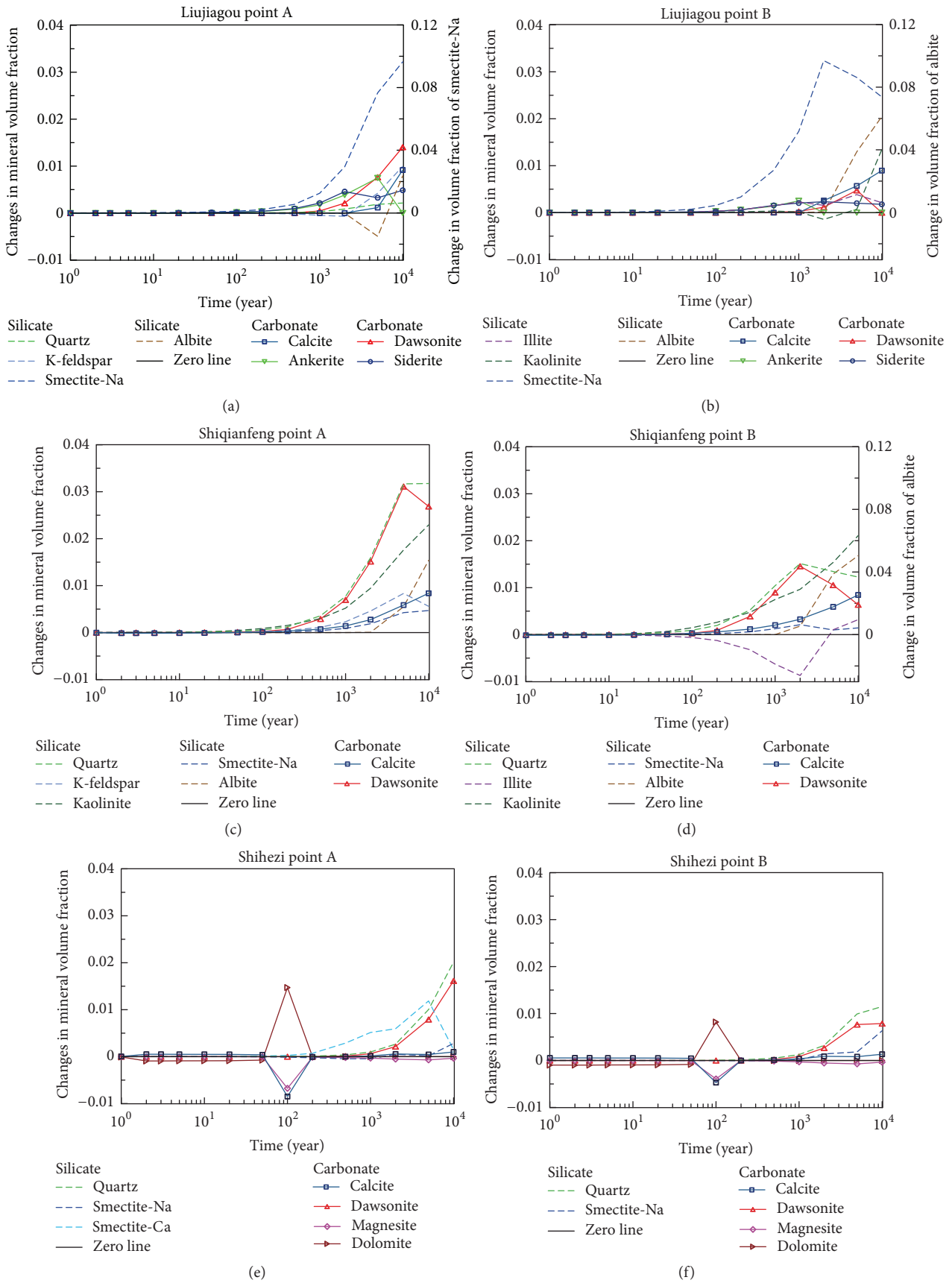


FIGURE 9: The evolution of mineral abundance changes at points A and B for the Liujiagou formation (a, b), Shiqianfeng formation (c, d), and Shihezi formation (e, f) over time.

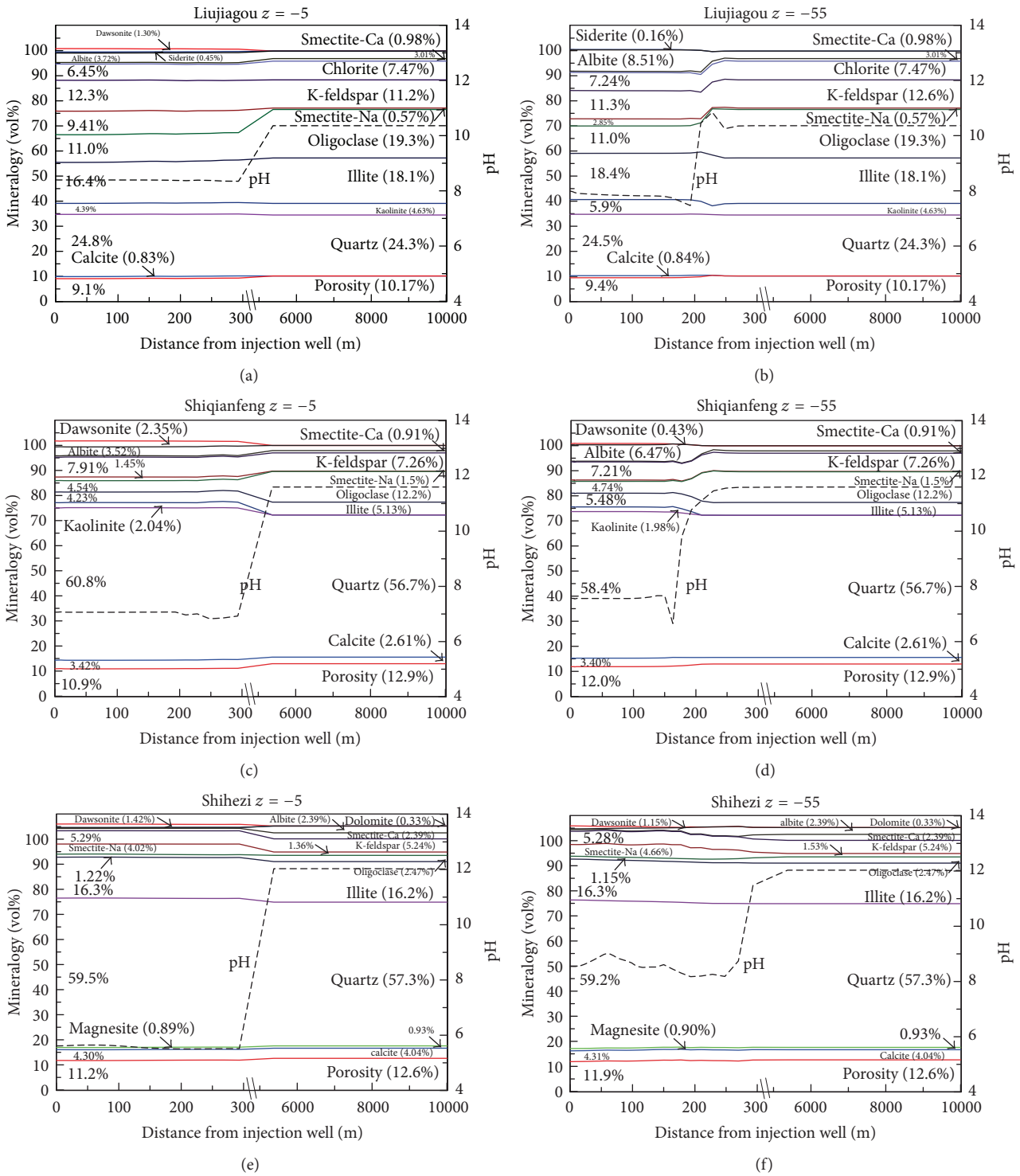


FIGURE 10: Mineral abundance of the Liujiagou formation (a, b), Shiqianfeng formation (c, d), and Shihezi formation (e, f) at the depths of -5 m and -55 m after 10,000 years.

To identify the mineral dissolution and precipitation induced by CO_2 -water-rock interactions, we compare mineral abundances of CO_2 bearing zone with far-well zone (Table 5). For silicate minerals, quartz and smectite-Na precipitate and oligoclase and smectite-Ca dissolve impacted by CO_2 -water-rock interactions in the three formations. For

carbonate minerals, the CO_2 trapping mineral assemblages and abundances of the three formations are different, which can be seen in Table 5 for details.

4.6. Porosity and Permeability Changes. Porosity changes of the formation are directly calculated from the volume

TABLE 5: The changes in abundance of mineral dissolution and precipitation after 10,000 years.

Minerals modelled	Chemical composition	Mineral dissolution (↑) and precipitation (↓)					
		Liujiagou		Shiqianfeng		Shihezi	
		-5 m	-55 m	-5 m	-55 m	-5 m	-55 m
<i>Primary minerals</i>							
Quartz	SiO ₂	↓	↓	↓	↓	↓	↓
K-feldspar	KAlSi ₃ O ₈	↓	↑	↓	↑	↓	↓
Oligoclase	Ca _{0.2} Na _{0.8} Al _{1.2} Si _{2.8} O ₈	↑	↑	↑	↑	↑	↑
Illite	K _{0.6} Mg _{0.25} Al _{1.8} (Al _{0.5} Si _{3.5} O ₁₀)(OH) ₂	↑	↓	↑	↓	↓	↓
Kaolinite	Al ₂ Si ₂ O ₅ (OH) ₄	↑	↓	↓	↓	/	/
Chlorite	Mg _{2.5} Fe _{2.5} Al ₂ Si ₃ O ₁₀ (OH) ₈	↑	↑	/	/	/	/
Smectite-Na	Na _{0.290} Mg _{0.26} Al _{1.77} Si _{3.97} O ₁₀ (OH) ₂	↓	↓	↓	↓	↓	↓
Smectite-Ca	Ca _{0.145} Mg _{0.26} Al _{1.77} Si _{3.97} O ₁₀ (OH) ₂	↑	↑	↑	↑	↑	↑
Calcite	CaCO ₃	↓0.83%	↓0.84%	↓0.81%	↓0.79%	↓1.68%	↓1.69%
Dolomite	CaMg(CO ₃) ₂	/	/	/	/	↑	↑
<i>Secondary minerals</i>							
Albite	NaAlSi ₃ O ₈	↓	↓	↓	↓	↑	↑
Ankerite	CaMg _{0.3} Fe _{0.7} (CO ₃) ₂	/	/	/	/	/	/
Dawsonite	NaAlCO ₃ (OH) ₂	↓1.30%	/	↓2.35%	↓0.43%	↓1.42%	↓1.15%
Siderite	FeCO ₃	↓0.45%	↓0.16%	/	/	/	/
Magnesite	MgCO ₃	/	/	/	/	↓0.04%	↓0.03%

Note. ↓ represents mineral precipitation; ↑ represents mineral dissolution; / represents nonexistent; data beside ↓ and ↑ is the volume fraction changes of minerals.

changes as a result of mineral precipitation and dissolution. As shown in Figure 11, porosity and permeability increase within the first 100 years and then decrease in the three formations. The maximum reduction of porosity and permeability occurs in the Shiqianfeng formation. It can be inferred that higher proportion of quartz in host rock is unfavorable for injectivity enhancing in large time scale.

The vertical distributions of porosity changes induced by CO₂-water-rock interactions at different times are shown in Figure 12. A column of model grids at a distance of 98.3 m from the injection well are selected to represent CO₂ bearing zone.

In the Liujiagou formation, porosity increases in the first 100 years and then decreases constantly. The larger decrease in porosity occurs at the top of the Liujiagou formation due to higher CO₂ saturation. However, the porosity at the top of the Liujiagou formation is greater than other parts at 5000 years due to ankerite dissolution. For the Shiqianfeng formation, porosity decreases with time. The increase in porosity in the first 100 years in Figure 11 is not shown in Figure 12, because single time points are used in Figure 12. The larger decrease in porosity at the top of the Shiqianfeng formation also occurs due to higher CO₂ saturation. But the greater porosity at the top of the Shiqianfeng formation occurs at 1000 years because of minor precipitation of quartz and kaolinite. In the Shihezi formation, porosity decreases after the initial increase within the first 100 years.

4.7. Comparisons with Previous Studies. Regarding the Shenhua CCS Project, the CO₂-water-rock interactions of major formations (the Liujiagou formation, the Shiqianfeng formation, and the Shihezi formation) have been studied by

experimental methods [25–27], which shows good qualitative agreement with our studies.

For the Liujiagou formation, we conduct the modelling at a temperature of 55°C and a pressure of 16 MPa, while Tao [27] uses the temperatures of 60–100°C and the same pressure 16 MPa in the CO₂-water-rock interaction experiment. Dissolution of K-feldspar, oligoclase, and chlorite and precipitation of siderite within the experimental period of 1–25 days are observed. This is well consistent with our results in much longer simulation period. For the Shiqianfeng formation and the Shihezi formation, Wang [25] and Yang [26] conduct experiments at temperatures of 55–100°C and the same pressures of 18 MPa for 24 days. The minerals that dissolve and precipitate in the experiments agree with our simulations.

Besides, more minerals are dissolved rather than precipitated in the experiments, which may lead to the porosity increase. This shows good agreement with our results that porosity and permeability increase in the first 100 years, which is also consistent with the observed increasing injectivity at the Shenhua CCS demonstration project. However, we have also found the decreases in porosity and permeability after a long time of simulation (after 100 years). This might be because the experiment is limited by time scale so that we could not predict the long-term CO₂-water-rock interactions and related porosity changes.

We also compare our results with previous modelling studies [14, 16, 40, 41]. The decreases in the porosity and permeability of the three formations after 100 years agrees with the simulation results of Xu et al. [16] and Wang et al. [41]. We find that the CO₂ mineral trapping is affected by rock types of injected formations, especially the content of quartz.

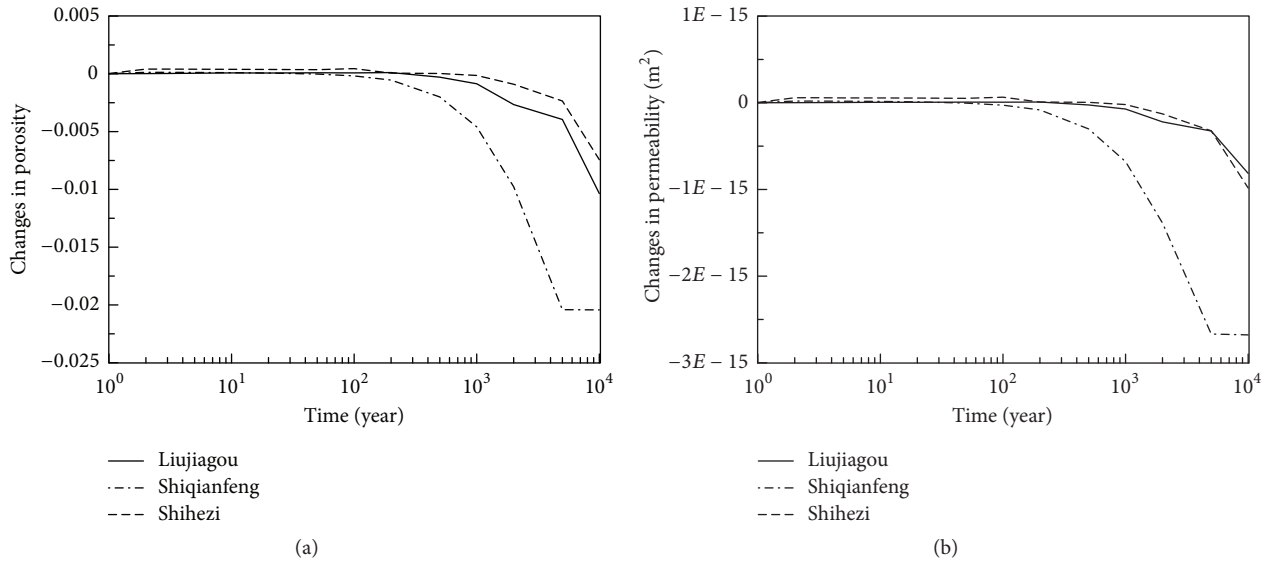


FIGURE 11: The evolution of changes in porosity (a) and permeability (b) at point A for the three formations over time.

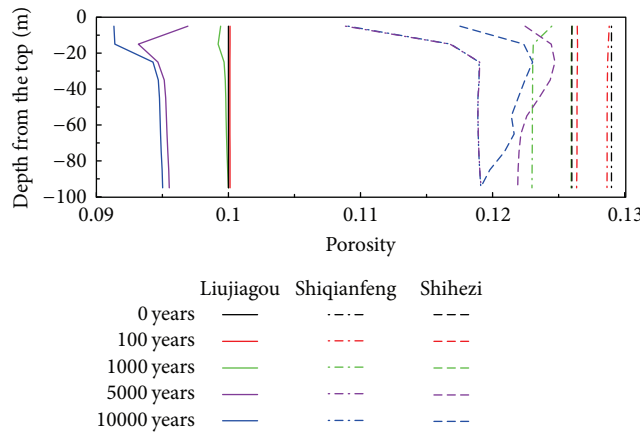


FIGURE 12: The vertical distributions of porosity changes in CO₂ bearing zone of the three formations at different times.

The volume fractions of quartz in the Shiqianfeng and Shihezi formations are 65% and 66%, respectively, which makes CO₂ mineral trapping capacities smaller than the Liujiagou formation. This is also demonstrated by Xu et al. [16] and Audigane et al. [14], and they found limited CO₂ sequestered by mineral trapping due to the high quartz content in the formations.

It can be seen that K⁺ exchanges between illite and K-feldspar when both of illite and K-feldspar are primary minerals in our study. However, this is different from Xu et al. [16] that they found illite and K-feldspar precipitation simultaneously. The differences can be explained by the fact that K⁺ is only from illite and K-feldspar in Liujiagou and Shiqianfeng formations, while the dissolution of glauconite could provide K⁺ for both illite and K-feldspar [16]. Chlorite as primary mineral provides Fe²⁺ and Mg²⁺ for precipitation of ankerite and siderite, which is consistent with Yang et al. [40] and Wang et al. [41]. The CO₂ trapping minerals are as follows: calcite, dawsonite, and siderite in the Liujiagou formation;

calcite and dawsonite in the Shiqianfeng formation; calcite, dawsonite, and magnesite in the Shihezi formation. These trapping minerals are also observed in the above studies.

5. Conclusions

CO₂ geological storage in deep saline aquifers has great potential for reducing CO₂ emissions in China. The Shenhua CCS Project has finished its goal of injecting 100,000 tons/year CO₂ into the onshore saline aquifers of the Ordos Basin by the end of 2013. As the CO₂-water-rock interactions have great effect on the long-term CO₂ geological storage, geochemical modelling for the three injected formations of the Shenhua CCS Project is conducted for 10,000 years in this study. The results show the following.

(1) 80% injected CO₂ remains in the three formations as free-gas at the end of injection period. Then CO₂ plume beneath caprocks barely moves without injection pressure as driven force. The differences of CO₂ phase partition

among the three formations (as free-gas, aqueous phase, and minerals) increase greatly from 100 years and peak at 1000–2000 years. CO₂-water-rock interactions should be the key factor for the evaluation of long-term CO₂ geological storage.

(2) The CO₂ trapping mineral assemblages and abundances in the three formations are different. Total CO₂ mineral trapping capacities of the Liujiagou, Shiqianfeng, and Shihezi formations are 2.99×10^8 kg, 2.85×10^8 kg, and 2.79×10^8 kg, respectively, which suggests quartz sandstone formations have lower CO₂ mineral trapping capability. The CO₂ trapping mineral assemblages are as follows: calcite, dawsonite, and siderite in the Liujiagou formation; calcite and dawsonite in the Shiqianfeng formation; calcite, dawsonite, and magnesite in the Shihezi formation. And calcite, dawsonite, and siderite are stable CO₂ trapping minerals, while dolomite, ankerite, and magnesite are not.

(3) The increase in porosity and permeability of the three formations in the first 100 years is consistent with the observed increasing injectivity at Shenhua CCS Project. The decrease in porosity and permeability after 100 years shows agreement with other modelling studies using the similar methods.

Numerical simulation of geochemical reactions depends on the precision and availability of the equilibrium constants, kinetic parameters, and properties of fluids and host rocks. More work about getting these parameters through experiments should be done. Numerical simulation not limited by time scale can predict a long-term scene. In the future we may have more field data to revise the models and gradually build the big data for CCS. More sensitivity analysis about the mineral assemblages will help to better understand the geochemical reactions. In the current stage, the results in this study have been compared with other studies; they can be useful for the evaluation of long-term CO₂ geological storage and the geochemical process for practical implementations of CCS.

Conflicts of Interest

The authors declare that there are no conflicts of interest regarding the publication of this paper.

Acknowledgments

This work was supported by the National Natural Science Foundation of China (NSFC, Grant no. 41572233) and a bilateral project China Australia Geological Storage of CO₂ Project Phase 2 (CAGS2).

References

- [1] World Meteorological Organization, *The Global Climate in 2011–2015*, 2016.
- [2] E. Bryant, *Climate process and change*, Cambridge University Press, Cambridge, UK, 1997.
- [3] C. J. Jepma and M. Munasinghe, "Climate change policy," in *Jepma CJ Munasinghe M*, p. 331, Cambridge University Press, New York, 1998.
- [4] S. Bachu, "Sequestration of CO₂ in geological media: Criteria and approach for site selection in response to climate change," *Energy Conversion and Management*, vol. 41, no. 9, pp. 953–970, 2000.
- [5] IPCC, *IPCC Special Report on carbon dioxide capture and storage. Prepared by Working Group III of the Intergovernmental Panel on Climate Change*, Cambridge University Press, Cambridge, United Kingdom/New York, NY, USA, 2005.
- [6] L. André, P. Audigane, M. Azaroual, and A. Menjot, "Numerical modeling of fluid-rock chemical interactions at the supercritical CO₂-liquid interface during CO₂ injection into a carbonate reservoir, the Dogger aquifer (Paris Basin, France)," *Energy Conversion and Management*, vol. 48, pp. 1782–1797, 2007.
- [7] N. Assayag, J. Matter, M. Ader, D. Goldberg, and P. Agrinier, "Water-rock interactions during a CO₂ injection field-test: Implications on host rock dissolution and alteration effects," *Chemical Geology*, vol. 265, no. 1-2, pp. 227–235, 2009.
- [8] G. Yang, Y. Li, and A. Atrens, "Reactive transport modelling of long-term CO₂ sequestration mechanisms at the Shenhua CCS Demonstration Project," *China Journal of Earth Science*, vol. 28, no. 3, pp. 457–472, 2016.
- [9] S. Bachu and D. B. Bennion, "Experimental assessment of brine and/or CO₂ leakage through well cements at reservoir conditions," *International Journal of Greenhouse Gas Control*, vol. 3, no. 4, pp. 494–501, 2009.
- [10] P. E. S. Bergmo, A.-A. Grimstad, and E. Lindeberg, "Simultaneous CO₂ injection and water production to optimise aquifer storage capacity," *International Journal of Greenhouse Gas Control*, vol. 5, no. 3, pp. 555–564, 2011.
- [11] Q. Fang and Y. Li, "Exhaustive brine production and complete CO₂ storage in Jiangnan Basin of China," *Environmental Earth Sciences*, vol. 72, no. 5, pp. 1541–1553, 2014.
- [12] F. Cipolli, B. Gambardella, L. Marini, G. Ottonello, and M. V. Zuccolini, "Geochemistry of high-pH waters from serpentinites of the Gruppo di Voltri (Genova, Italy) and reaction path modeling of CO₂ sequestration in serpentinite aquifers," *Applied Geochemistry*, vol. 19, no. 5, pp. 787–802, 2004.
- [13] I. Gaus, M. Azaroual, and I. Czernichowski-Lauriol, "Reactive transport modelling of the impact of CO₂ injection on the clayey cap rock at Sleipner (North Sea)," *Chemical Geology*, vol. 217, no. 3-4, pp. 319–337, 2005.
- [14] P. Audigane, I. Gaus, I. Czernichowski-Lauriol, K. Pruess, and T. Xu, "Two-dimensional reactive transport modeling of CO₂ injection in a saline aquifer at the Sleipner site, North Sea," *American Journal of Science*, vol. 307, no. 7, pp. 974–1008, 2007.
- [15] S. Amin, D. J. Weiss, and M. J. Blunt, "Reactive transport modelling of geologic CO₂ sequestration in saline aquifers: The influence of pure CO₂ and of mixtures of CO₂ with CH₄ on the sealing capacity of cap rock at 37°C and 100bar," *Chemical Geology*, vol. 367, pp. 39–50, 2014.
- [16] T. Xu, J. A. Apps, and K. Pruess, "Numerical simulation of CO₂ disposal by mineral trapping in deep aquifers," *Applied Geochemistry*, vol. 19, pp. 917–936, 2004.
- [17] T. Xu, J. A. Apps, and K. Pruess, "Mineral sequestration of carbon dioxide in a sandstone-shale system," *Chemical Geology*, vol. 217, no. 3-4, pp. 295–318, 2005.
- [18] T. Xu, E. Sonnenthal, N. Spycher, and K. Pruess, "TOUGHREACT—A simulation program for non-isothermal multiphase reactive geochemical transport in variably saturated geologic media: Applications to geothermal injectivity and CO₂ geological sequestration," *Computers & Geosciences*, vol. 32, pp. 145–165, 2006.

- [19] M. Wigand, J. W. Carey, H. Schütt, E. Spangenberg, and J. Erzinger, "Geochemical effects of CO₂ sequestration in sandstones under simulated in situ conditions of deep saline aquifers," *Applied Geochemistry*, vol. 23, no. 9, pp. 2735–2745, 2008.
- [20] Y. Okuyama, M. Sasaki, S. Nakanishi, N. Todaka, and S. Ajima, "Geochemical CO₂ trapping in open aquifer storage - the Tokyo Bay model," in *Proceedings of the 9th International Conference on Greenhouse Gas Control Technologies, GHGT-9*, pp. 3253–3258, usa, November 2008.
- [21] Y. K. Kharaka, D. R. Cole, S. D. Hovorka, W. D. Gunter, K. G. Knauss, and B. M. Freifeld, "Gas-water-rock interactions in Frio Formation following CO₂ injection: implications for the storage of greenhouse gases in sedimentary basins," *Geology*, vol. 34, no. 7, pp. 577–580, 2006.
- [22] S. D. Hovorka, S. M. Benson, C. Doughty et al., "Measuring permanence of CO₂ storage in saline formations: the Frio experiment," *Environmental Geosciences*, vol. 13, no. 2, pp. 105–121, 2006.
- [23] I. Hutcheon, M. Shevalier, K. Durocher et al., "Interactions of CO₂ with formation waters, oil and minerals and CO₂ storage at the Weyburn IEA EOR site, Saskatchewan, Canada," *International Journal of Greenhouse Gas Control*, vol. 53, pp. 354–370, 2016.
- [24] X. Wu, *Carbon Dioxide Capture and Geological Storage: The First Massive Exploration in China*, Beijing Science Press, 2013.
- [25] H. Wang, *Study on the Interaction of CO₂ Fluid with Sandstone in Shiqianfeng*, Jilin University, 2012.
- [26] X. Yang, *Experimental study of CO₂ fluid on the geological transformation of reservoir sandstone*, Jilin University, 2012.
- [27] Y. Tao, *Experimental study on the interaction of CO₂/CO₂-H₂S fluid with sandstone in Liujiagou*, Jilin University, 2013.
- [28] Q. Zhu, D. Zuo, and S. Zhang, "Simulation of geomechanical responses of reservoirs induced by CO₂ multilayer injection in the Shenhua CCS project, China," *International Journal of Greenhouse Gas Control*, vol. 42, pp. 405–414, 2015.
- [29] Q. Li, G. Liu, X. Liu, and X. Li, "Application of a health, safety, and environmental screening and ranking framework to the Shenhua CCS project," *International Journal of Greenhouse Gas Control*, vol. 17, pp. 504–514, 2013.
- [30] K. Zhang, J. Xie, C. Li, L. Hu, X. Wu, and Y. Wang, "A full chain CCS demonstration project in northeast Ordos Basin, China: Operational experience and challenges," *International Journal of Greenhouse Gas Control*, vol. 50, pp. 218–230, 2016.
- [31] T. Xu, N. Spycher, E. L. Sonnenthal, L. Zheng, and K. Pruess, "TOUGHREACT Users Guide: A simulation program for non-isothermal multiphase reactive transport in variably saturated geologic media," *Version*, vol. 2.0, 2012.
- [32] H. Tian, *Impacts of CO₂-brine-rock interaction on the caprock sealing efficiency: A case study of Shiqianfeng formation mudstone caprock in Ordos Basin*, Jilin University, 2014.
- [33] W. Zhang, Y. Li, and T. Xu, "Long-term variations of CO₂ trapped in different mechanisms in deep saline formations: A case study of the Songliao Basin, China," *International Journal of Greenhouse Gas Control*, vol. 3, no. 2, pp. 161–180, 2009.
- [34] A. C. Lasaga, J. M. Soler, J. Ganor, T. E. Burch, and K. L. Nagy, "Chemical weathering rate laws and global geochemical cycles," *Geochimica et Cosmochimica Acta*, vol. 58, no. 10, pp. 2361–2386, 1994.
- [35] I. Gaus, P. Audigane, L. André et al., "Geochemical and solute transport modelling for CO₂ storage, what to expect from it?" *International Journal of Greenhouse Gas Control*, vol. 2, no. 4, pp. 605–625, 2008.
- [36] A. Credo, O. Bildstein, M. Jullien et al., "Experimental and modeling study of geochemical reactivity between clayey caprocks and CO₂ in geological storage conditions," in *Proceedings of the 9th International Conference on Greenhouse Gas Control Technologies, GHGT-9*, pp. 3445–3452, usa, November 2008.
- [37] M. T. van Genuchten, "A closed-form equation for predicting the hydraulic conductivity of unsaturated soils," *Soil Science Society of America Journal*, vol. 44, no. 5, pp. 892–898, 1980.
- [38] A. T. Corey, "The interrelation between gas and oil relative permeabilities," in *Producers Monthly*, pp. 38–41, Producers Monthly, 1954.
- [39] J. Chen and Z. Zheng, *Probability and Statistics*, Peking University Press, Beijing, China, 2015.
- [40] G. Yang, Y. Li, and X. Ma, "Effect of chlorite on CO₂-water-rock interaction," *Earth Science Journal of China University of Geosciences*, vol. 39, no. 4, 2014.
- [41] K. Wang, T. Xu, H. Tian, and F. Wang, "Impacts of mineralogical compositions on different trapping mechanisms during long-term CO₂ storage in deep saline aquifers," *Acta Geotechnica*, vol. 11, no. 5, pp. 1167–1188, 2016.

Research Article

Numerical Modeling of CO₂ and Brine Leakage through Open Fracture in a Fault Zone: Open Channel Flow or Darcy Flow

Ning Liu,¹ Lehua Pan,² and Jianmei Cheng¹

¹*School of Environmental Studies, China University of Geosciences, Wuhan 430074, China*

²*Lawrence Berkeley National Laboratory, MS-9016, One Cyclotron Road, Berkeley, CA 94720, USA*

Correspondence should be addressed to Jianmei Cheng; jmcheng@cug.edu.cn

Received 13 July 2017; Revised 3 October 2017; Accepted 19 October 2017; Published 6 December 2017

Academic Editor: Xiaoqing Shi

Copyright © 2017 Ning Liu et al. This is an open access article distributed under the Creative Commons Attribution License, which permits unrestricted use, distribution, and reproduction in any medium, provided the original work is properly cited.

Understanding fluids migration and leakage risk along the fault zone is necessary to guarantee the safety of CO₂ geological storage. The validity of Darcy's law gets challenged in dealing with the flow in open fractures since the occurring of turbulence flow. In this study, we develop a 2D model with usage of T2Well, an integrated wellbore-reservoir simulator, to investigate the leakage problem along open fractures which are embedded in a fault zone from the deep injection reservoir to shallow aquifers. The results record a positive feedback of gas expansion and pressure response in fracture, which causes a quick downward propagation of highly gas saturated zone from the top of fracture and an easy gas breakthrough in the shallower aquifers. The decreasing of aperture size of fracture significantly enhances the leakage rates in fracture, but with less influences as aperture increases. In comparison, the Equivalent Porous Media models show a good approximation with the momentum model of large apertures but poor for the small one. Nevertheless, the differences are small in terms of final CO₂ distribution among various aquifers, suggesting that Darcy's law may be still "effective" in solving flow problem along fractures in a constant injection system at a large time scale.

1. Introduction

Injection of CO₂ into deep saline aquifers for CO₂ geological storage (CCS) is considered as an effective technology to mitigate greenhouse gas emission. Leakage through existing fault into shallow groundwater aquifers, which occurs in many natural systems (e.g., [1–4]), is an important risk associated with CCS. Many numerical studies highlight this risk [4–9]. Pruess and Garcia [10] investigate CO₂ discharge along a fault zone by a simplified 1D model of constant boundary conditions, to find that fluids dynamics in the fault zone are mainly constrained by relative permeability and capillary function. Lu et al. [11] set up a 2D fault model and use time-varying boundary conditions to investigate the risk of CO₂ leakage through a fault. The results suggest that fault permeability is the most sensitive factor affecting both CO₂ and brine leakage rate. Some studies further investigate the impacts of spatial heterogeneity about hydraulic parameters distribution in the fault zone on CO₂ leakage dynamics. Vialle et al. [6] develop a 2D model of CO₂ leakage along a fractured

cap rock, introduce heterogeneities in the initial permeability field of fractured damage zone, and find that the leakage of CO₂ into upper aquifer does not spread uniformly but most likely show one or several points' source leaks. Rinaldi et al. [12] suggest that the presence of hydraulic heterogeneity in the fault would influence the pressure diffusion when investigating the effect of hydraulic properties variation within a fault zone embedded in a multilayer sedimentary system. Jeanne et al. [9] get similar conclusion when studying the impact of hydraulic-property variations on fluids flow along a fault zone by two damage-zone models. They find that CO₂ is trapped in the fault zone and obtain a high fluid overpressure if the heterogeneous model is used. In contrast, the homogeneous model predicts an easy migration of CO₂ with lower overpressure. By recognizing the fact that fracture is usually the major flow pathway in a fault, a few researchers recently introduce the discrete fracture network (DFN) model to study fluids flow through fault zone or fractured rocks [13–15]. In general, these models divide reservoir system into fracture network and matrix rocks and

approximate a fracture as open space bounded by parallel plates. The equivalent permeability of a fracture is usually estimated using the cubic equation [16].

In the above studies, the fault is all assumed to be a kind of porous media so that the flow can be described by Darcy's law even in the models with preferred flow path such as open fractures. However, a fracture is fundamentally an open space bounded by two walls. Under some conditions, the aperture could be larger enough so that the flow in the fracture becomes turbulence or the momentum term is no longer negligible compared with the friction term. In this situation, Darcy's law is no longer proper to describe the flow dynamics and the full Navier-Stokes momentum equation would be needed. Furthermore, when free CO_2 phase evolves, the flow dynamics become more complicated because of complicated phase interference (e.g., gas-lifting phenomena) which may not be accounted by a Darcy law based model.

In this paper, we will present a numerical modeling study of CCS induced leakage from the deep injection aquifer to the shallow aquifer using T2Well [17], an integrated reservoir-wellbore simulator that solves the compressible two-phase Navier-Stokes momentum equations for flow in the subdomain of open space (e.g., well or fracture). The hypothetical leakage problem is formulated as a 2D problem (XZ -plane) so that the flow in open fractures can be simplified as a 1D problem to facilitate the usage of T2Well. The focus is on the impacts of open fractures on the possible leakage flow dynamics and under what conditions the flow in the open fracture can be properly approximated as Darcy flow.

2. Method

2.1. Concept Model and Numerical Grid. The problem we are interested in is the possible leakage through a fault from a deep injection aquifer to the shallow ones due to the injection of CO_2 (Figure 1). We take a profile of the system with a thickness of 2 m in Y -direction as our model that can be simplified as a 2D leakage problem without losing generality (Figure 1). As shown in Figure 1, in the XZ -plane, there are two sets of aquifers. The two shallow aquifers (Aquifers 3 and 4), separated by an aquitard in vertical direction, are open to constant boundary conditions on the left end but bounded by the fault at the right end. The two deep aquifers (Aquifers 1 and 2), also separated by an aquitard in vertical direction, are bounded by the fault at the left end. The fault zone is located at the distance of 4500 m from the left boundary and 500 m from the right boundary of the model. Aquifer 1 is the injection aquifer where a horizontal injection well is drilled at its right and bottom end for successive injection of CO_2 with a constant rate of 0.25 kg/s per unit meter for 5 years. As the pressure and CO_2 plume reach the fault, they may propagate further into the shallow aquifers (3 and 4). Aquifer 2 may serve as a buffer zone (or thief zone) in some degree depending on the pressure conditions at the nearby fault. The fault zone provides the critical pathway in this leakage problem. It is widely expected that the major flow pathway in a fault zone is the well-developed fracture network. Because flow modeling with detailed geometry of the fracture network

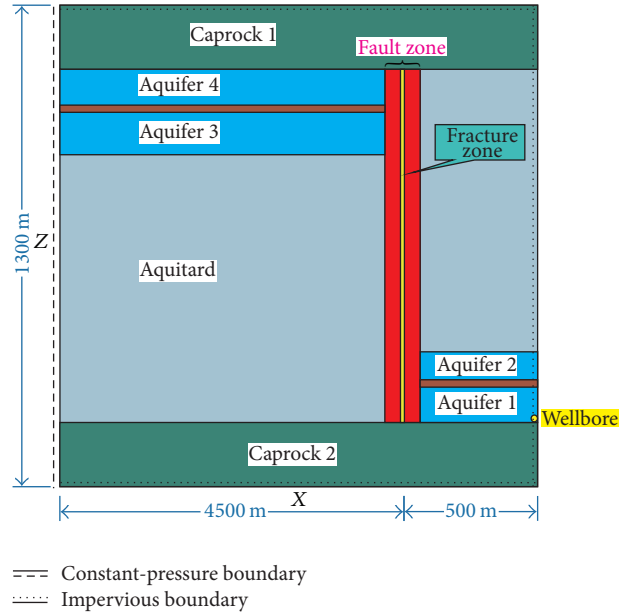


FIGURE 1: Concept model of CO_2 leakage along the fracture zone developed in the middle of a fault area which offsets and connects two sets of aquifers, the deep Aquifers 1 and 2 and shallow Aquifers 3 and 4. Open fractures of different apertures may grow inside the fracture zone and work as a fast pathway for CO_2 leakage. A horizontal well of 2 m length is drilled at the right and bottom side of Aquifer 1 for 5 years' CO_2 injection.

is often not practical (if not possible), we approximate the major flow pathway as a virtual fracture. The virtual fracture can represent different fracture network (i.e., the major flow pathway) with its effective aperture. To do so, we first define a fixed fracture zone in the numerical grid (e.g., 5 cm width in x -coordinate) and then use perimeter of the virtual fracture, Γ , and the effective porosity of the fracture zone, ϕ , defined as the fraction of the area occupied by fracture and total cross-section area of the fracture zone. Figure 2 shows the sketch of the virtual fracture model. As shown in Figure 2, with being fully fractured in Y direction of the fracture zone, the porosity can be calculated as the ratio of fracture aperture, h , over the width, w , of fracture zone. The fracture perimeter, Γ , can be calculated as $\Gamma = 2 \times (h + l)$. For example, a fracture aperture of 1 cm width (Case 1 in Figure 2) will result in a porosity of 0.2 and perimeter of 402 cm. If the aperture decreases to be 1 mm (Case 2 in Figure 2), the corresponding porosity is 0.02 and perimeter 400.2 cm. Similarly, we can have a porosity of 1.0 and perimeter of 410 cm if the effective fracture aperture is 5 cm. In this way, the virtual fracture as represented as the fracture zone can be seen as a lumped flow pathway representing the entire fracture network in the fault.

Figure 3 represents the mesh we construct based on the concept model. The dimension extends from -4500 m to 500 m in x -axis and -1500 m to -200 m in z -axis. The fault zone located at the zero in x -axis is composed of a 0.05 m wide fracture zone and several surrounded damage zones of width closing to 1 m. The horizontal resolution of the grid varies from 0.05 m near the fracture to the

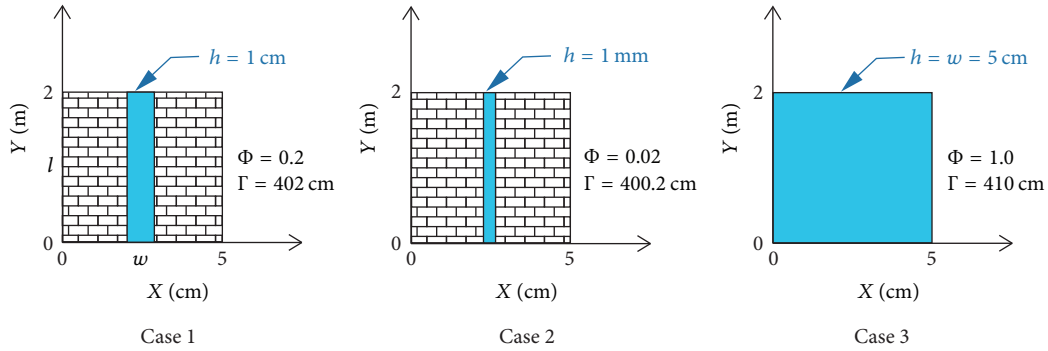


FIGURE 2: A cross-section (XY -plane) view of the fracture zone and relationships of the fracture aperture, h , and perimeter, Γ , and the porosity, ϕ , of the fracture zone in different cases of various aperture sizes. Note that the cross-section of the fracture zone remains unchanged in our numerical grid (2 m in length, l , and 5 cm in width, w) but the size of the virtual fracture (the blue colored area) can change and is defined by the perimeter of fracture space and the effective porosity of fracture zone and the ratio of fracture space over the total cross-sectional area of the fracture zone. In picture, the block-shaped area denotes the solid impermeable rocks in the fracture zone. In Case 1, a fracture of 1 cm wide aperture would have a perimeter of 402 cm ($2 \times 200 + 2 \times 1$ cm) and a porosity of 0.2 ($1 \times 200 \text{ cm}^2 / 5 \times 200 \text{ cm}^2$). The small aperture case ($h = 1$ mm) shown in Case 2 results in a porosity of 0.02 and perimeter of 400.2 cm. In particular, in Case 3, where a fracture fully develops among the fracture zone, its aperture finally equals the width of fracture zone of 5 cm, and the porosity becomes 1.0.

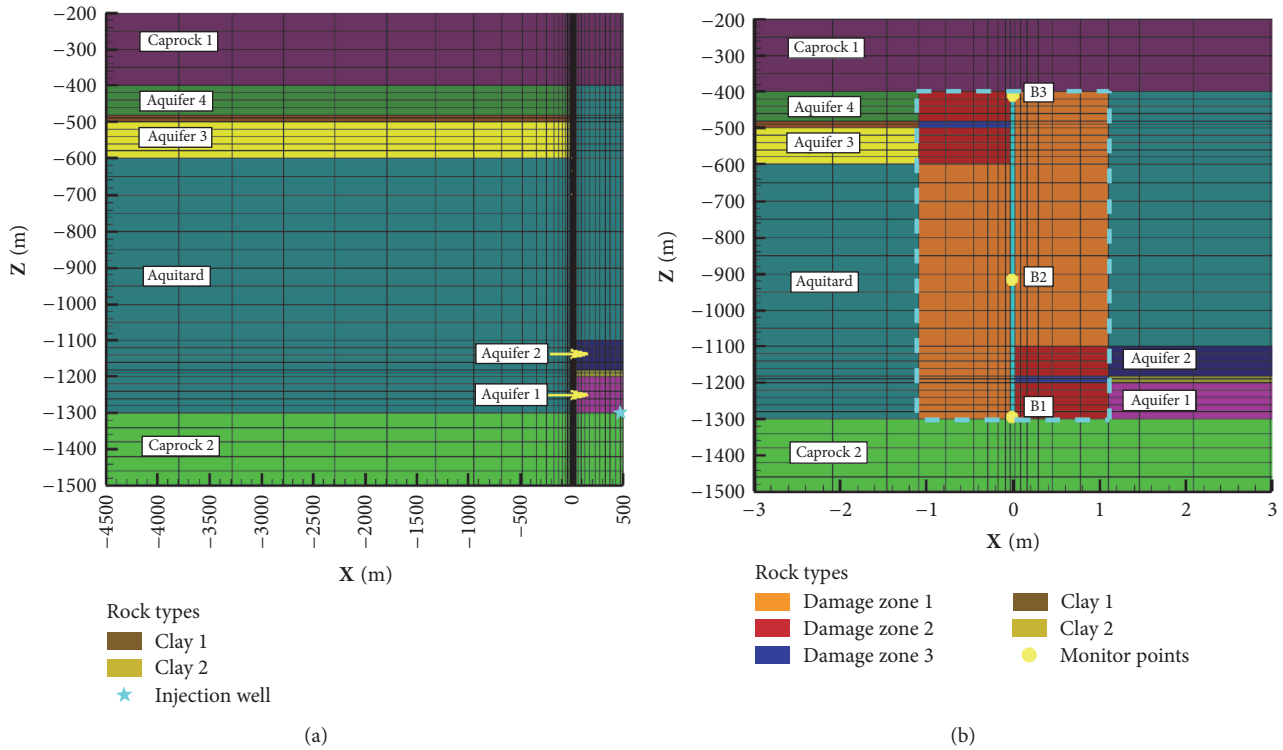


FIGURE 3: Mesh discretization based on the concept model shown in Figure 1. Picture (a) shows a full view of the grid in which a CO_2 injection well (the cyan star) is located at the right bottom side of Aquifer 1. Picture (b) is the zoom view of the fault zone, comprising a 0.05 m wide fracture zone in the middle and (highlighted by the cyan solid line) several surrounded damage zones of width closing to 1 m. The observation points B1, B2, and B3 are located at $Z = -1290, -975,$ and -410 m, respectively ($X = 0.0$ m).

maximum of 50 m and 500 m at the right and left boundary, respectively. Table 1 gives all hydraulic parameters of the porous medias used in this study while the information about fracture zone is summarized in Tables 2 and 3. The rock properties of porous media derive from the wellbores drilled at the Yaojia formation in SanZhao depression of Songliao

Basin, China. Commonly distributed sandstone strata with high porosity and permeability and the coupled upper shale of poor hydraulic property in Yaojia formation make the reservoir suitable for oil and CO_2 storage. In this study, we select a large porosity and corresponding permeability for the aquifers and small ones for aquitard, clays, and cap rocks,

to guarantee the most of injected CO₂ can be sequestered among aquifers instead of other media.

Before CO₂ injection, the whole system is saturated with water and under hydrostatics pressure. Surface temperature is 20°C and the temperature gradient is set to be 3°C/100 m. As shown in Figure 3, three points B1, B2, and B3 are located at the bottom ($Z = -1290$ m), middle ($Z = -975$ m), and top ($Z = -410$ m) of the fracture to monitor the pressure responses there associated with CO₂ injection. In addition, the fluids status and flow dynamics at injection well and the interfaces between the fracture and each aquifer are also monitored.

2.2. The Numerical Simulator. We use T2Well/ECO₂N [17] to simulate the fluid and heat flow associated with the leakage problems in this study. T2Well is an integrated reservoir-wellbore simulator. The major governing equations used in T2Well are listed in Table 4. As shown in Table 2, for the subdomain of porous media (e.g., formations), the multiple phase version of Darcy's law is used to obtain the phase velocity whereas the phase velocities are calculated as a function of the mixture velocity and the drift velocity in the subdomain of wellbore. By applying the empirical Drift Flux Model (DFM), the two-phase momentum equations can be simplified as a single momentum equation in terms of the mixture velocity:

$$\begin{aligned} \frac{\partial}{\partial t} (\rho_m u_m) + \frac{1}{A} \frac{\partial}{\partial z} [A (\rho_m u_m^2 + \gamma)] \\ = -\frac{\partial P}{\partial z} - \frac{\Gamma f \rho_m |u_m| u_m}{2A} - \rho_m g \cos \theta, \end{aligned} \quad (1)$$

where A is the cross-sectional area of the wellbore and the term $\gamma = S_G(\rho_G \rho_L \rho_m / \rho_m^{*2}) [(C_0 - 1)u_m + u_d]^2 / (1 - S_G)$ is caused by slip between the two phases. The terms ρ_m , u_m , and ρ_m^* are the mixture density ($\rho_m = S_G \rho_G + (1 - S_G) \rho_L$), the mixture velocity ($u_m = [S_G \rho_G u_G + (1 - S_G) \rho_L u_L] / \rho_m$), and the profile-adjusted average density of the mixture ($\rho_m^* = S_G C_0 \rho_G + (1 - S_G C_0) / \rho_L$). Γ is the perimeter of the cross-section, and f is apparent friction coefficient, a function of wall roughness and flow regime.

The details of the approach used in T2Well for modeling flow in wellbore can be found in the manual or other related papers [17–19] and would not be duplicated here. However, we have slightly modified the code to adapt the simulator to the case of fracture flow because the open space of a fracture is not of a circular shape as in the case of a wellbore. The momentum equation (1) uses the general terms, the perimeter Γ , and the cross-section area A , which should have no problem to apply to any geometric shape of open space including the rectangle shape of a fracture. The major difference is in the friction coefficient, f , which is calculated as a function of local Reynold number, the wall roughness, and the effective diameter of the pipe in T2Well [18, 19]:

$$f = \frac{64}{\text{Re}} \quad \text{for } \text{Re} \leq 2400,$$

$$\frac{1}{\sqrt{f}} = -4 \log \left[\frac{3\varepsilon/D_e}{3.7} - \frac{5.02}{\text{Re}} \log \left(\frac{3\varepsilon/D_e}{3.7} + \frac{13}{\text{Re}} \right) \right] \quad \text{for } \text{Re} > 2400, \quad (2)$$

where ε is the roughness of the wellbore and the Reynold number Re is defined as

$$\text{Re} = \frac{\rho_m u_m D_e}{\mu_m}, \quad (3)$$

where μ_m is the mixture viscosity. In both (2) and (3), the effective diameter D_e can be seen as the critical length for a pipe. Therefore, the modification we made is to let T2Well use the aperture in the place of the effective diameter in calculation of the Reynold number and the friction coefficient for the subdomain of open fractures.

ECO₂N is a TOUGH2 EOS module for modeling thermal physical behaviors of the H₂O-CO₂-NaCl system (Pruess, 2005) and has been widely used in modeling flow problems associated with CCS. In this study, we use an updated version of ECO₂N (i.e., Version 2.0, Pan et al., 2017) which provides more accurate calculations of the thermal physical properties of the CO₂-rich phase and can be applied to higher temperature range than the previous version (i.e., Version 1.0). Following the convention of ECO₂N, we will call the CO₂-rich phase gas phase thereafter although it could actually be gaseous, liquid, or supercritical CO₂ with dissolved water depending on local pressure and temperature.

3. Results and Discussions

3.1. CO₂ Migration Dynamics in Case 1 (Aperture = 1 cm). Injection of CO₂ increases the pressure at the injection point first (Figure 4). The pressure propagates quickly from injection point to the left end of Aquifer 1 which causes water to start flowing out from Aquifer 1 to the fault at about 0.1 days (Figure 5). The pressure responses at different depth in the open fracture (i.e., at Points B1 through B3) are almost identical indicating that the pressure propagation through the open fracture is much faster than through the porous formation (Figure 4). However, the responses in terms of gas phase saturation are very different. The gas saturation at shallow depth in the fracture can be higher than that at the injection well (Figures 4(a) and 4(d)) while the gas saturation at B1 (the deepest point in the fracture) is still below 0.012 at end of simulation (Figure 4(b)).

After about 4 days, CO₂ starts to flow into the fault as dissolved CO₂ in water (Figure 5). This period lasts for 254 days before breakthrough of gas phase. During this period, the CO₂-dissolved water flows up along the fracture and quickly reaches the top of fracture. As a result, the mass fraction of the dissolved CO₂ increases with time but its contour line is close to vertical above Aquifer 1 (Figure 6(a)).

Gas phase occurs first at bottom of the open fracture at day 257.9 although the gas saturation is very low (Figure 6(b)). The bubbling region expands to the depth of 700 m almost immediately although in much lower overall gas saturation

TABLE 1: Hydraulic parameters adopted in this study for all porous media.

Rock types	Permeability (m^2)		Parameters for relative permeability (van Genuchten-Mualem model and Corey model)			Parameters for capillary pressure (van Genuchten model)				Note		
	K_X	K_Z	Residual gas saturation (S_{gr})	m_{VG}	Residual liquid saturation (S_{lr})	Saturated liquid saturation (S_{ls})	Residual liquid saturation	m_{VG}	$1/P_0$ (Pa^{-1})		Maximum capillary pressure (Pa)	Saturated liquid saturation
Reservoirs (Aquifer 1 to Aquifer 4)	0.25	$3 \cdot e - 13$	0.05		0.3		0.25		$5.1 \cdot e - 5$	$1 \cdot e7$		(1) Thermal conductivity and specific heat are $2.51 \text{ Wm}^{-1} \text{ K}^{-1}$ and $920 \text{ J/kg} \cdot \text{C}$, respectively, keeping the same for all rocks.
Cap rocks, clays and aquitard	0.15	$1 \cdot e - 17$	0.15	0.46	0.4	1	0.35	0.46	$1.6 \cdot e - 5$	$1 \cdot e8$	1	(2) m_{VG} is an empirical parameter of van Genuchten capillary function and relative permeability function, and P_0 denotes a critical inlet pressure for fluids.
Damage zones of aquifers	0.3	$1 \cdot e - 12$	0.05		0.25		0.2		$5.1 \cdot e - 5$	$1 \cdot e7$		
Damage zones of aquitard	0.2	$1 \cdot e - 15$	0.1		0.3		0.25		$1.6 \cdot e - 5$	$5 \cdot e7$		

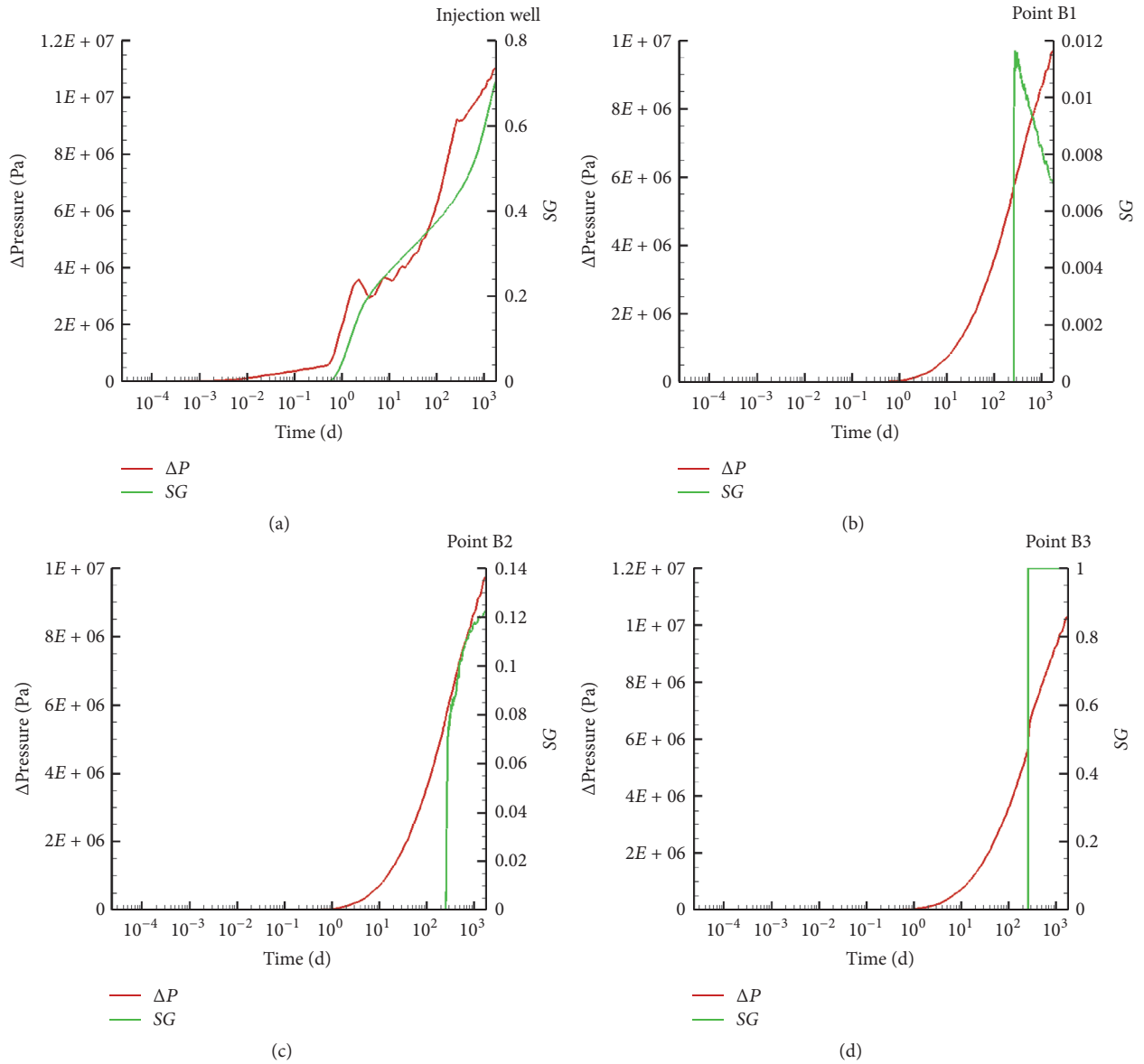


FIGURE 4: Pressure buildup and gas saturation changes at injection well and monitor points during CO₂ injection in Case 1.

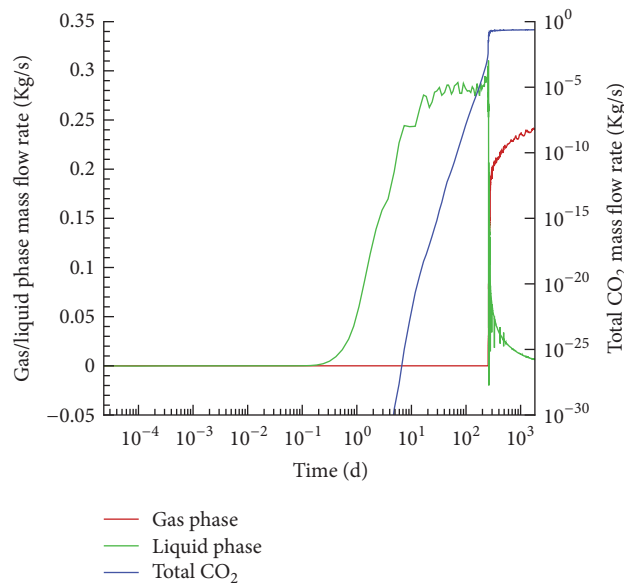


FIGURE 5: Mass flow rate evolution of the gas/liquid phase and total CO₂ at the outlet of Aquifer 1 in Case 1.

TABLE 2: Parameters of fracture zone in momentum models.

Case name	Aperture	Roughness	Capillary function	Relative permeability
Case 1	1 cm			Linear functions
Case 2	1 mm	$4.5 \cdot e - 4$ m	None	$S_{gr} = 0, S_{lr} = 0, S_{ls} = 1$
Case 3	5 cm			

TABLE 3: Parameters of fracture zone in EPM models.

Case name	Porosity	K_X (m ²)	K_Z (m ²)	Capillary function	Relative permeability
Case 4	0.2		$1.67 \cdot e - 6$		Linear functions
Case 5	0.02	$1.0 \cdot e - 12$	$1.67 \cdot e - 9$	None	$S_{gr} = 0, S_{lr} = 0, S_{ls} = 1$
Case 6	1.0		$2.08 \cdot e - 4$		

at day 258.2. After that, the gas saturation in the region gradually increases until a more significant increase occurs in the neighborhood of the 730 m depth where CO₂ transforms from supercritical to gaseous phase, which results in a large expansion. This period ends at day 258.5 as the bubble region suddenly reaches the top of the open fracture and, as a result, the overall gas saturation below 700 m depth decreases. The occurring of gas phase at top of the open fracture, where the pressure is the lowest in the fracture, starts positive feedback that results in a quick expansion of high gas saturation region downward (Figures 6(b) and 6(d)). This positive feedback can be described as follows. With increase of gas phase saturation at top of the fracture, the overall density of fluid mixture decreases significantly because the density of gas phase is much smaller than the aqueous phase. As a result, the gravity applied on the fluid below reduces greatly. This will in turn greatly reduce the pressure there which will cause more dissolved CO₂ to escape from the aqueous phase and the gas phase to occupy more volume. This process can go on until the difference in density between the gas phase and liquid phase is not large enough to make large change in gravity force due to change in gas saturation.

This downward propagation of high gas phase saturation region in the fracture has great impacts on the sequence of CO₂ breakthrough into each aquifer (Figure 7). The gas phase flow into aquifer occurs first at the shallowest aquifer (Aquifer 4) and then Aquifer 3 (deeper than Aquifer 4) about 11 days later (except a short lived inflow at day 258.5). For much deeper aquifer (Aquifer 2), there is no significant gas flow although it is the first aquifer in the leakage pathway after Aquifer 1. This is mainly because the gas saturation at that depth is too low (Figure 6(d)).

The change in fracture pressure associated with the quick expansion of the high gas saturation region in the fracture shows great impacts on the flow dynamics between the fracture and the aquifers since the fracture is opened to multiple aquifers at various depths. Although the gas flow from Aquifer 1 to the fracture increases with time and the liquid flow decreases in general and then tends to stabilize at certain level, such increase or decrease occurs at step-like way associated with some oscillations (Figure 7(a)). Such

oscillation is more profound at shallower depths (Figures 7(c) and 7(d)) and can even be found in the liquid flow rate between the fracture and Aquifer 2 (Figure 7(b)).

The profile of Reynold number shows that the flow in fracture is still mostly laminar flow with the maximum Reynold number < 2400 in the fracture (Figure 8(a)). The higher Reynold number region almost overlaps the gas phase dominant region while the Reynold number decreases with depth mainly because the velocity decreases with depth due to fluid leaking to Aquifers 3 and 4 on its way to top (Figures 8(a) and 8(c)). However, there are small regions where the momentum term is important because the ratio of the momentum over friction term is closing to or exceeds 1.0.

As shown in Table 5, after one year's injection, 77% of the injected CO₂ is still in Aquifer 1 and about 20% leaks into shallow aquifers, among which Aquifer 4 shows much potential to steal CO₂ than Aquifer 3. However, at end of 5 years' injection, only 20.2% of the injected CO₂ stays in Aquifer 1 while 42.5% leaks into Aquifer 3 and 35.3% into Aquifer 4 (Table 6). The time dependent characteristics of CO₂ mass distribution in each aquifer reflects the impacts of fluids dynamics at different time scale. Finally, there is no gas phase CO₂ sequestered in Aquifer 2 with the increase of injection duration, although the dissolved CO₂ slightly increases.

3.2. Impact of Fracture Aperture. In a real fault, the fracture network development could vary widely depending on local stress field and other factors. We did a series of simulations of the same leakage process using the fracture aperture as the parameter characteristic of the given open fracture system developed in a fault. Two additional cases with smaller (Case 2, 1 mm) or larger (Case 3, 5 cm) apertures, shown in Figure 2 and Table 2, are simulated to investigate how the aperture affects the CO₂ migration along fracture, in terms of pressure responses, gas saturation, fluids dynamics, and the final CO₂ distributions in aquifers. The smaller aperture case represents a scenario with a poor fracture network developed in the fault whereas the larger aperture case represents the other end. As shown in Figure 9(a), the injection pressure quickly increases with time in all cases until the gas phase

TABLE 4: Equations applied for different regions in T2Well.

Description	Equation	
Conservation of mass and energy	$\frac{d}{dt} \int_{V_n} M^\kappa dV_n = \int_{\Gamma_n} \mathbf{F}^\kappa \cdot n d\Gamma_n + \int_{V_n} q^\kappa dV_n$	
Mass accumulation	$M^\kappa = \phi \sum_{\beta} S_{\beta} \rho_{\beta} X_{\beta}^{\kappa}, \quad \text{for each mass component}$	
Mass flux	$\mathbf{F}^\kappa = \sum_{\beta} X_{\beta}^{\kappa} \rho_{\beta} \mathbf{u}_{\beta}, \quad \text{for each mass component}$	
Porous media		
Energy flux	$\mathbf{F}^\kappa = -\lambda \nabla T + \sum_{\beta} h_{\beta} \rho_{\beta} \mathbf{u}_{\beta}$	
Energy accumulation	$M^\kappa = (1 - \phi) \rho_R C_R T + \phi \sum_{\beta} \rho_{\beta} S_{\beta} U_{\beta}$	
Phase velocity	$\mathbf{u}_{\beta} = -k \frac{k_{r\beta}}{\mu_{\beta}} (\nabla P_{\beta} - \rho_{\beta} \mathbf{g})$	Darcy's Law
Wellbore		
Energy flux	$F^{NK1} = -\lambda \nabla T + \sum_{\beta} \rho_{\beta} S_{\beta} u_{\beta} \left(h_{\beta} + \frac{u_{\beta}^2}{2} + gz \cos \theta \right)$	
Energy accumulation	$M^\kappa = \sum_{\beta} \rho_{\beta} S_{\beta} \left(U_{\beta} + \frac{u_{\beta}^2}{2} + gz \cos \theta \right)$	
Phase velocity	$u_G = C_0 \frac{\rho_m}{\rho_m^*} u_m + \frac{\rho_L}{\rho_m^*} u_d$ $u_L = \frac{(1 - S_G C_0) \rho_m}{(1 - S_G) \rho_m^*} u_m - \frac{S_G \rho_G}{(1 - S_G) \rho_m^*} u_d$	Drift Flux Model

TABLE 5: CO₂ mass distribution in percentage among each aquifer after one year's injection.

Aquifers	Gas phase CO ₂	Dissolved CO ₂	Total CO ₂
Aquifer 1	64.60%	12.40%	77.00%
Aquifer 2	0.00%	0.03%	0.03%
Aquifer 3	7.03%	2.57%	9.60%
Aquifer 4	9.05%	3.03%	12.08%

TABLE 6: CO₂ mass distribution in percentage among each aquifer at end of five years' injection.

Aquifers	Gas phase CO ₂	Dissolved CO ₂	Total CO ₂
Aquifer 1	17.86%	2.33%	20.19%
Aquifer 2	0.00%	0.08%	0.08%
Aquifer 3	32.78%	9.72%	42.50%
Aquifer 4	27.36%	7.93%	35.29%

reaches the fault. After that point, the injection pressure increases much slowly because the leaking fluid accesses the lower resistance pathway (i.e., the open fracture). Different from the other cases, the injection pressure in the small aperture case (Case 2) significantly drops after that point which is accompanied with the similar pressure drop at bottom of the fracture and very fast pressure increase at top of the fracture (Figures 9(b) and 9(c)). In view of overall

pressure response in the fracture profile shown in Figures 9(e) and 9(f), Case 2 is also different from other cases that the pressure greatly increases at top and meanwhile decreases at bottom of the fracture. This is most likely because the gas saturation in fracture in Case 2 is much higher than other cases (Figures 10 and 6(d)) so that the resistance to gas flow is much smaller in Case 2 than in the other cases (Figure 11).

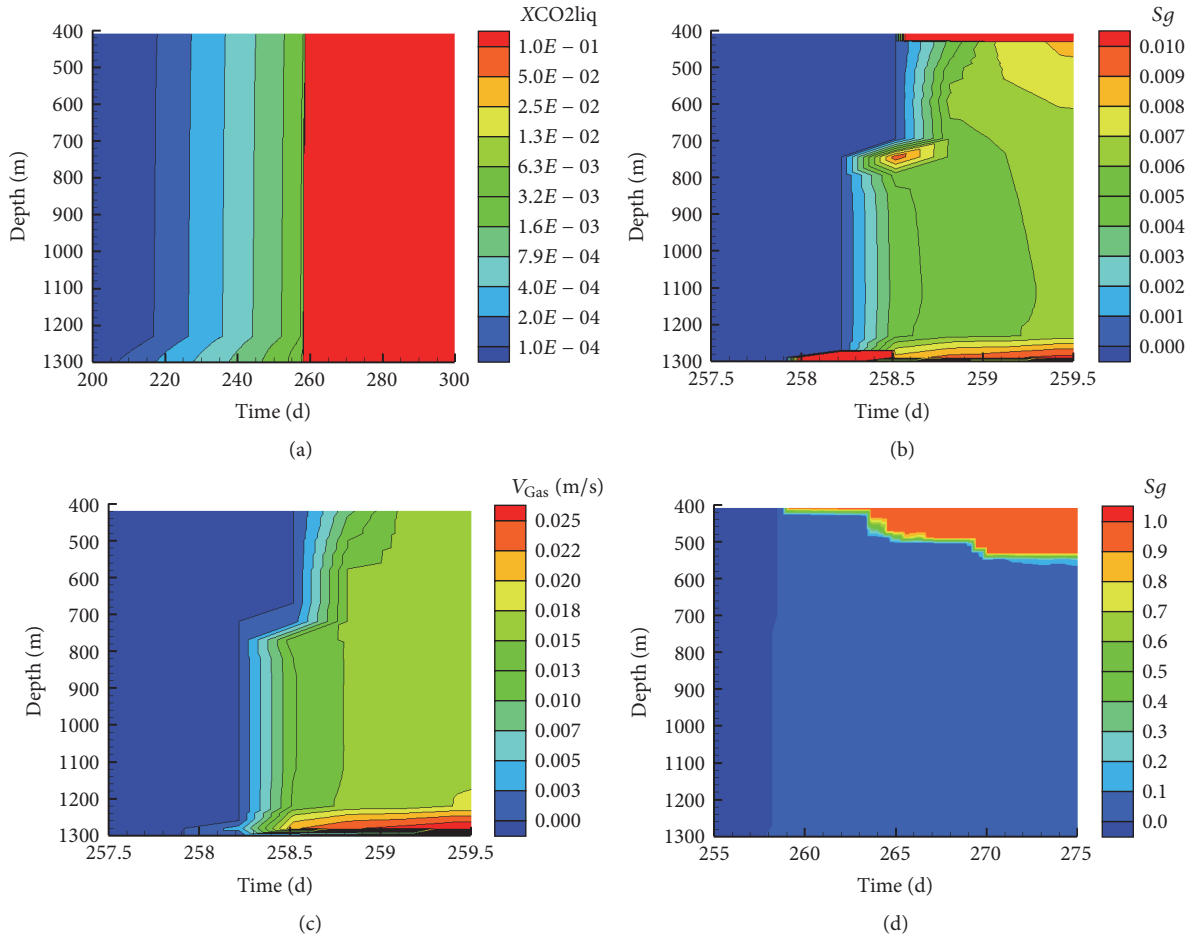


FIGURE 6: Distributions of the dissolved CO_2 mass fraction $X_{\text{CO}_2\text{liq}}$, gas saturation S_g , and gas phase flow rate V_{Gas} along the fracture profile in Case 1 during the few days around the breakthrough of CO_2 -rich phase at 258th day. Note that the fraction of dissolved CO_2 constantly becomes saturated if gas phase CO_2 evolves, working as a flag to trace the occurrence of two phases in fracture.

On the other hand, the fracture aperture shows great impacts on the flow dynamics in the fracture after two-phase flow has been established. The Reynold number increases as the aperture decreases from 1 cm (Case 1) to 1 mm (Case 2) because of increase in velocity (Figures 12(a) and 8(a)). However, the increase is quite small compared with Case 1 so that the maximum Reynold number is still below 2400 to prevail a laminar flow in the fracture. What is different is that the ratio of momentum term over friction becomes quite small as aperture decreases from 1 cm (Case 1) to 1 mm (Case 2), suggesting that the friction of side wall of fracture dominates fluids flow in the fracture other than the momentum term. In contrast, the Reynold number significantly increases over 2400 accompanied with momentum/friction ratio greater than 1.0 when aperture increases from 1 cm (Case 1) to 5 cm (Case 3). At these conditions, the fluids flow is of high turbulence and the momentum term becomes important in controlling the fluids flow rate in the fracture.

The larger the fracture aperture is, the earlier the gas phase arrives to the fracture from the injection well (Figure 13(a)) mainly because larger aperture means less resistance to fluid flow. The difference is quite small when the aperture increases

from 1 cm (Case 1) to 5 cm (Case 3) though. In contrast, when the aperture reduces from 1 cm (Case 1) to 1 mm (Case 2), occurring of the gas phase flow from Aquifer 1 to the fracture delays about 5 days but the mass flow rate quickly exceeds those in the case with larger aperture after gas phase reaches top of the fracture. This is consistent with pressure response pattern at fracture bottom (Figure 9(b)) that the pressure is much higher in Case 2 than in the other cases before gas phase breakthrough and the pressure in Case 2 after that point quickly drops to below those in other cases. As a result, the liquid phase flow rate from Aquifer 1 associated with CO_2 breakthrough drops slowly to be higher values than other cases in Case 2 (Figure 13(b)). The similar trend in terms of gas flow rate into shallow aquifers (Aquifer 3 and 4) can be found for aperture reduced to 1 mm, that is, Case 2 (Figures 13(c) and 13(d)). However, the occurring of gas flow into shallow aquifers delays as the aperture increases from 1 cm (Case 1) to 5 cm (Case 3) although the gas flow rate quickly approaches similar values in these two cases.

In general, the liquid phase mass flow rate decreases with time as the gas phase mass flow rate increases in all cases (Figure 14). The exemption is Case 2 (1 mm) where much

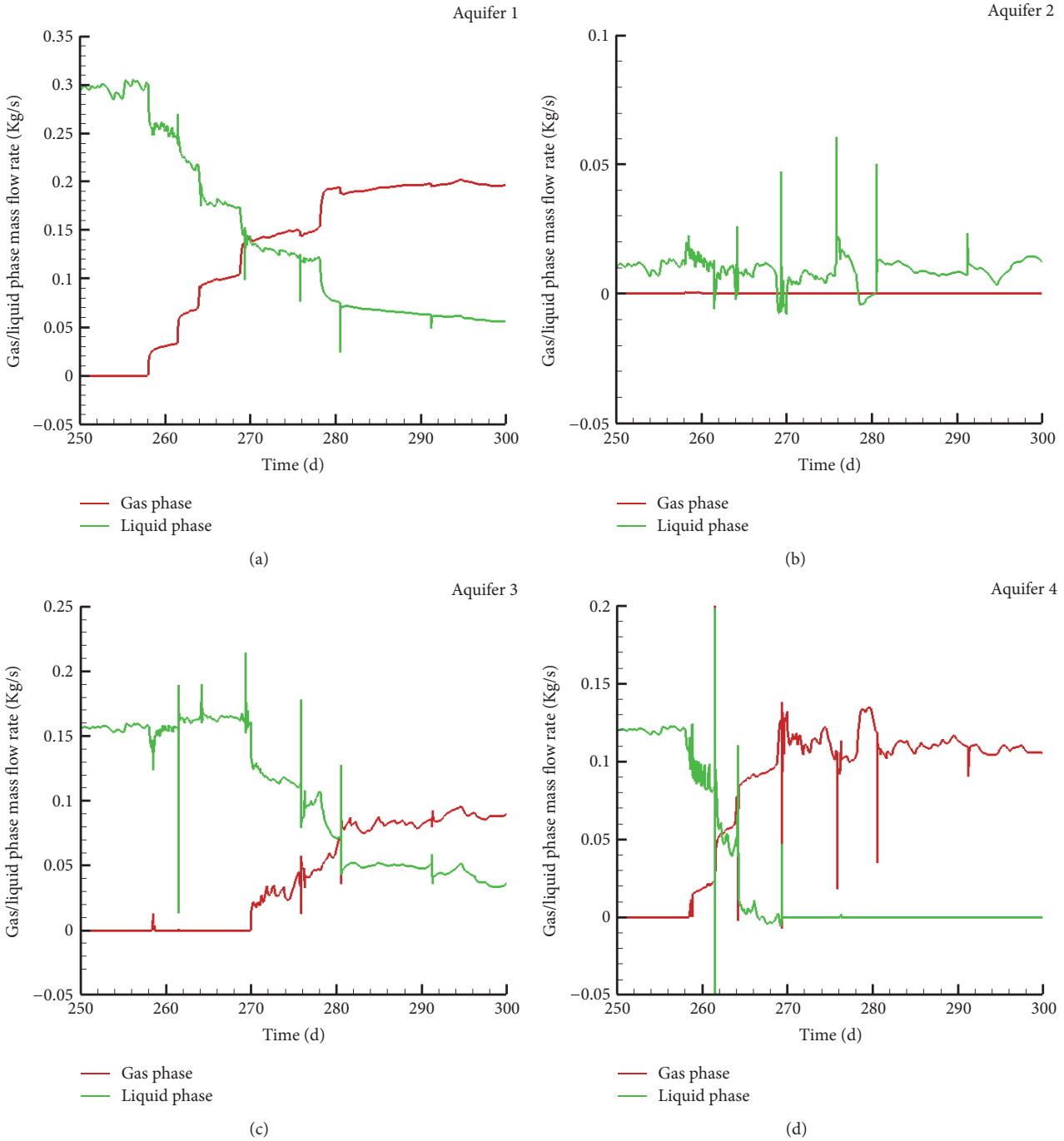


FIGURE 7: Phases mass flow rate at the interfaces of fracture and various aquifers in Case 1 before and after gaseous CO₂ breakthrough.

higher liquid flow rate into Aquifer 4 (including two peaks that exceed the rate during single liquid phase period) is found. This could be because the liquid is being lifted by the higher gas velocity in this smaller aperture case. The gas phase flow into Aquifer 2 is not significant in all cases probably because of very low gas saturation in the fracture at that depth. However, the liquid flow rate into Aquifer 2 shows different characteristics as aperture decreases from 1 cm to 1 mm (Figure 15). In general, the liquid flow rate is higher in

the small aperture case (Case 2) before gas CO₂ enters the fracture especially at the early injection stage (e.g., 50 days), which is also supposed as the reason for the higher amount of dissolved CO₂ stored in Aquifer 2 at end of 5 years' injection (Figure 16). With gas CO₂ breakthrough, the liquid reversely flows out from Aquifer 2 in Case 2 while other cases fail to observe this phenomenon. This is most likely because of the sudden pressure loss occurring at the fracture nearby Aquifer 2 as a result of the quick expansion of gas bubble zone at top of the fracture.

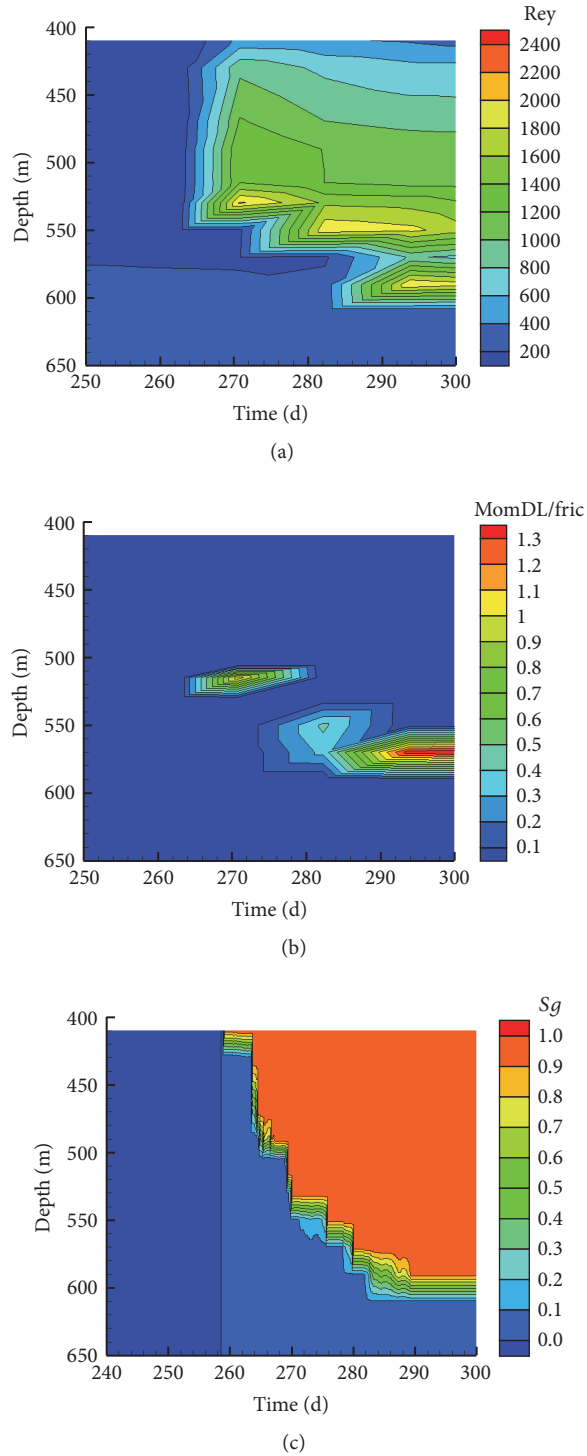


FIGURE 8: Profiles of Reynold number and the ratio of momentum over friction gradient at top zone of the fracture in Case 1 before and after gas phase evolves.

Despite many differences in flow dynamics caused by the fracture aperture during the first year of injection, especially during phase transition period in the fracture, the final distributions of the injected CO₂ are very similar for all

cases (Figure 16). This is because the gas flow rates into each aquifer approach the same values after first year (Figure 17), indicating that the fracture aperture only affects the flow dynamics at early time, especially during the phase transition

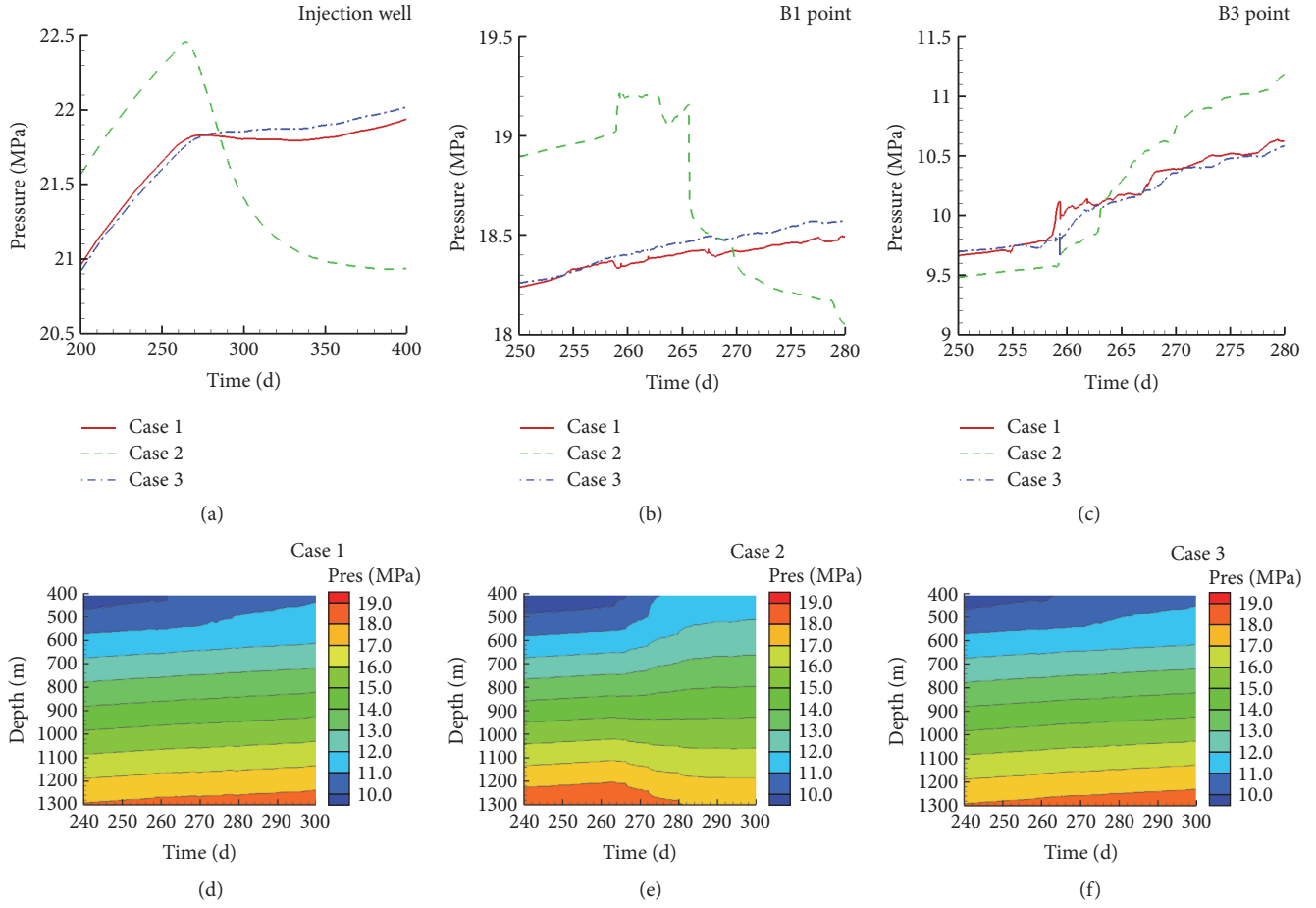


FIGURE 9: Pressure responses of CO₂ breakthrough at injection well and the fracture.

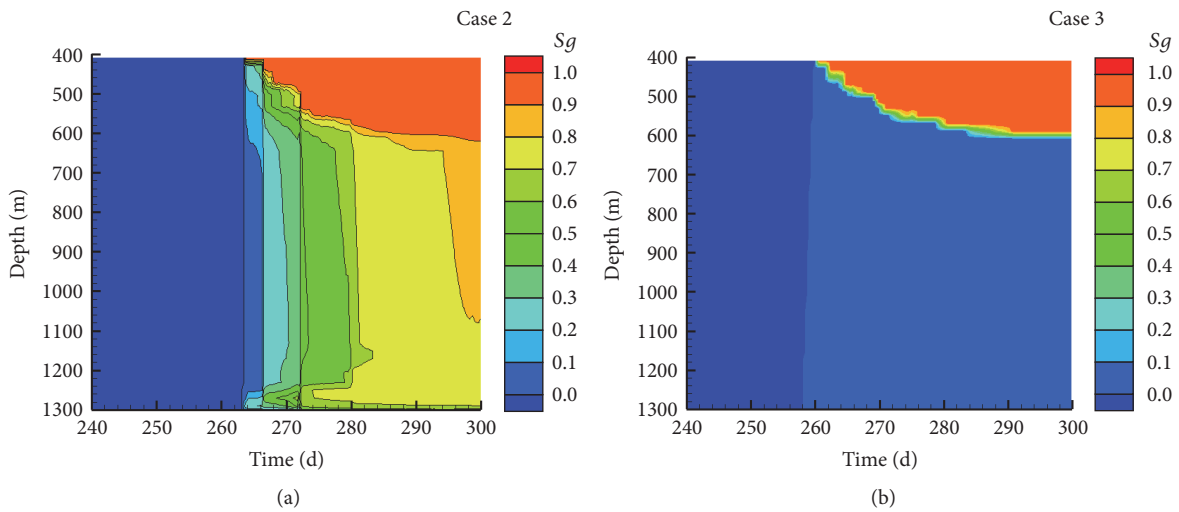


FIGURE 10: Gas saturation changes in the fracture in Case 2 and Case 3 associated with CO₂ breakthrough.

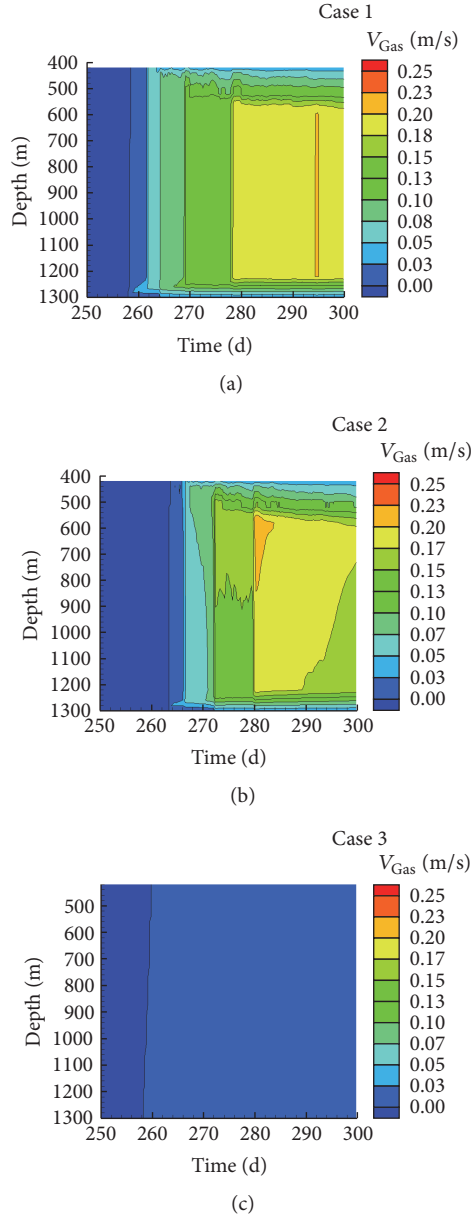


FIGURE 11: Distributions of gas velocity in the fracture profile for Cases 1 to 3 as gaseous CO₂ evolves.

period in the fracture, but it has insignificant effects on the quasi-steady state leakage corresponding to a fixed injection rate adapted in this study.

3.3. Equivalent Porous Media (EPM) Approximation. In many modeling studies of leakage through open fractures in a fault, the EPM approximation is often used that the Darcy law is assumed to be valid for describing the flow dynamics in open fractures. We have made a few EPM models of the same problem with the effective permeability of the open fractures, k_f being estimated as a function of the fracture aperture, h , suggested by Zimmerman and Bodvarsson [20] and Witherspoon et al., 1980:

$$k_f = \frac{h^2}{12}. \quad (4)$$

The effective permeability of fracture zone, k_e , can then be calculated as follows:

$$k_e = k_f \cdot \phi + k_m \cdot (1 - \phi), \quad (5)$$

where ϕ is the ‘‘porosity’’ of fracture zone, defined as the fraction of void space in fracture zone and k_m is the permeability of matrix rocks surrounding the virtual fracture. In this study, a value of zero is preferable for k_m since the virtual fracture is the only pathway for CO₂ leakage along the fracture zone. The calculated effective permeability of the fracture zone for Cases 4, 5, and 6 is shown in Table 3. Cases 4, 5, and 6 are corresponding to Cases 1, 2, and 3, respectively.

Figure 18 shows the differences of pressure response at the injection well and monitor points in the fracture for two pairs’ cases (Case 1 versus Case 4 and Case 2 versus Case 5)

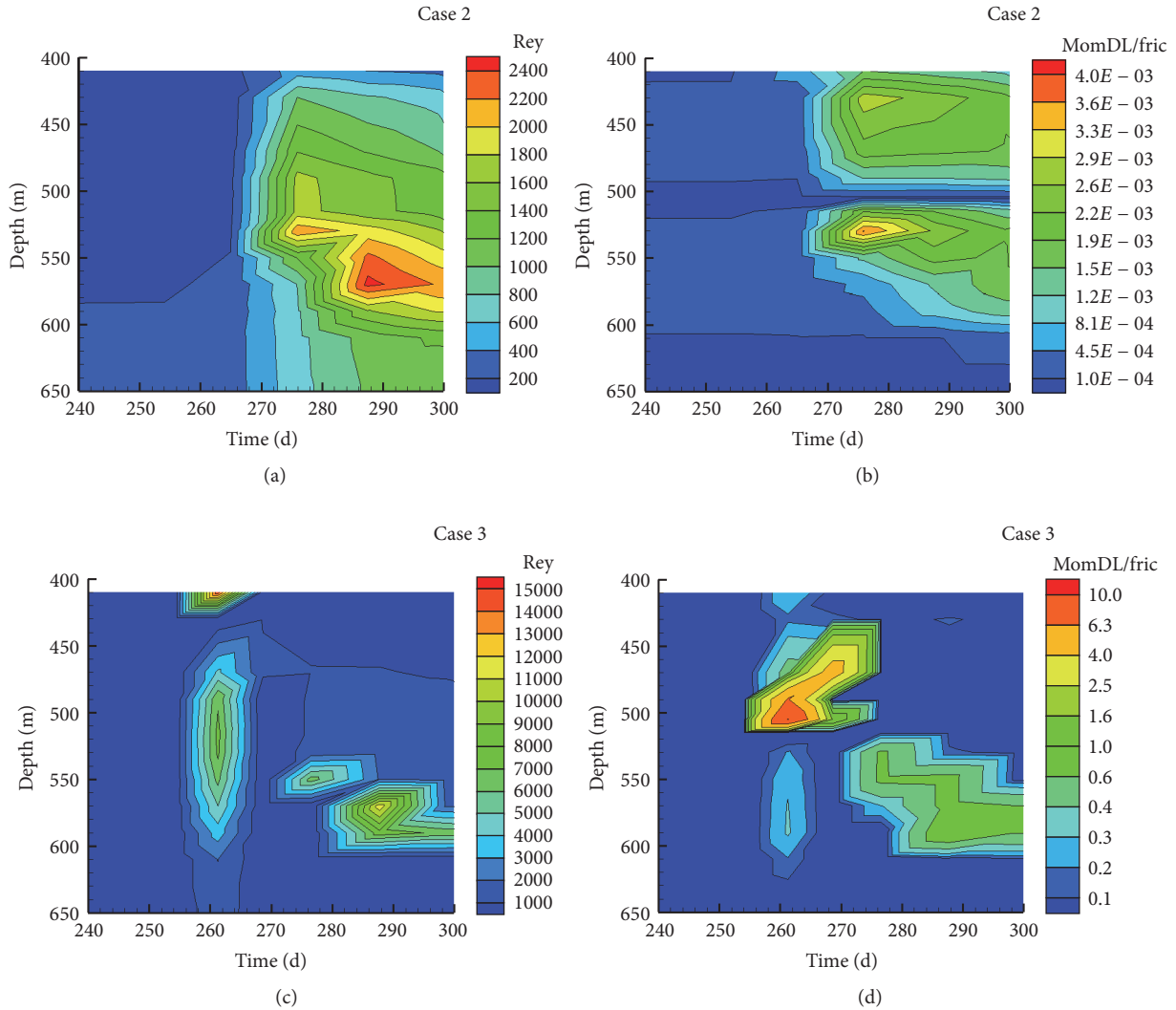


FIGURE 12: Changes of Reynold number and momentum/friction ratio in the fracture of Case 2 and Case 3 when CO_2 breakthrough occurs.

of the same aperture but different models. The pressure in large aperture cases ($h = 1$ cm in Case 1 versus Case 4) is similar although the EPM model records a bit higher pressure at injection well and the bottom of fracture after CO_2 breakthrough. With aperture increases from 1 cm to 5 cm, the pressure responses in Case 3 and Case 6 are almost identical (though they are not shown here to avoid too much crowd). However, when it comes to the small aperture cases ($h = 1$ mm in Case 2 versus Case 5), big differences are observed that (1) the injection pressure drops slowly in EPM model but fast in momentum model after CO_2 breakthrough; (2) the pressure of EPM model before CO_2 breakthrough at the bottom of fracture (B1 point) is much lower and drops less in response with the CO_2 breakthrough as compared with the momentum model; (3) what is more, the pressure in EPM model gets less increase when gas CO_2 reaches the top of fracture (B3 point).

These differences of pressure response further determine the various characteristics in terms of fluids flow dynamics at each aquifer/fracture interface (Figure 19). Overall, the larger aperture cases ($h = 1$ cm in Case 1 versus Case 5) show good approximations between two models while showing bad ones for the small aperture cases ($h = 1$ mm in Case 2 versus Case 4). For instance, Case 2 records a much higher gas and liquid phase flow rate from Aquifer 1 and gas phase leak rate into Aquifer 3 and Aquifer 4 when gas phase arrives at the top of fracture, in contrast with the small values predicted by EPM model (Case 4).

These seemingly strange results that the flow in larger fracture can be modeled by EPM better than in smaller fracture are for reasons. In general, larger fracture has less resistance to flow so as to be easy to develop high velocity flow regime which often causes turbulence flow and complex two-phase flow phenomena which may not be modeled properly by Darcy's law-based EPM model. However, in this particular study, the fracture is only the middle pathway

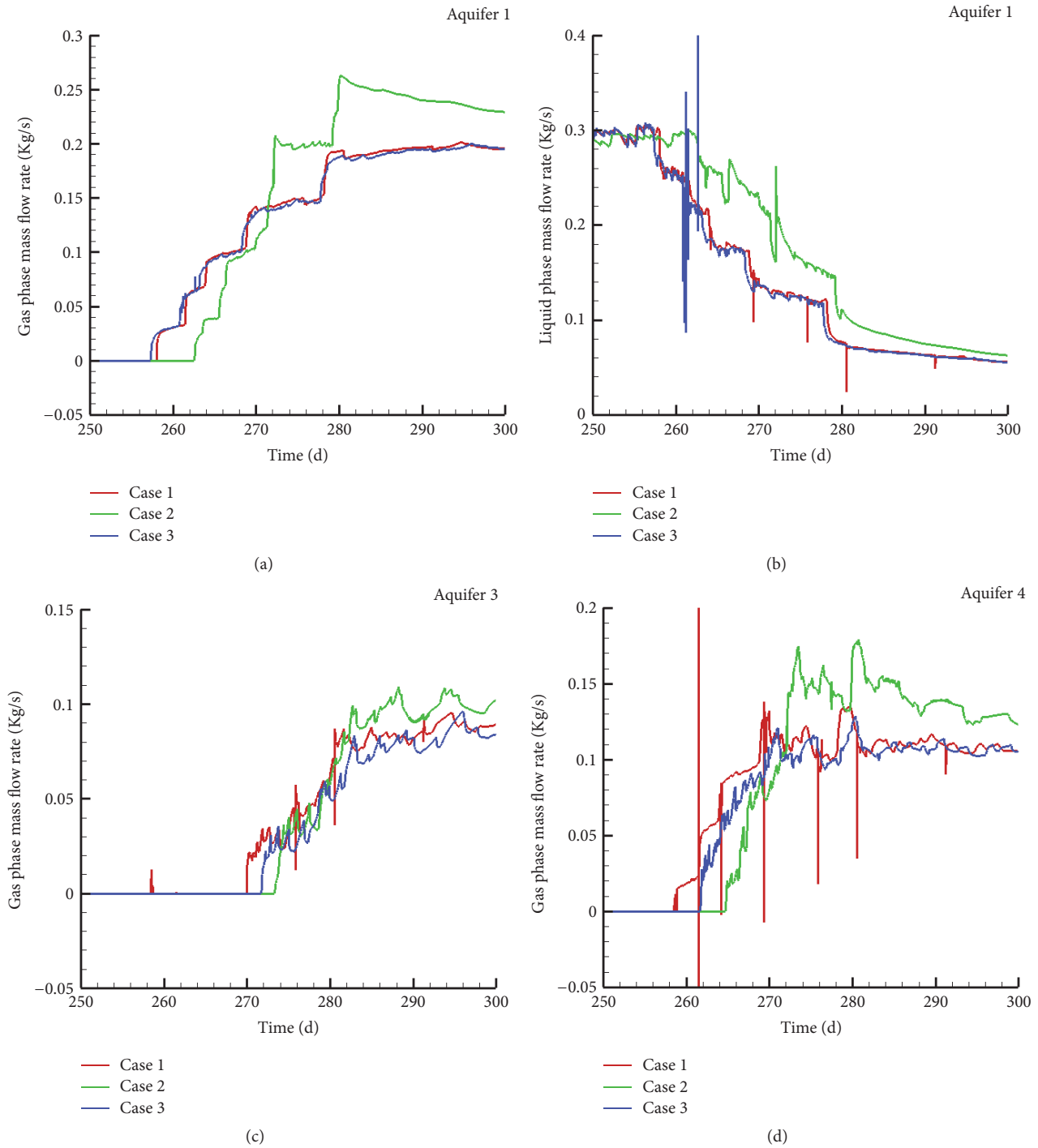


FIGURE 13: Fluids dynamics at the outlet/inlet of each aquifer in Cases 1–3 at early time (up to 300 days) after CO₂ breakthrough.

between porous aquifers and the mass flow rate is limited by the fixed injection rate. Under this condition, the large aperture will result in smaller velocity because of larger cross-section area or volume of the fracture (Figure 11). As a result, the gas velocity in the larger aperture cases (e.g., 1 cm and 5 cm) is too small to enhance the liquid flow in the fracture for the given injection rate adapted in this study. However, when

the aperture is reduced to 1 mm (Case 2), the gas velocity is high enough (Figure 11) to enhance the liquid flow in the fracture (Figure 19). This so-called gas-lifting effect cannot be captured by a Darcy's law-based EPM model even though the overall resistance of the fracture to flow can be described by the effective permeability. Therefore, whether or not the EMP model is a good approximation not only depends on

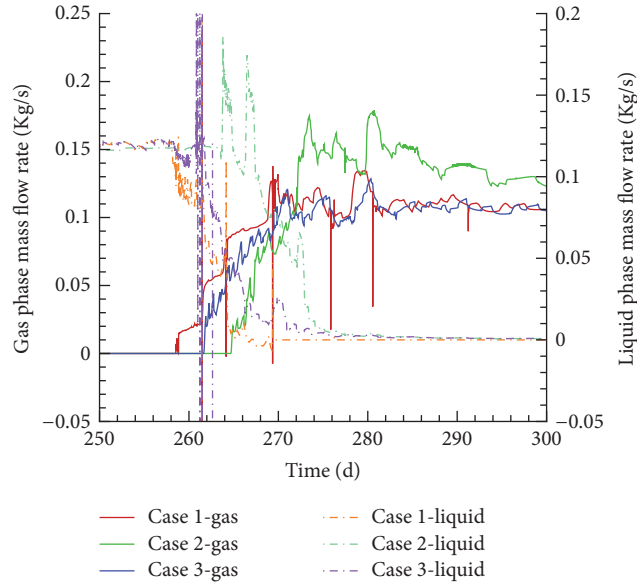


FIGURE 14: Fluids dynamics in Cases 1 to 3 at the interface of Aquifer 4 and the fracture with CO₂ breakthrough.

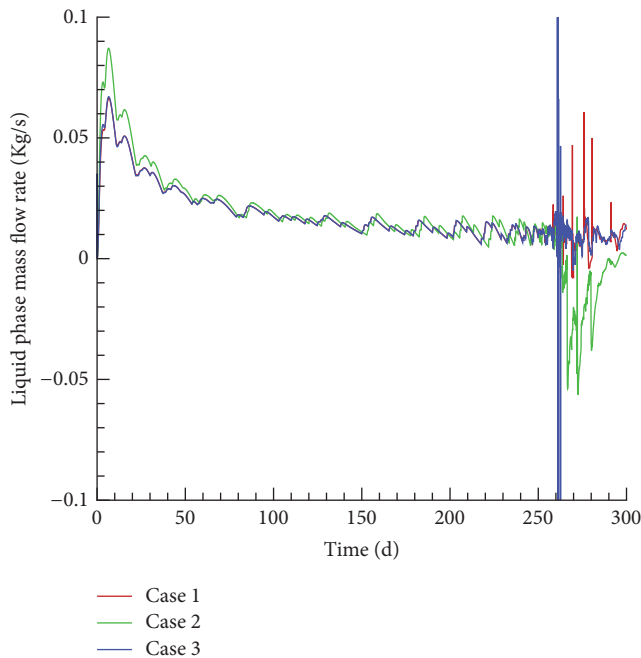


FIGURE 15: Evolution of liquid phase mass flow rate into Aquifer 2 from the beginning of CO₂ injection until the end of 300th days.

the geometry of the fractures but also depends on the flow conditions in a particular system. Nevertheless, from the view of CO₂ distribution among various aquifers at the end of 5 years' injection, the differences become quite small with aperture changes, suggesting that Darcy law may be still "effective" in solving fluids flow along fractures at large time scale, especially when the fractures are only an intermediate pathway between two porous media formations like the one studied here.

4. Conclusions

Fault area is one of the most concerns in conducting CCS projects for the safety of storage. Complex network of fractures developed in a fault area as a result of tectonic or anthropogenic activities may work as the fast pathway for CO₂ migration to favor a channel flow especially when two-phase flow occurs. In this study, we set up a 2D model of CO₂ leakage through a fault zone (simulated as a virtual vertical fracture) which connects two sets of aquifers at different

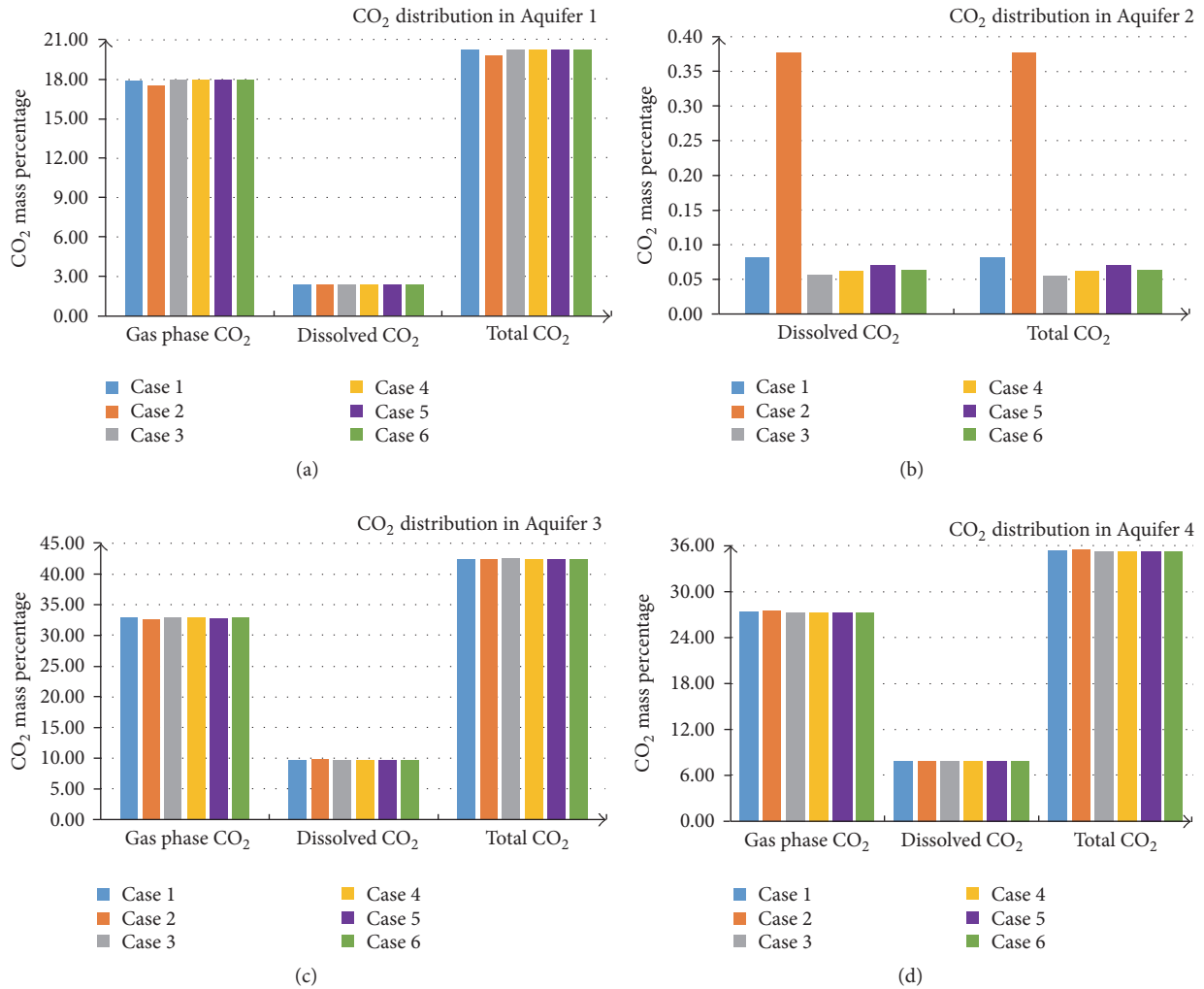


FIGURE 16: CO₂ mass distribution into each aquifer at the end of 5 year's injection in percentage.

depth. The momentum equation is applied for the calculation of fluids velocity in the fracture, with the DFM model to handle phase interactions in possible two-phase flow. Our motivation is to figure out what the differences are about channel flow and Darcy flow in open fractures and under what conditions the flow in the open fracture can be properly approximated as Darcy flow.

The results indicate that injection of CO₂ quickly increases the pressure in reservoir to facilitate the migration of water and gas into the fracture. When gas enters the fracture, it firstly evolves at the bottom at very low saturation and then quickly flows upward. Once it reaches the top, the bubble expands quickly because of low pressure which increases the local gas saturation and reduces the average density of the gas-liquid mixture. This will lower the pressure below and causes the increases of gas saturation there due to escape of the dissolved gas and expansion of the gas phase. Such positive feedback will propagate downward until the density difference between the gas phase and the aqueous phase becomes small or the local mass fraction of gas component becomes very small. As a result, the occurring of gas

phase flow into Aquifer 4 is earlier than Aquifer 3 although Aquifer 3 is below Aquifer 4. With aperture decreases from 1 cm to 1 mm, the friction force increases and, as a result, the momentum/friction ratio sharply decreases, although the Reynold number gets less influenced and remains below 2400 to prevail the laminar flow in the fracture. In contrast, when aperture increases from 1 cm to 5 cm, the Reynold number and momentum/friction ratio significantly increase to be the maximum of 15000 and 10, respectively, suggesting the occurrence of turbulent flow. In case of small aperture (1 mm), the gas phase velocity is high enough to enhance the liquid flow in the fracture by gas-lifting effects. As a result, the fracture dries quickly and the pressure drops quickly after two-phase flow developed in the fracture in this small aperture case. The differences of pressure responses further lead to diverse gas saturation profiles along fracture as well as the fluids dynamics of each aquifer. At the end of 5 years' injection, more dissolved CO₂ is stored in Aquifer 2 of Case 2.

With the relative small injection rate adapted in this study, the Equivalent Porous Media (EPM) model was found to be a good approximation of open fracture flow in cases of

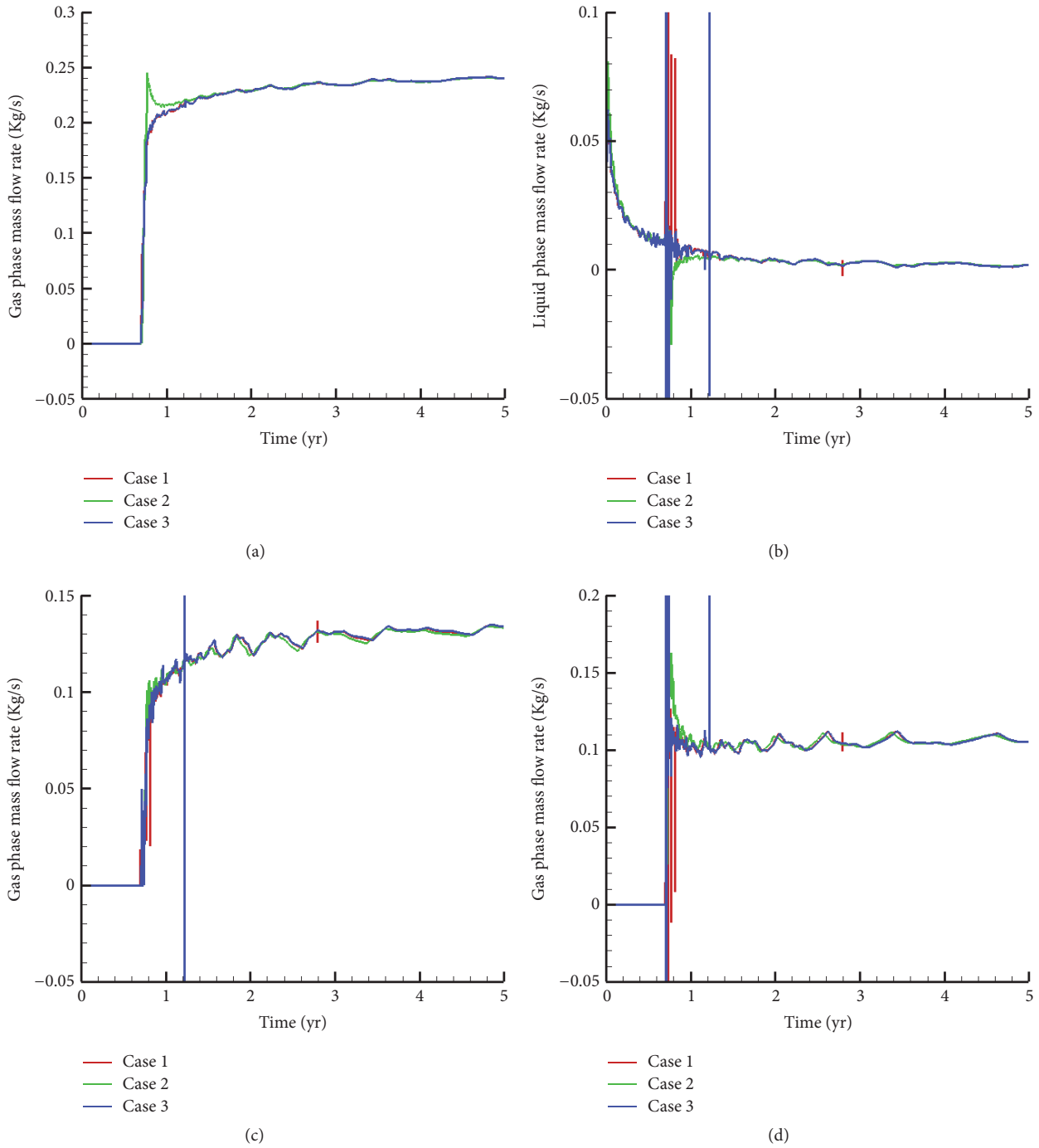
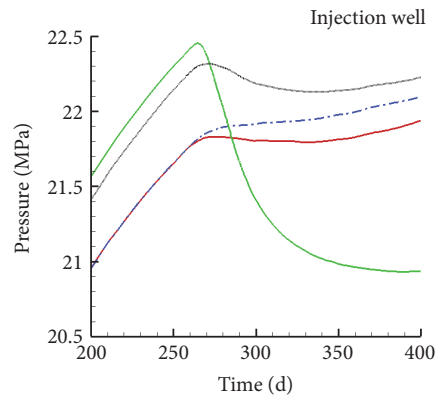


FIGURE 17: Fluids dynamics at the outlet/inlet of each aquifer in Cases 1-3 for whole time scale of CO₂ injection.

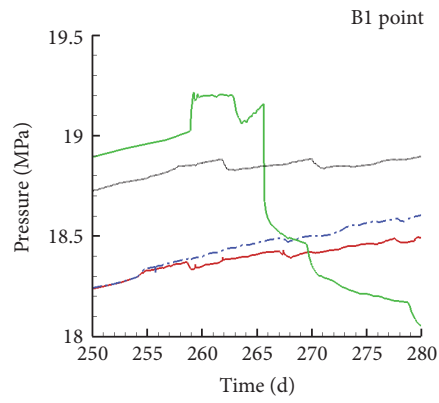
larger apertures but becomes poor if the aperture is reduced to 1 mm. The major reason is that, in the latter case, the gas velocity is high enough to enhance the liquid flow (i.e., the gas lifting) in the fracture which cannot be simulated by the EPM. Therefore, whether or not the EMP model is a good approximation not only depends on the geometry of the fractures but also depends on the flow conditions in a particular system.

In terms of CO₂ distribution among various aquifers at the end of 5 years' injection, the differences due to different aperture is quite small except for the dissolved CO₂ in Aquifer 2. This is because the open fracture is only the intermediate pathway sandwiched by porous aquifers. Even though the early time flow dynamics, especially during the phase transition period, could be very different, the long term quasi-steady state flow would be quite similar for the



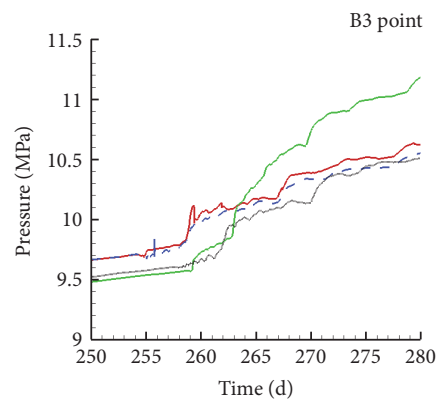
— Case 1 — Case 2
 - - - Case 4 — Case 5

(a)



— Case 1 — Case 2
 - - - Case 4 — Case 5

(b)



— Case 1 — Case 2
 - - - Case 4 — Case 5

(c)

FIGURE 18: Models comparison (Case 1 versus Case 4, Case 2 versus Case 5) in terms of pressure response at injection well and the bottom and top of fracture.

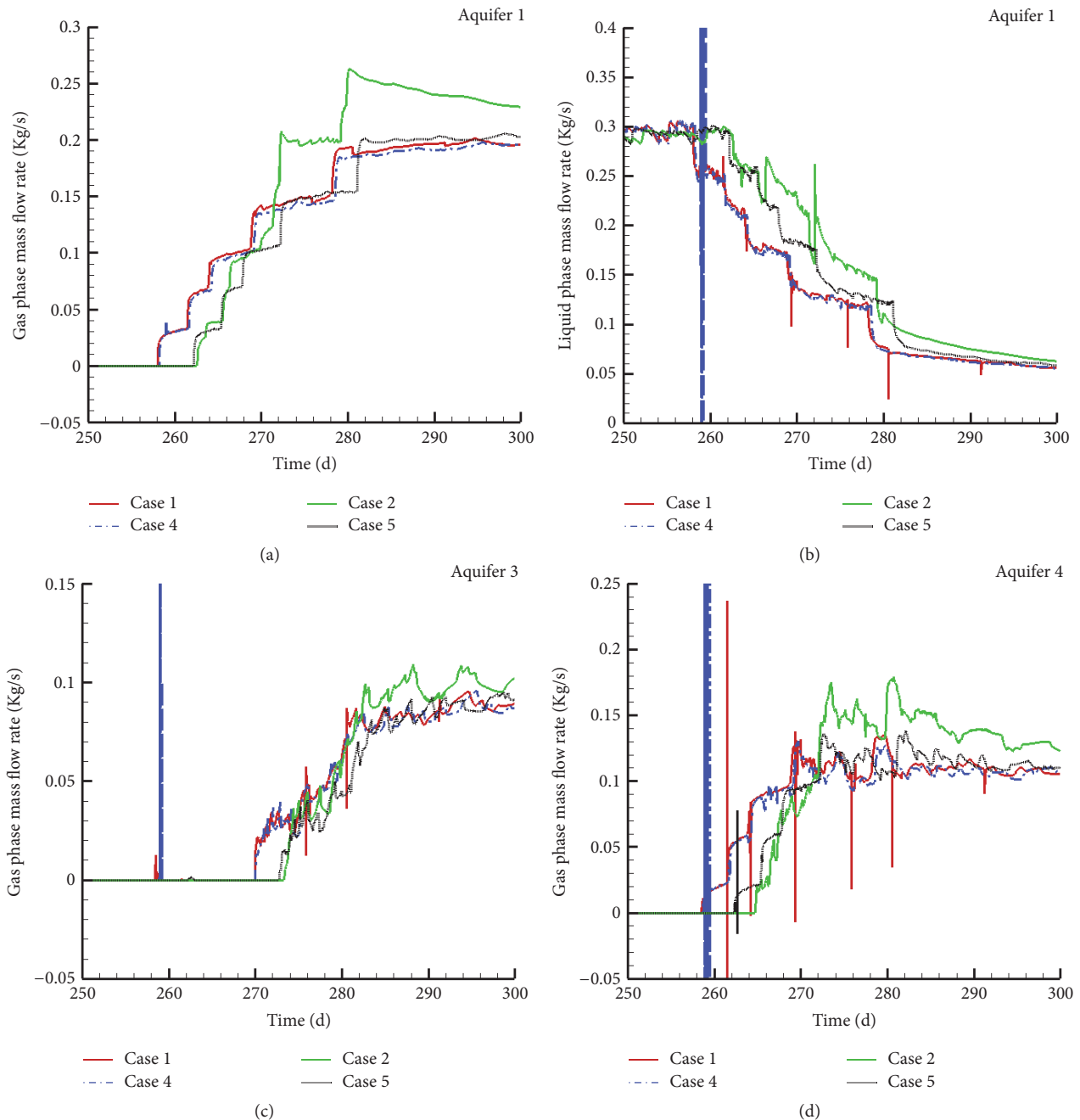


FIGURE 19: Differences of fluids dynamics at the outlet/inlet of each aquifer between momentum model and corresponding EPM model of various apertures.

given constant injection rate because the leakage is finally controlled by the high resistant media (i.e., the aquifers).

Conflicts of Interest

The authors declare that there are no conflicts of interest regarding the publication of this paper.

Acknowledgments

The authors gratefully acknowledge funding by the Project of National Sciences Foundation of China (no. 41172217).

References

- [1] J. L. Lewicki and S. L. Brantley, "CO₂ degassing along the San Andreas fault, Parkfield, California," *Geophysical Research Letters*, vol. 27, no. 1, pp. 5–8, 2000.
- [2] F. May, "Alteration of wall rocks by CO₂-rich water ascending in fault zones: natural analogues for reactions induced by CO₂ migrating along faults in siliciclastic reservoir and cap rocks," *Oil & Gas Science and Technology*, vol. 60, no. 1, pp. 19–32, 2005.
- [3] E. H. Keating, D. L. Newell, H. Viswanathan, J. W. Carey, G. Zyvoloski, and R. Pawar, "CO₂/brine transport into shallow aquifers along fault zones," *Environmental Science and Technology*, vol. 47, no. 1, pp. 290–297, 2013.

- [4] N.-H. Jung, W. S. Han, K. Han, and E. Park, "Regional-scale advective, diffusive, and eruptive dynamics of CO₂ and brine leakage through faults and wellbores," *Journal of Geophysical Research: Solid Earth*, vol. 120, no. 5, pp. 3003–3025, 2015.
- [5] F. Bu, T. Xu, F. Wang, Z. Yang, and H. Tian, "Influence of highly permeable faults within a low-porosity and low-permeability reservoir on migration and storage of injected CO₂," *Geofluids*, vol. 16, no. 4, pp. 769–781, 2016.
- [6] S. Vialle, J. L. Druhan, and K. Maher, "Multi-phase flow simulation of CO₂ leakage through a fractured caprock in response to mitigation strategies," *International Journal of Greenhouse Gas Control*, vol. 44, pp. 11–25, 2016.
- [7] T. Nakajima, Z. Xue, S. Chiyonobu, and H. Azuma, "Numerical simulation of CO₂ leakage along fault system for the assessment of environmental impacts at CCS site," *Energy Procedia*, vol. 63, pp. 3234–3241, 2014.
- [8] Q. Tao, D. Alexander, and S. L. Bryant, "Modeling potential CO₂ leakage rate along a fault in Mahogany Field," *Journal of Petroleum Science and Engineering*, vol. 111, pp. 15–24, 2013.
- [9] P. Jeanne, Y. Guglielmi, and F. Cappa, "Dissimilar properties within a carbonate-reservoir's small fault zone, and their impact on the pressurization and leakage associated with CO₂ injection," *Journal of Structural Geology*, vol. 47, pp. 25–35, 2013.
- [10] K. Pruess and J. Garcia, "Solutions of test problems for disposal of CO₂ in saline aquifers," Tech. Rep. LBNL-51812, Assistant Secretary for Fossil Energy, Berkeley, Calif, USA, 2003.
- [11] C. H. Lu, Y. W. Sun, T. A. Buscheck et al., "Uncertainty quantification of CO₂ leakage through a fault with multiphase and non-isothermal effects," *Greenhouse Gases: Science and Technology*, vol. 2, pp. 445–459, 2012.
- [12] A. P. Rinaldi, P. Jeanne, J. Rutqvist, F. Cappa, and Y. Guglielmi, "Effects of fault-zone architecture on earthquake magnitude and gas leakage related to CO₂ injection in a multi-layered sedimentary system," *Greenhouse Gases: Science and Technology*, vol. 4, no. 1, pp. 99–120, 2014.
- [13] I. H. Lee and C. F. Ni, "Fracture-based modeling of complex flow and CO₂ migration in three-dimensional fractured rocks," *Computers & Geosciences*, vol. 81, pp. 64–77, 2015.
- [14] S. Bigi, M. Battaglia, A. Alemanni et al., "CO₂ flow through a fractured rock volume: insights from field data, 3D fractures representation and fluid flow modeling," *International Journal of Greenhouse Gas Control*, vol. 18, pp. 183–199, 2013.
- [15] K. Zhang, Y.-S. Wu, G. S. Bodvarsson, and H.-H. Liu, "Flow focusing in unsaturated fracture networks: a numerical investigation," *Vadose Zone Journal*, vol. 3, no. 2, pp. 624–633, 2004.
- [16] P. A. Witherspoon, J. S. Y. Wang, K. Iwai, and J. E. Gale, "Validity of cubic law for fluid flow in a deformable rock fracture," *Water Resources Research*, vol. 16, no. 6, pp. 1016–1024, 1980.
- [17] L. Pan and C. M. Oldenburg, "T2Well-An integrated wellbore-reservoir simulator," *Computers & Geosciences*, vol. 65, pp. 46–55, 2014.
- [18] L. Pan, C. Oldenburg, Y. Wu, and K. Pruess, "T2Well/ECO2N version 1.0: multiphase and non-isothermal model for coupled wellbore-reservoir flow of carbon dioxide and variable salinity water," Tech. Rep. LBNL-4291E, Earth Sciences Division, Berkeley, Calif, USA, 2011.
- [19] L. Pan, S. W. Webb, and C. M. Oldenburg, "Analytical solution for two-phase flow in a wellbore using the drift-flux model," *Advances in Water Resources*, vol. 34, no. 12, pp. 1656–1665, 2011.
- [20] R. Zimmerman and G. Bodvarsson, "Hydraulic conductivity of rock fractures," Tech. Rep. LBNL-35976, USDOE, Washington, DC, USA, 1994.

Research Article

Multiphase Flow Behavior of Layered Methane Hydrate Reservoir Induced by Gas Production

Yilong Yuan, Tianfu Xu, Xin Xin, and Yingli Xia

Key Laboratory of Groundwater Resources and Environment, Ministry of Education, Jilin University, Changchun 130021, China

Correspondence should be addressed to Tianfu Xu; tianfu_xu@jlu.edu.cn

Received 12 July 2017; Accepted 12 October 2017; Published 29 November 2017

Academic Editor: Dan Lu

Copyright © 2017 Yilong Yuan et al. This is an open access article distributed under the Creative Commons Attribution License, which permits unrestricted use, distribution, and reproduction in any medium, provided the original work is properly cited.

Gas hydrates are expected to be a potential energy resource with extensive distribution in the permafrost and in deep ocean sediments. The marine gas hydrate drilling explorations at the Eastern Nankai Trough of Japan revealed the variable distribution of hydrate deposits. Gas hydrate reservoirs are composed of alternating beds of sand and clay, with various conditions of permeability, porosity, and hydrate saturation. This study looks into the multiphase flow behaviors of layered methane hydrate reservoirs induced by gas production. Firstly, a history matching model by incorporating the available geological data at the test site of the Eastern Nankai Trough, which considers the layered heterogeneous structure of hydrate saturation, permeability, and porosity simultaneously, was constructed to investigate the production characteristics from layered hydrate reservoirs. Based on the validated model, the effects of the placement of production interval on production performance were investigated. The modeling results indicate that the dissociation zone is strongly affected by the vertical reservoir's heterogeneous structure and shows a unique dissociation front. The beneficial production interval scheme should consider the reservoir conditions with high permeability and high hydrate saturation. Consequently, the identification of the favorable hydrate deposits is significantly important to realize commercial production in the future.

1. Introduction

Natural gas hydrate (NGH) is solid crystalline compound in which gas molecules are engaged inside the lattices of ice crystals under proper thermodynamic conditions [1, 2]. In nature, the dominant gas in NGH is methane, which forms at low temperature and high pressure with extensive distribution in the permafrost and in deep marine sediments [1, 3, 4]. The evaluation results show that the global quantity of hydrocarbon gas hydrates varies widely between 10^{15} and 10^{18} ST m³ (ST represents the standard conditions) [2, 5]. As an unconventional energy resource, the exploitation of NGH has attracted significant interest around the world [6].

Gas production from hydrate-bearing sediments (HBS) could be realized by dissociating solid-state hydrate into fluid phases (e.g., gas and water). Multiple methods have been proposed and employed to decompose hydrate for gas recovery from the HBS, such as depressurization, thermal stimulation, gas exchange, and the use of hydration inhibitors (such as salts and alcohols) [2, 5–8]. The above methods have

been compared in terms of energy efficiency, economic and technological feasibility, and environmental performance [1, 4, 9, 10]. Past laboratory and field tests and numerical studies showed that depressurization is the most potential method for gas recovery from HBS, while the other methods may be suitable for enhancing recovery or reservoir stimulation [4, 11, 12]. The obvious advantages of depressurization method include its simplicity and technical effectiveness [2, 13].

In order to seek the most technically and economically feasible method for production from the hydrate deposits, numerical simulation was considered the best way to achieve this objective. Moridis et al. [1, 2] investigated the gas production potential from Class 1 and Class 2 hydrate deposits through depressurization. They found that large volumes of gas can be produced at high rates for long times from Class 1 hydrate deposits by using conventional technology. Li et al. [14] investigated the effects of confined formation permeability on the gas production potential from marine hydrate deposit. They indicated that the hydrate deposit with impermeable boundaries was expected to be the potential gas

production target. Huang et al. [15] investigated the effects of geologic conditions on the hydrate dissociation and gas production through depressurization. Their results indicated that permeability, porosity, and initial hydrate saturation have significant effects on gas production performance. Hou et al. [16] numerically investigated the production characteristics of gas hydrate deposits by cyclic hot water stimulation with a separated-zone horizontal well. They indicated that the method combining depressurization and thermal stimulation can improve the hydrate production effectively. Based on the latest geological data in the Eastern Nankai Trough, the long-term production behavior was investigated by Sun et al. [17] and Konno et al. [4]. Both of their results indicated that the gas production rate is expected to increase with time and the simulated water recovery rate cannot match field measured data. In addition, the geomechanical behaviors (such as seafloor subsidence and sand production) of the marine HBS induced by gas production have been widely studied [3, 7, 18–21]. The geomechanical analysis indicated that the spatial evolution of the temperature, pressure, hydrate saturation, and gas saturation is the most relevant to the geomechanical behavior of HBS.

The above research has properly promoted the development of gas production from hydrate deposits; however, most of previous numerical studies assume homogeneous reservoirs with a single layer due to absence of substantial geological structure and field test data, resulting in inaccurate estimation of gas productivity and reservoir characteristics. In fact, the marine gas hydrate drilling explorations at the Eastern Nankai Trough of Japan and in Shenhu area of the South China Sea revealed the variable distribution of hydrate deposits. Gas hydrate reservoirs are composed of alternating beds of sand and clay in sediments with various conditions of permeability, porosity, and hydrate saturation [22, 25]. Consequently, the development of suitable geological model is critical to identify the dissociation layers and dissociation front induced by depressurization, which are key factors to ensure the success of the next long-term offshore production test [3, 4, 19, 22]. Additionally, the sensitivity analyses of gas production potential in previous studies were concentrated on production pressure, reservoir permeability, porosity, hydrate saturation, thickness, and initial temperature and pressure of HBS [11, 12, 14, 15, 26], whereas comprehensive studies related to the effects of well production interval on gas recovery have been reported sparsely, which are important for the optimization of gas production and reducing the water production rate.

In this paper, we extensively used the borehole geophysical logging, seismic interpretation, and core analyses at the production test site of the Eastern Nankai Trough reported previously by Japanese investigators. A more realistic reservoir model, which considers the layered heterogeneous structure of hydrate saturation, permeability, and porosity, was constructed to improve the simulation accuracy. The model we developed was validated by comparing the simulation results with actual test data of well production. The reservoir's responses and multiphase movement behaviors of water and gas during the production test were analyzed and discussed in detail. Furthermore, we use the validated model to investigate

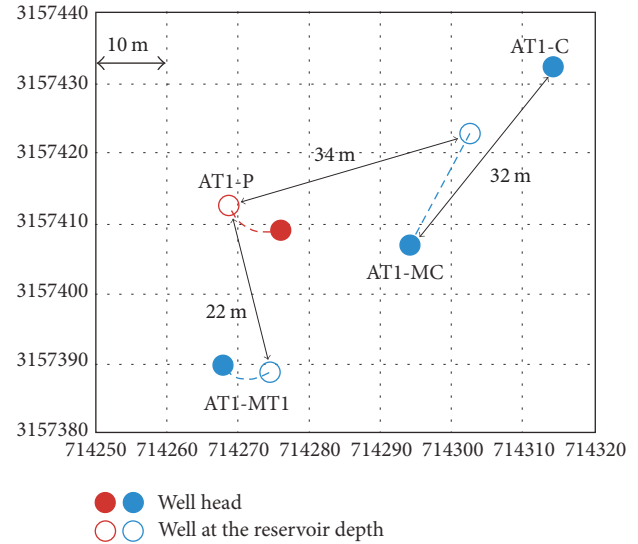


FIGURE 1: Horizontal section showing the locations of production, monitoring, and sampling wells at the AT1 site [4].

the effects of the placement of production interval on the production performance. Overall, this work may provide a useful method and some feasible suggestions for the subsequent test and future commercial production under similar reservoir conditions.

2. Overview of the Test Site of Nankai Trough

2.1. Site Conditions. The Eastern Nankai Trough is the most potential resource-rich area of gas hydrates in Japan [22, 27]. In this area, the total amount of CH_4 gas contained in HBS was estimated at an average value of $1.1 \times 10^{12} \text{ m}^3$, most of which was reserved in the 16 methane hydrate concentrated zones (MHCZs) [4, 22, 28]. MHCZ was characterized as sand-dominant methane hydrate with high saturation [4]. The AT1 site within the β -MHCZ, located in the north slope of Daini Atsumi Knoll area, is the 2013 production test site [22, 29]. The area of β -MHCZ is about 12 km^2 with the water depth ranging from 857 to 1405 m [22, 28]. The thickness of MHCZ is dozens of meters, which is composed of turbidite channel-type sediments [22].

2.2. Well Distribution and Formation Evaluations. In 2012, the production well (AT1-P), two monitoring wells (AT1-MC and AT1-MT1), and sampling well (AT1-C) were drilled at the AT1 site [22, 29]. The well locations and their trajectories projected in the horizontal section are shown in Figure 1. The extensive logging programs were conducted at wells AT1-P, MC, and MT1 in 2012 to evaluate reservoir properties and to determine the production interval [22, 28]. In addition, pressure coring was conducted at well AT1-C to collect essential geological and geochemical data and to correct in situ formation parameters [22, 30].

Figure 2 shows the detailed resistivity images at three wells (AT1-P, MC, and MT1) at the AT1 site. As shown in Figure 2, the target MHCZ (Unit IV) has a gross thickness of

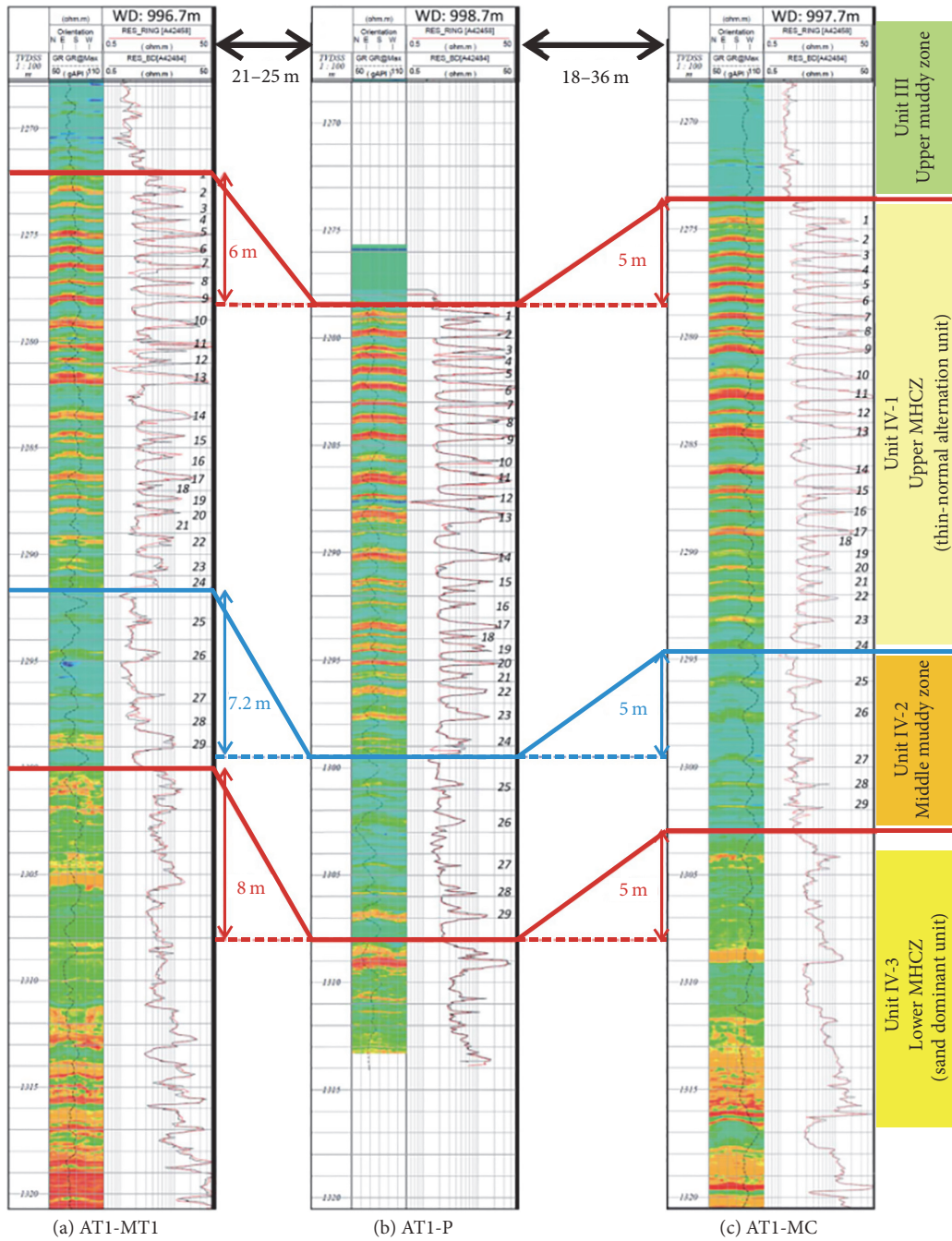


FIGURE 2: Resistivity images of three wells AT1-P, MT1, and MC at the AT1 site. The red color indicates the highly methane hydrate saturation sandy layers. The resistivity image logging indicated the stratum at the AT1 site with a dip angle approximately 20°; thus, well AT1-P was located slightly down-dip from wells AT1-MC and MT1 [22, 23].

61 m [22]. On the basis of lithological structure, the MHCZ is divided into three major subzones [22, 23]. Unit IV-1 is composed of thin alternating beds of sand and mud in the upper part and sand layers with thicknesses of 30–70 cm. Unit IV-2 also contains alternations of sand and silt in the middle part but with lower hydrate saturation. Unit IV-3 is composed of sand-dominant layers in the lower part with high hydrate saturation, and the thicknesses of sand layers range from dozens of centimeters to 2 m.

2.3. Quantification of Properties and Physical Conditions. Figure 3 shows the depth profiles of hydrate saturation, porosity, absolute permeability, and resistivity image. Hydrate saturation (Figure 3(a)) was estimated by using the Archie equation [31]. The validity of the derived saturation was confirmed by the pressure core data [22]. The porosities (Figure 3(b)) mainly ranging from 0.4 to 0.5 were determined from the density log. These are validated by the core derived porosities, which were measured under in situ confining

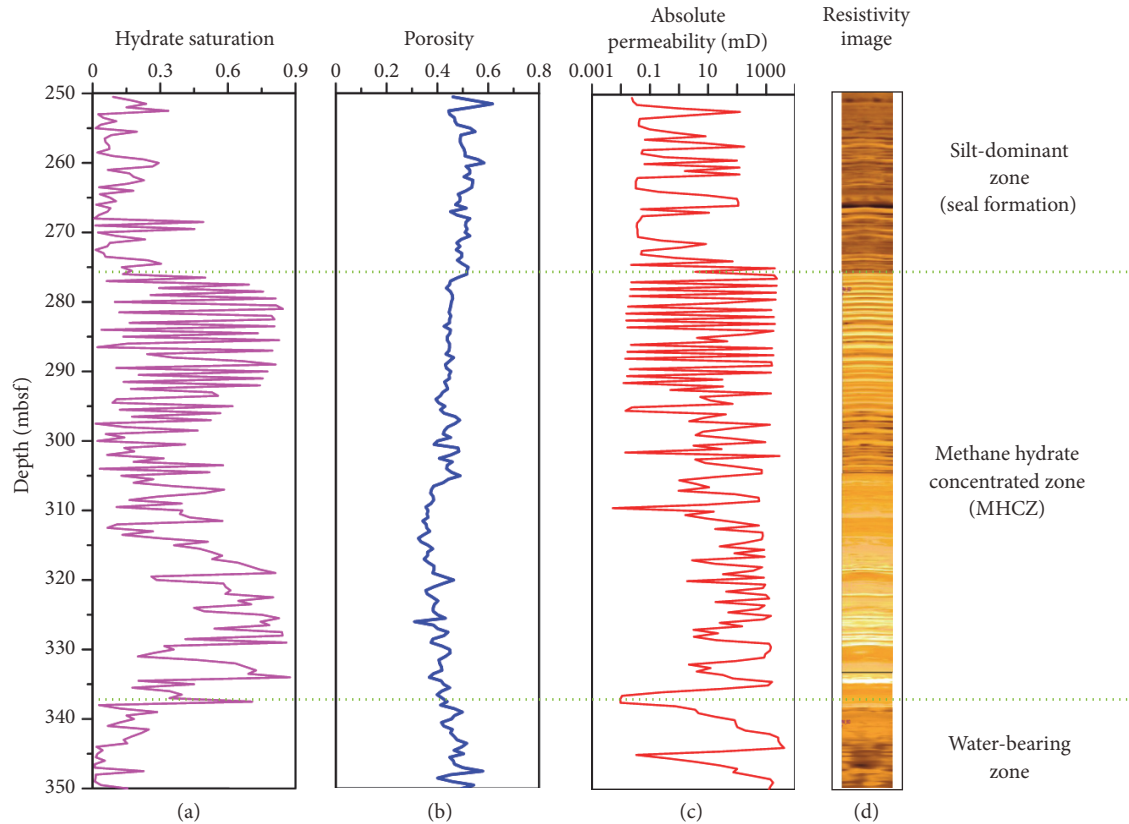


FIGURE 3: Depth profiles of hydrate saturation, porosity, and absolute permeability based on the well logging and core data with resistivity image [4, 22, 24]. Green dotted lines show the position of the top and bottom of the MHCZ.

pressure [22, 23]. The absolute permeability (intrinsic permeability, Figure 3(c)) was estimated by using the Kozeny-Carman model and calibrated with the core data collected from hydrate reservoirs at the Eastern Nankai Trough [23, 24].

3. Simulation Model

3.1. The Numerical Simulator. In this study, the TOUGH+HYDRATE simulator was used to investigate the multiphase flow behavior of layered methane hydrate reservoir induced by gas production. This code can model the nonisothermal hydration reaction, multiphase behavior, and flow of fluids and heat under conditions typical in geological media containing gas hydrates [1, 2, 5]. It includes both an equilibrium and a kinetic model of hydrate formation and dissociation [5]. The model accounts for heat and up to four mass components (i.e., H_2O , CH_4 , hydrate, and water-soluble inhibitors such as salts or alcohols). These components are partitioned among four possible phases (i.e., gas, liquid, ice, and hydrate) [2, 5]. The model can describe all possible hydrate dissociation mechanisms, such as depressurization, thermal stimulation, and salting-out effects.

3.2. Model Geometry, Boundaries, and Spatial Discretization. The geometry of the axisymmetric cylinder 2D model (RZ2D model) was constructed for the latter history matching simulation as shown in Figure 4. The model size in R -direction

is 1000 m to avoid the boundary effects. The total thickness of the entire model is 100 m with the thickness of MHCZ being 61 m. The production well with a radius of 0.1 m is located in the center of the cylinder [29, 32]. Production interval was 38 m from the top of the MHCZ for expecting the lower part of MHCZ as sealing layer to prevent water production [22]. Because the radius distance of 1000 m can effectively avoid the boundary effects in 6-day production test, there is no flow of fluids and heat through the lateral boundary. The top of the silt-dominant zone and the bottom of the water-bearing zone are designed as constant temperature and pressure boundaries [17]. For simulation of the varied depressurization processes (Section 3.5), the time-independent Dirichlet boundary (e.g., constant pressure) conditions are applied to the production well.

Previous studies had indicated that the critical process occurs within a limited range around the production well [1, 2, 7]. Therefore, the grids are refined surrounding the well with the minimum interval of 0.1 m. The grid sizes increase with the distance to the well, which reach a size of 75 m at the lateral boundary. The discretization for each fine layer at the vertical Z -direction is 0.5 m. Figure 5 shows the corresponding grids used in the simulations. The simulation domain was discretized into 200×100 grids in R - and Z -directions.

3.3. Initial Conditions. The initial reservoir pressure was assigned in line with the hydrostatic pressure, which was

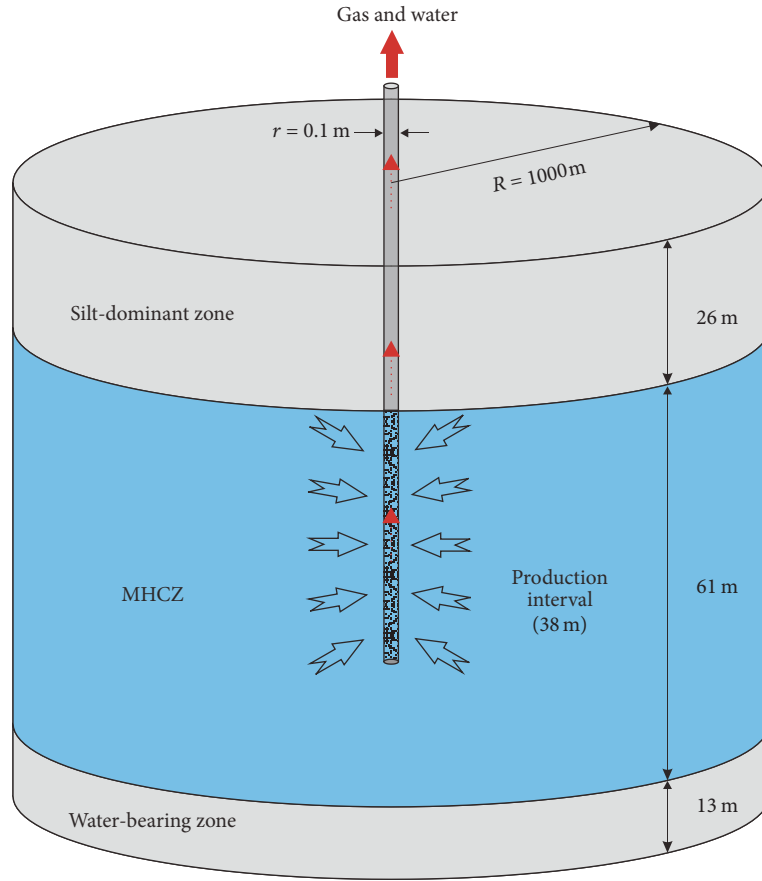


FIGURE 4: The geometry of the simulation domain and the configuration of production well.

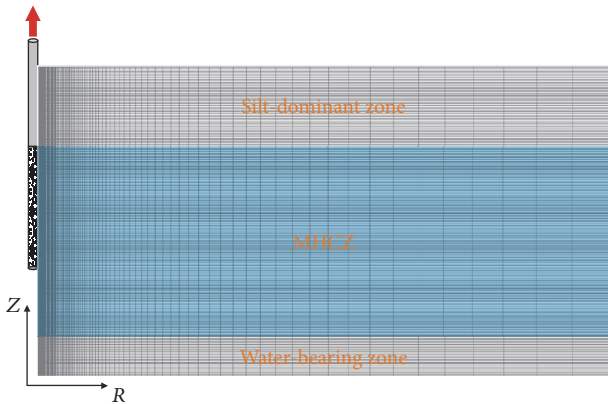


FIGURE 5: The corresponding grids used in the simulations, showing the main subzones at the AT1 site of the Eastern Nankai Trough.

computed according to the water depth and a pressure-adjusted saline water density [7, 17]. The initial temperature was specified to be 4°C at the seafloor [11, 17, 23]. The temperature profile was assigned to vary linearly as a function of depth with a geothermal gradient of 0.03°C/m. The initial hydrate saturation was varied in each fine layer and assumed to be horizontally uniform as shown in Figure 6(a).

3.4. Reservoir Properties and Parameters. Table 1 presents the main modeling parameters and physical properties for the AT1 site sediments at the Eastern Nankai Trough. These were based on the geophysical well logs and core samples analyses from published papers [4, 17, 22, 23, 27, 28]. The permeability and porosity are based on the logging data of AT1-MC and the pressure core data of AT1-C as shown in Figure 3. Hydrate saturations obtained from geophysical logging data were validated by those evaluated by pressure core analysis. The wellbore is simulated as a pseudoporous medium with porosity, permeability, capillary pressure, and low irreducible gas saturation of 1.0, $1.0 \times 10^{-8} \text{ m}^2$, 0 MPa, and 0.005, respectively. Earlier studies had shown the validity of this approximation [33, 34]. The composite thermal conductivity, relative permeability, and capillary pressure models are employed commonly in numerical simulations on gas production from hydrate deposits [2, 7, 17, 18]. The corresponding parameters for relative permeability and capillary pressure were determined from the field test data by Moridis and Reagan [34]. The changes of effective permeability and capillary pressure are consistent with the porosity and phase saturation during the simulation.

Well-to-well correlation between three wells (AT1-P, MC, and MT1) shown in Figure 2 exhibited that lateral continuity of these sand layers is fairly good, and the 3D seismic survey suggests the widespread deposits of the turbidite sediments

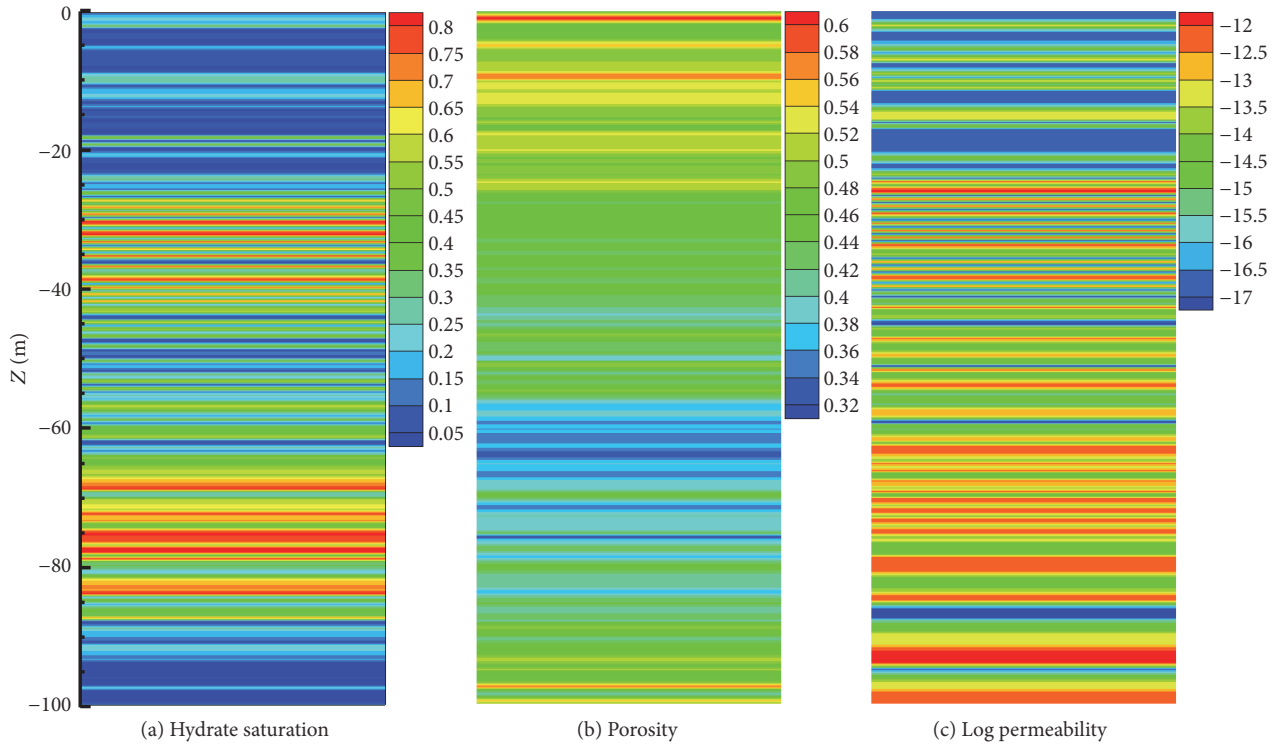


FIGURE 6: Cross-sectional view showing the initial reservoir-model properties: (a) hydrate saturation, (b) porosity, and (c) logarithmic value of absolute permeability.

beyond several kilometers [11, 22, 23]. Consequently, the reservoir properties were assumed to be uniform in each fine layer. Figure 6 shows the cross-sectional views of the initial hydrate saturation, porosity, and absolute permeability in the model.

3.5. Depressurization Scheme. The method used to decompose the solid hydrate was depressurization, which had been successfully applied at the Mallik site, Canada, in 2007 and 2008 [19, 37, 38]. Figure 7 shows the depressurization processes both in field test and in this simulation, which lasted for about 6 days. As shown in Figure 7, the wellbore pressure of production well was decreased from approximately 13 MPa to about 4 MPa during the first day and then remained almost stable for 5 days [29]. In the morning of the 6th day, sudden water rate increase was observed followed by strong sand production to the surface, and then the flow test was terminated [29]. During the stable production period, the volumetric rates of gas and water were approximately 20,000 and 200 m³/d, and the cumulative volume produced at the well during the period of 6 days was 119,500 m³ and 1,250 m³, respectively [4, 17, 29].

4. Simulation Results and Analysis

4.1. Gas and Water Production Behaviors. By decreasing the wellbore pressure of production well, gas and water flowed into the well due to the pressure gradient of the reservoir. Figure 8 indicates the evolution of the volumetric rate of (a) the model-predicted CH₄ production in the well (Q_{G1}), (b)

site measured CH₄ production in the well (Q_{G2}), and (c) gas released from hydrate dissociation (Q_R). As shown in Figure 8, the predicted volumetric rates of gas production match well with the measured data by site test. The accumulated volume of gas trapped (V_G) in 6 days is 122,861 m³; both Q_G and V_G are basically consistent with the field data observed.

Initially Q_R and Q_G increase quickly because of the significant decrease of borehole pressure during the first day (Figure 7). In the following days, both Q_R and Q_G begin oscillating around a coarsely invariable value, which clarify the struggle between the impacts of temperature and pressure on hydrate decomposition and gas production [3]. Decreasing pressure causes hydrate decomposition with the increase in Q_R and Q_G . The endothermic nature of hydrate decomposition results in temperature decline and makes further decomposition not easy, resulting in decrease in Q_R and Q_G . Note that the dramatic changes of Q_R at about 2.5 days are due to the wellbore pressure disturbance (Figure 7), which indicates that the decomposition of hydrate is extremely sensitive to production pressure. Further consideration of the difference between Q_R and Q_G suggests that the released gas cannot be trapped completely and most of which still remained in the hydrate reservoirs. Consequently, the optimization of well configuration and production strategies are needed to improve the gas recovery efficiency.

Figure 9 shows the evolution of volumetric rates of simulated (Q_{W1}) and measured (Q_{W2}) water production in the well. The predicted water production rate is about 300 m³/d, which is slightly higher than that of site measured rate of 200 m³/d. This may be because (1) the geomechanical

TABLE 1: Hydrate deposit properties at the AT1 site.

Parameter	Value
MHCZ thickness, H	61 m
Gas composition	100% CH ₄
Water salinity, X_i	3.50%
Pressure at the base of the MHCZ, P_b	14.7 MPa
Temperature at the base of the MHCZ, T_b	14.3°C
Critical mobile porosity, ϕ_{cri}	0.05
Rock grain density, ρ_R	2650 kg/m ³
Wet thermal conductivity, λ_W	3.1 W/m/K
Dry thermal conductivity, λ_D	1.0 W/m/K
Pore compressibility, α_p	1.0×10^{-8} Pa ⁻¹
Composite thermal conductivity model [35]	$\lambda = \lambda_D + (S_A^{1/2} + S_h^{1/2})(\lambda_W - \lambda_D) + \phi S_I \lambda_I$
Capillary pressure model [36]	$P_{cap} = -P_0([S_A^*]^{-1/m} - 1)^{1/m}$ $S_A^* = \frac{(S_A - S_{irA})}{(S_{mxA} - S_{irA})}$
S_{mxA}	1.0
m	0.45
P_0 [17]	1.0×10^5 Pa
Relative permeability model [7]	$k_{rA} = (S_A^*)^{n_A}$ $k_{rG} = (S_G^*)^{n_G}$ $S_G^* = \frac{(S_G - S_{irG})}{(1 - S_{irG})}$
n_A [34]	3.572
n_G	3.572
S_{irA}	0.20
S_{irG}	0.02

response during depressurization production from the HBS is not considered in our model, which means that the reservoir compression has immediate effects on decreases in formation porosity and intrinsic permeability and then on the fluid-flow behavior [3, 19]; (2) the well completion methods used at the field relate to prevent water from reservoir flow into the production well as explained by Yamamoto et al. [29] and Sun et al. [17]; (3) the exposure of clay minerals of marine deposit to fresh water (released from hydrate dissociation) can induce swelling and structural weakening [7, 18]; (4) the complex and inevitable horizontal heterogeneity in each fine layer is also neglected in our model. In fact, these factors mentioned above have little effect on gas production, because gas viscosity is much smaller than that of water and gas slippage effects in the low-permeability deposits exist [5]. As a consequence, the predicted gas production rates are basically consistent with the site measured data, while the predicted water production rates are higher than that in the field.

The stable depressurization and gas production at the AT1 site of the Eastern Nankai Trough proved that hydrate

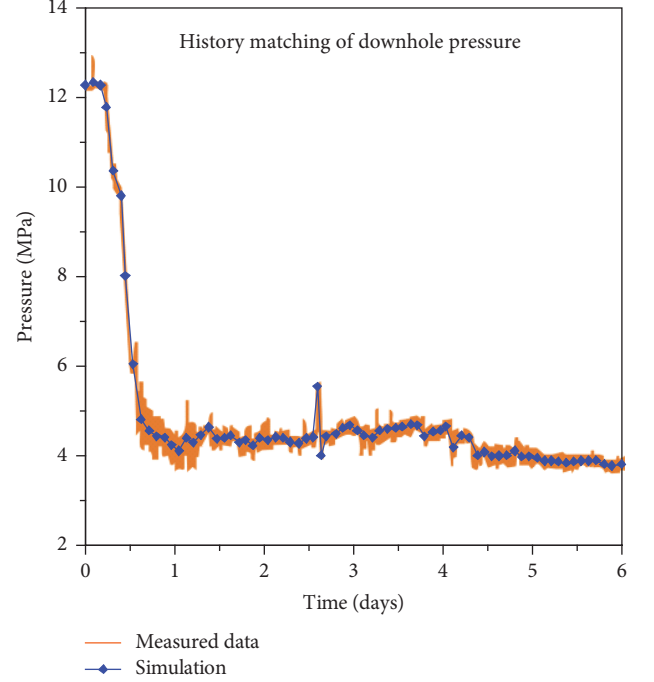
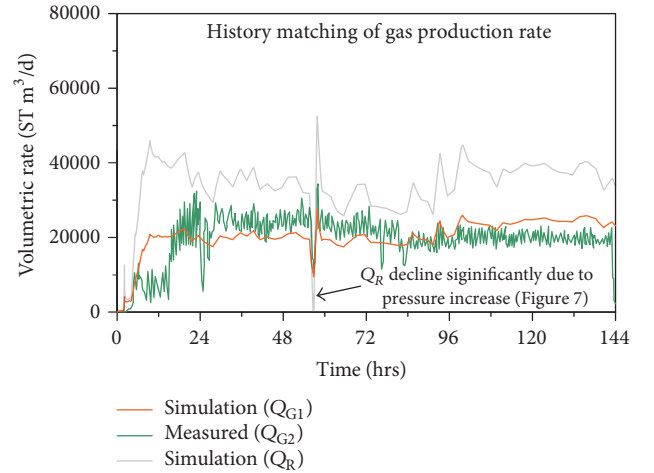


FIGURE 7: Depressurization processes of the production test at the AT1 site in the Eastern Nankai Trough.

FIGURE 8: Gas release (Q_R) and production (Q_G) rates during the 6-day production test at the AT1 site.

decomposition by depressurization is applicable even in the marine sediments. Over and above the absolute criteria of Q_R and Q_G to evaluate the production potential, the cumulative water/gas ratio R_{CWG} provides a relative criterion to evaluate the overall operation performance of the system, which is defined as [7]

$$R_{CWG} = \frac{\int Q_W dt}{\int Q_G dt}. \quad (1)$$

Figure 10 indicates the evolution of the simulated R_{CWG} during the 6-day production test at the AT1 site,

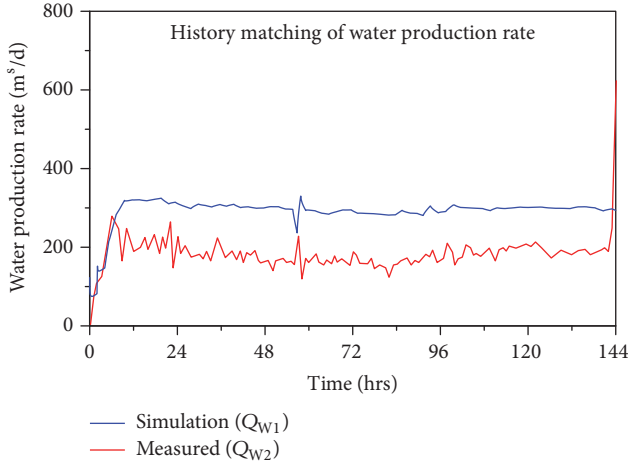


FIGURE 9: Measured and simulated water production rates (Q_w) during the 6-day production test at the AT1 site.

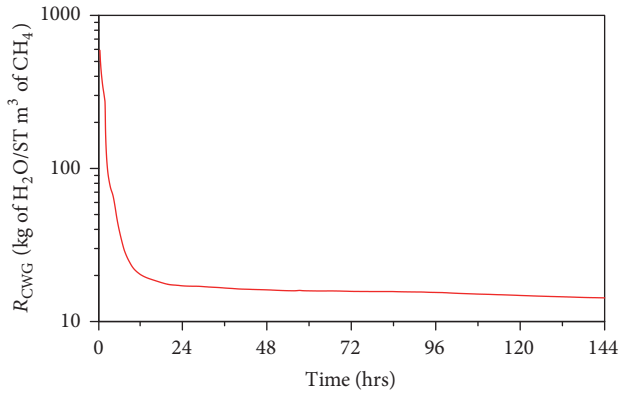


FIGURE 10: The cumulative water/gas ratio R_{CWG} during the 6-day production test at the AT1 site.

which declines monotonically with time. This is because of continuous improvement of the gas production. In the early stage, R_{CWG} drops rapidly because of significant hydrate dissociation in the reservoir and gas recovery at the production well (Figure 8). With time advancing, the stability of gas and water output results in slight changes of R_{CWG} . Consequently, R_{CWG} reaches very low levels of 20 in less than 1 day and is further reduced to $R_{CWG} = 14$ kg of H_2O/ST m^3 of CH_4 at 6 days.

4.2. History Matching of Temperature Changes at AT1-MT1. During the offshore production test, two monitoring wells (AT1-MT1 and MC) were designed for monitoring thermal disturbance around the production well (AT1-P). Figure 11 shows the monitored and simulated temperature changes at the location of the monitoring well AT1-MT1 on day 5. Measured data indicate that temperature decreases broadly occurred in the upper MHCZ and slightly in the lower MHCZ, which are mainly controlled by the location of production interval (Figure 4). The maximum changes of temperature reach the value of $0.6^\circ C$ [4, 39]; such a temperature decrease cannot be explained purely from the heat

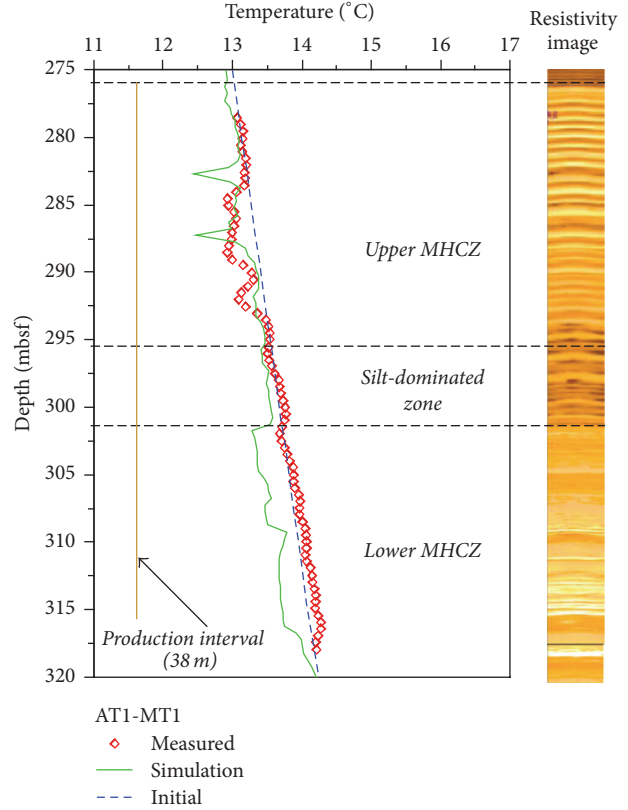


FIGURE 11: Measured and simulated temperature changes at the location of monitoring well AT1-MT1 on day 5 with resistivity image. Initial temperature profile is also shown in the figure with dashed blue line. The offset of the monitoring well AT1-MT1 from the production well AT1-P is 22 m at the reservoir depth as shown in Figure 1.

conduction (significantly long time is needed) according to Kanno et al. [39]. Therefore, the hydrate dissociations occurred at the location of the well AT1-MT1. The model-predicted temperature changes at well AT1-MT1 match well with the measured data, especially in the silt-dominated zone that showed slight change of temperature for both measured and simulated results.

4.3. Evolution of Physical Properties. For the multiphase flow system induced by depressurization, the dynamic evolutions of reservoir properties including pressure, temperature, hydrate, and gas saturation should be analyzed in detail. This is crucial knowledge for the later long-term production test of marine gas hydrate. In addition, the evolution of these variables is important to determine the geomechanical behaviors (such as sand production) in the Eastern Nankai Trough, which are key factors to ensure the success of the offshore production test.

4.3.1. Spatial Distribution of Pressure. Figure 12 indicates the evolution of pressure in the hydrate reservoir due to depressurization. White dashed lines show the position of the top and bottom of the MHCZ. Because the fine sand layers with high hydrate saturation and permeability

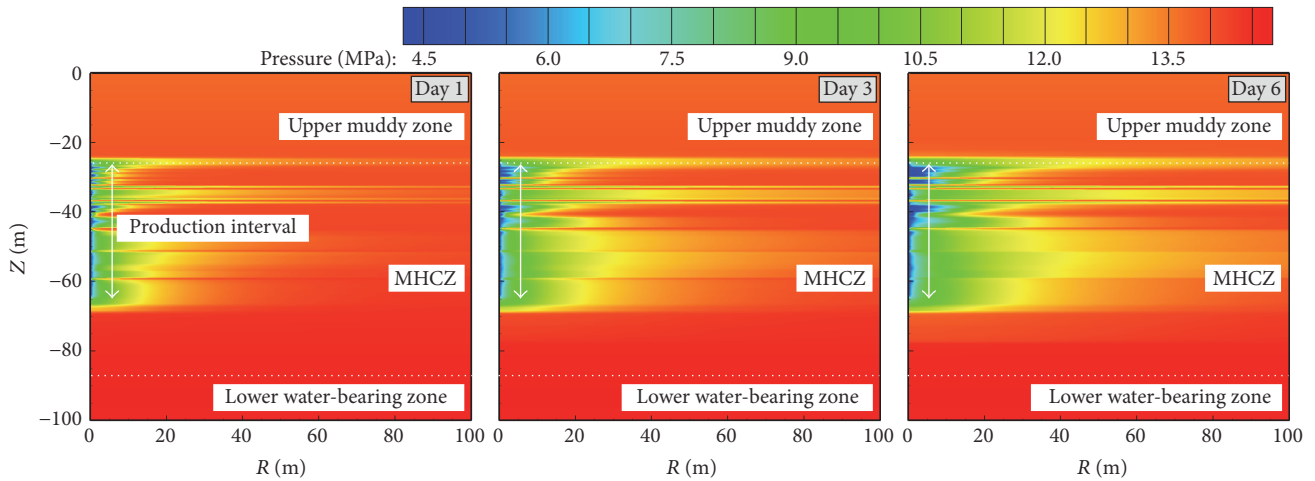


FIGURE 12: Evolution of spatial distribution of pressures in the hydrate reservoir at the AT1 site.

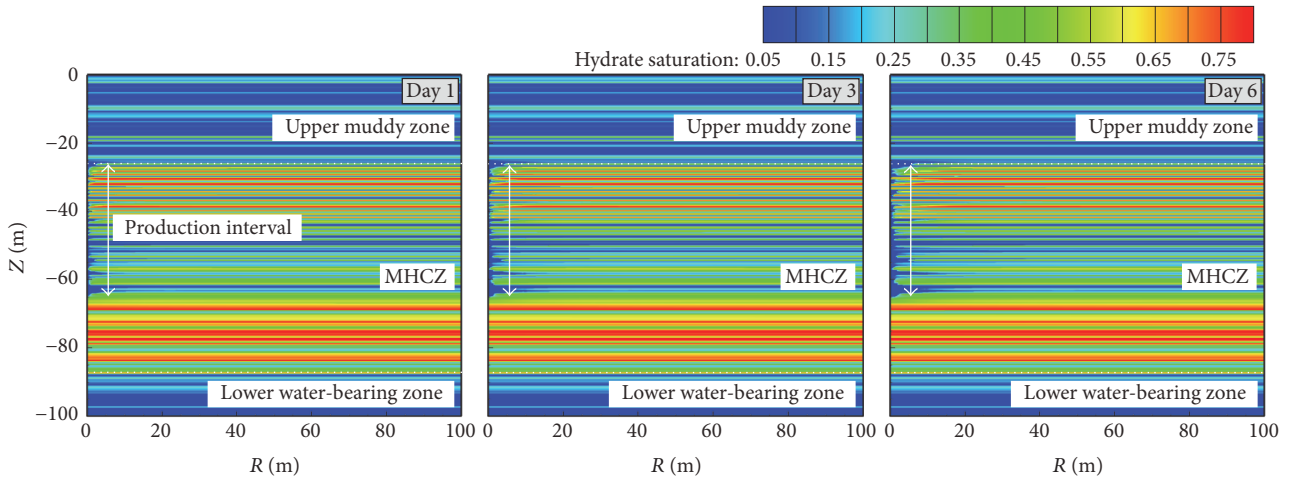


FIGURE 13: Evolution of spatial distribution of hydrate saturation in the hydrate reservoir at the AT1 site.

are hydraulically confined by silt/mud layers in MHCZ, depressurization is anticipated to be quickly and effectively propagated in the horizontal direction. In the early stage, the low pressure at the production well and the low effective permeability of MHCZ create a high pressure gradient near the production well. This pressure gradient extends laterally along the radial direction and tends to be stable with the gradual pressure diffusion. As hydrate dissociation results in increase of effective permeability, depressurization occurs more rapidly in the dissociated region. Due to the transmitted nature of pressure (e.g., even when fluid flow is restricted), the disturbance region of pressure is obviously larger than that of other reservoir properties (Figures 13–15). The effect of depressurization in the hydrate reservoir propagates laterally over 150 m during the 6-day production test.

4.3.2. Spatial Distribution of Hydrate Saturation. The decrease in pore-water pressure (Figure 12) drives the hydrate to dissociate around the well in the production interval (Figure 13). As mentioned above, hydrate dissociation increases the effective permeability of the deposits. This process and the anisotropic permeability conditions accelerate the pressure decrease in the radial direction. Consequently, the hydrate dissociates more in the radial direction than in the vertical direction (Figure 13). Overall, the dissociation zone is strongly affected by the vertical reservoir heterogeneity and shows a unique dissociation front. The spatial distribution of hydrate saturation indicates that hydrate has completely dissociated within a few meters around the well. Comparison with the initial hydrate distribution indicates the extent of dissociation zone within 35 m during the 6-day production test.

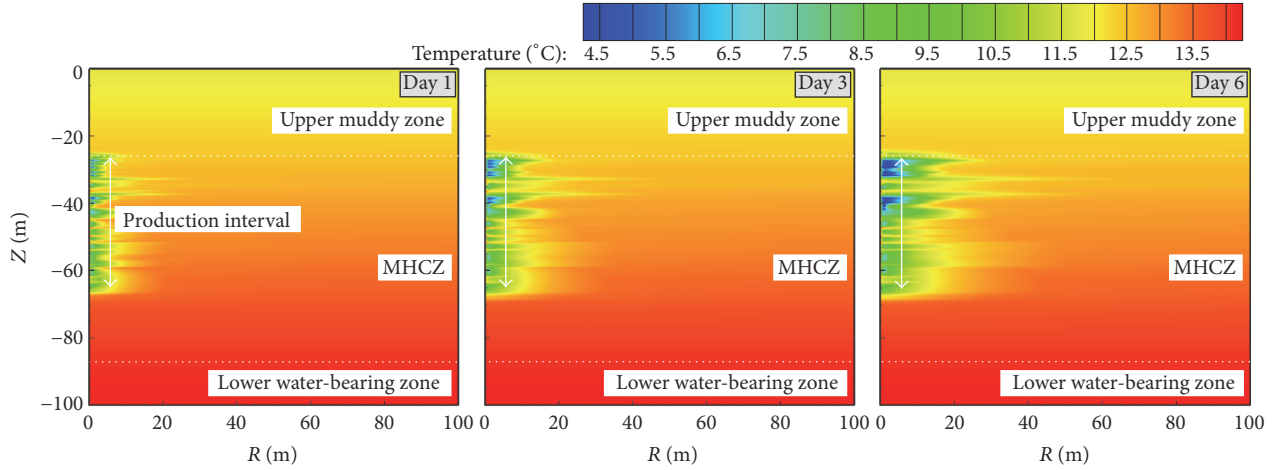


FIGURE 14: Evolution of spatial distribution of temperature in the hydrate reservoir at the AT1 site.

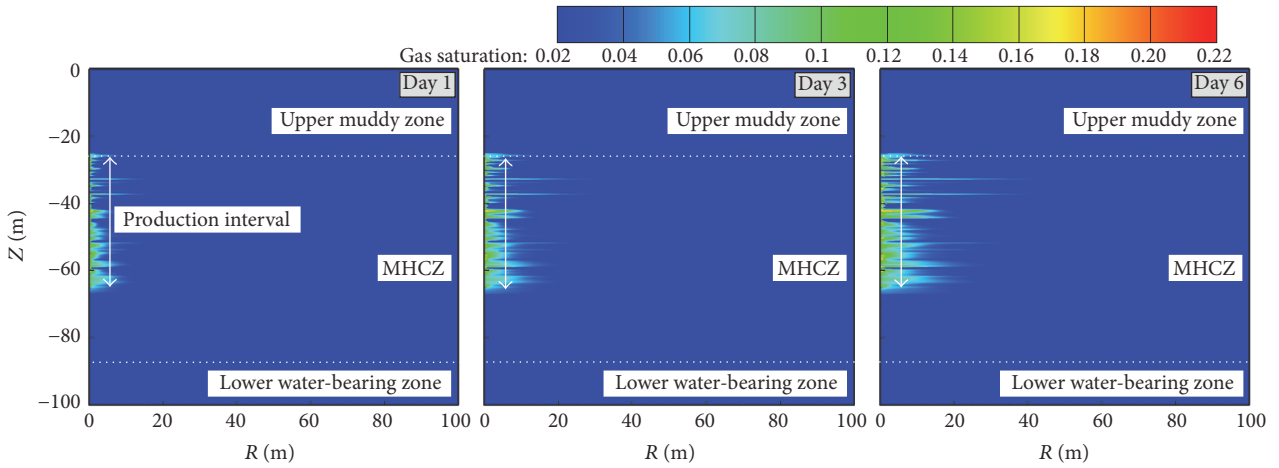


FIGURE 15: Evolution of spatial distribution of gas saturation in the hydrate reservoir at the AT1 site.

4.3.3. Spatial Distribution of Temperature. The temperature reduction is strongly related to the hydrate dissociation because of the endothermic function of hydrate dissociation (Figure 14). The spatial distribution of low temperature shows vertical heterogeneity as well. This is because of the drastic dissociation in the fine sand layers (with high hydrate saturation and high permeability) resulting in significant temperature decreases, whereas the silt-dominant zones with low hydrate saturation undergo slight temperature decreases. Generally, the evolution of low temperature region can reveal the dissociation performance directly.

4.3.4. Spatial Distribution of Gas Saturation. Figure 15 indicates the spatial distribution of gas saturation in the reservoir due to depressurization. The evolution of spatial distribution of free gas is very important for us to understand the gas production behaviors and to evaluate the formation of “secondary hydrate” [17]. As the depressurization begins, there gradually forms a gas bank around and below the production well with the maximum gas saturation of 0.22.

With time advancing, the region of gas zone gradually enlarges (Figure 15). Gas accumulation is observed around and below the production interval because of continuing hydrate dissociation. However, results of Rutqvist and Moridis [7] indicate that gas accumulation occurred under the bottom of the confined overburden, which results by buoyancy. This phenomenon did not occur in our modeling results, because the hydrate deposits in the case of the Eastern Nankai Trough are composed of alternating beds of sand and clay; thus, the low-permeability sealing formations can effectively prevent gas from migrating upward. This is very important for hydrate exploitation from marine sediments because lack of a confining overburden could result in gas diffusion into the sea floor [7].

5. Discussion

The design of production interval is recognized as a significant factor that affects the performance of hydrate exploitation [12, 17]. The production interval of 38 m from the

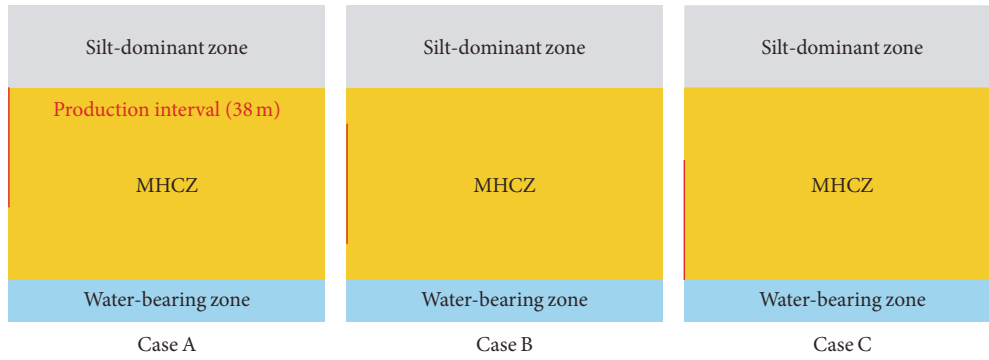


FIGURE 16: Different designs related to the location of production interval: Case A, from the top of the MHCZ (base case); Case B, at the center of the MHCZ; Case C, from the bottom of the MHCZ.

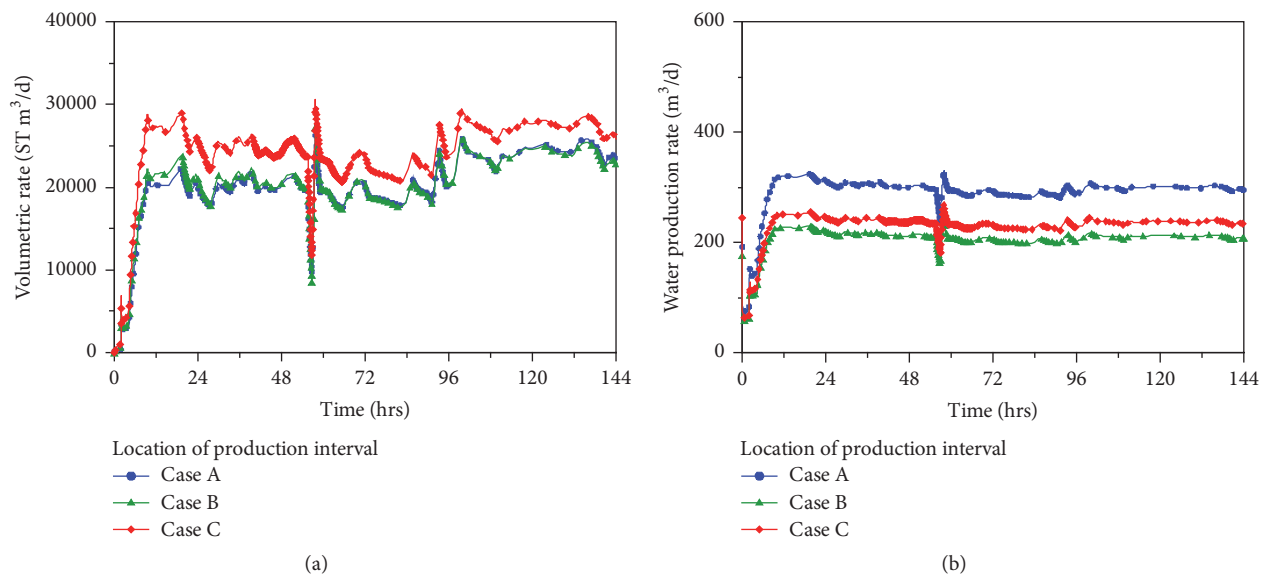


FIGURE 17: Evolution of volumetric rates of (a) gas production and (b) water production from hydrate reservoirs under different locations of production interval.

top of the MHCZ (total thickness of 61 m) was employed at the AT1 site of the Eastern Nankai Trough (Figure 16, Case A). For effective depressurization, the lower part of the MHCZ (i.e., with high hydrate saturation) was considered as sealing formation to block water production from the underlying water-bearing zones [22, 28]. Both the site test data and the modeling results indicate the effectiveness of this production interval design by depressurization at marine hydrate deposits. However, the significant gas accumulation is observed at the lower part of the MHCZ and could not sufficiently transport to the production well (Figure 15). This suggests that the gas recovery schemes should be optimized for the subsequent production test.

In this study, three different cases (Figure 16) with different locations of production interval are designed to investigate the effects of placement of production interval on gas production performance. The purpose is to provide some feasible suggestions for the subsequent site test and

future large-scale exploitation of gas hydrate. For the convenience of comparison, all of the thermophysical properties of the hydrate reservoirs and production method remain unchanged.

Figure 17 indicates the evolution of model-predicted volumetric rates of gas (Q_G) and water (Q_W) production from hydrate reservoirs under different locations of production interval (Figure 16). As shown in Figure 17(a), the gas production rate in Case C is significantly higher than that in Case A and Case B. The average values of Q_G in Case A, Case B, and Case C are about 20477, 20692, and 24307 ST m³/d, and the accumulated volumes of gas trapped (V_G) in 6 days are 122,861, 124,151, and 145,843 m³, respectively. On the other side, Q_W in Case B and Case C is significantly lower than that in Case A. The predicted average values of Q_W in Case A, Case B, and Case C are approximately 292, 207, and 231 m³/d, respectively.

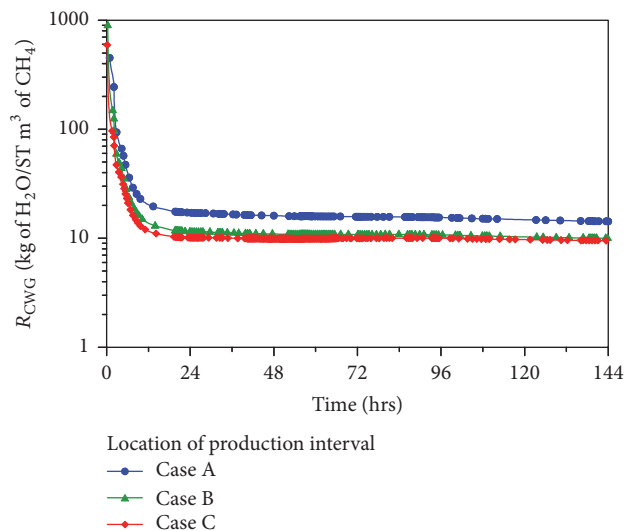


FIGURE 18: The evolution of simulated R_{CWG} during the 6-day production test under different locations of production interval.

Figure 18 shows the evolution of model-predicted R_{CWG} during the 6-day production test under different locations of production interval. As mentioned above, R_{CWG} drops rapidly in the early stage because of the significant hydrate dissociation and gas production (Figure 17(a)). The predicted average values of R_{CWG} in Case A, Case B, and Case C are approximately 15.7, 10.8, and 9.9 kg of $H_2O/ST m^3$ of CH_4 , respectively. Obviously, lower R_{CWG} indicates higher energy efficiency and economic efficiency of gas hydrate production from marine sediments, because lifting large water volumes to the surface could burden gas production with the cost. Particularly, the disposal of produced low-salinity water (released from hydrate dissociation) may pose environmental damage if released near the sea floor without mixing with sea water at suitable ratios [7].

Both the absolute criteria and relative criteria discussed earlier illustrate the obvious superiority of Case C, in which the production interval is located at the bottom of the MHCZ. This can be explained by the characteristic of flow-related reservoir properties, as shown in Figure 19. The main reasons include the following: (1) the lower part of MHCZ is composed of thick sand-dominant layers with high initial hydrate saturation and permeability (Figures 3 and 6); the pressure drops rapidly around production interval causing significant hydrate decomposition and gas production; (2) the extent of hydrate dissociation zone is enlarged due to hydrate dissociation which increases the effective permeability and accelerates the pressure reduction in the radial direction; (3) the fluid flow from bottom formations with higher temperature promotes the hydrate dissociation occurring in deeper sediments significantly; (4) the actual reservoir structure with low-permeability silt/mud layers in hydrate deposits can block the water flow through the formation into production well effectively. The simulation results suggest that the favorable production interval scheme should consider the reservoir conditions with high permeability and high hydrate

saturation in the subsequent field test and future commercial production. Furthermore, the production behaviors of the hydrate reservoir highly depend on the structure of lithofacies and reservoir properties such as the hydrate saturation and sediments permeability.

6. Conclusions

By incorporating the available geological data at the offshore production test site of the Eastern Nankai Trough, a multiphase fluid-flow model was constructed to investigate the gas production performance from the layered hydrate reservoirs by depressurization. The performance affected by the placement of production interval was discussed. Based on the numerical simulations, the following conclusions can be drawn:

- (1) The numerical model can match reasonably well with site-observed data of gas recovery. However, a slight deviation occurs between the predicted and measured water production rates. This is mainly due to the geomechanical responses such as reservoir compression, well completion method, clay minerals swelling, and lateral heterogeneity in each fine layer, which are not considered in our model.
- (2) Because the fine sand layers with high hydrate saturation are hydraulically confined by silt/mud layers in MHCZ, depressurization is anticipated to be rapidly and effectively propagated, leading to fast hydrate dissociation in the radial direction. As hydrate dissociation results in an increase of effective permeability, this process and the anisotropic permeability conditions accelerate the pressure reduction and hydrate dissociation in the radial direction. Overall, the dissociation zone is strongly affected by the vertical reservoir heterogeneity and shows a unique dissociation front.
- (3) The actual reservoir structure with low-permeability silt/mud layers in hydrate reservoirs can block the water flow through the formation into production well. Gas accumulation is observed around and below the production interval, because the low-permeability sealing formations can effectively prevent gas from migrating upward.
- (4) The location of production interval is significantly important for the optimization of gas recovery and reduction of water production. The beneficial production interval scheme should consider the reservoir conditions with high permeability and high initial hydrate saturation. Consequently, the identification of favorable hydrate sediments is significantly important to realize commercial production in the future.

Conflicts of Interest

The authors declare that they have no conflicts of interest.

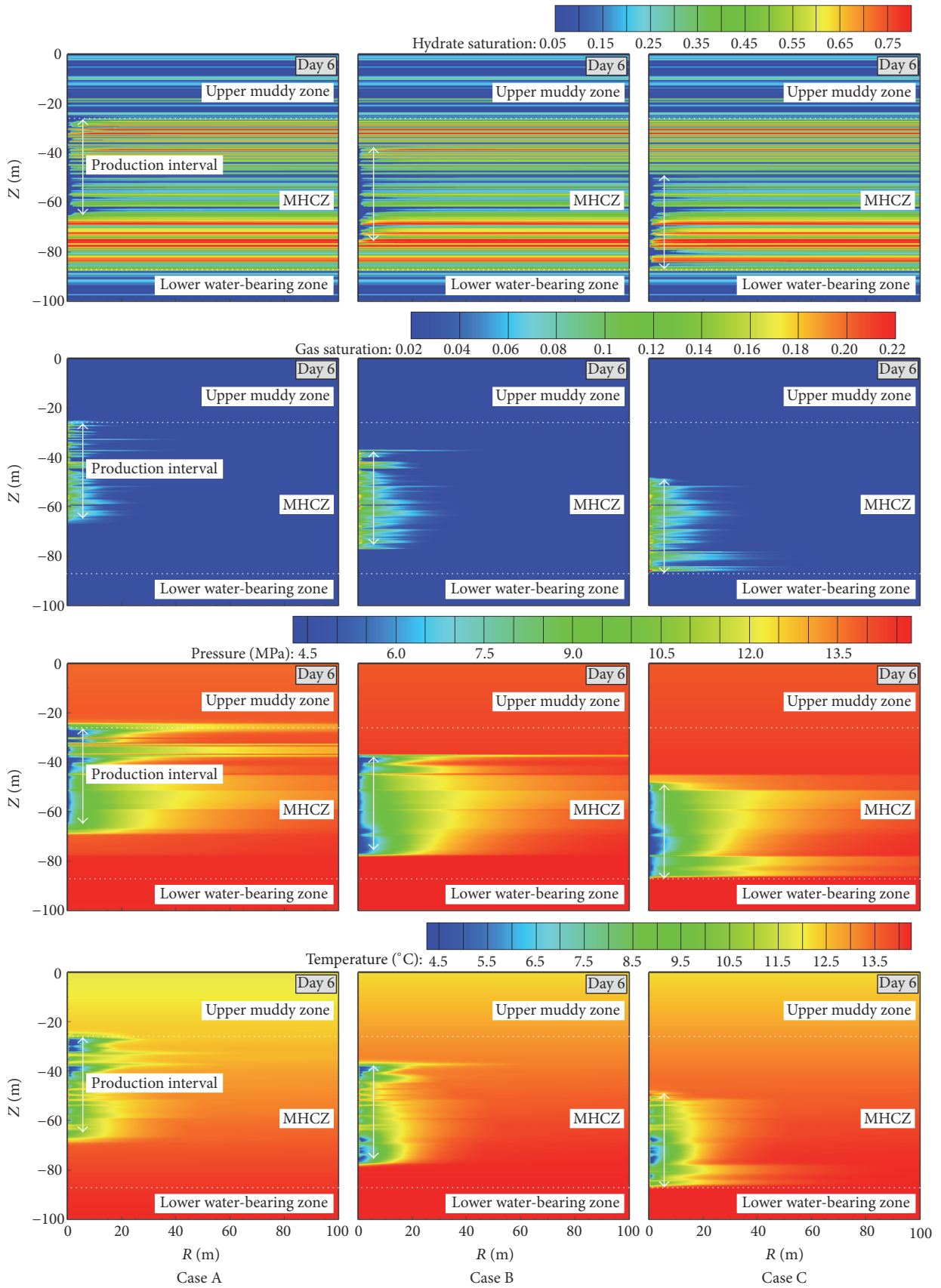


FIGURE 19: The predicted spatial distribution of hydrate and gas saturation, pressure, and temperature at day 6 under different placement of production interval.

Acknowledgments

This work was supported by the National Program on Key Research and Development Project (no. 2017YFC0307304) and the Graduate Innovation Fund of Jilin University (no. 2017018).

References

- [1] G. J. Moridis and M. B. Kowalsky, "Depressurization-induced gas production from Class 1 and Class 2 hydrate deposits," *SPE Reservoir Evaluation and Engineering*, vol. 10, no. 5, pp. 458–481, 2005.
- [2] G. J. Moridis and M. T. Reagan, "Estimating the upper limit of gas production from Class 2 hydrate accumulations in the permafrost: 2. Alternative well designs and sensitivity analysis," *Journal of Petroleum Science and Engineering*, vol. 76, no. 3–4, pp. 124–137, 2011.
- [3] J. Rutqvist, G. J. Moridis, T. Grover, and T. Collett, "Geomechanical response of permafrost-associated hydrate deposits to depressurization-induced gas production," *Journal of Petroleum Science and Engineering*, vol. 67, no. 1–2, pp. 1–12, 2009.
- [4] Y. Konno, T. Fujii, A. Sato et al., "Key Findings of the World's First Offshore Methane Hydrate Production Test off the Coast of Japan: Toward Future Commercial Production," *Energy & Fuels*, vol. 31, pp. 2607–2616, 2017.
- [5] G. Moridis, "User's Manual for the Hydrate v1.5 Option of TOUGH+ v1.5: A Code for the Simulation of System Behavior in Hydrate-Bearing Geologic Media," Tech. Rep. LBNL-6869E, 2014.
- [6] G. Jin, T. Xu, X. Xin, M. Wei, and C. Liu, "Numerical evaluation of the methane production from unconfined gas hydrate-bearing sediment by thermal stimulation and depressurization in Shenhu area, South China Sea," *Journal of Natural Gas Science and Engineering*, vol. 33, pp. 497–508, 2016.
- [7] J. Rutqvist and G. J. Moridis, "Numerical studies on the geomechanical stability of hydrate-bearing sediments," *SPE Journal*, vol. 14, no. 2, pp. 267–282, 2009.
- [8] X. S. Li, C. G. Xu, Y. Zhang, X. K. Ruan, G. Li, and Y. Wang, "Investigation into gas production from natural gas hydrate: A review," *Applied Energy*, vol. 172, pp. 286–322, 2016.
- [9] B. Li, X.-S. Li, G. Li, J.-C. Feng, and Y. Wang, "Depressurization induced gas production from hydrate deposits with low gas saturation in a pilot-scale hydrate simulator," *Applied Energy*, vol. 129, pp. 274–286, 2014.
- [10] B. Li, Y.P. Liang, Li. XS, and L. Zhou, "A pilot-scale study of gas production from hydrate deposits with two-spot horizontal well system," *Applied Energy*, vol. 176, pp. 12–21, 2016.
- [11] M. Kurihara, A. Sato, H. Ouchi et al., "Prediction of gas productivity from eastern Nankai trough methane-hydrate reservoirs," *SPE Reservoir Evaluation and Engineering*, vol. 12, no. 3, pp. 477–499, 2009.
- [12] M. Kurihara, H. Ouchi, A. Sato et al., "Prediction of performances of methane hydrate production tests in the eastern Nankai Trough," in *Proceedings of the 7th International Conference on Gas Hydrates*, 2011.
- [13] R. Swindell and S. Belfroid, "Gas production from oceanic class 2 hydrate accumulations," in *Proceedings of Offshore Technology Conference*, 2007.
- [14] G. Li, X.-S. Li, K. Zhang, B. Li, and Y. Zhang, "Effects of impermeable boundaries on gas production from hydrate accumulations in the shenhu area of the South China sea," *Energies*, vol. 6, no. 8, pp. 4078–4096, 2013.
- [15] L. Huang, Z. Su, N. Wu, and J. Cheng, "Analysis on geologic conditions affecting the performance of gas production from hydrate deposits," *Marine and Petroleum Geology*, vol. 77, pp. 19–29, 2016.
- [16] J. Hou, Z. Xia, S. Li, K. Zhou, and N. Lu, "Operation parameter optimization of a gas hydrate reservoir developed by cyclic hot water stimulation with a separated-zone horizontal well based on particle swarm algorithm," *Energy*, vol. 96, pp. 581–591, 2016.
- [17] J. Sun, F. Ning, L. Zhang et al., "Numerical simulation on gas production from hydrate reservoir at the 1st offshore test site in the eastern Nankai Trough," *Journal of Natural Gas Science and Engineering*, vol. 30, pp. 64–76, 2016.
- [18] J. Rutqvist and G. J. Moridis, "Coupled hydrologic, thermal and geomechanical analysis of well bore stability in hydrate-bearing sediments," in *Proceedings of Offshore Technology Conference*, 2008.
- [19] S. Uchida, K. Soga, A. Klar, and K. Yamamoto, "Geomechanical study of the Mallik gas hydrate production field trials," *Bulletin of the Geological Survey Canada*, vol. 601, pp. 191–204, 2012.
- [20] M. Jiang, H. Chen, M. Tapias, M. Arroyo, and R. Fang, "Study of mechanical behavior and strain localization of methane hydrate bearing sediments with different saturations by a new DEM model," *Computers & Geosciences*, vol. 57, pp. 122–138, 2014.
- [21] S. Uchida, A. Klar, and K. Yamamoto, "Sand production model in gas hydrate-bearing sediments," *International Journal of Rock Mechanics and Mining Sciences*, vol. 86, pp. 303–316, 2016.
- [22] T. Fujii, K. Suzuki, T. Takayama et al., "Geological setting and characterization of a methane hydrate reservoir distributed at the first offshore production test site on the Daini-Atsumi Knoll in the eastern Nankai Trough, Japan," *Marine and Petroleum Geology*, vol. 66, pp. 310–322, 2015.
- [23] K. Yamamoto, T. Kanno, X.-X. Wang et al., "Thermal responses of a gas hydrate-bearing sediment to a depressurization operation," *RSC Advances*, vol. 7, no. 10, pp. 5554–5577, 2017.
- [24] K. Suzuki and H. Narita, "Estimation of Permeability of methane hydrate-bearing strata of Nankai Trough, in comparison to core measurement vs. CMR analysis," *Journal of the Japanese Association for Petroleum Technology*, vol. 75, pp. 98–105, 2010.
- [25] X. Wang, T. S. Collett, M. W. Lee, S. Yang, Y. Guo, and S. Wu, "Geological controls on the occurrence of gas hydrate from core, downhole log, and seismic data in the Shenhu area, South China Sea," *Marine Geology*, vol. 357, pp. 272–292, 2014.
- [26] L. Huang, Z. Su, and N.-Y. Wu, "Evaluation on the gas production potential of different lithological hydrate accumulations in marine environment," *Energy*, vol. 91, pp. 782–798, 2015.
- [27] Y. Komatsu, K. Suzuki, and T. Fujii, "Sedimentary facies and paleoenvironments of a gas-hydrate-bearing sediment core in the eastern Nankai Trough, Japan," *Marine and Petroleum Geology*, vol. 66, pp. 358–367, 2015.
- [28] T. Fujii, S. Noguchi, T. Takayama, K. Suzuki, K. Yamamoto, and T. Saeki, "Site selection and formation evaluation at the 1st offshore methane hydrate production test site in the Eastern Nankai Trough, Japan," in *Proceedings of the 75th EAGE Conference and Exhibition Incorporating SPE EUROPEC 2013*, gbr, June 2013.
- [29] K. Yamamoto, Y. Terao, T. Fujii et al., "Operational overview of the first offshore production test of methane hydrates in the Eastern Nankai Trough," in *Proceedings of the Offshore*

- Technology Conference 2014, OTC 2014*, pp. 1802–1812, usa, May 2014.
- [30] S. Yang, M. Zhang, J. Liang et al., “Preliminary results of China’s third gas hydrate drilling expedition: a critical step from discovery to development in the South China Sea,” *Fire in the Ice*, vol. 15, pp. 1–5, 2015.
- [31] G. Archie, “The Electrical Resistivity Log as an Aid in Determining Some Reservoir Characteristics,” *Transactions of the AIME*, vol. 146, no. 01, pp. 54–62, 2013.
- [32] Y. Terao, M. Duncan, B. Hay, and L. Dang, “Deepwater methane hydrate gravel packing completion results and challenges,” in *Proceedings of the Offshore Technology Conference 2014, OTC 2014*, pp. 2682–2695, usa, May 2014.
- [33] G. J. Moridis and M. T. Reagan, *Strategies for gas production from oceanic class 3 hydrate accumulations*, Lawrence Berkeley National Laboratory, 2007.
- [34] G. J. Moridis and M. T. Reagan, “Estimating the upper limit of gas production from Class 2 hydrate accumulations in the permafrost: 1. Concepts, system description, and the production base case,” *Journal of Petroleum Science and Engineering*, vol. 76, no. 3–4, pp. 194–204, 2011.
- [35] G. J. Moridis, Y. Seol, and T. J. Kneafsey, *Studies of reaction kinetics of methane hydrate dissociation in porous media*, Lawrence Berkeley National Laboratory, 2005.
- [36] M. T. van Genuchten, “A closed-form equation for predicting the hydraulic conductivity of unsaturated soils,” *Soil Science Society of America Journal*, vol. 44, no. 5, pp. 892–898, 1980.
- [37] M. Kurihara, K. Funatsu, H. Ouchi et al., “Analysis of 2007/2008 JOGMEC/NRCan/Aurora Mallik gas hydrate production test through numerical simulation,” in *Proceedings of the 7th International Conference on Gas Hydrates*, Edinburgh, Scotland, United Kingdom, 2011.
- [38] M. Uddin, F. Wright, S. Dallimore, and D. Coombe, “Gas hydrate dissociations in Mallik hydrate bearing zones A, B, and C by depressurization: Effect of salinity and hydration number in hydrate dissociation,” *Journal of Natural Gas Science and Engineering*, vol. 21, pp. 40–63, 2014.
- [39] T. Kanno, M. Takekoshi, X. Wang et al., “In-situ temperature measurement of gas hydrate dissociation during the world-first offshore production test,” in *Proceedings of the Offshore Technology Conference 2014, OTC 2014*, pp. 1709–1713, usa, May 2014.

Research Article

Computational Efficiency of Decoupling Approach in Solving Reactive Transport Model: A Case Study of Pyrite Oxidative Dissolution

Jixiang Huo,¹ Fuheng Ma,¹ and Hanzhou Song²

¹State Key Laboratory of Hydrology-Water Resources and Hydraulic Engineering, Nanjing Hydraulic Research Institute, Nanjing 210029, China

²College of Earth Science and Engineering, Hohai University, Nanjing 210098, China

Correspondence should be addressed to Jixiang Huo; jixianghuo@hotmail.com

Received 13 July 2017; Revised 5 October 2017; Accepted 7 November 2017; Published 26 November 2017

Academic Editor: Keni Zhang

Copyright © 2017 Jixiang Huo et al. This is an open access article distributed under the Creative Commons Attribution License, which permits unrestricted use, distribution, and reproduction in any medium, provided the original work is properly cited.

Pyrite existed widely in nature and its oxidative dissolution might lead groundwater to become acidic, which was harmful to the environment and indeed to artificial building materials. The reactive transport model was a useful tool to predict the extent of such pollution. However, the chemical species were coupled together in the form of a reaction term, which might lead the equations to be nonlinear and thus difficult to solve. A decoupling approach was presented: linear algebraic manipulations of the stoichiometric coefficients of the chemical reactions for the purpose of reducing the number of equation variables and simplifying the reactive source were used. Then the original and decoupled models were solved separately, by both a direct solver and an iterative solver. By comparing the solution times of two models, it was shown that the decoupling approach could enhance the computational efficiency, especially in situations using denser meshes. Using a direct solver, more solution time was saved than when using an iterative version.

1. Introduction

Pyrite is a common, naturally occurring mineral. In the open atmosphere pyrite oxidative dissolution occurs under the action of groundwater. On one hand the resulting acid water may cause environmental problems, such as contamination of surface and ground waters directed to urban and agricultural supply [1–3]. Some toxic elements especially, such as arsenic, are closely associated with pyrite. The kinetic oxidative dissolution of As-bearing pyrite due to dissolved oxygen in the ambient groundwater is an important mechanism for arsenic release in groundwater under both natural conditions and engineering applications [4, 5]. On the other hand the formation of acid water also has some impacts on artificial building materials because of sulfate attack and acid attack [6, 7]. All the above lead the management of potentially acid generating waste rock to be very important [8]. To study the extent and scope of acidic water pollution, some

hydrogeochemical models and transport ones are developed to simulate such a system [9–11].

In recent years reactive transport model is widely used to simulate the contaminant transport, water-rock interaction, and other processes in earth science fields [12, 13]. To improve computational efficiency of the model, Friedly and Rubin [14] present a general, concise formulation (decoupling approach) by means of linear algebraic manipulations of the stoichiometric coefficients of the chemical reactions, which can reduce the number of unknown variables and simplify the reaction source/sink terms. Based on this, De Simoni et al. [15] and Molins and Mayer [16] build up the decoupling matrix according to the equilibrium and kinetic reactions. And Huo et al. [17] extend its applications to heterogeneous media. Some efficiency tests are done by Kräutle and Knabner [18] and Hoffmann et al. [19] to study the resulting improvement. In recent years, the decoupling approach is widely used in both engineering applications and laboratory

experiments. Saaltink et al. [20] apply the approach into the modelling of multiphase flow for CO₂ injection and storage in deep saline aquifers. And the approach is also used in the simulation of two-phase multicomponent flow with reactive transport in porous media [21, 22]. And in identifying geochemical processes using end member mixing analysis, Pelizardi et al. [23] uses the decoupling approach to help in the identification of both end members and such reactions, so as to improve mixing ratio calculations. In laboratory experiments and its simulation, the approach is applied in a laboratory experiment where a sand column saturated with a MgSO₄ solution is subject to evaporation [24]. And some programs and models are built up based on the decoupling approach for hydrogeochemical calculations, such as CHEPROO++ [25] and MRWM [26].

In this paper, a reactive transport model of pyrite oxidative dissolution is built up in COMSOL Multiphysics, a finite element software platform for the simulation of physics-based problems. COMSOL is a multiphysics modelling tool that solves various coupled physical problems based on Finite Element Analysis and Partial Differential Equations. It provides a user-friendly interface for mesh generation, equations configuration, and results visualization. And it is widely applied in earth science field. For example, Shao et al. [27] uses it to couple a dual-permeability model with a soil mechanics model for landslide stability evaluation on a hillslope scale. Azad et al. [28] build up an interface between COMSOL and GEMS, a chemical modelling platform, for the reactive transport modelling in variably saturated porous media, while Nardi et al. [29] and Jara et al. [30] couple two standalone simulation programs, COMSOL and PHREEQC, for the reactive transport modelling.

Although some studies have been done on computational efficiency, they are carried out from different research directions. Hoffmann et al. [19] mainly study the impact from theory view, while Kräutle and Knabner' work [18] is based on a transient model to study computational efficiency in different time steps of two approaches. In this paper, we focused on the number of meshes and different solvers. Based on a brief introduction to the theories and mathematical methods behind the decoupling approach, a reactive transport model of pyrite oxidative dissolution is solved by a traditional method and a decoupling approach separately to compare their computational efficiencies. In both 1D and 2D models, the study area is meshed to different grid refinements in each situation. The original and decoupled models are solved and their solution times are compared. Meanwhile, the 2D models are solved by both a direct and an iterative solver to study the effect on the computational efficiency of the decoupling approach compared to different solvers. It is aimed at providing a more convenient and efficient method of calculation to solve the reactive transport model of pyrite oxidative dissolution.

2. Mathematical Description

The chemical reactions involved in aqueous species are divided into two kinds, equilibrium reaction and kinetic one. Reaction rates of the former are fast in comparison to

transport, so that local chemical equilibrium can be assumed at every point within the system. Kinetic laws are applied to represent the processes of latter one, which is not sufficiently fast enough. So without considering the influence of activity, the mass balance of each species can be written in concise vector notation as follows:

$$\frac{\partial(\mathbf{m})}{\partial t} = \mathbf{M}\mathbf{L}(\mathbf{c}) + \mathbf{S}^T \cdot \mathbf{r} = \mathbf{M}\mathbf{L}(\mathbf{c}) + \mathbf{S}_e^T \mathbf{r}_e + \mathbf{S}_k^T \mathbf{r}_k, \quad (1)$$

where vector \mathbf{m} contains the mass of species per unit volume of porous medium, and it can be split into two parts, \mathbf{m}_c and \mathbf{m}_a , respectively, related to the constant activity species (such as minerals in solid phase and gases) and to the remaining species. Matrix \mathbf{M} is diagonal and its diagonal terms are unity when a given species is mobile and zero otherwise. \mathbf{c} contains species concentrations in mol/mass of liquid ($\mathbf{m} = \theta \cdot \mathbf{c}$ for mobile species, θ is porosity) and $\mathbf{c} = (\mathbf{c}_1 \ \mathbf{c}_2)^T$, while \mathbf{c}_1 , \mathbf{c}_2 are primary and secondary species: the number of secondary species is equal to the number of reaction equilibrium, and the linear operator L in (1) is defined as $L(\mathbf{c}) = -\nabla \cdot (\mathbf{q} \cdot \mathbf{c}) + \nabla \cdot (\theta \cdot \mathbf{D}\nabla \mathbf{c})$, where \mathbf{q} is the water flux and \mathbf{D} is dispersion coefficient; \mathbf{S} is a matrix containing the stoichiometric coefficients of reactions involving reactants and product(s) and $\mathbf{S} = (\mathbf{S}_e/\mathbf{S}_k)$, where \mathbf{S}_e and \mathbf{S}_k represent the matrices of equilibrium and kinetic reactions such that $\mathbf{S}_e = (\mathbf{S}_1 \ | \ \mathbf{S}_2)$ due to the primary and secondary species. \mathbf{S}_1 is stoichiometric coefficients matrix of primary species and \mathbf{S}_2 is stoichiometric coefficients matrix of secondary species. Vector \mathbf{r} contains the reaction rate and is also divided into two parts: \mathbf{r}_e and \mathbf{r}_k .

A full rank matrix, \mathbf{U} , can be established, orthogonal to \mathbf{S}_e , which satisfies $\mathbf{U} \cdot \mathbf{S}_e^T = 0$. The component matrix \mathbf{U} can be calculated by means of Gauss-Jordan elimination which leads to the following expression [31]:

$$\mathbf{U} = \left[\mathbf{I}_{N_s - N_e} \ | \ -\mathbf{S}_1^T \cdot (\mathbf{S}_2^T)^{-1} \right], \quad (2)$$

where $\mathbf{I}_{N_s - N_e}$ is a diagonal matrix of dimension $N_s - N_e$, with all diagonal elements equal to one; N_e and N_s are the number of reactions and species. Now a component vector of \mathbf{u} is defined as $\mathbf{u} = \mathbf{U} \cdot \mathbf{c}$ and its number, N_u , can be calculated by $N_u = N_s - N_e$. Writing the transport equations in terms of \mathbf{u} is helpful because the source/sink term becomes simple. Species concentration \mathbf{c} can also be solved with the equilibrium reaction constants.

According to Molins et al. [32], four types of reactive transport systems are classified by the types of reactions, as shown in Table 1.

It can be seen that four types of reactive transport systems are classified. The characteristics and calculation of component matrix \mathbf{U} of each system are shown as follows.

(1) The first is tank system, in which all reactions take place in equilibrium in the aqueous phase, which means a large aqueous reservoir with residence times long enough for aqueous species to reach equilibrium, and no interaction with other solid or gas phases assumed. The component matrix

TABLE 1: Types of reactive transport system.

Paradigm	Homogeneous		Heterogeneous	
	Fast (Equilibrium)	Slow (Kinetic)	Fast (Equilibrium)	Slow (Kinetic)
Tank	√			
Canal	√	√		
River	√	√		√
Aquifer	√	√	√	√

of this system, \mathbf{U}^{tank} , can be calculated by the following equation.

$$\mathbf{U}^{\text{tank}} = \mathbf{U}^e = [\mathbf{I} \ \mathbf{S}_{e1}^t], \quad (3)$$

where \mathbf{S}_{e1}^t is stoichiometric coefficients matrix of equilibrium reactions corresponding to primary species.

(2) The second is canal system, in which all reactions are homogeneous, but some may be slow (kinetic). The component matrix of this system, $\mathbf{U}^{\text{canal}}$, can be calculated by the following equation.

$$\mathbf{U}^{\text{canal}} = \mathbf{U}_k \cdot \mathbf{U}_e, \quad (4)$$

where $\mathbf{U}_k = \begin{bmatrix} \mathbf{I} & \mathbf{S}_{k1}^t \\ \mathbf{0} & \mathbf{I} \end{bmatrix}$ and \mathbf{S}_{k1}^t is stoichiometric coefficients matrix of kinetic reactions corresponding to primary species.

(3) The third is river system, in which heterogeneous reactions also take place, but they are slow relative to flow. The component matrix of this system, $\mathbf{U}^{\text{river}}$, can be calculated by the following equation.

$$\mathbf{U}^{\text{river}} = \mathbf{F} \cdot \mathbf{U}^{\text{canal}}, \quad (5)$$

where \mathbf{F} is a factor matrix which is multiplied by $\mathbf{U}^{\text{canal}}$ to eliminate the immobile kinetic species. More detailed solution steps of \mathbf{F} can be seen in Molins et al. [32].

(4) The fourth is aquifer system, where some heterogeneous reactions are fast enough to be considered in equilibrium. Some fixed activity species (e.g., minerals and H₂O) can be found among the equilibrium reactions. These species can be eliminated from the equations by reducing the components to be solved. The component matrix of this system, $\mathbf{U}^{\text{aquifer}}$, can be calculated by the following equation.

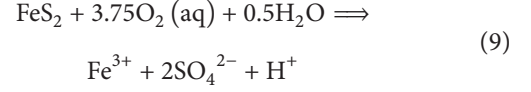
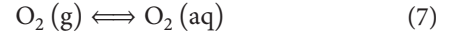
$$\mathbf{U}^{\text{aquifer}} = \mathbf{E} \cdot \mathbf{U}^{\text{river}}, \quad (6)$$

where \mathbf{E} is a factor matrix which is multiplied by $\mathbf{U}^{\text{river}}$ to eliminate constant activity species and reduce the number of components. More detailed solution steps of \mathbf{E} can be seen in Molins et al. [32].

3. Decoupling Approach in Pyrite Oxidative Dissolution

3.1. The Chemical System and Its Decoupling Matrix. It is important to build up a chemical reaction system for pyrite oxidative dissolution reactive transport. When the initial

solution is assumed to be formed in deionized water, the main reactions occurring in the open system are as follows.



where there are equilibrium reactions in both (7) and (8), with reaction rates of R_1 and R_2 and (9) reflects the process of pyrite oxidative dissolution, which depends on the concentration of H^+ and $\text{O}_2(\text{aq})$ in solution. According to these, the stoichiometric coefficient matrix of the system \mathbf{S} could be written as

$$\mathbf{S} = \begin{matrix} & \text{O}_2(\text{aq}) & \text{H}^+ & \text{OH}^- & \text{SO}_4^{2-} & \text{Fe}^{3+} & \text{FeS}_2 & \text{O}_2(\text{g}) & \text{H}_2\text{O} \\ = & \begin{bmatrix} 1 & 0 & 0 & 0 & 0 & -1 & 0 \\ 0 & 1 & 1 & 0 & 0 & 0 & -1 \\ -3.75 & 1 & 0 & 2 & 1 & -1 & 0 & -0.5 \end{bmatrix} & \cdot & \end{matrix} \quad (10)$$

Since the reactions involved both aqueous and solid phases, it satisfied the aquifer system in Section 2. So the component matrix, \mathbf{U} , could be calculated as

$$\mathbf{U} = \begin{bmatrix} 0 & -1 & 1 & 0 & 1 & 0 & 0 & 0 \\ 0 & 0 & 0 & 1 & -2 & 0 & 0 & 0 \\ 0 & 0 & 0 & 0 & 1 & 0 & 0 & 0 \end{bmatrix}. \quad (11)$$

And a new vector of components, \mathbf{u} , was defined as

$$\mathbf{u} = \mathbf{U} \cdot \mathbf{c} = \begin{bmatrix} -c_2 + c_3 + c_5 \\ c_4 - 2 \cdot c_5 \\ c_5 \end{bmatrix} = \begin{bmatrix} u_1 \\ u_2 \\ u_3 \end{bmatrix}, \quad (12)$$

where the vector \mathbf{c} in this system comprised eight species: $\text{O}_2(\text{aq})$, H^+ , OH^- , SO_4^{2-} , Fe^{3+} , FeS_2 , $\text{O}_2(\text{g})$, and H_2O in order. The calculated aqueous components were u_1 , u_2 , u_3 . As (12) shows (1) the component vector \mathbf{u} is a linear combination of species, which is readily calculated; (2) the number of unknowns to be solved in the equations is reduced, from eight species to three components. In this system, the number of all species is defined as N_s , with $N_s = 8$ and the number of equilibrium reactions N_e is 2, while the number of secondary species with fixed activity is defined as N_0 , which includes pyrite, H_2O , and $\text{O}_2(\text{g})$. In this system $N_0 = 3$, so the number of components, N_c , could be calculated as

$$N_c = N_s - N_e - N_0 = 8 - 2 - 3 = 3. \quad (13)$$

Meanwhile, the reaction terms of species in the transport equations were as follows:

$$\mathbf{S}^T \cdot \mathbf{R} = [R_1 - 3.75 \cdot R_3, R_2 + R_3, R_2, 2 \cdot R_3, R_3, -R_3, -R_1, -R_2 - 0.5 \cdot R_3]^T. \quad (14)$$

TABLE 2: Chemical parameters of pyrite oxidation dissolution.

K_{sp1}	K_{sp2}	k	m	n
$10^{-2.8983}$	10^{-14}	$10^{-10.19}$	0.5	-0.11

Multiplying by the decoupling matrix, U , this term could be expressed as

$$U \cdot S^T \cdot R = \begin{bmatrix} 0 & 0 & 0 \\ 0 & 0 & 0 \\ 0 & 0 & 1 \end{bmatrix} \cdot \begin{bmatrix} R_1 \\ R_2 \\ R_3 \end{bmatrix} = \begin{bmatrix} 0 \\ 0 \\ R_3 \end{bmatrix}. \quad (15)$$

It could be seen that the reaction term of the original model was more complicated and contained the expressions of the equilibrium reaction rates R_1 and R_2 , both of which were difficult to obtain explicitly which introduced some difficulties when solving the model. However, it was expressed in the form of extremely simple items by means of the decoupling approach. As shown in (15), the reaction terms of components, u_1 and u_2 , were 0, and the one of component u_3 involved only R_3 . Then the transport equations of component \mathbf{u} could be solved. Once system components had been evaluated, the original species, c , was obtained from the nonlinear algebraic system of (12) and corresponding equilibrium constants of (7) and (8).

3.2. Verification. In order to verify the influence of the decoupling approach on the calculation accuracy, firstly a batch reactor system of pyrite oxidation dissolution was taken as an example. In this system the pyrite was completely immersed in deionized water in a stirred vessel, which meant there was no need to consider the transport problem. The simulation results by both original approach and decoupling one were compared. The chemical parameters are shown in Table 2.

K_{sp1} and K_{sp2} are the equilibrium constant of (7) and (8), while k , m , and n are reaction parameters of pyrite oxidative dissolution. Its reaction rate could be calculated by the following equation.

$$R_3 = \frac{A_{\text{solid}}}{V_{\text{water}}} \cdot k \cdot c_1^m \cdot c_2^n, \quad (16)$$

where A_{solid} is solid phase surface area and V_{water} is water volume; c_1 and c_2 are concentration of $O_2(\text{aq})$ and H^+ .

The ratio of solid phase surface area to water volume was set as 3 dm^{-1} and simulated time was 10 days. The variation and error of pH value and Fe^{3+} concentration in two models are shown in Figure 1.

It can be seen from Figure 1 that the results of two models are basically the same. Maximum relative error of pH value is -0.04725% , while the one of Fe^{3+} is 0.59542% , which means that decoupling approach has little effect on the accuracy of the calculation.

3.3. Comparison of Computational Efficiency. The decoupling approach not only simplified the reaction term but also

reduced the number of unknown variables in the transport equations. As a result, the new transport model of each component should now be solvable with improved computational efficiency. Deionized water flows through a single smooth fracture of pyrite can be simplified to either a 1D or 2D parallel plate model with model parameters as shown in Table 3.

Initially the fracture was deemed to have been full of deionized water, with a constant flow velocity v through the fracture. Without considering the change in the aperture size caused by dissolution, the distribution of aqueous species reached dynamic equilibrium, which can be regarded as a steady state. The two models were thus simulated. One of the two models involved transport of species c and the original model was designated: the other involved transport of decoupled component \mathbf{u} and the decoupled model was designated.

Then the two models were separately established in COMSOL 3.5a, a software platform for the simulation of physics-based problems. The central processing unit (CPU) of the computer was an Intel Core Duo P8400 with a clock speed of 2.26 GHz and the motherboard had 3 GB of random access memory. There were two main categories of solver in the software: direct and iterative. The former included UMFPACK, SPOOLES, PARDISO, and TAUCS Cholesky, which solved a linear system by Gaussian elimination. The iterative solvers, GMRES, FGMRES, conjugate gradients, BiCGStab, and geometric multigrid, were more memory-efficient to deal with models with many degrees of freedom.

When the model was solved in COMSOL, the mesh generator partitioned the study domains into mesh elements: the number of elements depended on the maximum element size when they were uniformly subdivided. Then the 1D and 2D models (original and decoupled types) were solved separately. First the direct solver, UMFPACK, was chosen and the model was solved three times in each case. To solve the nonlinear equations in both original model and decoupled one, Damped Newton Method (DNM) was adopted. Relative tolerance was set as 1.0×10^{-6} and maximum number of iterations was set as 25. The average solution times are shown in Tables 4 and 5.

It can be seen from Tables 4 and 5 that:

(1) Solution by direct solver, UMFPACK, costs much more time in the original model than when adopting a decoupling approach in both 1D and 2D models.

(2) The solution time in both 1D models increases with the number of elements, but it saves more time by using a decoupling approach when the number of elements becomes large. When there are only 25 elements in the model, it costs 0.234 s and 0.094 s to solve each model. With the increase in the number of elements, the solution times reach 1.079 s and 0.297 s for 500 elements (some 4.61 and 3.16 times the requirements at 25 elements).

(3) As in 1D, the computing time in 2D also increases with the number of elements in both of the two models and it saves more time when using a decoupling approach for large numbers of elements. At 7,800 elements, the original model cannot be solved due to an out of memory error during LU factorisation. However, by using a decoupling approach it only costs 21.033 s. Compared to the 1D model, it has a better

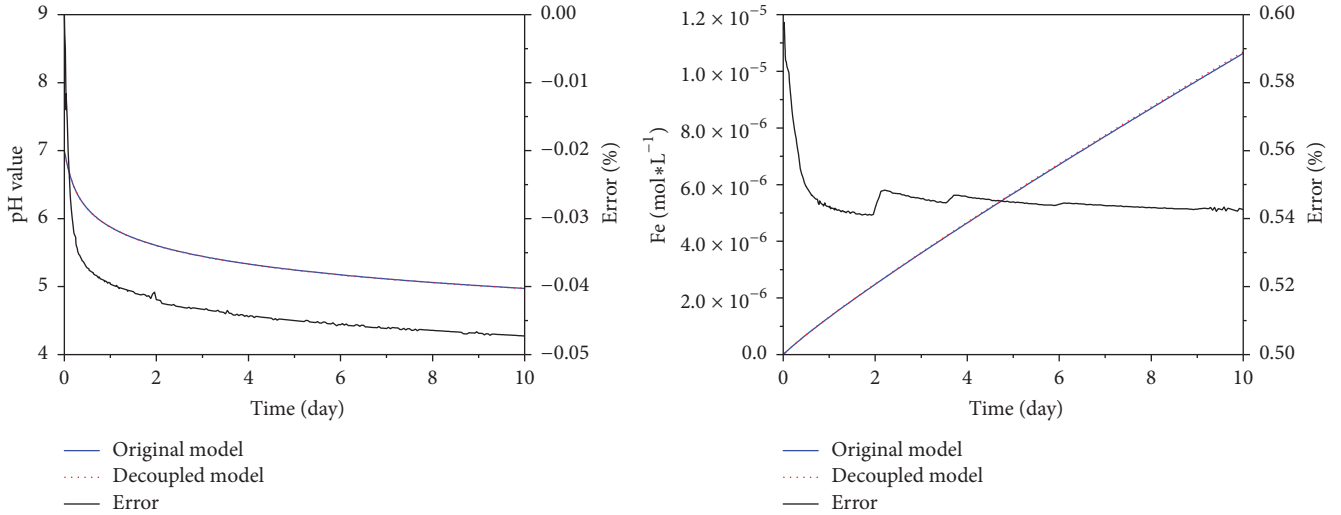


FIGURE 1: Variation and error of pH value and Fe^{3+} concentration.

TABLE 3: Parameters for the 1D and 2D models.

	L/m	W/m	$\nu/m \cdot s^{-1}$	α_l/m	α_T/m	$D_m/m^2 \cdot s^{-1}$
1D	5	—	0.001	0.05	—	$1.34e-9$
2D	5	1	0.001	0.05	0.02	$1.34e-9$

TABLE 4: Comparison of solution time in 1D model using direct solver, UMFPAK.

Maximum element size	Number of elements	Original solution time, t_1/s	Decoupled solution time, t_2/s	t_2/t_1 %
0.01	500	1.079	0.297	27.53
0.02	250	0.625	0.203	32.48
0.04	125	0.406	0.141	34.73
0.05	100	0.359	0.125	34.82
0.08	63	0.313	0.109	34.82
0.10	50	0.282	0.109	38.65
0.20	25	0.234	0.094	35.47

TABLE 5: Comparison of solution time in 2D model using direct solver, UMFPAK.

Maximum element size	Number of elements	Original solution time, t_1/s	Decoupled solution time, t_2/s	t_2/t_1 %
0.04	7800	-	21.033	-
0.05	5036	246.141	11.767	4.78
0.08	2038	43.644	4.141	9.49
0.10	1310	18.095	2.344	12.95
0.12	944	11.032	1.719	15.58
0.15	616	6.062	1.141	18.82
0.20	308	2.672	0.626	20.08
0.25	206	1.750	0.485	23.43
0.30	148	1.344	0.406	27.71

computational efficiency costing only 4.78% to 27.71% of the original.

Then the iterative solver GMRES was chosen to solve the 2D model. The solution set of nonlinear equations was the same as the direct solver, UMFPAK. Three replicates were run and the average solution times are shown in Table 6.

The following can be seen from Table 6.

(1) Like the results in Table 3, the decoupling approach also enhances the computational efficiency when solving the two models by use of the iterative solver. The decoupled solution time is only 17.92% to 52.34% of that needed for the original model and the solution time increases with the number of elements no matter whether in the original or decoupled model.

(2) Unlike the situation in Table 3, t_2/t_1 does not reduce with increased numbers of elements: at 5,036 and 7,800

- represents the absence of a result because of an out of memory error during LU factorisation.

elements, t_2/t_1 is only 51.54% and 52.34% of that required originally. It shows that the decoupling approach does not have as significant an effect as expected when used iteratively on a large model.

(3) Solving the original model with a direct solver costs much more time than when using an iterative version. However, when dealing with a decoupled model, the direct solver is faster and t_2/t_1 (Table 3) ranges from 4.78% to 27.71%, while it is 17.92% to 52.34% in Table 4. This means that solving the decoupled model by using an iterative solver does not save as much time as the direct solver does.

TABLE 6: Comparison of solution time in 2D model using iterative solver, GMRES.

Maximum element size	Number of elements	Original solution time, t_1/s	Decoupled solution time, t_2/s	t_2/t_1 %
0.04	7800	89.644	46.923	52.34
0.05	5036	50.955	26.313	51.64
0.08	2038	18.251	8.235	45.12
0.10	1310	11.016	5.062	45.95
0.12	944	7.328	3.454	47.13
0.15	616	4.531	0.812	17.92
0.20	308	2.172	0.484	22.28
0.25	206	1.547	0.406	26.24
0.30	148	1.219	0.360	29.53

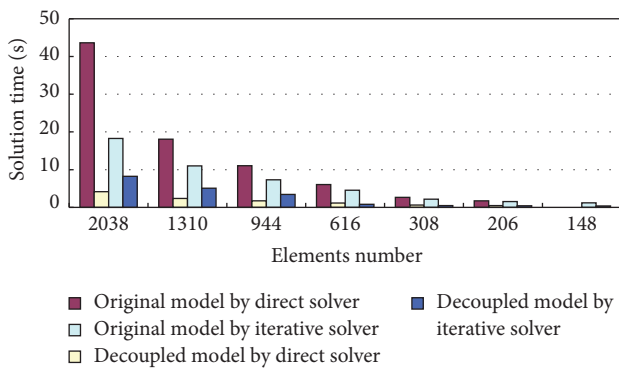


FIGURE 2: Comparison of solution times.

According to Tables 5 and 6, solution times for original and decoupled models with direct and iterative solvers are shown in Figure 2.

Figure 2 shows that solving an original model takes more time than a decoupled one, no matter whether by direct solver or iterative solver. In general sorted by time taken: the decoupled model by direct solver < decoupled model by iterative solver < original model by iterative solver < original model by direct solver.

4. Conclusions

The present work described the basic theory and mathematical methods of the decoupling approach and then took pyrite oxidative dissolution as an example. Based on the analysis of its chemical reaction system, the decoupling matrix U was calculated. When multiplied by U , the concentration vector \mathbf{c} was converted to the component vector \mathbf{u} , which had fewer variables and simpler reaction terms. Then the original and decoupled models were established in COMSOL Multiphysics 3.5a. Then the study domain was meshed at different degrees of refinement. In each case it was solved by direct and iterative solvers. The results show the following.

(1) Decoupling enhances the computational efficiency in both 1D and 2D models while saving more time for 2D models than 1D models.

(2) The more mesh grids the domain generates, the more efficiently the decoupled model finds a solution by direct solver, whether in 1D or 2D.

(3) Although the iterative solver takes less time than the direct solver for the original 2D model, it is more efficient to use a direct solver in solving a decoupled problem.

(4) The solution times in ascending order are the decoupled model solved by direct solver, a decoupled model solved by an iterative solver, the original model solved by an iterative solver, and the original model solved by a direct solver.

As a conclusion, the decoupling approach is of assistance when solving reactive transport of pyrite oxidative dissolution problems, especially over a large domain with more mesh elements. Its applicability is thus demonstrated.

Conflicts of Interest

The authors declare that there are no conflicts of interest regarding the publication of this article.

Acknowledgments

This work was supported by Young Scientists Fund of the National Natural Science Foundation of China (Grant no. 51609150), the China Postdoctoral Science Foundation (Grant no. 2016M590477), the National Natural Science Foundation of China (Grant no. 41272265), and the Special Scientific Research Fund of Public Welfare Profession of Ministry of Water Resources of China (Grants nos. 201501033 and 201501036).

References

- [1] J. A. Grande, R. Beltrán, A. Sáinz, J. C. Santos, M. L. De La Torre, and J. Borrego, "Acid mine drainage and acid rock drainage processes in the environment of Herrerías Mine (Iberian Pyrite Belt, Huelva-Spain) and impact on the Andevalo Dam," *Environmental Geology*, vol. 47, no. 2, pp. 185–196, 2005.
- [2] J. A. Grande, M. Santisteban, M. L. de la Torre, T. Valente, and E. Pérez-Ostalé, "Characterisation of AMD Pollution in the Reservoirs of the Iberian Pyrite Belt," *Mine Water and the Environment*, vol. 32, no. 4, pp. 321–330, 2013.
- [3] P. M. Heikkinen, M. L. Räisänen, and R. H. Johnson, "Geochemical characterisation of seepage and drainage water quality from two sulphide mine tailings impoundments: Acid mine drainage versus neutral mine drainage," *Mine Water and the Environment*, vol. 28, no. 1, pp. 30–49, 2009.
- [4] M. M. Rahman, M. Bakker, C. H. L. Patty et al., "Reactive transport modeling of subsurface arsenic removal systems in rural Bangladesh," *Science of the Total Environment*, vol. 537, pp. 277–293, 2015.
- [5] S. Fakhreddine, J. Lee, P. K. Kitanidis, S. Fendorf, and M. Rolle, "Imaging geochemical heterogeneities using inverse reactive transport modeling: An example relevant for characterizing arsenic mobilization and distribution," *Advances in Water Resources*, vol. 88, pp. 186–197, 2016.
- [6] A. Rodrigues, J. Duchesne, B. Fournier, B. Durand, P. Rivard, and M. Shehata, "Mineralogical and chemical assessment of

- concrete damaged by the oxidation of sulfide-bearing aggregates: Importance of thaumasite formation on reaction mechanisms," *Cement and Concrete Research*, vol. 42, no. 10, pp. 1336–1347, 2012.
- [7] T. Schmidt, A. Leemann, E. Gallucci, and K. Scrivener, "Physical and microstructural aspects of iron sulfide degradation in concrete," *Cement and Concrete Research*, vol. 41, no. 3, pp. 263–269, 2011.
- [8] M. F. Lengke, A. Davis, and C. Bucknam, "Improving management of potentially acid generating waste rock," *Mine Water and the Environment*, vol. 29, no. 1, pp. 29–44, 2010.
- [9] C. Kohfahl and A. Pekdeger, "Rising groundwater tables in partly oxidized pyrite bearing dump-sediments: Column study and modelling approach," *Journal of Hydrology*, vol. 331, no. 3–4, pp. 703–718, 2006.
- [10] B. Blunden and B. Indraratna, "Pyrite oxidation model for assessing ground-water management strategies in acid sulfate soils," *Journal of Geotechnical and Geoenvironmental Engineering*, vol. 127, no. 2, pp. 146–157, 2001.
- [11] R. Abbassi, F. Khan, and K. Hawboldt, "Prediction of minerals producing acid mine drainage using a computer-assisted thermodynamic chemical equilibrium model," *Mine Water and the Environment*, vol. 28, no. 1, pp. 74–78, 2009.
- [12] C. I. Steefel, D. J. DePaolo, and P. C. Lichtner, "Reactive transport modeling: An essential tool and a new research approach for the Earth sciences," *Earth and Planetary Science Letters*, vol. 240, no. 3–4, pp. 539–558, 2005.
- [13] C. I. Steefel, C. A. Appelo, and B. Arora, "Reactive transport codes for subsurface environmental simulation," *Computational Geosciences*, vol. 19, no. 3, pp. 445–478, 2015.
- [14] J. C. Friedly and J. Rubin, "Solute transport with multiple equilibrium-controlled or kinetically controlled chemical reactions," *Water Resources Research*, vol. 28, no. 7, pp. 1935–1953, 1992.
- [15] M. De Simoni, J. Carrera, X. Sánchez-Vila, and A. Guadagnini, "A procedure for the solution of multicomponent reactive transport problems," *Water Resources Research*, vol. 41, no. 11, Article ID W11410, pp. 1–16, 2005.
- [16] S. Molins and K. U. Mayer, "Coupling between geochemical reactions and multicomponent gas and solute transport in unsaturated media: A reactive transport modeling study," *Water Resources Research*, vol. 43, no. 5, Article ID W05435, 2007.
- [17] J.-X. Huo, H.-Z. Song, and Z.-W. Wu, "Multi-component reactive transport in heterogeneous media and its decoupling solution," *Journal of Contaminant Hydrology*, vol. 166, pp. 11–22, 2014.
- [18] S. Krättele and P. Knabner, "A new numerical reduction scheme for fully coupled multicomponent transport-reaction problems in porous media," *Water Resources Research*, vol. 41, no. 9, Article ID W09414, pp. 1–17, 2005.
- [19] J. Hoffmann, S. Krättele, and P. Knabner, "A general reduction scheme for reactive transport in porous media," *Computational Geosciences*, vol. 16, no. 4, pp. 1081–1099, 2012.
- [20] M. W. Saaltink, V. Vilarrasa, F. De Gaspari, O. Silva, J. Carrera, and T. S. Rötting, "A method for incorporating equilibrium chemical reactions into multiphase flow models for CO₂ storage," *Advances in Water Resources*, vol. 62, pp. 431–441, 2013.
- [21] E. Ahusborde, M. Kern, and V. Vostrikov, "Numerical simulation of two-phase multicomponent flow with reactive transport in porous media: application to geological sequestration of CO₂," in *Proceedings of the ESAIM: Proceedings and Surveys*, vol. 50, pp. 21–39.
- [22] E. Ahusborde and M. El Ossmani, "A sequential approach for numerical simulation of two-phase multicomponent flow with reactive transport in porous media," *Mathematics and Computers in Simulation*, vol. 137, pp. 71–89, 2017.
- [23] F. Pelizardi, S. A. Bea, J. Carrera, and L. Vives, "Identifying geochemical processes using End Member Mixing Analysis to decouple chemical components for mixing ratio calculations," *Journal of Hydrology*, vol. 550, pp. 144–156, 2017.
- [24] P. Gamazo, M. W. Saaltink, J. Carrera, L. Slooten, S. A. Bea, and M. Gran, "Modeling the influence of MgSO₄ invariant points on multiphase reactive transport process during saline soil evaporation," *Physics and Chemistry of the Earth*, vol. 64, pp. 57–64, 2013.
- [25] F. d. Gaspari, "Mixing and speciation algorithms for geochemical and reactive transport problems," 2015.
- [26] J. Soler-Sagarra, L. Luquot, L. Martínez-Pérez, M. W. Saaltink, F. De Gaspari, and J. Carrera, "Simulation of chemical reaction localization using a multi-porosity reactive transport approach," *International Journal of Greenhouse Gas Control*, vol. 48, pp. 59–68, 2016.
- [27] W. Shao, T. Bogaard, and M. Bakker, "How to Use COMSOL Multiphysics for Coupled Dual-permeability Hydrological and Slope Stability Modeling," *Procedia Earth and Planetary Science*, vol. 9, pp. 83–90, 2014.
- [28] V. J. Azad, C. Li, C. Verba, J. H. Ideker, and O. B. Isgor, "A COMSOL-GEMS interface for modeling coupled reactive-transport geochemical processes," *Computers & Geosciences*, vol. 92, pp. 79–89, 2016.
- [29] A. Nardi, A. Idiart, P. Trincherro, L. M. De Vries, and J. Molinero, "Interface COMSOL-PHREEQC (iCP), an efficient numerical framework for the solution of coupled multiphysics and geochemistry," *Computers & Geosciences*, vol. 69, pp. 10–21, 2014.
- [30] D. Jara, J.-R. d. Dreuzy, and B. Cochepein, "TReacLab, An object-oriented implementation of non-intrusive splitting methods to couple independent transport and geochemical software," *Computers & Geosciences*.
- [31] M. W. Saaltink, C. Ayora, and J. Carrera, "A mathematical formulation for reactive transport that eliminates mineral concentrations," *Water Resources Research*, vol. 34, no. 7, pp. 1649–1656, 1998.
- [32] S. Molins, J. Carrera, C. Ayora, and M. W. Saaltink, "A formulation for decoupling components in reactive transport problems," *Water Resources Research*, vol. 40, no. 10, pp. W103011–W1030113, 2004.

Research Article

Numerical Modeling of Soil Evaporation Process and Its Stages Dividing during a Drying Cycle

Jiangbo Han, Jin Lin, and Yunfeng Dai

State Key Laboratory of Hydrology-Water Resources and Hydraulic Engineering, Nanjing Hydraulic Research Institute, Nanjing 210029, China

Correspondence should be addressed to Jiangbo Han; jbhan@nhri.cn

Received 19 July 2017; Revised 16 October 2017; Accepted 25 October 2017; Published 14 November 2017

Academic Editor: Xiaoqing Shi

Copyright © 2017 Jiangbo Han et al. This is an open access article distributed under the Creative Commons Attribution License, which permits unrestricted use, distribution, and reproduction in any medium, provided the original work is properly cited.

The soil water evaporation is a critical component of both the surface energy balance and water balance, affecting the mass and energy exchange between the land and the atmosphere. Evaporation process is involved in the highly complex interactions between media properties, transport processes, and boundary conditions. So, it is difficult to accurately determine these near-surface highly dynamic processes based only on the sparse field data and on the measurement-based methods. The objective of this paper was to obtain a detailed description of the soil water evaporation process and to better understand the evolutions of variables involved in the evaporation process during different stages of evaporation. To do this, a numerical simulation experiment in a bare silt soil was conducted to reproduce the soil drying process during a 20-d period after a 2-cm rainfall event. According to simulation results, the whole 20-d simulation period was divided into two main stages as well as a transient period from stage 1 to stage 2. Diurnal patterns of energy and water balance components, soil moisture, soil temperature, water fluxes, evaporation rate, dry surface layer (DSL), and evaporation zone during this drying process were fully described, which, in turn, could be as the possible indicators for judging the shift of stages of evaporation.

1. Introduction

Infiltration and soil water movement play a key element in surface runoff, groundwater recharge, evapotranspiration, soil erosion, and transport of chemicals in surface and subsurface waters [1]. In particular, soil water evaporation and storage during natural wetting/drying cycle exert critical influences on land-atmosphere exchange of water and energy [2, 3], thereby affecting the local or global climate changes. In addition to the important role in the hydrological process, drying and evaporation processes are also of interest for many engineering and industrial applications, such as food processing and preservation, production of ceramics and paper, eye and skin care, and numerous construction activities [4].

During drying of soils after a rainfall or irrigation event, shifts between atmospheric demand to soil control evaporation occur with the progressive drying of soils [3]. Soil water evaporation is a dynamic process and this process has frequently been divided into three major stages. Stage 1 evaporation has a relatively high and constant evaporation

rate followed by a lower rate (stage 2) [5, 6]. During stage 1 when the soil surface has available water, evaporation takes place at the soil surface and is limited by atmospheric demand. At stage 1, a large portion of net radiation is readily dissipated as latent heat of vaporization. With the soil continuing to dry, evaporation eventually occurs within the subsurface when the soil water content is depleted; and stage 2 evaporation begins, during which the evaporation drops below the potential rate and decreases with time. Stage 3 is characteristic of a very low and relatively constant evaporation rate. When the soil moisture is not available at the soil surface, a dry surface layer (DSL) forms near the soil surface, in which moisture transfer occurs only in the vapor phase [7] with the profile below this layer remaining much wetter [8]. The diffusive vapor transfer within the dry layer is supplied by the liquid water flow from sites below the evaporation zone (where the phase change from liquid water to water vapor is occurring). The transition from the surface to subsurface evaporation also has a significant effect on the surface energy balance and profiles of soil temperature

and moisture because the energy required for vaporization of liquid water must be transported from the soil surface to subsurface evaporation zone [4, 9]. Formation of DSL and the shift of the evaporation front from the surface to the subsurface result in a significant change in the surface energy balance as the location of latent heat sink moves from surface to subsurface. The latent heat flux associated with this phase change is important for assessing the surface energy balance during the soil drying [10–12]. The evaporation stage could be an indicator for total water loss, evaporation rate, and soil water content [5], as well as surface energy balance [9]. Therefore, it is important to understand soil evaporation stages for water resource management, environmental conservation, and agricultural production.

To evaluate the evaporative drying process in the field condition, especially to determine the timing of stages of evaporation process, there is need to determine the evaporation rate from soils. The approaches for measuring soil water evaporation include the Bowen ratio [13], eddy correlation and automatic weighing lysimeter methods [1]. These techniques are widely used for field measurements to study the water balance dynamics near the soil surface. However, there are some limitations in these measurement methods; for example, it is somewhat time costly and laborious and cannot accurately measure the dynamics of soil water evaporation with time and depth, especially for evaluating the effect of the evaporation process on the surface energy balance and soil temperature and moisture profiles. Although there are some new approaches developed recently to determine the process of soil water evaporation, it is difficult for these measurement-based approaches to capture the highly dynamic near-surface soil water and heat processes involved in soil water evaporation. For instance, some researchers [3, 14] introduced a measurement approach based on sensible heat balance to determine in situ soil water evaporation dynamics by means of heat pulse probes. However, this approach was not available for stage 1 evaporation [3] during which evaporation likely occurred in the days after rainfall or irrigation. And this approach could result in underestimation of total subsurface evaporation due to the existence of undetectable zone [4]. Deol et al. [15] quantify the millimeter-scale subsurface evaporation profiles by using eleven-needle heat pulse probes in the soil column over a drying event. Since these profiles were limited to depth-integrated evaporation rates, the accurate shape and variation of evaporation zone with time and depth remained uncertain, particularly for some cases whereas the width of evaporation zone was less than 1 mm [4, 9]. Thus, because the evaporation process is involved in the highly complex interactions between media properties, transport processes, and boundary conditions, the direct measurement approaches have a limitation to accurately determine the highly dynamic soil water evaporation process. And numerical modeling is an alternative means.

The growing computational capacity provides the possibility of numerically reproducing evaporation processes by applying the theory of the coupled heat and moisture transport in variable saturated soils, which is developed in Philip and de Vries [16], henceforth PDV. Currently, there are several numerical codes, for example, SVAT, SHAW, and

HYDRUS, developed for simulating coupled water and heat flow in the vadose zone. HYDRUS-ID is a widely used finite-element model for simulating one-dimensional movement of water, heat, and multiple solutes in variably saturated porous media [17] and is applied widely in the study of vadose process. The objective of this paper was to evaluate the process of evaporative drying from a silt soil after a rainfall event by using the HYDRUS-ID model under the field-like atmospheric conditions and to better understand the evolutions of variables involved in the evaporation process.

2. Materials and Methods

2.1. Water Flow Equations. The general partial differential equation for describing the one-dimensional transient water flow in the soil under variably saturated, nonisothermal conditions can be expressed as [4, 16]

$$\frac{\partial(\theta_L + \theta_v)}{\partial t} = -\frac{\partial q_w}{\partial z} = -\frac{\partial q_L}{\partial z} - \frac{\partial q_v}{\partial z}, \quad (1)$$

where θ_L is the volumetric liquid water content ($\text{m}^3 \text{m}^{-3}$), θ_v is the volumetric water vapor content (expressed as an equivalent water content, $\rho_v \theta_{\text{air}} / \rho_L$, $\text{m}^3 \text{m}^{-3}$), θ_{air} is volumetric air content ($\text{m}^3 \text{m}^{-3}$), ρ_L is the density of liquid water (kg m^{-3}) at T ($^{\circ}\text{C}$), q_w ($= q_L + q_v$) is the total water flux (m s^{-1}), q_L and q_v are the flux densities of liquid water and water vapor (expressed as an equivalent water flux density m s^{-1}), respectively, t is time (s), and z is the spatial coordinate positive upward (m).

The PDV model describes liquid water and water vapor movements driven both by the temperature and matric potential gradients. Thus, the flux densities of liquid water, q_L , and water vapor, q_v are given by, respectively,

$$q_L = q_{TL} + q_{hL} = -D_{TL} \frac{\partial T}{\partial z} - K \left(\frac{\partial h}{\partial z} + 1 \right) \quad (2)$$

$$q_v = q_{Tv} + q_{hv} = -D_{Tv} \frac{\partial T}{\partial z} - D_{hv} \frac{\partial h}{\partial z}, \quad (3)$$

where q_{TL} and q_{hL} are the thermal and isothermal liquid water fluxes (m s^{-1}), respectively; q_{Tv} and q_{hv} are the thermal and isothermal water vapor fluxes (m s^{-1}), respectively; T is the soil temperature ($^{\circ}\text{C}$); h is the pressure head (m); D_{TL} ($\text{m}^2 \text{K}^{-1} \text{s}^{-1}$) and K (m s^{-1}) are the thermal and isothermal hydraulic conductivities for liquid phase fluxes, respectively; and D_{Tv} ($\text{m}^2 \text{K}^{-1} \text{s}^{-1}$) and D_{hv} (m s^{-1}) are the thermal and isothermal hydraulic conductivities for water vapor fluxes, respectively. The hydraulic conductivities and related parameters are summarized in Table 1. Combining (1) to (3), the governing liquid water and water vapor equation can be expressed as

$$\begin{aligned} & \frac{\partial(\theta_L + \theta_v)}{\partial t} \\ &= \frac{\partial}{\partial z} \left[D_{TL} \frac{\partial T}{\partial z} + K \frac{\partial h}{\partial z} + D_{Tv} \frac{\partial T}{\partial z} + D_{hv} \frac{\partial h}{\partial z} + K \right]. \end{aligned} \quad (4)$$

TABLE 1: Hydraulic conductivities for liquid-water and water vapor flux and related parameters.

Hydraulic conductivity	Parameter	Expression/constant
$K = K_s S_e^l [1 - (1 - S_e^{1/m})^m]^2$	Pore connectivity coefficient	$l = 0.5$
	Gain factor	$G_{wT} = 7$
	Surface tension of soil water, g s^{-2}	$\gamma = 75.6 - 0.1425T - 2.38 \times 10^{-4}T^2$
	Surface tension at 25°C, g s^{-2}	$\gamma_0 = 71.89$
$D_{TL} = K \left(hG_{wT} \frac{1}{\gamma_0} \frac{\partial \gamma}{\partial T} \right)$	Vapor diffusivity in soil, $\text{m}^2 \text{s}^{-1}$	$D = D_a \Omega \theta_{\text{air}}$
	Tortuosity factor in gaseous phase	$\Omega = \theta_{\text{air}}^{2/3}$
	Vapor diffusivity in air, $\text{m}^2 \text{s}^{-1}$	$D_a = 2.12 \times 10^{-5} \left(\frac{(T + 273.15)}{273.15} \right)$
$D_{Tv} = \frac{D}{\rho_L} \eta \left[H_r \frac{d\rho_{sv}}{dT} + \rho_{sv} \frac{dH_r}{dT} \right]$	Density of liquid water, kg m^{-3}	$\rho_L = 1000 - 7.3 \times 10^{-3} (T - 4)^2 + 3.79 \times 10^{-5} (T - 4)^3$
	Saturation vapor density, kg m^{-3}	$\rho_{sv} = 10^{-3} \times \exp \left(19.84 - \frac{4975.9}{(T + 273.15)} \right)$
	Relative humidity of soil surface	$H_r = \exp \left(\frac{hMg}{R(T + 273.15)} \right)$
	Molecular weight of water, kg mol^{-1}	$M = 0.01805$
	Gravitation acceleration, m s^{-2}	$g = 9.81$
	Universal gas constant, $\text{J mol}^{-1} \text{K}^{-1}$	$R = 8.314$
$D_{hv} = \frac{D}{\rho_L} H_r \frac{Mg}{RT} \rho_{sv}$	Enhancement factor	$\eta = 9.5 + \frac{3\theta_L}{\theta_s} - 8.5 \exp \left\{ - \left[\frac{(1 + 2.6/\sqrt{f_c}) \theta_L}{\theta_s} \right]^4 \right\}$
	Mass fraction of clay	0.02

TABLE 2: Soil hydraulic properties used in numerical simulations.

Sample	θ_r ($\text{m}^3 \text{m}^{-3}$)	θ_s ($\text{m}^3 \text{m}^{-3}$)	α (cm^{-1})	n	K_s (cm d^{-1})
silt	0.034	0.46	0.016	1.37	6

The van Genuchten model which described the soil water retention relation was used for the silt [18]:

$$\theta_L = \theta_r + (\theta_s - \theta_r) [1 + |\alpha h|^n]^{-m}, \quad (5)$$

where θ_s is the saturated water content ($\text{m}^3 \text{m}^{-3}$), θ_r is the residual water content ($\text{m}^3 \text{m}^{-3}$), and α (m^{-1}), n , and m ($= 1 - 1/n$) are empirical shape parameters. The parameters employed for the soil are shown in Table 2.

2.2. Heat Transport Equations. The governing equation for the one-dimensional movement of energy in a variably saturated vadose zone is given by [19]

$$\frac{\partial S_h}{\partial t} = -\frac{\partial q_h}{\partial z}, \quad (6)$$

where S_h is the storage of heat in the soil (J m^{-3}) and q_h is the total soil heat flux density ($\text{J m}^{-2} \text{s}^{-1}$). The storage of heat S_h (J m^{-3}) in the soil is

$$S_h = C_s (T - T_r) \theta_n + C_v (T - T_r) \theta_v + C_w (T - T_r) \theta_L + L_0 \theta_v, \quad (7)$$

where C_s ($= 1.92 \text{ MJ m}^{-3} \text{K}^{-1}$) C_w ($= 4.18 \text{ MJ m}^{-3} \text{K}^{-1}$) and C_v ($= 1.8 \text{ MJ m}^{-3} \text{K}^{-1}$) are the volumetric heat capacities of dry soil particles, liquid water, and water vapor, respectively;

T_r is the reference temperature ($^\circ\text{C}$); and θ_n is the volumetric fraction of solid phase ($\text{m}^3 \text{m}^{-3}$). The soil heat flux density q_h ($\text{J m}^{-2} \text{s}^{-1}$), accounting for the sensible heat of the conduction, sensible heat by the convection of liquid water and water vapor, and latent heat by vapor flow, can be described as

$$q_h = -\lambda \frac{\partial T}{\partial z} + C_v (T - T_r) q_v + C_w (T - T_r) q_L + L_0 q_v, \quad (8)$$

where λ is the apparent soil thermal conductivity ($\text{W m}^{-1} \text{K}^{-1}$) described by [20]

$$\lambda = b_1 + b_2 \theta_L + b_3 (\theta_L)^{0.5}, \quad (9)$$

where b_1 , b_2 , and b_3 are empirical parameters ($\text{W m}^{-1} \text{K}^{-1}$) (for silt: $b_1 = 0.243$, $b_2 = 0.393$, and $b_3 = 1.534$); L_0 ($= \rho_L * (2.501 \times 10^6 - 2369.2T)$) is the volumetric latent heat of vaporization of water (J m^{-3}). Combining the continuity equation with (6) to (8) produces the governing equation for the movement of energy in soils:

$$C_p \frac{\partial T}{\partial t} + L_0 \frac{\partial \theta_v}{\partial t} + C_v (T - T_r) \frac{\partial \theta_v}{\partial t} + C_w (T - T_r) \frac{\partial \theta_L}{\partial t} = \frac{\partial}{\partial z} \left(\lambda \frac{\partial T}{\partial z} \right) - C_v \frac{\partial T q_v}{\partial z} - C_w \frac{\partial T q_L}{\partial z} - L_0 \frac{\partial q_v}{\partial z}, \quad (10)$$

where C_p ($= C_s \theta_n + C_v \theta_v + C_w \theta_L$) represents the volumetric heat capacity of the moist soil ($\text{J m}^{-3} \text{K}$), and the contribution of air to C_p is considered negligible.

2.3. Surface Water and Energy Boundaries. Surface precipitation, evaporation, and heat fluxes are used as boundary conditions for liquid water and water vapor flow and heat

transport in field soils. Surface boundary conditions for the water and energy equations are, respectively, given by [21, 22]

$$q_L(0, t) + q_v(0, t) = E \quad (11)$$

$$R_n - H - LE - G = 0, \quad (12)$$

where $q_L(0, t)$ and $q_v(0, t)$ are liquid water and water vapor fluxes through the soil surface, respectively, E is the evaporation rate (m s^{-1}) from the soil, R_n is net radiation (W m^{-2}), H is the sensible heat flux density (W m^{-2}), LE is the latent heat flux density (W m^{-2}), L is the latent heat (J kg^{-1}), and G is the surface heat flux density (W m^{-2}). While R_n and G are positive downward, H and LE are positive upward [19]. R_n is defined as

$$R_n = R_{ns} + R_{nl} = (1 - a) S_t + \epsilon_s \sigma (\epsilon_a T_a^4 - T_s^4), \quad (13)$$

where R_{ns} and R_{nl} are net shortwave and longwave radiations (W m^{-2}), respectively, a is soil albedo (unitless), S_t is incoming (global) shortwave solar radiation (W m^{-2}), σ is the Stefan Boltzmann constant ($5.6704 \times 10^{-8} \text{ W m}^{-2} \text{ K}^{-4}$), ϵ_s is soil longwave emissivity (unitless), and ϵ_a is the effective atmospheric emissivity (unitless). The sensible heat flux can be defined as [23]

$$H = C_a \frac{T_s - T_a}{r_h}, \quad (14)$$

where C_a is the volumetric heat capacity of air ($1200 \text{ J m}^{-3} \text{ K}^{-1}$), T_s and T_a are temperature ($^{\circ}\text{C}$) of the soil surface and the air, respectively, and r_h is the aerodynamic resistance to heat transfer (s m^{-1}). The soil surface evaporation rate can be calculated from the difference between the water vapor densities of the air, ρ_{va} (kg m^{-3}), and the soil surface ρ_{vs} (kg m^{-3}):

$$E = \frac{\rho_{vs} - \rho_{va}}{r_v + r_s}, \quad (15)$$

where r_v is the aerodynamic resistance to water vapor flow (s m^{-1}) and r_s is the soil surface resistance to water vapor flow that acts as an additional resistance along with the aerodynamic resistance (s m^{-1}). r_v and r_h can be defined as [24]

$$r_v = r_h = \frac{1}{uk^2} \left[\ln \left(\frac{z_{\text{ref}} - d + z_h}{z_{\text{oh}}} \right) + \psi_h \right] \cdot \left[\ln \left(\frac{z_{\text{ref}} - d + z_m}{z_{\text{om}}} \right) + \psi_m \right], \quad (16)$$

where u is wind speed (m s^{-1}), k is von Karman constant (which has a value of 0.41), d is the zero plane displacement (m), z_h and z_m are the height of temperature and wind speed measurement (m), respectively, z_{oh} and z_{om} are the surface roughness length for heat flux and momentum flux (m), respectively, and ψ_h and ψ_m are the atmospheric stability correction factors for heat flux and momentum flux (—), respectively. And r_s can be expressed as [25, 26]

$$r_s = 10 \exp(35.63(0.15 - \theta_{\text{top}})), \quad (17)$$

where θ_{top} is the surface water content ($\text{m}^3 \text{ m}^{-3}$). Details on these variables also can be found in Saito et al. [19, 27].

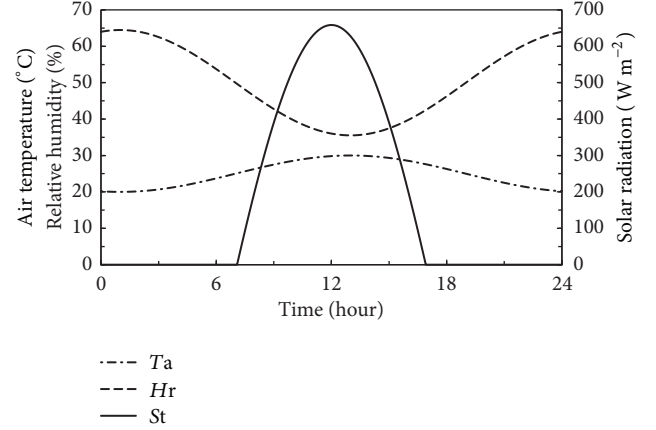


FIGURE 1: Diurnal variations of air temperature T_a , relative humidity H_r , and incoming shortwave solar radiation S_t .

2.4. Numerical Modeling Procedure. The soil profile used in this simulation was considered a 50-cm deep silt horizon. The simulated period lasted for 21 days including a day with a 2-cm daily rainfall following a 20-d soil drying process under clear sky conditions. Boundary conditions at the soil surface for liquid water, water vapor, and heat transport were determined from the surface water and energy balance equations described above. The soil surface was imposed to the field-like atmospheric forcing condition. Thus, the diurnally varying air temperature and air relative humidity could be determined by trigonometric functions with a period of 24 h [4]:

$$T_a = \frac{T_{\text{max}} + T_{\text{min}}}{2} + \frac{T_{\text{max}} - T_{\text{min}}}{2} \cdot \cos \left[2\pi \left(\frac{t - 13}{24} \right) \right] \quad (18)$$

$$H_r = \bar{H}_r + \frac{H_{r\text{max}} - H_{r\text{min}}}{2} \cdot \cos \left[2\pi \left(\frac{t - 1}{24} \right) \right], \quad (19)$$

where T_{max} and T_{min} are the maximum and minimum air temperatures, respectively, and \bar{H}_r , $H_{r\text{max}}$, and $H_{r\text{min}}$ are the average, maximum, and minimum air relative humidity, respectively. The incoming shortwave solar radiation, S_t , at any given time can be calculated as follows [19]:

$$S_t = f \times \max \left\{ S_t^{\text{d}} \left[\sin \varphi \sin \sigma + \cos \varphi \cos \sigma \cos 2\pi(t - 12) \right], 0 \right\}, \quad (20)$$

where S_t^{d} is the daily solar radiation (W m^{-2}), φ is the site latitude (rad), and σ is the solar declination (rad); f is used to adjust the daily summation of S_t equal to S_t^{d} . In this study, we assumed $T_{\text{max}} = 30^{\circ}\text{C}$ and $T_{\text{min}} = 20^{\circ}\text{C}$, $\bar{H}_r = 30\%$, $u = 1.2 \text{ m s}^{-1}$, and $S_t^{\text{d}} = 230 \text{ W m}^{-2}$ for all the days. Figure 1 shows the diurnal variations of T_a , H_r , and S_t for a period of 24 h.

Zero pressure head (free drainage) and temperature gradients were used as the bottom boundary conditions of the soil domain. These conditions assume that the water table is located far below the domain of interest and that heat transfer across the lower boundary occurs only by convection of liquid

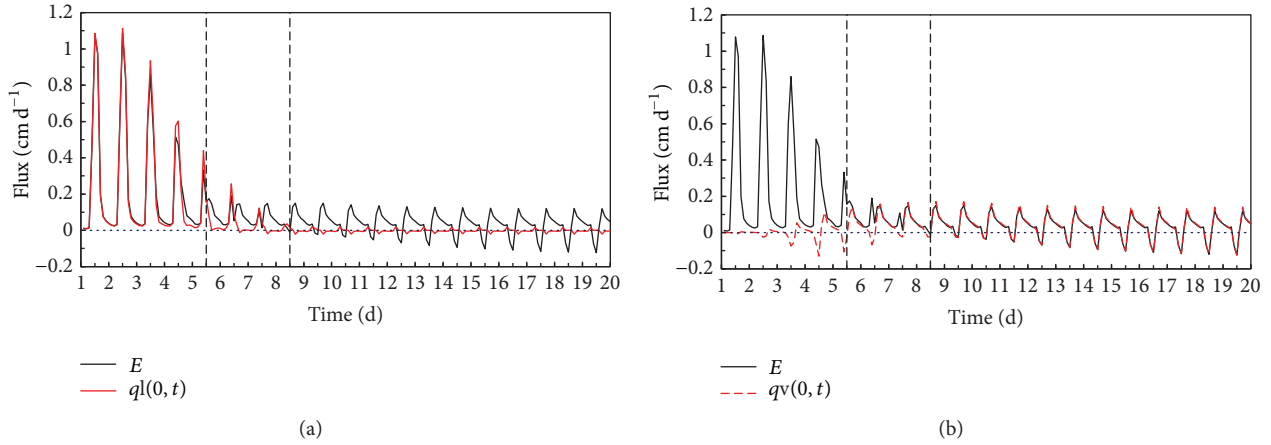


FIGURE 2: The liquid water (red solid line), water vapor (red dashed line) water fluxes, and the total flux (black solid line) at the soil surface. The left vertical dashed lines represent timing point of shift of evaporation process from stages 1 and 2, and periods between the two dashed line indicate the transient stage of evaporation process (same below).

water and water vapor. The initial temperature of 25°C and uniform water content of $0.2\text{ m}^3\text{ m}^{-3}$ were applied to the soil.

The variably saturated water flow and heat transport equations as well as the surface energy and water balances were solved numerically using HYDURUS-1D software package. The 50-cm long soil profile for simulation was divided into 500 elements, with the mesh thickness increasing linearly from 0.03 cm at the soil surface to 0.27 cm at the bottom of the soil domain. The time step was allowed to vary between the initial and maximum time steps of 1×10^{-5} and 0.01 day, respectively.

3. Results and Discussion

During soil drying after a rainfall or irrigation event, the soil continues to dry with the surface water loss by evaporation. This process also affects or is accompanied by changes in the water content, soil temperature, surface energy balance, and soil water balance. In the following sections, the soil water evaporation stages are divided and variables associated with evaporation are discussed at different stages.

3.1. Soil Water Evaporation (Drying) Process. As shown in (11), the evaporation rate E (equals the total water flux at the soil surface), actually could be expressed as the sum of surface liquid and vapor water fluxes. Figure 2 presents diurnal variations of the two components of actual surface evaporation rate E . The surface liquid water flux $q_L(0, t)$ indicates vaporization of water occurring at the soil surface as long as its values are larger than 0, while the positive surface water vapor flux $q_v(0, t)$ indicates that water vaporized within the subsurface and its negative values represent that some water vapor was moving downward from the soil surface to deeper profiles. As shown in Figure 2(a), $q_L(0, t)$ totally dominated E until about the noon of day 5, indicating that evaporation was occurring at the soil surface. During this period, the soil was wet enough to supply water to accomplish vaporization of water, and soil evaporation was limited only

by the supply of energy. This could also be determined from Figure 3 which shows that the actual evaporation rate E equals to the potential evaporation rate during this period. $q_v(0, t) < 0$ (Figure 2(b)) is observed around the noon for some days, suggesting that some water vapor produced at the soil surface was moving downward driven by the large downward temperature gradient at noon. Between days 5 and 8 $q_L(0, t)$ was the dominant source early in the day and $q_v(0, t)$ took over for the rest of the day with some overlap where both $q_L(0, t)$ and $q_v(0, t)$ occurred simultaneously. During this period, the actual evaporation rate became less than the potential one (Figure 3) during afternoons. Beginning on day 9 values of $q_L(0, t)$ were close zero for the all days, and $q_v(0, t)$ became the dominant source of evaporation E (Figure 3), suggesting that vaporization of water occurred in the subsurface at most time of the day during this period. It is also notable that a very small negative $q_L(0, t)$ occurred around late afternoon after day 8, which resulted from the condensation of water vapor at the soil surface or in air when atmospheric evaporation demand decreased. From day 9 on, E/E_0 presented negative values around the noon, which was caused by the negative $q_v(0, t)$ during the same period in the result of the downward temperature gradient. In this case, E actually does not represent the rate of evaporation from the soil but indicates that the flux at the soil surface is moving towards deeper layers as the form of water vapor.

Thus, based on these results, the stages of evaporation process for the silt soil could be reasonably determined. Stage 1 evaporation was maintained from day 1 to the noon of day 5, indicated by $E/E_0 = 1$. Thereafter, stage 2 was maintained until the end of this numerical experiment, with a period as a transient stage in which the shift between $q_L(0, t)$ and $q_v(0, t)$ occurred alternately every day (from days 5 to 8). Stage 2 was also referred as falling rate stage evaporation because during this stage the actual evaporation rate E fell below the potential evaporation rate E_0 . There was no clear limit between stage 2 and stage 3 evaporation according to data shown in Figures 2 and 3. The so-called stage 3 evaporation,

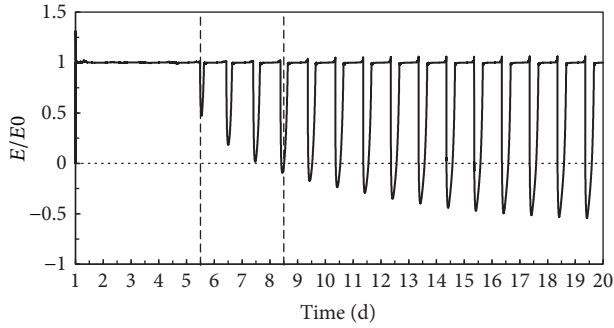


FIGURE 3: The temporal variation of ratio of actual evaporation rate (E) and potential (E_0) rate E/E_0 during the simulation period.

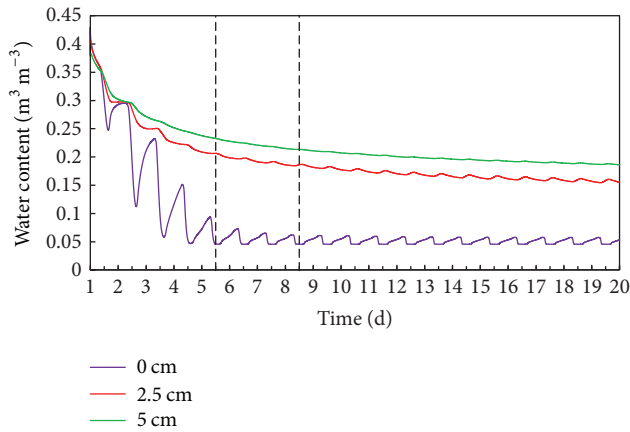


FIGURE 4: Simulated temporal variations of soil water contents at depths of 0, 2.5, and 5 cm during the soil drying after a rainfall event.

which was characteristic of the low and constant evaporation rate, was not considered to be very important and often merged into stage 2.

3.2. Soil Water Content and Temperature. Figure 4 presents temporal changes in the volumetric soil water contents at selected depths near the soil surface during a 20-d drying period immediately following a rain event before day 1 (i.e., at day 0). Soil water redistribution and soil drying began at day 1. Water contents near the soil surface decreased rapidly for the first few days, caused by gravity drainage and evaporation imposed by the hot and dry atmospheric conditions (Figure 1). The extent of water loss in the profile declined with depth, with more pronounced decrease occurring at the soil surface (0 cm) where the water content had a significant decrease from the maximum value of $0.43 \text{ m}^3 \text{ m}^{-3}$ at the beginning of day 1 to the minimum value of $0.046 \text{ m}^3 \text{ m}^{-3}$ at the noon of days 5 to 20 during stage 2. It is also notable that the water content near the soil surface (e.g., at 0 and 2.5 cm depths) displayed a distinct diurnal pattern, with it decreasing from late morning through the afternoon and then increasing from afternoon to late morning on the following day. This pattern during evaporation process was consistent with the findings from a number of field measurements [14, 28–31]. This diurnal pattern for surface water content

TABLE 3: Maximum and minimum values of soil water content and the corresponding time points.

Day	Min ($\text{m}^3 \text{ m}^{-3}$)	Day	Max ($\text{m}^3 \text{ m}^{-3}$)
1.6	0.247	1.0	0.43
2.6	0.112	2.2	0.30
3.6	0.058	3.3	0.23
4.6	0.047	4.3	0.15
5.5	0.046	5.3	0.09
6.5	0.046	6.3	0.07
7.5	0.046	7.3	0.07
8.5	0.046	8.2	0.06
9.5	0.046	9.2	0.06
10.5	0.046	10.2	0.06
11.5	0.046	11.2	0.06
12.5	0.046	12.2	0.06
13.5	0.046	13.2	0.06
14.5	0.046	14.2	0.06
15.5	0.046	15.2	0.06
16.5	0.046	16.2	0.06
17.5	0.046	17.2	0.06
18.5	0.046	18.2	0.06
19.5	0.046	19.2	0.06

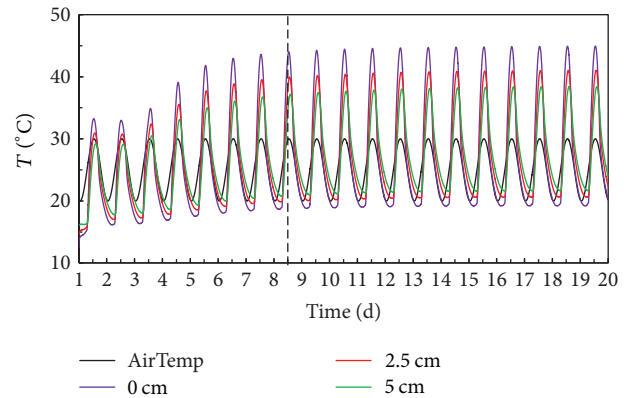


FIGURE 5: Simulated temporal variations of air temperature and soil temperatures at depths of 0, 2.5, and 5 cm during the soil drying.

derived from evaporation during daytime and subsequent soil rewetting during nighttime. The consistency between simulated patterns of soil water content in this study and observations in the field conditions supports the reliability of our models on reproducing the evaporative drying process of soils. The amplitude of diurnal pattern decreased with depth, with presenting a small fluctuation at 2.5 cm and no apparent trace for the deeper soil layer, for example, at 5 cm. After day 8, this diurnal pattern of soil water content at the soil surface maintained the same amplitude and magnitude, with maximum values of surface water content maintained at the same value of $0.06 \text{ m}^3 \text{ m}^{-3}$ and the maximum values of surface temperature at around 44.5°C (Table 3).

Figure 5 is the same as Figure 4 but for temporal changes in soil temperatures during the simulation period. It is clear

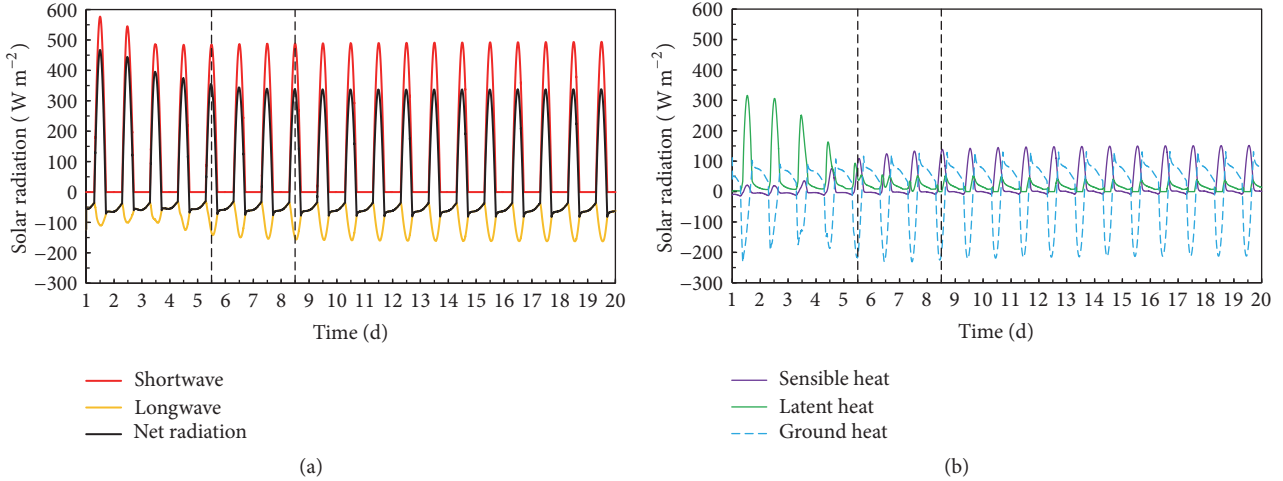


FIGURE 6: Simulated diurnal variations in surface energy balance components (namely, shortwave radiation, long radiation, net radiation, sensible heat flux, latent heat flux, and surface heat flux) during a 20-day drying period following a rainfall event.

that the soil temperatures at three depths all display a typical diurnal sinusoidal pattern over all the days, with its maximum temperatures occurring around noon (e.g., at 1 pm at 0 cm) and its minimum temperatures occurring just before the sunrise. In the early few days, the relatively uniform and large water content near the soil surface resulted in the uniform and large soil heat capacity (remember that soil heat capacity varies only as function of water content in soil). This resulted in a relatively uniform soil temperature profile for this period, with the daily temperature magnitudes and amplitudes being a little different between the three depths. On the other hand, the initially wet soil conditions combined with high-radiation atmospheric conditions caused a large amount of vaporization of water near the soil surface, causing more incoming solar radiation to be applied to accomplish vaporization rather than heating the soil. These effects caused relatively lower daily temperature magnitudes and amplitudes for the first few days. With the soil drying, both minimum and maximum temperatures in the shallow profile were increasing from day 1 to about day 8 (Table 4) during the first and transient stages since less and less incoming radiation energy was used for evaporation and a growing residual energy was applied to heat this soil during this period. The diurnal amplitude of soil temperature was also increasing during this period resulting from increase in the nonuniformity of soil heat properties in response to an increasing difference between soil water content values at the three depths for the corresponding period (Figure 4). The minimum and maximum temperatures reached around 19 and 44°C at the noon of day 8, respectively, showing larger diurnal temperature difference in the soil surface (23°C) than in air (10°C). Because of attenuation of the heat energy transported from the soil surface, the daily amplitudes of the soil temperature fluctuation also decreased with depth. The diurnal variation of temperature presented the similar magnitude and amplitude after day 8 (Table 4), which also may indicate a timing at which the transient stage was over.

TABLE 4: Maximum and minimum values of soil temperature and the corresponding time points.

Day	Min (°C)	Day	Max (°C)
1.0	12.5	1.5	33.2
2.2	16.1	2.5	33.0
3.2	16.3	3.6	34.9
4.2	16.9	4.6	39.1
5.2	17.5	5.5	41.8
6.2	18.0	6.5	43.0
7.2	18.4	7.5	43.6
8.2	18.6	8.5	44.0
9.2	18.8	9.5	44.3
10.2	18.9	10.5	44.5
11.2	19.0	11.5	44.6
12.2	19.1	12.5	44.6
13.2	19.1	13.5	44.7
14.2	19.2	14.5	44.8
15.2	19.2	15.5	44.8
16.2	19.2	16.5	44.9
17.2	19.2	17.5	44.9
18.2	19.2	18.5	44.9
19.2	19.2	19.5	44.9

3.3. Surface Energy Balance Components. Simulated diurnal variations of surface energy balance components are depicted in Figure 6. R_n and its two components (R_{ns} and R_{nl} in (12)) all reached maximum values at noon and both R_n and R_{nl} had minimum values just before the sunrise, with R_{ns} being values of 0 during nights. R_{ns} dominated R_n during daytime and R_{nl} dominated it during nighttime. Net radiation R_n and shortwave R_{ns} presented larger amplitudes for the first few days when the soil was relatively wet as compared than those for the rest of days. The relatively higher soil

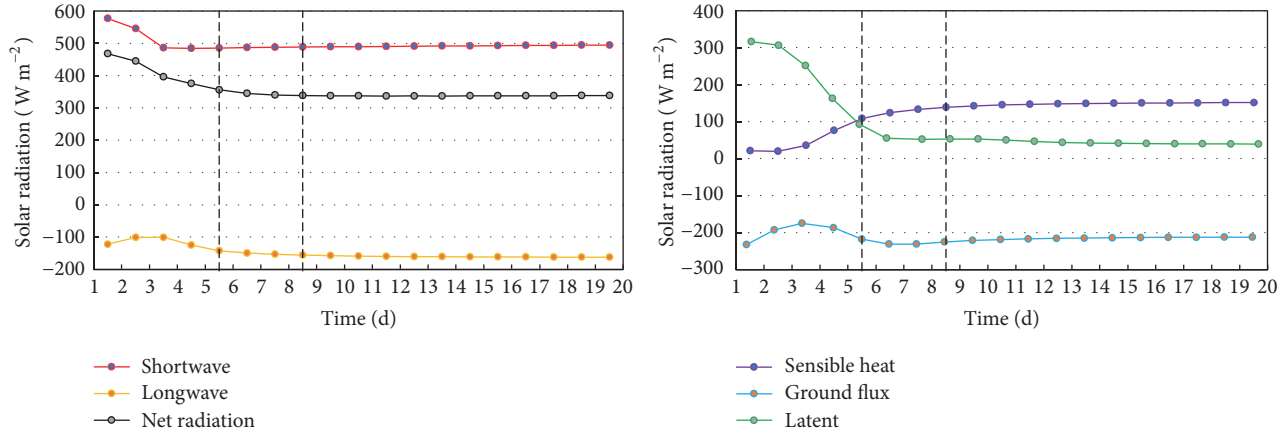


FIGURE 7: Diurnal maximum values of surface energy balance components depicted in Figure 4 (for R_{ns} and LE , negative diurnal maximum values are demonstrated).

moisture at the soil surface before about day 5 caused a lower soil albedo a (it had a negative relation with the surface water content in (12)); this, in turn, resulted in a smaller reflection of shortwave radiation which caused the higher shortwave R_{ns} and net radiations R_n . With the drying of the soil, the amplitudes in R_{ns} were decreasing until day 4 after which they remained constant (changes in amplitudes are indicated in Figure 7 which shows diurnal maximum values of surface energy balance components) when diurnal changes of the surface water content and its corresponding soil albedo were kept constant for the remaining days (Figure 4). The longwave radiation R_{nl} presented increasing amplitude with the increasing soil surface temperature at 1 and transient stages and then approached approximately constant value for the rest of days. R_{nl} was always downward (negative values), suggesting it would decrease the soil temperature by emitting the surface energy into the atmosphere. Net radiation R_n presented a rapid decrease amplitude at stage 1 and a slow decrease one at the transient stage and then kept a relative constant maximum value for the rest time (Figure 7).

The net radiation flux at the soil surface must accomplish the partitioning between the latent heat, sensible heat, and ground surface heat fluxes (11), depending on the hydraulic and thermal properties of the near-surface zone. The latent heat flux LE was typically high during the early few days when the soil was very moist and there was adequate water in the soil to maintain the high evaporation rate. As shown in Figure 7, the maximum value of LE approached $316 W m^{-2}$ at the noon of day 1, which accounted for 68% of the net radiation R_n at same time. LE decreased rapidly with the decreasing soil moisture at stage 1 and presented a very slow decrease at stage 2 (Figure 7). The maximum value of LE approached $55 W m^{-2}$ at the noon of day 5, which accounted for only 16% of R_n at same time, and with a constant ration of LE to R_n being 12% at the last six days when the water stored in surface layer was depleted. The sensible heat flux H , which was more related to the changes of surface soil temperature than the surface moisture, showed an inverse trend with LE and increased from very small values during the first two days to a relatively high and constant amplitude

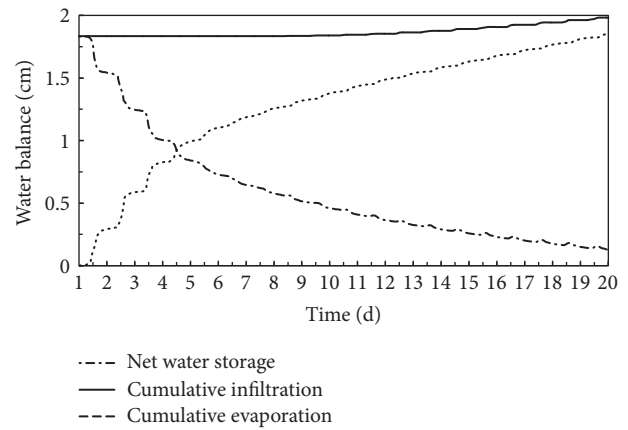


FIGURE 8: Temporal changes in the accumulation infiltration (solid line) and evaporation (dashed line) as well as the net water storage during the simulation period.

after day 8. The ground heat flux G did not present a distinct variation trend with the changes in the soil moisture or soil temperature during stage 1 and transient stage (Figure 7). That was because G was controlled by both the temperature gradient and moisture-dependent thermal conductivity λ of the soil, both of which had a positive relationship with the value of G . Thus, G reached its lowest value at the noon of day 3 when there were relatively lower values of both soil surface moisture and temperature and a highest value at the noon of day 6 when there were relatively higher values of both soil surface moisture and temperature. G presented a slow decreasing value after transient stage.

3.4. Soil Water Balance. In this section, variations of soil water balance during the drying process were analyzed to provide an additional way to improve the understanding of the soil water evaporation process. Calculated cumulative infiltration, cumulative evaporation, and change in the net water storage for the whole soil profile during the simulation period are shown in Figure 8. The net water storage change

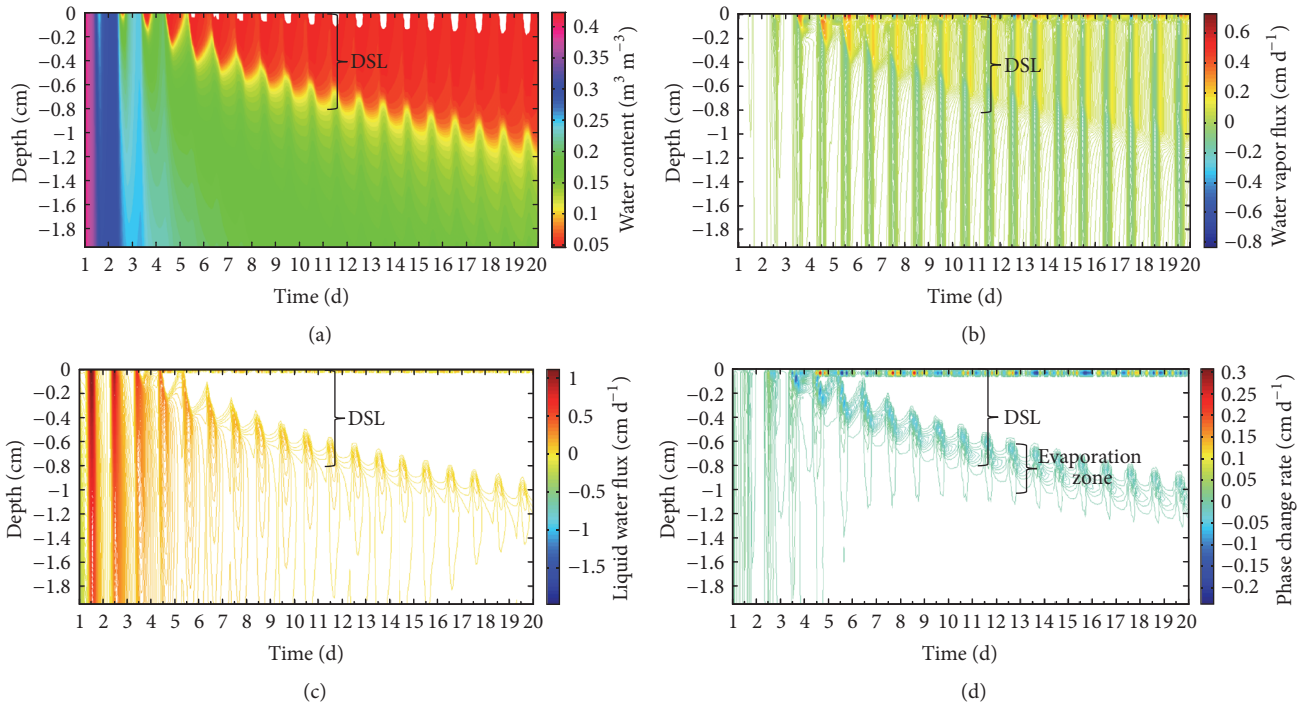


FIGURE 9: The spatiotemporal evolutions of (a) water content, (b) water vapor flux, (c) liquid water flux, and (d) evaporation zone during the drying period.

was obtained by subtracting the initial water storage value within the 50-cm profile from the water storage values for every node time. Because there was no runoff on the land and no water flowed out from the lower boundary of the soil domain from the result of this simulation, the infiltration water would be totally changed to the storage of water in the soil profile. Therefore, the change in the water storage was due only to the water loss of evaporation from the soil, namely, the water loss in the soil should be equal to the amount of evaporation. Clearly, the water infiltration process began on the rain day (not shown in Figure 8) during which there was a 2-cm precipitation. When this rainfall process terminated at 0 hour of day 1, the amount of cumulative infiltration reached 1.84 cm, which all were contributed to the increased amount of water storage in the profile indicated by the equal values between the cumulative infiltration and net water storage at 0 hour on day 1. At the same time, the cumulative evaporation was equal to 0 before the sunrise. The significant evaporation began before the noon of day 1 and then kept rapidly increasing during each afternoon period until around day 6, which was accompanied by the rapid decrease in the net water storage. At stage 1, it was clearly found that the shapes of “step” on the evaporation or net water storage curves were seen in Figure 8. This step indicated that the evaporation process concentrated on a certain period at each day (e.g., from 10 to 17 hours on day 2) under atmospheric demand conditions, with the little evaporation occurring at the rest of the day. After day 5, cumulated evaporation also kept increasing but with a relatively slow rate until the end of this simulation.

It is notable that the cumulated infiltration had a small increase from about the day 8 when the transient stage of

evaporation terminated. This may be surprising because there was no extra rainfall event to induce the infiltration during these days. Actually, this part of increase in infiltration was due to the condensation of water vapor in atmosphere or at the soil surface. This process occurs when the near-surface soil is extremely dry so that the air humidity exceeds the soil pore humidity and then the water vapor in the atmosphere will diffuse towards soil surface according to Fick’s law and condense there or within the soil. The amount of the increased infiltration due to condensation was about 0.148 cm until the end of day 20. This process may be a relatively important water production mechanism in semiarid or arid regions, especially in the desert areas.

3.5. DSL and Evaporation Zone. Once the surface moisture was depleted (i.e., the surface water content dropped too close to the critical value), the soil came in equilibrium with the overlying air and became approximately air-dry. This resulted in formation of DSL at the end of stage 1 evaporation. Figure 9 presents the spatiotemporal evolutions of water content, water vapor flux, and liquid water flux in the near-surface zone (the upper 2-cm profile) during the drying period, through which we could find the structure of DSL and its diurnal changes with the soil drying. As shown in Figure 9(a), the critical water content (the minimum value of water content under the drying condition) was about $0.05 \text{ m}^3 \text{ m}^{-3}$, which was also inferred from the temporal change in the water content at 0 cm in Figure 4. There was a distinct line which divided the plot of water content into two zones during the transition and stage 2 evaporation, with the upper zone being the DSL and the lower zone remaining wetter.

We also could infer the evolution information of the DSL from the diurnal dynamics of vapor and liquid fluxes in the profile; based on that water vapor flux dominated the DSL and liquid water flux dominated the layer below the evaporation zone. As shown in Figures 9(b) and 9(c), within the DSL, the liquid water flux was approximately the zero value, while the water vapor flux had a sharp increase within the DSL during daytime hours. From Figures 9(a)–9(c), it was found the distribution of the DSL presented the diurnal pattern, with it being at deeper profiles during daytime hours and shallower profiles during nighttime hours. With the drying of soil, the width of DSL became larger and finally reached a value of about 1.2 cm at the end of simulation.

It was also interesting to know the shape and width of the evaporation zone, in which the liquid water changed to the water vapor. This could be found from Figure 9(d), in which the distribution of phase change rate was presented. The phase change rate e was calculated from the following expression [4]:

$$e = \left(\frac{\partial q_v}{\partial z} + \frac{\partial \theta_v}{\partial t} \right) * dz, \quad (21)$$

where dz was the node distance in the numerical simulation. As depicted in this figure, the evaporation zone also displays a diurnal fluctuation with its distribution being more apparent during day time. With the progression of drying, the evaporation zone moved deeper in the soil and its width became narrower.

4. Conclusions

In this paper, we conducted a numerical simulation on the continuously evaporative drying process with 20-d clear sky conditions immediately following a 2-cm rainfall using the HYDRUS-1D software package. Our simulations provided a range of soil conditions from very wet after rainfall to thorough dry. Various stages of evaporation process could be determined from results of simulation. At stage 1, the actual evaporation rate was same as the potential evaporation rate before the noon of day 5 during which the liquid water flux at the soil surface was the sole source of evaporation. During the transient stage between days 6 and 9, the evaporation of the soil came from both the liquid water and vapor fluxes at the soil surface accompanying the ratio of actual to potential evaporation rates E/E_0 less than 1. And after day 9, the water vapor flux became the dominant source of evaporation for stage 2. There was a distinct rewetting of soils during the soil cooling period at stage 2, either because of the liquid water moving upwards from below or condensation of water vapor from the atmosphere. When the soil moisture was depleted, the location of evaporation zone moved into the subsurface and DSL formed immediately above the evaporation zone. Both the DSL and evaporation zone displayed a diurnal pattern during the transition and stage 2 evaporation. The width of DSL became wider with the progressive drying of the soil, while the width of evaporation zone behaved in the inverse trend. The corresponding changes in the soil moisture, soil temperature, surface energy balance, and soil water balance during different stages of evaporation were fully discussed in

this paper, which, in turn, may be as some indicators for the division of stages for the evaporation process.

Conflicts of Interest

The authors declare that there are no conflicts of interest regarding the publication of this paper.

Acknowledgments

This study was supported by the National Natural Science Foundation of China (Grant no. 41602263) and the National Key Research and Development Program of China (Grant no. 2016YFC0402804).

References

- [1] D. R. Maidment, *Handbook of hydrology*, McGraw-Hill Inc, New York, NY, USA, 1992.
- [2] J. Han, Z. Zhou, Z. Fu, and J. Wang, "Evaluating the impact of nonisothermal flow on vadose zone processes in presence of a water table," *Soil Science*, vol. 179, no. 2, pp. 57–67, 2014.
- [3] J. L. Heitman, X. Xiao, R. Horton, and T. J. Sauer, "Sensible heat measurements indicating depth and magnitude of subsurface soil water evaporation," *Water Resources Research*, vol. 44, Article ID W00D05, 2008.
- [4] M. Sakai, S. B. Jones, and M. Tuller, "Numerical evaluation of subsurface soil water evaporation derived from sensible heat balance," *Water Resources Research*, vol. 47, no. 2, Article ID W05901, 2011.
- [5] G. Y. Qiu and J. Ben-Asher, "Experimental determination of soil evaporation stages with soil surface temperature," *Soil Science Society of America Journal*, vol. 74, no. 1, pp. 13–22, 2010.
- [6] X. Xiao, R. Horton, T. J. Sauer, J. L. Heitman, and T. Ren, "Cumulative soil water evaporation as a function of depth and time," *Vadose Zone Journal*, vol. 10, no. 3, pp. 1016–1022, 2011.
- [7] J. W. Gowing, F. Konukcu, and D. A. Rose, "Evaporative flux from a shallow watertable: The influence of a vapour-liquid phase transition," *Journal of Hydrology*, vol. 321, no. 1–4, pp. 77–89, 2006.
- [8] M. Gran, J. Carrera, S. Olivella, and M. W. Saaltink, "Modeling evaporation processes in a saline soil from saturation to oven dry conditions," *Hydrology and Earth System Sciences*, vol. 15, no. 7, pp. 2077–2089, 2011.
- [9] M. D. Novak, "Dynamics of the near-surface evaporation zone and corresponding effects on the surface energy balance of a drying bare soil," *Agricultural and Forest Meteorology*, vol. 150, no. 10, pp. 1358–1365, 2010.
- [10] D. A. De Vries and J. R. Philip, "Soil heat flux, thermal conductivity, and the null-alignment method," *Soil Science Society of America Journal*, vol. 50, no. 1, pp. 12–18, 1986.
- [11] B. A. Kimball and R. D. Jackson, "Soil heat flux determination: a null-alignment method," *Agricultural and Forest Meteorology*, vol. 15, no. 1, pp. 1–9, 1975.
- [12] C. L. Mayocchi and K. L. Bristow, "Soil surface heat flux: some general questions and comments on measurements," *Agricultural and Forest Meteorology*, vol. 75, no. 1–3, pp. 43–50, 1995.
- [13] J. Hatfield, J. Baker, L. J. Fritschen, and C. L. Fritschen, "Bowen Ratio Energy Balance Method," in *Micrometeorology in Agricultural Systems*, 2005, 397–405.

- [14] J. L. Heitman, R. Horton, T. J. Sauer, and T. M. DeSutter, "Sensible heat observations reveal soil-water evaporation dynamics," *Journal of Hydrometeorology*, vol. 9, no. 1, pp. 165–171, 2008.
- [15] P. Deol, J. Heitman, A. Amoozegar, T. Ren, and R. Horton, "Quantifying nonisothermal subsurface soil water evaporation," *Water Resources Research*, vol. 48, no. 11, Article ID W11503, 2012.
- [16] J. R. Philip and D. A. de Vries, "Moisture movement in porous materials under temperature gradients," *Eos, Transactions American Geophysical Union*, vol. 38, no. 2, pp. 222–232, 1957.
- [17] J. Šimůnek, M. T. van Genuchten, and M. Šejna, "Recent developments and applications of the HYSDRUS computer software packages," *Vadose Zone Journal*, vol. 15, no. 7, 2016.
- [18] M. T. van Genuchten, "A closed-form equation for predicting the hydraulic conductivity of unsaturated soils," *Soil Science Society of America Journal*, vol. 44, no. 5, pp. 892–898, 1980.
- [19] H. Saito, J. Šimůnek, and B. P. Mohanty, "Numerical analysis of coupled water, vapor, and heat transport in the vadose zone," *Vadose Zone Journal*, vol. 5, no. 2, pp. 784–800, 2006.
- [20] S. Chung and R. Horton, "Soil heat and water flow with a partial surface mulch," *Water Resources Research*, vol. 23, no. 12, pp. 2175–2186, 1987.
- [21] G. Boulet, I. Braud, and M. Vauclin, "Study of the mechanisms of evaporation under arid conditions using a detailed model of the soil-atmosphere continuum. Application to the EFEDA I experiment," *Journal of Hydrology*, vol. 193, no. 1-4, pp. 114–141, 1997.
- [22] K. Noborio, K. J. McInnes, and J. L. Heilman, "Two-dimensional model for water, heat, and solute transport in furrow-irrigated soil: I. Theory," *Soil Science Society of America Journal*, vol. 60, no. 4, pp. 1001–1009, 1996.
- [23] C. H. M. van Bavel and D. I. Hillel, "Calculating potential and actual evaporation from a bare soil surface by simulation of concurrent flow of water and heat," *Agricultural and Forest Meteorology*, vol. 17, no. 6, pp. 453–476, 1976.
- [24] P. J. Camillo and R. J. Gurney, "A resistance parameter for bare-soil evaporation models," *Soil Science*, vol. 141, no. 2, pp. 95–105, 1986.
- [25] M. Bittelli, F. Ventura, G. S. Campbell, R. L. Snyder, F. Gallegati, and P. R. Pisa, "Coupling of heat, water vapor, and liquid water fluxes to compute evaporation in bare soils," *Journal of Hydrology*, vol. 362, no. 3-4, pp. 191–205, 2008.
- [26] A. A. van de Griend and M. Owe, "Bare soil surface resistance to evaporation by vapor diffusion under semiarid conditions," *Water Resources Research*, vol. 30, no. 2, pp. 181–188, 1994.
- [27] J. Šimůnek, M. T. Van Genuchten, and M. Šejna, "Development and applications of the HYDRUS and STANMOD software packages and related codes," *Vadose Zone Journal*, vol. 7, no. 2, pp. 587–600, 2008.
- [28] A. T. Cahill and M. B. Parlange, "On water vapor transport in field soils," *Water Resources Research*, vol. 34, no. 4, pp. 731–739, 1998.
- [29] R. Bruce and R. D. Jackson, "Diurnal changes in soil water content during drying," in *Field Soil Water Regime*, 1973, 37–55.
- [30] C. W. Rose, "Water transport in soil with a daily temperature wave. I. theory and experiment," *Australian Journal of Soil Research*, vol. 6, no. 1, pp. 31–44, 1968.
- [31] A. Verhoef, J. Fernández-Gálvez, A. Diaz-Espejo, B. E. Main, and M. El-Bishti, "The diurnal course of soil moisture as measured by various dielectric sensors: Effects of soil temperature and the implications for evaporation estimates," *Journal of Hydrology*, vol. 321, no. 1-4, pp. 147–162, 2006.

Research Article

Cl⁻ as a Chemical Fingerprint of Solute Transport in the Aquitard-Aquifer System of the North Jiangsu Coastal Plain, China

Qin Ge,¹ Xing Liang,^{1,2} Menggui Jin,^{1,3} Jing Li,¹ and Yan Liu⁴

¹School of Environmental Studies, China University of Geosciences, Wuhan 430074, China

²Hubei Province Key Laboratory of Wetland Evolution and Ecology Restoration, China University of Geosciences, Wuhan 430074, China

³State Key Laboratory of Biogeology and Environmental Geology, China University of Geosciences, Wuhan 430074, China

⁴Key Laboratory of Ministry of Land and Ground Fissure Disaster, Nanjing 210018, China

Correspondence should be addressed to Qin Ge; geqin90827@126.com and Xing Liang; xliang@cug.edu.cn

Received 14 July 2017; Revised 4 October 2017; Accepted 17 October 2017; Published 9 November 2017

Academic Editor: Xiaoqing Shi

Copyright © 2017 Qin Ge et al. This is an open access article distributed under the Creative Commons Attribution License, which permits unrestricted use, distribution, and reproduction in any medium, provided the original work is properly cited.

Detailed vertical profiles of Cl⁻ in porewaters through the aquitard-aquifer system were used to yield solute transport mechanism and build a conceptual model regarding evolution processes and transport time of natural tracer migration in North Jiangsu coastal plain, China. One-dimensional vertical simulated models of Cl⁻ profiles illustrate that diffusion appeared to be the dominant solute transport mechanism in the aquitard-aquifer system. A downward groundwater flow did not improve the fitness between simulated and measured values. Several simulated models were constructed and suggested that the evolution of the Cl⁻ profiles is mainly ascribed to the introduction of seawater and freshwater of transgression-regression to the first confined aquifer and the upper boundary. Groundwater in the first confined aquifer recharged by the Late Pleistocene glacial meltwater (25–15 ka BP) was supported in response to the low Cl⁻ concentrations. The shallow groundwater in the first confined aquifer and porewater with high salt were attributable to the Holocene seawater intrusion. These timeframes were also consistent favorably with the results of previous studies into the palaeohydrology of the study area.

1. Introduction

Aquitards frequently seem to have the ability to contain high salinity relative to aquifers [1, 2]. Many researches have been conducted on the thicker, nonfractured clay-rich and shale units with the bulk hydraulic conductivity (K) below 1×10^{-10} m/s [3–6]. Under such conditions, solute transport in the aquitards is demonstrated to be dominated by molecular diffusion [7, 8].

Shaw and Hendry [9] suggest that the thickness of clay-rich aquitard was requested to be >60 m in order to avoid the occurrence of the initial interferences among the advective-diffusive solute profiles. However, the water-bearing units (aquifers or sand streaks) with various thicknesses were often interspersed within aquitards [6, 10–12] and particularly marked in the late Quaternary sediments of coastal plains

in China due to the transgression-regression effect [13]. Critically, these occurrences could cause perturbations in transport paths and partial advection solute transport in porewater profiles and lead to problems with the interpretation of the palaeohydrogeological information [12]. Despite the potential for significant advective migration during tracer profiles, diffusion was determined as the pure transport mechanism controlling solute transport in the aquitard-aquifer system based on the researches of Kuang et al. [14, 15]. Geochemical tracers were used to define and constrain long-term transport mechanisms and preserve a historical record of the major palaeohydrologic events at the aquitard scale [6, 10–12, 16]. Although solute transport in the aquitards had been conducted in many studies, the porewater transport mechanism and processes in clay-rich aquitards interspersed with the cooccurrence of multiple aquifers

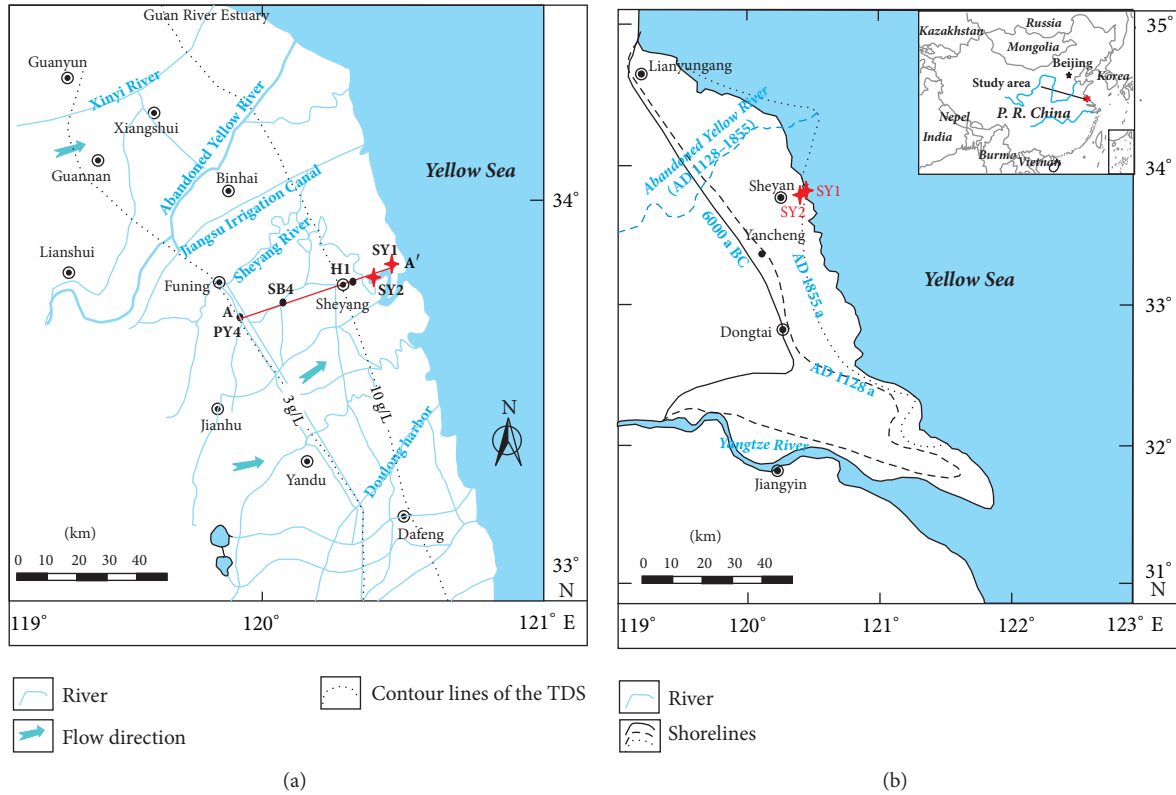


FIGURE 1: (a) Location map of the research area and (b) various shorelines of different time in the study area (modified after Liu et al. [22]).

of coastal area need more studies to support and further confirm.

North Jiangsu coastal plain (NJCP) is located in the eastern part of China, adjacent to the south Yellow Sea (Figure 1). This study area belongs to the part of the new Silk Road, where groundwater resource plays a pivotal role in promoting social and economic development. However, groundwater in this region has been mostly seriously affected by seawater intrusion because of the Quaternary transgressions [17, 18]. To ensure the sustainable development of the new Silk Road, the management of the groundwater resource should be given considerable attention. Most of the previous studies in this area have focused on the detailed investigation of the change and evolution of regional groundwater quality [19, 20]. Additionally, saline groundwater in the aquitards and aquifers has been studied to investigate the hydrogeochemical characteristics and chemical evolution processes [21]. Nevertheless, an understanding of the saline transport mechanism and processes in the aquitard-aquifer system is still very limited in such coastal areas.

The aim of this work is to investigate the solute transport mechanism and evolution processes in the aquitard-aquifer system and provide additional palaeohydrogeologic information using Cl^- concentration vertical profiles. The specific objectives of this study are to (1) obtain the effective diffusion coefficients (D_e) and K of the studied vertical deposition profiles on the basis of laboratory experiments, (2) apply 1D vertical transport model of the Cl^- profiles to gain insight into the dominant solute transport mechanism in the

aquitard-aquifer system, and (3) explore a more detailed synthesis of the time of paleohydrologic and formative geologic events for tracer profiles in the aquitard-aquifer system.

2. General Description of the Field Site

2.1. Hydrogeological Setting. The current study is conducted on the Late Pleistocene and Holocene clay-rich deposits in NJCP, a part of China's Eastern Plain (Figure 1). The NJCP has a continental and maritime climate and the average annual temperature of 13–16°C. Annual precipitation averaged approximately 800–1,200 mm and nearly 30–60% of the annual precipitation falls between June and September [25]. The annual evaporation is about 900–1,050 mm.

The depositional facies of the deposits change from west to east, progressing from alluvium to proluvial sediments and then marine sediments on the coastal plain, mainly because of the development of the Huai River, the Yellow River, and the sea level change [23, 26, 27]. A gradual and vertical Quaternary sediment shift is observable from the single continental alluvial to the transitional sediments between land and marine facies [17, 18]. The depositional facies of the research area can be classified into three groups: continental facies, marine facies, and transitional facies. Quaternary continental facies mainly refer to fluvial alluvial facies and fluvial-lacustrine alluvial facies [17, 18]. Marine facies are composed of littoral facies and shallow sea facies. Transitional facies occurred along the coast consist of estuarine, lagoon, intertidal, and residual seawater zone.

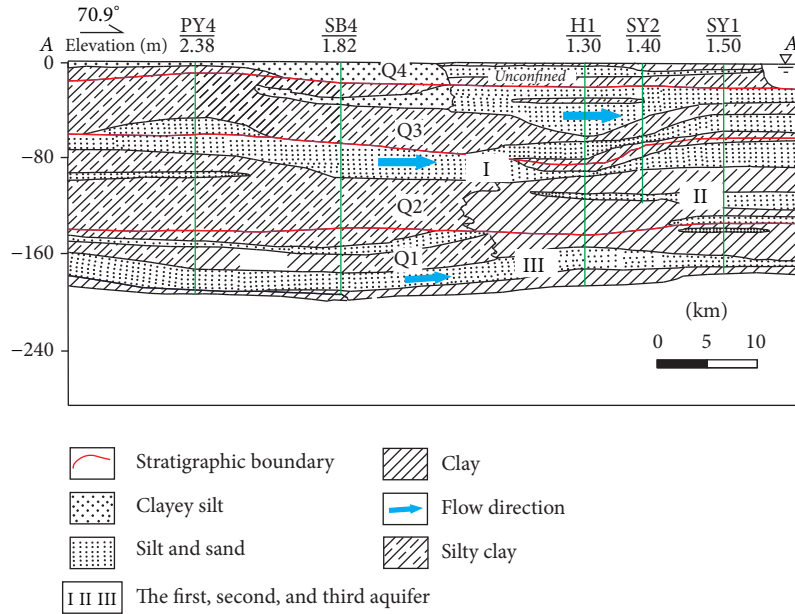


FIGURE 2: A–A' cross section of the study area (modified after Fu [20]). I, II, and III represent first, second, and third confined aquifers.

The major aquifer is composed of the multilayered aquifer groups on the east coast (Figure 2). The phreatic aquifer and the first, second, and third confined aquifers are recognized in this study area and composed of Quaternary sediments with a thickness of 10–50 m [19]. These aquifers consist of sandy gravel, medium-fine sand, and fine sand and are separated by silt- and clay-dominated aquitards. The aquifers are characterized by a complex multilayered framework due to the special geographical position and complex climate conditions (Figure 2).

The burial depth of the phreatic aquifer and the first confined aquifer are generally less than 5 and 60 m, respectively. Groundwater in the phreatic aquifer and the first confined aquifer corresponding to the Holocene and the Late Pleistocene formations is mostly saline with total dissolved solids (TDS) generally over 3 g/L. Freshwater can be found in the bottom of the first confined aquifer. The TDSs of saline water exhibit an increasing trend from the west to east. Groundwater in these aquifers belongs to Cl-Na water type, with a small amount of HCO₃-Cl-Ca-Na type, which was derived from the Holocene seawater [20] and then mixed with the recharge of precipitation and irrigation water. Evaporation and exploitation are the main discharge pathways. Groundwater exploitation is limited due to the high salinity.

The burial depths of the second and third confined aquifers were usually shallower than 140 and 250 m, respectively. Groundwater in the second confined aquifer illustrated the chemical signature of fresh water and was trapped in the fluvial deposits during the Middle Pleistocene, which was possibly recharged during a colder period in the Late Pleistocene [28]. The third confined aquifer groundwater is mainly characterized by less saline with TDS below 2.0 g/L, except some areas in the northeast with TDS values extremely higher than 2.0 g/L [19, 20]. The salinity of some groundwater in the third aquifer was attributed to the entrapped relict

seawater of the Late Pleistocene. The hydrochemical compositions of groundwater in the second and third confined aquifer are mostly HCO₃-Na, HCO₃·Cl-Na-Ca, Cl-Na, and Cl-Ca-Na. Groundwater runoff conditions are poor and the water circulation is slow gradually, which are current targets for exploitation and major water resource for local residents. Groundwater ages in the second and third aquifers were assumed to be around 30 ka BP on the basis of carbon isotopic dating (¹⁴C) [20, 28]. As a result of the lack of clay aquitards locally, the leakage recharge from the upper shallow groundwater is possibly regarded as the main sources for deep confined groundwater during groundwater exploitation, and the corresponding discharge is artificial extraction.

2.2. Transgressions and Regressions. It is believed that this study area has undergone many times of transgressive-regressive processes since Quaternary [29, 30]. In the early Middle Pleistocene, climate warming, strong surface runoff, and enhancement of river erosion caused the deposition of the clayey sediment interbedded with silt. Subsequently, the first transgression occurred as a result of sea level rise, and the range and degree were smaller.

The scope of the two other transgressions in the Late Pleistocene (Marine Isotope Stage (MIS) 5, about 110–70 ka BP; MIS 3, about 40–25 ka BP) expanded gradually [31]. These two transgressions corresponded to the depth of approximately 30–90 m in the study region. The shoreline of the second transgression (MIS 5) reached the above 5–7 m of the modern coastline, and all of the study area suffered from marine environment [29]. The transgression in the MIS 3 was relatively small, and the deposition environment might be subaerial exposure [32]. The sea level in MIS 3 seemed to not reach the location of the modern sea level in the study area and generally agreed that the coastline was close to or below 10–20 m of the modern shoreline [29]. In other

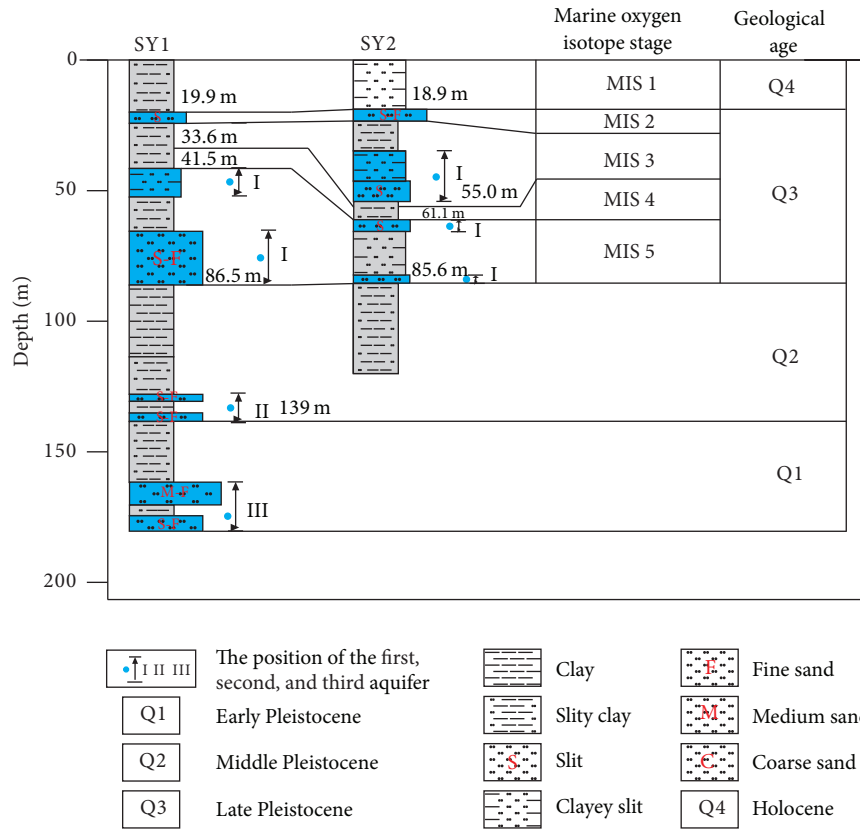


FIGURE 3: Geological profiles, time periods of the drilled boreholes in NJCP, along with hydrostratigraphic interpretation. The marine oxygen isotope stages are determined by the marine micropaleontology identification. I, II, and III represent the positions of first, second, and third confined aquifers.

words, the sea level regressed from this region with the time of 70–10 ka BP (MIS 2–4), and the corresponding sediments probably suffered from weathering denudation [33]. In the Holocene (MIS 1), the sea level rose rapidly and large-scale seawater intrusion occurred, resulting in an interactive marine and terrestrial deposit with a whole transgression-to-regression succession [22, 34]. It was not until AD 1,128 that the coastline then moved eastward rapidly and seawater gradually retreated from this region [35].

2.3. Boreholes Description. Two stratigraphic boreholes were drilled about 10 km apart (Figure 1). The first borehole (SY1) had a depth of 250 m and was located approximately 10 km west of the southern Yellow Sea shore (33.86° N, 120.43° E). In this study, the upper section with the depth of 2–182 m was conducted. The second borehole had a depth of 120 m and was located approximately 20 km west of the southern Yellow Sea shore (33.80° N, 120.32° E). The stratigraphic columns of the two boreholes were presented in Figure 3 reference to the field logs. 1–2 m below ground was considered to be the oxidized and fractured layer due to the fluctuation of water table, and the underlying deposits were regarded as unoxidized zone. There was a lack of downward water flow in the oxidized layer because of its fractured features and discontinuity [36]. The oxidized layer was outside the range of this study. Although the two boreholes were very close to each other, the marine

layers have different degrees of inclination toward the sea because of neotectonic activity [13].

Three transgressive events were confirmed to have occurred in the study area and were named, from the earliest to the latest: *the Asterorotalia* transgression, *the False Rotifer* transgression, and *the Winding Worms* transgression. Species such as *Ammonia annectens*, *A. beccarii* var., and *Rosalina bradyi* were found in the surficial aquitard (grey-yellow) with a depth of 0–19.9 m in borehole SY1 and 0–18.9 m in borehole SY2, suggesting that these depths belonged to MIS 1 period. Correspondingly, the occurrence of a large number of *Pseudorotalia schroeteriana* indicates the underlying aquitard at depth of 23.8–33.6 m in SY1 and 23.3–54.2 m in SY2 formed in MIS 3. Deposits at depth of 41.5–86.5 m in SY1 and 61.1–85.6 m in SY2 developed during the MIS 5 period and were attributable to the presence of the warm species *Pseudorotalia indopacifica* and *Asterorotalia pulchella*.

3. Material and Methods

3.1. Borehole Sampling and Analysis. In this study, core samples were collected from 2 to 182 m in borehole SY1 between January and February 2013 using a rotary drill. Additional core samples were collected from 10.6 m to 120 m in borehole SY2 in December 2014. For these study profiles, subsamples were taken every 2–5 m at the SY1 and SY2 drilling sites. To

ensure that no drilling fluid contaminated the collected samples, immediately after retrieval and before packing, the outer 2–3 cm of the samples were removed and discarded. Sample was packaged in a sealable aluminum barrel (in length of 20 cm and diameter of 8 cm) and sealed with wax, which was prepared for chemical analysis. Samples were collected on-site by 10 mL glass bottles to extract porewater for stable isotopic analysis and were sealed using raw adhesive tape immediately after sampling to prevent fractionation caused by evaporation. The packaged borehole samples were placed in coolers (at approximately 4–5°C) with ice bags in the field for transport to the School of Environmental Studies of the China University of Geoscience, where samples were stored at 4–5°C prior to analysis, to minimize the growth of microorganisms.

The high-pressure mechanical squeezer (HPMS) using nitrogen was employed on the sealed core samples for porewater extraction. The HPMS was designed and developed based on the *ex situ* squeezing device described in detail by Li et al. [37]. The application of a pressure-controlled noble gas to a sample forced porewater to separate from the sediment. The operational pressure of the HPMS was controlled within an allowable range of 0–8 MPa, with an analytical precision of 0.2 MPa. The outermost 1–2 cm of the prepared core samples was scraped to discard any materials that could have been altered by exposure to the atmosphere (oxidation). Approximately 1,000 g soil samples were conducted to ensure that enough porewater was provided for analysis. To avoid overconsolidation or destruction of the clay-pore system, the applied stress was increased to 8 MPa gradually rather than in a single step. First, a small stress of approximately 1 MPa was initially applied to expel most of the air in the sample chamber and to ensure that the sample was bedded. Second, the applied stress was increased by 1 MPa every 4–5 hours during the day. Finally, core samples were compressed and consolidated under pressure for 3–4 days. Meanwhile, porewater flowed out from the center hole of the bottom endplate through 0.45 μm filter paper and was collected in a clean plastic bottle. The water samples were weighed and filtered through a 0.45 μm membrane and immediately stored in a refrigerator at 4°C before being analyzed.

For stable isotopes analysis, porewater was extracted from the collected core samples using vacuum distillation, reducing the influence of air during the porewater collection process. The final distillation temperature keeps 120°C for 6–7 h. All extracted water samples were kept in a refrigerator at around 4°C.

Porewater samples of borehole SY1 ($n = 27$) and SY2 ($n = 24$) were analyzed for Cl^- and Br^- concentration analysis using ion chromatography (ICS-1100, Dionex, Sunnyvale, CA, USA) at the School of Environmental Studies, China University of Geosciences. The analytical precision for Cl^- and Br^- concentration was greater than 0.01 mg/L.

Stable isotope analysis in borehole SY1 and SY2 was conducted at the State Key Laboratory of Water Resources and Hydropower Engineering Science of Wuhan University and the Laboratory of Geological Survey Institute, China University of Geosciences in Wuhan, respectively. These isotope samples of SY1 and SY2 boreholes were analyzed with mass gas isotopic ratio mass spectrometry (MAT 253, Thermo

Fisher Scientific, Waltham, MA, USA, with an analytical precision of $\pm 0.2\text{‰}$ and $\pm 2\text{‰}$, resp.) and a liquid water isotope analyzer (LGR, IWA-45EP, USA, with an analytical precision of $\pm 0.1\text{‰}$ and $\pm 0.5\text{‰}$, resp.), with values reported relative to Vienna Standard Mean Ocean Water (V-SMOW).

3.2. Laboratory Test

3.2.1. Porosity. The porosities of the soil samples from the saturated zone were determined. To avoid samples being in an unsaturated state caused by the release of confining pressure during the sampling process, samples were secondarily saturated using the vacuum saturation method for more than 72 h. The porosity of selected samples was determined using a cutting ring with a specific volume ($119.9 \times 10^{-6} \text{ m}^3$). Eight samples from the borehole SY1 and 25 samples from the borehole SY2 were dried at 105°C for 48–72 h for analysis of their total porosities (n_T), as shown in Figure 4.

3.2.2. Hydraulic Conductivity. The K values of the samples in the profiles were determined using a laboratory testing method on undisturbed samples. A laboratory hydraulic conductivity tester was designed on the basis of a TST-55 permeameter, consisting of a cutting ring, two porous plates, a lantern ring, a top cover, a bottom cover, several screws, and pressure-resistant water supply bottle [38]. An external vacuum compressor was added to ensure that the K of low-permeability clay was measured with high efficiency (Figure 5). The tester functioned within the operating pressure range of 0–0.6 MPa which was controlled with a precision regulator with an analytical precision of 0.02 MPa. The water flow in the low-permeability samples approximately followed at a constant pressure head. The external pressure generated by the air compressor was the most influential factor controlling water flow in the laboratory experiment. The change in the water supply bottle level was much lower than the external pressure head, and its function could be neglected (verifying test has been done but not present in this paper). Hydraulic pressure was produced in the water outlet if water flowed through the samples quickly during the experimental process, and then drip leakage was allowed in the test. For high-permeability samples (e.g., sand or silt deposits), an external vacuum compressor was ineffective, and the pressure head was provided by the water level of the supply bottle. K was calculated using falling down head equations in accordance with *highway engineering test methods for soils* (2007) [39]. Testing results show that K of the clay-rich zone varied with depth in the borehole SY1 from 7.3×10^{-10} to 1.5×10^{-11} m/s, and K of silt-rich samples were between 2.6×10^{-8} and 1.8×10^{-9} m/s (Figure 4).

3.2.3. Diffusion Testing. Many different laboratory diffusion testing techniques for low-permeability materials have been reviewed [40]. The radial diffusion method was selected to apply in this study, because of its suitability for low-permeability aquitards and its high efficiency [41–43]. The radial diffusion device was developed with special stainless steel, consisting of a tube, the upper cap, and the lower cap [44]. The height and internal diameter of the tube were 10 cm

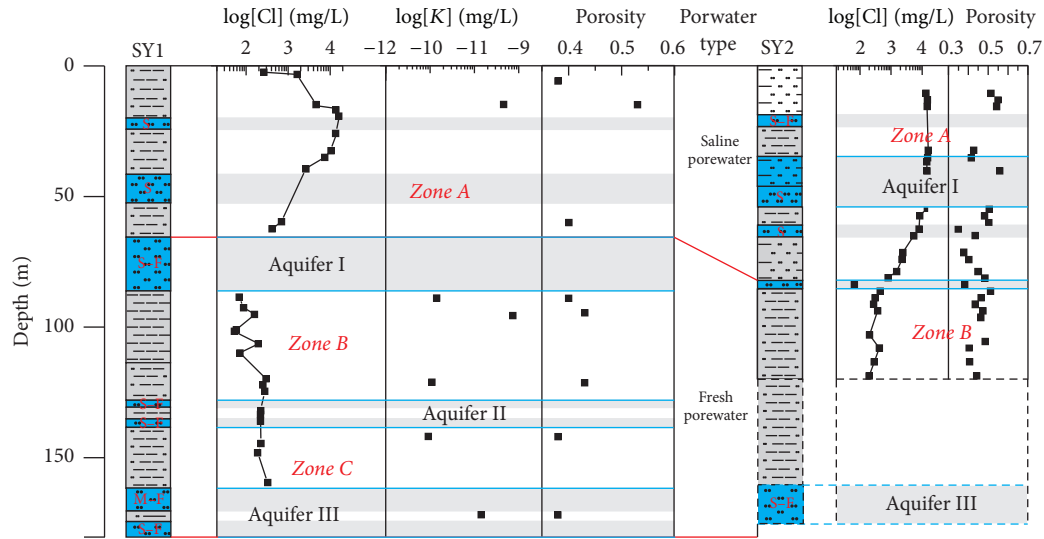


FIGURE 4: Geologic profiles and hydrogeologic zones, the measured Cl^- concentrations, hydraulic conductivity, porosity versus depth, and porewater types. The black dotted bordered rectangles represent the sediments that were not revealed in the borehole SY2.

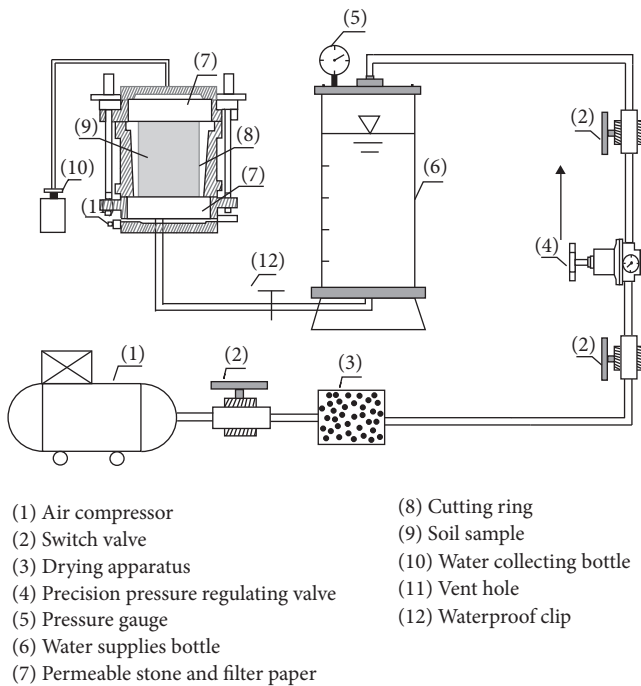


FIGURE 5: Device for measuring the K of saturated clay-rich deposits.

and 7 cm, respectively, as shown in Figure 6. A hole (length of 9 cm and diameter of 3 cm) was drilled along the central axis of the sample as a reservoir. Subsequently, water with a certain Cl^- concentration was injected into the reservoir. The application of Cl^- online monitoring in the reservoir assisted the recording of the concentration variation. To ensure that the probe of Cl^- online monitoring contacted the water in the reservoir easily, a spiral hole with the diameter of 3.0 cm was drilled on the upper cap.

Diffusing testing results were analyzed using the COMSOL software (COMSOL 4.4, Burlington, MA, USA) [45, 46]

according to the initial and boundary conditions of the experimental model. The measured D_e of Cl^- was $4.5 \times 10^{-10} \text{ m}^2/\text{s}$ for a SY1 core sample (porosity, 0.4, depth 54.95–55.15 m, and laboratory temperature 12°C), and $3.5 \times 10^{-10} \text{ m}^2/\text{s}$ for a SY2 core sample (porosity, 0.5, depth 32.8–33.0 m, and laboratory temperature 24°C). The measured D_e values were corrected to the mean groundwater temperature (14°C) on the basis of the relationship between temperature and viscosity [47]. The corrected D_e values of Cl^- for borehole SY1 and SY2 samples were $4.3 \times 10^{-10} \text{ m}^2/\text{s}$ and 2.7×10^{-10} , respectively.

4. Results and Discussion

4.1. Salt Source of Porewater. Salt in groundwater derives from several possible sources. The relationship of Cl^- and Br^- was always applied to determine the origin of groundwater salinity, since the Cl/Br ratios keep constant during the dilution and evaporation process of seawater prior to halite precipitation [48, 49]. Besides, Cl^- concentrations together with $\delta^{18}\text{O}$ and $\delta^2\text{H}$ values were further to characterize the salinization process of groundwater [50].

The Cl/Br mass ratios of SY1 saline porewater have a mean value of 203.6 below the near-shore seawater values. For SY2 saline porewater, Cl/Br mass ratios scatter around the near-shore seawater values with a mean value of 315.7. The quasilinear relationship of Cl^- and Br^- (Figure 7(a)) and the plot of Cl^- and $\delta^2\text{H}$ (Figure 7(b)) suggest saline porewater salinity was derived from seawater. Most of the saline porewater plotted closely to the diluted line of standard seawater, indicating that the original porewater has been mixed by freshwater. The relationship of Cl^- and $\delta^2\text{H}$ in SY1 suggests that the low Cl/Br mass ratios were probably attributed to the release of Br^- from diagenesis of marine organic material [51]. Thus, Cl^- could be assumed to behave conservatively and serve as a good natural tracer to quantify mechanism of solute transport.



FIGURE 6: Radial diffusion system and Cl⁻ online monitor.

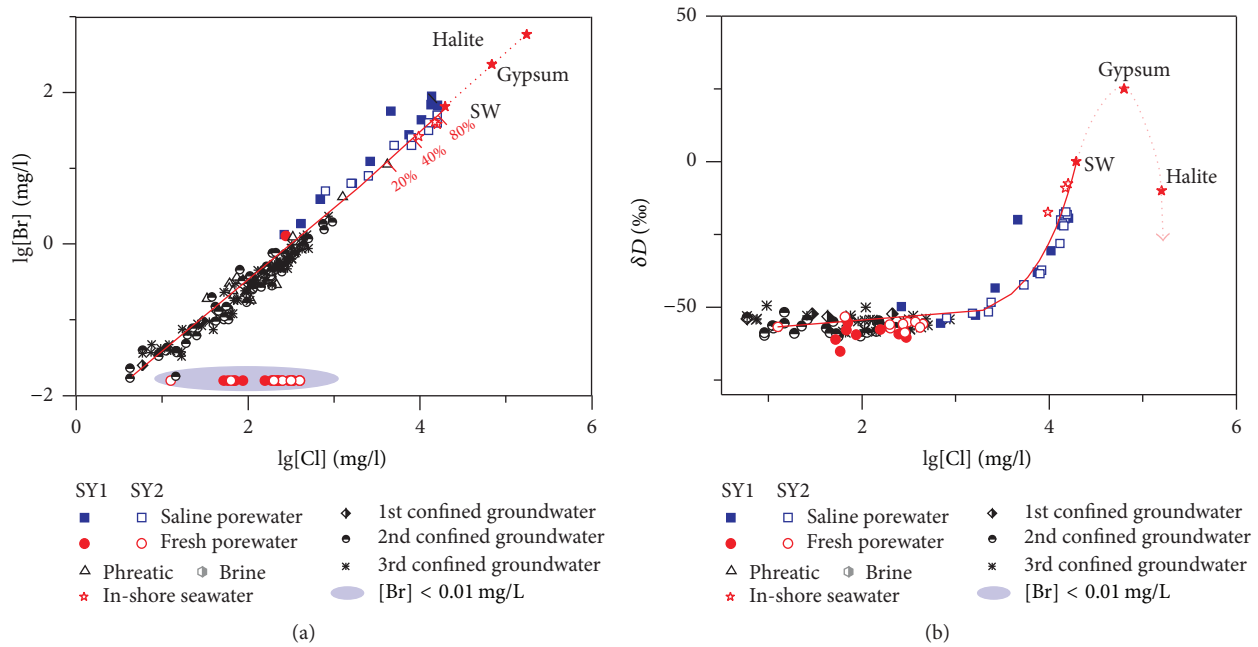


FIGURE 7: Cl⁻ versus (a) Br⁻ concentrations and (b) δ²H of porewaters in the aquitards and groundwater in aquifers. The groundwater samples are referred from Fu [20]. The red line represents the diluted line of standard seawater (SW), and the red dotted line represents SW evaporated trajectory. The paths for evaporating seawater are from Fontes and Matray (1993) [24].

4.2. Chloride-Depth Profiles. The extracted porewater Cl⁻ distributions of two boreholes along with the profiles were presented in Figure 4. The Cl⁻ concentrations yielded a well-defined 1D depth profile and indicated the presence of three distinct hydrogeologic zones interrupted by the aquifers. Two gradual decreases in Cl⁻ concentrations of borehole SY1 were observed from 334.8 to 60.0 mg/L (depth 162.2–86.5 m in zone B) and 16,086.1 to 262.2 mg/L (depth 19.8–2.0 m in zone A) as the depth decreases. Between 62.2 and 19.8 m, Cl⁻ concentrations increased rapidly from 16,086.1 to 412.3 mg/L. In borehole SY2, the high Cl⁻ concentrations were presented steadily ranging from 13,000 to 15,576.6 mg/L (mean 14,223.8 mg/L, depth 55.1–10.6 m). Then Cl⁻ concentration decreased with depth and attained its minimum value of

around 250 mg/L at 85.6 to 120 m. The bad agreement between Cl⁻ concentrations in SY1 and borehole SY2 suggests that the chemical vertical variability in the profiles was assumed to be complex and large over distances [19].

The decreasing trend in observed Cl⁻ concentrations in the zone A from 19.8 m to the top of borehole SY1 could be attributed to the diluted mixture of modern meteoric water after the Holocene transgression. The shape of the Cl⁻ profile through the remaining zone A and the underlying deep first confined aquifer (aquifer I, Figure 4) suggests that Cl⁻ diffused from the zone A downward into the aquifer and upward toward the top of zone A. The lower Cl⁻ values (about 60 mg/L) from 108 to 89 m, attached to aquifer I, imply that the invasion of the different glacial meltwater into the aquifer

I resulted in porewater in the underlying aquitards (zones B and C) suffering from vertical solute diffusive mixing.

The Cl^- concentrations of zone A in borehole SY2 were centered on the sand-rich deposits, especially for the depth of 54.2–10.6 m. It yielded a maximum Cl^- concentration of 15,576.6 mg/L, similar to the Cl^- concentrations of near-shore seawater values (about 9,000–16,000 mg/L). This could explain that the Holocene seawater rapidly travelled through the deposits and replaced the original porewater due to the coarse logic section. The B zone yielded Cl^- concentrations that were relatively constant at around 250 mg/L and showed a signature of freshwater, consisting with the constant Cl^- concentrations in borehole SY1 C zone and aquifer II (Figure 4). It shows that the deep first confined aquifer did not exert a significant impact on the adjoining Cl^- aquitard profile in borehole SY2 due to its thin thickness (about 3 m, depth 85.6–82.6 m). Due to their freshwater signatures, porewaters in the B and C zone of the two boreholes were assumed to derive from postdepositional glacial meltwater recharge with different time in the Late Pleistocene relative to groundwater in aquifer I.

4.3. Conceptual Transport Model. Vertical solute transport in a saturated medium can be simulated using the advection-diffusion equation:

$$\frac{\partial C}{\partial t} = D \frac{\partial^2 C}{\partial Z^2} - V \frac{\partial C}{\partial Z}, \quad (1)$$

where V is the average linear porewater velocity, D is the coefficient of hydrodynamic dispersion, C is the mass concentration of the solute, Z is the distance, and t is the time. The coefficient of hydrodynamic dispersion is defined as $D = D_e + \alpha V$, where D_e is the effective diffusion coefficient and α is dispersivity. The average linear porewater velocity is defined as $V = v/n_e$, where v is the Darcy velocity and n_e is the effective porosity. We assumed that advection in the aquitard-aquifer system follows Darcy's law and no threshold hydraulic gradient exists in the porewater transport process [52]. The effective porosity was supposed to be equal to the porosity, namely, $n_e = n_T$ (total porosity) [5, 42]. More, compaction-driven flow was also ignored according to the previous researches on aquitard-aquifer system [14, 15, 53]. Beyond that, the aquifer and aquitard were assumed to be individually homogeneous.

The porosities (n_T s) for the borehole SY1 are uniform with depth (except depth of 14.82–15.02 m) and have a mean value of 0.41. For borehole SY2, n_T s of aquitards are mostly around 0.5 and approximately 0.4 for the aquifers. Then, n_T s of the aquitards and aquifers of borehole SY1 are set to be 0.41. Correspondingly, 0.5 and 0.4 are set to be n_T s of the aquitards and aquifers in borehole SY2, respectively.

Based on the estimated D_e values of two borehole aquitards using laboratory diffusion testing technique, the corrected D_e values of Cl^- for boreholes SY1 and SY2 samples are presented in Table 1. The D_e values for Cl^- in the aquitards and aquifers within 162.2 m were assumed to be $4.3 \times 10^{-10} \text{ m}^2/\text{s}$ since no indication of pore structure occurred in these units [6]. The estimated D_e for borehole SY2 was assumed to be $2.7 \times 10^{-10} \text{ m}^2/\text{s}$.

4.4. Initial and Boundary Conditions. The vertical distributions of Cl^- in the aquitard-aquifer system at the time of their deposition are unknown. The Cl^- profiles are probably attributed to several historical palaeohydrological events. The higher Cl^- concentrations in zone A originated from seawater during the Holocene transgression, and the low concentrations in aquifer I of SY1 possibly resulted from the invasion of glacial meltwater. However, the time of this intrusion of melt water is uncertain. The intrusion also had been described as aquifer "activation" of Hendry et al. (2013) [6] and Hendry and Harrington (2014) [11]. Defining the time of aquifer I recharge needed to depend on a great of assumptions. It is supposed that the recharge time for aquifer I was selected to coincide with the onset of the last glacial maximum, and the simulations were developed from 25 to 15 ka BP [29]. The relative constant values (around 250 mg/L) at depth of 159–120 m in borehole SY1 indicate that the aquitards and aquifers at depth of 182–19.8 m were assumed to be filled with freshwater (Cl^- , 250 mg/L) before "activation" of aquifer I. Afterwards, the later invasion with glacial meltwater (the last glacial maximum) into aquifer I resulted in Cl^- diffusion mixing transport at the top of zone B and the bottom of zone A. In fact, no realistic physical mechanism, other than perpetual flushing of the aquifer could be presented by a constant value throughout the aquifer I. A near-instantaneous change in Cl^- concentration within the aquifer I was assumed during the activation of aquifer [6]. And an instantaneous value of 60 mg/L was used in aquifer I after the activation of aquifer in keeping with the lower porewater values in the adjacent aquitard and groundwater values in aquifer I of the study area [20].

The sea level of the last glacial maximum was –130 m below the modern coastline [54]. In the Holocene, the sea level rose rapidly, and the study area was submerged by seawater [55], which seemed to result in the porewater salinization in the deposits, as Yi et al. (2012) [31] described occurring in the North China Plain. Due to the uncertainty of sedimentation rate and the relative thin thickness of the Holocene deposits, the fixed upper BC was set to locate at the surface of the Late Pleistocene since the onset of the Holocene, which was assumed to be the sediment-water interface (19.9 m). Theoretically, the Cl^- concentration for the upper BC should be the value of standard seawater (19.0 g/L). Actually, most of the near-shore seawater had low Cl^- concentrations (approximately 10,000–16,000 mg/L [20]), and the highest Cl^- concentration of 16,086.1 mg/L was observed in the two boreholes. Porewater salinity distribution in coastal plain aquitard-aquifer system was probably complex and mostly different from the standard seawater [15]. The assumed fixed Cl^- concentration of 16,100 mg/L was adopted as the upper BC.

The study area stayed in a marine environment until the appearance of Yellow River captured Huai River in AD 1,128. Since then, seawater retreated from the study area, and the shoreline gradually reached the present level (Figure 1(b)) [26]. It could believe that the Holocene deposits had been filled with seawater during the period of transgression, and the Cl^- concentration of seawater was set to be 16,100 mg/L. A freshening upper BC (fixed Cl^- concentration of 100 mg/L)

TABLE 1: Initial and boundary concentrations adopted for Cl⁻ concentrations at SY1 bore and SY2 bore.

Borehole	Depth range (m)	Time	Parameters	Upper BC (mg/L)	Lower BC (mg/L)	The confined aquifer BC (mg/L)	Initial concentration (mg/L)			
SY1	182.0–2.0									
	162.0–19.9	15–10 ka BP	D_e (m ² /s)	60	Aquifer III 182–162.2 m	Aquifer I 86.5–62.6 m	Zone B and zone C 162.2–86.5 m	Aquifer I 86.5–62.6 m	Zone A 62.6–19.9 m	
	162.0–19.9	10 ka BP–AD 1,128	4.3×10^{-10}	16,100	250	60	250	60	250	
SY1	162.0–2.0	AD 1,128–present		100	250	60	The simulation Cl ⁻ concentration of 15 ka BP	The simulation Cl ⁻ concentration of 10 ka BP	The simulation Cl ⁻ concentration of 15 ka BP	
	162.0–2.0	AD 1,128–present		100	250	60	The simulation Cl ⁻ concentration of 15 ka BP	The simulation Cl ⁻ concentration of 10 ka BP	The simulation Cl ⁻ concentration of 15 ka BP	
SY2	About 180.0–2.0									
	About 180.0–18.9	15–10 ka BP		60	Aquifer III about 180–160 m	Aquifer I 54.2–34.8 m	About 160.0–54.2 m	54.2–34.8 m	34.8–18.9 m	18.9–2 m
SY2	About 180.0–18.9	10 ka BP–AD 1,128	2.7×10^{-10}	16,100	250	16,100	The simulation Cl ⁻ concentration of 15 ka BP	16,100	16,100	16,100
	About 180.0–2.0	AD 1,128–present		100	250	16,100	The simulation Cl ⁻ concentration of 10 ka BP	16,100	16,100	16,100

Note. “/” represents no data.

was applied to the oxidation-nonoxidation interface (about 2 m) since AD 1,128, coinciding with the time of marine regression of this area.

For the borehole SY2, the depth of this study extends to the underlying aquifer III at the depth of approximately 160–180 m on the basis of the distributions of regional aquifers (Figures 2 and 4), because the drilled borehole did not reveal the underlying confined aquifer which should serve as the lower BC. Before the “activation” of aquifer I, the aquitards and aquifers at depth of about 160–18.9 m were assumed to be filled with freshwater (Cl^- , 250 mg/L). Subsequently, the glacial meltwater (the last glacial maximum; Cl^- , 60 mg/L) and the Holocene seawater intrusion led to Cl^- diffusion mixing transport of this profile. At the beginning of the Holocene, the initial Cl^- concentration of porewater at depth of 54.2–18.9 m was assigned as 16,100 mg/L since the relative coarser sediments occurred in this profile (described in Section 4.2). Beyond that, the similar various initial conditions and BC with different timeframes were assigned consisting with the setting for borehole SY1. Specific initial conditions and BC could refer to Table 1 for a summary of the boundary conditions.

4.5. Simulations of Aquitard-Aquifer System Cl^- Profiles. Previous researches on solute transport in the thick, regional aquitards have suggested that thin, sand-filled layers or permeable conduits might result in facilitating Cl^- “halos” laterally through an aquitard [56] and major deviations from one-dimensional diffusion profiles [12]. In this study, the sand layers (aquifers or sand streaks) are commonly encountered in the aquitards. Determining the influence of sand layers on the Cl^- transport simulations is crucial to palaeohydrological interpretation of porewaters.

The solute transport mechanism could be inferred to be advection if solute concentrations had no obvious vertical change; otherwise, curvilinear concentration profiles were attributed to molar diffusion transport [57, 58]. In order to detect the influence of sand layers on Cl^- transport, vertical 1D diffusion transport (see (1)) was postulated to be the dominant migration mechanism throughout the aquitard-aquifer system, because obvious vertical distributions appeared in the Cl^- concentration profiles (Figure 4).

As shown in Figure 4, the thickness of aquifer has an obvious influence on the Cl^- concentration profiles, for example, aquifer I (86.5–62.6 m) of SY1 borehole. The thick aquifer I is observed in borehole SY1, and Cl^- concentrations in the neighboring aquitards display the notable diffusion mixing trends occurring in the aquitard-aquifer interfaces. However, when the aquifer is relatively thin (the deep first confined aquifer with the thickness of about 3 m in the borehole SY2, depth of 85.6–82.6 m), the impact on Cl^- concentration profile in the neighboring aquitards is so little that even can be ignored. Namely, the thick aquifer should be regarded as the fixed concentration BC since the diffusion front does not reach the bottom of the aquifer in the simulations, while, for thin aquifer, the diffusion front reaches the bottom of aquifer in a short time, and the corresponding Cl^- concentration in the thin entire aquifer will keep changing with time on the basis of the Cl^- concentrations of the adjacent aquitards

[15]. Besides that, the relatively thick aquifer (silt) is also found at depth of 52.3–41.5 m in borehole SY1. Groundwater in the aquifer entrapped palaeoseawater of the Holocene was similar to the constituents of the adjacent aquitards and was renewed more rapidly than the deep confined aquifers due to their shallow depth [19]. The Cl^- concentrations in the aquifer are also dynamic just like values in the thin sand layers. Thus, in this study, the thin aquifer II, the shallow first confined aquifer in borehole SY1, and the deep first confined aquifer (mentioned above, 85.6–82.6 m) in the borehole SY2 are supposed to be regarded as aquitards in the simulations.

To determine whether palaeohydrological change events affect the interpretation of the measured Cl^- profiles, the various boundary conditions were evaluated and applied to the modeling simulations. The transient constant upper and lower BC, initial conditions, aquifer boundary encountered in aquitards, and D_e 's were shown in Table 1. The starting time of aquifer I was reconstructed broadly varying from 30 to 12 ka BP to assess the impact of the last glacial maximum on the measured profile.

As is illustrated in Figure 8(a), the simulations with 20–15 ka BP are the best fit to the measured data at the depth of 162.2–62.6 m in borehole SY1. Using 15 ka BP simulation as the new initial condition and applying a subsequent saline BC (16,100 mg/L) with the transport time of about 10 ka and 70 ka are to develop the historical SY1 Cl^- concentration profile in the Holocene (Figure 8(b)). The obtained best fit simulation with transport time of 10 ka is consistent with the onset timescale of the Holocene. Subsequently, utilizing fresher upper BC with Cl^- concentration of 100 mg/L (the mean concentration of rainfall) which is referenced from Zhang et al. (2000) [59] and Zhang et al. (2003) [60] followed by saline BC, this model is used to simulate the shorter timescale (since AD 1,128). It provides a very good fit to the measured porewater Cl^- profile (Figure 8(c)), suggesting that the observed relatively large vertical scatter in Cl^- profile is closely related to the various upper BC.

Due to the thin deep first confined aquifer existing in borehole SY2, this aquifer activation is not considered in the simulations (*note*: the simulations related to the deep aquifer activation are modeled but not presented). As Figure 8(d) shows, the meltwater intrusion into the aquifer I has less of an impact on the Cl^- profile. According to the simulative result of the SY1 (Figure 8(a)), 15 ka BP simulation was selected as the new initial condition, and a series of simulations were performed, first by implementing a saline phase in the surface of the Late Pleistocene and then a freshening phase (Cl^- , 100 mg/L) in the oxidation-nonoxidation interface (about 2 m). Apart from the low Cl^- concentration in aquifer I (depth of 85.6–82.6 m), good fits between the simulated and measured Cl^- values are yielded (Figures 8(e) and 8(f)). These results could be explained that the realistic assumption is traceable in reasonable selection of the BC and initial conditions associations with the palaeohydrology events in the simulations.

4.6. Effects on the Diffusion Simulations of Cl^- Profiles

4.6.1. Effects of Effective Diffusion Coefficient on the Evolution of the Cl^- Profiles. Although simulations have the capacity to

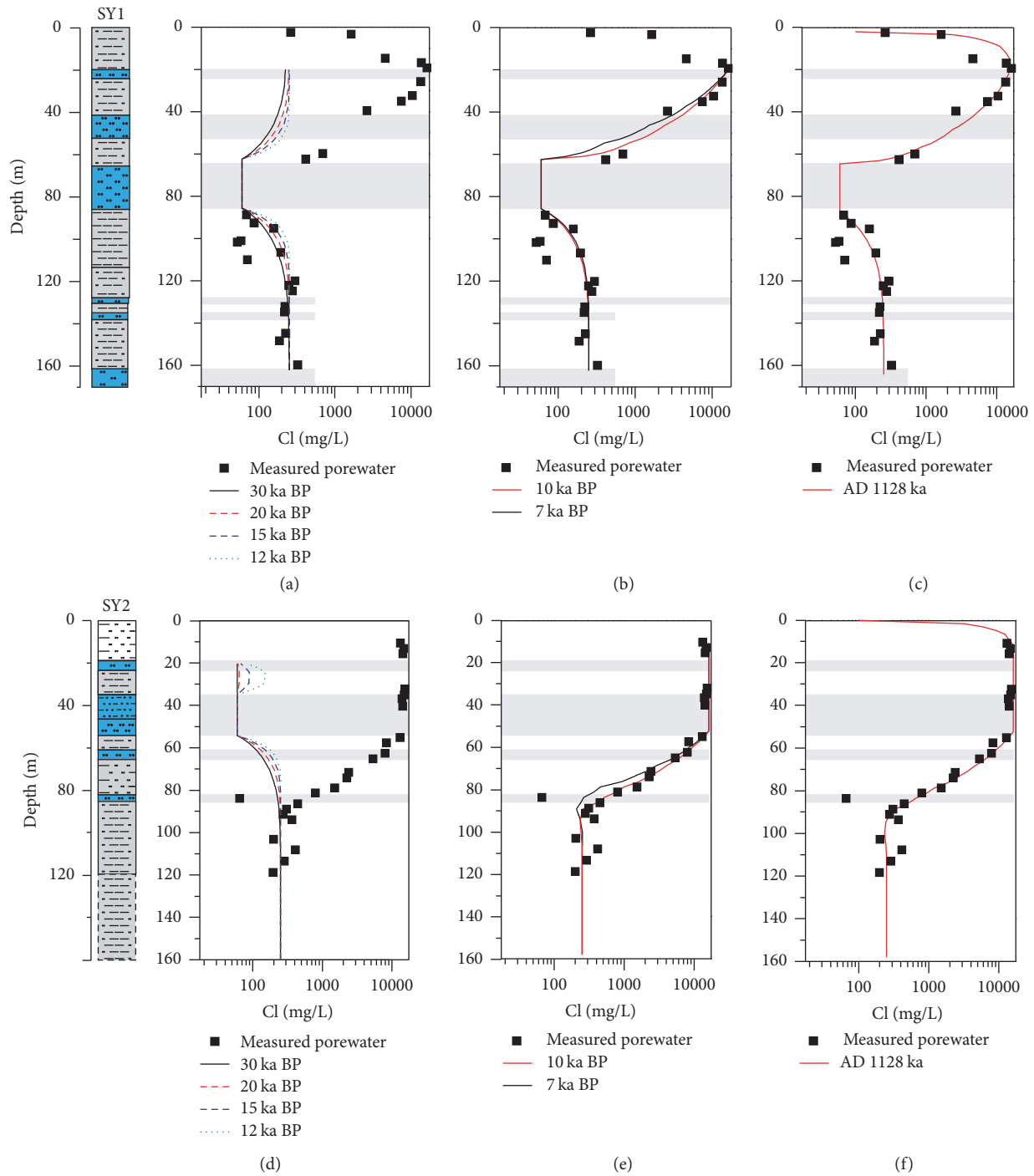


FIGURE 8: Measured and modeled Cl^- concentration profiles in aquitard-aquifer system at the studied boreholes. (a, d) SY1 and SY2 profiles between 30 and 12 ka BP with a fresher boundary condition of the Aquifer I. (b, e) Using the simulation result of 15 ka BP as the new initial condition, simulated borehole profiles after a further 10 ka BP and 7 ka BP with a saline upper BC. (c, f) Using the simulation result of 10 ka BP as the new initial condition, simulated SY1 profiles after a further AD 1,128 with a fresher upper BC. The black dotted bordered rectangles in the borehole SY2 profile represent the sediments that were not revealed in the borehole SY2.

reflect tracer transport time, the simulated profiles cannot be unique because of the selection of values to material properties [61]. Sensitivity analyses of parameters in solute transport processes in aquitards have been conducted, and the results indicate that the diffusion model was most sensitive to the

choice of D_e values [62]. However, obtaining D_e values using field or laboratory test methods is difficult because of the heterogeneity of deposits, test operations, and sampling. The selected unsuitable parameters for the simulation possibly lead to deviations in transport time [10]. In this study, the

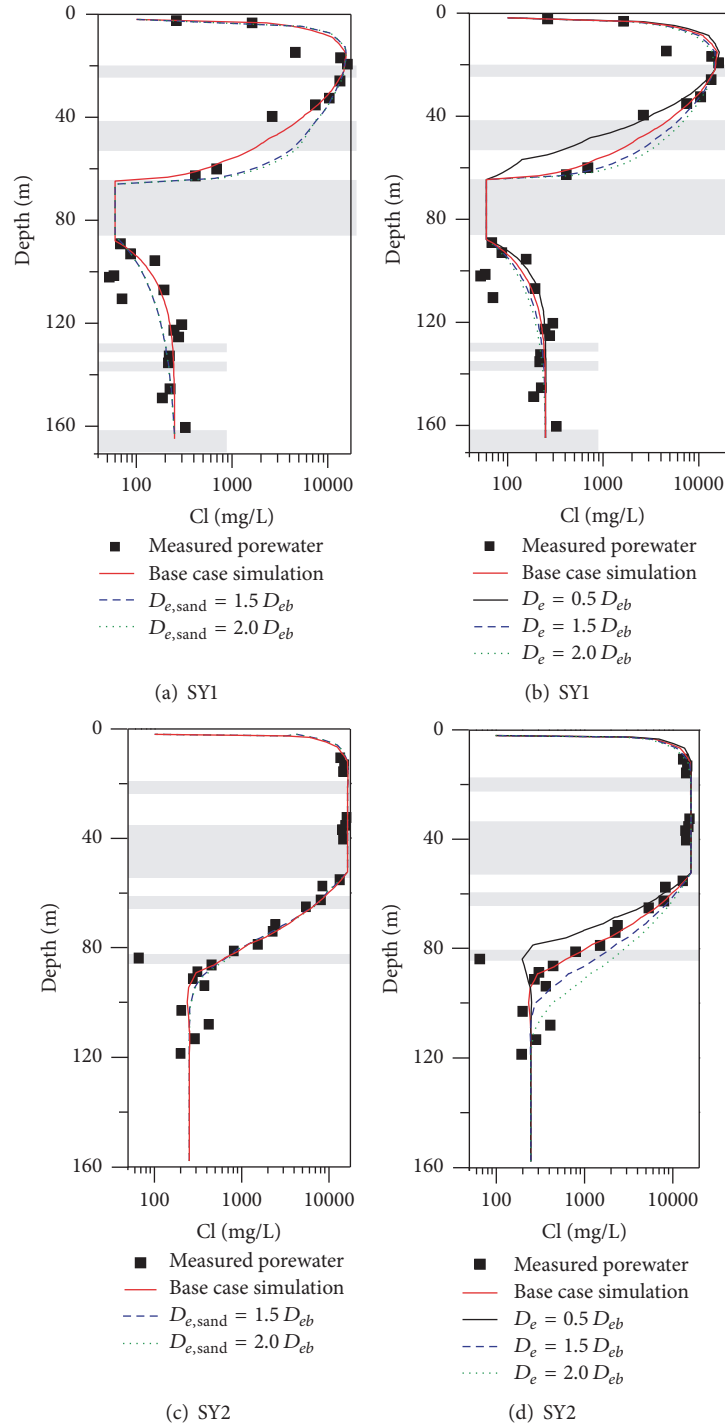


FIGURE 9: Results of D_e sensitivity analyses on simulations; (a) and (c) show the simulation profiles of the two boreholes through simply modifying effective diffusion coefficients of sand layers ($D_{e,sand}$) by various increase factors. (b) and (d) show the modified simulation tracer profiles of the two boreholes using various D_e for the whole profiles. D_{eb} represents the D_e value applied for the base case simulation.

D_e values of the sand layers (aquifers and sand streaks) are estimated similar to the aquitards in the two boreholes due to the absence of laboratory measurements of sand layers. To illustrate the influence of D_e of the aquitard-aquifer systems on the simulated Cl^- concentration profiles, different D_e values are selected for aquitard and aquifer deposits.

In order to describe convenience, the simulated results of SY1 (Figure 8(c)) and SY2 (Figure 8(f)) are called “base case simulations,” as illustrated in Figure 9.

As the results shown in Figures 9(a) and 9(c), there is no greater difference between the base case simulation and the reconstruction simulations due to the thin sand layers

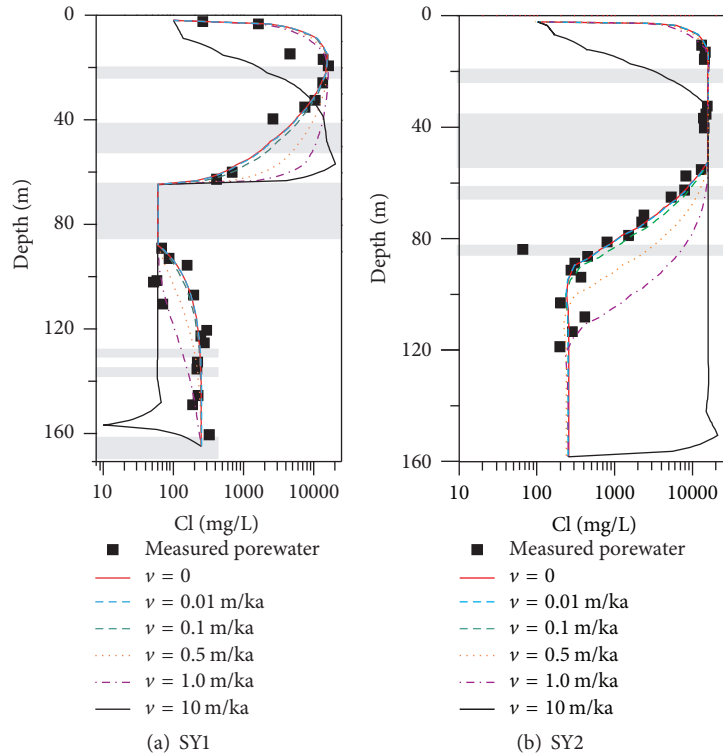


FIGURE 10: Porewater Cl^- measurements of (a) SY1 and (b) SY2 profiles, and simulations with the different groundwater velocities for the two studied boreholes.

in the borehole SY2. These also exhibit that same D_e for the aquitards and aquifers would not result in the obvious offsets of the Cl^- simulation profiles in this study. The obvious differences were observed in the Figures 9(b) and 9(d), suggesting that the Cl^- simulations in the aquitard-aquifer system are affected by different chosen D_e values. The best fits are obtained when $D_e = 4.3 \times 10^{-10} \text{ m}^2/\text{s}$ for SY1 and $D_e = 2.7 \times 10^{-10} \text{ m}^2/\text{s}$ for SY2 core samples, coinciding with the measured D_e values.

4.6.2. Effects of Velocity Coefficient on the Evolution of the Cl^- Profiles. Advection transport is another factor that may influence solution migration [3, 62]. On the basis of the dynamic data of groundwater table monitored in the study area for numerous years, the mean water table level in the study area is generally 0.4 m; the mean piezometric level of the first and second confined aquifers is -4.5 m and -15.4 m , respectively. The determined vertical hydraulic gradient is fairly uniform with a value of 0.25 across the aquitards, assuming Darcy's law is valid at very low velocities. Accordingly, the average downward porewater velocities through the clay-rich deposits are calculated to be between 0.118 m/ka and 5.76 m/ka for the K values determined through the lab experiment method. In these simulations, groundwater velocities are supposed to range broadly from 0.01 to 10 m/ka.

The simulated profiles for downward velocities of 0.01, 0.1, 0.5, 1, and 10 m/ka and the measured Cl^- concentrations of the two boreholes are presented in Figure 10. The best fits simulated profiles for the two boreholes are obtained

for velocity of 0.1 m/ka and less. The higher velocity cases evidently depart from the measured Cl^- profiles. However, the added advective velocity produces no marked change in the simulated profiles, and the minimum deviation does not affect the transport profiles. Therefore, it can surmise that diffusion solely is adequate to reconstruct the transport of Cl^- in the aquitard-aquifer system.

However, the Cl^- concentrations of porewater in the aquitards which are below aquifer I, and above aquifer III in boreholes present significant horizontal distribution and they do not show a coherent diffusion trend, it is likely that the strong overpressure in aquifers results in an advective component to the reversal of the Cl^- profiles [3]. Besides that, lateral advection was also not involved in these simulations, which probably contributes a horizontal advective component to the Cl^- profiles [63].

5. Conclusion

Numerical simulations of diffusive Cl^- transport were used to define the recharge processes of the aquifer I and explore the long-term evolution of porewater chemistry in aquitard-aquifer system of NJCP. Based on the preexisting knowledge of the sedimentary depositional environments and the events of transgression and regression since the Late Pleistocene, the various initial and upper boundary conditions over geological time were implemented. Diffusion has been approved to be the dominant transport mechanism of Cl^- in the aquitard-aquifer system. The thickness of the sand layers

had significant influence on the shapes of the simulated Cl^- concentration in the aquitards. The simulations yielded well-defined 1D Cl^- profiles, suggesting that the assumed geological timeframes for the simulations are applicable and the high Cl^- profiles through the upper aquitards of the two boreholes are consistent with the onset of the Holocene (10 ka BP).

The results of this study present an understanding of the vertical solute transport in the aquitard-aquifer system based on the measured tracer profiles and transport parameters. The good agreement obtained between simulated and measured profiles suggests that the simulations can not only help one to understand solute transport mechanism in the aquitard-aquifer system but also provide insight into the timing of major geologic events (e.g., glaciations, transgression). The model simulation mechanisms are also suitable to other areas of the new Silk Road with the similar hydrogeological characteristics of NJCP.

Conflicts of Interest

The authors declare that there are no conflicts of interest regarding the publication of this paper.

Acknowledgments

This study was funded by the National Natural Science Foundation of China (Grants nos. 41502231 and 41272258). The authors would like to thank Professor Zhang Wen and two anonymous reviewers for their helpful comments and advice, as well as all the members of the Geological Survey of Jiangsu Province, China, for their assistance and support in the process of sampling and data collection.

References

- [1] M. Cyr and A. Daidié, "Optimization of a high-pressure pore water extraction device," *Review of Scientific Instruments*, vol. 78, no. 2, article 023906, 2007.
- [2] A. K. Steen, J. A. Nunn, and J. S. Hanor, "Indications of formation water flow and compartmentalization on the flank of a salt structure derived from salinity and seismic data," *Geofluids*, vol. 11, no. 2, pp. 199–208, 2011.
- [3] T. A. Al, I. D. Clark, L. Kennell, M. Jensen, and K. G. Raven, "Geochemical evolution and residence time of porewater in low-permeability rocks of the Michigan Basin, Southwest Ontario," *Chemical Geology*, vol. 404, pp. 1–17, 2015.
- [4] A. Burg and R. Gersman, "Hydrogeology and geochemistry of low-permeability oil-shales – Case study from HaShfela sub-basin, Israel," *Journal of Hydrology*, vol. 540, pp. 1105–1121, 2016.
- [5] M. J. Hendry and L. I. Wassenaar, "Implications of the distribution of σD in pore waters for groundwater flow and the timing of geologic events in a thick aquitard system," *Water Resources Research*, vol. 35, no. 6, pp. 1751–1760, 1999.
- [6] M. J. Hendry, S. L. Barbour, K. Novakowski, and L. I. Wassenaar, "Paleohydrogeology of the Cretaceous sediments of the Williston Basin using stable isotopes of water," *Water Resources Research*, vol. 49, no. 8, pp. 4580–4592, 2013.
- [7] D. E. Desaulniers, J. A. Cherry, and P. Fritz, "Origin, age and movement of pore water in argillaceous Quaternary deposits at four sites in southwestern Ontario," *Journal of Hydrology*, vol. 50, no. C, pp. 231–257, 1981.
- [8] M. J. Hendry and L. I. Wassenaar, "Controls on the distribution of major ions in pore waters of a thick surficial aquitard," *Water Resources Research*, vol. 36, no. 2, pp. 503–513, 2000.
- [9] R. J. Shaw and M. J. Hendry, "Hydrogeology of a thick clay till and Cretaceous clay sequence, Saskatchewan, Canada," *Canadian Geotechnical Journal*, vol. 35, no. 6, pp. 1041–1052, 1998.
- [10] G. A. Harrington, W. P. Gardner, B. D. Smerdon, and M. J. Hendry, "Palaeohydrogeological insights from natural tracer profiles in aquitard porewater, Great Artesian Basin, Australia," *Water Resources Research*, vol. 49, no. 7, pp. 4054–4070, 2013.
- [11] M. J. Hendry and G. A. Harrington, "Comparing vertical profiles of natural tracers in the Williston Basin to estimate the onset of deep aquifer activation," *Water Resources Research*, vol. 50, no. 8, pp. 6496–6506, 2014.
- [12] M. J. Hendry and L. I. Wassenaar, "Inferring heterogeneity in aquitards using high-resolution δd and $\delta^{18}\text{O}$ Profiles," *Groundwater*, vol. 47, no. 5, pp. 639–645, 2009.
- [13] D. Y. Yang, "Quaternary transgressive sediments and neotectonic movement in the coastal area of Jiangsu Province (in Chinese with English abstract)," *Journal of Disaster Prevention & Mitigation Engineering*, vol. 01, pp. 24–32, 1986.
- [14] X. Kuang, J. J. Jiao, and K. Liu, "Numerical studies of vertical Cl^- , $\delta^2\text{H}$ and $\delta^{18}\text{O}$ profiles in the aquifer-aquitard system in the Pearl River Delta, China," *Hydrological Processes*, vol. 29, no. 19, pp. 4199–4209, 2015.
- [15] X. Kuang, J. J. Jiao, and Y. Wang, "Chloride as tracer of solute transport in the aquifer-aquitard system in the Pearl River Delta, China," *Hydrogeology Journal*, vol. 24, no. 5, pp. 1121–1132, 2016.
- [16] M. J. Hendry, D. K. Solomon, M. Person et al., "Can argillaceous formations isolate nuclear waste? Insights from isotopic, noble gas, and geochemical profiles," *Geofluids*, vol. 15, no. 3, pp. 381–386, 2015.
- [17] , *Radiative sAndy Ridge Field on Continental Shelf of the Yellow Sea*, Y. Wang, Ed., China Environment Science Press, Beijing, China, 2002.
- [18] Y. Wang, Z. K. Zhang, D. K. Zhu, J. H. Yang, L. J. Mao, and S. H. Li, "Riversea interaction and the North Jiangsu Plain formation," *Quaternary Sciences*, vol. 26, pp. 301–320, 2006.
- [19] X. Shi, F. Jiang, Z. Feng, B. Yao, H. Xu, and J. Wu, "Characterization of the regional groundwater quality evolution in the North Plain of Jiangsu Province, China," *Environmental Earth Sciences*, vol. 74, no. 7, pp. 5587–5604, 2015.
- [20] C. C. Fu, *The Hydrochemical Characteristics and Processes for Salinity Sources of the Deep Confined Groundwater in the Coastal Plain of Huai River Basin*, Jilin University, 2015.
- [21] H. C. Zhou, "Origin, distribution, and evolution of salt-fresh groundwater in North Jiangsu Basin, China," *Environmental Geology and Water Sciences*, vol. 12, no. 1, pp. 15–22, 1988.
- [22] J. Liu, Y. Saito, H. Wang, L. Zhou, and Z. Yang, "Stratigraphic development during the Late Pleistocene and Holocene offshore of the Yellow River delta, Bohai Sea," *Journal of Asian Earth Sciences*, vol. 36, no. 4–5, pp. 318–331, 2009.
- [23] C. T. Xue, Y. Q. Zhou, and G. L. Wang, "Reviews of the Yellow River Delta Superlobes Since 700 BC," *Marine Geology and Quaternary Geology*, vol. 23, pp. 23–30, 2003.
- [24] J. C. Fontes and J. M. Matray, "Geochemistry and origin of formation brines from the Paris Basin, France. 1. Brines associated with Triassic salts," *Chemical Geology*, vol. 109, no. 1–4, pp. 149–175, 1993.

- [25] J. Wang, X. Huang, T. Zhong, and Z. Chen, "Climate change impacts and adaptation for saline agriculture in north Jiangsu Province, China," *Environmental Science & Policy*, vol. 25, pp. 83–93, 2013.
- [26] C. T. Xue, J. Liu, and X. H. Kong, "Preliminary study of Holocene Huaihe River delta on west coastal plain of Yellow Sea, China," *Quaternary Sciences*, vol. 30, pp. 892–901, 2010.
- [27] C. Y. Ha, J. Q. Zhu, N. J. Ye, J. J. Huang, and J. S. Gong, "The forgotten delta the formation and evolution of Huaihe Delta River," *Geological Bulletin of China*, vol. 24, pp. 1094–1106, 2005.
- [28] B. Kang, *The study of groundwater evolution and rational exploitation and utilizing in Jiangsu Coastal area*, Jilin University, 2017.
- [29] J. T. Wang and P. X. Wang, "Relationship between sea-level changes and climate fluctuations in east China since the Late Pleistocene," *Acta Geographica Sinica*, vol. 35, no. 4, pp. 299–312, 1986.
- [30] P. Y. Wang, "Strata of quaternary transgressions in east China: a preliminary study," *Acta Geologica Sinica*, vol. 55, no. 1, pp. 1–13, 1981.
- [31] L. Yi, H.-J. Yu, J. D. Ortiz et al., "Late Quaternary linkage of sedimentary records to three astronomical rhythms and the Asian monsoon, inferred from a coastal borehole in the south Bohai Sea, China," *Palaeogeography, Palaeoclimatology, Palaeoecology*, vol. 329–330, pp. 101–117, 2012.
- [32] Y. Z. Yan, H. Wang, F. L. Li, J. F. Li, C. R. Zhao, and F. Lin, "Sedimentary environment and sea-level fluctuations revealed by borehole bq1 on the west coast of the Bohai bay, China," *Geological Bulletin of China*, vol. 25, no. 3, pp. 357–382, 2006.
- [33] Y. Zong, W. W.-S. Yim, F. Yu, and G. Huang, "Late Quaternary environmental changes in the Pearl River mouth region, China," *Quaternary International*, vol. 206, no. 1–2, pp. 35–45, 2009.
- [34] S. Ling, "Changes of the palaeogeographic environment in north Jiangsu Plains since the Holocene," *Journal of Oceanography of Huanghai Bohai & Seas*, vol. 8, no. 4, pp. 20–28, 1991.
- [35] Y. Saito, H. Wei, Y. Zhou, A. Nishimura, Y. Sato, and S. Yokota, "Delta progradation and chenier formation in the Huanghe (Yellow River) delta, China," *Journal of Asian Earth Sciences*, vol. 18, no. 4, pp. 489–497, 2000.
- [36] C. Stumpp and M. J. Hendry, "Spatial and temporal dynamics of water flow and solute transport in a heterogeneous glacial till: The application of high-resolution profiles of $\delta^{18}\text{O}$ and $\delta^2\text{H}$ in pore waters," *Journal of Hydrology*, vol. 438–439, pp. 974–977, 2012.
- [37] J. Li, X. Liang, M. Jin, and X. Mao, "Geochemical signature of aquitard pore water and its paleo-environment implications in Caofeidian Harbor, China," *Geochemical Journal*, vol. 47, no. 1, pp. 37–50, 2013.
- [38] Q. Ge, X. Liang, X. L. Gong, and Y. Liu, "The application and comparison of various methods for determining hydraulic conductivity in saturated clay-rich deposits—a case study of clay-rich sediments in North Jiangsu coastal plain," *Earth Science*, vol. 42, no. 5, pp. 793–803, 2017.
- [39] The Professional Standards Compilation Group of People's Republic of China. JTG E40—2007 "Test methods of soils for highway engineering", Beijing: China Communications Press, 2007.
- [40] C. D. Shackelford, "Laboratory diffusion testing for waste disposal — A review," *Journal of Contaminant Hydrology*, vol. 7, no. 3, pp. 177–217, 1991.
- [41] K. S. Novakowski and G. Van Der Kamp, "The radial diffusion method. 2. A semianalytical model for the determination of effective diffusion coefficients, porosity, and adsorption," *Water Resources Research*, vol. 32, no. 6, pp. 1823–1830, 1996.
- [42] G. Van Der Kamp, D. R. Van Stempvoort, and L. I. Wassenaar, "The radial diffusion method. 1. Using intact cores to determine isotopic composition, chemistry, and effective porosities for groundwater in aquitards," *Water Resources Research*, vol. 32, no. 6, pp. 1815–1822, 1996.
- [43] B. Mahmoudzadeh, L. Liu, L. Moreno, and I. Neretnieks, "Solute transport through fractured rock: Radial diffusion into the rock matrix with several geological layers for an arbitrary length decay chain," *Journal of Hydrology*, vol. 536, pp. 133–146, 2016.
- [44] Q. Ge, X. Liang, X. L. Gong, and Y. Liu, "Laboratory determination and analysis of effective diffusion coefficients for low-permeability rock and clay," *Hydrogeology & Engineering Geology*, vol. 44, no. 3, pp. 93–99, 2017.
- [45] G. Kourakos and T. Harter, "Vectorized simulation of groundwater flow and streamline transport," *Environmental Modelling & Software*, vol. 52, no. C, pp. 207–221, 2014.
- [46] Q. Wang, H. Zhan, and Z. Tang, "Two-dimensional flow response to tidal fluctuation in a heterogeneous aquifer-aquitard system," *Hydrological Processes*, vol. 29, no. 6, pp. 927–935, 2015.
- [47] L. Yuan-Hui and S. Gregory, "Diffusion of ions in sea water and in deep-sea sediments," *Geochimica et Cosmochimica Acta*, vol. 38, no. 5, pp. 703–714, 1974.
- [48] I. Cartwright, T. R. Weaver, and L. K. Fifield, "Cl/Br ratios and environmental isotopes as indicators of recharge variability and groundwater flow: An example from the southeast Murray Basin, Australia," *Chemical Geology*, vol. 231, no. 1–2, pp. 38–56, 2006.
- [49] A. M. Stueber and L. M. Walter, "Origin and chemical evolution of formation waters from Silurian-Devonian strata in the Illinois basin, USA," *Geochimica et Cosmochimica Acta*, vol. 55, no. 1, pp. 309–325, 1991.
- [50] D. M. Han, X. F. Song, M. J. Currell, J. L. Yang, and G. Q. Xiao, "Chemical and isotopic constraints on evolution of groundwater salinization in the coastal plain aquifer of Laizhou Bay, China," *Journal of Hydrology*, vol. 508, pp. 12–27, 2014.
- [51] S. N. Davis, D. O. Whitemore, and J. Fabryka-Martin, "Uses of chloride/bromide ratios in studies of potable water," *Groundwater*, vol. 36, no. 2, pp. 338–350, 1998.
- [52] C. E. Neuzil, "Groundwater Flow in Low-Permeability Environments," *Water Resources Research*, vol. 22, no. 8, pp. 1163–1195, 1986.
- [53] X.-S. Wang, J. J. Jiao, Y. Wang et al., "Accumulation and transport of ammonium in aquitards in the Pearl River Delta (China) in the last 10,000 years: Conceptual and numerical models," *Hydrogeology Journal*, vol. 21, no. 5, pp. 961–976, 2013.
- [54] S. L. Zhao, G. F. Yang, S. X. Gang, and H. C. Zhang, "On the marine stratigraphy and coastlines of the western coast of the gulf of Bohai," *Oceanologia et Limnologia Sinica*, vol. 9, no. 1, pp. 15–25, 1978.
- [55] C. X. Li, J. Q. Zhang, D. D. Fan, and B. Deng, "Holocene regression and the tidal radial sand ridge system formation in the Jiangsu coastal zone, east China," *Marine Geology*, vol. 173, no. 1–4, pp. 97–120, 2001.
- [56] G. A. Harrington, M. J. Hendry, and N. I. Robinson, "Impact of permeable conduits on solute transport in aquitards: Mathematical models and their application," *Water Resources Research*, vol. 43, no. 5, pp. 198–208, 2007.

- [57] M. J. Hendry, S. L. Barbour, J. Zettl, V. Chostner, and L. I. Wasseenaar, "Controls on the long-term downward transport of $\delta^2\text{H}$ of water in a regionally extensive, two-layered aquitard system," *Water Resources Research*, vol. 47, no. 6, 2011.
- [58] M. Mazurek, S. Buschaert, and O. N. E. Agency, *Natural Tracer Profiles across Argillaceous Formations: The Claytrac Project*, Nuclear Energy Agency Organisation for Economic Cooperation and Development, 2009.
- [59] J. L. Zhang, Z. G. Yu, and J. Zhang, "Wet deposition (precipitation) of major elements at two sites of northwestern Yellow Sea," *Environmental Chemistry*, vol. 19, no. 4, pp. 352–356, 2000.
- [60] G. S. Zhang, H. T. Chen, J. Zhang, and H. Z. Xin, "Major anions in the wet deposition at the Yellow Sea and the East China Sea," *Bulletin of Mineralogy, Petrology and Geochemistry*, vol. 22, no. 2, pp. 159–162, 2003.
- [61] M. Jim Hendry, S. Lee Barbour, E. E. Schmeling, S. O. C. Mundle, and M. Huang, "Fate and transport of dissolved methane and ethane in cretaceous shales of the Williston Basin, Canada," *Water Resources Research*, vol. 52, no. 8, pp. 6440–6450, 2016.
- [62] V. H. Remenda, G. Van Der Kamp, and J. A. Cherry, "Use of vertical profiles of $\delta^{18}\text{O}$ to constrain estimates of hydraulic conductivity in a thick, unfractured aquitard," *Water Resources Research*, vol. 32, no. 10, pp. 2979–2987, 1996.
- [63] J. C. McIntosh, G. Garven, and J. S. Hanor, "Impacts of Pleistocene glaciation on large-scale groundwater flow and salinity in the Michigan Basin," *Geofluids*, vol. 11, no. 1, pp. 18–33, 2011.

Research Article

Modeling of Two-Phase Flow in Rough-Walled Fracture Using Level Set Method

Yunfeng Dai,^{1,2} Zhifang Zhou,³ Jin Lin,^{1,2} and Jiangbo Han^{1,2}

¹State Key Laboratory of Hydrology-Water Resources and Hydraulic Engineering, Nanjing Hydraulic Research Institute, Nanjing 210029, China

²Groundwater Research Center, Nanjing Hydraulic Research Institute, Nanjing 210029, China

³School of Earth Sciences and Engineering, Hohai University, Nanjing 211100, China

Correspondence should be addressed to Yunfeng Dai; yfdai@nhri.cn

Received 12 July 2017; Revised 6 October 2017; Accepted 16 October 2017; Published 8 November 2017

Academic Editor: Keni Zhang

Copyright © 2017 Yunfeng Dai et al. This is an open access article distributed under the Creative Commons Attribution License, which permits unrestricted use, distribution, and reproduction in any medium, provided the original work is properly cited.

To describe accurately the flow characteristic of fracture scale displacements of immiscible fluids, an incompressible two-phase (crude oil and water) flow model incorporating interfacial forces and nonzero contact angles is developed. The roughness of the two-dimensional synthetic rough-walled fractures is controlled with different fractal dimension parameters. Described by the Navier–Stokes equations, the moving interface between crude oil and water is tracked using level set method. The method accounts for differences in densities and viscosities of crude oil and water and includes the effect of interfacial force. The wettability of the rough fracture wall is taken into account by defining the contact angle and slip length. The curve of the invasion pressure–water volume fraction is generated by modeling two-phase flow during a sudden drainage. The volume fraction of water restricted in the rough-walled fracture is calculated by integrating the water volume and dividing by the total cavity volume of the fracture while the two-phase flow is quasistatic. The effect of invasion pressure of crude oil, roughness of fracture wall, and wettability of the wall on two-phase flow in rough-walled fracture is evaluated.

1. Introduction

Two-phase flow through fractured rock is encountered in many industrial activities such as oil and gas recovery, carbon dioxide storage, and underground oil storage. It is also an important phenomenon related to non-aqueous-phase-liquid (NAPL) contamination of groundwater. A three-dimensional numerical simulator simulating two-phase flow was developed for fractured reservoirs [1] and was later used to simulate water–oil displacement in a fractured network [2].

The research of two-phase flow in fracture networks contained in fractured rock is based on that for single fracture. The numerical models that describe the two-phase flow in a single rough-walled fracture use different size scales and theories. The one-dimensional variable-aperture fracture model was initially derived, and the model was the conceptual basis used to evaluate the effect of aperture variation on two-phase flow [3, 4]. This conceptual model

employed a local cubic law (LCL). An active capillary pressure between the wetting and nonwetting phases was developed to simulate two-phase flow in rough-walled rock fractures, from which the relative permeability for the lognormal aperture distribution was calculated [5]. Based on a finite volume implementation of the cubic law and the conservation of mass, a conceptual model of two phases in a single fracture was developed, and the results of simulations were compared with a one-dimensional analytic solution [6]. A composition simulator based on Darcy's law and Brooks–Corey functional relationship was used to simulate the migration of dense NAPLs through a single fracture in a clay aquitard and to evaluate the effect of fracture aperture [7, 8]. Based on a modified TOUGH2 simulator, a continuum-based approach was used to simulate two-phase flow in a single heterogeneous fracture, and the results were compared with the invasion-percolation model [9, 10]. The multicomponent multiphase lattice Boltzmann method was used to investigate the effect of

wettability on the NAPL flow in a microscale single fracture [11, 12].

In recent years, the Navier–Stokes equations and Eulerian techniques have been used to simulate two-phase flow aided in computations from such methods as the level set method, volume of fluid method, and phase field method.

The level set method was adopted in tracking the movement of this interface under this complicated force [13–15]. The level set method was presented to simulate the motion of air bubbles in water and falling water drops in air; this method included large density and viscosity ratios as well as surface tension [16, 17]. The level set method was applied to track the motion of interfaces of pore-scale displacements of two-phase in real porous media [18]. The progressive quasistatic algorithm based on the level set method was applied in an analysis of the matrix–fracture transfer and the shape of the two-phase interface during drainage and imbibition in low permeability rock [19, 20]. The level set method was also employed to simulate quasistatic drainage and imbibition for different contact angles in porous media [21]. The level set method and phase field method were used to simulate two-phase flow with viscosity contrast through complex porous media using COMSOL software [22]. In addition, within the COMSOL platform the level set method was used to model two-phase flow in a 3 mm minichannel [23].

The foregoing methods including the ideal conceptual model, cubic law model, and continuum model have been used in simulating two-phase flow in a single fracture with reasonable success, but there were some shortcomings: (1) the ideal conceptual model based on the parallel plate theory cannot describe the rough surfaces of real rock fractures; (2) the classical LCL cannot calculate the fluid inertia and in general overestimates flow through real fractures without considering the wettability of the fracture wall; (3) the continuum model is unable to capture the characteristic of two-phase flow in an unfilled single fracture; (4) the lattice Boltzmann method is limited to model two-phase flow in a large-scale single fracture because this method needs very long calculation time; (5) the effect of the roughness on two-phase flow in an unfilled single fracture is not clearly evaluated.

To prevent crude oil from damaging the underground environment during the future operation period of underground oil storage caverns, the property of two-phase flow around oil storage caverns is a key research object. The two-phase flow in rough-walled fracture is not easily accessible experimentally, so an aperture-scale simulation of the two-phase displacement in a rough-walled fracture can provide valuable information. The main aim of the study was to simulate the two-phase (crude oil and water) flow in a rough-walled fracture using the level set method. A two-dimensional synthetic rough-walled fracture was created, based on the computational fluid dynamics adopted in COMSOL; simulations were performed. The moving interface between crude oil and water was tracked in a large-scale unfilled single fracture by overcoming the shortcomings of the previous methods, and the process of crude oil displacing water was presented under different conditions. The effect of the invasion pressure of crude oil, roughness of the

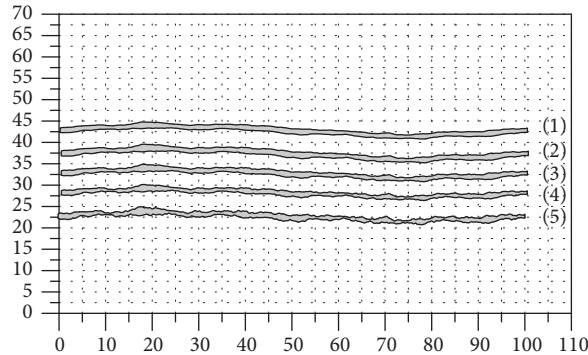


FIGURE 1: Single rough-walled fractures with fractal dimension ranging from 2.0 to 2.4 (unit: mm).

fracture wall, and wettability of the rough wall on the flow characteristics during drainage was evaluated at the same time. The methods and results are described and discussed below.

2. Synthetic Rough-Walled Fractures Based on Fractal Dimension

For the purpose of modeling two-phase flow in rough-walled fractures, synthetic rough fractures were used. These fractures were generated using the software SynFrac, which enables a numerical configuring of fractures of different roughness and average apertures, and it provides much more realistic numerically synthesized fractures than previous methods [25–28]. SynFrac was also used to generate a series of similar fractures with increasing roughness, to allow the effect of roughness on transport in fractures to be evaluated [29].

A series of similar rough-walled fractures with increasing roughness was created by controlling its associated fractal dimension (FD). A 100 mm two-dimensional profile was selected from the data of a three-dimensional fracture, while ensuring that the two-dimensional fracture had no contact point. With FD ranging from 2.0 to 2.4, the mean aperture of the synthetic rough fractures is 1.5 mm. The input parameters for the SynFrac software are listed in Table 1. The resolution (1024×1024), standard deviation (1 mm), and anisotropy factor (1.0) are kept constant. The five different fractures are drawn in Figure 1.

3. Numerical Model of Two-Phase Flow with Level Set Method

When the two-phase immiscible fluids are in contact with the wall in an unfilled fracture, the pressure difference at the interface of the two fluids is defined as the capillary pressure written as [3]

$$p_c = p_{nw} - p_w = 2\sigma \frac{\cos \theta}{r}, \quad (1)$$

where p_c is capillary pressure (Pa), p_{nw} the pressure in the NAPL (Pa), p_w the pressure in aqueous phase liquid (Pa),

TABLE 1: Input parameters of SynFrac for generation of fractures with various roughness.

	Fracture 1	Fracture 2	Fracture 3	Fracture 4	Fracture 5
Resolution	1024 × 1024	1024 × 1024	1024 × 1024	1024 × 1024	1024 × 1024
Random number generator	Park & Miller				
Length (mm)	100	100	100	100	100
Mismatch length	15	15	15	15	15
Standard deviation (mm)	1.0	1.0	1.0	1.0	1.0
Anisotropy factor	1	1	1	1	1
Fractal dimension	2.0	2.1	2.2	2.3	2.4

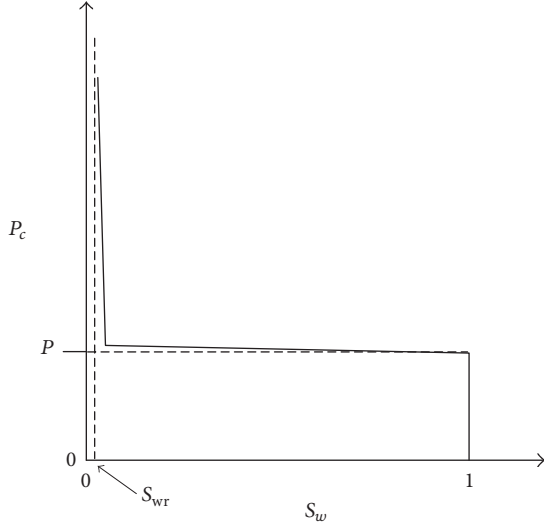


FIGURE 2: Capillary pressure-saturation relationship at the local position in a single fracture (S_w is water saturation and S_{wr} the residual wetting phase saturation) [10, 24].

σ the interfacial force (N/m), θ the contact angle of the two-phase fluid interface with the fracture wall (rad), and r the average radius of curvature in the single rough-walled fracture (m).

To describe the process in which the NAPL displaces the aqueous phase liquid, a specific capillary pressure-saturation curve (Figure 2) at the local position of the fracture was proposed [10, 24]. At this local position for a single fracture, the NAPL entry pressure P can be calculated:

$$P = \frac{2\sigma \cos \theta}{b}, \quad (2)$$

where b is the local aperture of the single fracture (m).

To analyze similar process for a single unfilled rough-walled fracture around an oil storage cavern, it is necessary to simulate the two-phase flow considering the effect of the NAPL invasion pressure and the capillary pressure at the interface of the two-phase fluids. Interface tracking is the key element of the modeling of this two-phase flow.

Level set tracking of the interface uses an auxiliary function on the fixed finite element mesh. The differences in densities, viscosities, and interfacial forces of the two immiscible fluids are considered in level set method [30]. For

the horizontal single fracture of this study, the effect of gravity on the two fluids is ignored. The incompressible formation of the Navier–Stokes equations is used to calculate the two-phase flow in an unfilled fracture [30, 31]:

$$\rho \frac{\partial \mathbf{u}}{\partial t} + \rho (\mathbf{u} \cdot \nabla) \mathbf{u} = \nabla \cdot [-p\mathbf{I} + \mu (\nabla \mathbf{u} + \nabla \mathbf{u}^T)] + \mathbf{F}_{st} \quad (3)$$

$$\nabla \cdot \mathbf{u} = 0, \quad (4)$$

where ρ is the average density of the two immiscible fluids (kg/m^3), \mathbf{u} the velocity vector, \mathbf{I} the position vector, t the time (s), p the pressure in fluid (Pa), μ the average dynamic viscosity of two immiscible fluids ($\text{Pa}\cdot\text{s}$), \mathbf{F}_{st} the interfacial force (N/m), and ∇ the Laplace operator.

The auxiliary function added to track the interface is defined by [23, 30, 31]

$$\frac{\partial \phi}{\partial t} + \mathbf{u} \cdot \nabla \phi = \gamma \nabla \cdot \left(\varepsilon \nabla \phi - \phi (1 - \phi) \frac{\nabla \phi}{|\nabla \phi|} \right), \quad (5)$$

where the auxiliary level set function ϕ representing the interface is a smooth continuous function; where $\phi < 0.5$, the fracture cavity regions are filled with NAPL; where $\phi = 0.5$, the regions are part of the interface; where $\phi > 0.5$, the regions are filled with aqueous phase liquid. The parameter γ controls the intensity of reinitialization (m/s) and ε controls the interface thickness (m).

The density and dynamic viscosity vary smoothly over the interface, and the average density and dynamic viscosity can be defined using the level set function [30, 31]:

$$\rho = \rho_1 + (\rho_2 - \rho_1) \phi \quad (6)$$

$$\mu = \mu_1 + (\mu_2 - \mu_1) \phi,$$

where ρ_1 and ρ_2 are constants representing the densities of NAPL and aqueous phase liquid; μ_1 and μ_2 are constants representing dynamic viscosities of NAPL and aqueous phase liquid.

The interfacial force of the right-hand side in (3) can be calculated using [30]

$$\mathbf{F}_{st} = \sigma \kappa \delta \mathbf{n}, \quad (7)$$

where σ is the interfacial force coefficient (N/m), \mathbf{n} the unit normal to the interface, δ Dirac's delta-function specifying the interface (1/m), and κ the second derivative of the level set function.

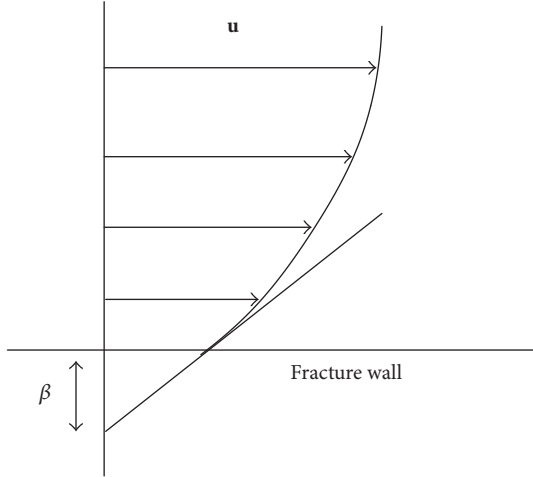


FIGURE 3: Definition of the slip length.

To avoid poor accuracy in calculating the interfacial force derived from κ , the formulation of this force is developed further [30, 32]:

$$\mathbf{F}_{st} = \nabla \cdot (\sigma (\mathbf{I} - (\mathbf{nn}^T)) \delta |\nabla \phi| |\phi (1 - \phi)|). \quad (8)$$

The initial condition imposed in this model of two-phase flow in a rough-walled fracture is

$$\begin{aligned} p(x, t) &= 0, & t &= 0 \\ S_{wat}(t) &= 1, & t &= 0, \end{aligned} \quad (9)$$

where x is the position in the fracture and S_{wat} the volume fraction of water in the fracture cavity.

The boundary conditions include those for the inlet and outlet boundaries and the wetted wall boundary of the fracture. The inlet boundary is a constant-pressure boundary, and a pressure equals the invasion pressure p_o of the NAPL. The outlet boundary is also a constant-pressure boundary but with the pressure equal to zero.

The properties of the wetted wall boundary include adopting the slip wall condition and setting the contact angle between the interface of two-phase fluid and the fracture wall. In the level set method, the slip wall condition of the interface along the fracture wall adds a frictional force [30]:

$$\begin{aligned} \mathbf{u} \cdot \mathbf{n}_{wall} &= 0 \\ \mathbf{F}_{fr} &= -\frac{\mu}{\beta} \mathbf{u}, \end{aligned} \quad (10)$$

where \mathbf{n}_{wall} is the unit normal to the wall, \mathbf{F}_{fr} the frictional force on the wall (N/m), and β the slip length (m) (see Figure 3). In simulations, the slip length is set equal to the size of the mesh element.

The contact angle between the interface and fracture wall (Figure 4) is used to reflect the wettability of the rough-walled fracture [12]. In the level set method, given the contact angle

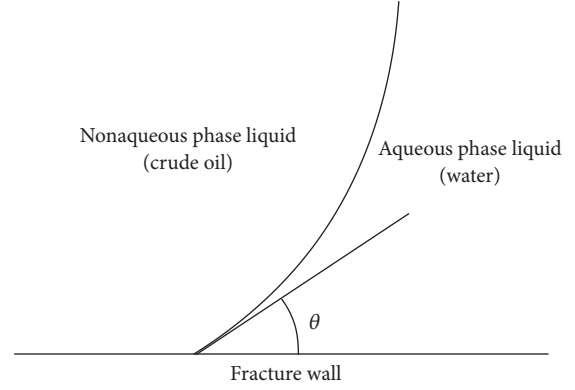


FIGURE 4: Definition of the contact angle.

θ , a weak boundary term is added in the wetted wall boundary condition [30]:

$$\int_{\partial\Omega} \text{test}(\mathbf{u}) \cdot [\sigma (\mathbf{n}_{wall} - (\mathbf{n} \cos \theta)) \delta] dS. \quad (11)$$

The modeling of this two-phase flow using the level set method employs the computational fluid dynamics module of COMSOL Multiphysics and was run on a 2.5 GHz PC with 8 G memory. The solver for the two-phase flow interface was automatically selected for this purpose in COMSOL, and the linear system solver with direct methods was chosen in this paper.

4. Effect of Important Parameters on Two-Phase Flow in Rough-Walled Fracture

Water-sealed underground oil storage caverns are generally artificially excavated in fresh rock below a certain groundwater level [33]. After the excavation of oil storage caverns some fractures in the rock will open or be generated; it is necessary to study drainage process of crude oil invasion of a saturated single rough-walled fracture around oil storage caverns. The effects of invasion pressure, fracture roughness, and wettability of the fracture wall were evaluated by calculating volume-fraction curves of water in the fracture cavity.

4.1. Main Parameters of Simulation. In simulating crude oil displacing water in single unfilled fractures, various roughness was set by allowing the FD to range from 2.0 to 2.4. Three different contact angles were chosen: 30° , 45° , and 60° .

The single fractures were subdivided with triangular meshes using the finite element method. The size of the maximum/minimum element is 0.2 mm/0.01 mm. Hence, for example, if the FD is 2.0, the number of elements is 22716 after triangular subdivision.

The two immiscible fluids, crude oil and water, and the values of their physical properties are listed in Table 2 [34].

4.2. Effect of Invasion Pressure of Crude Oil. Fracture 1 with FD of 2.0 was chosen for the analysis of the effect of the invasion pressure. During the simulation, the contact angle

TABLE 2: Parameter values of the physical properties of crude oil and water.

	Temperature	Density (Kg/m ³)	Dynamic viscosity (Pa·s)	Interfacial force (N/m)
Crude oil (40API)	15.6°C	8.25×10^2	8.0×10^{-3}	0.0307
Water		9.99×10^2	1.1×10^{-3}	

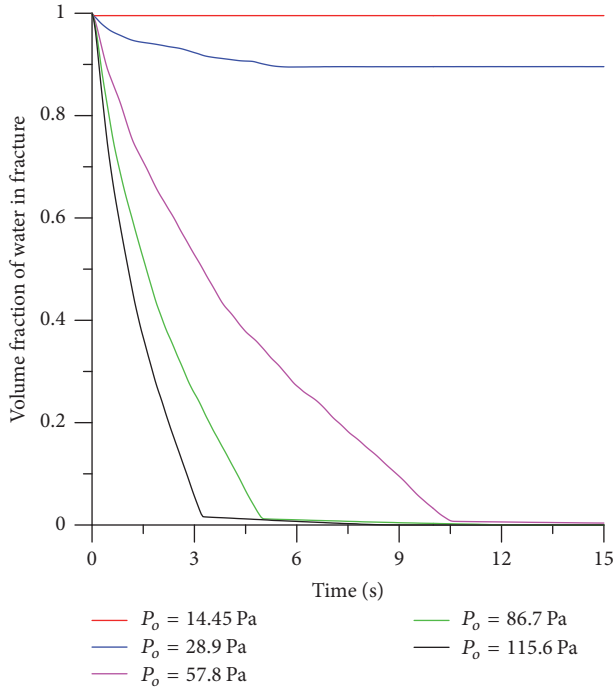


FIGURE 5: Volume fraction of water in fracture for different invasion pressures of crude oil.

was maintained constant at 45°. The single rough-walled fracture was saturated initially with water. The crude oil invades the fracture from the left-hand side as the invasion pressure increases from 14.45 Pa to 115.6 Pa. The curves of the volume fraction of water in the fracture decrease with increasing invasion pressure (Figure 5). For an average aperture 1.5 mm, (2) gives an entry pressure of 28.9 Pa. While the invasion pressure of the crude oil is less than or equal to 28.9 Pa, the crude oil is unable to break through the fracture. With apertures less than the average aperture, crude oil is trapped in local positions after displacing some water from the fracture. Figure 6 presents the distribution of crude oil trapped in the fracture and the aperture distribution along the fracture for invasion pressures of 14.45 Pa and 28.9 Pa. At the low pressure, crude oil nearly does not displace water, whereas at the higher pressure crude oil is trapped at the position 11 mm where the local aperture is 1.07 mm, and the volume fraction of water is 0.896. As evident in Figure 5, the invasion pressure is greater than 28.9 Pa, the crude oil can break through the fracture. Increasing the invasion pressure from 57.8 Pa to 115.6 Pa leads to faster displacements with times falling from 10.5 s to 3.25 s. The plots of invasion pressure of crude oil and volume fraction of water in the fracture at different times are presented in Figure 7. As the

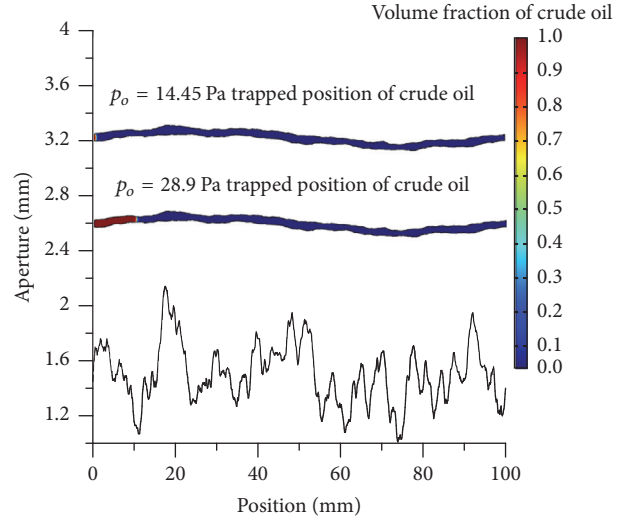


FIGURE 6: Distribution of aperture and trapped crude oil in the fractures.

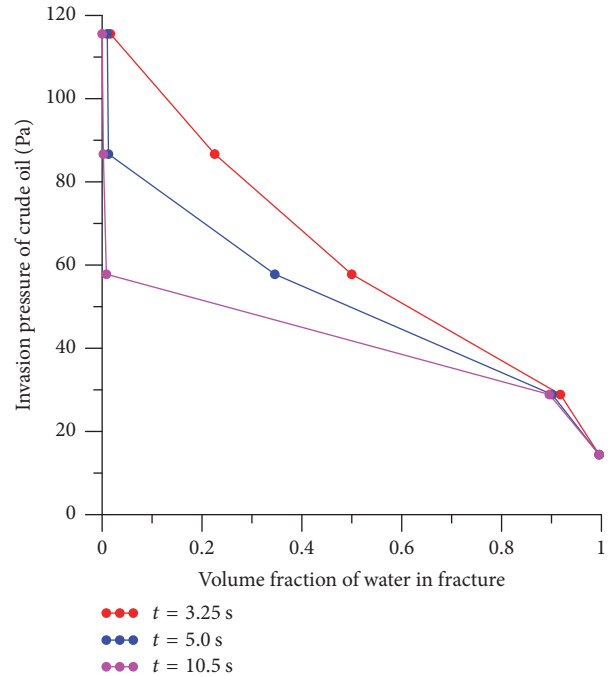


FIGURE 7: Relationship curves of the invasion pressure of crude oil and the volume fraction of water in the fracture at different times.

invasion time increases, the shape of the curve approaches that for capillary pressure-saturation (Figure 2). With the level set method, the drainage of water from the saturated

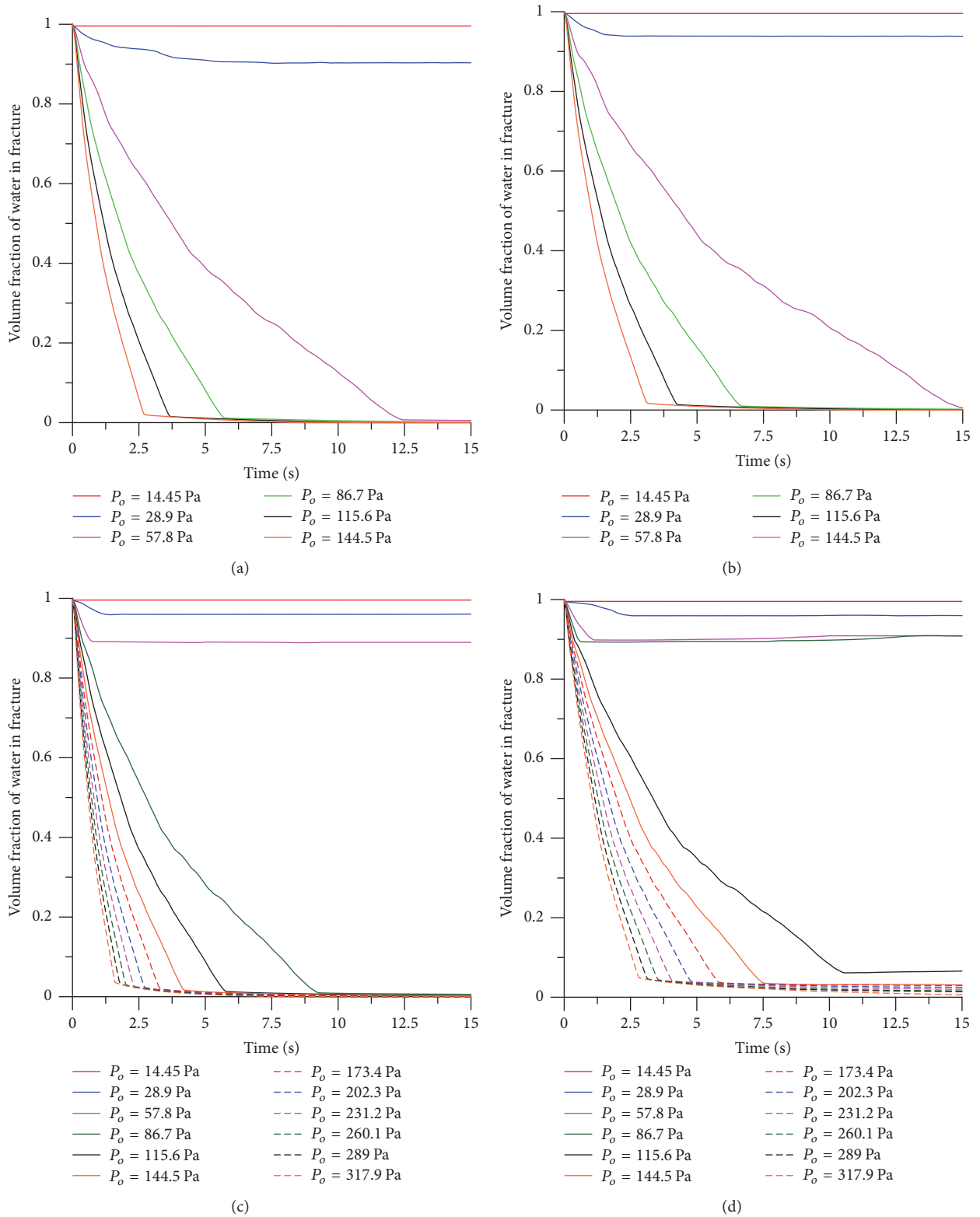


FIGURE 8: Volume fraction of water for different roughness fractures during drainage: (a) $FD = 2.1$; (b) $FD = 2.2$; (c) $FD = 2.3$; (d) $FD = 2.4$.

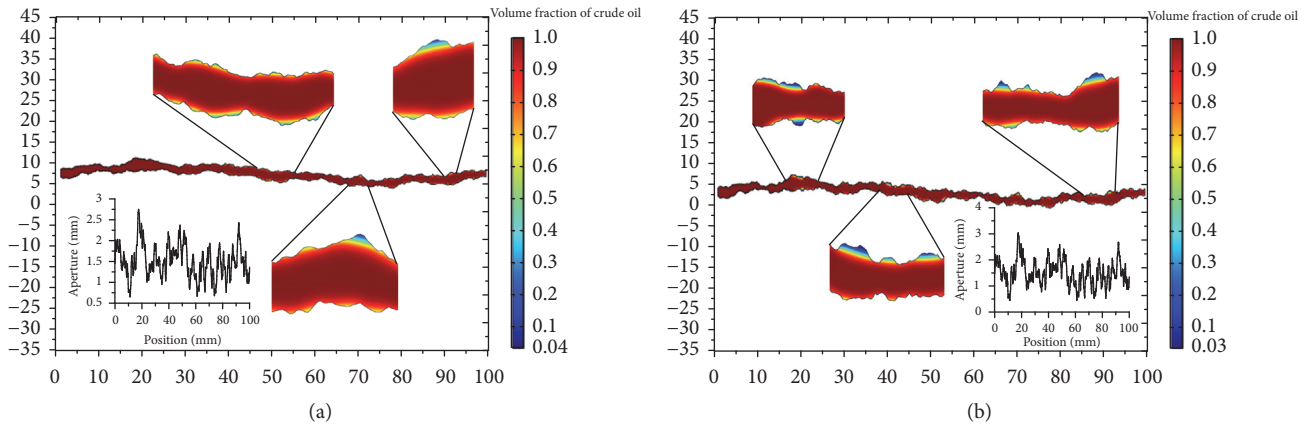


FIGURE 9: Distribution of aperture and restrict position of water while the crude oil is breaking through the fractures: (a) $FD = 2.3$ and $P_o = 317.9$ Pa; (b) $FD = 2.4$ and $P_o = 317.9$ Pa.

fracture has been simulated accurately, and the residual water saturation can be calculated directly.

4.3. Effect of Fracture Roughness. To analyze the effect of fracture roughness on the displacement of water by crude oil, five rough-walled fractures were generated using different FD values (Figure 1) from 2.0 to 2.4 in steps of 0.1; the contact angle of the wall is set to 45° . During drainage, the volume fraction of water decreases with different fracture roughness and FD from 2.1 to 2.4 (Figure 8). With invasion pressure less than or equal to 28.9 Pa crude oil becomes trapped in fracture 2 ($FD = 2.1$) and fracture 3 ($FD = 2.2$), and the volume fraction of the water in fracture 2 ($FD = 2.1$) is less than that in fracture 3 ($FD = 2.2$). Clearly, the crude oil is more easily trapped in fractures with high roughness. As the invasion pressure rises to 57.8 Pa, the crude oil begins to break through fracture 2 ($FD = 2.1$) and fracture 3 ($FD = 2.2$) but is trapped in fracture 4 ($FD = 2.3$) and fracture 5 ($FD = 2.4$). With invasion pressures exceeding 115.6 Pa, crude oil can break through all four fractures.

As crude oil is breaking through the fractures some water still exists in the fracture at that instant (Figure 8). Higher invasion pressures lead to rapid crude oil breaking through the fracture with more water existing in the fracture. As time elapses, the volume fraction of water in the fracture decreases slowly. While the crude oil is breaking through fracture 4 and fracture 5 (at times 1.6 s and 2.85 s), the distributions of the crude oil in the fractures are obtained (Figure 9). In the left half of the fracture 4 ($FD = 2.3$) almost all water is displaced by crude oil, whereas in the right half of the fracture some water is restricted on the rough wall where local apertures are comparatively large. Because the left half of the fracture 4 is less rough than the right half, the average aperture of the left hand is larger than that of the right hand. The water in the left half was more easily displaced by crude oil which needs low NAPL entry pressure. Unlike fracture 4 some of water is restricted on the rough wall along the fracture 5 ($FD = 2.4$). The results obtained by modeling the two-phase flow indicates that a large roughness leads to more water restricted between crude oil and the wall of the fracture.

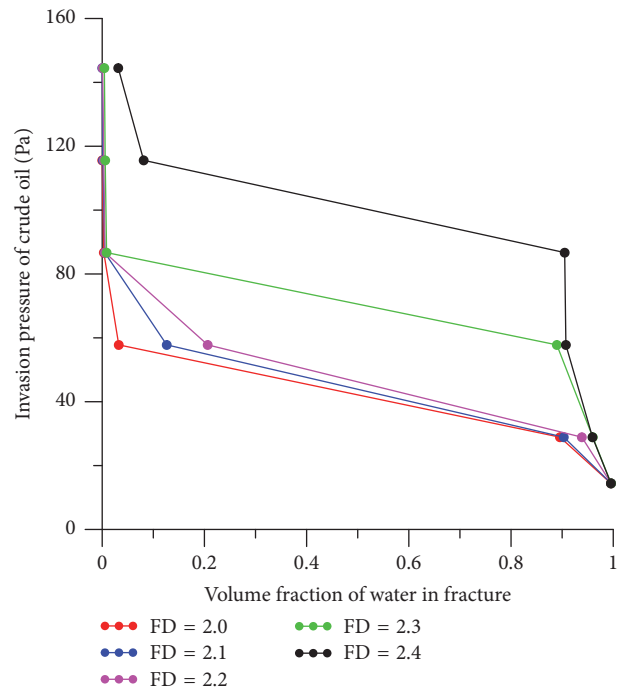


FIGURE 10: Relationship curves of the invasion pressure of crude oil and the volume fraction of water in the fracture for different roughness at time 10 s.

To analyze the effect of roughness on the two-phase flow further, the relationship curves of invasion pressure of crude oil and the volume fraction of water in the fracture for different roughness at time 10 s are calculated (Figure 10). The results from modeling show that, with large fracture roughness, water is not easily displaced by crude oil, and increasing the roughness changes the rate of drainage noticeably.

4.4. Effect of Wettability of the Fracture Wall. To evaluate the effect of wettability of the fracture wall on the two-phase flow, three fractures (fractures 1, 3, and 5) with contact angles 30° and 60° were used in the numerical calculations.

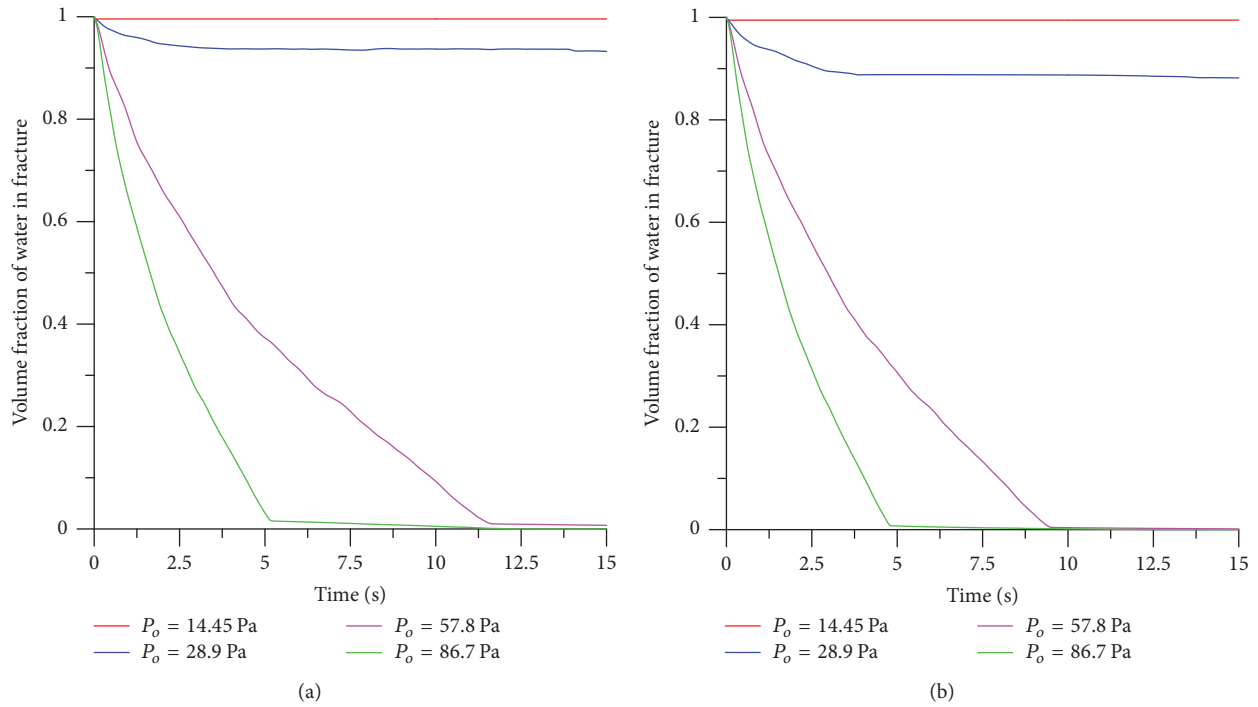


FIGURE 11: Volume fraction of water in the fracture for different wettability setting for fracture wall: (a) $FD = 2.0$, contact angle 30° ; (b) $FD = 2.0$, contact angle 60° .

The volume fraction of water in fracture 1 ($FD = 2.0$) shows a decline with contact angles 30° and 60° (Figure 11). A comparison of simulation results presented in Figures 11(a) and 11(b) indicates that as crude oil is trapped in the fracture, the volume fraction of water decreases with increasing contact angle from 30° to 60° . While the crude oil is breaking through the fracture, an increase in contact angle leads to a decrease of the breakthrough time. The simulation results are in accord with (2), from which entry pressure decreases as contact angle increases at each local position. The relation between invasion pressure of crude oil and the volume fraction of water in the fracture for different contact angles at time 15 s is presented in Figure 12. The change in contact angle does not make any significant difference on the shape of curves during drainage.

The decreasing curves for the volume fraction of water for fracture 3 ($FD = 2.2$) with contact angles 30° and 60° are shown in Figure 13. The relationship between the invasion pressure of crude oil and the volume fraction of water in the fracture for different contact angles at time 15 s is given in Figure 14. The increase in contact angle leads to a decrease in the breakthrough time but does not make a large difference on the curves of invasion pressure and volume fraction of water in the fracture. With invasion pressures of 28.9 Pa and 57.8 Pa, the volume fraction of water in the fracture decreases slightly for the contact angles of 30° and 60° .

Figure 15 shows a decreasing trend for the volume fraction of water in fracture 5 ($FD = 2.4$) with contact angle set at 60° . With contact angle of 30° , the numerical calculation of the two-phase flow was not stable. With the level set method,

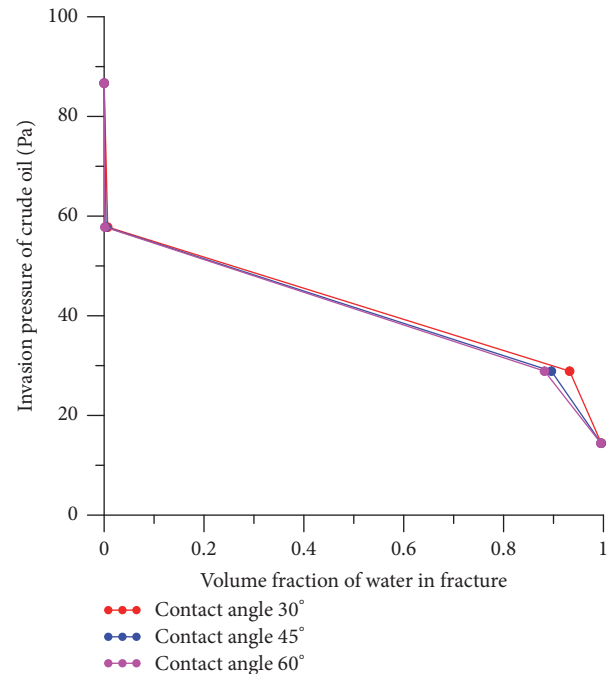


FIGURE 12: Relationship between the invasion pressure of crude oil and volume fraction of water in the fracture for different contact angles at time 15 s ($FD = 2.0$).

the small contact angle requires a large local entry pressure causing an oscillation in simulation results after crude oil

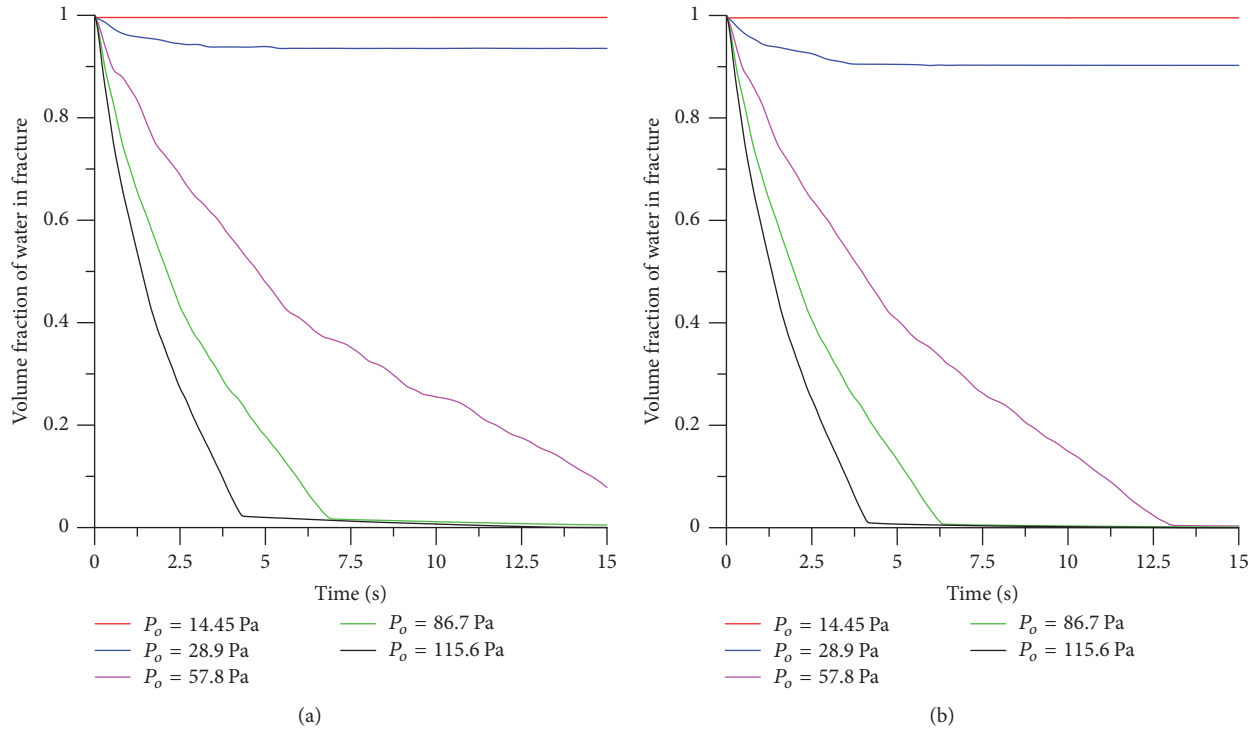


FIGURE 13: Volume fraction of water in the fracture for different wettability setting of the fracture wall: (a) FD = 2.2, contact angle 30°; (b) FD = 2.2, contact angle 60°.

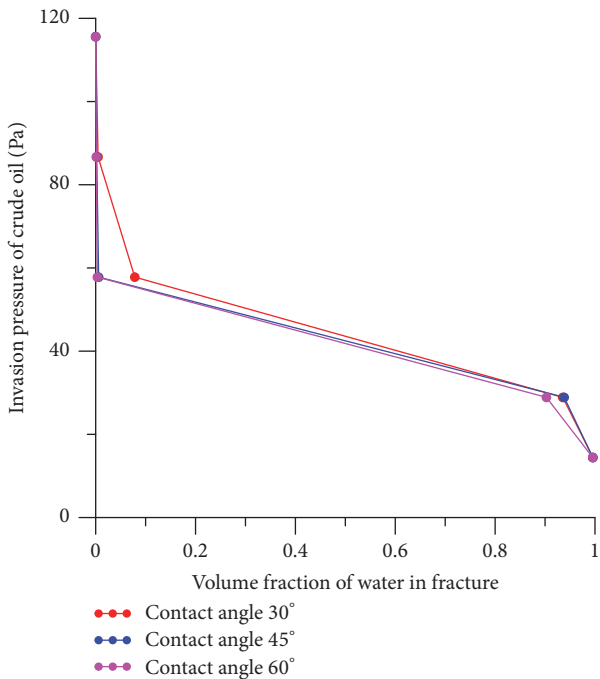


FIGURE 14: Relationship between the invasion pressure of crude oil and the volume fraction of water in the fracture for different contact angles at time 15 s (FD = 2.2).

being trapped in the very rough wall of the fracture. The relationship between the invasion pressure of crude oil and

volume fraction of water in the fracture for different contact angles at time 10 s (Figure 16) indicates that after crude oil breaks through the fracture, the volume fraction of water decreases noticeably because of the addition 15° of the contact angle.

5. Conclusions

In this study, the level set method was used to simulate the process of crude oil invasion into an unfilled two-dimensional rough-walled fracture saturated by water and to investigate the influences of the fracture roughness and wettability of the fracture wall on the relationship between the invasion pressure of crude oil and the volume fraction of water.

Increasing the invasion pressure decreases the breakthrough time, whereas the water volume fraction in the fracture is inversely proportional to the invasion pressure of crude oil as it breaks through the fracture. Larger roughness leads to more water being restricted between crude oil and the wall of fracture. The breakthrough times of crude oil decrease for large contact angles (high wettability), along with the volume fraction of residual water. Compared with the wettability of the fracture wall, wall roughness significantly affects the relationship between the invasion pressure of crude oil and volume fraction of water.

These simulation results are useful to understanding of the characteristics of two-phase (crude oil and water) flow in fractures around underground oil storage caverns.

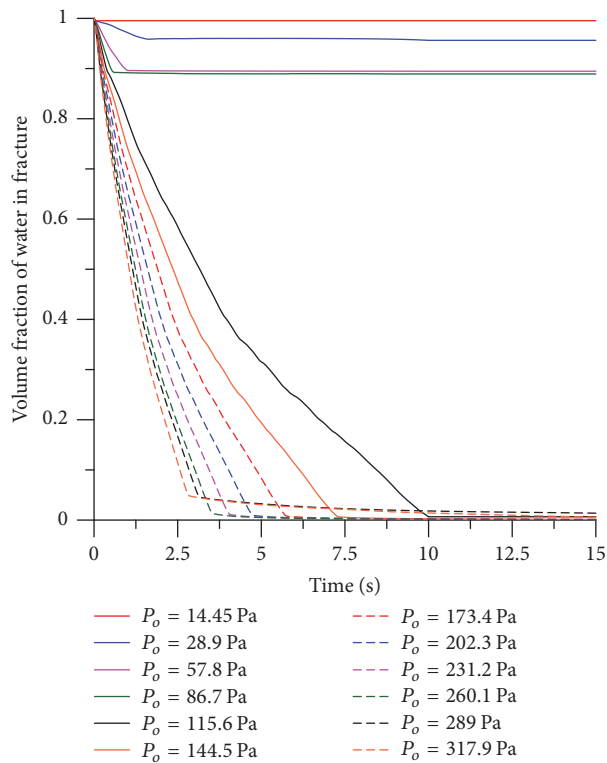


FIGURE 15: Volume fraction of water in a fracture with a wettable fracture wall (FD = 2.4, contact angle 60°).

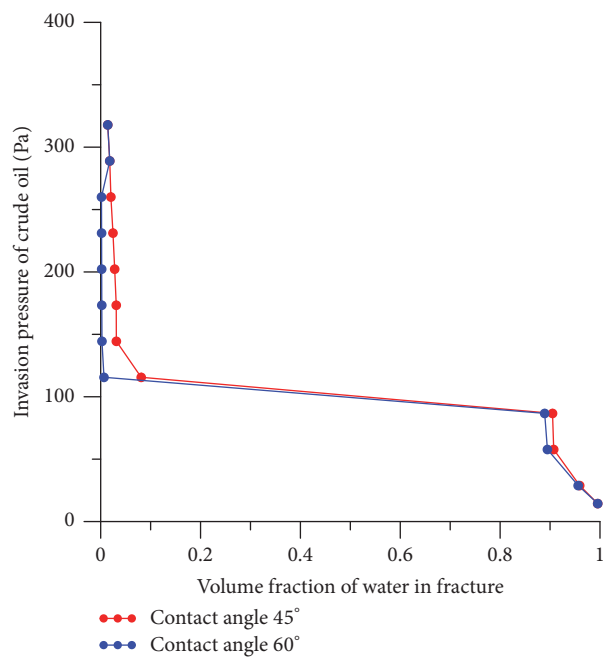


FIGURE 16: Relationship between the invasion pressure of crude oil and the volume fraction of water in the fracture for different contact angles at time 10 s (FD = 2.4).

Conflicts of Interest

The authors declare that there are no conflicts of interest regarding the publication of this paper.

Acknowledgments

The study is financially supported by National Key R&D Program of China (Grant no. 2016YFC0402800), project supported by National Natural Science Foundation of China (Grant no. 51709186), Special Funds for Basic Research and Business Expenses of Central Level Public Welfare Research Institutes (Grant no. Y516030), project supported by Basic Research Program (Natural Science Foundation) of Jiangsu Province (Grant no. BK20170154), and China Postdoctoral Science Foundation funded project (Grant no. 2017M611863). The authors also thank Richard Haase, Ph.D., from Liwen Bianji, Edanz Group China (<https://www.liwenbianji.cn/ac>), for editing the English text of a draft of this manuscript.

References

- [1] J. E. Warren and P. J. Root, "The behavior of naturally fractured reservoirs," *Old SPE Journal*, vol. 3, no. 3, pp. 245–255, 1963.
- [2] H. Kazemi, L. S. Merrill, K. L. Porterfield, and P. R. Zeman, "Numerical simulation of water-oil flow in naturally fractured reservoirs," *Society of Petroleum Engineers Journal*, vol. 16, pp. 317–326, 1976.
- [3] W. F. Zhou, H. S. Wheeler, K. Kovar, and J. Krasny, "Effect of aperture variation on two phase flow in fractures," *International Journal of Rock Mechanics & Mining Sciences & Geomechanics Abstracts*, vol. 7, 325A, 1995.
- [4] W. Zhou, "Numerical simulation of two-phase flow in conceptualized fractures," *Environmental Geology*, vol. 40, no. 7, pp. 797–808, 2001.
- [5] K. Pruess and Y. W. Tsang, "On two-phase relative permeability and capillary pressure of rough-walled rock fractures," *Water Resources Research*, vol. 26, no. 9, pp. 1915–1926, 1990.
- [6] J. R. Murphy and N. R. Thomson, "Two-phase flow in a variable aperture fracture," *Water Resources Research*, vol. 29, no. 10, pp. 3453–3476, 1993.
- [7] D. A. Reynolds and B. H. Kueper, "Multiphase flow and transport in fractured clay/sand sequences," *Journal of Contaminant Hydrology*, vol. 51, no. 1-2, pp. 41–62, 2001.
- [8] D. A. Reynolds and B. H. Kueper, "Numerical examination of the factors controlling DNAPL migration through a single fracture," *Groundwater*, vol. 40, no. 4, pp. 368–377, 2002.
- [9] Z. Yang, A. Niemi, F. Fagerlund, and T. Illangasekare, "Effects of single-fracture aperture statistics on entrapment, dissolution and source depletion behavior of dense non-aqueous phase liquids," *Journal of Contaminant Hydrology*, vol. 133, pp. 1–16, 2012.
- [10] Z. Yang, A. Niemi, F. Fagerlund, and T. Illangasekare, "A generalized approach for estimation of in-plane curvature in invasion percolation models for drainage in fractures," *Water Resources Research*, vol. 48, no. 9, Article ID W09507, 2012.
- [11] Z. Dou, Z.-f. Zhou, Y. Huang, and W. Wu, "Numerical study of non-aqueous phase liquid transport in a single filled fracture by lattice boltzmann method," *Journal of Hydrodynamics, Ser. B*, vol. 24, pp. 130–137, 2012.

- [12] Z. Dou, Z. Zhou, and B. E. Sleep, "Influence of wettability on interfacial area during immiscible liquid invasion into a 3D self-affine rough fracture: lattice Boltzmann simulations," *Advances in Water Resources*, vol. 61, pp. 1–11, 2013.
- [13] S. Osher and J. A. Sethian, "Fronts propagating with curvature-dependent speed: algorithms based on Hamilton-Jacobi formulations," *Journal of Computational Physics*, vol. 79, no. 1, pp. 12–49, 1988.
- [14] J. A. Sethian, *Level Set Methods and Fast Marching Methods: Evolving Interfaces in Computational Geometry, Fluid Mechanics, Computer Vision, and Material Science*, vol. 3 of *Cambridge Monographs on Applied and Computational Mathematics*, Cambridge University Press, Cambridge, UK, 2nd edition, 1999.
- [15] S. Osher and R. Fedkiw, *Level Set Methods and Dynamic Implicit Surfaces*, Springer-Verlag, New York, NY, USA, 2003.
- [16] M. Sussman, P. Smereka, and S. Osher, "A level set approach for computing solutions to incompressible two-phase flow," *Journal of Computational Physics*, vol. 114, no. 1, pp. 146–159, 1994.
- [17] M. Sussman, E. Fatemi, S. Osher, and P. Smereka, "A level set approach for computing solutions to incompressible two-phase flow II," in *Proceedings of the 6th international symposium on computational fluid dynamics*, pp. 4–8, Lake Tahoe, NV, USA, Sep 1995.
- [18] M. Prodanovic and S. L. Bryant, "A level set method for determining critical curvatures for drainage and imbibition," *Journal of Colloid and Interface Science*, vol. 304, pp. 442–458, 2006.
- [19] M. Prodanovic and S. L. Bryant, "Physics-Derived interface modeling for drainage and imbibition in fractures," *SPE Journal*, vol. 14, pp. 532–542, 2007.
- [20] M. Prodanović, S. L. Bryant, and Z. T. Karpyn, "Investigating matrix/Fracture transfer via a level set method for drainage and imbibition," *SPE Journal*, vol. 15, no. 1, pp. 125–136, 2010.
- [21] E. Jettestuen, J. O. Helland, and M. Prodanović, "A level set method for simulating capillary-controlled displacements at the pore scale with nonzero contact angles," *Water Resources Research*, vol. 49, no. 8, pp. 4645–4661, 2013.
- [22] H. A. Akhlaghi Amiri and A. A. Hamouda, "Evaluation of level set and phase field methods in modeling two phase flow with viscosity contrast through dual-permeability porous medium," *International Journal of Multiphase Flow*, vol. 52, pp. 22–34, 2013.
- [23] H. Grzybowski and R. Mosdorf, "Modelling of two-phase flow in a minichannel using level-set method," *Journal of Physics: Conference Series*, vol. 530, article 012049, 2014.
- [24] Z. Yang, A. Niemi, F. Fagerlund, and T. Illangasekare, "Two-phase flow in rough-walled fractures: Comparison of continuum and invasion-percolation models," *Water Resources Research*, vol. 49, no. 2, pp. 993–1002, 2013.
- [25] S. R. Brown, H. W. Stockman, and S. J. Reeves, "Applicability of the Reynolds Equation for modeling fluid flow between rough surfaces," *Geophysical Research Letters*, vol. 22, no. 18, pp. 2537–2540, 1995.
- [26] P. W. J. Glover, K. Matsuki, R. Hikima, and K. Hayashi, "Fluid flow in synthetic rough fractures and application to the Hachimantai geothermal hot dry rock test site," *Journal of Geophysical Research: Solid Earth*, vol. 103, no. 5, pp. 9621–9635, 1998.
- [27] P. W. J. Glover, K. Matsuki, R. Hikima, and K. Hayashi, "Synthetic rough fractures in rocks," *Journal of Geophysical Research: Solid Earth*, vol. 103, no. 5, pp. 9609–9620, 1998.
- [28] S. R. Ogilvie, E. Isakov, and P. W. J. Glover, "Fluid flow through rough fractures in rocks. II: A new matching model for rough rock fractures," *Earth and Planetary Science Letters*, vol. 241, no. 3–4, pp. 454–465, 2006.
- [29] S. Briggs, B. W. Karney, and B. E. Sleep, "Numerical modelling of flow and transport in rough fractures," *Journal of Rock Mechanics and Geotechnical Engineering*, vol. 6, no. 6, pp. 535–545, 2014.
- [30] Comsol, "Computational Fluid Dynamics User's Guide. Version 4.2, 2011".
- [31] E. Olsson and G. Kreiss, "A conservative level set method for two phase flow," *Journal of Computational Physics*, vol. 210, no. 1, pp. 225–246, 2005.
- [32] B. Lafaurie, C. Nardone, R. Scardovelli, S. Zaleski, and G. Zanetti, "Modelling merging and fragmentation in multiphase flows with SURFER," *Journal of Computational Physics*, vol. 113, no. 1, pp. 134–147, 1994.
- [33] Y. Dai and Z. Zhou, "Steady seepage simulation of underground oil storage caverns based on Signorini type variational inequality formulation," *Geosciences Journal*, vol. 19, no. 2, pp. 341–355, 2015.
- [34] J. P. Everett and C. F. Weinaug, "Physical Properties of Eastern Kansas Crude Oils," in *Kansas Geological Survey, Part 7, Bulletin 114*, 1955.

Research Article

Numerical Investigation of the Influences of Wellbore Flow on Compressed Air Energy Storage in Aquifers

Yi Li,¹ Keni Zhang,² Litang Hu,¹ and Jinsheng Wang¹

¹College of Water Sciences, Engineering Research Centre of Groundwater Pollution Control and Remediation of Ministry of Education, Beijing Normal University, Beijing 100875, China

²Institute of Groundwater and Earth Sciences, Jinan University, Guangzhou 510632, China

Correspondence should be addressed to Litang Hu; litanghu@bnu.edu.cn

Received 7 July 2017; Accepted 8 October 2017; Published 31 October 2017

Academic Editor: Marco Petitta

Copyright © 2017 Yi Li et al. This is an open access article distributed under the Creative Commons Attribution License, which permits unrestricted use, distribution, and reproduction in any medium, provided the original work is properly cited.

With the blossoming of intermittent energy, compressed air energy storage (CAES) has attracted much attention as a potential large-scale energy storage technology. Compared with caverns as storage vessels, compressed air energy storage in aquifers (CAESA) has the advantages of wide availability and lower costs. The wellbore can play an important role as the energy transfer mechanism between the surroundings and the air in CAESA system. In this paper, we investigated the influences of the well screen length on CAESA system performance using an integrated wellbore-reservoir simulator (T2WELL/EOS3). The results showed that the well screen length can affect the distribution of the initial gas bubble and that a system with a fully penetrating wellbore can obtain acceptably stable pressurized air and better energy efficiencies. Subsequently, we investigated the impact of the energy storage scale and the target aquifer depth on the performance of a CAESA system using a fully penetrating wellbore. The simulation results demonstrated that larger energy storage scales exhibit better performances of CAESA systems. In addition, deeper target aquifer systems, which could decrease the energy loss by larger storage density and higher temperature in surrounding formation, can obtain better energy efficiencies.

1. Introduction

Compressed air energy storage (CAES) can be considered as a potential storage technology combined with intermittent energy sources (e.g., wind energy and solar energy). Compressed air is injected into a “storage vessel” using excess electricity and can be produced to generate electricity as needed [1–3]. The scale of the stored energy depends on the choice of the storage vessel. Porous rock reservoirs (aquifers) and cavern reservoirs (salt domes or caverns in hard rock) are candidates for large-scale storage vessels (Figure 1). The Huntorf plant in Germany (290 MW) and the McIntosh plant in the USA (110 MW) are two existing commercial large-scale compressed air energy storage plants [4, 5]. They both use a salt dome (cavern reservoir) as the air storage vessel. Thermodynamic and hydrodynamic studies of compressed air energy storage in caverns (CAESC) have been conducted to describe the pressure and temperature variances [6–10].

Additionally, an advanced CAES system (adiabatic compressed air energy storage) with no reheating requirements to regenerate electricity has been investigated [9, 11–13].

Compressed air energy storage in aquifers (CAESA), which costs less and has a wider availability, is becoming more attractive compared with CAESC [2, 14]. The feasibility of CAESA was investigated by Oldenburg and Pan using numerical modelling, which showed its energy efficiency well using the operation scheme in the Huntorf plant [15]. Later, they proposed and simulated the utilization of CO₂ as a cushion gas for a CAESA system [16]. The impact factors on the variances of pressure and temperature have been studied, including the reservoir permeability, gas bubble volume, gas bubble boundary permeability, and geological structures and thicknesses [17–19]. In addition, the ranking criteria for candidate sites were suggested by Succar and Williams [2]. The Iowa Stored Energy Park (ISEP) planned to build a 270 MW CAESA plant, but the project had to be cancelled

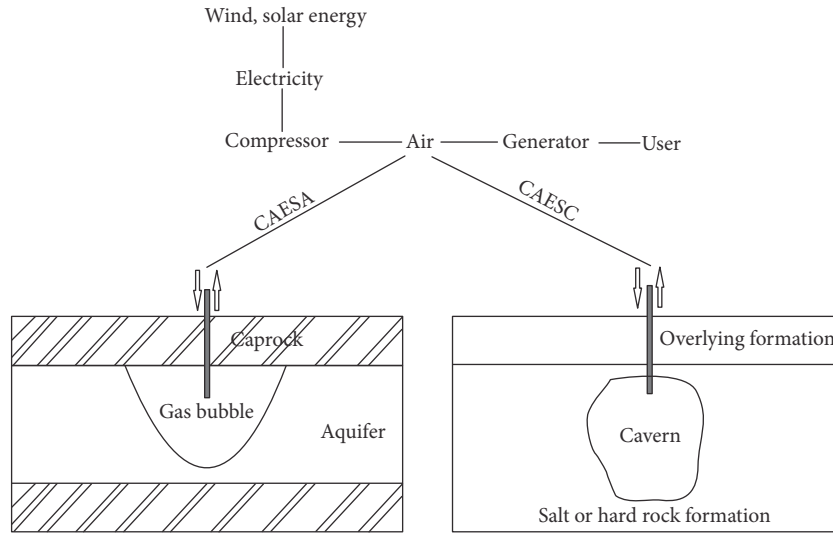


FIGURE 1: Schematic diagrams of CAESA and CAESC systems.

due to geological limitations [20]. The Pacific Northwest National Laboratory (PNNL) evaluated the technical and economic feasibility of CAESA in the Columbia Basin and designed a hybrid CAES plant that integrated geothermal energy [21].

Generally, the cyclic processes of compressed air can be divided into daily cycles and weekly cycles. Because compressed air is cyclically injected and produced frequently through the wellbore, the wellbore will play an important role in a CAESA system regarding the energy transfer from the formation and the energy deliverability. Kushnir et al. studied the relationship between the well screen length and water suction in CAESA, where the existence of an air-water interface was assumed in anticline structure. Their results showed that longer well screens can decrease pressure fluctuations while increasing the risk of water suction [22, 23]. Pan and Oldenburg developed a T2WELL simulator to integrate the wellbore and reservoir, and it has shown good performance when describing the wellbore-reservoir system in different fields, including CO₂ geological sequestration, geothermal energy, and CAESA [24]. Li et al. investigated the heat transfer in a single wellbore by investigating CAESA using a semianalytical solution. Their studies were mainly concentrated on the thermodynamic analysis of the well section in the overlying impermeable formation and ignored the impacts of energy transfer in the target aquifer. Their study showed that the small wellbore overall heat transfer coefficient and thermal diffusivity of the formation can help to decrease the heat loss [25]. Meanwhile, the initial gas bubble make-up can also be influenced by the wellbore and affect the subsequent cycle processes. The make-up of the initial gas bubble is the first step in the operation of a CAESA system, during which the amount of air needs to be injected into the aquifer to displace the water to build a bubble. This gas bubble can provide the necessary pressure to keep the next operation of the cycle sustainable. In previous studies, the initial gas bubble was always assumed to be under ideal

conditions, wherein the gas is fully saturated in the target storage space. However, this assumption is not practical in a CAESA system. Aimed at the studies concerning the initial gas bubble make-up, Guo et al. investigated the impact factors on the creation of the initial gas bubble, and TOUGH2/EOS3 was used to simulate the gas bubble creation [17]. However, their study was limited because their simulator was not sufficiently precise in describing the air flow in the wellbore, which is controlled by non-Darcian flow, and the well screen was simply fixed on the top of the aquifer.

Given the aforementioned gaps in the previous studies, we will study and analyse the effect of the wellbore on a CAESA system, thereby concentrating on the impact of the well screen length in the target aquifer. We will discuss the impact of the well screen length on the initial gas bubble formation and the CAESA system performance. On the basis of optimizing the well screen length configuration, we will also study the impacts of the energy storage scale and reservoir depth on the energy storage efficiency. Due to the lack of practical engineering applications of CAESA, numerical modelling is a valid method to study these key problems. The initial gas bubble make-up and subsequent cycle operations will be simulated using T2WELL/EOS3. The results will help to optimize the CAESA system.

2. Model Setup

2.1. Numerical Method. T2WELL is an integrated wellbore-reservoir simulator that can describe the nonisothermal, multiphase and multicomponent flow in a porous or fractured system. In the simulator, the drift-flux model is used to solve for the mixture flow within the wellbore, and the flow in the reservoir is described similarly as with TOUGH2 [26]. Different fluid state modules are integrated into T2WELL for applications in different fields. T2WELL/EOS3 was developed to describe a H₂O-air-heat system, which is appropriate for simulating the CAESA process [15]. In the EOS3 module, the

air is considered as an ideal gas and the water properties are described by the steam table equations. The detailed mechanics process and chemical reaction process are not considered in the module. The selected three primary thermodynamic variables (pressure, air mass fraction, and temperature for single-phase and gas phase pressure, gas saturation, and temperature for two phases) can describe the system condition. The air dissolution in the water can be estimated by Henry's law, where the air pressure is proportional to air solubility in water (mol fraction dissolved in water) and the proportional constant is Henry's constant. Henry's constant slowly varies with temperature, so a constant is adopted in the module [26]. A comparison study of the simulation results from T2WELL/EOS3 with monitoring data from the Huntorf plant has shown the feasibility of the simulator application in previous studies [18].

2.2. Numerical Model and Scheme Design

2.2.1. Grid Design. A radial symmetric grid was created to describe the entire aquifer system in the CAESA system using the mesh generator Wingridder [27]. To eliminate boundary effects, the radial domain of the model covers 1000 m away from the centre wellbore. The thickness of target aquifer is set as 50 m, which ranges from -650 m to -700 m with a grid resolution of 2 m, and the formation above the aquifer is considered impermeable. The vertical resolution of the mesh is refined near the wellhead, as well as the interface between the overlying formation and the target aquifer. In the radial direction, the grid resolution varies from 0.25 m near the wellbore to 70 m in the far field. The diameter of the wellbore is set as 0.5 m. Figure 2 and Table 1 show the profile of the radial symmetric mesh from 0 m to 200 m and the aquifer parameters, respectively. The van Genuchten-Mualem model and van Genuchten function are used for calculating the gas and liquid relative permeability and capillary pressure. The functions can be referred to in [26]. They both depend on the saturation (gas or liquid) in the latest time step and some other parameters (power in expression, aqueous phase residual saturation, gas phase residual saturation, capillary pressure strength between aqueous and gas phases, and maximum capillary pressure). The model is initially assumed to be fully water saturated. The distribution of the pressure is based on hydrostatic equilibrium, and the atmospheric pressure is set as that of the land surface. The temperature is initially calculated by the geothermal gradient ($38.5^\circ\text{C}/\text{km}$) with a surface temperature of 15°C . In addition, a constant lateral boundary condition is set during the entire process.

2.2.2. Scheme Design. A daily cycle operating scheme was more common in the previous studies. As no commercial CAESA plant exists, we choose the daily cycle based on Guo's research (the same as that in the Huntorf plant), which includes an injection stage (12 h), a shut-in stage (4.5 h), a production stage (3 h), and another shut-in stage (4.5 h) [17]. Meanwhile, a larger energy scale will be simulated compared with Guo's research. We design the operation cycle with an injection of 5 kg/s and a production of 20 kg/s, which can

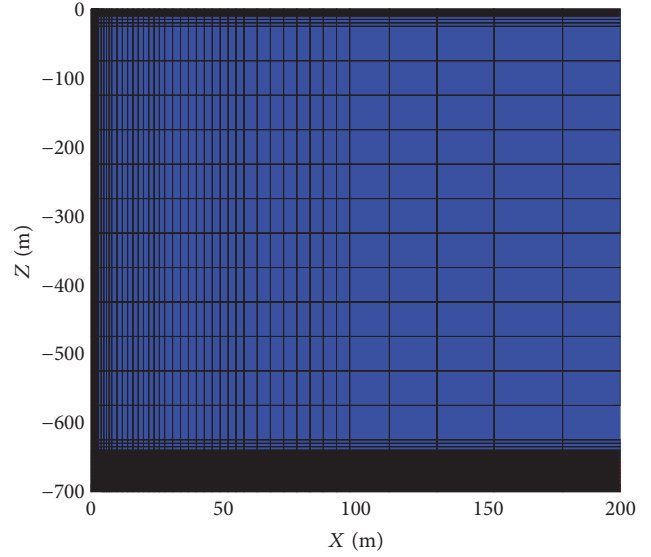


FIGURE 2: Profile of the radial symmetric mesh in a range of 200 m (blue represents the Caprock domain and red represents target domain).

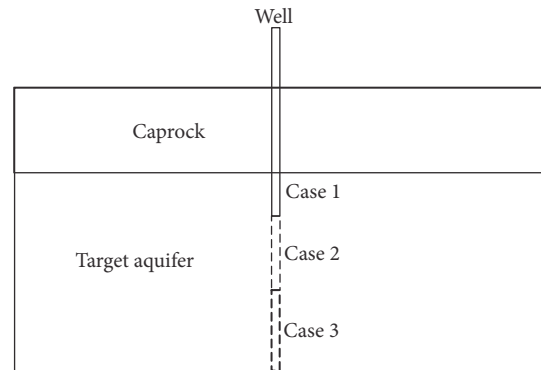


FIGURE 3: Schematic figure of the three cases with a different penetrating well to the target aquifer.

maintain the total gas mass balance. The enthalpy of injected air is 0.328 MJ/kg. The injection and production processes adopt constant flow rate at the wellhead. The well is closed to mass flow transfer with surrounding formation along its length except where it is perforated, but the energy flow transfer exists along all length. In the simulation, the flow and energy transfer both in wellbore and between wellbore and reservoir can be detailedly described in [24]. In the initial stage of the gas bubble make-up, air is injected into the aquifer at 50 kg/s for 30 days based on a preliminary model, which is used to estimate the initial gas volume consideration with the planned operation cycle scheme. To address the aforementioned questions about the well screen, three cases with different penetrating well screens will be developed in our model (Figure 3), which are 10 m penetration (Case 1), 30 m penetration (Case 2), and 50 m penetration (Case 3).

TABLE 1: List of the key parameters of the aquifer.

Parameters	Value	Unit
Grain density	2600	kg/m ³
Permeability (horizontal)	3.0×10^{-13}	m ²
Permeability (vertical)	3.0×10^{-14}	m ²
Porosity	0.2	
Compressibility	1.0×10^{-10}	Pa ⁻¹
Heat conductivity	2.51	W/(m·°C)
Rock grain special heat	920	J/(kg·°C)
Relative permeability function	van Genuchten-Mualem model	
Capillary pressure function	van Genuchten function	
Power in expression	0.60	
Aqueous phase residual saturation	0.12	
Gas phase residual saturation	0.05	
Capillary pressure strength between aqueous and gas phases	675.68	Pa
Maximum capillary pressure	5.0×10^5	Pa

3. Results and Analysis

3.1. Initial Gas Bubble. After 30 days of air injection, an initial gas bubble is created for the three cases (Figure 4). The different penetrating cases result in the evolution of different shapes of the gas bubble. Considering the domain in which the gas saturation is larger than 0.5 after 30 days, Case 1 has a wider horizontal scale (increasing to approximately 60 m) but has a smaller scale in the vertical direction (approximately 25 m) when compared with those of Case 2 (40 m × 41 m) and Case 3 (25 m × 50 m). A decreasing well screen length can cause the gas bubble to trend along the horizontal direction, which may induce larger gas diffusion and pressure fluctuation during the operation cycle. The reason for this is that a short well screen has a small interface area for air that is being injected into the aquifer, and thus, the air tends to remain at the top and move horizontally owing to the buoyancy force and a high horizontal permeability.

The pressure will gradually decrease with time (Figure 5) and become stable with a continued injection time. It is easier to inject the same amount of gas with an increasing gas volume in the aquifer. The pressure will increase inversely with the length of the well screen, which can also be caused by the smaller interface area for gas injection into the aquifer. The maximum pressure at the wellhead will increase to over 22 MPa for a short well screen (Case 1), during which any possible hazards caused by pressure build-up should be considered [28]. Also the high pressure during initial gas bubble injection process can change the permeability and porosity of aquifer near the wellbore [29], which may cause the subsequent injection pressure variance. In the practice engineering, the high build-up pressure in the initial gas bubble injection process can be avoided by possible injection method or process (e.g., constant pressure injection or the intermittent injection). The total amount of initial injection gas varies with the energy scale and characteristic of reservoir and also it depends on the economy. In the engineering practice, a prior

model is needed to make a decision for the total amount of initial injection gas.

3.2. Performance of the CAESA System

3.2.1. Change of Pressure and Temperature in the CAESA System. Figure 6(a) shows the change in the wellhead pressure with time during the cycle processes in the three different penetrating cases. The maximum pressure with the short well screen length is higher than that with the longer well screen length cases. However, the minimum wellhead pressure during production is lower with a decrease in the well screen length, which is probably the result of a small area for gas flow during the injection and production process as a consequence of the short well screen length that penetrates into the target aquifer. In the same cycle scheme, the wellhead pressure needs to be higher in order to inject the necessary amount of gas; meanwhile, it needs to be lower to meet the required deliverability. Additionally, as the pressurized air is needed in order to regenerate electricity, the lower pressure during the production process with a shorter screen length may be not available.

Variances of the wellhead temperature with time during the operation cycle for the three cases are shown in Figure 6(b). In the first shut-in stage, the wellhead temperature decreases owing to the decompression of the air and the cooling of the wellhead temperature. In this stage, the wellhead temperature with a short screen length (Case 1) is lower than in the other two cases, which can be caused by a larger pressure reduction (Figure 6(a)). In the production stage, the decline in the wellhead temperature is caused by multiple factors, including air decompression, energy loss in the aquifer, and heat transfer between the well and the formation. During the production process, the air temperature at the wellhead (Case 1) is lower. As a higher background geothermal temperature occurs at deeper locations within the aquifer, the well

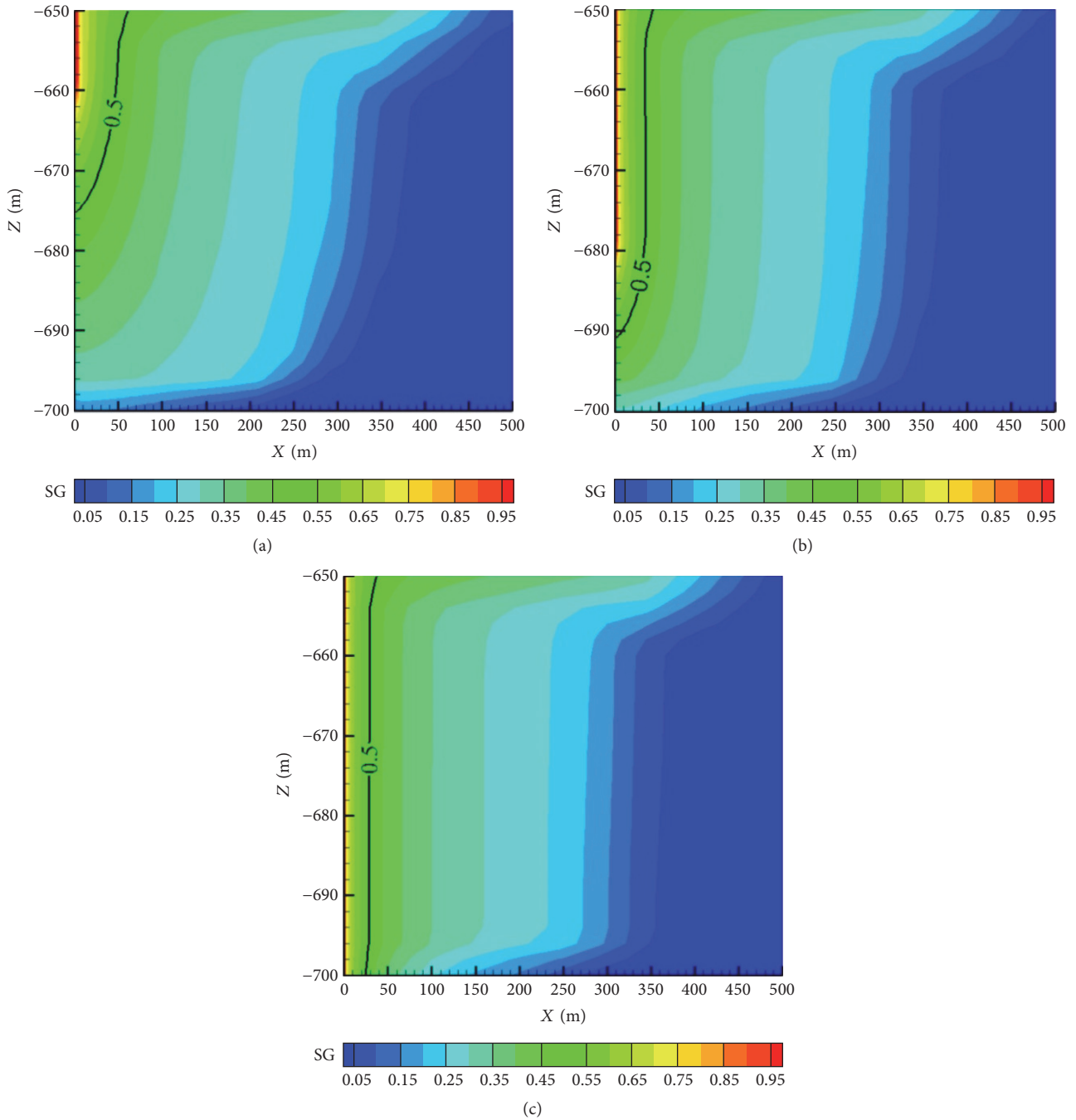


FIGURE 4: Gas saturation distribution for the three cases after a 30-day injection period in the aquifer. (a) Case 1 (10 m). (b) Case 2 (30 m). (c) Case 3 (50 m).

screen lengths used to penetrate the aquifer in Case 2 and Case 3 can reduce the heat loss and keep the temperature higher at the wellhead than that in Case 1. In the shut-in stage after production, the wellhead temperature increases due to the heat of compression caused by the wellhead pressure recovery phase, and an increase in the temperature will accompany a more prolonged pressure recovery stage (Case 1) (Figure 6(a)). Also, the variance differences in pressure and temperature among the three cases demonstrate the more

sensitive to the shorter wellbore screen case. The variances are more obvious between Case 1 and Case 2, compared with that between Case 2 and Case 3, with the same well screen length difference (20 m).

3.2.2. Comparison of the Energy Storage Efficiency among the Three Cases. The energy flow rates in the cycle operations for the three cases are calculated by the model (Figure 7), the differences within which occur during the production period.

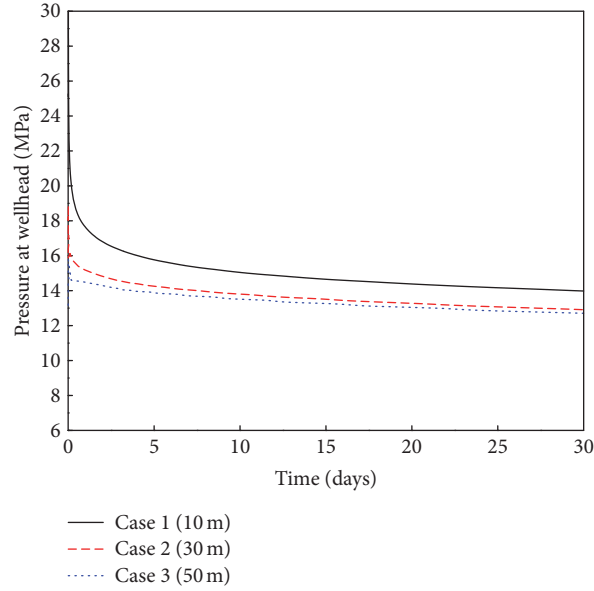


FIGURE 5: Change of pressure at the wellhead with time for the three cases.

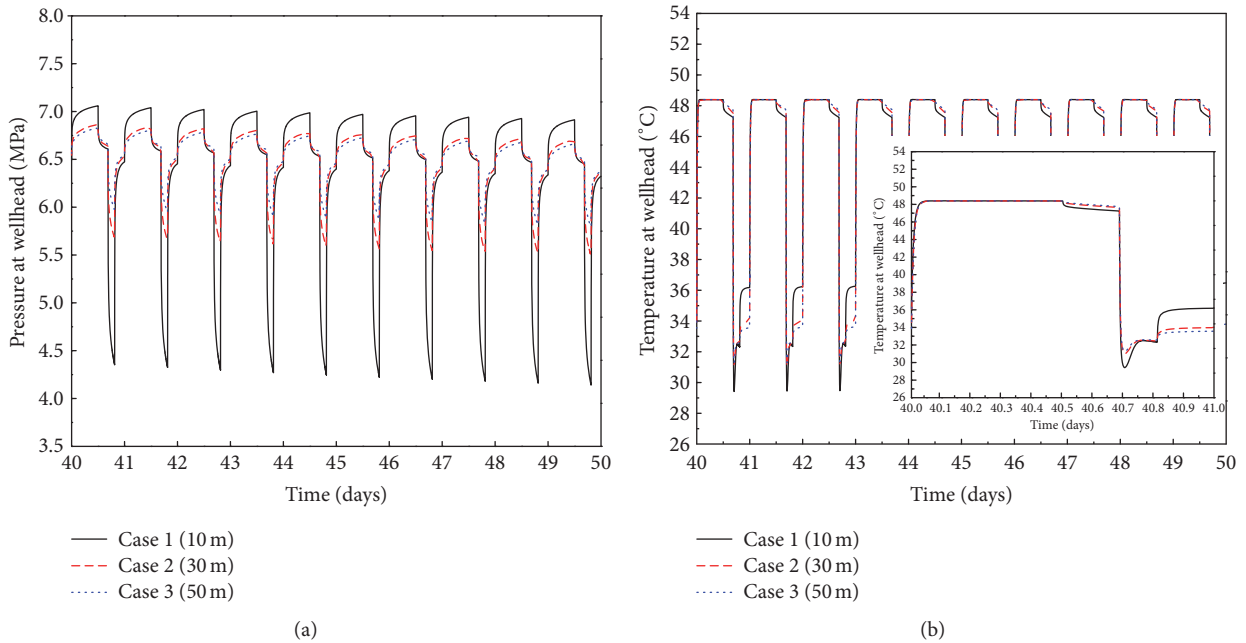


FIGURE 6: Comparisons of the variances of pressure and temperature at the wellhead during the cycle processes among the three different well penetrating cases. (a) Pressure. (b) Temperature.

The energy flow rate is slightly higher in the cases with a longer well screen length. The changes in the energy flow rate with time for the three cases are almost consistent with the change in the temperature with time during the production period (Figure 6(b)). More energy can be produced with air at a higher pressure and temperature when using a long well screen length.

Ignoring the efficiencies of the compressor and turbine, we only consider the energy loss from the underground storage vessel caused by the cycle processes. The energy

storage efficiency per cycle process can be calculated as follows:

$$E_{\text{efficiency}} = \frac{E_{\text{Injection}}}{E_{\text{Production}}}, \quad (1)$$

where $E_{\text{efficiency}}$ is the energy efficiency per cycle; $E_{\text{Injection}}$ is the total injection energy; and $E_{\text{Production}}$ is the total production energy.

The energy efficiency gradually increases with the continuation of the cycle, which varies from 93.6% to 95.4% over 50

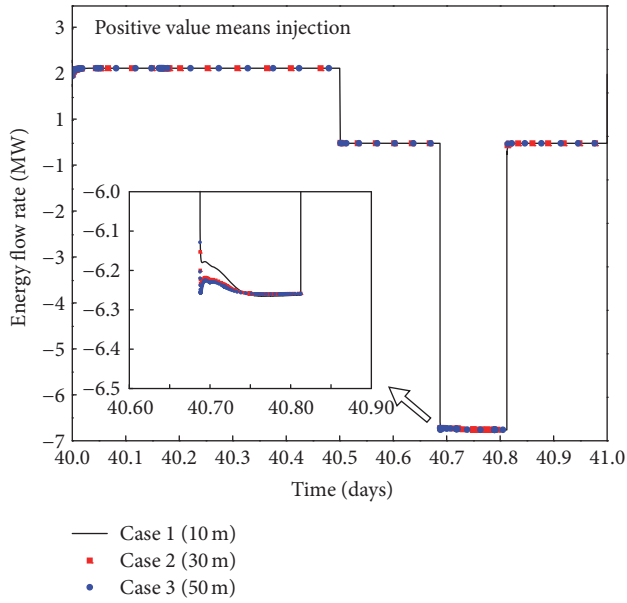


FIGURE 7: The energy flow rates at the wellhead in the three different cases.

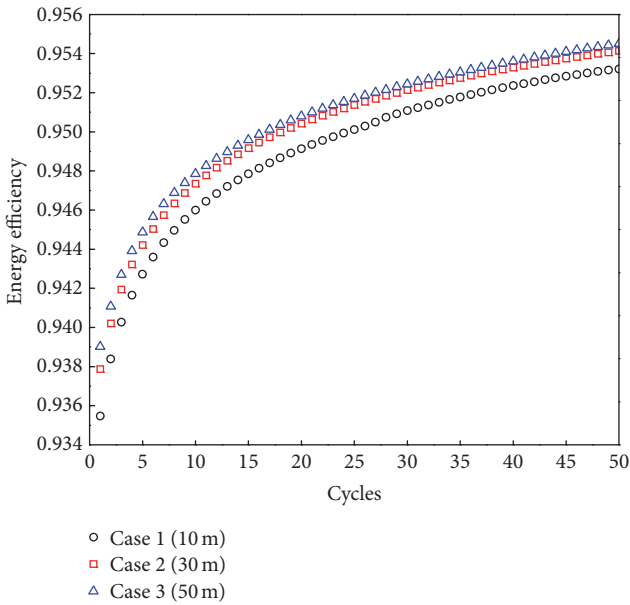


FIGURE 8: Changes of the energy efficiency of the CAESA system in the three different cases with the continuation of cycles.

cycles (Figure 8). The reason for this is that the temperature near the wellbore in the aquifer and in the overlying cap formation will gradually become higher due to heat transfer with the higher temperature injected air, which causes less energy loss over the continued cycle processes. In addition, a longer well screen length performs with slightly better energy efficiency. The energy efficiency in Case 3 is 0.2% (13.2 kW total energy) higher than Case 1 per cycle and the variance is more sensitive to shorter well screen length. Although the differences of the energy efficiency among the three cases are not obvious in this model, the total energy loss can be more

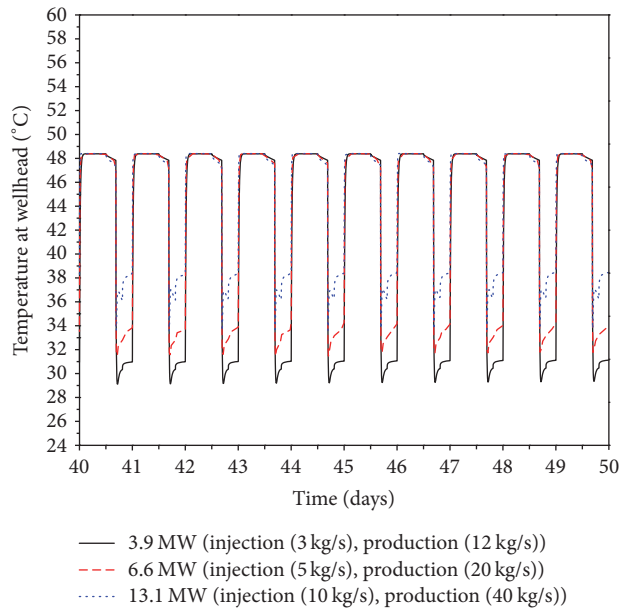


FIGURE 9: Changes in the wellhead temperature with time among the three energy storage scales of the CAESA system.

significant if a large-scale CAESA system is being implemented.

A comparison of the CAESA system performance with the three kinds of well screen lengths penetrating into the aquifer suggests that longer well screen lengths can perform with better energy storage efficiencies, especially for the case penetrating through the entire target aquifer. Additionally, longer well screen length will contribute more stable and sufficiently pressurized output air for the regeneration of electricity. Furthermore, the greater deliverability with a longer well screen could extend the energy storage scale in a single well or reduce the number of wells required for a large-scale CAESA system.

4. Discussion

As discussed above, well screens that entirely penetrate through the target aquifer can perform with better energy efficiencies in a CAESA system. In this section, we will investigate the effects of the energy storage scale and reservoir depth under the conditions of a well penetrating through the entire aquifer using numerical modelling.

4.1. Impact of the Energy Storage Scale on the System Performance. In a fixed CAESA system, different energy storage scales can be reflected by variances in the injection and production rates. To evaluate the influences of the energy storage scale, we design three cases of the energy storage scale, the corresponding injection and production rates of which are shown in Table 2. The wellbore is perforated through the entire aquifer. The initial gas bubble and other aquifer parameters are the same as those mentioned previously.

Figure 9 demonstrates the temperature variance among the three cases of the energy storage scale at the wellhead

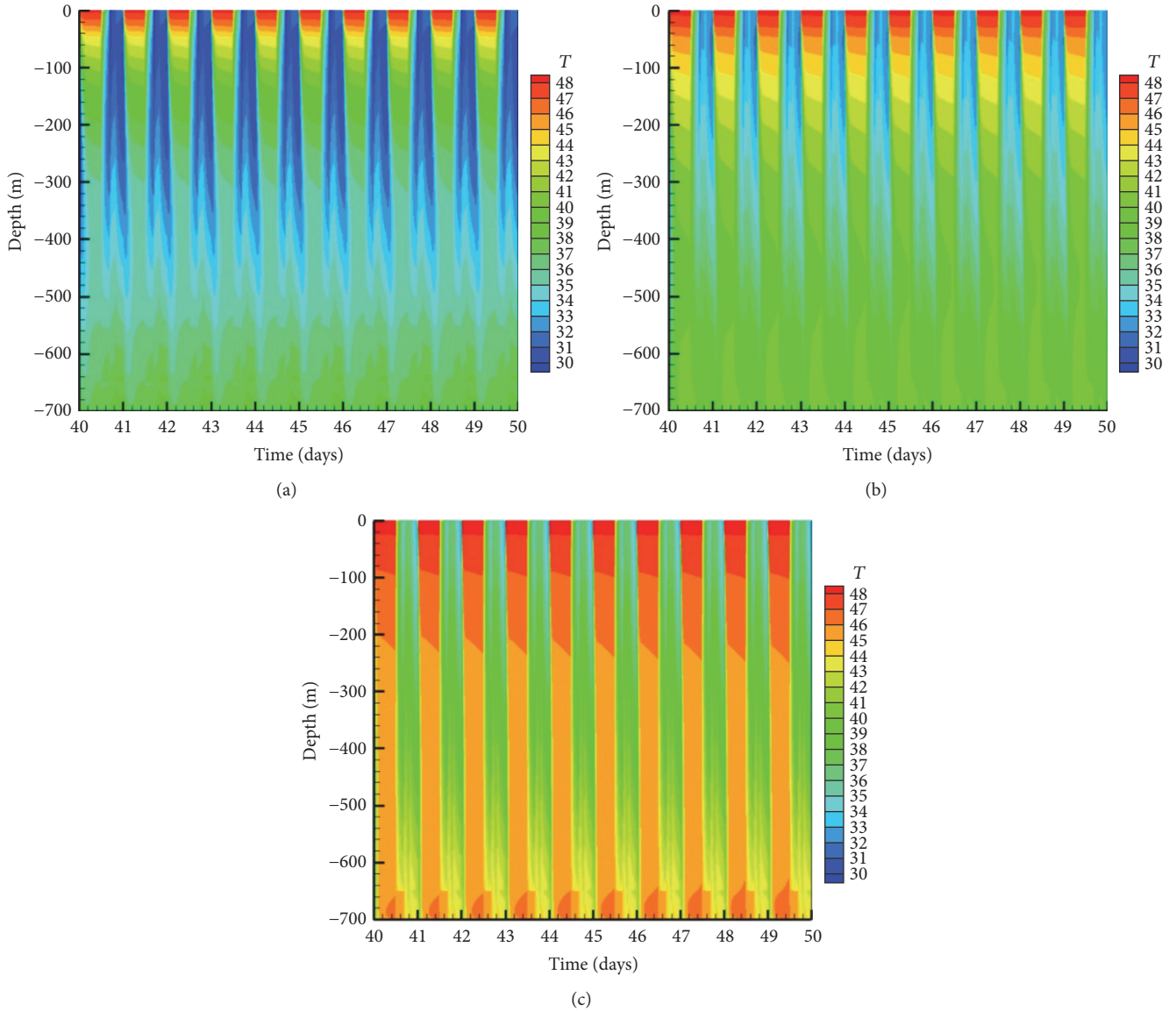


FIGURE 10: Temperature profiles along the wellbore among the three energy storage scales of the CAESA system during the 40–50 cycles. (a) 3.9 MW (injection 3 kg/s, production 12 kg/s); (b) 6.6 MW (injection 5 kg/s, production 20 kg/s); (c) 13.1 MW (injection 10 kg/s, production 40 kg/s).

TABLE 2: The injection and production rates in the three energy storage scale systems.

Scale (MW)	Injection rate (kg/s)	Production rate (kg/s)
3.9	3	12
6.6	5	20
13.1	10	40

during the operation cycle. The minimum wellhead temperature reaches 34°C, 31°C, and 29°C for the 3.9 MW, 6.6 MW, and 13.1 MW scales, respectively. In addition, the maximum temperature is the same (approximately 48°C) in the different cases during the injection period. Larger energy storage

scales, which correspond to larger air mass cycles, result in higher air temperatures during the production period.

The temperature profiles along the wellbore during the operation cycle are drawn in Figure 10. The temperature distribution is controlled by heat transfer between the air in the wellbore and the surrounding formation. Taking the injection process as an example, the high-temperature injected air transfers heat to the surrounding cooler formation, which results in a temperature drop in the wellbore. As the depth increases, the temperature in the surrounding formation rises and the temperature difference with the air in the wellbore could decrease. When the temperature in the surrounding formation is higher (the temperature can reach 42°C at the bottom of the aquifer as calculated by the aforementioned geothermal gradient) than the air temperature in the wellbore

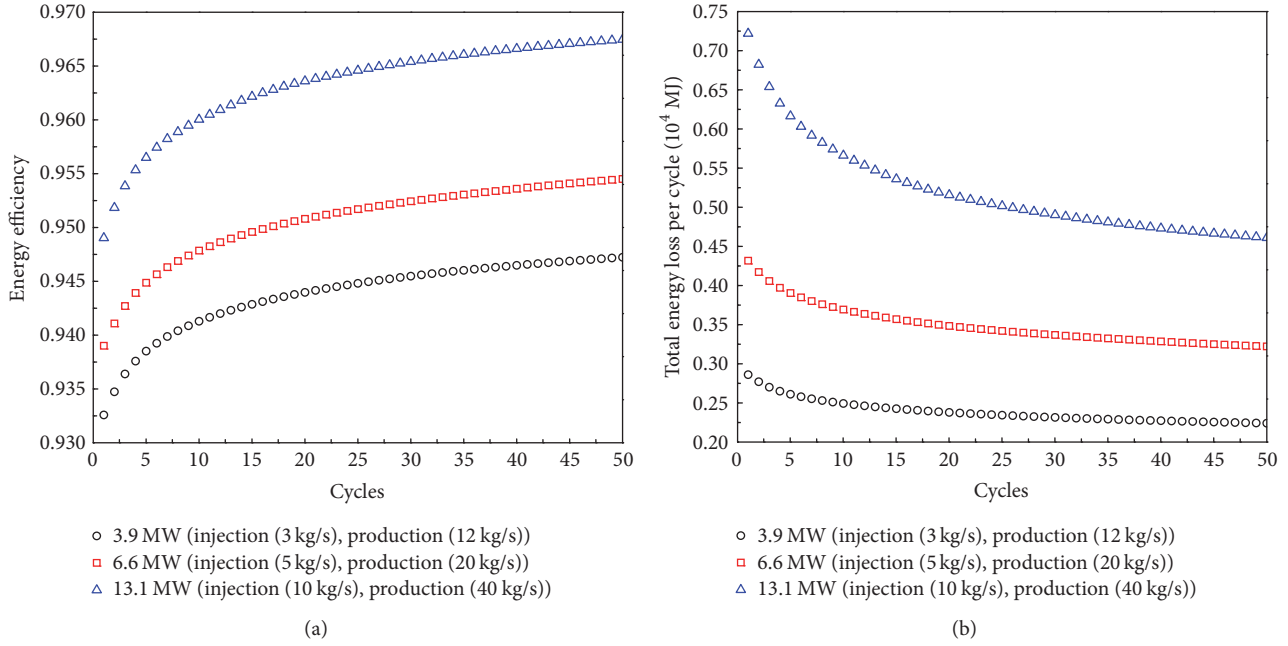


FIGURE 11: Comparison of the energy efficiencies and total energy losses during the 50 cycles under the three energy storage scales of a CAESA system. (a) Energy efficiency. (b) Total energy loss.

(in the 3.9 MW and 6.6 MW cases), the heat transfer process is reversed, which means that heat will be transferred to the wellbore from the surrounding formation. In the 3.9 MW and 6.6 MW cases, the temperature drops and then rises with depth along the wellbore during the injection. During the operation cycle, a larger energy storage scale represents a higher temperature distribution. The difference could be explained as the consequence of the larger air flow velocity in the wellbore relative to larger energy storage scales, which will cause a smaller heat loss of the unit air mass to the surrounding formation.

The variances in the energy efficiency and total energy loss during the 50 cycles in the three energy storage scales are described in Figure 11. A larger energy storage scale can cause a greater total energy loss in a CAESA system. However, the case with the 13.1 MW scale has a better energy storage efficiency (96.8%) when compared with those at the 6.6 MW scale (95.3%) and 3.9 MW scale (94.5%) in the 50th cycle. The opposite trends between the energy efficiency and total energy loss are caused by the total energy storage scale. The ratio of the total energy loss in these different cases is smaller than the ratio of the energy storage scale, which means that the energy loss of the unit air mass is smaller in larger energy storage scales, which can be reflected by the temperature variances during the cycle (see Figures 9 and 10) due to larger air flow velocities. Under the condition of guaranteeing the sustainability of the system, these numerical results reveal that a larger energy storage scale design could perform with better energy efficiency.

4.2. Impact of the Reservoir Depth on the System Performance. In this section, we will discuss the reservoir depth impact on the CAESA system performance. Different reservoir depths

TABLE 3: Scenario sets for different target aquifer depths in a CAESA system.

Case	Target aquifer location depth
Case 4	150 m–200 m
Case 5	250 m–300 m
Case 6	450 m–500 m
Case 7	650 m–700 m
Case 8	850 m–900 m

could impact both the performance of the initial gas bubble formation and changes in the pressure and temperature. At the same time, we further investigate the interaction between geothermal and CAESA systems, as shown in the previous section. Five different target aquifer depth cases are investigated as shown in Table 3. The thickness of the target aquifer remains constant (50 m) and the ranges in their values represent the location depth. The selection ranges for the target aquifer location depths are based on the literature, which suggests that the depth to the top of the aquifer should be larger than 140 m [2]. The other basic parameters of the aquifer are the same as above, and the overlying formation is impermeable. The wellbore entirely penetrates the target aquifer. The grid is generated depending on the different cases with the same resolution in the aquifer.

Different depths of the target aquifer will produce different initial gas bubbles. During the first stage, the initial gas bubble is generated using the simulator. The injection scheme is the same as that mentioned previously (50 kg/s for 30 days) among the five cases. Figure 12 illustrates the gas saturation distribution after injection for the different cases. The gas saturation distribution only shows minor differences

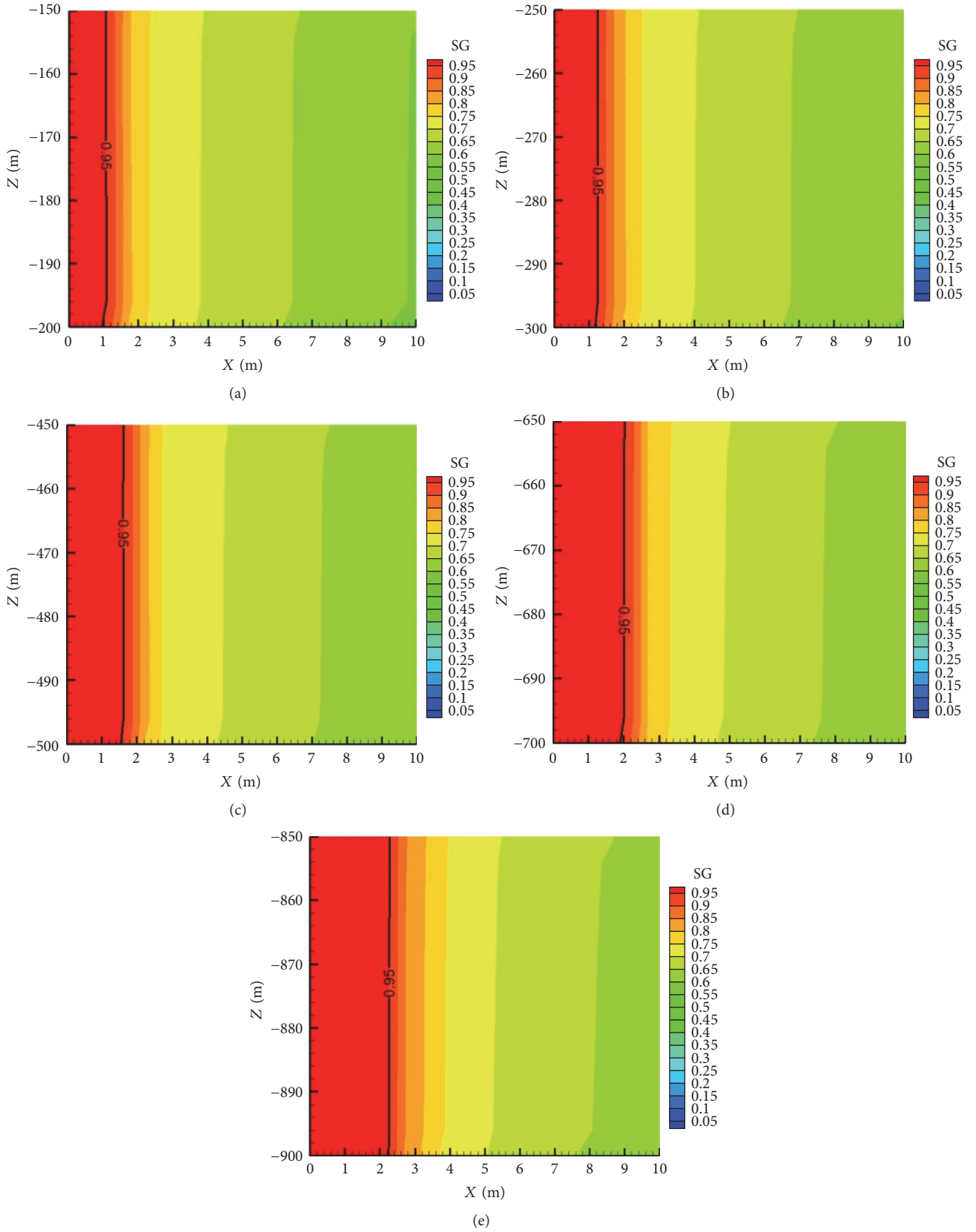


FIGURE 12: Distribution of the initial gas saturation within a lateral distance of 10 m before the cycle process for five cases. (a) Case 4 (150 m–200 m); (b) Case 5 (250 m–300 m); (c) Case 6 (450 m–500 m); (d) Case 7 (650 m–700 m); (e) Case 8 (850 m–900 m).

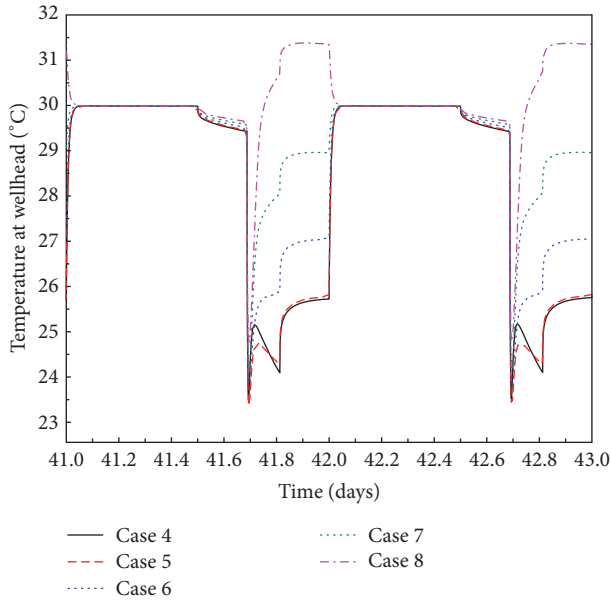


FIGURE 13: Comparison of the temperate changes at the wellhead during the operation cycle processes among the five depth cases.

for the five cases. As the 0.95 gas saturation contour shows, larger distances away from the wellbore are observed in the deeper cases, and they vary from 1 m for Case 4 to 2.2 m for Case 8. This could be explained insomuch that greater depths correlate to higher storage densities and a smaller plume area, which makes the gas accumulate near the wellbore.

Within the cycle process, we design the cycle scheme as the basic model (5 kg/s injection for 12 h and 20 kg/s production for 3 h). The injection air temperature is set to 30°C, which is different from the temperature in the base model, in consideration of the geothermal gradient (38.5°C/km) and the different depth cases. A comparison of the wellhead temperature changes in 41–43 days after the start of the operation cycle is shown in Figure 13. As the in situ temperature in the formation increases with depth, the heat in the wellhead can be replenished from the formation when the temperature in the formation is higher than the injection air temperature. This can result in the fact that the wellhead temperature is higher in deeper cases, and it even reaches a temperature that is higher than the injection temperature during the production period in Case 8.

Figure 14 displays the temperature profile at the wellhead in the 40th cycle for the five cases. For Case 4 and Case 5, the background temperature (i.e., the undisturbed formation temperature) is lower than the injection air temperature. Therefore, in the entire operation cycle, the heat will constantly flow into the surrounding formation. With an increase in the depth (from Case 6 to Case 8), the background temperature will gradually become higher than the injection temperature (30°C), which may reverse the heat transfer process at certain depths, and the injected air could be heated by the geothermal.

The energy efficiencies in the five depth cases are drawn in Figure 15. A CAESA system with a deeper aquifer performs

with better energy efficiency. The differences may be caused by two main reasons. First is the effect of the geothermal. Heat is lost to the surrounding cooler formation when the background temperature in the aquifer is lower (Figures 14(a) and 14(b) for Case 4 and Case 5, resp.). A deeper aquifer system will enlarge the area of the heat loss, which may result in a worse energy efficiency (the energy efficiency in Case 4 will become better than Case 5 with the continuation of the cycle). When the background temperature is higher (Figures 14(c), 14(d), and 14(e) for Cases 6, 7, and 8, resp.), a longer wellbore with a deeper aquifer will reduce the heat loss and sometimes can obtain thermal supplement from surrounding formation, which can result in better energy efficiency in a CAESA system. Second reason could be the higher energy storage densities and pressure. Greater depths correlate to higher storage densities and a smaller gas diffusion area could decrease the energy loss and higher storage pressure could maintain the thermal energy by compression heat. The two reasons result in the fact that the energy efficiency can be approached 100% in Case 8. We can also infer that the energy efficiency may exceed 100% with a deeper aquifer system and higher in situ temperature. These results show that a deeper target aquifer with an entirely perforated wellbore could perform with a better energy efficiency, which could reduce the heat loss and obtain thermal supplement by higher surrounding formation temperature and decrease the energy loss by large storage densities and high pressure. However, in practical engineering applications, a CAESA system with a deeper target aquifer may increase the cost for well drilling, which means the total economic performance needs to be considered.

However, there are two aspects of limitations in this study. First, in the conceptual model, the aquifer is assumed to be horizontal, homogeneous, and embedded with the impermeable formation. While in the natural condition, the aquifer is often heterogeneous, which may affect the initial gas bubble distribution and the pressure variance in cycle process. Also the energy efficiency can become worse caused by gas loss with the poor Caprock. Second, in the T2WELL/EOS3 module, the gas is considered as ideal gas. The property differences between ideal gas and real gas may affect the simulation results. The permeability and porosity variance, as well as the possible hazards caused by pressure build-up, will not be considered as the mechanics process is ignored in the module. Despite the limitations existing in this study, it can answer the foundation questions about the wellbore influence in the CAESA system mentioned in the paper.

5. Conclusions

A wellbore-reservoir numerical model was developed to evaluate the influence of wellbore flow on the performance of a CAESA system. The integrated operation processes, including the formation of the initial gas bubble formation and the cycle injection and production process, were simulated in detail. A wellbore that is fully penetrating into the target aquifer can provide the most reliable pressurized air output, and a comparison of the energy efficiency calculated using the ratio of input energy and output energy from the storage

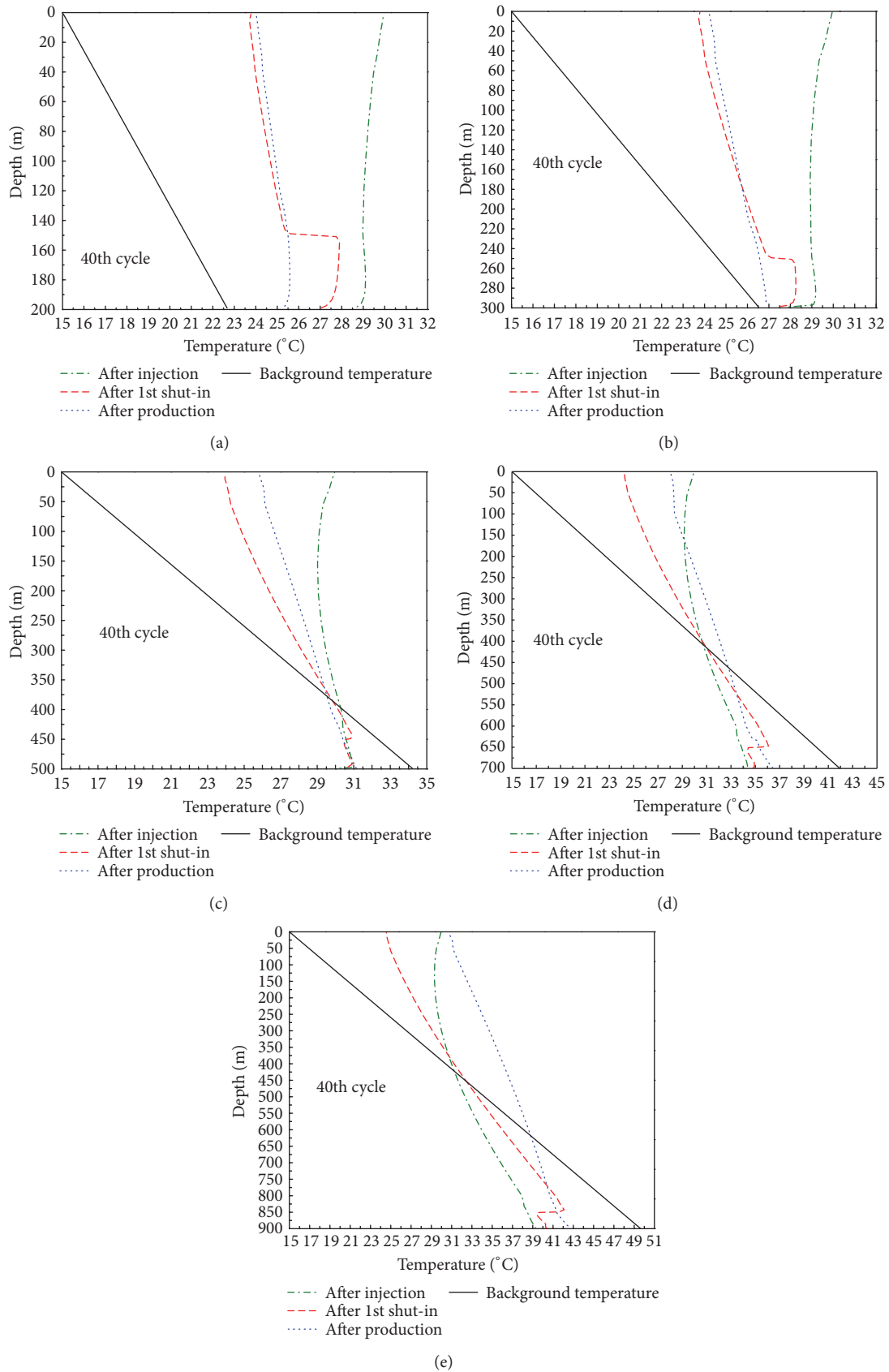


FIGURE 14: The temperature profiles along the wellbore in the 40th cycle for the different cases. (a) Case 4 (150–200 m); (b) Case 5 (250–300 m); (c) Case 6 (450–500 m); (d) Case 7 (650–700 m); (e) Case 8 (850–900 m).

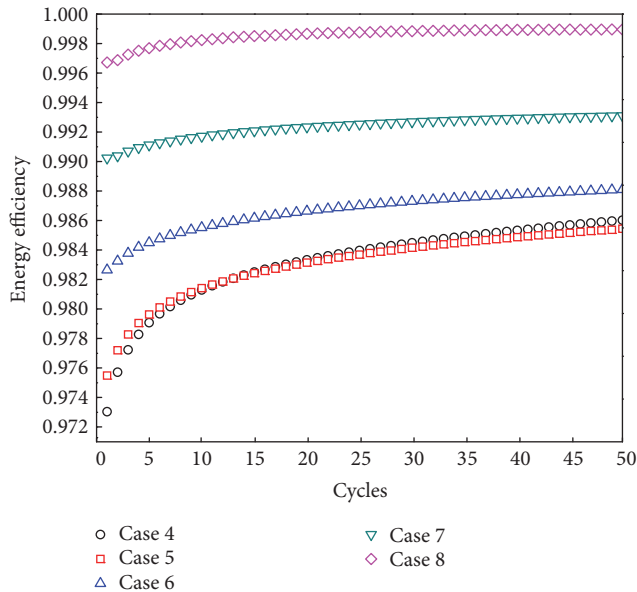


FIGURE 15: Comparison of the energy efficiencies in the continued cycles among the five depth cases.

vessel shows that it can help improve the performance of a CAESA system due to heat transfer with the formation.

On the basis of the wellbore study results, the impacts of the energy storage scale and reservoir depth on the performance of a CAESA system were investigated through numerical modelling. The results show that larger energy storage scales with larger injection and production rates can help improve the performance of a CAESA system, which is represented by a smaller energy loss to the surrounding formation relative to the unit air mass. The geothermal effect and energy storage density can impact the total energy efficiency, and a deeper target aquifer can improve the performance of a CAESA system. The results can help the system design and extend the prospects of CAESA system combined with geothermal system.

There still remain some problems concerning the influences of wellbore flow on a CAESA system, which need to be studied in the future. One important challenge is how to build an initial gas bubble at a larger scale, which can support larger scale energy storages. In addition, the impact of geothermal effect on CAES is an interesting research issue and should be further studied. Other inevitable aspects, including the reaction of oxygen with minerals, the corrosion of the wellbore, and the associated risk assessments, should be investigated.

Conflicts of Interest

The authors declare that there are no conflicts of interest regarding the publication of this paper.

Acknowledgments

This research was funded by the Fundamental Research Funds for the Central Universities through Beijing Normal University (no. 2015KJJCBI7) and the National Natural

Science Foundation of China (Grant no. 41572220). It was also supported by the China Scholarship Council (CSC) for the first author's visit to the Lawrence Berkeley National Laboratory.

References

- [1] M. Budt, D. Wolf, R. Span, and J. Yan, "A review on compressed air energy storage: Basic principles, past milestones and recent developments," *Applied Energy*, vol. 170, pp. 250–268, 2016.
- [2] S. Succar and R. H. Williams, "Compressed air energy storage: theory, resources, and applications for wind power," *Princeton Environmental Institute report*, p. 8, 2008.
- [3] R. Allen, T. Doherty, and L. Kannberg, "Summary of selected compressed air energy storage studies," Tech. Rep. PNL-5091, 1985.
- [4] D. R. Mack, "Something new in power technology," *IEEE Potentials*, vol. 12, no. 2, pp. 40–42, 1993.
- [5] F. Crotogino, K. U. Mohmeyer, and R. Scharf, *Huntorf CAES: More than 20 Years of Successful Operation*, Orlando, Florida, USA, 2001.
- [6] R. Kushnir, A. Dayan, and A. Ullmann, "Temperature and pressure variations within compressed air energy storage caverns," *International Journal of Heat and Mass Transfer*, vol. 55, no. 21–22, pp. 5616–5630, 2012.
- [7] M. Raju and S. Kumar Khaitan, "Modelling and simulation of compressed air storage in caverns: a case study of the Huntorf plant," *Applied Energy*, vol. 89, no. 1, pp. 474–481, 2012.
- [8] E. Barbour, D. Mignard, Y. Ding, and Y. Li, "Adiabatic Compressed Air Energy Storage with packed bed thermal energy storage," *Applied Energy*, vol. 155, pp. 804–815, 2015.
- [9] N. Hartmann, O. Vöhringer, C. Kruck, and L. Eltrop, "Simulation and analysis of different adiabatic Compressed Air Energy Storage plant configurations," *Applied Energy*, vol. 93, pp. 541–548, 2012.
- [10] J. Rutqvist, H.-M. Kim, D.-W. Ryu, J.-H. Synn, and W.-K. Song, "Modeling of coupled thermodynamic and geomechanical performance of underground compressed air energy storage in lined rock caverns," *International Journal of Rock Mechanics and Mining Sciences*, vol. 52, pp. 71–81, 2012.
- [11] C. Bullough, C. Gatzen, C. Jakiel, M. Koller, A. Nowi, and S. Zunft, "Advanced adiabatic compressed air energy storage for the integration of wind energy," in *European Wind Energy Conference, EWEC*, vol. 22, p. 25, London, UK, 2004.
- [12] Z. Guo, G. Deng, Y. Fan, and G. Chen, "Performance optimization of adiabatic compressed air energy storage with ejector technology," *Applied Thermal Engineering*, vol. 94, pp. 193–197, 2016.
- [13] X. Luo, J. Wang, C. Krupke et al., "Modelling study, efficiency analysis and optimisation of large-scale Adiabatic Compressed Air Energy Storage systems with low-temperature thermal storage," *Applied Energy*, vol. 162, pp. 589–600, 2016.
- [14] M. Sánchez, A. Shastri, and T. M. Le, "Coupled hydromechanical analysis of an underground compressed air energy storage facility in sandstone," *Geotechnique Letters*, vol. 4, no. April/June, pp. 157–164, 2014.
- [15] C. M. Oldenburg and L. Pan, "Porous Media Compressed-Air Energy Storage (PM-CAES): Theory and Simulation of the Coupled Wellbore-Reservoir System," *Transport in Porous Media*, vol. 97, no. 2, pp. 201–221, 2013.

- [16] C. M. Oldenburg and L. Pan, "Utilization of CO₂ as cushion gas for porous media compressed air energy storage," *Greenhouse Gases: Science and Technology*, vol. 3, no. 2, pp. 124–135, 2013.
- [17] C. Guo, K. Zhang, C. Li, and X. Wang, "Modelling studies for influence factors of gas bubble in compressed air energy storage in aquifers," *Energy*, vol. 107, pp. 48–59, 2016.
- [18] C. Guo, L. Pan, K. Zhang, C. M. Oldenburg, C. Li, and Y. Li, "Comparison of compressed air energy storage process in aquifers and caverns based on the Huntorf CAES plant," *Applied Energy*, vol. 181, pp. 342–356, 2016.
- [19] A. S. Jarvis, *Feasibility study of porous media compressed air energy storage in South Carolina, United States of America*, Clemson University, 2015.
- [20] Schulte R. H., N. Critelli, K. Holst, and G. Huff, *Lessons from Iowa: development of a 270 Megawatt compressed air energy storage project in midwest independent system operator*, Sandia National Laboratories, Albuquerque, New Mexico, USA, 2012.
- [21] B. McGrail, J. Cabe, C. Davidson et al., *Technoeconomic performance evaluation of compressed air energy storage in the Pacific Northwest*, Pacific Northwest National Laboratory, Richland, USA, 2013.
- [22] R. Kushnir, A. Ullmann, and A. Dayan, "Compressed air flow within aquifer reservoirs of CAES plants," *Transport in Porous Media*, vol. 81, no. 2, pp. 219–240, 2010.
- [23] R. Kushnir, A. Ullmann, and A. Dayan, "Thermodynamic and hydrodynamic response of compressed air energy storage reservoirs: a review," *Reviews in Chemical Engineering*, vol. 28, no. 2-3, pp. 123–148, 2012.
- [24] L. Pan and C. M. Oldenburg, "T2well-an integrated wellbore-reservoir simulator," *Computer Geosciences*, vol. 65, pp. 46–55, 2014.
- [25] Y. Li, K. Zhang, L. Hu, and J. Wang, "Thermodynamic analysis of heat transfer in a wellbore combining compressed air energy storage," *Environmental Earth Sciences*, vol. 6, no. 76, pp. 1–10, 2017.
- [26] K. Pruess, C. Oldenburg, and G. Moridis, "TOUGH2 User's Guide Version 2," Tech. Rep. LBNL-43134, Lawrence Berkeley National Laboratory, Berkeley, Calif, USA, 1999.
- [27] L. Pan, *Wingridder-an interactive grid generator for TOUGH2*, Lawrence Berkeley National Laboratory, Berkeley, USA, 1999.
- [28] Y. Li, Y.-F. Chen, G.-J. Zhang, Y. Liu, and C.-B. Zhou, "A numerical procedure for modeling the seepage field of water-sealed underground oil and gas storage caverns," *Tunnelling and Underground Space Technology*, vol. 66, pp. 56–63, 2017.
- [29] M. Liu, Y. Chen, K. Wei, and C. Zhou, "Interpretation of gas transient pulse tests on low-porosity rocks," *Geophysical Journal International*, vol. 210, no. 3, pp. 1845–1857, 2017.

Research Article

Quantitative Evaluation and Case Study of Risk Degree for Underground Goafs with Multiple Indexes considering Uncertain Factors in Mines

Longjun Dong, Weiwei Shu, Xibing Li, Zilong Zhou, Fengqiang Gong, and XiLing Liu

School of Resources and Safety Engineering, Central South University, Changsha 410083, China

Correspondence should be addressed to Longjun Dong; lj.dong@csu.edu.cn

Received 23 June 2017; Accepted 14 September 2017; Published 16 October 2017

Academic Editor: Xiaoqing Shi

Copyright © 2017 Longjun Dong et al. This is an open access article distributed under the Creative Commons Attribution License, which permits unrestricted use, distribution, and reproduction in any medium, provided the original work is properly cited.

The accidents caused by underground goafs are frequent and destructive due to irregular geometric shapes and complex spatial distributions, which caused severe damage to the environment and public health. Based on the theories of uncertainty measurement evaluation (WME) and analytic hierarchy process (AHP), the comprehensive risk evaluation of underground goafs was carried out using multiple indexes. Considering the hydrogeological conditions, mining status, and engineering parameters of underground goafs, the evaluation index system was established to evaluate the risk degrees considering quantified uncertain factors. The single index measurement values were solved by the semiridge measurement function. The weights for evaluation vectors were calculated through the entropy theory and AHP. Finally, the risk level was evaluated according to the credible degree recognition criterion (CDRC) and the maximum membership principle. The risk levels of 37 underground goafs in Dabaoshan mine were evaluated using 4 coupled methods. The order for underground goafs risk degrees was ranked and classified on account of the uncertainty important degree. According to the ranked order, the reasonability of 4 coupled methods was evaluated quantitatively. Results show that the UME-CDRC can be applied in the practical engineering, which provides an efficient guidance to both reduce the accident risk and improve the mining environment.

1. Introduction

Underground mining projects are the basic energy source and resource guarantee of the national economic development. The mining industry develops rapidly in the countries like South Africa, Australia, Canada, Poland, and China. With the large land area and relatively small population, it is viable to carry out the open pit mining in Australia and Canada, where little underground goafs are distributed [1–4]. Compared to these countries, a large number of underground goafs formed in the process of mining in China, especially in the underground mines using open stope mining methods [5–7]. Since the 1980s, the illegal mining was rising up in China, which caused numerous unknown underground goafs around the mines. There is no doubt that they present a very serious threat to safety and viability of efficient and sustainable mining, due to the characteristics of irregular

geometric shapes, complex spatial distributions, and being strongly concealed [8–10].

In recent years, many collapse accidents of underground goafs have occurred, which have caused huge economic losses, casualties, and serious ecological damage. Particularly, the damage to our vegetation, water, and land from numerous underground goafs induced by large-scale mining has posed severe threats to the environment and public health [11–17]. There are more than 9000 state-owned mines in China. The annual amount of mineral production has reached 9 billion tons and the volume of underground goafs has reached billions of cubic meters. In Shanxi Province, the area of underground goafs has been as large as 1/8 of the whole provincial area. Numerous mines in China are mining with underground goafs, including Dachang mine, Changba lead-zinc mine, Shizishan copper mine, Luanchuan molybdenum mine, Lanping lead-zinc mine, and Dabaoshan mine. The



FIGURE 1: The damage of roads caused by the collapse of underground goafs in Shengda iron mine, where the vibration intensity was equal to an earthquake with the magnitude 3.1.



FIGURE 2: The huge and numerous collapse pits distributed in the Hulun Buir, where the vegetation, environment, and ecological system were damaged seriously.

distribution range of underground goafs is extremely large and the locations are strongly concealed, which threatens the safety of mine production and surrounding environment.

The statistical results show that more than 180 places with large area of ground subsidence have been found in 21 provinces of China, which have caused more than 1592 collapse pits and more than 200 deaths. Based on the analysis of these accidents, two significant aspects for the harm of underground goafs are summarized [18]. One aspect is the large area falling of underground goafs roofs, which results in the subsidence and cracking of surface, the destruction of mine environment, and heavy casualties. For example, a ground subsidence accident occurred at Shengda mine [19]. The nearby roads and buildings were damaged with different levels by an induced vibration, where the vibration intensity was equal to an earthquake with the magnitude 3.1 (Figure 1). In addition, a large number of collapse pits were found in Hulun Buir (Figure 2). The vegetation was damaged seriously due to the large-scale coal mining, which led to the environmental disruption and imbalance of the ecological system [20]. Another aspect is the groundwater inrush accident caused by numerous underground goafs and blasting vibration. Since, in the mining process, the rock fractures in the surrounding rock of underground goafs will

develop due to the impact of blasting vibration and even connect to the surface or the chamber which contains water fully, thus the tunnels and working face will be inundated and causing huge losses. For example, a groundwater inrush accident occurred at Nandan, Guangxi Province, on 7 July 2001. In this disastrous accident, two mines were inundated at the same time and 81 people were killed. The volume of groundwater inrush was more than $34 \times 10^4 \text{ m}^3$ and the direct economic losses reached 80 million yuan [21].

Furthermore, the environmental engineering geological problems induced by underground goafs also have a serious impact on the mine production, transportation, pipeline, land, and water movement. It is typical to note that there are a total of 1982 locations with different degrees of ground subsidence in the Fankou lead-zinc mine, Guangdong Province. The area of ground subsidence has reached 675 km^2 and the area of damaged farmland is about 66.7 km^2 . The area of the removed surrounding buildings is 7 km^2 . Besides, a national highway between Laizhou and Zhaoyuan suffered serious ground subsidence, which resulted in the destructions of traffic and surrounding buildings. At the same time, the adjacent underground goafs are more likely to penetrate each other and cause large-scale collapse of domino type [22]. Thus, the evaluation of underground goafs risk degrees is a significant and urgent problem.

Focusing on the problems of underground goafs, some remarkable methods including the accurate detection methods and stability analysis have been developed for underground goafs [23–28]. Measurement works include shear movements [29], water [30], and locations of underground goafs [31]. The stability analysis of underground goafs focused on mechanism and stability evaluation in the ground subsidence [26], numerical analysis [27], and prediction model for mining subsidence [28].

However, the evaluation of underground goaf risk degree is carried out through the single index in the existing methods, where the area of underground goafs is considered commonly [32]. The application of comprehensive evaluation method for underground goaf risk degree using multiple

TABLE 1: Classification criteria for evaluation of risk levels with qualitative indexes.

Evaluation indexes	Classification			
	Risk level C_1	Risk level C_2	Risk level C_3	Risk level C_4
Rock mass structure (X_1)	Complete structure	Stratified structure	Cracked structure	Loose structure
Geological structure (X_2)	Without faults or folds	Impact of folds is small	Impact of folds is huge	The faults penetrate surrounding rock
Groundwater (X_4)	Without water spraying	Little water spraying when rainfall exists	Water spraying when rainfall is huge	Water spraying in rainy season
Impact of groundwater (X_5)	Without impact for surrounding rock	Little impact for surrounding rock	General impact for surrounding rock	Huge impact for surrounding rock
Mining impact (X_6)	Little blasting impact	General blasting impact	Huge blasting impact	Great blasting impact
Condition of adjacent underground goaf (X_7)	No more underground goafs in the influencing area	The area of underground goafs is medium and the number is small	The area of underground goafs is large and the number is great, while the distribution is scattered	The area of underground goafs is large, the number is great, and the distribution is concentrated
Pillar size and layout (X_{11})	The pillar exists and the layout is standard	The pillar exists but the layout is nonstandard	Without pillar or the layout is nonstandard; the pillar begins to be damaged	Without pillar or the layout is nonstandard; the pillar is damaged seriously
¹ Size of underground goaf (X_{13})	$r < 1$	$1 \leq r < 2$	$2 \leq r < 3$	$r \geq 3$
Engineering layout (X_{14})	Reasonable	Generally reasonable	Partly reasonable	Extremely unreasonable

¹ r is the ratio of span to height.

indexes is scarce. As for the existing risk evaluation methods considering multiple evaluation indexes, most of them perform risk evaluation through the safety checklist, which is of qualitative evaluation. Actually, the weights of evaluation indexes will be affected seriously due to the subjective judgment, which leads to the inaccuracy and deviation of evaluation results. Recently, some comprehensive evaluation methods have been developed including grey fixed weight clustering method, grey relational analysis method, and neural network method [21, 33–35]. In fact, the difficulty for evaluating underground goaf risk degree lies in the uncertainties and concealments of the influencing factors, which should be considered and analyzed together. Thus, a comprehensive method for evaluating the underground goaf risk degree, as well as ranking the order, is necessary and important. According to the ranked order of underground goafs risk degrees, it is feasible to provide theoretical support for the management order of underground goafs with higher safety hazards. Then, the underground goafs with severe safety threats can be managed timely, to avoid casualties and environmental destruction.

In this paper, UME and AHP theories are applied to evaluate underground goafs risk degrees comprehensively [36–38]. The recognition criteria CDRC and TMMP are used to evaluate the risk levels of underground goafs. The multiple factors that influence the stability of underground goafs are considered and integrated comprehensively, which include the quantitative and qualitative factors, instead of a single factor. In addition, the quantitative and qualitative analysis

are combined, and the qualitative factors are calculated with the quantitative form. According to the comparison and analysis of the 4 coupled methods formed through the combination of UME, AHP, CDRC, and TMMP, it is expected to develop a reasonable method for the evaluation of underground goaf risk degree, which is beneficial for the protection of environment and the sustained development of green mining.

2. Materials and Methods

2.1. The Index System for the Evaluation of Underground Goaf Risk Degree. The underground goafs are of irregular geometric shapes and complex spatial distributions, where numerous factors have effects on the risk degrees. Based on the analysis of factors that influence the stability of underground goafs, 9 factors are selected as the qualitative single evaluation indexes including rock mass structure, geological structure, groundwater, impact of groundwater, mining impact, condition of adjacent underground goaf, pillar size and layout, the size of underground goaf (the ratio of the span to the height), and engineering layout, which are represented with X_1 , X_2 , X_4 , X_5 , X_6 , X_7 , X_{11} , X_{13} , and X_{14} , respectively. In addition, 5 factors are selected as the quantitative single evaluation indexes including rock quality designation (RQD), span, area, height, and buried depth, which are represented with X_3 , X_8 , X_9 , X_{10} , and X_{12} , respectively. Tables 1 and 2 show the classification criteria of the 9 qualitative indexes and the 5 quantitative indexes,

TABLE 2: Classification criteria for evaluation of risk levels with quantitative indexes.

Evaluation indexes	Classification			
	Risk level C_1	Risk level C_2	Risk level C_3	Risk level C_4
RQD (X_3)/%	>60	50–60	40–50	<40
Span (X_8)/m	<40	40–80	80–120	>120
Area (X_9)/m ²	<800	800–1200	1200–2400	>2400
Height (X_{10})/m	<8	8–20	20–30	>30
Buried depth (X_{12})/m	<100	100–200	200–400	>400

respectively. In order to evaluate the risk degrees comprehensively and reasonably, the risk degrees are classified into 4 levels, which are C_1 , C_2 , C_3 , and C_4 . The risk levels C_1 , C_2 , C_3 , and C_4 represent little dangerous, generally dangerous, very dangerous, and extremely dangerous, respectively. For the underground goafs with different risk levels, the management methods are listed as follows:

- (i) For the underground goafs that belong to the risk level C_1 , they should be monitored on schedule. The management process should be accomplished within twelve months.
- (ii) For the underground goafs that belong to the risk level C_2 , they should be closed and separated. In addition, the distinct sign should be set up and the filling operation should be prepared in the meanwhile. The whole process should be accomplished within six months.
- (iii) For the underground goafs that belong to the risk level C_3 , the distinct sign should be set up. The filling operation should be carried out within three months.
- (iv) For the underground goafs that belong to the risk level C_4 , they should be closed and filled immediately. Moreover, the caving method should be applied as long as the safety requirements are satisfied. The whole process should be accomplished within one month.

2.2. Determination of the Single Index Measurement Value.

The underground goaf to be evaluated is represented as the symbol R . The variable X_i represents a single evaluation index. As the number of selected evaluation indexes is 14, the evaluation index space is represented as $X = \{X_1, X_2, \dots, X_{14}\}$. For the underground goaf R to be evaluated, x_i is the measured value corresponding to the single evaluation index X_i . Therefore, the parameter R can be represented as a vector $R = \{x_1, x_2, \dots, x_{14}\}$. It is known that there are 4 risk levels for the underground goaf. The k th risk level is represented as C_k ($k = 1, 2, 3, 4$) and it is safer than the $(k + 1)$ th risk level, which can be rewritten as $C_k < C_{k+1}$. The degree that the measured value x_i belongs to the risk level C_k is represented as $\mu_{ik} = \mu(x_i \in C_k)$. The parameter μ is exactly the single index measurement value, which is determined through the single index measurement function. Based on the analysis and comparison of different single

index measurement functions, the semiridge distribution is selected to calculate the single index measurement values, which is shown as follows:

$$\mu(x) = \begin{cases} 0 & x \leq a \\ \frac{1}{2} + \frac{1}{2} \sin \frac{\pi}{b-a} \left(x - \frac{b+a}{2} \right) & a < x < b \\ 1 & x \geq b \end{cases} \quad (1)$$

$$\mu(x) = \begin{cases} 1 & x \leq a \\ \frac{1}{2} - \frac{1}{2} \sin \frac{\pi}{b-a} \left(x - \frac{b+a}{2} \right) & a < x < b \\ 0 & x \geq b, \end{cases} \quad (2)$$

where a and b are the lower and upper limit of the value range. Equation (1) is the rising semiridge distribution for the quantitative positive indexes, where the risk levels of underground goafs increase with the increase of single evaluation index. Equation (2) is the descending semiridge distribution for the quantitative negative indexes, where the risk levels increase with the decrease of single evaluation index. The semiridge functions of the 9 qualitative evaluation indexes and 5 quantitative evaluation indexes are shown in Figure 3. Thus, it is feasible to solve the single index measurement values of 14 evaluation indexes. The evaluation matrix $(\mu_{ik})_{14 \times 4}$ of single index measurement value is shown as follows:

$$(\mu_{ik})_{14 \times 4} = \begin{bmatrix} \mu_{11} & \mu_{12} & \cdots & \mu_{14} \\ \mu_{21} & \mu_{22} & \cdots & \mu_{24} \\ \vdots & \vdots & \ddots & \vdots \\ \mu_{141} & \mu_{142} & \cdots & \mu_{144} \end{bmatrix}. \quad (3)$$

2.3. The UME Theory

2.3.1. Determination of Evaluation Index Weight.

Based on the summary of UME theory proposed by Wang [37], we improve the theory to fit the evaluation of underground goafs risk degrees. It is assumed that w_i is a parameter which represents the relatively important degree between the evaluation index X_i and other indexes. The parameter w_i can be taken as the weight of the evaluation index X_i , which should satisfy the requirements that $0 \leq w_i \leq 1$ and $\sum_{i=1}^{14} w_i = 1$.

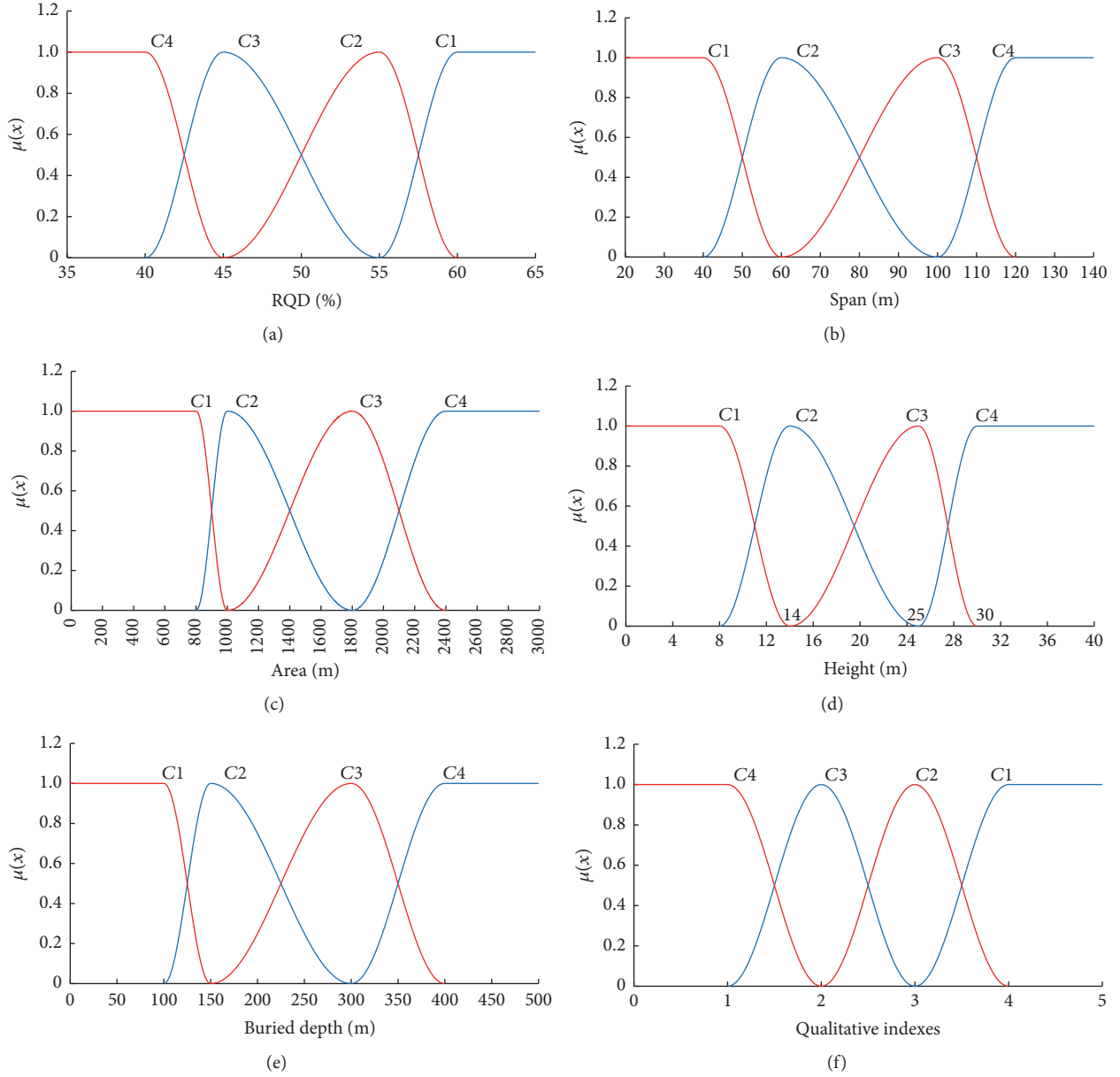


FIGURE 3: The single index measurement functions for evaluation indexes of underground goafs. The graphs (a), (b), (c), (d), and (e) show the functions of RQD, span, area, height, and buried depth, respectively. The graph (f) shows the function of rock mass structure, geological structure, groundwater, impact of groundwater, mining impact, condition of adjacent underground goaf, pillar size and layout, and engineering layout.

The weight w_i can be determined by the entropy theory through the following equations:

$$v_i = 1 + \frac{1}{\lg 4} \sum_{k=1}^4 \mu_{ik} \lg \mu_{ik} \quad (4)$$

$$w_i = \frac{v_i}{\sum_{i=1}^{14} v_i}.$$

The evaluation matrix $(\mu_{ik})_{14 \times 4}$ of single index measurement value is known, and the weight w_i can be determined through (4).

2.3.2. *The Comprehensive Evaluation Vector of Multiple Index Measurements.* The degree of the underground goaf R belongs to the risk level C_k , which is represented as $\gamma_k = \gamma (R \in C_k)$. It can be obtained through

$$\gamma_k = \sum_{i=1}^{14} w_i \mu_{ik} \quad (k = 1, 2, 3, 4). \quad (5)$$

It is obvious that the requirements $0 \leq \gamma_k \leq 1$ and $\sum_{k=1}^4 \gamma_k = 1$ are satisfied here. Therefore, $\{\gamma_1, \gamma_2, \gamma_3, \gamma_4\}$ is the comprehensive evaluation vector of multiple indexes measurements for the underground goaf R .

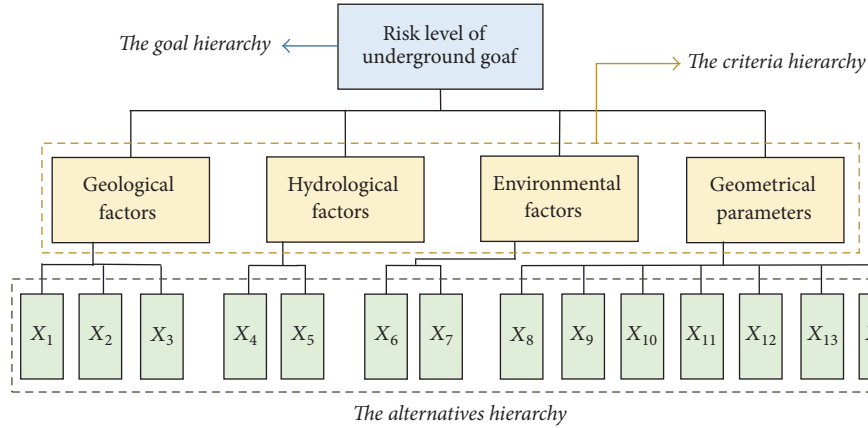


FIGURE 4: The hierarchical model for AHP, which consists of the goal hierarchy, the criteria hierarchy, and the alternatives hierarchy.

2.4. The AHP Theory

2.4.1. Establishment of a Hierarchical Model. According to the ideas and methods of AHP presented by Orenco and Fujii [36], the hierarchical model is established as shown in Figure 4, which consists of the goal hierarchy G , the criteria hierarchy P , and the alternatives hierarchy X . The problem to be solved is taken as the goal hierarchy G , which is the risk level C_k of the underground goaf R in this paper. The criteria hierarchy P is determined based on the analysis of the practical problem and the relationships between single evaluation indexes, which consists of geological factors, hydrological factors, environmental factors, and geometrical parameters. Specifically, the geological factors contain X_1 , X_2 , and X_3 . The hydrological factors contain X_4 and X_5 . The environmental factors contain X_6 and X_7 . The geometrical parameters contain X_8 , X_9 , X_{10} , X_{11} , X_{12} , X_{13} , and X_{14} . All the single evaluation indexes make up the alternatives hierarchy, which is the lowest hierarchy.

2.4.2. Determination of the Judgment Matrix. According to the importance degree for the 4 criteria in the middle hierarchy P , the relative importance degree can be determined by 1–9 comparison scale method, which is clarified as follows. The number 9 indicates the greatest importance degree, while the number 1 indicates the smallest importance degree. It is assumed that P_{ab} ($1 \leq a, b \leq 4$) is the judgment value of the criterion P_a with respect to the criterion P_b , which indicates the importance degree. On the contrary, P_{ba} is the judgment value of the criterion P_b with respect to the criterion P_a , which is equal to the reciprocal of P_{ab} . The detailed steps for determining P_{ab} and P_{ba} are shown in Table 3. Through (6), the judgment values can be solved by comparing P_a and P_b . Therefore, the judgment matrix G for the goal hierarchy can be obtained, which is shown as (7). Then, the greatest characteristic root and corresponding normalized feature vector of the judgment matrix G can be solved. Similarly, the judgment matrixes, greatest characteristic roots, and corresponding normalized feature vectors of the criteria hierarchies P_1 , P_2 , P_3 , and P_4 can be solved.

TABLE 3: The judgment values for determining the importance degree between the criteria P_a and P_b .

The importance degree for comparing P_a and P_b	P_{ab}	P_{ba}
a and b are “equally important”	1	1
a is “a little more important” than b	3	1/3
a is “obviously important” compared to b	5	1/5
a is “significantly more important” than b	7	1/7
a is “extremely important” compared to b	9	1/9
The importance degree of P_a with respect to P_b is between the above levels	2, 4, 6, 8	$1/P_{ab}$

TABLE 4: The values for average random consistency index (RI).

T	1	2	3	4	5	6	7	8	9	10	11
RI	0	0	0.58	0.90	1.12	1.24	1.32	1.41	1.45	1.49	1.51

$$g_{ab} = \frac{P_a}{P_b}, \quad (6)$$

$$g_{ba} = \frac{P_b}{P_a}$$

$$G_{4 \times 4} = \begin{bmatrix} g_{11} & g_{12} & g_{13} & g_{14} \\ g_{21} & g_{22} & g_{23} & g_{24} \\ g_{31} & g_{32} & g_{33} & g_{34} \\ g_{41} & g_{42} & g_{43} & g_{44} \end{bmatrix}. \quad (7)$$

2.4.3. The Consistency Check of the Judgment Matrix. The consistency check should be performed for the judgment matrixes to determine whether they are qualified. According to (8), the consistency index (CI) is solved. The average random consistency index (RI) can be found from Table 4.

Then, we can calculate the consistency ratio (CR) through (9), which is equal to the ratio of CI to RI. The consistency of the judgment matrix is qualified when there is $CR < 0.1$. Otherwise, the judgment matrix should be determined again with different criteria.

$$CI = \frac{\lambda_{\max} - t}{t - 1} \quad (8)$$

$$CR = \frac{CI}{RI}, \quad (9)$$

where t is the number of rows for the judgment matrix to be checked.

2.4.4. Determination of the Synthetic Weight. As the judgment matrixes, the greatest characteristic roots, and the corresponding feature vectors of $G, P_1, P_2, P_3,$ and P_4 are known, the consistency check can be performed for these judgment matrixes. The results of the judgment matrixes, the greatest characteristic roots, and the corresponding feature vectors are shown in (10). The synthetic weights of all the evaluation indexes are represented as W_i , which are shown in Table 5.

$$\begin{aligned}
 G &= \begin{bmatrix} 1.0000 & 1.8000 & 1.2857 & 0.8889 \\ 0.5556 & 1.0000 & 0.6667 & 0.4444 \\ 0.7778 & 1.5000 & 1.0000 & 0.6667 \\ 1.1250 & 2.2500 & 1.5000 & 1.0000 \end{bmatrix}, \quad \sigma_G = (0.2873, 0.1528, 0.2252, 0.3348)^T, \quad \lambda_{\max} = 4.0011, \quad CR < 0.10 \\
 P_1 &= \begin{bmatrix} 1.0000 & 0.6667 & 0.8889 \\ 1.5000 & 1.0000 & 1.2857 \\ 1.1250 & 0.7778 & 1.0000 \end{bmatrix}, \quad \sigma_{P_1} = (0.2762, 0.4093, 0.3145)^T, \quad \lambda_{\max} = 3.0002, \quad CR < 0.10 \\
 P_2 &= \begin{bmatrix} 1.0000 & 0.6667 \\ 1.5000 & 1.0000 \end{bmatrix}, \quad \sigma_{P_2} = (0.4000, 0.6000)^T, \quad \lambda_{\max} = 2.0000, \quad CR < 0.10 \\
 P_3 &= \begin{bmatrix} 1.0000 & 1.5000 \\ 0.6667 & 1.0000 \end{bmatrix}, \quad \sigma_{P_3} = (0.6000, 0.4000)^T, \quad \lambda_{\max} = 2.0000, \quad CR < 0.10 \\
 P_4 &= \begin{bmatrix} 1.0000 & 1.1250 & 1.2857 & 1.1250 & 1.5000 & 1.5000 & 1.5000 \\ 0.8889 & 1.0000 & 1.1250 & 1.0000 & 1.2857 & 1.2857 & 1.2857 \\ 0.7778 & 0.8889 & 1.0000 & 0.8889 & 1.1250 & 1.1250 & 1.1250 \\ 0.8889 & 1.0000 & 1.1250 & 1.0000 & 1.2857 & 1.2857 & 1.2857 \\ 0.6667 & 0.7778 & 0.8889 & 0.7778 & 1.0000 & 1.0000 & 1.0000 \\ 0.6667 & 0.7778 & 0.8889 & 0.7778 & 1.0000 & 1.0000 & 1.0000 \\ 0.6667 & 0.7778 & 0.8889 & 0.7778 & 1.0000 & 1.0000 & 1.0000 \end{bmatrix}, \\
 &\quad \sigma_{P_4} = (0.1803, 0.1574, 0.1387, 0.1574, 0.1221, 0.1221, 0.1221)^T, \quad \lambda_{\max} = 7.0003, \quad CR < 0.10
 \end{aligned} \quad (10)$$

2.4.5. Determination of the Evaluation Vector. The degree that the underground goaf R belongs to the risk level C_k is represented as η . Since the evaluation matrix $(\mu_{ik})_{14 \times 4}$ of single index measurement value and the weights of hierarchical model are known, the comprehensive evaluation vector $\{\eta_1, \eta_2, \eta_3, \eta_4\}$ can be obtained by multiplying the weights and evaluation matrix from the alternatives hierarchy to the goal hierarchy.

2.5. The Recognition Criteria for UME and AHP. In order to make sure that the evaluation results for underground goafs are reasonable and reliable, CDRC and TMMP are applied to compare the evaluation results and verify the reasonability.

2.5.1. The Credible Degree Recognition Criterion (CDRC). The credible degree is represented as ξ ($\xi \geq 0.5$). It is credible that the underground goaf R belongs to the evaluation level C_k when the following requirements are satisfied:

$$\begin{aligned}
 &C_1 < C_2 < C_3 < C_4 \\
 &k = \min \left\{ k : \sum_{j=1}^k \mu_j \geq \xi, (k = 1, 2, 3, 4) \right\}. \quad (11)
 \end{aligned}$$

2.5.2. The Maximum Membership Principle (TMMP). The membership for the evaluation level C_k of the underground goaf R is exactly the corresponding weight. In UME method, it is equal to γ_k , whereas it is equal to η_k in the AHP method.

TABLE 5: The results of the weights in the hierarchical model.

Weight of the goal hierarchy (G)	Weights of the criteria hierarchy (P)	Weights of the alternatives hierarchy (X)	The synthetic weights (W)
The risk level C_k , the underground goaf R	P_1 -geological factors (0.2873)	X_1 (0.2762)	0.0793
		X_2 (0.4093)	0.1176
		X_3 (0.3145)	0.0903
	P_2 -hydrological factors (0.1528)	X_4 (0.4000)	0.0611
		X_5 (0.6000)	0.0917
		X_6 (0.6000)	0.1351
	P_3 -environmental factors (0.2252)	X_7 (0.4000)	0.0901
		X_8 (0.1803)	0.0604
		X_9 (0.1574)	0.0527
		X_{10} (0.1387)	0.0464
	P_4 -geometrical parameters (0.3348)	X_{11} (0.1574)	0.0527
		X_{12} (0.1221)	0.0409
		X_{13} (0.1221)	0.0409
		X_{14} (0.1221)	0.0409

It is credible that the underground goaf R belongs to the evaluation level C_k when the corresponding weight is the maximum among all the weights.

2.6. The Method for Ranking the Order of Underground Goafs. There is not only a need to evaluate the risk level C_k of the underground goaf R , but also a requirement to rank the order for many underground goafs according to the risk degrees. If there is $C_1 < C_2 < C_3 < C_4$ and I_k is the score value of C_k , then we can obtain the following equations:

$$I_k < I_{k+1} \quad (12)$$

$$q_R = \sum_{k=1}^4 I_k \mu_k, \quad (13)$$

where q_R is the uncertainty important degree of the underground goaf R . Therefore, the order for risk degrees of many underground goafs can be ranked by the values of q_R .

2.7. The Evaluation Process for Risk Levels of Underground Goafs. Firstly, the single index measurement value can be solved based on the semiridge distribution. Then, we can obtain the evaluation matrix $(\mu_{ik})_{14 \times 4}$ of single index measurement value. Secondly, the weights of single evaluation indexes in UME can be solved through the entropy theory. In the AHP theory, all the weights can be solved through the AHP. Then, it is feasible to obtain the comprehensive evaluation vectors of UME and AHP. Finally, the recognition criteria including CDRC and TMMP are applied to evaluate the risk level of the underground goaf. Therefore, there are 4 coupled evaluation methods for the risk level through the combination of UME, AHP, CDRC, and TMMP. The comprehensive evaluation process for the risk level C_k of the underground goaf R , which mainly includes UME-CDRC, UME-TMMP, AHP-CDRC, and AHP-TMMP, is shown in Figure 5.

3. Results

3.1. The Dabaoshan Mine. The Dabaoshan mine is located in Guangdong Province, China, where there is a superimposition place of one fault belt and another tectonic belt. Due to the open stope mining and illegal mining, numerous underground goafs formed and caused the continuous increase of geostress. Figures 6(a) and 6(b) show the distinct geostatic activities such as pillar cracking and roof falling, which threaten the safety of ground, slope, and underground production system. In the mining process, the sizes of some underground goafs were large, while the sizes of pillars were too small to bear the pressure. Then, the pillar cracking and the large area falling caused a serious landslide accident, which caused threat and destruction to workers and environment. Figure 6(c) shows the landslide accident caused by the collapse of underground goafs.

The statistical results of Dabaoshan mine show that the number of underground goafs is 254, and most geometric shapes are irregular. The volume of the smaller underground goaf is about 400 m^3 , whereas the larger volume is greater than $10 \times 10^4 \text{ m}^3$ and the height is greater than 100 m. In view of the current status, the evaluation of underground goafs risk degrees is important and urgent.

Combined with the hydrogeologic conditions, environmental factors, mining status, and structural parameters of underground goafs, a total of 37 underground goafs are selected to evaluate the risk levels. The data for 14 single evaluation indexes of 37 underground goafs are listed in Table 6 [39]. According to the estimated and measured data provided in Table 6, as well as the single index measurement values solved in Figure 3, the evaluation matrixes $(\mu_{ik})_{14 \times 4}$ of single index measurement value for the 37 underground goafs can be obtained. The underground goaf R_1 is taken as an example to calculate the evaluation matrix $(\mu_{ik})_{14 \times 4}$ of single index measurement value, which is shown as follows:

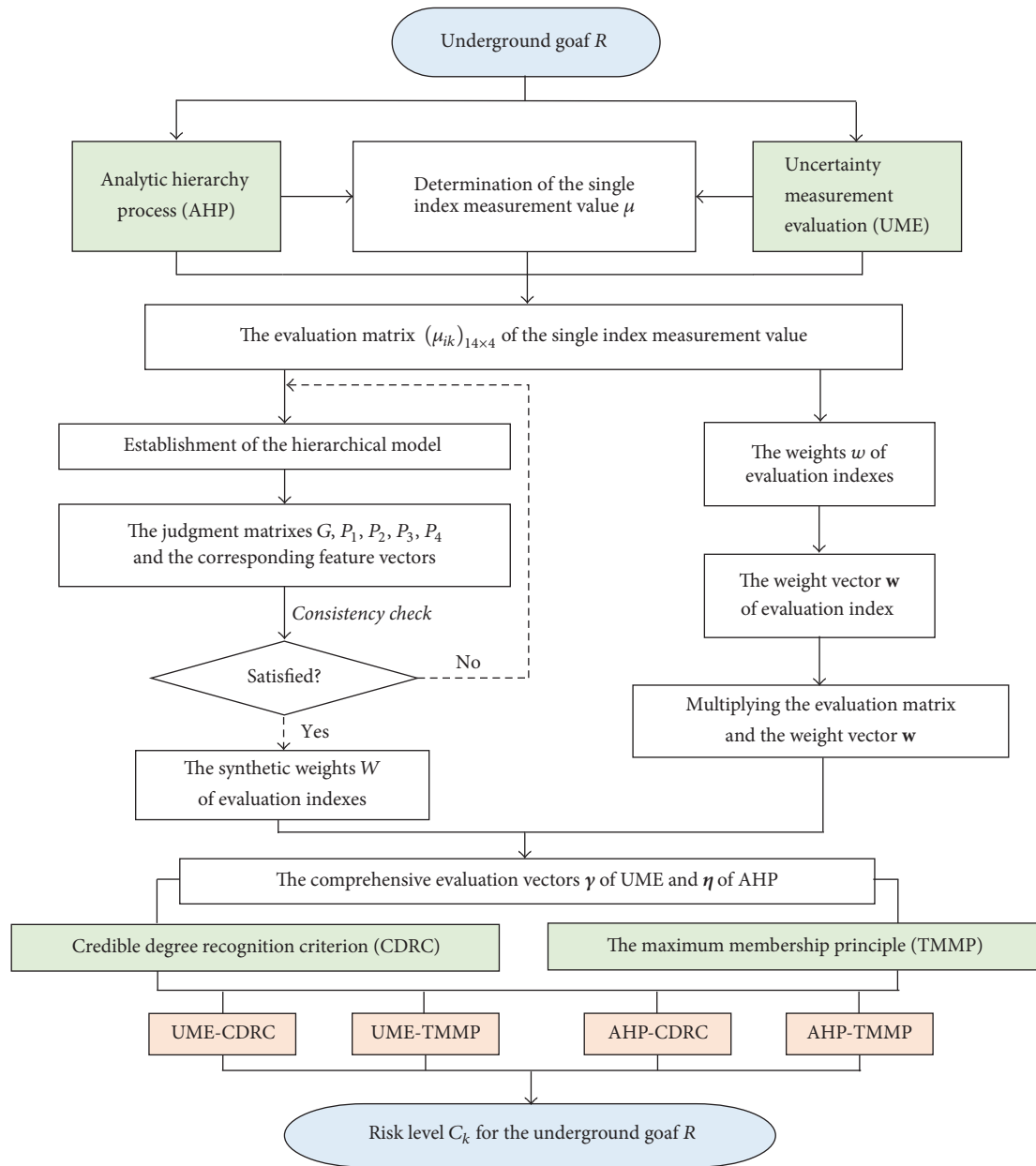


FIGURE 5: The flowchart for evaluating the risk level C_k of the underground goaf R comprehensively, where 4 coupled methods including UME-CDRC, UME-TMMP, AHP-CDRC, and AHP-TMMP are applied.

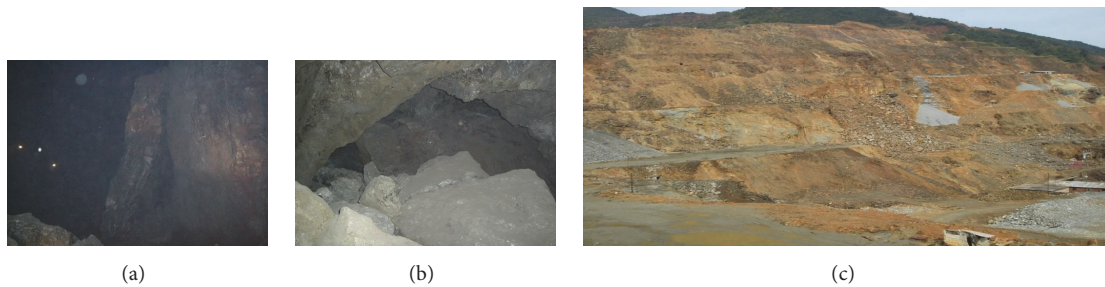


FIGURE 6: The distinct geostatic activities and scene of accident of Dabaoshan mine. (a) shows the pillar cracking phenomenon, (b) shows the large-scale falling in a underground goaf, and (c) shows the landslide accident caused by the collapse of underground goafs.

TABLE 6: Estimated and measured data for single evaluation indexes of 37 underground goafs.

Number	The risk evaluation indexes of underground goaf													
	X_1	X_2	$X_3/\%$	X_4	X_5	X_6	X_7	X_8/m	X_9/m^2	X_{10}/m	X_{11}	X_{12}/m	X_{13}	X_{14}
R_1	2	4	38	3	3	1	1	85	5190	15	1	260	3	3
R_2	3	3	56	3	3	1	1	60	1230	8	2	260	3	4
R_3	2	2	35	3	3	1	1	62	2560	14.5	1	290	2	3
R_4	2	3	48	3	3	1	1	73	1740	22	1	280	1	2
R_5	2	3	43	3	3	1	1	60	1920	16.5	1	280	2	3
R_6	2	2	47	3	3	1	1	160	6890	26.3	1	305	1	2
R_7	3	4	55	4	4	4	4	26	2870	15.8	3	305	4	4
R_8	3	4	57	3	3	1	1	96	2260	21	2	335	3	4
R_9	4	4	67	3	3	4	4	60	1200	10	4	335	4	4
R_{10}	4	3	53	2	2	1	1	85	3970	60	1	240	3	3
R_{11}	4	3	59	4	4	4	4	40	2260	15	4	305	3	4
R_{12}	4	4	62	3	3	4	4	35	1450	13	4	290	4	4
R_{13}	4	4	52	3	3	2	2	35	2590	6	4	201	4	4
R_{14}	4	4	55	4	4	2	2	65	2430	12	4	208	4	4
R_{15}	2	2	56	3	3	2	2	83	2350	4.5	2	208	4	3
R_{16}	4	4	54	4	4	2	2	68	1800	10	4	208	3	4
R_{17}	4	3	57	3	3	1	1	55	1600	16	3	411	2	3
R_{18}	4	4	54	3	3	4	4	74	2000	8	2	300	3	4
R_{19}	4	4	55	4	4	2	2	59	1950	23	3	201	3	4
R_{20}	4	4	52	4	4	2	2	110	5000	7.5	4	195	4	4
R_{21}	4	4	51	4	4	2	2	85	3270	13	3	180	3	4
R_{22}	4	3	54	4	4	1	2	65	1300	7.5	2	180	3	3
R_{23}	4	3	55	4	4	1	1	73	1730	6.2	2	180	3	4
R_{24}	4	4	53	4	4	2	2	74	1870	6	4	230	4	4
R_{25}	4	4	53	4	4	2	2	68	1170	14	4	230	3	4
R_{26}	4	4	54	4	4	4	4	65	2490	16	4	230	3	4
R_{27}	4	4	53	4	4	4	4	78	2440	13	4	230	3	4
R_{28}	4	4	43	3	3	1	1	80	3480	23	1	230	2	2
R_{29}	4	4	55	4	4	4	4	85	1410	8	3	230	3	4
R_{30}	3	4	44	2	2	2	2	65	1750	85	1	350	2	3
R_{31}	4	4	52	4	4	4	4	70	1210	10	4	350	4	3
R_{32}	4	4	56	4	4	2	2	65	1320	13	1	375	3	3
R_{33}	4	4	57	4	4	2	2	65	3690	7.5	3	210	3	4
R_{34}	3	3	41	2	2	2	2	48	1420	18	2	210	2	2
R_{35}	4	3	40	2	2	1	2	62	1680	26	1	290	2	3
R_{36}	3	3	43	1	1	1	1	89	1290	63	1	290	2	3
R_{37}	4	3	42	3	3	1	1	120	4580	28	1	400	2	3

$$(\mu_{R_1})_{14 \times 4} = \begin{bmatrix} 0 & 0 & 1.0000 & 0 \\ 1.0000 & 0 & 0 & 0 \\ 0 & 0 & 0 & 1.0000 \\ 0 & 1.0000 & 0 & 0 \\ 0 & 1.0000 & 0 & 0 \\ 0 & 0 & 0 & 1.0000 \\ 0 & 0 & 0 & 1.0000 \\ 0 & 0.3087 & 0.6913 & 0 \\ 0 & 0 & 0 & 1.0000 \\ 0 & 0.9797 & 0.0203 & 0 \\ 0 & 0 & 0 & 1.0000 \\ 0 & 0.1654 & 0.8346 & 0 \\ 0 & 1.0000 & 0 & 0 \\ 0 & 1.0000 & 0 & 0 \end{bmatrix}. \tag{14}$$

3.2. *The Results for Evaluation of Risk Levels.* The underground goaf R_1 is taken as an example. According to UME theory, the weights of 14 single evaluation indexes can be obtained through the entropy theory, which are $w_1 = 0.0760$, $w_2 = 0.0760$, $w_3 = 0.0760$, $w_4 = 0.0760$, $w_5 = 0.0760$, $w_6 = 0.0760$, $w_7 = 0.0760$, $w_8 = 0.0421$, $w_9 = 0.0760$, $w_{10} = 0.0706$, $w_{11} = 0.0760$, $w_{12} = 0.0514$, $w_{13} = 0.0760$, and $w_{14} = 0.0760$, respectively. Therefore, the comprehensive evaluation vector can be solved as $\gamma_1 = \{0.0760, 0.3946, 0.1494, 0.3800\}$. Based on the recognition criterion CDRC, it can be obtained that $k = 0.0760 + 0.3946 + 0.1494 = 0.6200 > \xi = 0.5$ when the credible degree ξ is set as 0.5. Thus, the risk level of the underground goaf R_1 is level C_3 . The risk level is evaluated as level C_2 while applying the recognition criterion TMMP.

According to the AHP theory, the weights of the criteria hierarchy and the alternatives hierarchy, as well as the

TABLE 7: The comparison results for UME and AHP of 37 underground goafs, as well as the risk levels evaluated by CDRC and TMMP.

Number	UME-CDRC, UME-TMMP					AHP-CDRC, AHP-TMMP				
	C_1	C_2	C_3	C_4	(CDRC, TMMP)	C_1	C_2	C_3	C_4	(CDRC, TMMP)
R_1	0.0760	0.3946	0.1494	0.3800	(3, 2)	0.1176	0.3054	0.1561	0.4209	(3, 4)
R_2	0.1583	0.4837	0.1289	0.2290	(2, 2)	0.1726	0.4260	0.1235	0.2779	(2, 2)
R_3	0.0000	0.3601	0.2915	0.3485	(3, 2)	0.0000	0.3003	0.2819	0.4178	(3, 4)
R_4	0.0000	0.3967	0.2795	0.3238	(3, 2)	0.0000	0.3585	0.3228	0.3187	(3, 2)
R_5	0.0000	0.4366	0.3157	0.2477	(3, 2)	0.0000	0.4141	0.2745	0.3114	(3, 2)
R_6	0.0000	0.1544	0.3188	0.5268	(4, 4)	0.0000	0.1614	0.3588	0.4797	(3, 4)
R_7	0.5797	0.2735	0.0043	0.1425	(1, 1)	0.6376	0.2658	0.0033	0.0933	(1, 1)
R_8	0.1807	0.3752	0.2227	0.2215	(2, 2)	0.1897	0.3472	0.1810	0.2822	(2, 2)
R_9	0.6562	0.2910	0.0202	0.0326	(1, 1)	0.6817	0.2697	0.0189	0.0297	(1, 1)
R_{10}	0.0777	0.3153	0.2182	0.3887	(3, 4)	0.0793	0.3138	0.2299	0.3770	(3, 4)
R_{11}	0.6603	0.2265	0.0202	0.0930	(1, 1)	0.6930	0.2125	0.0266	0.0679	(1, 1)
R_{12}	0.6812	0.2245	0.0943	0.0000	(1, 1)	0.7103	0.2178	0.0719	0.0000	(1, 1)
R_{13}	0.5340	0.2241	0.1766	0.0652	(1, 1)	0.4381	0.2548	0.2563	0.0508	(2, 1)
R_{14}	0.5649	0.2104	0.1850	0.0397	(1, 1)	0.4957	0.2108	0.2517	0.0418	(2, 1)
R_{15}	0.1675	0.3445	0.4585	0.0294	(2, 3)	0.0959	0.3261	0.5427	0.0354	(3, 3)
R_{16}	0.5024	0.2424	0.2552	0.0000	(1, 1)	0.4781	0.2227	0.2992	0.0000	(2, 1)
R_{17}	0.1011	0.5329	0.1304	0.2356	(2, 2)	0.1194	0.5250	0.0895	0.2661	(2, 2)
R_{18}	0.4534	0.3260	0.2141	0.0065	(2, 1)	0.5094	0.3257	0.1588	0.0062	(1, 1)
R_{19}	0.3682	0.2964	0.3313	0.0041	(2, 1)	0.3910	0.2476	0.3580	0.0035	(2, 1)
R_{20}	0.6267	0.0787	0.1967	0.0979	(1, 1)	0.5306	0.1042	0.2824	0.0829	(1, 1)
R_{21}	0.3985	0.3144	0.2083	0.0788	(2, 1)	0.3937	0.2516	0.3020	0.0527	(2, 1)
R_{22}	0.3047	0.4438	0.1753	0.0762	(2, 2)	0.2786	0.4189	0.1675	0.1351	(2, 2)
R_{23}	0.3757	0.3138	0.1603	0.1503	(2, 1)	0.3194	0.3327	0.1227	0.2252	(2, 2)
R_{24}	0.6251	0.1050	0.2688	0.0011	(1, 1)	0.5306	0.1439	0.3248	0.0008	(1, 1)
R_{25}	0.4686	0.3356	0.1958	0.0000	(2, 1)	0.4433	0.2889	0.2678	0.0000	(2, 1)
R_{26}	0.6237	0.2889	0.0383	0.0492	(1, 1)	0.6685	0.2481	0.0375	0.0459	(1, 1)
R_{27}	0.6573	0.2437	0.0564	0.0426	(1, 1)	0.6716	0.2191	0.0668	0.0426	(1, 1)
R_{28}	0.1621	0.2058	0.2930	0.3392	(3, 4)	0.1969	0.2050	0.2363	0.3618	(3, 4)
R_{29}	0.6370	0.2896	0.0734	0.0000	(1, 1)	0.6622	0.2461	0.0917	0.0000	(1, 1)
R_{30}	0.0762	0.2370	0.5287	0.1581	(3, 3)	0.1176	0.1992	0.5755	0.1077	(3, 3)
R_{31}	0.6975	0.2536	0.0489	0.0000	(1, 1)	0.7033	0.2404	0.0564	0.0000	(1, 1)
R_{32}	0.3248	0.3670	0.2215	0.0867	(2, 2)	0.3614	0.2993	0.2806	0.0587	(2, 1)
R_{33}	0.4775	0.2741	0.1713	0.0772	(2, 1)	0.4682	0.2375	0.2416	0.0527	(2, 1)
R_{34}	0.0294	0.2658	0.6461	0.0587	(3, 3)	0.0395	0.3016	0.5771	0.0817	(3, 3)
R_{35}	0.0738	0.2231	0.4762	0.2269	(3, 3)	0.0793	0.2217	0.4163	0.2826	(3, 3)
R_{36}	0.0000	0.2773	0.2365	0.4862	(3, 4)	0.0000	0.2862	0.2055	0.5083	(4, 4)
R_{37}	0.0000	0.3060	0.1048	0.5892	(4, 4)	0.0000	0.3112	0.0843	0.6044	(4, 4)

synthetic weights, are solved in Table 5. Combined with the evaluation matrix $(\mu_{ik})_{14 \times 4}$ of single index measurement value, we can obtain the evaluation vector $\eta_1 = \{0.1176, 0.3054, 0.1561, 0.4209\}$. The risk level is evaluated as level C_3 by CDRC, while the risk level is evaluated as level C_4 by TMMP.

The evaluation vectors using UME and AHP of all the 37 underground goafs, as well as the risk levels evaluated by CDRC and TMMP, are listed in Table 7. The comparison results for risk levels evaluated by CDRC and TMMP of 37 underground goafs are shown in Figure 7.

3.3. *The Results for Ranking the Order of Underground Goafs.* As I_k is the score value of C_k and the risk level C_k is safer than C_{k+1} , it can be assumed that $I_1 = 1, I_2 = 2, I_3 = 3$, and $I_4 = 4$. Then the uncertainty important degree q of the underground goaf R can be solved according to (13). The uncertainty important degree of UME is represented as q_{UME} , whereas the uncertainty important degree of AHP is represented as q_{AHP} . The results of q_{UME} and q_{AHP} are shown in Figure 8. Based on the calculation results, we can rank the order of risk degree for 37 underground goafs from lower to higher, which is $R_{31}, R_{12}, R_9, R_{29}, R_{27}, R_{26}, R_{11}, R_{24}, R_{14}$,

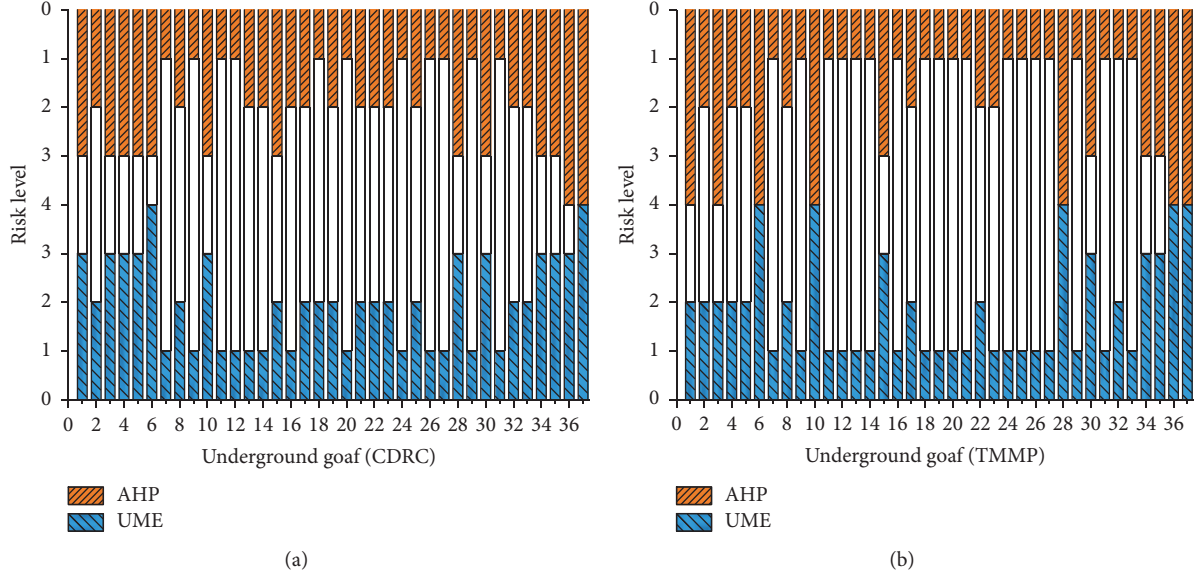


FIGURE 7: The comparison results for risk levels of 37 underground goafs. The graph (a) shows the risk levels of underground goafs using CDRC, and the graph (b) shows the risk levels using TMMP, where the blue part represents the risk levels of UME and the orange part represents the risk levels of AHP.

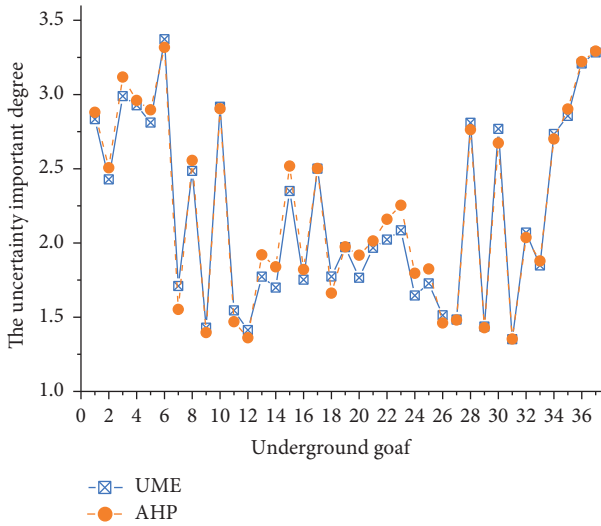


FIGURE 8: The comparison results for the uncertainty important degree of 37 underground goafs using UME and AHP, where the blue symbols represent values of q_{UME} and the orange symbols represent values of q_{AHP} .

$R_7, R_{25}, R_{16}, R_{20}, R_{13}, R_{18}, R_{33}, R_{21}, R_{19}, R_{22}, R_{32}, R_{23}, R_{15}, R_2, R_8, R_{17}, R_{34}, R_{30}, R_{28}, R_5, R_1, R_{35}, R_{10}, R_4, R_3, R_{36}, R_{37},$ and R_6 for both UME and AHP. It is proved that UME and AHP have the similar ability and effect for ranking the order of risk degree. Furthermore, the ranking results can provide theoretical and reasonable guidance for the management of underground goafs. Actually, it is difficult to manage numerous underground goafs at the same time due to the great need of time, manpower, and environmental factors. Therefore, the underground goaf of higher risk degree can be

managed firstly according to the order of risk degree. As a result, it is feasible to manage underground goafs reasonably without influencing the normal production.

4. Discussion

For the risk levels of underground goafs to be evaluated, there are 4 coupled methods, which are UME-CDRC, UME-TMMP, AHP-CDRC, and AHP-TMMP, respectively. Table 8 shows the underground goafs of four risk levels with 4 coupled methods.

It is obvious that the order of risk degree is higher and the risk level of the underground goaf is higher. As the ranking results are the same for both UME and AHP, we can arrange all the underground goafs along a straight horizontal line from the lower risk degree to the higher risk degree, which is shown in Section 3.3. Then, we can divide this straight line into four sets $D_1, D_2, D_3,$ and D_4 by setting three dividing lines artificially. In addition, the setting of three dividing lines is different based on the method to be analyzed. Also, the setting of dividing lines should be the optimal for every method. Therefore, there will be four sets of all the underground goafs with every method. Then, the underground goafs of four sets can be compared to the underground goafs of four risk levels quantitatively. The results shown in Table 8 are taken as standard data. Compared to the underground goafs of four sets $D_1, D_2, D_3,$ and D_4 , the detailed evaluation criteria are stated as follows:

- (i) If the risk level of an underground goaf is equal to the level of the divided four sets, then the score value for the underground goaf is 0.
- (ii) If the difference between the risk level of an underground goaf and the level of the divided four sets is

TABLE 8: The underground goafs of four risk levels with 4 coupled methods.

Risk level	Underground goafs using 4 coupled methods			
	UME-CDRC	UME-TMMP	AHP-CDRC	AHP-TMMP
C_1	$R_7, R_9, R_{11}, R_{12}, R_{13}, R_{14}, R_{16}, R_{20}, R_{24}, R_{26}, R_{27}, R_{29}, R_{31}$	$R_7, R_9, R_{11}, R_{12}, R_{13}, R_{14}, R_{16}, R_{18}, R_{19}, R_{20}, R_{21}, R_{23}, R_{24}, R_{25}, R_{26}, R_{27}, R_{29}, R_{31}, R_{33}$	$R_7, R_9, R_{11}, R_{12}, R_{18}, R_{20}, R_{24}, R_{26}, R_{27}, R_{29}, R_{31}$	$R_7, R_9, R_{11}, R_{12}, R_{13}, R_{14}, R_{16}, R_{18}, R_{19}, R_{20}, R_{21}, R_{24}, R_{25}, R_{26}, R_{27}, R_{29}, R_{31}, R_{32}, R_{33}$
C_2	$R_2, R_8, R_{15}, R_{17}, R_{18}, R_{19}, R_{21}, R_{22}, R_{23}, R_{25}, R_{32}, R_{33}$	$R_1, R_2, R_3, R_4, R_5, R_8, R_{17}, R_{22}, R_{32}$	$R_2, R_8, R_{13}, R_{14}, R_{16}, R_{17}, R_{19}, R_{21}, R_{22}, R_{23}, R_{25}, R_{32}, R_{33}$	$R_2, R_4, R_5, R_8, R_{17}, R_{22}, R_{23}$
C_3	$R_1, R_3, R_4, R_5, R_{10}, R_{28}, R_{30}, R_{34}, R_{35}, R_{36}$	$R_{15}, R_{30}, R_{34}, R_{35}$	$R_1, R_3, R_4, R_5, R_6, R_{10}, R_{15}, R_{28}, R_{30}, R_{34}, R_{35}$	$R_{15}, R_{30}, R_{34}, R_{35}$
C_4	R_6, R_{37}	$R_6, R_{10}, R_{28}, R_{36}, R_{37}$	R_{36}, R_{37}	$R_1, R_3, R_6, R_{10}, R_{28}, R_{36}, R_{37}$

TABLE 9: The four sets and the corresponding final score values of every coupled method.

Sets	Comparison results of 4 coupled methods							
	UME-CDRC	Score	UME-TMMP	Score	AHP-CDRC	Score	AHP-TMMP	Score
D_1	$R_{31}, R_{12}, R_9, R_{29}, R_{27}, R_{26}, R_{11}, R_{24}, R_{14}, R_7, R_{25}, R_{16}, R_{13}, R_{20}$	-1	$R_{31}, R_{12}, R_9, R_{29}, R_{27}, R_{26}, R_{11}, R_{24}, R_{14}, R_7, R_{25}, R_{16}, R_{20}, R_{13}, R_{18}, R_{33}, R_{19}, R_{21}$	0	$R_{31}, R_{12}, R_9, R_{29}, R_{27}, R_{26}, R_{11}, R_{24}$	0	$R_{31}, R_{12}, R_9, R_{29}, R_{27}, R_{26}, R_{11}, R_{24}, R_{14}, R_{25}, R_{16}, R_{20}, R_{13}, R_{18}, R_{33}, R_{21}, R_{19}, R_{22}, R_{32}$	-1
D_2	$R_{18}, R_{33}, R_{21}, R_{19}, R_{22}, R_{32}, R_{23}, R_{15}, R_2, R_8, R_{17}$	0	$R_{22}, R_{32}, R_{23}, R_{15}, R_2, R_8, R_{17}$	-2	$R_{14}, R_7, R_{25}, R_{16}, R_{20}, R_{13}, R_{18}, R_{33}, R_{21}, R_{19}, R_{22}, R_{32}, R_{23}, R_{15}, R_2, R_8, R_{17}$	-4	$R_{23}, R_{15}, R_2, R_8, R_{17}$	-1
D_3	$R_{34}, R_{30}, R_{28}, R_5, R_1, R_{35}, R_{10}, R_4, R_3, R_{36}$	0	$R_{34}, R_{30}, R_{28}, R_5, R_1, R_{35}, R_{10}, R_4, R_3$	-6	$R_{34}, R_{30}, R_{28}, R_5, R_1, R_{35}, R_{10}, R_4, R_3$	0	$R_{34}, R_{30}, R_{28}, R_5, R_1, R_{35}$	-3
D_4	R_{37}, R_6	0	R_{36}, R_{37}, R_6	0	R_{36}, R_{37}, R_6	-1	$R_{10}, R_4, R_3, R_{36}, R_{37}, R_6$	-2
Final score	-1		-8		-5		-7	

equal to 1, then the score value for the underground goaf is -1.

- (iii) If the difference between the risk level of an underground goaf and the level of the divided four sets is equal to 2, then the score value for the underground goaf is -2.
- (iv) If the difference between the risk level of an underground goaf in and the level of the divided four sets is equal to 3, then the score value for the underground goaf is -3.

If the final score value is higher, it means that the corresponding method is more reasonable and suitable for the evaluation of risk level. UME-CDRC is taken as an example: the first dividing line is set between R_{13} and R_{18} , the second dividing line is set between R_{17} and R_{34} , and the third

dividing line is set between R_{36} and R_{37} . Therefore, there are $D_1 = \{31, 12, 9, 29, 27, 26, 11, 24, 7, 25, 16, 20, 13\}$, $D_2 = \{18, 33, 21, 19, 22, 32, 23, 15, 2, 8, 17\}$, $D_3 = \{34, 30, 28, 5, 1, 35, 10, 4, 3, 36\}$, and $D_4 = \{37, 6\}$. Compared to the risk levels of UME-CDRC shown in Table 8, it is obvious that only the risk level of the underground goaf R_{25} is different from the standard data, where the difference is equal to 1. Then, the final score value of UME-CDRC is determined as -1. Similarly, the final score value of UME-TMMP, AHP-CDRC, and AHP-TMMP can be solved as -8, -5, and -7, respectively. The four sets and the corresponding score values of every method are listed in Table 9.

Obviously, the score value of UME-CDRC is the maximum among the 4 coupled methods. As a result, UME-CDRC is the most reasonable method for the evaluation of underground goafs risk degrees. Through the comparisons

of UME-CDRC and UME-TMMP, AHP-CDRC, and AHP-TMMP, the score value of UME-CDRC is much smaller than UME-TMMP and the score value of AHP-CDRC is smaller than AHP-TMMP. Thus, it can be concluded that CDRC is more reasonable than TMMP. Sometimes, the difference between the greatest weight and the second greatest weight in the evaluation vector is little. In this case, the risk level evaluated through TMMP will not be reasonable and reliable. On the contrary, CDRC is suitable for evaluation of underground goafs risk levels whatever the difference between the greatest weight and the second greatest weight. As for AHP, it is more subjective than UME because the process of establishing the hierarchical model and the determination of weights for evaluation indexes are more subjective. The evaluation vector of UME is determined through the measured values, which is more objective. Therefore, it is concluded that UME-CDRC is reasonable for evaluation of underground goafs risk degrees in the practical engineering application.

5. Conclusions

As the special characteristics of underground goafs are with irregular geometric shapes, concealed locations, and huge amount, they have caused numerous safety accidents and destructive disasters, which influence the normal production in mines and the surrounding environment. Therefore, the evaluation of underground goafs risk degrees is an urgent and significant problem. In this paper, the theories of UME and AHP were applied to comprehensively evaluate the risk levels of underground goafs. According to the hydrogeological conditions, mining status, and engineering parameters, 14 factors were selected to establish the evaluation index system. Based on the estimated and measured data, the semiridge distribution is selected as the single index measurement functions. Then, the single index measurement values were solved quantitatively according to the single index measurement functions. Furthermore, the weights of evaluation vector were determined by applying the entropy theory and AHP. Once the evaluation vectors of UME and AHP were obtained, the risk levels of underground goafs can be evaluated through the recognition criteria CDRC and TMMP. Also, the order of risk degree can be ranked per the values of uncertainty important degree. Combining the calculation methods UME and AHP with the recognition criteria CDRC and TMMP, there are 4 coupled methods UME-CDRC, UME-TMMP, AHP-CDRC, and AHP-TMMP. The data of underground goafs in Dabaoshan mine were used to evaluate the risk levels using the 4 coupled methods, as well as ranking the order of risk degree. On account of the ranked order, it is proved that UME-CDRC is the most reasonable method through both quantitative and qualitative analysis. Results show that UME-CDRC not only can evaluate the underground goafs risk degrees reasonably, but also can rank the order of risk degree, which insures that the most dangerous underground goaf can be managed at the first time to reduce the probability of accidents. The developed UME-CDRC provides a reasonable and reliable methodology to evaluate the underground goafs risk degrees, which is not only a beneficial complement for the management methods of underground goafs, but also a

big improvement for environmental protection as well as for the sustained development of green mining.

Conflicts of Interest

The authors declare that there are no conflicts of interest regarding the publication of this paper.

Acknowledgments

The authors wish to acknowledge financial support from the State Key Research Development Program of China (2016YFC0600706), the National Basic Research Program of China (2015CB060200), National Natural Science Foundation of China (41630642, 51504288), China Postdoctoral Science Foundation (2015M570688, 2016T90639), The Young Elite Scientists Sponsorship Program by CAST (2016QNR001), and Innovation-Driven Project of Central South University (2016CXS001).

References

- [1] L. J. Dong, J. Wesseloo, Y. Potvin, and X. B. Li, "Discriminant models of blasts and seismic events in mine seismology," *International Journal of Rock Mechanics and Mining Sciences*, vol. 86, pp. 282–291, 2016.
- [2] L. Dong, J. Wesseloo, Y. Potvin, and X. Li, "Discrimination of mine seismic events and blasts using the fisher classifier, naive bayesian classifier and logistic regression," *Rock Mechanics and Rock Engineering*, vol. 49, no. 1, pp. 183–211, 2016.
- [3] M. Bukowska, "The rockbursts in the Upper Silesian Coal Basin in Poland," *Journal of Mining Science*, vol. 48, no. 3, pp. 445–456, 2012.
- [4] X. T. Feng, S. Webber, and M. U. Ozbay, "Neural network modeling on assessing rockburst risks for South African deep gold mines," *Transactions of Nonferrous Metals Society of China*, vol. 8, no. 2, pp. 1–7, 1998.
- [5] M. S. Diederichs and P. K. Kaiser, "Rock instability and risk analyses in open stope mine design," *Canadian Geotechnical Journal*, vol. 33, no. 3, pp. 431–439, 1996.
- [6] X. Li, S. J. Wang, T. Y. Liu, and F. S. Ma, "Engineering geology, ground surface movement and fissures induced by underground mining in the Jinchuan Nickel Mine," *Engineering Geology*, vol. 76, no. 1–2, pp. 93–107, 2004.
- [7] L. Dong, W. Shu, X. Li, G. Han, and W. Zou, "Three Dimensional Comprehensive Analytical Solutions for Locating Sources of Sensor Networks in Unknown Velocity Mining System," *IEEE Access*, vol. 5, pp. 11337–11351, 2017.
- [8] State Administration of Work Safety and State Administration of Coal Mine Safety, *State Technological Development Programming of Work Safety—Non-Coal Mine Domain Research Bulletin*, State Administration of Work Safety, State Administration of Coal Mine Safety, Beijing, China, 2010.
- [9] H. Ma, J. Wang, and Y. Wang, "Study on mechanics and domino effect of large-scale goaf cave-in," *Safety Science*, vol. 50, no. 4, pp. 689–694, 2012.
- [10] Y.-X. Hu and X.-B. Li, "Bayes discriminant analysis method to identify risky of complicated goaf in mines and its application," *Transactions of Nonferrous Metals Society of China*, vol. 22, no. 2, pp. 425–431, 2012.

- [11] R. G. Corbett, "Effects of coal mining on ground and surface water quality, Monongalia County, West Virginia," *Science of the Total Environment*, The, vol. 8, no. 1, pp. 21–38, 1977.
- [12] X. Huang, M. Sillanpää, E. T. Gjessing, S. Peräniemi, and R. D. Vogt, "Environmental impact of mining activities on the surface water quality in Tibet: Gyama valley," *Science of the Total Environment*, vol. 408, no. 19, pp. 4177–4184, 2010.
- [13] F. J. Martín Peinado, A. Romero-Freire, I. García Fernández, M. Sierra Aragón, I. Ortiz-Bernad, and M. Simón Torres, "Long-term contamination in a recovered area affected by a mining spill," *Science of the Total Environment*, vol. 514, pp. 219–223, 2015.
- [14] P. Huang and X. Wang, "Applying environmental isotope theory to groundwater recharge in the jiaozuo mining area, china," *Geofluids*, vol. 2017, Article ID 9568349, 11 pages, 2017.
- [15] P. Achtziger-Zupančič, S. Loew, A. Hiller, and G. Mariethoz, "3D fluid flow in fault zones of crystalline basement rocks (Poehla-Tellerhaeuser Ore Field, Ore Mountains, Germany)," *Geofluids*, vol. 16, no. 4, pp. 688–710, 2016.
- [16] X. Shi, F. Jiang, Z. Feng, B. Yao, H. Xu, and J. Wu, "Characterization of the regional groundwater quality evolution in the North Plain of Jiangsu Province, China," *Environmental Earth Sciences*, vol. 74, no. 7, pp. 5587–5604, 2015.
- [17] X. Shi, S. Jiang, H. Xu, F. Jiang, Z. He, and J. Wu, "The effects of artificial recharge of groundwater on controlling land subsidence and its influence on groundwater quality and aquifer energy storage in Shanghai, China," *Environmental Earth Sciences*, vol. 75, no. 3, article 195, 2016.
- [18] X. B. Li, D. Y. Li, G. Y. Zhao, Z. L. Zhou, and F. Q. Gong, "Detecting, disposal and safety evaluation of the underground goaf in metal mines," *Journal of Mining and Safety Engineering*, vol. 23, pp. 24–29, 2006.
- [19] Future net, An earthquake with the magnitude 3.1 occurred in Pingyi County, Shandong Province http://news.k618.cn/society/shwx//_7017577.html.
- [20] The first financial net, Thousands of collapse pits occurred in the Hulun Buir prairie. <http://www.afinance.cn/new/gncj//488504.html>.
- [21] Xinhuanet, The groundwater inrush accident occurred at the mines in Nandan County, Guangxi Province. http://news.xinhuanet.com/china/2001-08/08/content_76694.htm.
- [22] X. B. Li, L. J. Dong, G. Y. Zhao et al., "Stability analysis and comprehensive treatment methods of landslides under complex mining environment—a case study of Dahu landslide from Linbao Henan in China," *Safety Science*, vol. 50, no. 4, pp. 695–704, 2012.
- [23] D. J. Yancey, M. G. Imhof, J. E. Feddock, and T. Gresham, "Analysis and application of coal-seam seismic waves for detecting abandoned mines," *Geophysics*, vol. 72, no. 5, pp. M7–M15, 2007.
- [24] L. Dong and X. Li, "Comprehensive models for evaluating rockmass stability based on statistical comparisons of multiple classifiers," *Mathematical Problems in Engineering*, vol. 2013, Article ID 395096, 9 pages, 2013.
- [25] S. Lou, B. Yang, and Z. Luo, "Three-dimensional information acquisition and visualization application in goaf," *Procedia Engineering*, vol. 84, pp. 860–867, 2014.
- [26] Y. Sun, X. Zhang, W. Mao, and L. Xu, "Mechanism and stability evaluation of goaf ground subsidence in the third mining area in Gong Changling District, China," *Arabian Journal of Geosciences*, vol. 8, no. 2, pp. 639–646, 2015.
- [27] Z.-Q. Luo, C.-Y. Xie, J.-M. Zhou, N. Jia, X.-M. Liu, and H. Xu, "Numerical analysis of stability for mined-out area in multi-field coupling," *Journal of Central South University*, vol. 22, no. 2, pp. 669–675, 2015.
- [28] L. Nie, H. Wang, Y. Xu, and Z. Li, "A new prediction model for mining subsidence deformation: the arc tangent function model," *Natural Hazards*, vol. 75, no. 3, pp. 2185–2198, 2015.
- [29] K. W. Mills, O. Garratt, B. G. Blacka, L. C. Daigle, A. C. Rippon, and R. J. Walker, "Measurement of shear movements in the overburden strata ahead of longwall mining," *International Journal of Mining Science and Technology*, vol. 26, no. 1, pp. 97–102, 2016.
- [30] B. Su, R. Malekian, J. Yu, X. Feng, and Z. Liu, "Electrical Anisotropic Response of Water Conducted Fractured Zone in the Mining Goaf," *IEEE Access*, vol. 4, pp. 6216–6224, 2016.
- [31] B. Su, J. Yu, and C. Sheng, "Borehole electromagnetic method for exploration of coal mining goaf," *Elektronika ir Elektrotechnika*, vol. 22, no. 4, pp. 37–40, 2016.
- [32] J.-H. Hu, J.-L. Shang, K.-P. Zhou et al., "Hazard degree identification of goafs based on scale effect of structure by RS-TOPSIS method," *Journal of Central South University*, vol. 22, no. 2, pp. 684–692, 2015.
- [33] K.-L. Du, "Clustering: A neural network approach," *Neural Networks*, vol. 23, no. 1, pp. 89–107, 2010.
- [34] Q.-H. Wu, S.-M. Wan, and W.-X. Peng, "A comprehensive evaluation method about stability of poly laminate goafs," *Journal of Central South University (Science and Technology)*, vol. 43, pp. 2324–2330, 2012.
- [35] M. Shao, Z. Gong, and X. Xu, "Risk assessment of rainstorm and flood disasters in China between 2004 and 2009 based on gray fixed weight cluster analysis," *Natural Hazards*, vol. 71, no. 2, pp. 1025–1052, 2014.
- [36] P. M. Orenco and M. Fujii, "A localized disaster-resilience index to assess coastal communities based on an analytic hierarchy process (AHP)," *International Journal of Disaster Risk Reduction*, vol. 3, no. 1, pp. 62–75, 2013.
- [37] G. Y. Wang, "Uncertainty information and its mathematical treatment," *Journal of Harbin Architecture and Engineering Institute*, vol. 23, pp. 52–58, 1990.
- [38] H. J. He, Y. M. Yan, C. X. Qu, and Y. Fan, "Study and application on stability classification of tunnel surrounding rock based on uncertainty measure theory," *Mathematical Problems in Engineering*, vol. 2014, Article ID 626527, 5 pages, 2014.
- [39] Y. Duan, *Fuzzy synthetic assessment of the hazard degree of underground goaf disaster [M.S. dissertation]*, Safety Engineering, Central South University, Changsha, China, 2005.